Springer Series in Optical Sciences 140

Vesselinka Petrova-Koch
Rudolf Hezel
Adolf Goetzberger *Editors*

High-Efficient Low-Cost Photovoltaics

Recent Developments

Second Edition

Springer

Springer Series in Optical Sciences

Volume 140

Springer Series in Optical Sciences is led by Editor-in-Chief William T. Rhodes, Florida Atlantic University, USA, and provides an expanding selection of research monographs in all major areas of optics:

- lasers and quantum optics
- ultrafast phenomena
- optical spectroscopy techniques
- optoelectronics
- information optics
- applied laser technology
- industrial applications and
- other topics of contemporary interest.

With this broad coverage of topics the series is useful to research scientists and engineers who need up-to-date reference books.

More information about this series at http://www.springer.com/series/624

Vesselinka Petrova-Koch ·
Rudolf Hezel · Adolf Goetzberger
Editors

High-Efficient Low-Cost Photovoltaics

Recent Developments

Second Edition

Springer

Editors
Vesselinka Petrova-Koch
Gate East
Garching, Germany

Rudolf Hezel
University of Hannover
Pullach, Germany

Adolf Goetzberger
Fraunhofer Institute for Solar Energy System
Freiburg, Baden-Württemberg, Germany

ISSN 0342-4111 ISSN 1556-1534 (electronic)
Springer Series in Optical Sciences
ISBN 978-3-030-22863-7 ISBN 978-3-030-22864-4 (eBook)
https://doi.org/10.1007/978-3-030-22864-4

Preface to the Second Edition

The second edition of our book on High-Efficient Low-Cost PV appears exactly 10 years after its first edition. In the last decade, the global warming and the climate change became stronger pronounced, the population on earth increased from 6.7 Billion in 2008 by almost one billion to 7.6 Billion in 2018, and also the demand of electricity and of food worldwide. In the age of digitalization and e-mobility, the electricity consumption will increase further, and clean electricity will become mandatory if we care for the equilibrium of the climate on our planet. 100 renewables do not have an alternative. Industries like the PV managed to grow fast in the last decade, to reach globally 500 GWp! accumulated volume by the end of 2018.

Unfortunately, Germany and Europe, where the Renewable Energy Law EEG was first introduced, and the PV industry pioneered, lost its leading position in PV manufacturing and also in installed capacity. Wacker, headquartered in Germany, remains a leader, and producing 80 000 t/year solar-grade polysilicon today is the number one worldwide manufacturer. Also, US position is not much different from this of Europe.

Asia took leading position and China alone manufactures today the biggest fraction of the c-Si PV, where companies like Jinko and Trina Solar occupying the top two positions in 2017 followed by Canadian Solar.

The second edition is reviewing the recent development the high-efficient low-cost PV, of the next-generation PV cells and modules, which targeted in the last decade single-junction cells with an efficiency 20 plus %, no matter if wafer c-Si technology or thin-film technology, while decreasing the costs to 0.30 €C/Wp.

We cover recent cutting edge developments of c-Si wafer technologies like *PERC*—Passivated Emitter Rear Cell; *Bifacial*—Dual-sided panels and cells; *Multi Busbar*—Multi-ribbon and wire busbars; *Split panels*—using half-cut cells; *Dual Glass*—Frameless; *HJT*—Heterojunction cells.

A new chapter reviewing the most widely used *passivation layers SiN and Al2O3* and their prospectives for the next-generation PV to come is offered in the second edition.

The most recent development of *III-V Heterojunction High-Efficient Cells for Concentrator PV* (*CPV*) is reviewed on its way to reach 50% efficiency.

Among the thin-film technologies, we present a review of the development of *CIGS PV—on glass—and on flexible substrates*, targeting 20 plus% efficiencies, and chapter about *Perovskite* (inkjet printed). Perovskite was selected because it became a hype in the last several years, and a promising candidate to reduce the cost of PV below 30 €C/Wp in the near future.

A chapter about *Augsburger Tubular PV* (*ATPV*), which promised better solar sharing between generation of Solar Electricity and Agro, is also presented. It is time for a paradigm change in direction of affordable Agro PV.

The chapter devoted *Fluorescing Collectors* pioneered by Prof. Götzbereger in 1977 (more than 40 years ago) deserves further development and interest, and is included in this edition.

During the 35th PC SEC Europe in Brussels in September 2018, targets like 30% plus efficient tandem cells by 2022 and costs less than 10 €C/Wp in 2035 have been put in focus. We only mention these developments to come but did not include in the second edition on a c-Si tandem with perovskite.

Garching, Germany — Vesselinka Petrova-Koch
Pullach, Germany — Rudolf Hezel
Freiburg, Germany — Adolf Goetzberger

Preface to the First Edition

Global warming and climate change are a result of excessive emission of greenhouse gases in the recent decades. During the same period, we have experienced a dramatic *increase in energy demand to support the global industry and a "modern life style"*. These events, combined with the astronomic increase of the *energy prices* since the beginning of the twenty-first century, make it obvious that the *global energy mix* needs to be changed in favor of *clean renewable energy sources*. At the same time, we must improve the *energy efficiency* of all technologies.

Solar energy conversion, particularly *Photovoltaics* (PV), represents one of the most interesting and dynamically growing branches of the industry at the moment. Although today the cost of PV is still relatively high, it has dropped considerably in the past years and will continue to do so. A main driving force behind the development of solar energy is its enormous, practically unlimited potential. Unlike other renewable energy sources like wind or water, solar energy can be utilized everywhere on the globe. The cost of PV will have to continue to drop if the goal of economic viability is to be reached. Prices of PV modules and systems follow a well-determined learning curve. If present trends continue, it has been predicted that grid parity (cost of PV equal to grid electricity at the consumer's site) will be reached in about 10 years in favorable locations. An important aspect of the learning curve is that it includes not only scale effects of mass production but also technical advances and new concepts. It can be shown that for most applications *high efficiency* is a prerequisite *for lowering cost*. It is the purpose of this book to give a survey of the most important technologies for increasing efficiency and lowering cost of PV.

In the last five to six years the PV market has grown exponentially: not all over the world yet, but in some countries like Germany and Spain in the EU, and Japan in Asia. Japan and Germany may be considered as front-runners and engines of the newborn *PV Mega Industry.* The German *preferential feed-in tariff for solar electricity* and the new RES Law (*called EEG in German*) opened new market dimensions and made it possible that the German market outgrew a country like Japan, which was and is still the biggest PV producer worldwide. Germany reached this state in spite of the fact that it is not the sunniest part of Europe, due to the *joint*

efforts of politics, industry, and academia. About one-fourth of all PV modules produced worldwide till the end of 2007 are installed in the southern part of Germany (mainly in Bavaria and Baden-Wuerttemberg)! The exceptionally successful *EEG* law also influenced many other countries. In the last 5 years, more than 30 countries copied and/or modified it. In this way, a *PV network* was formed. This network spawned a very active PV development in several countries of the EU like Italy, Portugal, Greece, and even new member-states like Bulgaria. PV is becoming accepted also in countries like USA, Australia, and Russia, as well as in the newly developing economies like China, India, and Turkey, which are on their way to sign the Kyoto Protocol and to support the targets for Clean Energy.

So far, the PV market is dominated by the so-called *first-generation* PV, the production and installation of which recently reached the gigawatt scale. First-generation PV, which can be seen on many solar roofs today, is based mainly on mono- and poly-crystalline Si, and these wafers are not made of low-cost material. This generation is characterized by relatively low efficiencies of the cells and modules, considerably below the theoretical limits and below results that have been obtained in the laboratory. In spite of this fact, the demand for PV is increasing exponentially so that several crises along the value chain of the PV industry have occurred, for example, the shortage of solar-grade poly-Si feedstock since 2005, or the one for solar glass, appearing on the skyline now. The crises of the Si feedstock are causing a deviation from the learning curve. The fast growth of the PV demand at one side and the shortage of Si at the other have generated not only supply problems, but they also led to a change of perspectives and to a search for innovative solutions, based on new materials, cells, and module systems. These new solutions are based on reduced consumption of expensive semiconductor material using, for example, *thin-film PV technology* (*second-generation PV*), or on improved efficiency of crystalline cells and systems, while making use of cost-effective *concentrators for solar radiation* (*third-generation PV*).

The aim of this book is to present some important trends and achievements that are shaping the *High-Efficient Low-Cost Photovoltaic* (*HELCPV) Industry*.

Our intention here is not to deal with the basics of PV, which are covered elsewhere. We also do not focus in this book on thin-film PV. Our ambition is to present here the most important strategies and developments in the *transition period for the PV industry between* 2000 *and* 2007 on its way *to a gigawatt industry*, and to predict some of the tendencies of development of the near future, focusing on innovative *highly efficient wafer-based solar cell* and innovative *modules* and systems, making use of *concentrated sun radiation.*

The book consists of 13 chapters, written by 25 authors. In chapter 1, an attempt is made to put together in a chronologic manner the milestones of the PV since the discovery of the photovoltaic effect in 1839 and to focus the attention on the important steps to develop a powerful and sustainable PV industry. In Chap. 2, a comprehensive review of PV for space applications as a for-runner of the PV Industry and its impact on the terrestrial PV is demonstrated. Chapter 3 focuses on

the development of the terrestrial PV from a niche market at the beginning of the 21st century to one of the most important mainstream markets for electricity at the moment.

Chapter 4 reviews state-of-the-art poly-Si technology based on the Siemens process, which remains the major technology also after the recent shortage for poly-Si. In Chap. 5, the recent advances of the so-called ribbon technology, which gives the unique chance to reduce the consumption of poly-Si during wafer manufacturing, are described. In Chap. 6, an unambiguous answer to the question "Why high efficient, bifacial c-Si PV cells?" is given, and a novel high-efficient rear contact c-Si cell with bifacial sensitivity and elegant simple manufacturing steps is described. Chapter 7 reviews the commercially available power c-Si PV cells, like the Point-Contact Solar Cell of Sun Power, the HIT Solar Cells of Sanyo, and the Buried-Contact Solar Cell manufactured by BP. This gives opportunity to the reader to compare the concepts available already on the market with the one presented and analyzed in Chap. 6.

Chapter 8 reviews the development of III–V multi-junction PV cells with efficiency close to 40%, on relatively less expensive c-Ge substrates. The ability of such cells to operate under extreme conditions (more than 1,000 suns) is emphasized. Cost-effective concentrator systems based on Fresnel mini-lenses arrays, prepared out of silicone, and sun truckers for such concentrator modules are described here. In Chap. 9, the economic perspectives of the III–V concentrator PV when manufactured on megawatt scale is discussed and compared to the first-generation c-Si PV. It is argued why CPV should be considered as a promising candidate on the market, capable to compete with the c-Si PV particularly in the very sunny regions in the solar belt countries.

In Chap. 10, the attention is focused on an alternative device concentrating the sun radiation, named Fluorescent Concentrator, which is less popular than the one based on Fresnel optics, but which is unique in its ability to concentrate diffuse radiation in a sophisticated way. The basics and the more recent advances to develop further and to simplify this device are reviewed in this part. Chapter 11 deals with a concept of a novel hybrid photovoltaic/thermal concentrator. Chapter 12 points the attention then to some innovative PV installation concepts and future PV applications.

Chapter 13 reviews the recent advances in the field of Organic Solar Cells and deals with some design rules, helping to make the organic PV relatively high efficient. We believe that OPV will continue to develop similar to the OLEDs and will be able to supply the market with high-efficient low-cost PV in a very near future.

Garching, Germany — Vesselinka Petrova-Koch
Pullach, Germany — Rudolf Hezel
Freiburg, Germany — Adolf Goetzberger

To the Memory of Zhores Alferov

Zhores Ivanovich Alferov, distinguished Soviet and Russian scientist in the field of semiconductor physics, winner of the Lenin and state awards, winner of the Nobel Prize for Physics in 2000, vice-president of the Russian Academy of Science in 1991–2017, Director of the Ioffe Institute in 1987–2003 passed away on March 1, 2019.

Zhores Ivanovich Alferov was born on March 14, 1930, in Vitebsk. In 1952, he graduated from the Faculty of Electronic Engineering of V. I. Ulyanov (Lenin) Electro-Technical Institute in Leningrad. In 1953, he went to work at the Ioffe Institute, where, since the first half of the 50s, research on physics of semiconductor devices was carried out. At that time, the task was to grow Ge single crystals (they had not been produced by the Soviet industry) and create planar diodes and triodes basing on them. Zhores Alferov joined to its accomplishment. He took an active part in the development of the first Soviet transistors, and, in 1954, the domestic power Ge devices were created, which quickly found numerous technical applications in various industries. Fulfillment of this task had required deep insight into the physics of the processes in semiconductors and into technological processes for their production. In those years, he worked as a physicist, as a technologist, and as an engineer, introducing the new items into production: the devices were transferred for mass manufacturing.

On the basis of a set of works (for which he received the first government award in 1959), Zhores Alferov defended his Ph.D. thesis, which drew a line under his 10-year work. He faced the question of choosing a future direction of research. It is needless to say that with development of Ge and Si valves, in the creation of which Alferov made such a large contribution, the complex of physical and technical problems associated with power semiconductor devices had not been exhausted. And the experience gained by him allowed us to hope for further successful developments in this field. Their start ensured further rapid progress.

According to Zhores Alferov, "The ability to choose promising areas of research, courage in this choice, patience and perseverance in the work in the absence of quick success in its conduct" characterizes his search strategy and his research work itself.

In the early 60s, he addressed the problem of heterojunctions and began research in this area with a small group of his employees.

Technological bases of the research were epitaxial methods allowing one to grow single-crystalline layers of semiconductor materials with different chemical compositions on an initial substrate. He and his group presented opportunity to control such fundamental semiconductor parameters as the forbidden gap, the electron affinity, the effective charge carrier mass, refraction index, and so on inside one single crystal. Creation of perfect heterostructures could lead to a qualitative leap in semiconductor physics and techniques. This had been understood by not only Alferov but also scientists in many scientific centers abroad, who deployed intensive study of heterojunctions. As promptly as by 1967, in the large number of publications, it was judged on that defects and imperfections of real heterostructures made it impossible to obtain and realize the effects, which had been expected in the ideal case. In the same year, he and his staff obtained completely opposite result: they created a heterostructure in the AlAs–GaAs system, which was close by its properties to an ideal model.

The main thing in such a structure is not only that materials of a heterojunction pair are characterized by the proximity of lattice parameters and chemical nature of atoms comprising them, but also that the energy band structure of these materials is optimal one from the point of view of electrical, optical, and luminescent properties. This had determined the possibility to produce a wide range of semiconductor devices and to create a set of experimental methods for studying physical processes in heterojunctions.

Successful solution of a problem in heterojunctions by Zhores Alferov was determined by a number of circumstances. Among them there was a physical approach typical for him to phenomena being studied, his wide coverage of a problem, his deep intuition, which helped him often to find optimal versions, and, the last but not least, his ability to captivate a team of young employees with a quite interesting albeit very difficult task. Discovery made by Alferov in ideal heterojunctions and in such new physical phenomena as the “super-injection” and also the electronic and optical limitations in heterostructures has allowed improving dramatically parameters of the majority of known semiconductor devices and creating fundamentally new ones, particularly promising for applying in optical and quantum electronics.

This new stage in investigating heterojunctions in semiconductors was summarized by Zhores Alferov in his doctoral thesis successfully defended in 1970. In 1972, he became a corresponding member and, in 1979, academician of the Academy of Sciences of the USSR.

The fundamental research of Zhores Ivanivish formed the basis for a number of new scientific and technical directions. Some of them went beyond his laboratory and continued to be developed under his supervision in some industrial institutes. Since then, a diversity of such devices with heterojunctions (lasers, light diodes, light indicators, traffic lights, photodetectors, and sunlight converters) are being produced by industry. Power diodes, transistors, and thyristors based on heterojunctions are also being introduced into production.

In using the technology of high-efficient radiation-tolerant solar cells based on AlGaAs/GaAs heterostructures developed by Zhores Alferov in 70s, the Scientific Production Association "Kvant" organized for the first time in the world large-scale production of heterostructure solar cells for space arrays. One of such arrays installed in 1986 on the basic module of the Space Station "MIR" had worked on this space station for the entire lifetime without noticeable reduction in power.

Among works performed under the supervision of Zhores Alferov, special attention was paid to the search of new heterostructures, to investigation of physical processes on the interface of heterojunction materials, to application of heterostructures in investigations of luminescence and quantum-dimensional effects, and also to development of new principles for designing solid-state devices for electronics and integral optics.

On the basis of ideal heterojunctions in the InGaAsP compound proposed in 1970 by Alferov with his staff, semiconductor lasers operating in a substantially wider spectral range than lasers in the AlGaAs system were created. They have found a wide application as radiation sources in fiber-optic extended range communication lines.

As a result of the Alferov's investigation of charge carrier radiative recombination and of photovoltaic phenomena in heterostructures, conditions for obtaining the 100% internal quantum yield have been established, what means practically entire internal conversion of electric power into light one and vice versa. This has opened new prospects in creating high-effective sources for coherent and spontaneous radiation and photovoltaic and other power converters. In the mid-70s, Zhores Alferov together with his staff created spontaneous radiation sources, in which, owing to the reduction of losses inside a crystal, it was managed to achieve record values of the external quantum yield of 45% in the IR spectral range and more than 10%—in the "red" one.

Investigation of processes of generation, propagation, and conversion of light waves in waveguide heterostructures resulted in the development of new principles for creating monolithic integral optical schemes capable to control light fluxes effectively. The semiconductor direction in the integral optics based on heterostructures, which is associated with the works of Zhores Alferov and his employees, is now considered as one of the most promising in this area of physics at the junction of modern optics and electronics.

In 80–90s, Alferov with his staff have proposed extensive investigation of solar cells based on heterostructures, which resulted in the creation of photovoltaic converters of the concentrated sunlight with the efficiency of greater than 30% at sunlight concentration ratio of 100–500. These converters create a base for developing works at a new level on space and terrestrial power engineering.

In the Center of Nano-heterostructure Physics of the Ioffe Institute organized by Alferov, different techniques for fabricating heterostructures are being developed and applied successfully: liquid, metal-organic, and molecular-beam epitaxy, which has allowed creating a new generation of optoelectronic components based on heterostructures. Among them, there are injection quantum-dimensional lasers of IR and visual ranges with the record radiation conversion efficiency, single-mode

lasers with a distributed reverse bias, picosecond lasers and photodetectors, and optoelectronic integral circuits for computers.

Starting from 1993, one of the main directions of the Center is the investigation of properties of nanostructures of lessened dimension: quantum wires and quantum dots. Proposed and realized were new ways for obtaining self-organizing nanostructures with high uniformity in size and with crystalline perfection. Investigated were processes of charge carrier capture, relaxation, and recombination in nano-heterostructures. In 1993–1994, for the first time in the world, hetero-lasers on "artificial atoms" (narrowband nano-dimensional inclusions of In, Ga, and As in the GaAs matrix) are realized. In 1995, Alferov et al. demonstrate for the first time an injection hetero-laser on quantum dots operating at room temperature through the main state of quantum dots. For the first time, a continuous mode of operation of such a laser was demonstrated. A fundamentally important event was widening of the laser spectral range with using quantum dots on the GaAs substrates up to 1.3 μm, which is important for application in the fiber-optic communication. For the first time, surface-irradiating lasers on quantum dots in the In-Ga-N system operating in the UV range at optical pumping at room temperature were realized. Thus, Alferov's investigations laid a basis for fundamentally new electronics based on heterostructures with a very wide range of application known as "band engineering".

Contents

Contributors

S. N. Abolmasov R&D Center of Thin Film Technologies in Energetics, St. Petersburg, Russia

A. S. Abramov Ioffe Institute, St. Petersburg, Russia;
R&D Center of Thin Film Technologies in Energetics, St. Petersburg, Russia

Zh. I. Alferov St Petersburg Academic University, St.-Petersburg, Russia

V. M. Andreev Ioffe Institute, St.-Petersburg, Russia

D. A. Andronikov Ioffe Institute, St. Petersburg, Russia;
R&D Center of Thin Film Technologies in Energetics, St. Petersburg, Russia

Thorsten Dullweber Institut für Solarenergieforschung Hameln, Emmerthal, Germany

D. Forgacs Director of Knowledge Management, Saule Technologies, Wroclaw, Poland

Adolf Goetzberger Fraunhofer Institute for Solar Energy Systems, Freiburg, Germany

D. Hariskos ZSW – Zentrum für Sonnenenergie- und Wasserstoff-Forschung Baden-Württemberg, Stuttgart, Germany

Karl Hesse Wacker Chemie AG, Wacker Polysilicon, Burghausen, Germany

R. Hezel University of Hannover and ZAE Bayern, Pullach, Germany

Winfried Hoffmann Hanau, Germany

H. P. Huber Laserzentrum Hochschule München, Fakultät für angewandte Wissenschaften und Mechatronik, Hochschule für angewandte Wissenschaften München, Munich, Germany

K. Jaeger-Hezel Munich University of Applied Sciences, Pullach, Germany

F. Kessler ZSW – Zentrum für Sonnenenergie- und Wasserstoff-Forschung Baden-Württemberg, Stuttgart, Germany

E. Lotter ZSW – Zentrum für Sonnenenergie- und Wasserstoff-Forschung Baden-Württemberg, Stuttgart, Germany

O. Malinkiewicz Chief Technology Officer, Saule Technologies, Wroclaw, Poland

J. Mayer Ledvance GmbH, Equipment Engineering, Augsburg, Germany

J. W. Müller Hanwha Q CELLS GmbH, Bitterfeld-Wolfen OT Thalheim, Germany

V. Petrova-Koch Gate-East, Garching, Germany

Ewald Schindlbeck Burghausen, Germany

M. Z. Shvarts Ioffe Institute, St.-Petersburg, Russia

S. Spiering ZSW – Zentrum für Sonnenenergie- und Wasserstoff-Forschung Baden-Württemberg, Stuttgart, Germany

E. I. Terukov Ioffe Institute, St. Petersburg, Russia;
R&D Center of Thin Film Technologies in Energetics, St. Petersburg, Russia

K. Wojciechowski Scientific Director, Saule Technologies, Wroclaw, Poland

R. Wuerz ZSW – Zentrum für Sonnenenergie- und Wasserstoff-Forschung Baden-Württemberg, Stuttgart, Germany

Chapter 1
Milestones of Solar Conversion and Photovoltaics

V. Petrova-Koch

1.1 Prehistory

Seventh century BC: In ancient *Egypt* the houses were built so that the solar radiation could be collected during the day and used during the night.

Fifth century BC: The *Greeks* oriented their houses so that they could receive solar energy in the wintertime *to heat the buildings*.

Third century BC: *Archimedes* used *mirrors* to reflect *direct sun radiation* and to defend Syracuse from invasion by the Romans.

Second century BC: the first *windows* made out of *transparent mica* were inserted in houses in northern Italy, with the aim to increase the use of solar radiation in wintertime.

First century AD: the so-called *heliocaminos* started to be used. These solar baths with big mica windows oriented to the south found their maximum application in Italy around the fifth century.

Fourteenth century: the first *solar law* was introduced in Italy.

1767 in Russia: *M.V. Lomonossov* suggested the use of lenses to concentrate the solar radiation.

1767 in Switzerland: *Horace de Saussure* discovers the amplification and increased heat efficiency in Matjoshka-type fivefolded glass boxes.

1830 in South Africa: *J. Hershel* uses the first *solar cooker*.

Around 1830: *H. Repton* constructs the first (*glass*) *greenhouses in Europe.*

V. Petrova-Koch (✉)
Gate-East, Schleissheimer str. 17, 85748 Garching, Germany
e-mail: vpkoch@yahoo.de

V. Petrova-Koch et al. (eds.), *High-Efficient Low-Cost Photovoltaics*,
Springer Series in Optical Sciences 140,
https://doi.org/10.1007/978-3-030-22864-4_1

1.2 Milestones of the Photovoltaics

1839: *Alexandre-Edmund Becquerel*, a young experimental physicist in France, discovered the photovoltaic effect at age of 19, while assisting his father, experimenting with electrolytic cells made up of two metal electrodes.

1873: *W. Smith, working in the UK*, discovered the photoconductivity of selenium, which led to the invention of the photoconductive cell.

1883: *Ch. Frits*, an American inventor, described the first solar cell made from Se selenium wafers.

1887: *H. Hertz* discovered in Germany that ultraviolet light altered the lowest voltage capable of causing a spark between two metal electrodes.

1888: *Ed. Weston* receives the first patent for solar cells (U.S. 389124 and US3891-25).

1904: *W. Hallwachs* discovered the photosensitivity in a copper/cuprous oxide pair.

1904: *A. Einstein* publishes his pioneering theoretical work on the photoelectric effect (he received the Nobel Prize in 1921 for this work).

1916: *R.A. Millikan* provides experimental proof of the photoelectric effect.

1916: *Y. Czochralski* (Polish scientist) develops a new method to grow single-crystal silicon.

1930: *W. Schottky* discovers a new cuprous oxide photoelectric cell.

1931: *A.F. Ioffe* guides a project at the Physico-Technical Institute in St. Petersburg on thallium sulphide photocells, which reach a record efficiency at that time of more than 1%. He submitted a proposal to the Soviet government concerning the use of solar PV roofs for providing electricity.

1932: *Audobert and Stora* discover the photovoltaic effect in CdS.

1948: *W. Schottky* presents the first theoretical concept for semiconductor PV.

1951: at *Bell Labs* the first p–n junction was grown in germanium.

1953: *D. Trivich* publishes the first theoretical calculations on the conversion efficiency of the solar spectrum with materials of different bandgaps.

1953: *G. Pearson at Bell Labs* begins research of Li-doped Si solar cells.

1953: *D. Chapin*; *C. Fuller and G. Pearson* realized a two cm^2 Si solar cell with an efficiency of 4% (published on *NY Times* cover page).

1954: *D. Chapin*, *C. Fuller and G. Pearson* improve the efficiency of a Si Cell to 6%; first AT&T solar cell demonstration in Murray Hill, NJ.

1954: At *Siemens in Germany*, *G. Spenke* and his team develop an efficient *method for poly-Si growth*: Scientists and experts from *Wacker* and TU Munich participate in this work as part of a joint team with Siemens. The so-called *Siemens Method* is the main technology for the production of solar and semiconductor grade Si.

1954: *J.J. Loferski and Jenny* at RCA reported a pronounced PV effect in Cd*S*.

1954: *The International Solar Energy Society* (*ISES*) *was founded in Phoenix*, *AZ*, USA.

1957–1959: *Hoffmann Electronics* achieves 8, 9 and 10% efficiency and develops the grid contact, significantly reducing the series resistance of the device.

1954: *J.J. Loferski and Jenny* at RCA reported a pronounced PV effect in Cd*S*.

1954: *The International Solar Energy Society* (*ISES*) was founded in Phoenix, AZ, USA.

1970: Its headquarters was later moved to Melbourne, Australia, and in 1995 it was moved again to Freiburg, Germany.

1978: *R. Hezel* introduced Silicon Nitride as antireflection and passivation layer which is presently applied for almost all Commercial Silicon Solar Cells.

1980: *M. Riel* starts the famous *1,000 solar roof program* in Zurich, Switzerland.

1980: *BP* enters solar business.

1981: *The Fraunhofer Institute for Solar Energy ISE* in Freiburg, Germany, was founded by A. Goetzberger.

1981: *Reflective solar concentrators* used for the first time with solar cells at Ioffe Institute St. Petersburg.

1982: *The PV Production* worldwide reaches the value *of 10 MW.*

1982: *A 1-MW PV plant*—built by *ARCO Solar* with 100 Dual-Axis trackers with c-Si modules—goes online in CA, USA.

1983: The PV production worldwide exceeds *20 MW*, *and sales exceed* 250 million USD.

1983: *International Science and Engineering Conference* (the Asian ISE-Conference) is started.

1984: *M.A. Green and S. Wenham* introduced the *laser-grooved buried-contact* solar cell (*LGBC*).

1985: *M. Green* at the University of New South Wales, Australia, *breaks the 20% efficiency barrier for c-Si solar cell under one sun* in the research lab.

1985: *R. Swanson* founded *Sun Power in CA* with the goal to commercialize the high-efficiency c-Si solar cell.

1985: *R. Hezel* and *K. Jaeger* introduced Aluminum Oxide as passivation layer for a new generation of Silicon Solar Cells.

1986: *ARCO Solar releases the first commercial thin-film power module.*

1987: *The Solar Challenge is inaugurated, and PV-powered cars race across Australia.*

1987: The *Institute for Solar Energy Research (ISFH)* is founded in Hamelin/Emmerthal, Germany.

1988: The *Centre for Solar Energy and Hydrogen Research (ZSW)* is founded in Stuttgart, Germany.

1989: *V.D. Rumyantsev at Ioffe Institute, St. Petersburg,* introduces a solar concentrator lens-cell system with radically reduced size.

1990: *ARCO Solar* is sold to *Siemens* and renamed *to Siemens Solar*.

1991: *Nukem GmbH* (*later Schott Solar*) built *1 MW pilot PV plant* out of *mono- and bifacial MIS-inversion-layer solar cells*, developed by the team of *R. Hezel at the University of Erlangen*.

1991: *M. Graetzel* invents the *dye-sensitized electrochemical solar cell*. An efficiency more than 10% was obtained within 5 years after the discovery.

1992: *BP* commercializes the *Laser Grooved c-Si Solar Cell* (*patented by M.A. Green and S. Wenham*).

1994: *NREL* develops and demonstrates *a two-terminal*, *high-efficiency GaInAsP/GaAs solar cell*, which under 180 suns shows more than 30% efficiency. The third generation CPV was born.

1997: *The biggest PV roof* with more than 3 MW is installed in Munich, Germany.

1997: *Sanyo* starts mass production of its *high-efficiency HIT c-Si/a-Si:H PV cells*.

1998: *SolarWorld A.G.* is founded in Germany, the *first vertically integrated PV company*.

1999: *M.A. Green and J. Zhao* achieved a *record efficiency of 24.7% for laboratory c-Si solar cells*.

1999: *Total PV power* installed worldwide exceeds *1 GW.*

2000: In April, Germany introduces the new *Renewable Energy Sources Act or EEG* (German: Erneuerbare-Energien-Gesetz) (feed-in law), the law which, in 2008, was translated into more than 40 languages. Germany becomes the largest PV market worldwide.

2002: *First Solar Silicon Conference* dealing with the crisis of Si feedstock *was* organized by Photon in Munich, Germany.

2002: *Cypress Corp. and Sun Power* in the USA start pilot production of the high efficiency c-Si Sun Power PV cell. Mass production is set up in the Philippines.

2002: *Siemens Solar* sold its solar activities to *Shell Solar*, *in 2004 Shell Solar* c-Si solar cell activities were divested to *SolarWorld.*

2004: *General Electric* enters PV, after becoming owner of *AstroPower.*

2005: *Sharp* remains *the biggest producer* of PV cells worldwide.

2005: *Q-Cells*, which was founded in 2002, is the *fastest growing PV cell producer* worldwide.

2005: *Solyndra*, the first manufacturer of tubular PV so far was founded in CA, USA.

2006: *SolFocus in USA*, *Concentrix-Solar in Freiburg*, *Germany*, *and SolarTec AG* in Munich, Germany, start *pilot-production of concentrator III–V PV* (*CPV*). CPV Modules consisting of GaAs triple cells on Ge substrates with efficiency more than 35%, and Fresnel concentrator lenses made out of UV-resistive silicone, capable of providing up to 800 suns.

2006: *Wacker* expands the production of solar-grade poly-Si in *Burghausen*, *Germany*, up to 16,000 tons per year to become the second biggest company in this field worldwide. The new investment is about 500 million €.

2006: *First Int. Solar Glass Conference* is organized by Photon in Munich.

2007: *Hemlock* announces its mega-expansion of poly-Si production up to 3,600 metric tons per year in *MI*, *USA*, and will start producing in 2010. The investment is about $1 billion U.S. Hemlock remains the biggest poly-Si producer worldwide.

2006: *InterSolar*, the *biggest International Solar Fair* takes place for a 10th and last time in Freiburg, Germany. In 2008 it will continue to operate in Munich.

2007: *SunPower* and *Sanyo* both announce the *highest efficiency* for mass produced solar cell under one sun solar radiation of *22%*.

2007: *Al Gore and IPCC* receive the *Nobel Peace Price.*

2007: *UN-Conference* devoted to climate change takes place *in Bali*.

2008: *Q-Cells* bypasses *Sharp* to become the world biggest PV cell producer.

2009: T. Miyasaka et al. demonstrated first Perovskite cells with 3.8% efficiency.

2009: Hemlock announced PolySi production for a Giga-Scale PV at Intersolar NA.

2010: Oxford PV Ltd. founded to develop and commercialize Perovskite photovoltaics.

2010: ZSW announced efficiency record of 20.1% for CIGS cells (0.5 cm^2).

2011: Sanyo HIT became Panasonic.

2011: Solyndra's spectacular foul in the US. Other PV companies went bankrupt.

2011: *Avancis* and *Lasercenter Munich University* improve *CIGS solar cell efficiency by 15%* with the first *all-laser* monolithical serial Interconnects and *picosecond* laser pulses.

2012: Soitec and ISE Fraunhofer announced 36,7% efficient III-V CPV module.

2012: Hanwha acquired Q-Cells.

2012: First Solar demonstrated cost competitive CdTe modules with 17% efficiency.

2012: Siemens exits completely the Solar Business.

2012: 15.5% efficient flexible lightweight modules by MiaSole.

2012: H. Snaith and M. Lee demonstrated the first solid state perovskite PV cell.

2013: Heliatek in Germany achieved Organic PV Cells with efficiency of 12%.

2013: Perovskite PV cells reach 15% efficiency (O. Malinkiewicz and J. Burschka).

2013: Schott Solar exits PV manufacturing.

2014: Panasonic reports 25.6% world record for c-Si HIT cell technology.

2014: Perovskite cells reached 20.1% efficiency at KRCT (Korea).

2014: Sauletech, Poland pioneered first ink-jet printed perovskite PV.

2015: EPFL in Switzerland reports 21% world record efficiency for Perovskite cells.

2015: Solar Frontier reaches one 1 GW_p manufacturing per year of CIGS PV.

2016: Panasonic HIT-Module reached 23.8% efficiency.

2016: Kaneka Corporation achieved 26.33% world record with a heterojunction cell.

2016: First manufacturing site of Oxford PV for c-Si/Perovskite tandem cells and modules, located in Germany.

2016: UNIST (South Korea) reached 22.1% efficiency with Perovskite cells.

2016: UC Berkeley and Stanford reported first graded junction all perovskite PV.

2017: Panasonic HIT cell turns its 20th anniversary.

2017: Wacker Poly Silicon reaches 80 000 tones/year, to become the number one manufacturer of solar-grade polysilicon (corresponding to a production of 16–20 GW_p PV).

2017: Tesla started production of HE cells with Panasonic for solar roof tiles.

2017: First industry-sized perovskite/silicon tandem cells produced at Oxford PV in Germany.

2017: Hevel Solar started manufacturing of Hetero Junction HJT c-Si cells with efficiency more than 22% and modules in Russia.

2018: Solar World Germany went bankrupt.

2018: Longi Solar (China), the biggest manufacturer of mono c-Si PERC cells demonstrated a half-cut bifacial PERC modules (120 half cells) with 340 Wp.

2018: Hevel Solar and TFTE (Ioffe Institute) demonstrated 144 Half Cell HJT Module with 460 Wp.

2018: Energetica in Austria announced a Next Generation Module Manufacturing Gigafab (the biggest in Europa) with cells based on the Blue Chip Technology.

Chapter 2
PV as a Major Contributor to the ~100% Renewably Powered World and Solving the Climate Battle

Winfried Hoffmann

Abstract This paper aims to demonstrate in a comprehensive yet clearly arranged and short digest how we are able to end an unfair, dangerous, environmentally unfriendly, and increasingly expensive energy supply and usage towards a fair, clean, and lower cost energy situation for everyone in the future. The important role which Photovoltaics (PV) has to play is emphasized but also the necessary portfolio of other renewables, notably wind, together with the large scale introduction of electricity storage. With today's existing power purchase agreements for PV, wind and also new nuclear power stations it is shown that already with current prices, renewable electricity is 5–10 times less expensive compared to new nuclear and clean fossil power stations. Especially the economic argument will quickly drive the development towards a 100% renewably powered world within this century and provide energy at lowest price for everyone, highest security of supply everywhere and helping best to solve the climate battle.

2.1 Today's Energy Situation

In the years around 2015, the world's energy situation is shown in Fig. 2.1 [1, 2]. The primary energy (PE) was around 160 PWh (P = Peta = 10^{15}) and consisted of ~83% fossil and ~4% nuclear exhaustible energy sources. The contribution of renewables—mainly firewood and hydro—was around 13%. The conversion of primary energy into usable secondary energy (SE, also named Final Energy Consumption) is associated with considerable losses and amounted to ~100 PWh. The highest loss originates from conversion of fossil and nuclear primary energy sources into electricity and is around 2/3 on an average level. The last column on the right shows the energy content for what we really need: hours of light with a given intensity from a light source, transport with a car from A to B, comfortable living in well air-conditioned houses, power and process heat for the industry, and many more. The machines and devices,

W. Hoffmann (✉)
Bergstrasse 48, 63456 Hanau, Germany
e-mail: Winfried@Hoffmann-ase.de

V. Petrova-Koch et al. (eds.), *High-Efficient Low-Cost Photovoltaics*,
Springer Series in Optical Sciences 140,
https://doi.org/10.1007/978-3-030-22864-4_2

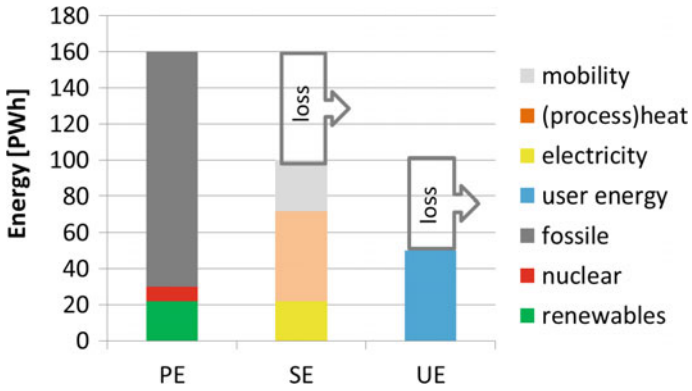

Fig. 2.1 Primary (PE), secondary (SE) and end user energy (UE) in ~2015

which convert secondary energy into what we really need, have energy losses which decrease the end user energy (UE) to ~50 PWh. There was an old rule of thumb for the relation between these three energy forms: PE: SE: UE = 3: 2: 1. This relation has today changed to 3.3: 2: 1. It is the goal of this paper to demonstrate that in a renewably powered world this ratio will significantly change towards ~1.5: 1.5: 1.

The energy sectors within the SE on a global level are shown in Fig. 2.2 and are 27% for mobility, 28% for low-temperature heat, 23% industry (process) heat, 9% industry electricity, and 13% rest of electricity. For an easy remembering the fractions can be approximated to ~1/4 mobility, ~1/4 low-temperature heat, ~1/4 industry (process) heat, and ~1/4 electricity (total).

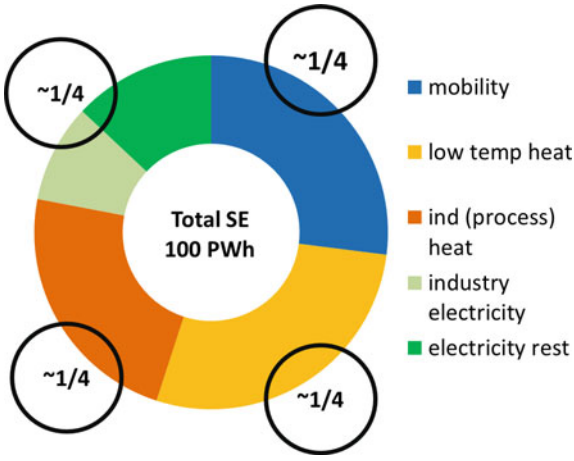

Fig. 2.2 Energy sectors within secondary energy globally (~2015)

2.2 Energy Efficiency Measures

Although energy efficiency measures have nothing directly to do with renewable energies they are important as they will be able to increase the fraction of renewables for a given contribution. Two types of efficiency measures are shown in Fig. 2.3: (1) to use machines and devices which convert SE much more efficiently to the needed UE. Examples are LED's instead of light bulbs, electric cars instead of petrol-driven ones, phase angle modulated power for the millions of pumps instead of constant power for all flow rates, and many more. (2) to provide the specific needs with measures which do not require SE; examples are proper insulation, thoughtful planning of future urban districts to minimize traffic, etc. The arrow (3) shows what by convention has been agreed, namely that the SE provided by renewable sources is equal to the PE (the convention for measuring the primary energy content is either the Physical Energy Content Method (PECM) or the Direct Energy Equivalency Method (DEEM); as a physicist I would have equated the PE for electricity from a PV module—or other renewable technologies—as the energy content within the solar energy received, i.e., for a 20% efficient solar module, producing 10 kWh electricity, the PE would then be 5 times higher, i.e., 50 kWh—but let us continue with what has been agreed).

There is one important consequence with many of the new and higher efficient devices: in most cases, they are more expensive to buy for the same service compared with old and low-efficiency products (example LED vs. light bulb). Only the total cost over the lifetime of the respective product shows that in most cases the service will be cheaper with the new devices by taking into account lower energy consumption and in some cases longer lifetime. So in future the decision for a product will be no longer as easy as it was in the past by only comparing the investment cost—what is still done in many cases today. Only the total cost over lifetime determines which product delivers a less expensive service. The same argumentation applies also to renewable energies as their specific investment is typically more expensive compared to old

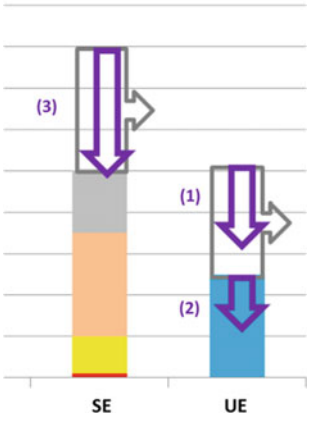

Fig. 2.3 Energy efficiency measures (1 and 2) and removing the losses (3) from PE to SE to obtain secondary energy with renewables only

fossil and nuclear technologies but they have no fuel and other necessary running costs and their cost over the product life cycle are already today less expensive.

It is a straightforward exercise with the examples given and some additional obvious ones to conclude that with today's available machines and devices together with ongoing improvements a significant efficiency increase should be possible. It has been shown in recent years by von Weizsäcker et al. [3, 4] that an efficiency increase up to a factor of 5 is feasible. In order to be more realistic, we may define a factor of only 2.5. This would imply an annual decrease for the needed energy to power the same service of 3.5% or 1.8%, if we would like to have this accomplished in 2050 or 2075, respectively.

This "realistic" efficiency increase includes the change from oil for transportation to electricity and electricity based fuels [hydrogen from hydrolysis of water, methane by reacting CO_2 with hydrogen ($2H_2 + CO_2 = CH_4 + O_2$) as well as the production of methanol ($CO + 2H_2 = CH_3OH$)]. With these assumptions, there will be a significant change for the relative share of the energy sectors. In particular, the fraction of electricity will show a substantial increase.

2.3 Future Energy Needs

The important question arises how many billion people we will have to satisfy with energy. The United Nations [5] have made several scenarios for future development. The medium one is shown in Fig. 2.4 with an interesting result. Until the 1980s we had a steep increase for the 10 year average of annual population increase, there is since the 1990s a decrease observed. With the assumed further decrease in the coming decades as shown, there is good evidence that the global population towards the end of this century could level off at around 10 billion people.

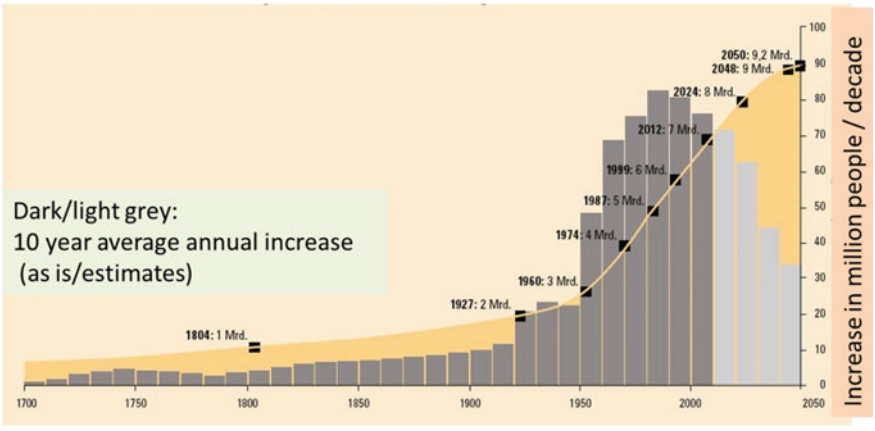

Fig. 2.4 History and future estimate for the global population [5]

One important aspect for the future is also to solve the existing inequity for energy use globally in different regions. If we do not care for a solution we may see emigration of nations at a level which will manifold exceed the immigration to Europe in recent years. A simplified calculation is as follows: With today's ~8 billion people using ~100 PWh SE we have ~1/4 of people using ¾ of SE. From this, we can conclude that 1 billion of people enjoying "high-quality of life" are using ~37.5 PWh of SE. Hence with business as usual and allowing 10 billion people the same "high-quality life" we would have to provide 375 PWh of SE. With our "realistic" energy efficiency measures (factor 2.5) this number decreases to 150 PWh.

2.4 Technologies and Market Development for Renewables

2.4.1 Photovoltaics (PV)

One of the most fascinating and quickest developing technologies in recent years has been PV. After the discovery in the mid-1950s of the first Silicon solar cell it was first used for powering at lowest cost satellites starting in the 1960s. The replacement of small button cells in millions of calculators and other small devices by integrating cheaper small solar cells in the housing of these systems happened in the 1970/80s. This was also the time to power remote places like repeater stations for industry and solar home systems in developing countries with the lowest cost of electricity. First support mechanisms allowed the demonstration of grid-connected PV systems in households (1,000 rooftop in Germany in 1990, 70,000 rooftop in Japan in 1994). It was the introduction of the best market support program ever installed, namely the feed-in tariff starting in Switzerland and Germany, where it was further optimized in 2000 with the so-called "Renewable Energy Sources Act" (H.-J. Fell, H. Scheer and others) providing for all renewable technologies an individual fixed payment for each produced kWh from these systems over 20 years and allowing a fair return of investment. This catapulted the PV market from only 0.3 GW in 2000 to 17 GW in 2010 and realistically towards 100 GW in 2020. This also because other European countries first (and more than 50 countries worldwide afterward) adopted this support scheme. As seen in Fig. 2.5 it was Europe which until 2011 dominated the global annual installations and created an average market growth of 50% p.a. Unfortunately, Europe experienced thereafter a strong decrease in annual market but fortunately other regions, notably US, China, and Japan (part of APAC) helped the global market to increase by 24% p.a. until 2015.

If only an average 14% growth is assumed for the time between 2015 and 2025 the annual and cumulative PV market is shown in Fig. 2.6. The annual market will be around 100 GW in 2020 and 200 GW in 2025. With this, the cumulated market of ~250 GW in 2015 will increase to 500 GW in 2019 and approach the first TW in 2023. Major drivers for this development will be China, India, US, South America and later Africa, and also Europe again.

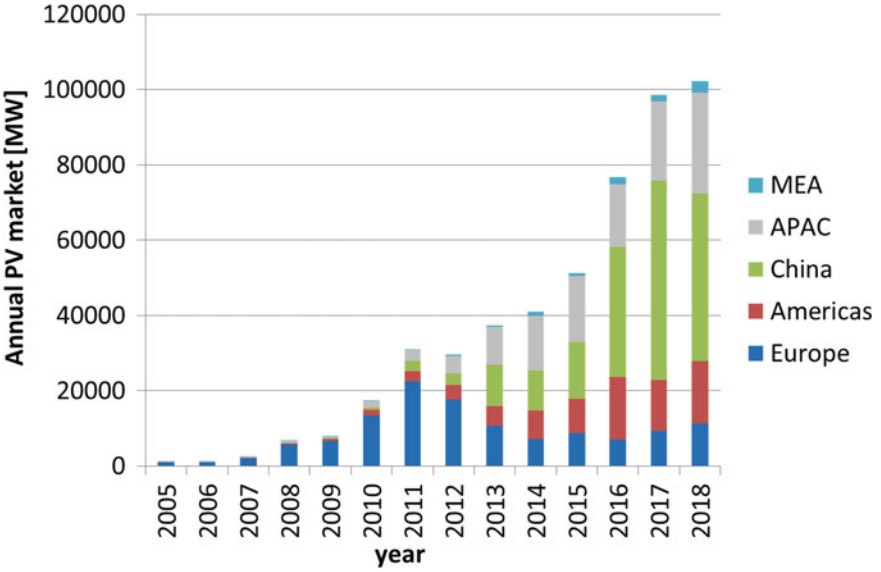

Fig. 2.5 History of annual growth for PV market (SolarPower Europe [6])

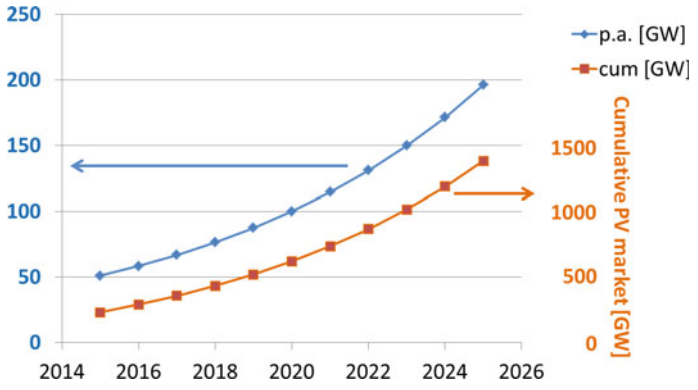

Fig. 2.6 PV market projection in coming years (own research in 2016)

When I sketched the Fig. 2.6 in 2016 it was ambitious to state a market of 100 GW in 2020. But with the unexpectedly strong growth of the Chinese market of 50 GW in 2017, we reached already in this year almost 100 GW. Most associations and market researchers quickly predicted at this moment more than 130 GW by 2020. However, these people forgot the vulnerability of the PV market as long as it is driven by state support. In the past 20 years this "vulnerability" was positive, i.e., more support measures were granted in many countries as anticipated, resulting in a stronger growth compared with expectations. When China published in June 2018 a

cut of subsidies resulting in ~20 GW fewer installations for this and next year, we had all of a sudden for the first time in 20 years the situation that most probably the annual market in 2018 will be smaller than in 2017. Fortunately we have now additional strong markets like India, Middle East, and others which will help to reach 100 GW in 2020. I am confident that the market will grow as in Fig. 2.6 and the vulnerability will fade away as we no longer need state support for our PV systems, because of their competitiveness compared to new nuclear and clean fossil counterparts. This, of course, needs a level playing field for all technologies (i.e., no or at least equal subsidies for each one).

The most important driver for the market increase until today was the decrease for PV module price, which contributed in 2000 ~70% and in 2015 still, ~40% to the total installed system price. The price development for a globally traded mass-produced product is best characterized by the so-called Price Experience Curve (PEC) [7]. Here the logarithm of the average price is plotted versus the logarithm of the respective cumulated market volume. Typically a straight line is obtained with a product-specific slope. The slope gives the decrease in price in % when the cumulative volume is doubled and is called Learning Rate (LR) or Price Experience Factor (PEF). Figure 2.7 shows such a graph for PV modules starting in the 1970s when at the cumulative volume of ~0.5 MW the module price was ~100$/W. 2015 we had 250 GW cumulative volume at prices ~0.5 $/W. The PEF is slightly above 20%.

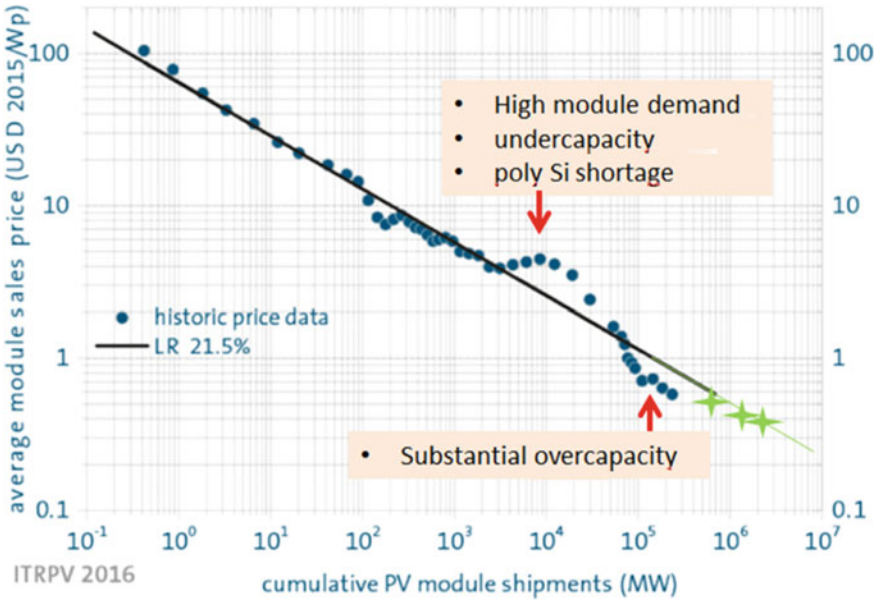

Fig. 2.7 Price Experience Curve for PV modules (ITRPV [8])

As seen in the graph the prices followed nicely the best-fit line until a cumulative volume of ~2 GW was reached, which was in the year around ~2005. Thereafter, we had even a slight price increase and then a downturn to below the straight line. The understanding of this behavior needs no scientific explanations but a good understanding of the market mechanisms and how prices are formed. Until 2000 the small PV industry was able to obtain the polysilicon for the wafers from a scrap of the electronic industry. In 2005 was the time when all existing polysilicon production capacities for the electronic industry were fully loaded, but with a quick market growth there was higher demand compared to production capability. As it takes a few years until complex chemical companies can be operational, the price for polysilicon skyrocketed and the price for modules increased in these times of under capacity along the complete value chain. This was the advent of Chinese production companies. The Chinese state government had just made the decision to heavily invest in the production of goods with high future global potential (wind energy, PV modules, batteries, etc.). In only a few years Chinese companies could use ~40 billion $ investment money at very favorable conditions from the Chinese state bank to ramp up the production capacity quickly with the newest production machines from Europe and the US. In parallel many Chinese companies also went successfully public at the New York Stock Exchange and by 2010 Chinese companies had taken over the lead in global solar cell and module production. This capacity increase even surpassed the 50% annual market growth by a factor of 2. Consequently in 2010 and later we had an overcapacity of ~100% which resulted in significant price erosion as seen in Fig. 2.7. The upside was that many new markets could kick start in these years but the down side was a quick consolidation of the global production industry with heavy losses in the years 2011/12. For the future years I wish for the sake of a healthful industry a return to the straight line as indicated by the green stars in Fig. 2.7.

From a technological point of view the observed massive decrease of price between the 1970s and today is due to a manifold cost reduction: efficiency increase for solar modules, decrease for specific material cost, lowering the investment needs along the value chain, automation, and high volume manufacturing. In the following some examples are given:

- **Efficiency increase**
  In the 1970s the efficiency for industrially produced c-Si solar cells was around 10% which resulted in ~8% module efficiency. This relative 20% reduction was due to round wafers leading to a low package density. The cell architecture was a simple BSF (back surface field)-back side and not passivated front side. Si-Nitride as AR coating resulted also in good passivation thereby increasing the cell efficiency. In recent years the state of the art for solar cells was the introduction of narrow screen-printed front metallization and PERC back structure (passivated emitter rear cell), which gives for monocrystalline wafers efficiency of above 20%, resulting in ~18% module efficiency. With Heterojunction (HIT) cells and Back-contacted solar cells the efficiency for solar cells in mass production is well above 23% with module efficiency above 20%. It is important to highlight the increase

of efficiency for all applications, where area cost per installed power is important, as this decreases inversely proportional.

- **Decrease for specific material cost**
  One important material cost component for solar cells is poly-silicon. During the ~40 years the following achievements could be made:
  # decrease of wafer thickness from ~700 μm to 150 μm (inside hole saw → wire saw)
  # decrease of kerf loss from ~500 μm to 100 μm (same as above)
  The weight reduction could be decreased with these measures from 28 to 6 g/dm^2
  # Decrease for the price of poly-Si from ~60 to 15 $/kg
  The material cost for poly-Si decreased then from ~1.68 to 0.09 $/dm^2
  Together with the efficiency increase from ~8 to 20% we obtain a reduction for the specific material cost from 2.10 to 0.045 $/W, which is an impressive reduction by a factor of ~50!
- **Lowering the investment needs**
  Along the value chain for the production of solar modules the specific investment needs for a production capacity of 1 GW p.a. could be decreased substantially in the years from 2000 to 2018 as seen in Fig. 2.8.
  Keeping in mind that new capacities are in the range of many GW's and this achievement is quite crucial.
- **Automation and high volume manufacturing**
  In the early days the capacity for one production line in a 4 shift operation (24/7) for solar cells was in the range of ~5 MW p.a. without robots. Meanwhile, this capacity has increased to ~200 MW p.a. using quick kinematic robots and highly sophisticated in-line characterization for high uptime and highest yield.

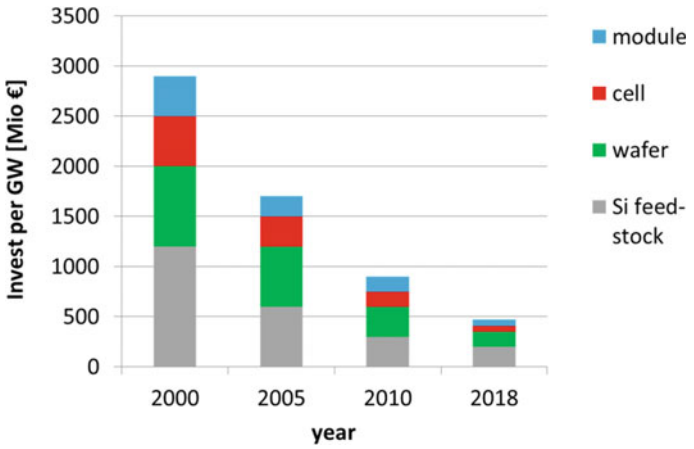

Fig. 2.8 Development of investment needs for Si-feed-stock, waferWafer-, cell- and module manufacturing

An interesting question arises as to the end of the shown price decrease in the Price Experience Curve. If we assume for a single band-gap silicon solar cell the following strongly simplified parameters for the OPEX cost:

- **Feed stock Silicon** at 12 $/kg and a 200 × 200 mm^2 wafer (thickness 80 μm, kerf loss 70 μm), producing a back-contacted solar cell with an efficiency of 25% to ~2 ct/W
- Crystallization and other materials for **wafer** production using wire saws → ~1–2 ct/W
- For the **cell** production (Cu or Al as contact material) → 1–2 ct/W
- The **module** consists of 2 glass plates, each 1.4 mm → 4 ct/W
  plus encapsulation material, etc. → 2–3 ct/W
  finish by cables, back rails, etc. → 2–3 ct/W

In total, the OPEX cost amounts to **12–16 ct/W**.

For a mass-produced component, one could envisage the OPEX cost to amount to ~80% of the total cost. Hence this total cost would be ~15–20 ct/W. This would imply that in our Price Experience Curve the limiting price number would be—dependent on the assumed margin—around 18–24 ct/W. This price would be expected at a cumulative volume of around 24 TW, which can be reached with reasonable growth rates—as shown in the last section—in a few decades from today.

It is often argued that with today's (2018) spot market module prices approaching already 20 ct/W the above estimates are too much on the high side. However, the above numbers are based on full cost—including depreciation, financing cost and no subsidies for energy, waste treatment, and other items. In addition, a healthy industry must also have reasonable margins to be able to further invest in new and additional capacities and to do the necessary R&D—together with institutes—to reach the ambitious further cost reductions. Unfortunately, the observed low spot market prices today are driven by overcapacity of the global sector leading to consolidation. Before going bankrupt smaller companies sell often below their cost and larger corporations being able to survive such difficult times invest in further cost reductions which—hopefully soon—will allow a positive margin with today's low prices.

Is this number really the ultimate cost and price? Fortunately not, as Research is underway to increase the efficiency for c-Si wafer based solar cells even further by using tandem structures which will allow efficiencies well above 30% with only a small increase in the cell-associated cost, but a substantial decrease for the 8–10 ct/W, stated above for the manufacturing of the module (glass, encapsulation, and finish). If we increase the cell cost by 50% due to additional thin film layers for the tandem structure we have 2–3 ct/W. However, if a very optimistic module efficiency of 35% (instead the above stated 25%) is assumed, the module add-on cost is decreased by a factor 1.4, i.e., ~6–7 ct/W. Using a kerfless wafer production could decrease the wafer add-on from 3–4 ct/W from above to 2 ct/W. The total OPEX would decrease to 10–12 ct/W with a total cost of 12–15 ct/W. Hence the limiting price would decrease towards 14–18 ct/W! These rather simplified thoughts underline the needs for further Research & Development for quite some decades in order to reach these ambitious goals. These numbers also demonstrate that it is not necessary—as PV is already

today the lowest cost electricity producing technology - and even dangerous for the global producing industry—see above arguments - to discuss publicly prices of 10 ct/W in only a few years from now. A more bottom-up calculation for the future cost- and price development has concluded that a fair price for modules at 10 ct/W can be expected at around 2040 [9].

The given price level today and the one expected in the years to come, depending on the growth rate, seen in the Price Experience Curve, have an important consequence and any new technology entering the market place has two possibilities:

1. A higher price per power may be paid, if other and/or additional customer needs can be served compared to the mainstream c-Si modules. Examples are flexible thin-film modules, including organic cell structures, colored dye solar modules or tubular solar modules, well suited for agricultural applications. These products are normally said to serve niche markets—however, at a total market of 100 GW now and 500 GW p.a. in a few years, a niche market of 10% from the total can be an interesting market place to be. The resulting 10 and 50 GW represent a module turnover of ~25 billion and ~100 billion €.
2. Any new product intending to enter the mainstream market can only be successful at a lower price. Even if a new technology would be cheaper at the same production level compared to c-Si technology it has to start at the beginning with a small production volume resulting in a high cost and price. Consequently it will be more and more difficult to replace c-Si wafer based products as the mainstream product.

2.4.2 Solar Power—CSP and CPV

2.4.2.1 Concentrated Solar Power (CSP)

In the mid-1980s a total capacity of ~350 MW solar parabolic trough power plants were built in the US which was seen for several years as the preferred technology for large scale centralized solar power plants. The challenge to increase the steam temperature for the turbines (increase of Carnot efficiency) could not be solved until today. As a result the production cost for a kWh from these systems is still ~7 €ct/kWh [10], which is ~4 times higher compared to large PV plants in the same locations. One big advantage which was already demonstrated is the storage of heat during sunshine and storing for the hours after the sunset. This increases the operational time of the system and utilizes the turbines much better. Experiments are ongoing to improve the steam temperature by replacing the limiting heat exchange fluid (oil) of today.

Another possibility is the use of Dish sterling units or large Power Tower systems which receive concentrated light from 1,000 s of 2-axis tracking mirrors. Here the temperature is very high and a high efficiency can be obtained. First commercial

systems have been built and it will be interesting to see the development of the associated cost/kWh.

2.4.2.2 Concentrated PV

Based on 40% efficient multi-junction III-V compound (GaAs) solar cells, typically used for satellite powering today, highly concentrated PV modules with a 2-axis tracking mechanism have been commercially built in recent years. The module efficiency could be demonstrated to be above 30% solar light to electricity. As with all concentrating devices they can only be used in places with high direct sunshine over the year. Similar to the CSP systems it will be interesting to see the development of the reachable cost/kWh.

2.4.3 Wind Energy

The technology for windmills has shown a remarkable development. The size for a single machine in the 1980s was ~75 kW with a rotor diameter of 17 m and a hub height of ~25 m. Today commercial systems have a power of ~7.5 MW with a rotor diameter of 126 m and a hub height up to 140 m. A major drive for this development is the strong dependence of rotor diameter and average wind speed (which is for a given site higher at higher hub heights) on the power output (P):

P ~ (rotor diameter)^2 and P ~ (average wind speed)^3

Parallel to this technology development the annual market increased from ~3.8 GW in 2000 to 51.5 GW in 2014 [11] which gives a CAGR of 20% during this time.

2.5 Need for Storage as Solution to Variable Renewable Energies

The most important types of renewable energies, PV and wind, are by nature variable, however, increasingly predictable. Only a minor part has uncertainties, e.g., local clouds decreasing the PV output in those shaded areas. With today's weather satellites there is high predictability at least for the day-ahead forecast. Nonetheless if we are to provide all electricity needs of a country only with renewables we must provide some storage for periods when no or too little sun and wind cannot provide the actual need. In Fig. 2.9 the electricity load curve for Germany is shown (upper blue curve). The area below corresponds to the annual electricity consumption which is ~600 TWh. If we oversimplifying, assume that this 600 TWh should be produced only from PV and wind we would need ~200 GW wind and ~250 GW PV installations. The annual energy would be ~400 TWh for wind and 250 TWh for PV. With this the

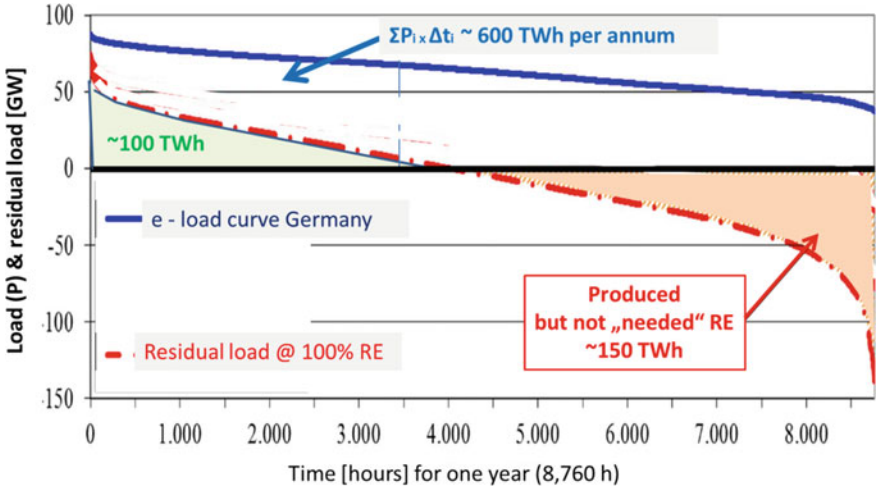

Fig. 2.9 Electricity load curve and residual load for Germany [12]

residual load curve (lower red dash-dotted line) is obtained which also shows that ~ half of the year we produce electricity at times when it is not needed (~150 TWh) whereas the other half year we need electricity at times when there is no wind and sun (~100 TWh). The good news is that we have more electricity produced from wind and PV at times when it was not needed; hence we have energy available to account for losses associated with storage, e.g., charging/discharging batteries and conversion of electricity to hydrogen or methane (P2G, Power to Gas).

The ratio between wind and PV is very much dependent on location. For Germany's load curve we have the best balance for a power ratio of ~1:1. In this case, we have a monthly average which is almost constant during the year, only in winter months slightly higher (due to wind contribution) and matching well the German load pattern. It is important to note that this pattern helps to overcome an old fear: namely the need for seasonal storage, which is no longer necessary. With Germany's irradiation and wind profile this gives energy-wise a ratio of ~2:1 for wind: PV (~2 kWh/W_{wind} and ~1 kWh/W_{PV}). Other regions with different load profiles and different climatic conditions may have significant differences. For example Near and Middle East regions have a pronounced load peak in summer times, much higher irradiation (~2 kWh/W_{PV}) and less wind. Therefore, the power ratio would be in favor of PV. In contrast we may look to Scotland with less sunshine compared to Germany but much more wind; here the power ratio would be in favor of wind. Of course specific regions have also additional renewable sources which can be used to optimize the portfolio for the various renewables to reach the lowermost need for storage.

The storage of electricity has a diversity of solutions: pumped hydro, chemical batteries and also the long-term storage via P2G (power to gas: hydrolysis, methane formation and, when needed, re-electrification with fuel cells). Pumped hydro is only

in few countries in Europe a viable solution (Austria, Switzerland, and Scandinavia) and in most others can only provide a small portion of the needed storage. Example Germany: here 7 GW are installed and in the "old times" (2006) they produced ~4 TWh electricity. Compared to the needed storage of 100 TWh this will not be a solution. Discussions to transport surplus electricity from Germany to Scandinavia have the problem that additional high voltage grids have to be built.

Most likely the solution will be a combination of various technologies. This will start with electricity storage in individual homes (several kWh with lead-acid or Li-ion batteries) where the self-consumption of PV can be increased significantly from ~20% up to 80% (especially when an e-car is also present). For offices, stores, and many SME's (Small and Medium Enterprises) appropriate storage capacities may go up to the several 100 kWh ranges. In a municipality there is still surplus electricity which can be collected and stored in M- to GWh batteries (e.g., NaS, redox flow batteries). Municipalities may run jointly a P2G unit for the small rest of long-term storage needs.

It is interesting to analyze the potential of price decrease for kWh storage in homes and SME's. For this, it is useful to construct a Price Experience Curve for the Li-ion battery cells, the most costly part of such a storage unit. The result is shown in Fig. 2.10 for automotive kWh-units which has a Price Experience Factor of ~15%, i.e., each doubling of the cumulative volume of sold battery cells will decrease the price by ~15%. At the time the curve was made we had a cumulative volume at the end of 2015 of ~40 GWh of sold Li-ion battery cells with a price of ~250 €/kWh. The interesting question is—when could we expect a cell price of 100 €/kWh? For this we extrapolate the straight line and obtain at ~1 TWh cumulated capacity this envisaged price. The next question is—at which time would we like to have this cumulative volume reached, bearing in mind that a meaningful growth rate should be in place. If we assume that in 2030 (or 2025) we would like this price, we can calculate the necessary growth rate, which is 24 (or 38) % p.a. These growth numbers may seem ambitious but if we compare this with the growth rate for the cumulated

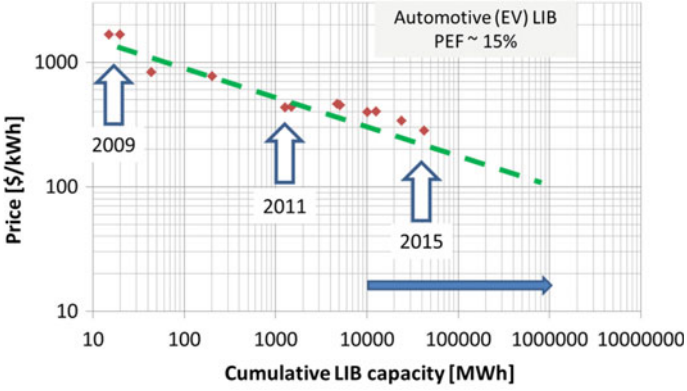

Fig. 2.10 Price experience curve for Li-ion batteries [13]

PV modules in the time 2000 and 2010 the industry was capable to demonstrate 41%. So this is a realistic goal to be reached.

To complete a battery we must add the assembly cost which is assumed to be ~25% of the cell price. The assumptions for a simplified calculation to obtain the storage cost in €ct/kWh are as follows:

- Lifetime of battery: 5,000 cycles
- Finance cost: 50% up to ~same as investment
- Usable capacity per cycle: ~90%
- → cost per kWh = (Invest + finance cost)/(5,000 × 0.9)

The storage cost is expected to decrease from ~15 €ct/kWh today down to ~(4–5.5) €ct/kWh in 2025/2030. Even if we have to add some electronic hardware for the stationary house storage we have a very favorable price for a stored kWh of PV electricity when compared to a purchased kWh from the utility. This price development for battery storage also gives a very good prospect for the running cost of future e-cars. If we assume a petrol-driven car with 5 l/100 km the cost is 7.5 € at 1.5 €/l. An e-car using PV electricity with 15 kWh/100 km has a cost of only (1.5–2.2) € which is 3-5 times less (PV (5–10)€ct/kWh in southern and northern regions, storage cost 5 €ct/kWh).

2.6 The ~100% Renewably Powered World

Assuming realistic energy efficiency measures of a factor 2.5 from today to 2050 we have a completely different energy picture in a 100% renewably powered world as shown in Fig. 2.11. This also takes into account that the unfair energy distribution of today is changed to a situation in 2050 where the global population has a similar

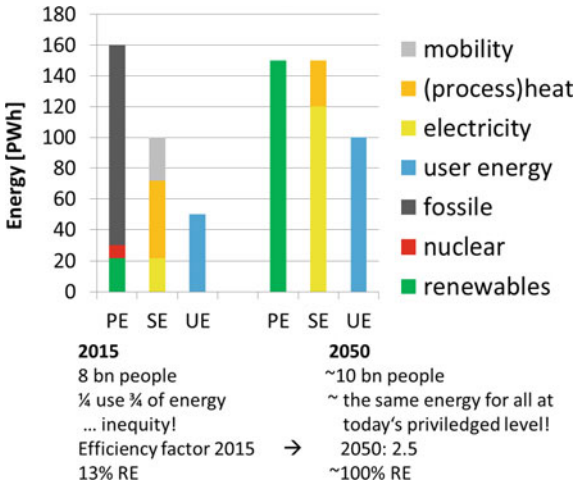

Fig. 2.11 Energy picture from today towards a fair and 100% renewably powered world in 2050+

Table 2.1 Technical and sustainable potential for various renewable technologies [14]

	Technical potential [PWh/year]	Sustainable potential [PWh/year]	
Biomass	224	28.0	
Geother	202	6.2	~1%
Hydro	45	3.4	
Solar	78,400	2,800.0	~90%
Wind	476	280 .0	~9%
total	79,347	3,117.6	100%

access to energy. Important to note is that primary energy equals SE, and the electricity makes up 80% of SE (120 PWh, which also contains the energy for mobility) and the total losses to convert SE into EE are significantly reduced. This is obviously very different to the situation as of today and results in the ratio PE: SE: EE = ~1.5: ~1.5: 1.

When it comes to the needed portfolio of the different renewable sources it is important to understand what the respective technical and—even more important—the sustainable potential is. A comprehensive review for this topic was done in a detailed publication [14] and is shown in Table 2.1. The technical potential summarizes all land based areas (and near coastal areas for offshore wind) which would technically allow the utilization for a given renewable source. In contrast, the sustainable potential, which is only ~4% of the technical one, takes into account important ecological, economical, and environmental aspects to be fulfilled. Fortunately the 150 PWh annual needs are only ~5% of the sustainable potential—hence there is no obvious or unsurmountable hurdle to have the needs covered only by renewables. Also important is the fraction for solar, wind, and all others (including hydro, geothermal, biomass, etc.) of the sustainable potential which is 90%, 9%, and only 1%, respectively.

In order to account for local opportunities especially for "all others" we should increase the share for our 150 PWh from 1% up to ~20% which would imply that 30 PWh should come from these sources. Some thoughts about why this is not likely to increase significantly:

- *Hydropower*
  The last 50 years had an almost linear increase of ~0.5 PWh per decade to 3.5 PWh today. Even if we assume the same capacity addition—which becomes more difficult in the future—we arrive in 50 years at a cumulative capacity of ~6 PWh.
- *Geothermal*

There are limited places with high surface temperature. In addition, most places have only a rather low steam temperature level for the turbine resulting in a low Carnot efficiency. From today's installed capacity of ~15 GW, producing ~0.09 PWh there is even with the globally available capacity potential of ~200 GW an annual electricity production of ~1.2 PWh is possible [15]. Even if we double this number, not more than 2–3 PWh will be produced from this technology.

- *Bioenergy*
  If biogas is produced with the fastest growing plants and electricity made with a 40% power station there is only ~20 MWh/ha electricity p.a. Compared with PV in the sun belt 80 times electricity in the same area is produced, in northern countries like Germany it is still 40 times more.
  For biodiesel the situation is even worse: while in an area of 10 m^2 with plants for biodiesel a diesel-fuelled car can only drive 110 km (5 l/100 km), an e-car can drive with PV generated electricity in the same area as far as 10,000 or 20,000 km p.a. for northern areas and sun belt regions, respectively.
  Nonetheless we have substantial amounts of bio-waste which should be used in the best possible way, also to produce electricity—but a major portion of the 30 PWh is difficult to imagine.
- *Ocean energy (wave and tidal)*
  Although the theoretical energy production from these sources is huge there are severe practical limitations for harnessing cost-efficiently this energy resource. Some favored areas may well be used for this technology but again it is difficult to see a big part for the 30 PWh coming from here.

For wind, there is also good reason to increase the relative 9% towards ~20% of our needed SE. Major reasons for this are:

- Wind and solar are balancing very well
- Wind onshore is cost-effective and has a good capacity factor (2–3 kWh/($W_{wind\ inst}$ x a))
- Wind offshore has an excellent capacity factor (3–5 kWh/($W_{wind\ inst}$ x a)) and shows the good prospect of low cost (just recently a PPA was awarded to Vattenfall at <5€ct/kWh)
- From today's installed capacity of ~420 GW in 2015, the annual growth can be smaller than 10% p.a. to reach the 30 PWh electricity production

For solar we will decrease the relative fraction from 90% down to 60% for our 150 PWh scenario. Three technologies should contribute in this area: (a) solar PV (decentralized), (b) solar power centralized and (c) solar thermal (process) heat.

- *Solar PV (decentralized)*
  The development of this fascinating technology was described in the preceding section. The annex "decentralized" should cover all PV systems from the small W-range (pico-PV) via the kW-installations (rooftop for houses) up to the MW- and even GW-range (commercial rooftops, community owned green fields). The question is whether we can reasonably assume that these systems are able to grow in order to be able to supply for example 30 PWh of electricity let us say around

Table 2.2 Necessary growth rates (simplified) to provide 20% PV for the future 150 PWh of SE

	V 1	V 2
Decade	% growth	p.a.
1990 - 2000	*20*	*20*
2000 - 2010	*50*	*50*
2010 - 2020	20	20
2020 - 2030	14	15
2030 – 2040	8	10
2040 – 2050	4	5
cumulative PV power in 2050 [TW]	**23**	**30**
Annually produced energy [PWh] in 2050 at 1.3 kWh/W (average)	**30**	**38**

2050. Table 2.2 illustrates a quick exercise for such a growth: Coming from the past two decades with a proven CAGR of 20 and 50% p.a. and as shown earlier that the running decade is realistic to demonstrate 20% we only need much lower GAGR's for the coming three decades to reach a cumulated capacity of 23 TW for such PV installations. If we take a conservative average number of only 1.3 kWh/($W_{PV\ inst}$ × a) these PV systems would produce in 2050 about 30 PWh electricity.

Of course, this simple approach does not take into account dismounting old installations after ~30 years and would assume an unrealistic stop of installations in 2051 with a gradual increase again as in the years 2010–2015. More realistic is a logistic growth curve to reach asymptotically the 23 TW as shown in Fig. 2.12 [16]. Here the increase for PV systems is shown for the major regions worldwide with adjusting the respective growth to the local situation and the relative share is taken in proportion of the expected population [5] in the various regions.

In order to arrive at the cumulative capacity, the annual market growth is shown as a black dotted line (right ordinate). The peaks and valleys derive from the assumption of an average lifetime of the PV systems of 30 years. In the steady state after ~2040, the annual installations are in the range of ~800 GW per year (±100). From our today's ~70 GW in 2016 we have still a way to go but as we have neither material limitations nor manufacturing bottlenecks this ambitious goal could be well reached, given the track record of the last decade.

There is another very important point why this PV growth will really happen. If the increasing PV installations could only be achieved with subsidies and support against less expensive alternatives, I would not dare to make such projections. However, with recently published power purchase agreements (PPA's) for new nuclear power stations and new PV systems, we are now able to compare the price for electricity for the alternatives in a fair manner.

For new nuclear we refer to the agreed contract between Great Britain and France to build two Areva EPR 1,600 MW nuclear reactors with a planned investment of

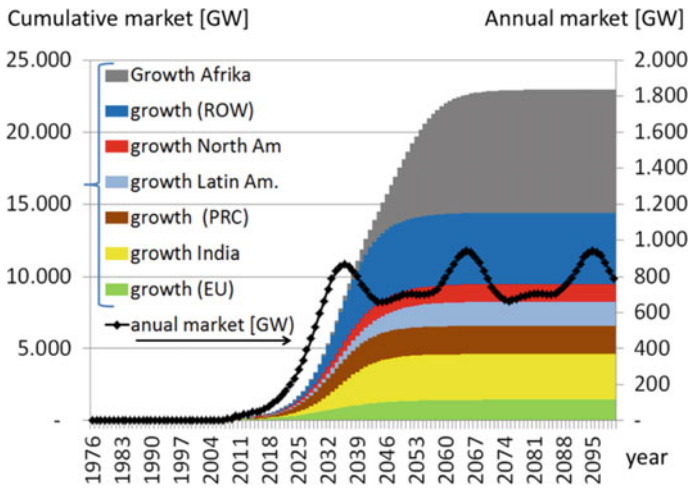

Fig. 2.12 Logistic growth curve to reach the 23 TW-PV installations (=~30 PWh electricity p.a.)

26.5 bn €. EdF will only build these reactors if GB accepts a guaranteed price for each produced kWh with the following conditions:

(a) 92.5 BP/MWh = ~12 €ct/kWh,
(b) duration 35 years after start of operation,
(c) adjustment according to inflation, starting with the reference year 2012,
(d) expected completion 9.5 years after start of work.

With these numbers the price to be paid (in today's currency) is calculated and shown in Fig. 2.13 for two inflation rates assumed (1 and 2.5% p.a.) and an expected start of operation in 2027 (earliest start in 2017 plus 9.5 years). Although inflation rates were rather low in recent years, it is expected that in the long run, an average inflation rate will be around 2%. With this the first kWh in 2027 has a price of ~16 €ct/kWh and will increase towards ~35 €ct/kWh at the end of the 35 years. The average or "effective" price for this new nuclear power is ~25 €ct/kWh (at 2% inflation rate).

In contrast to this agreement, there have been several PPA's for new PV MW-sized green fields recently signed. In several calls for tender in Germany for green-field PV plants with a size of ~100 MW, the contracts were awarded (a) at and below 5 €ct/kWh guaranteed price, (b) duration 20 years, (c) no adjustment with inflation, and (d) expected completion ~1 year. Another PPA was signed recently by Dubai Electricity and Water Authority (DEWA) and Abu Dabi Future Energy Company (Masdar) for a solar park at 2.99 $ct/kWh with similar boundary conditions as in Germany. Another PPA was signed in Chile at 2.91 $ct/kWh. The lower PPA in Dubai and Chile reflect the differences of irradiation for Germany (~1 kWh/W_{PV}), Dubai (~1.9 kWh/W_{PV}) and Chile (~2.3 kWh/W_{PV}). In the case of PV we can realistically assume a lifetime of ~30 years. If we conservatively take ~1 €ct/kWh for maintenance and repair for the 3rd decade for those PV systems we can calculate the "effective" price for the PV systems in Germany as follows: two decades with ~7 €ct/kWh and

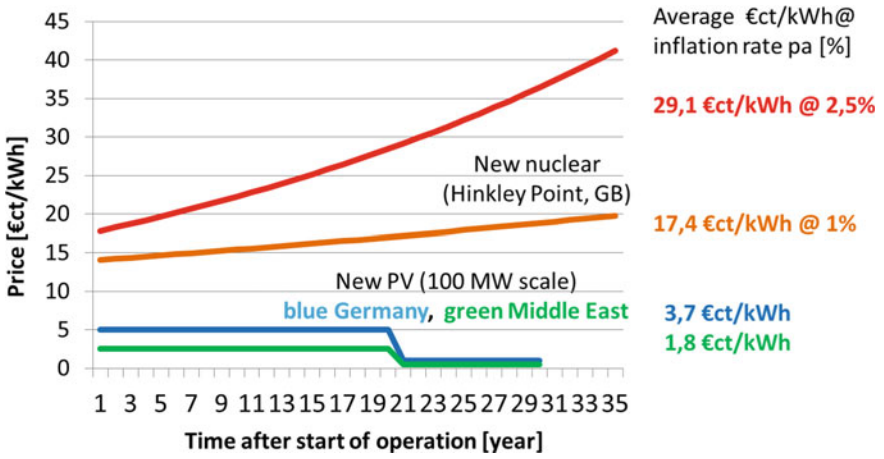

Fig. 2.13 Price development for new nuclear (Great Britain) and new PV (in Germany and Dubai) based on existing PPA's (power purchase agreements)

one decade with 1 €ct/kWh → "effective" price = (2 × 5 + 1)/3 = 3.7 €ct/kWh. Similarly in Dubai and Chile the "effective" price is ~1.8 €ct/kWh. This calculation is based from the point of view of a user for these systems; an investor running the systems should remember that for the above mentioned PV PPA's he will receive the price after inflation as shown in Fig. 2.12.

In summary, we have already today the situation that with current prices a PV-kWh in less sunny Germany is 5 times cheaper compared to a new nuclear power station. This factor increases in sunnier regions like South America and Middle East to more than 10. Whenever the financial world has understood this interesting result the 100 s of billions of € investment money will no longer go into new nuclear but in new PV (and wind, see above PPA for wind). There is no longer any meaningful reason why a country should decide for new nuclear. Similar arguments are with clean coal (CCS, carbon sequestration, and storage) as this will add cost and make a clean fossil kWh also very expensive at above 10 €ct/kWh.

Until a mandatory CCS will be in place there may be due to the Paris agreement a possible move to a reasonable Carbon price. This started in Europe some years ago with ~30 €/t-CO_2 collapsed to ~5 and is today at ~20. It is expected that in the years 2019–2023 this price will average at ~35–40 €/t-CO_2 . With the goal to keep temperature increase well below 2°C, we may anticipate that a price of 50 €/t-CO_2 may become realistic. This would add a cost to fossil power plants of ~6 €ct/kWh for lignite, ~5 €ct/kWh for hard coal and 2.2 €ct/kWh for gas—plus running the power plant and buying fuel—for sure more expensive than new renewables as demonstrated before.

- *Solar power centralized*
  While PV (and wind) systems up to the multi MW-range are well suited to cover the energy needs regionally for private homes, SME's, hotels and offices, the

question remains how to provide the necessary energy for the large and energy-intensive industry. There has always been a tendency to move such industries to regions with low energy costs, which in the past was predominantly in areas with hydropower. Examples are metallurgical silicon plants in Scandinavia and aluminum production from bauxite in Iceland. For all those countries lacking hydropower a great opportunity could arise to keep or attract the industrial location of such energy-intensive industries in their region if they have good solar (or wind) potentials. Regions around the Mediterranean area, desert regions like Gobi in China, Sahara in Africa, Atacama in Chile, large areas in Australia and many more could provide multi TW power stations for lowest price electricity and heat. First TW-PV plants are already built in China and many more could use either huge standard PV plants (fixed plate), concentrated PV (2-axis tracking systems with 500x concentration using multi band-gap GaAs solar cells) and/or concentrated solar power (parabolic trough, solar dish or power tower, which can provide not only electricity but also process heat for industry). An interesting approach is a hybrid PV and parabolic trough system at the same site to provide cheap continuous power for industrial production companies: lowest price during sunshine with PV and lowest price during the night with cheapest heat storage from the parabolic trough converted to electricity by the turbines. Such hybrid plants are capable to provide continuous power at ~5 ct/kWh, cheaper than anything else.
A quick exercise shows that with such large centralized systems energy of 30 PWh in 30 years can be provided with reasonable growth rates: If we assume an average size of 5 GW we need an annual growth of ~31% p.a. to reach 30 PWh. In the next 10 years 14 of such systems should then be built. Looking to the plans in India, Africa, Middle East, and China for similar large scale systems this seems feasable.

- *Solar thermal (process) heat*
  At the end of 2010 we had globally ~270 million m^2 cumulative solar thermal installations, with more than 70% installed in China. This corresponds to ~190 $GW_{thermal}$ and an energy equivalent of ~130 TWh. While most of these installations are used to cover the low-temperature heat for warm water it is increasingly used also for district heating (example Denmark).
  An additional business opportunity for thermal systems will arise which is medium temperature process heat for many industrial applications from SME's up to big companies. Whether the annual global energy needs for this technology segment will approach 30 PWh remains to be seen; it all depends on how the customer needs can be satisfied most efficiently in comparison with electricity based solutions from a cost and convenience point of view.

In summary, we have summarized the portfolio of renewables to cover the future SE needs of 150 PWh in the following Table 2.3.

The above split should only emphasize the relative importance for all renewables and not be taken as a quantitative forecast for 2050. It could well be that Solar PV becomes bigger and Solar power and/or Solar thermal smaller. But this does not change the basic message from this exercise: namely that renewables will for

Table 2.3 Portfolio and split of renewable technologies to cover 100% global secondary energy needs

	Fraction (%)	Energy (PWh)
Solar PV (decentralized)	20	30
Solar power centralized (CPV and CSP)	20	30
Solar thermal (process) heat (CSP and solar thermal collectors)	20	30
Wind energy (on- and offshore)	20	30
All other (hydro, biomass, ocean tidal and wave, geothermal etc.)	20	30
Total	100	150

economic and environmental reasons take over the global energy supply in the coming decades from today's fossil and nuclear technologies.

Acknowledgements I would like to thank C. Pillot from Avicenne for providing the market data for Li-ion batteries and M. Fischer from Hanwha Q-Cells for calculating the logistic growth curve.

References

1. IEA (International Energy Agency), World Energy Outlook (2017)
2. Own research by Winfried Hoffmann
3. E.U. von Weizsäcker, A.B. Lovins, L.H. Lovins, *Factor Four: Doubling Wealth–Halving Resource Use: The New Report to The Club of Rome* (Earthscan, London, 1998)
4. E.U. von Weizsäcker, K. Hargroves, M. Smith, Factor 5. Transforming the Global Economy through 80% Improvements in Resource Productivity, (Earthscan, London, 2009)
5. UN (United Nations), World Population Prospects: The 2012 Revision, Highlights and Advance Tables (Working Paper No. ESA/WP.228 2013)
6. SolarPower Europe, Global Market Outlook (2019)
7. W. Hoffmann, *The Economic Competitiveness of Renewable Energy*, (Scrivener publishing/Wiley 2014) (chapter 7, ISBN 978-1-118-23790-8)
8. ITRPV (International Technology Roadmap for PhotoVoltaics), www.itrpv.net/Reports/Downloads/2016
9. W. Hoffmann, A. Metz, *Modules at a Price of 10 $ct/Wp - Dream or Reality?* New Approach for Future Cost and Price Predictions, (EU PVSEC, Marseille, 2019)
10. Personal information DLR institute (2018)
11. GWEC (Global Wind Energy Council) www.gwec.net
12. Hartmann, Dissertation Stuttgart (2012) and Jülich, Fraunhofer-ISE (2014)
13. C. Pillot, personal communication, avicenne, Paris (2014)
14. WBGU (Advisory Board to the German Government on global change), Flagship report 2011, World in transition: a social contract for sustainability, ISBN 978-3-936-191-37-0 (2011)
15. Geothermal Energy Association, Annual US and global geothermal power production report, (2016)
16. Data by W. Hoffmann and calculation of logistic growth curve by M. Fischer, Hanwha Q-Cells GmbH (2015)

Chapter 3
Advanced Solar-Grade Si Material

Karl Hesse and Ewald Schindlbeck

Abstract Silicon-based technologies account for more than 90% of global PV installations. Since decades, scientists around the world have been searching for the right technology to produce silicon feedstock for the photovoltaic industry, which fulfils the needs for "low cost" as well as the needs for sufficient quality. The urgency of this task has intensified since 1998, when it became clear that the PV demand could no longer be met with by-products from the electronic industry.

3.1 Introduction

Silicon-based technologies account for more than 90% of global PV installations. Since decades, scientists around the world have been searching for the right technology to produce silicon feedstock for the photovoltaic industry, which fulfils the needs for "low cost" as well as the needs for sufficient quality. The urgency of this task has intensified since 1998, when it became clear that the PV demand could no longer be met with by-products from the electronic industry. The established producers of polysilicon developed specific products for the solar industry, and expanded their production capacities significantly. Despite these efforts, a severe Si shortage was observed in 2008 triggering very high spot prices for solar-grade silicon. New entrants entered the field of polysilicon production to capitalize on fast growing demand of photovoltaics. Production capacities were expanded at fast pace and the market situation changed from "undersupply" to "oversupply" rather quickly. As a consequence, spot prices for solar-grade polysilicon continuously declined. Today, the polysilicon market is characterized by a highly competitive environment. Successful polysilicon producers must have the capabilities to produce high-quality polysilicon at lowest

K. Hesse (✉)
Wacker Chemie AG, Wacker Polysilicon, Johannes-Hess-Straße 24, 84489 Burghausen, Germany
e-mail: karl.hesse@wacker.com

E. Schindlbeck
Anton-Riemerschmid-Str. 40, 84489 Burghausen, Germany
e-mail: schindlbeck.ewald@t-online.de

V. Petrova-Koch et al. (eds.), *High-Efficient Low-Cost Photovoltaics*,
Springer Series in Optical Sciences 140,
https://doi.org/10.1007/978-3-030-22864-4_3

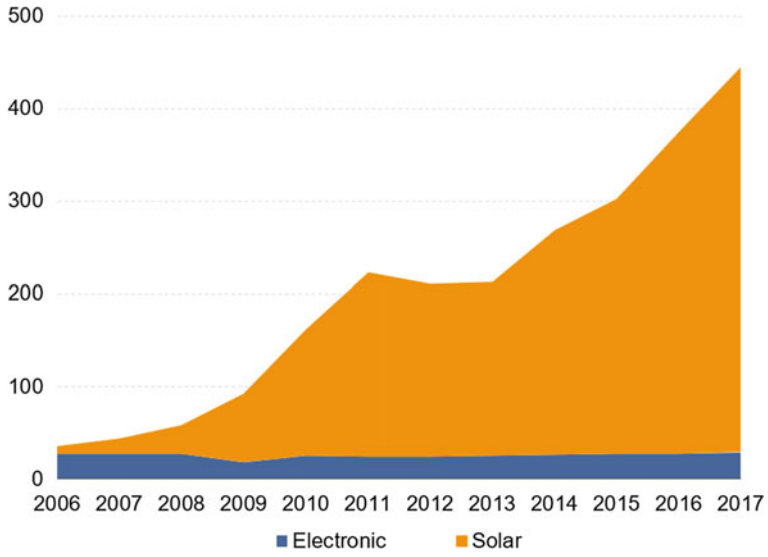

Fig. 3.1 Development of global polysilicon demand (kt). *Source* Analysis Wacker Chemie AG September 2018 production pathways solar silicon feedstock

possible cost. Besides the established Siemens and fluidized-bed technologies, there are still alternative production methods under discussion which potentially could even be more suitable to serve the needs of the photovoltaics industry. Here requirements and possibilities have to be checked very carefully. Also old knowledge and experience about the different possibilities to produce silicon should not be forgotten. The future supply of silicon to the PV industry has to be seen in the tense environment of quality, costs and time of implementation (Fig. 3.1).

3.1.1 Metallurgical-Grade Silicon: Carbothermic Reduction of Silica as Starting Point for Most Pathways

Most pathways for the production of solar silicon feedstock are starting with metallurgical silicon ("silicon metal", purity >98%) and ending with hyperpure silicon (purity in the parts per billion range), so the challenge is to do this purification as efficient as possible.

The silicon metal is produced in submerged electric arc furnaces (electrical consumption between 10 and 30 MW) according to the formula:

$$SiO_2 + 2C = Si + 2CO$$

Feedstocks are woodchips, high-purity quartz lumps and high-purity coal, charcoal and coke.

The silicon melt has to be refined and solidified in the casting process to get a multicrystalline structure and then crushed.

An important by-product is silica fumes, formed in by a side reaction according to the formulas:

$$2Si + O_2 = 2SiO$$

$$2SiO + O_2 = 2SiO_2$$

Owing to economy of scale and process improvements, the electric consumption of 10–11 kWh/kg has already reached compared to more than 14 kWh/kg in the past [1].

As the worldwide production capacity for metallurgical silicon is far more than 1 mio mto/a (most of it for the metal/aluminium industry), there is no supply bottleneck to see in the future (cf. [2]).

Regarding the quartz as feedstock, it is certainly true that SiO_2 is one of the most abundant materials available on earth (as "sand"). But if you are looking for high-purity quartz as it is necessary for high-purity metallurgical silicon, the availability is much more limited to special mines, for example in Spain or Brazil, which is not so much an issue of availability but costs (for mining and transport).

The purity of typical metallurgical-grade silicon with respect to metallic impurities is approximately six orders of magnitude worse than that of typical solar-grade silicon. So purification for the solar needs is inevitable.

3.1.2 Established Production Methods: Purification of Metallurgical Silicon via the "Silane Route" Is Dominating

The extreme purity required for silicon in photovoltaic or electronics applications is achieved by converting metallurgical-grade silicon into silanes (large-scale industrial processes are based on trichlorosilane or monosilane), which are then distilled and decomposed to yield hyperpure silicon. The conventional method is the so-called Siemens process in which TCS is decomposed in bell jar type reactors in the presence of hydrogen with the deposition of polysilicon on thin silicon rods [3]. The silicon tetrachloride (STC) produced as a by-product is hydrogenated back to TCS or is used as a feedstock for pyrogenic silica. The fluidized-bed CVD process used to deposit polysilicon appears to be a very attractive alternative to the Siemens deposition process. Wacker has successfully developed a fluidized-bed deposition process for granular solar-grade polysilicon based on TCS [4]. In contrast, two completely

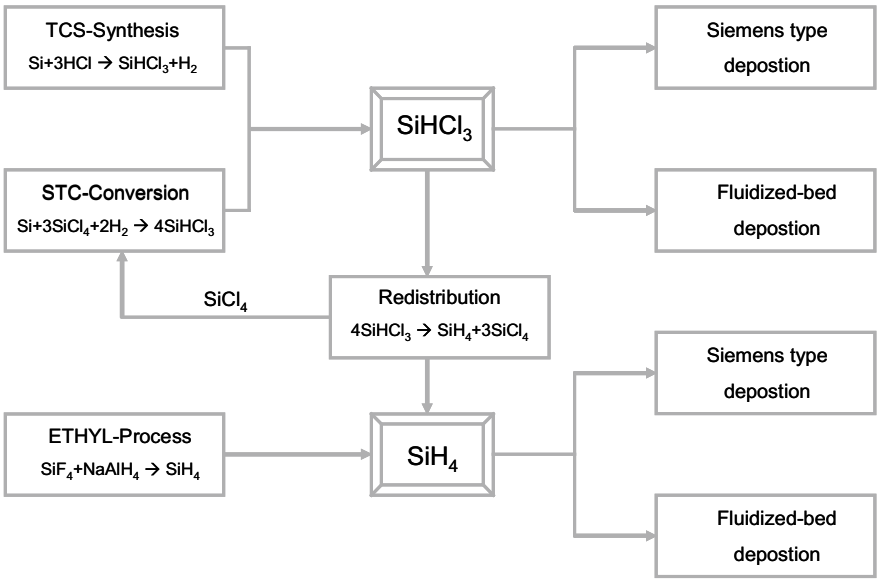

Fig. 3.2 Pathways for polysilicon production

different processes use monosilane (SiH_4) as the feedstock for deposition of polysilicon. As shown in Fig. 3.2, one of these processes uses TCS as a feedstock to afford SiH_4, whereas the other process is based on SiF_4, a by-product from the production of superphosphate fertilizers. The latter process was used by SunEdison on an industrial scale until 2016. Semiconductor-grade monosilane can be used in a modified low-temperature Siemens process or in a fluidized-bed deposition reactor to produce polysilicon.

Approximately 94% of the global capacity of polysilicon used the Siemens process and TCS as a feedstock in 2016 [5].

3.1.3 Differences in Utilizing TCS or Silane as Feedstock

Lobreyer and Hesse [6] demonstrated that comparable qualities of semiconductor-grade polysilicon could be obtained from Siemens deposition of polysilicon, regardless of the type of silane feedstock (TCS or monosilane).

There are pros and cons associated with the use of both monosilane and TCS to deposit polysilicon. Breneman and Dawson [7] published a detailed review discussing the key advantages and disadvantages.

The deposition of polysilicon from monosilane can be carried out at a temperature as low as 650 °C, whereas temperatures >900 °C are necessary for TCS. If monosilane is used, the main problem appears to be the production of silicon dust by

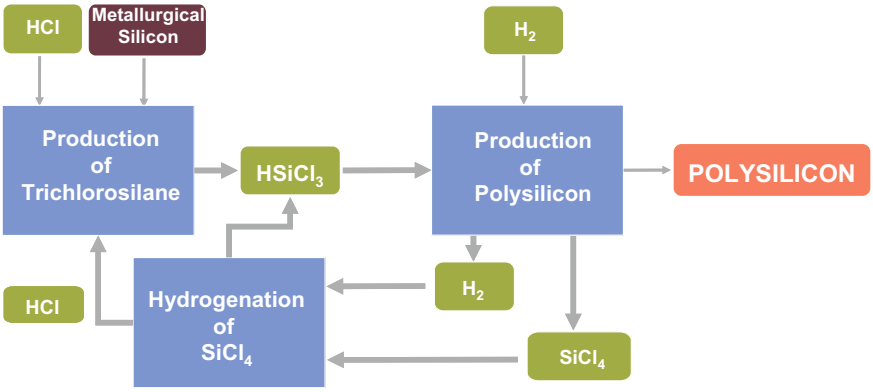

Fig. 3.3 Wacker polysilicon: closed loops for hydrogen and chlorine yield significant cost advantages

homogeneous vapour deposition, which decreases yields and limits deposition rates; it also negatively affects the product morphology (pores, density, microroughness). If TCS is used, approx. 1/4 reacts to form silicon, 3/4 is converted into STC which leaves the reactor in the off-gas. On the other hand, if monosilane is used, conversion rates of nearly 100% are obtained and hydrogen is practically the only by-product. The main pathway to produce monosilane is redistribution of TCS to monosilane and STC; here ¼ of the TCS reacts to monosilane, ¾ is converted to STC; so the system with monosilane deposition has to deal with the same amounts of chlorosilanes as the TCS-based deposition system. There are also major differences in handling of the individual silanes. The self-ignition and the very low boiling point of monosilane necessitate extremely strict safety-engineering requirements and a complex cryodistillation system.

Regarding the process complexity, the Wacker TCS process achieves a closed-loop production system based on only three chemical reactions (Fig. 3.3):

$$\mathrm{mgSi} + 3\mathrm{HCl} \rightarrow \mathrm{SiHCl_3} + H_2 \quad \text{metallurgical Si to TCS} \quad (3.1)$$

$$4\mathrm{SiHCl_3} \rightarrow \mathrm{Si} + 3\mathrm{SiCl_4} + 2\mathrm{H_2} \quad \text{deposition of Si} \quad (3.2)$$

$$3\mathrm{SiCl_4} + 3\mathrm{H_2} \rightarrow 3\mathrm{SiHCl_3} + 3\mathrm{HCl} \quad \text{hydrogenation of STC} \quad (3.3)$$

$\mathrm{mgSi} \rightarrow \mathrm{Si}$ sum: purification of metallurgical silicon to hyperpure silicon, closed loops of hydrogen and chlorine

So the decisive point appears to be how the polysilicon deposition process is integrated into the manufacturer's particular product flow. The objective here is to either recycle all the by-products and waste products or use them to synthesize other products to minimize losses of silicon, chlorine and hydrogen. It is also important to use any waste heat arising from the various processes within the integrated system.

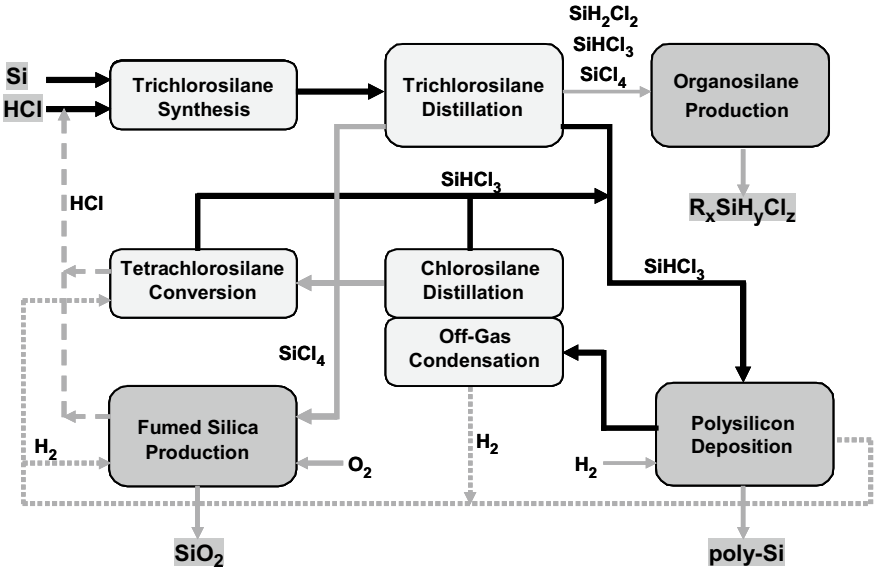

Fig. 3.4 Integrated product flow at Wacker Chemie AG, besides polysilicon the production of other value-added products is possible

The integrated product system used at Wacker takes the additional advantage of value-added products by linking the production of polysilicon to that of pyrogenic silica, organofunctional silanes, silicates and silicones (Fig. 3.4).

3.1.4 Accommodation of the Processes to the PV Requirements

An alternative to the "silane route" has been sought for many years, particularly for the production of solar-grade silicon. The purity of solar-grade silicon with respect to metallic impurities is approximately six orders of magnitude higher than that of typical metallurgical-grade silicon. It is questionable as to whether there is an alternative to the "silane route" that can achieve this purity at acceptable costs. A very important parameter in photovoltaics is solar cell efficiency (around 19–24% in 2018 [8]). The highest cell efficiencies with low specific material usage are only possible via high-quality feedstock. For the production of solar-grade feedstock Wacker Chemie AG has optimized its existing semiconductor-grade production process taking into account the requirements of the solar industry:

- The deposition process was optimized for maximum deposition rate.
- The purification of the surface by chemical cleaning or etching after crushing of the rods could be avoided by a new crushing process. This process leads to

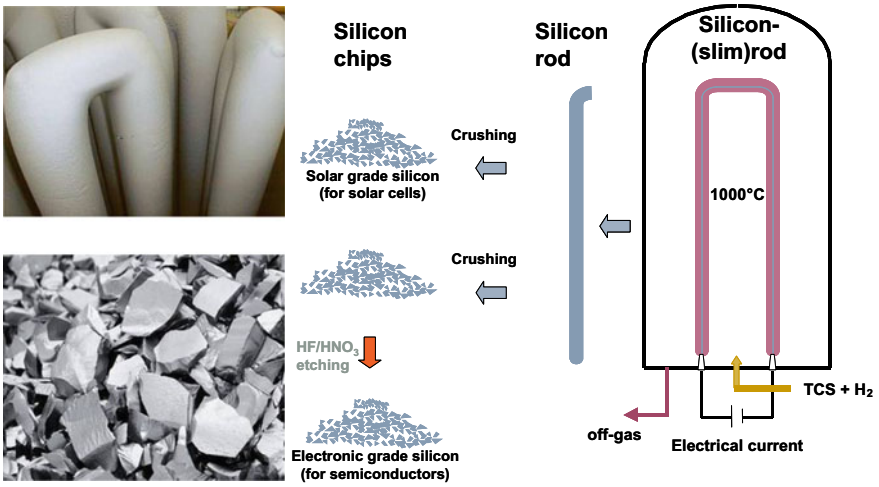

Fig. 3.5 Rod deposition: optimized process of deposition handling and crushing for the solar Industry

lower contaminations, especially for metals, so that the solar requirements (metals contaminations in the low parts per billion per atom (ppba) range) can be fulfilled; the metal contaminations of cleaned prime electronic-grade polysilicon are two orders of magnitude lower) (Fig. 3.5).

The fundamentals for a cost-effective production of solar-grade silicon at Wacker polysilicon are:

- Highly integrated, but flexible production system: value-added use of by-products
- Economy of scale: investments, costs, productivity
- Advanced reactor technology: high output, yield, quality
- Flexible reactor technology: solar or electronic polysilicon according to demand
- Over 60 years of experience in polysilicon production.

Deposition of Granular Polysilicon with Trichlorosilane

A fluidized-bed deposition process might be a reasonable supplement to the "main route" rod deposition technology (Fig. 3.6). In this process, a fluidized bed of silicon particles is heated to the necessary decomposition temperature of the silicon containing gas which is passed through the bed. Ideally, elemental silicon is deposited on the silicon particles that start growing. It is possible to operate this process continuously by regularly withdrawing particles from the fluidized bed and adding smaller seed particles to the bed. The withdrawn particles are already the ready-to-use product. Seed particles can be obtained for example by milling of product granules. Besides the advantage of continuous operation, the process has the potential of lower specific energy consumption. For customers granular polysilicon has a lot of advantages

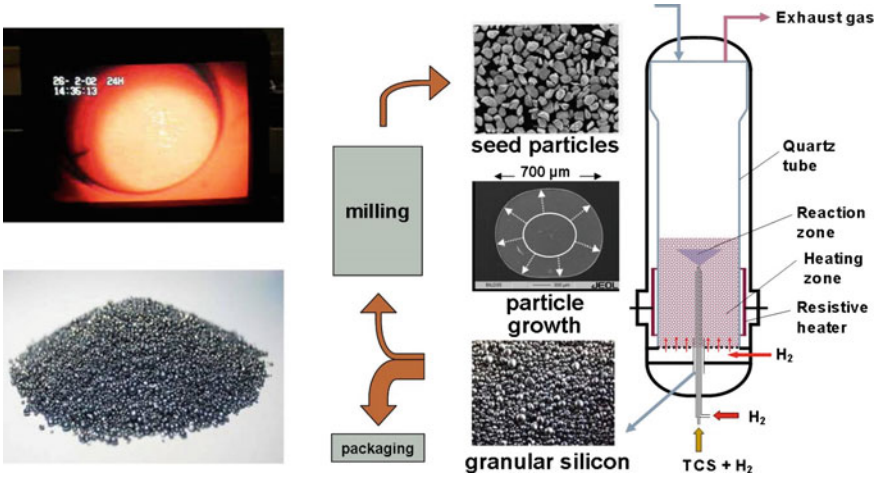

Fig. 3.6 Granular deposition

regarding handling, for high crucible filling grade (in combination with chunk material) and for applications which need a finely tunable continuous recharging. Wacker polysilicon is establishing this granular product to supplement its product portfolio.

3.1.5 The Myths of the "High Energy/High Cost" Rating of Established Silane-Based Polysilicon Deposition Technologies

There is a public understanding that the production of solar-grade feedstock via gas phase deposition is "too costly" because of the "high" energy consumption of the deposition process. And purification of silicon via metallurgical processes, that is, different melting und crystallization steps, slag refining, treatment with different gases and so on, is much less energy-consuming and therefore less expensive. But is this really true?

1. *Myth: High temperature = high energy consumption?* The first misunderstanding is that high temperature in a process equals high energy consumption. But if there is no energy-consuming reaction involved, the consumed energy is mainly influenced by the *energy losses*—a thermosbottle with hot fluid inside is also hot inside without being "energy intensive". It is a similar situation with the gas phase deposition. Energy consumption can be influenced a lot by scale, reactor design and process design. So the energy consumption figures given by O'Mara et al. [3] are much lower now. Also, the general belief that monosilane deposition is less energy-consuming than trichlorosilane deposition because of the lower deposition temperature is not correct if you consider the maximum

possible deposition rate: Trichlorosilane deposition rate can be much higher because heterogeneous monosilane deposition rate is much earlier limited by homogenous gas phase deposition (i.e. dust formation). The faster the deposition rate, the lower the energy losses. In addition, the high energy consumption for monosilane cryodistillation and storage have to be taken into account.

2. *Myth: The sum of chemical reactions, condensation and distillation steps of the silicon purification via silanes is more energy intensive than "direct" metallurgical purification*

Let us compare the trichlorosilane-based purification with typical metallurgical purification involving several melting/crystallization steps (e.g. JFE-process, Apollon solar process, [9, 10]) to reach the minimum required purity regarding metals by segregation. At established polysilicon producers the total energy consumption of the total TCS process is lower than 80 kWh/kg with a total silicon yield of much more than 90% [11]. In metallurgical refining one melting/directed solidification step of silicon needs about 10 [12] to 16 [13] kWh/kg for the target product. To reach a similar metal purity as the TCS process, you need at least three melting/solidification steps and still some elements cannot be efficiently removed due to their unfavourable segregation coefficient. In addition, you have energy losses by the melt treatment, for example, with slag refining, gases, electron beam guns (for elimination of phosphorus), plasma torches (removal of boron) and so on to bring the dopant concentrations to an acceptable level. The remaining purity regarding carbon and dopants will still be worse compared to the TCS process. And you have high yield losses by slag and metal contaminated parts after segregation.

So there is no reason to condemn the "chemical" silicon purification methods in favour of "metallurgical" methods with respect to the needed energy or yield.

3.1.6 *Alternative Technologies for the Production of Solar-Grade Feedstock: Purification of Metallurgical Silicon via Melt Treatment/Crystallization Is Dominating*

If you look at metallurgical methods you will find that they need energy-intensive melting and crystallization processes and special treatments for the removal of dopants which are connected with yield losses. The achievable quality is still far lower compared to gas phase deposition processes. The situation is similar to the carbothermic direct reduction of pure quartz with pure carbon as well as for the melt electrolysis of quartz. Other, already in the past evaluated and practised methods like the reduction of silicon compounds with metals, for example, $SiCl_4$ with zinc in vapour phase or aluminothermic reduction proved to be not competitive in the past regarding the achievable quality and costs. Important, limiting factors are the purities of the feed materials, contaminations during the process steps, low yields of reaction steps and complex reprocessing of by-products [14].

3.1.7 Alternative Vapour Phase Deposition Technologies?

In a closed-loop chlorosilane system, the above-mentioned problems are already solved in a large production scale; dominating technology is the heterogenous vapour phase deposition on rods. Thereby maximum purity is achieved. For solar-grade silicon also fluidized bed deposition of granules is a possibility. Others tested the deposition of silicon on hot surfaces with temperatures above melting point—"vapour to liquid" deposition [9]. The extremely corrosive nature of fluid silicon is here limiting the achievable quality. The lowest energy consumption in deposition is reached in so-called "free space" reactors; here silanes are decomposed in a homogenous gas phase reaction. But the resulting silicon is in the form of very fine particles ("dust"), which was not usable in this form in the past because of the highly reactive, respectively oxidized surface and the low density which led to melting problems and the contamination problem during handling of the material.

3.2 Quality Requirements from the PV Market

As shown in Fig. 3.7 solar cell efficiencies are expected to increase further. High efficiency approaches such as PERC, HIT or back contact cells are likely to gain market share over the next years. In addition, the solar industry is working hard to improve process efficiencies, yields and quality at each step of the value chain (ingot, wafer, cell and module). Highest charge carrier lifetimes, highest yields and most efficient production strategies are accessible with high-quality polysilicon feedstock. As a consequence, high-quality polysilicon enables the PV industry to produce highest

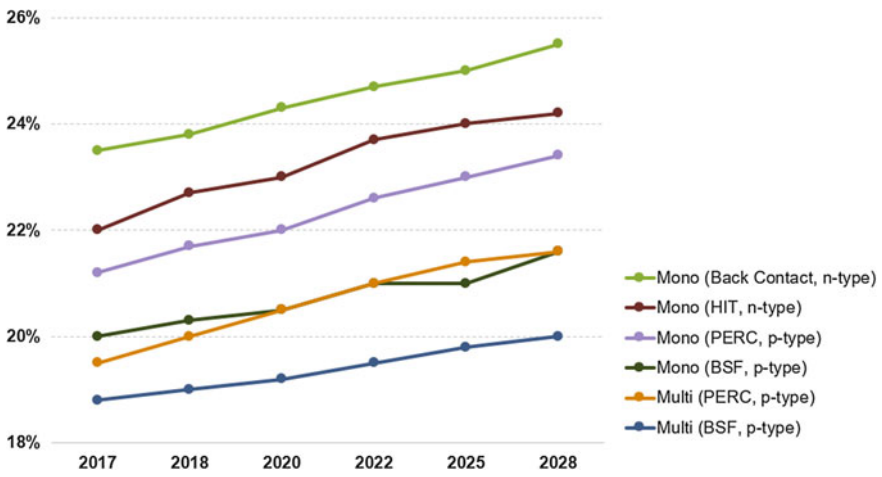

Fig. 3.7 Expected development of solar cell efficiencies [8]

quality PV products with reliable long-term stability at lowest possible cost—one of the key drivers for the success of photovoltaics also in the future.

3.3 Summary

TCS will remain one of the semiconductor and photovoltaic industries' most important feedstock in the future, regardless of whether used as a direct feedstock to produce polysilicon in the Siemens and granulate processes or as a raw material for monosilane production. For more than 60 years, the Wacker group is using and improving polysilicon production based on vapour phase deposition of TCS in a closed-loop process. Hydrogen and chlorine are processed in a cycle, and process heat is used efficiently in the chemical plant system. This process is safe and environmentally friendly and has plenty of potential for further improvement. Wacker Chemie AG is operating three world-scale production sites for polysilicon with a total production capacity of 80,000 metric tons in 2017 (Fig. 3.8).

In parallel, the downstream users are continuously improving their processes and product qualities. Besides higher cell efficiencies and reliable long-term stabilities (based on high-quality feedstock), advanced crystallization techniques, smaller wafer thicknesses, lower kerf loss during sawing and overall higher process yields, there is still huge potential to lower costs further—the basis to establish photovoltaics as one of the major energy sources of our future (Fig. 3.9).

Fig. 3.8 Integrated polysilicon production of Wacker Chemie AG in Burghausen, Nünchritz (both Germany), and Tennessee (USA)

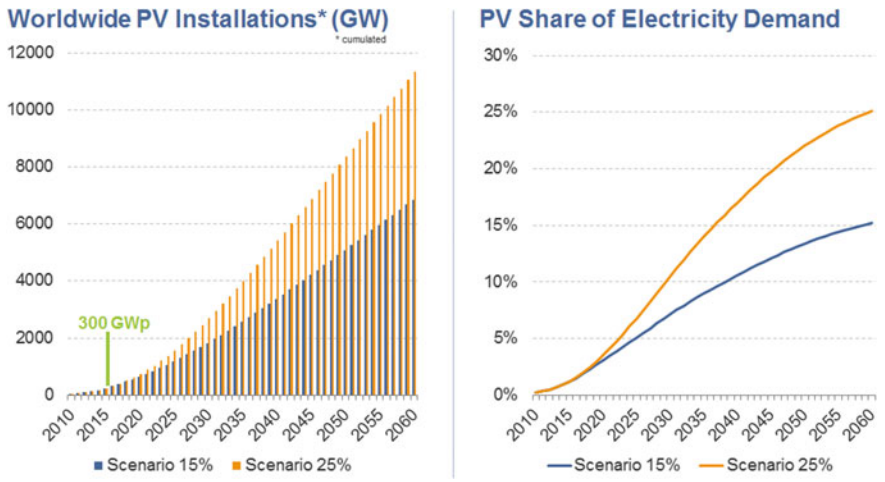

Fig. 3.9 Projected development of photovoltaics [15, 16]

References

1. A. Schei, J. Tuset, H. Tveit, *Production of High Silicon Alloys* (1998)
2. Ferroglobe presentation, Inaugural Investor Day, 17 October 2017, p. 8
3. W.C. O'Mara, R.B. Herring, L.P. Hunt (eds.), *Handbook of Semiconductor Silicon Technology* (1990)
4. D. Weidhaus, E. Schindlbeck, K. Hesse, *Silicon for the Chemical Industry VII* (2004), p. 165. ISBN 82-90265-25-5
5. Analysis Wacker Chemie AG, June 2017
6. T. Lobreyer, K. Hesse, *Silicon for the Chemical Industry IV* (1998), p. 93. ISBN 82-90265-20-4
7. W.C. Breneman, H.J. Dawson, *Silicon for the Chemical Industry IV* (1998), p. 101. ISBN 82-90265-20-4
8. ITRPV Roadmap 2018, www.itrpv.net
9. 3rd Solar Silicon Conference, 2, München. April 2006
10. 21st European Photovoltaic Solar Energy Conference, Dresden, 4–8 Sept. 2006
11. China PV Industry Association, China PV Roadmap (2016), p. 7
12. E. Sirtl, The WACKER approach to low-cost silicon material technology, in *Proceedings 3rd EC PV Solar Energy Conference*, Cannes (1980), p. 236 ff
13. J.O. Odden, G. Halvorsen, H.M. Rong, R. Glockner, Comparison of the energy consumption in different production processes for solar grade silicon, in *Silicon for the Chemical and Solar Industry IX* (2008), p. 87. ISBN: 978-82-997357-5-9
14. Flat-Plate Solar Array Project Final Report, vol. II: Silicon Material, JPL Publication 86-31, October 1986
15. W. Storm, Wacker Chemie AG, Photovoltaik – Vom Silicium zur Sonnenenergie, Presentation Wacker Wissensforum, 4 April 2017
16. International Energy Agency (IEA), World Energy Outlook 2017. www.iea.org

Chapter 4
Silicon Nitride and Aluminum Oxide—Multifunctional Dielectric Layers Crucial for the Progress of Silicon Solar Cells

R. Hezel and K. Jaeger-Hezel

Abstract The achievement of high efficiencies for crystalline silicon solar cells is highly dependent on the reduction of carrier recombination at both cell surfaces. As a new era in PV, this loss of charges can be minimized by simply depositing silicon nitride or aluminum oxide layers at low temperatures. Due to their fascinating properties, both dielectric films became key components of present and future monofacial and bifacial silicon solar cells. As a special highlight, by an innovative aluminum oxide-based rear side scheme, high efficiency industrial cells (PERC) could be developed which are generally regarded to become next-generation solar cells.

4.1 Introduction

The achievement of high efficiencies for crystalline silicon solar cells is highly dependent on the reduction of carrier recombination at both cell surfaces. For high-efficiency laboratory solar cells thermally grown silicon dioxide (SiO_2) layers have been applied to obtain very low effective surface recombination velocities (SRV) [1]. Despite thermal SiO_2 has excellent passivation properties on phosphorous diffused silicon surfaces as well as on n- and p-type silicon wafers it requires high processing temperatures (>900 °C) and long processing time. This treatment can severely degrade the bulk minority carrier lifetimeLifetime, particularly of lower quality silicon material, e.g., multicrystalline silicon. Very clean production equipment, expensive electronic grade gases, and thorough cleaning of the samples are needed to avoid contamination and diffusion of unwanted impurities into the bulk.

R. Hezel (✉)
University of Hannover and ZAE Bayern, Josef-Heppner-Straße 26, 82049 Pullach, Germany
e-mail: rudolf.hezel@t-online.de

K. Jaeger-Hezel
Munich University of Applied Sciences, Josef-Heppner-Straße 26, 82049 Pullach, Germany
e-mail: jaeger-hezel@lrz.fh-muenchen.de

V. Petrova-Koch et al. (eds.), *High-Efficient Low-Cost Photovoltaics*,
Springer Series in Optical Sciences 140,
https://doi.org/10.1007/978-3-030-22864-4_4

This is undesirable from production cost and throughput considerations [2]. Similar problems arise with the implementation of a back surface-field (BSF) which provides only moderate surface passivation. This fabrication step is still used for the rear side of the present mainstream solar cells [3]. Furthermore, thermal SiO_2 does not provide efficient reflection reduction because of its low refractive index. Traditional antireflection layers such as TiO_x or Ta_2O_3 can be deposited in a rather cheap low-temperature process but they do not provide good surface passivation and delamination problems are reported.

In order to obtain reliable high-efficiency solar cells with a simple technology low-temperature-processed dielectric layers had to be found providing excellent surface passivation together with good optical and surface protecting properties.

Inspired by our research activity in microelectronics [4, 5] the two multifunctional dielectric films, silicon nitride (SiN_x) and aluminum oxide (Al_2O_3), appeared to us to be also attractive for photovoltaics and in 1978 low-temperature surface passivation of silicon solar cells could be first introduced at the University of Erlangen (FAU) by these two dielectric materials [6–8].

As to silicon nitride, our pioneering work was starting with its first application as a passivating antireflection layer for solar cells, followed by intensive basic and applied research for further optimization [7]. In 1981 plasma-enhanced chemical-vapor-deposited (PECVD silicon nitride) was introduced in our lab for silicon solar cells [9]. In 2004 these activities were culminating in the development of a high-throughput in-line machine for large-scale low-temperature plasma deposition of silicon nitride [10, 11]. Providing high-quality SiN_x passivation and antireflection layers on an industrial scale was a decisive contribution to the first mass production of reliable solar cells. Subsequently, the production volume increased dramatically. Today, for worldwide 90% of the mainstream silicon solar cells plasma silicon nitride layers are used. They are gaining even more importance for next-generation solar cells.

As another highlight, in 1985 Al_2O_3 layers were first applied by us for silicon solar cells in order to substitute the conventional back surface-field to further reduce carrier recombination at the rear side and their unique properties were investigated [8, 12]. An innovative rear surface configuration with gridded base contacts and Al_2O_3 as passivation between the line-shaped contact fingers was established and successfully implemented in silicon solar cells [8, 12–14]. Decades later this early work was reintroduced and intensively studied in many research labs all over the world [15, 16]. Our rear surface design was implemented in the so-called PERC solar cells which are regarded as the next-generation silicon solar cells [3, 17, 18]. Both Al_2O_3 and SiN_x layers are applied for these devices. Mass production started in 2013.

In this article, the fascinating properties of both dielectric films are reviewed and their crucial role for present and future commercial silicon solar cells is outlined. Among others, the early history and our pioneering contributions at the University of Erlangen and later at the Institute for Solar Energy Research in Hameln (ISFH) are extensively discussed.

4.2 Silicon Nitride Layers for Solar Cells

4.2.1 Protection Properties

Long-term stability is a prerequisite for the successful utilization of solar electricity. Due to their outstanding protective properties, SiN_x coatings turned out to be determining the ultimate reliability of solar cells. At the University of Erlangen much basic work was done including physico-chemical analysis to characterize and understand the properties of SiN_x films.

By a combination of Auger electron spectroscopy (AES) and low energy electron energy loss spectroscopy (ELS) quantitative information about the chemical bonding states in thin amorphous SiN_x films were obtained. The ground and excited states of the Si–N bonds could be characterized and an electron level scheme for silicon nitride was derived [19–22].

Electron and ion bombardment in the course of electron spectroscopy and scanning electron microscopy revealed outstanding stability of silicon nitride with chemical bonds much stronger compared to silicon oxide [23, 24]. This is demonstrated in Fig. 4.1, where for thermal SiO_2 and Si_3N_4 the effect of a 3 keV irradiation on the Si_{LVV} Auger spectrum is shown as a function of the beam exposure time [24]. In

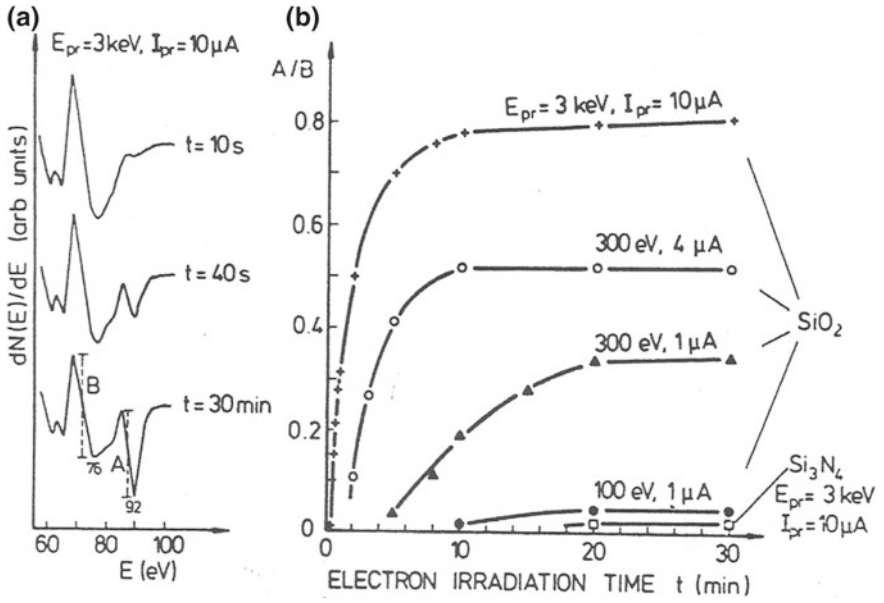

Fig. 4.1 **a** Effect of electron beam irradiation on the Si_{LVV} Auger spectrum of SiO_2 at Epr = 3 keV and I_{pr} = 10 μA. **b** The p-p heights ratio A (92 eV)/B(76 eV) for various electron beam parameters as a function of irradiation time. The ratio A(92 eV)/B(83 eV) of the Si_{LVV} spectra of Si_3N_4 is also plotted

all cases in the Si_{Lvv} spectrum the irradiation results in the appearance of the 92 eV line which is characteristic for elemental silicon (Fig. 4.1a). The p-p height A of the 92 eV line relative to the height B of the main peak of 76 eV in the spectrum is taken as a measure for the creation of "free" silicon by breaking of Si–O bonds and subsequent electron-stimulated desorption (ESD) of oxygen (Fig. 4.1b) [25].

For the Si_{LVV} Auger spectra of silicon nitride (not shown in Fig. 4.1) the p-p height A of the 92 eV line—breaking of Si–N bonds and formation of Si–Si bonds—relative to the height B of the corresponding main peak at 83 eV is also plotted in Fig. 4.1b. As a striking result, in comparison to silicon oxide for silicon nitride an almost negligible irradiation effect can be observed. Qualitatively similar results as for the case of electron irradiation were obtained for argon ion bombardment [21].

According to these and other experimental results it can be concluded, that silicon nitride layers, unlike SiO_2, can provide excellent protection of the surface and bulk of silicon solar cells.

It is well known that silicon nitride provides excellent protection against contamination by blocking all kinds of foreign species from diffusing into the sensitive silicon substrate [26]. Already extremely small quantities are deleterious for the carrier lifetime and thus for the cell efficiency. As a positive exception, only hydrogen is mobile in the nitride layer which is beneficial in minimizing charge recombination at the surface and within the bulk of silicon by saturation of dangling bonds (see Sect. 4.2.3). The excellent barrier of SiN_x for moisture together with scratch and crack resistance and low mechanical film stress have to be mentioned [5]. SiN_x also serves as mask against etching and high-temperature diffusion of dopants during device fabrication. Progress in contact formation for solar cells could be achieved since SiN_x proved to withstand the firing of metal contacts through the already deposited surface film [27].

4.2.2 Optical Properties

The power output of a solar cell is directly dependent upon the amount of incident sunlight which is absorbed by the cell. Therefore, a major consideration in the design of solar cells is the reduction of losses caused by reflection and shadowing. Minimizing reflection losses from the non-metallized area of the cell is generally accomplished by coating the surface with one or more highly transparent dielectric layers of lower refractive index than the silicon itself and/or by texturing the surface of crystalline substrates via chemical etching the wafers in anisotropic etchants resulting in an array of pyramids. PECVD (**P**lasma-**E**nhanced **C**hemical **V**apor **D**eposition) silicon nitride acts as excellent surface-passivation and antireflection coating, a combination which is not met by the standard coatings on silicon solar cells [28]. As a special advantage of PECVD silicon nitride, the refractive index n can be varied over a wide range (from about 1.6–2.6). It thus can be easily optimized for a single and multilayer AR coating by the CVD preparation conditions. The refractive index is linearly correlated to the Si/N ratio of the films. For stoichiometric Si_3N_4 n is about 1.95,

higher indexes are obtained if the films contain excess Si. On the front surface of solar cells n should be close to the optimum of 2.0 in order to minimize optical losses due to reflection and absorption. Light absorption by the nitride films in the visible and near UV region of the solar spectrum can be kept very low. With silicon nitride on a textured silicon surface reflection of sunlight below 3% is achieved making the cell appearing dark.

4.2.3 Passivation Properties

One of the most outstanding advantages of the thin multifunctional PECVD silicon nitride layers is their ability to drastically reduce the loss of light generated charge carriers on front and rear side as well as in the bulk of the solar cell and thus considerably increasing cell efficiency.

Surfaces of silicon represent rather severe defects in the crystal structure owing to non-saturated ("dangling") bonds. These "surface states" act as recombination centers for the light generated electron hole pairs hence reducing the number of charge carriers. Passivation, i.e., minimizing surface recombination is thus a prerequisite for achieving high efficiency solar cells. Extrinsic silicon surface passivation is based upon the Shockley-Read-Hall theory [12, 29]. According to this the recombination of charge carriers via surface states is dominated by those centers that are located near the middle of the forbidden energy gap. The recombination rate reaches its maximum in case of depletion when the electron and hole concentrations at the surface are equal. If the concentration of one partner is strongly reduced in case of inversion or accumulation, a much lower recombination rate results. This can be realized by the formation of an internal electric field below the silicon surface, e.g., by fixed positive or negative charges in a surface dielectric film thus as SiN_x or Al_2O_3. As a special advantage, the low-temperature processed PECVD films are combining two very effective mechanisms for passivation of the silicon surface [12]. (i) Reducing the density of surface states by chemical passivation and (ii) field effect passivation via fixed insulator charges.

Chemical Passivation by Intrinsic Hydrogen

During nitride deposition, e.g., by the reaction of the two gases silane (SiH_4) and ammonia (NH_3) in a glow discharge hydrogen is released and up to 30% are incorporated in the amorphous films which are, therefore, often designated as a-SiN_x:H, abbreviated as SiN_x throughout this work [30]. By ELS spectroscopy a new electron energy loss peak at 8.6 eV was detected and was related to the presence of chemically bonded hydrogen [31]. The very active hydrogen species terminates unsaturated bonds at the silicon surface thus lowering the density of surface states. The low interface state density of 8×10^9 cm^{-2} eV^{-1} for nitride films deposited at 270 °C and annealed at 500 °C is attributed to the saturation of unsaturated bonds at the silicon surface by hydrogen originating from N–H bonds [32].

To a certain degree also other electronic states caused by crystal defects in the bulk such as dislocations or grain boundaries in multicrystalline silicon including silicon ribbons [33] are inactivated by hydrogen diffusing into the wafer during film deposition or by a post-deposition heat treatment. Hence also the bulk diffusion length can be improved resulting in a further increase of the cell efficiency [34].

Field Effect Passivation by Fixed Insulator Charges
SiN_x contains a high density of long-term-stable positive charges causing strong inversion consisting of electrons at the surface of p-type silicon. Hence, as outlined above, low surface recombination rates are achievable by field effect passivation. For PECVD SiN_x fixed charge densities up to $Qn/q = 7.2 \times 10^{12}$ cm^{-2} are observed [9, 32, 35]. By incorporation of sodium [36] or cesium [37] the charge densities can be further drastically increased up to 1.5×10^{13} cm^{-2} without significantly affecting the low surface state density.

The combined effects of charge induced and hydrogen passivation are reflected in the surface recombination velocity S_{eff} which is discussed further below.

4.2.4 First Application of Silicon Nitride for Solar Cells

In 1981 the first and most demanding application of PECVD SiN_x layers for silicon surface passivation was its use as charged dielectric in a novel type of solar cells, the so-called inversion layer cell [9]. Simple low-temperature fabrication and the use of aluminum instead of expensive silver for metallization are attractive advantages compared to the conventional pn-junction solar cells. Worldwide extensive research was performed with similar structures whereby as transparent dielectrics the previously used antireflection layers such as thermal SiO_2 [38], TiO_x and CVD-SiO_2 [39], SiO_x [40, 41] and Ta_xO_y [42] were applied. Efficiencies up to 16% are reported [42]. However, a major shortcoming of all these solar cells was that they were suffering under severe stability problems.

For the inversion layer solar cells studied at the University of Erlangen, the simple fabrication consists of deposition of the highly transparent positively charged PECVD SiN_x layer on undiffused p-type silicon and a tunnel MIS (**M**etal **I**nsulator **S**ilicon) contact grid with a tunnel Si oxide of 1.5 nm in thickness [9]. In the area between the parallel grid lines an inversion layer is induced at the silicon surface, which is responsible for surface passivation and provides a conducting path to the MIS contacts for the light generated electrons. Therefore, in addition to a high density of stable insulator charges and a low density of fast interface states also a low inversion layer sheet resistance is required [12]. Creation of interface states during cell operation, in addition to surface recombination, also leads to a reduction of the electron mobility and thus to an increase of the inversion layer sheet resistance. Both effects are significantly contributing to the loss of solar cell efficiency.

As a conclusion, inversion layer solar cells are extremely surface sensitive electronic devices and are, therefore, excellent test tools for the quality and particularly

long-term stability and industrial applicability of passivation layers for silicon solar cells. In the eighties silicon nitride was further optimized for inversion layer solar cells and in 1990 the technology was transferred from the University lab to a 1 MW industrial pilot line [43]. This transfer was honored by the German Industry with the Innovation Award 1992.

The 10 × 10 cm^2 solar cells using plasma SiN_x as charged dielectric successfully passed the specific endurance tests [44]. Peak efficiencies exceeding 15% could be obtained [43]. (About 10 years later laboratory cells reached efficiencies up to 19.6% [45].)

In 1994 as a joint Spanish/German project 450 kW of the cells encapsulated in novel large area double glass modules were installed in Europe's largest photovoltaic plant in Toledo/Spain (1 MW total). Encouraging results could be reported clearly demonstrating the excellent long-term stability of the inversion layer modules [46]. For the next step towards a 10 MW production line cost-competitive high-rate evaporation of aluminum for front and back-contacts were required. However, such an evaporation machine was not available from the equipment manufactures at this time, so that the successful project could not be continued [47].

From the above over decades successful field test using the surface sensitive inversion layer solar cell structure the important conclusion can be drawn, that PECVD SiN_x films have been proven to be excellent candidates for the reliable large-scale passivation of future industrial silicon solar cells.

4.2.5 *Further Optimization of PECVD Silicon Nitride*

Stimulated by these promising results from 1995 onward further research was focused on the optimization of the SiN_x/Si interface quality, now at the Institute for Solar Energy Research (ISFH) and elsewhere. Figure 4.2 shows the dependence of the

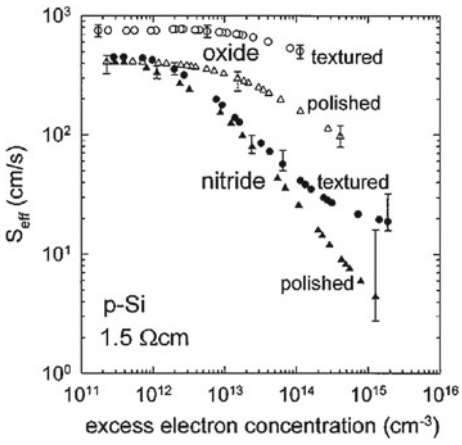

Fig. 4.2 Measured $S_{eff}(\Delta n)$ dependence at polished and textured 1.5 Ωcm p-Si wafers passivated by remote plasma silicon nitride and thermally grown silicon dioxide

surface recombination velocity S_{eff} on the bulk excess carrier concentration Δn for polished and chemically textured 1.5 Ωcm p-Si wafers passivated by thermally grown silicon dioxide and remote PECVD silicon nitride [48]. This configuration corresponds, e.g., to the non-metallized passivated rear surface regions including bifacial solar cells. As can be seen, for injection levels of relevance for photovoltaic applications (i.e., $\Delta n > 10^{13}$ cm^{-3}) the remote SiN_x film provides far better surface passivation than the thermal Si oxide. At the highest measured injection levels of 10^{15} cm^{-3} the polished SiN_x passivated surface yields a surface recombination velocity (SRV) of 4 cm/s compared to 100 cm/s for the thermally oxidized surface. This is one of the lowest SRV that has ever been obtained on a low resistivity p-Si wafer passivated by a solid film. Even for the nitride passivated textured wafer to reduce light reflection a S_{eff} value of only 19 cm/s is obtained. High-quality surface passivation could also be obtained in an industrial type in-line remote microwave silicon nitride deposition system with S_{eff} values of 10 cm/s, making the surface passivation in this system practically equivalent to that of the best laboratory PECVD reactor [10, 49].

Most of the present laboratory as well as industrial silicon solar cells are based on p-type wafers with a front-side phosphorous diffused n^+-emitter, screen-printed metallization, and a full-area Al-p^+ back surface-field (Al-BSF). Passivation of these devices by PECVD SiN_x is the topic of several papers [50]. Also a systematic optimization of remote PECVD SiN_x films for n^+-emitters was performed in our lab [10, 51]. With remote plasma as well as with HF direct plasma SiN_x films very good surface passivation can be obtained if the refractive index is greater than about 2.0, i.e., if silicon-rich SiN_x films are applied. Furthermore, these plasma SiN_x passivated emitters exhibit an excellent thermal stability and are perfectly stable against UV exposure. Efficiencies up to 21% could be achieved for lab type diffused junction solar cells [52, 53].

To summarize, compared to thermal oxides grown at high temperatures, low-temperature remote PECVD SiN_x films provide about equal surface passivation on phosphorous diffused Si–surfaces and significantly superior surface passivation on low resistivity p-Si wafers. Together with the higher refractive index, these films can perfectly be applied as reliable passivating AR coatings for high-efficiency silicon solar cells.

4.3 Plasma-Enhanced Deposition Techniques

Initially silicon nitride layers prepared by atmospheric pressure (APCVD) and low-pressure chemical vapor deposition (LPCVD) were studied in our lab at the University of Erlangen and successfully applied for solar cells [7, 19, 22]. These films were deposited in a hot wall reactor at temperatures between 630 and 900 °C by the reaction of silane (SiH_4) and ammonia (NH_3). Good interface properties could be demonstrated [32, 35].

In 1981, for the sake of lower deposition temperatures and several other advantages, as an alternative plasma-enhanced chemically-vapor-deposited (PECVD) silicon nitride layers were first introduced by us as passivation and antireflection films for silicon solar cells [9, 32]. It could be realized by a variety of experiments that the properties of PECVD SiN_x depend strongly on the type of the reactor as well as on the deposition parameters. There are two fundamentally different plasma reactor designs, parallel plate (often referred to as "direct") and "remote".

4.3.1 Parallel Plate Plasma Reactor

In this version, the wafer is placed onto one of two electrodes where the processing gases silane and ammonia are excited by an electric field and the wafers are in direct contact with the plasma. The electromagnetic field has a frequency of either 13.56 MHz ("high frequency" or HF mode) or lies in the 10–500 kHz range ("low frequency" or LF mode). The systems are made up of an array ("boat") of disk-like metal plates in a long furnace tube enabling the simultaneous processing of a large number of silicon wafers. A special phenomenon could be observed by extensive investigations in our lab, that the plasma excitation frequency has a strong impact on the electronic properties of the silicon/silicon nitride interface [54–56]. It was found that the nitride deposition by low frequency direct PECVD does not significantly affect the initial performance of the surface sensitive inversion layer solar cells as well as the interface properties. However, under UV light severe degradation occurs. This behavior is attributed to the generation of interface states during the direct LF plasma deposition process accompanied by their simultaneous passivation with hydrogen. These "latent" states (apparently weak Si–H bonds) are activated by UV light. As to the interface state generation during film deposition, below the so-called plasma frequency (about 4 MHz) ions are able to follow the plasma excitation frequency producing significant surface bombardment. In the high frequency regime (HF) bombardment of the substrate surface is minimized since the ions cannot follow the excitation of the electromagnetic field. Hence SiN_x films prepared by direct PECVD at high frequency (13.6 MHz) provide better surface passivation and excellent UV stability than SiN_x films prepared at low frequency (10–500 kHz) [57].

Inspite of its success the direct plasma batch method has a number of major drawbacks and technical limitations with regard to the low-cost mass production of SiN_x-coated silicon solar cells [58].

4.3.2 Remote Plasma Reactor

The second and most successful class of plasma reactors is formed by the downstream or remote system which was introduced into photovoltaics in 1989 by the author's group at the University of Erlangen [59]. An important feature of the remote PECVD

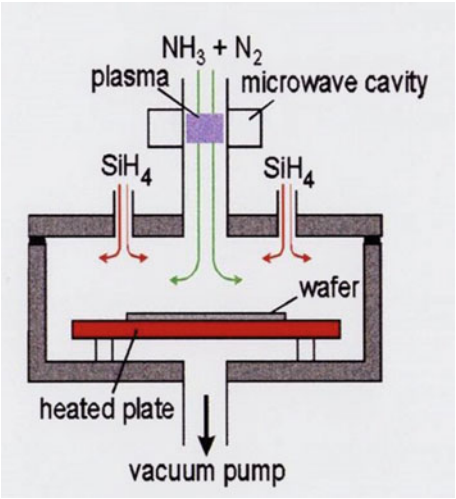

Fig. 4.3 Schematic of a static remote PECVD reactor

systems is that the silicon wafer is located outside the plasma region, allowing the deposition of SiN_x films with no surface damage to the wafers and making the frequency relatively unimportant.

Figure 4.3 shows a schematic of the static laboratory-type remote PECVD system with downstream geometry (Oxford Plasmalab 80). A mixture of ammonia and nitrogen is excited by passing through a 2.45 GHz-microwave cavity and mixes with silane downstream of the plasma. The reaction takes place above the substrate which is placed on a heated plate. It has been shown to give excellent surface passivation on both p- and n^+-type silicon and was successfully used for the coating of high efficiency solar cells in our lab [49, 51, 52].

Development of an Industrial In-Line Remote PECVD System

For industrial production of SiN_x coatings, a high–throughput PECVD system is required. In 1998 the first industrial solar cell line in Germany began its operation at the ASE company. Direct PECVD was used for SiN_x deposition. Due to several drawbacks of these parallel plate batch mode reactors for the second production line a remote PECVD in-line system should be developed [60]. In 2000 this development occurred in tight cooperation between our research institute ISFH, the solar cell producer ASE (later Schott Solar) and the equipment manufacturer Roth&Rau. Figure 4.4 shows a cross section of the deposition system which consists of a processing chamber and two load looks for the entry and exit of the wafer carriers [10, 11]. Inside the evacuated processing chamber two heating plates form an isothermal tunnel as a second preheating stage. In the plasma source two quartz tubes are mounted perpendicular to the wafer transport direction. The microwave antennae are located in the center of these quartz tubes. Two rows of magnets are installed alongside the tubes which stabilize the plasma in the low-pressure regime by forcing electrons on curved paths.

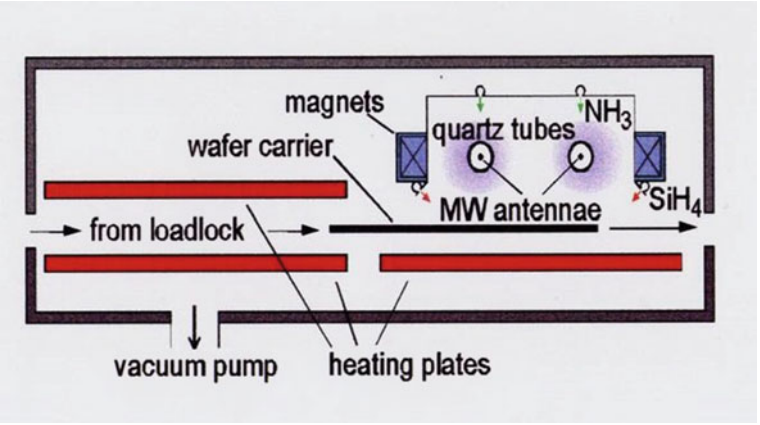

Fig. 4.4 Schematic cross section of a microwave in-line remote PECVD system

Ammonia is fed into the source above the tubes, whereas silane is added below at the sides of the plasma source. The plasma is excited around the quartz tubes by means of two continuous-wave magnetron microwave generators with a frequency of 2.45 GHz. The carrier rests on rollers, by which it is transported linearly through the vacuum chambers. A throughput of several thousand wafers/hour can be obtained in continuous operation.

Due to our long experience with silicon nitride the in-line deposition system has been set up for process development at the ISFH laboratory. After demonstrating that industrial scale throughput can be obtained while maintaining good surface passivation the deposition system was transferred by the ISFH staff to ASE GmbH and successfully implemented into the solar cell production line. Roth&Rau subsequently commercialized this tool under the name "SINA" and very soon became the world-leading supplier for remote in-line PECVD systems [61]. This importantly paved the way for the economic mass production of silicon solar cells worldwide since reliable low-temperature passivating antireflection SiN_x layers could be provided on a large-scale [10, 11].

4.4 Silicon Nitride Passivated Bifacial Solar Cells

Excellent passivation of both surfaces is of prime importance for highly efficient solar cells. This also allows a further increase in power output density by utilizing the light incident on the solar cell from the front and rear side. By the proper installation of such bifacially sensitive solar modules directing light also onto the rear surface, power gains up to 50% is achievable [43, 62, 63, 64].

Bifacial cells have a long history and great efforts have been made regarding both development as well as the application of these devices for space and terrestrial

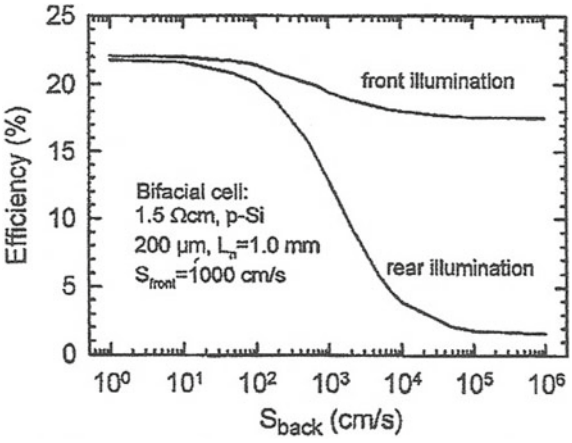

Fig. 4.5 Calculated dependence of the 1-sun efficiency of a bifacial Si solar cell on the area-averaged rear surface recombination velocity S_{back}

systems [64]. In the eighties low-temperature dielectric rear surface passivation was applied for monofacial and bifacial solar cells in order to substitute the complex high-temperature-processed back surface-field of the standard silicon cells [12, 13, 65].

In Fig. 4.5 the importance of rear surface passivation is demonstrated by the calculated dependence of the cell efficiencies on the rear surface recombination velocity S_{back} [66]. As can be seen for the special case of Fig. 4.5, the front efficiency increases significantly with decreasing S_{back}, however, the improvement of the rear efficiency is much more pronounced. For a poorly passivated rear surface ($S_{back} > 10^4$ cm/s) the rear efficiency is smaller than 5% whereas for a well passivated rear surface ($S_{back} < 10^2$ cm/s) rear efficiencies higher than 20% can be reached.

As already shown in Fig. 4.2, much lower surface recombination velocities down to record values of 4 cm^2/s are experimentally possible for p-Si using remote plasma silicon nitride layers [49]. These SiN_x films together with their excellent optical properties also provide very good surface passivation on phosphorous diffused emitters so that highly efficient bifacial n^+p silicon solar cells are obtainable by deposition of silicon nitride on front and rear side [56].

Based on our successful application of PECVD silicon nitride as charged passivating antireflection film for the front-side of inversion layer solar cells, in 1986 this multifunctional dielectric layer was applied by us for rear side passivation according to the novel scheme consisting of a line-shaped aluminum base contact grid in combination with the passivation layer between the grid fingers [13, 65, 12].

As the first application for 100 µm thick induced junction bifacial solar cells efficiencies of 15 and 13.2% for front and rear illumination, respectively, could be achieved [43, 65]. Extensive outdoor measurements for various albedo-conditions were performed with 100 µm 10 × 10 cm^2 bifacial cells in glass/glass modules of different size up to 0.43 × 1.15 m^2 [67].

With the fabrication of a 100 cm^2 CZ-Si n^+p-solar cell in a pilot production line at ASE 16.5% front and 13.8% rear efficiencies, respectively, were resulting [68].

Another fully nitride passivated 4 cm^2 bifacial n^+p-silicon solar cell was introduced in 1997 with efficiencies up to 20.1% under front illumination [69] and up to 18.1% under rear illumination [66]. As can be seen from Fig. 4.6, this cell combines the excellent surface passivation properties of remote PECVD SiN_x/SiO_x double layers with a simple local Al back surface-field. It was the first bifacial silicon solar cell to exceed 20% front efficiency [69].

A completely different nitride passivated diffused pn-junction device is characterized by a corrugated rear surface and both contact grid systems placed on the steep flanks of the ridges at the rear side [70, 63]. Bifacial sensitivity is automatically included with extremely low grid shadowing together with the advantages of back-contact solar cells for efficiency, module fabrication and visual appearance. A schematic of this back collecting bifacial "BACK OECO" (**O**bliquely **E**vaporated **Co**ntacts) cell is shown in Fig. 4.7. Solar cells, 4 cm^2 in size, were processed

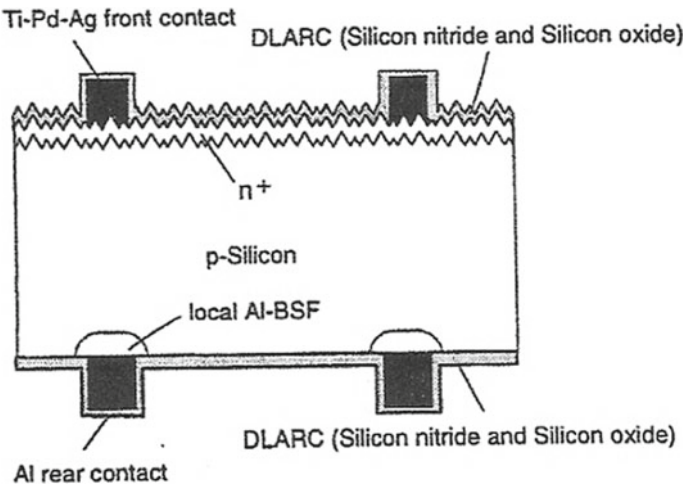

Fig. 4.6 Schematic representation of a bifacial n^+p-silicon solar cell with double layer AR coatings [69]. Monolayer SiN_x coatings are applied in [66]

Fig. 4.7 Schematic of the nitride passivated back collecting and bifacially sensitive BACK OECO solar cell. Both contact lines are placed on the steep flanks of the ridges at the rear side

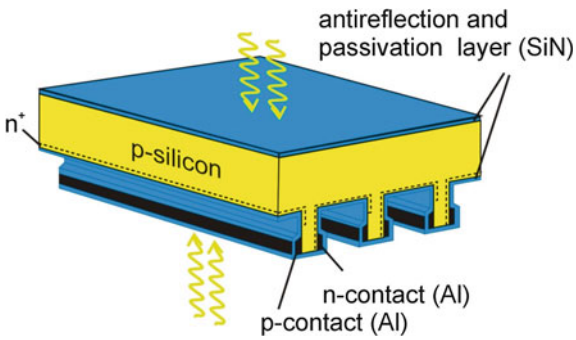

using 0.5 Ωcm silicon wafers with an effective base thickness of 150 μm. Efficiencies of 21.5% and 17.7% could be achieved for front and rear side illumination, respectively [70].

4.5 Aluminum Oxide for Next-Generation Solar Cells

The future of solar cell production still lies in further increasing cell efficiency while simultaneously reducing production costs. Upgrading the present standard n^+p-silicon technology by replacing the efficiency limiting full-area Al-p^+ back surface-field (BSF) is commonly regarded as an effective procedure without much additional costs. Low-temperature dielectric passivation of the rear surface plays a crucial role.

Already in the eighties, a substitute for the conventional BSF was introduced at the University of Erlangen with a novel rear side scheme suitable both for monofacial and bifacial solar cells in order to drastically reduce carrier recombination. As described above for the rear side of bifacial solar cells this novel design is achieved by gridding the base contact to minimize its area and depositing a thin passivating dielectric layer on the silicon surface between the contact fingers [8, 12, 13, 65].

It was demonstrated in the preceding chapter that PECVD SiN_x turned out to be a reliable antireflection and passivation layer and is now used on the front-side of the mainstream silicon solar cells worldwide. However, if the nitride layers are incorporated in the above mentioned rear surface passivation scheme parasitic effects have been identified by us which, to a certain extent, decrease cell performance [71, 66]. The performance loss is mainly due to a lower short-circuit current of the cells. Our experiments clearly revealed parasitic shunting of the inversion layer induced by the positively charged SiN_x films with the rear contact grid [71]. The coupling of the inversion layer with the base contacts can be mitigated by several means, e.g., lowering the inversion layer sheet conductance by the introduction of a thin plasma SiO_x film beneath SiN_x. This step was already applied for the bifacial cell shown in Fig. 4.6 [69] and later by Agostinelli et al. [72]. In 2011 a SiO_x/SiN_x stack was implemented in a production line [73].

Alternatively, a thin Si-rich SiN_x layer (refractive index $n = 2.5$) beneath the standard nitride ($n = 2.05$) was introduced in the back-contacted bifacial solar cell shown in Fig. 4.7 [70, 63]. In all cases by the double layer the fixed positive insulator charge density and thus the shunting effect is reduced.

4.5.1 Al_2O_3—Based Rear Surface Passivation Scheme

In 1985 significant progress with respect to rear surface passivation and parasitic shunting could be achieved at the University of Erlangen by the introduction of aluminum oxide as another outstanding charged dielectric in combination with a novel rear side scheme based on line-shaped local rear contacts (see Fig. 4.8). The

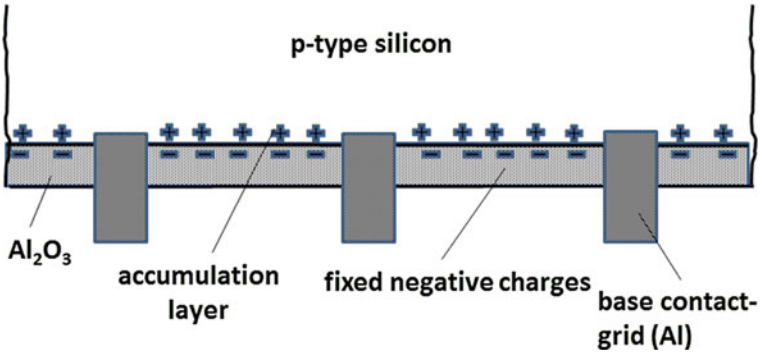

Fig. 4.8 Basic structure of the innovative rear side scheme of locally contacted and Al_2O_3—passivated p-type silicon solar cells for monofacial and bifacial application [8, 12, 13]

crucial properties for low-temperature passivation were already investigated [8, 12, 13]. As demonstrated in Fig. 4.9, this early innovation became the basic element of the industrial PERC device, which is world-wide regarded as the next-generation solar cell.

Most relevant for rear side passivation are the fixed negative charges present in the Al_2O_3 film which are attracting holes as the majority carriers to form an accumulation layer on p-type silicon [8]. This positively charged layer acts as a barrier for electrons so that recombination and hence loss of light generated charge carriers is significantly reduced ("field effect passivation"). As shown in Fig. 4.8 the novel rear side scheme is made up of a parallel base contact grid and an Al_2O_3 layer on the silicon surface between the grid fingers. The area of the base contacts with their high recombination rate has to be minimized without significantly increasing the contact resistance. By this also grid shadowing for back surface illumination is reduced. Full-area back metallization with contact openings in the Al_2O_3 layer as well as a local back surface-field at the base contact lines are some of the further options (see Figs. 4.6 and 4.9).

The crucial property of this back surface system is that due to the presence of the accumulation layer also the parasitic shunting effect is completely avoided [71]. In

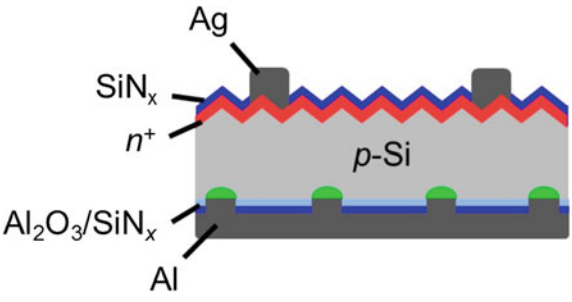

Fig. 4.9 Schematic cross section of an industrial type PERC solar cell with full-area back metallization and line-shaped local contacts (picture taken from [81])

contrast to the case of inversion present with positively charged SiN_x as passivation layer, the flow of electrons along the rear surface towards the highly recombinative base contacts is suppressed. This, as one of the main advantages of Al_2O_3 together with excellent surface passivation has a high potential for significantly increasing the efficiency of conventional solar cells at low cost including the application as bifacial devices [8, 12, 74].

4.5.2 Early Laboratory Results for Al_2O_3

For the first application of Al_2O_3 for solar cells we used the simple deposition technique of atmospheric pressure chemical vapor deposition (APCVD) with an open tube laboratory furnace at temperatures between 300 and 500 °C. A very good level of surface passivation of p-type solar cells could already be demonstrated [8, 12]. It was confirmed that the reported fixed negative charge density $Q_f/q = -3 \times 10^{12}$ cm^{-2} and the mid-gap interface state density $D_{it} = 8 \times 10^{10}$ cm^{-2} eV^{-1} lies within the range of typical values of present-day well passivating Al_2O_3 layers indicating S_{eff} values below 100 cm/s on 2 Ωcm p-type silicon [74]. As in the case of SiN_x also for Al_2O_3, in addition to charge induced ("field effect") passivation, reduction of the interface state density D_{it} via saturation of unsaturated bonds by intrinsic hydrogen plays another important role for surface passivation. However, in comparison to SiN_x, Al_2O_3 provides an even more effective field-effect passivation since less recombination occurs due to the absence of a space charge region at the surface of p-type silicon [75].

As to the reliability of the interface properties, an interesting observation could be made. Under strong UV light irradiation the fixed charge density Q_f/q is increasing due to an internal photo injection process [12]. Thus by UV light the passivation properties of Al_2O_3 are improved via enhancement of accumulation. As a surprising result, the interface state density D_{it} is not affected by the UV light. Similar to SiN_x (Fig. 4.1), also Al_2O_3 is known for its excellent radiation hardness and strong chemical bonding. Thus Al_2O_3 represents an extremely effective and reliable transparent insulator film for silicon surface passivation, preferably for the rear side of p-type solar cells to replace the conventional back surface-field. The effectiveness of the passivation technique was first demonstrated on the front-side of a new back collecting silicon solar cell, the performance of which is extremely sensitive to front surface recombination [8]. A dramatic increase of the cell efficiency could be observed by changing the deposition temperature of Al_2O_3 from 290 to 500 °C.

Based on the encouraging results at this early stage together with other outstanding properties, there was clear evidence that Al_2O_3 could play a crucial role for efficient and long-term stable monofacial and bifacial silicon solar cells [8, 12].

However, in the nineties, our R+D work at the FAU Erlangen and later at the ISFH was focused on the further optimization of silicon nitride to provide a reliable passivating antireflection layer for standard solar cells. This was an urgent goal at

that time, also for future solar cells. As a result, silicon nitride paved the way for mass production of solar cells worldwide.

4.5.3 Revival of Al_2O_3 as Passivation Layer for PERC Solar Cells

With the introduction of the Al_2O_3—based rear surface passivation scheme including line-shaped local contacts at the University of Erlangen, in 1985 a novel concept was realized that, according to Fig. 4.8, the rear metal makes direct contact with the p-type substrate on a restricted area while most of the silicon surface is passivated by a dielectric layer [8, 13]. In 2006 a reintroduction of this configuration occurred which is considered a key technology in future industrial high efficiency solar cell production [17, 18, 74].

Four years after the introduction of the innovative passivation scheme shown in Fig. 4.8, in 1989 a laboratory cell named PERC ("**P**assivated **E**mitter and **R**ear **C**ell") demonstrated the high-efficiency potential of the abovementioned general concept [1]. The PERC cell is characterized by a high-temperature thermal SiO_2 film at the rear and a full-area metal layer forming point-shaped local rear contacts by openings in the passivating oxide. With sophisticated processing, a record efficiency of 22.8% was resulted, a value which at present is already obtained for Al_2O_3—based industrial cells. The name PERC is now generally used for these latter cells (see, e.g., Fig. 4.9).

The Al_2O_3 films were intensively studied in many research labs all over the world and an extremely large number of publications appeared during the following years [3, 15, 16, 74]. Soon the interest of the PV industry grew rapidly due to the encouraging results obtained for the first Al_2O_3—based solar cells. Various types of production processes were developed together with advanced technologies, e.g., for layer deposition, laser contact opening, screen printing, and firing of Al-contacts. From 2012 onward the majority of solar cell manufacturers are already introducing PERC-like solar cells into industrial mass production upgrading their conventional BSF production lines for improved cell performance. For this purpose the innovative basic rear side scheme shown in Fig. 4.8 was extended by a conventional local back surface-field at the Al-contact lines and by a SiN_x capping layer on top of Al_2O_3. In most cases a full-area rear metallization is applied by screen printing and firing, which contacts the silicon wafer at line-shaped areas where the rear passivation layer has been removed by laser contact opening (LCO) [76]. An industrial type PERC solar cell is schematically shown in Fig. 4.9. The crucial role of the two innovative charged dielectric layers can clearly be seen. It should be mentioned, that for the manufacturing process point-shaped local rear contacts turned out to be less suitable than the line-shaped contact scheme [77, 78].

There is increased interest in PERC solar cells with bifacial sensitivity since due to the open-gridded back contact structure on the one hand light incident on the

rear can be used to increase power output and on the other hand aluminum paste consumption is reduced [13, 65, 79, 80].

A bifacial version based on the open rear surface configuration shown in Fig. 4.8 is obtained by simply applying a line-shaped Al-grid at the contact openings. Referring to Sect. 4.4, already since 1986 the novel rear surface scheme was used for the development of bifacial PERC-like solar cells.

4.5.4 Al_2O_3/SiN_x Stacks for PERC Solar Cell

For almost all industrial PERC cells thanks to its unique properties silicon nitride films play an even more important role compared to the present mainstream solar cells. As can be seen from Fig. 4.9, in addition to the use of SiN_x as passivation and antireflection coating at the n^+-diffused front-side, the rear is made up of a stack consisting of thin Al_2O_3 capped by a thicker PECVD SiN_x layer. The SiN_x capping layer has the following benefits. The Al_2O_3 field effect back surface passivation is enhanced by further chemical passivation provided by the active hydrogen species released during the SiN_x deposition. As outlined in Sect. 4.2.1 SiN_x also provides an outstanding protection layer, e.g., for further improving the firing stability of Al_2O_3 against the Al-paste for the surface passivation of industrial screen-printed silicon solar cells [82]. The rear side covered by the Al_2O_3/SiN_x stack acts as a mirror for incident light and thus enhances its absorption within the solar cell. Therefore, a higher portion of the light is used for the generation of charge carriers [83]. Both effects, excellent back surface passivation, as well as the mirror action, are further key factors for boosting cell conversion efficiency of the PERC cells. Furthermore, by a proper combination of the two films an optimized antireflection coating for light incident on the rear side of the cell is provided.

There are various techniques for industrial low-temperature deposition of Al_2O_3. Despite atomic layer deposition (ALD) yields the best passivation, PECVD is most widely used since high-throughput and low-cost are the inherent advantages [3]. S_{eff} values below 10 cm/s are achieved [74]. The Roth&Rau company (now Meyer&Burger) have adapted their successful SINA microwave PECVD system (see Fig. 4.4, codeveloped at ISFH) for Al_2O_3 deposition resulting in a multiple application in-line apparatus (MAIA). Implemented into a standard Al-BSF cell line for the establishment of a PERC cell line the MAIA equipment is capable of depositing both the front SiN_x AR coating and the rear Al_2O_3/SiN_x stack within one machine and in one run [84].

4.6 Conclusions

Minimizing recombination of charge carriers on both surfaces is a prerequisite for achieving cost-effective high-efficiency solar cells. In the eighties, an important era

for PV began with the extrinsic low-temperature passivation of silicon solar cells by the two dielectric layers silicon nitride (SiN_x) and aluminum oxide (Al_2O_3) introduced at the University of Erlangen. Both multifunctional films became key components of present and future monofacial and bifacial solar cells.

Due to its unique properties, the positively charged SiN_x-layers clearly outperformed all other candidates as efficient long-term stable passivating antireflection coating. Thanks to the successful development of high-throughput plasma deposition of these films economic mass production of reliable silicon solar cells was possible. Hence, almost 50 years after the demonstration of a silicon solar cell in 1954 at the Bell Labs in USA the way was paved for the first large area application of solar cells in the history of photovoltaics, soon culminating in a worldwide boom of solar electricity.

A similar extraordinary progress as achieved by SiN_x for the present mainstream solar cells can also be predicted for the high-efficiency PERC devices as the next-generation silicon cells by the outstanding properties of Al_2O_3 as a negatively charged surface passivation layer in combination with a gridded Al rear contact scheme. This latter structure, pioneered by the authors already in 1985 is generally regarded as a key technology for future silicon solar cells. But still, SiN_x plays an important role. So it took almost 25 years since their introduction, that both charged SiN_x and Al_2O_3 layers are now together implemented in the novel silicon solar cell. By the modifications for upgrading the mainstream cell production lines for PERC cell manufacturing large investments are avoided compared to the development of new technologies.

The international technology roadmap for photovoltaics (ITRPV) forecasts a market share of PERC solar cells up to 60% and record efficiencies approaching 24% within the next few years. For the present Al-BSF mainstream solar cells efficiencies up to 20% are achievable. A comprehensive review with further details about monofacial and bifacial industrial PERC solar cells is presented in the following two articles of this book.

References

1. A. Blakers, A. Wang, A. Milne, J. Zao, M. Green, Appl. Phys. Lett. **55**, 1363 (1989)
2. A.G. Aberle, Crystalline Silicon Solar Cells—Advanced Surface Passivation and Analysis. Centre for Photovoltaic Engineering, University of New South Wales, Sydney NSW 2052 (1999)
3. T. Dullweber, J. Schmidt, IEEE J. Photovolt. **6**(5), 1366 (2016)
4. R. Hezel, *Siemens Forschungs- und Entwicklungsberichte*, *Bd.1, Nr.1/72* (1972), p. 153
5. R. Hezel, E. Hearn, J. Electrochem. Soc. **125**, 1848 (1978)
6. R. Hezel, German patent application (1978)
7. R. Hezel, R. Schörner, T. Meisel, in *Proceedings of the 3rd. European Photovoltaic Solar Energy Conference, Cannes* (1980), p. 866
8. K. Jaeger, R. Hezel, in *Proceedings of the 18th IEEE Photovoltaic Specialist Conference, Las Vegas* (1985), p. 1752
9. R. Hezel, R. Schörner, J. Appl. Phys. **52**, 3076 (1981)

10. J. Moschner, J. Henze, J. Schmidt, R. Hezel, Prog. Photov. Res. Appl. **12**, 21 (2004)
11. K. Roth, F. Chen, M. Fritzsche, M. Kirschmann, J. Müller, H. Schlemm, in *Proceedings of the 21st European Photovoltaic Solar Energy Conference, Dresden* (2006), p. 1137
12. R. Hezel, K. Jaeger, J. Electrochem. Soc. **136**(2), 518 (1989)
13. K. Jaeger, R. Hezel, in *Proceedings of the 7th European Photovoltaic Solar Energy Conference, Seville* (1986), p. 806
14. R. Hezel, K. Jaeger, *Fall Meeting of the Electrochemical Society, Honolulu, Extended Abstracts*, vol. 87(2) (1987), p. 1134
15. *Photon International* (March 2011)
16. *Sun and Wind Energy* (Nov. 2010)
17. B. Hoex, S. Heil, F. Langereis, M. van de Sanden, W. Kessels, Appl. Phys. Lett. **89**, 042112 (2006)
18. G. Agostinelli, A. Delabie, P. Vitanov, Z. Alexieva, H. Dekker, S. Wolf et al., Sol. Energy Mater. Sol. Cells **90**, 3438 (2006)
19. N. Lieske, R. Hezel, Thin Solid Films **61**, 217 (1979)
20. N. Lieske, R. Hezel, in *Proceedings of the Conference in Insulating Films on Semiconductors 1979*, vol. 50 (1980), p. 206
21. R. Hezel, N. Lieske, J. Appl. Phys. **51**, 2566 (1980)
22. R. Hezel, *Habilitationsschrift Universität Erlangen-Nürnberg (FAU)* (1981)
23. R. Hezel, Solid St. Electron., 735 (1979)
24. R. Hezel, Radiat. Eff. **65**, 101 (1982)
25. J. Johannessen, W. Spicer, Y. Strausser, J. Appl. Phys. **47**, 3028 (1976)
26. A. Sinha, H. Levinstein, T. Smith, G. Quintana, S. Haszko, J. Electrochem. Soc. **125**(4), 601 (1978)
27. B. Lenkeit, S. Steckemetz, A. Mücklich, A. Metz, R. Hezel, in *Proceedings of the 16th European Photovoltaic Solar Energy Conference, Glasgow* (2000), p. 1332
28. R. Hezel, in *Silicon Nitride in Electronics, Gmelin Handbook Si Supplement*, vol. B 5c (1991), p. 321
29. W. Shockley, W. Reed, Phys. Rev. **87**, 835 (1952)
30. W. Lanford, M. Rand, J. Appl. Phys. **49**, 2473 (1978)
31. R. Hezel, N. Lieske, J. Appl. Phys. **53**(3), 1671 (1982)
32. R. Hezel, K. Blumenstock, R. Schörner, in *Proceedings of the Symposium on Silicon Nitride Thin Insulating Films*, vol. 83-8, ed. by H.S.V.J. Kapoor (1983), p. 280
33. G.Schwuttke, K. Yang, R. Hezel, *ERDA/JPL Contract Nr. 954144-76/05*, Technical Progress Report, USA, 5 (1976), pp. 1–34
34. A. Cuevas, M. Kerr, J. Schmidt, in *Proceedings of the 3rd World Conference on Photovoltaic Solar Energy Conversion, Osaka* (2003), p. 913
35. R. Hezel, Solid St. Electron. **24**, 863 (1981)
36. R. Hezel, in *Insulating Films on Semiconductors*, Springer Series in Electrophysics, vol. 7 (Springer, Berlin, 1981), p. 219
37. R. Hezel, in *Proceedings of the 16th IEEE Photovoltaic Specialists Conference* (1982), p. 1237
38. T. Salter, R. Thomas, Solid St. Electron. **20**, 95 (1977)
39. P. van Halen, R. Mertens, R. van Overstraten, R. Thomas, J. van Meerbergen, IEEE Trans. El. Dev. **ED-25**, 507 (1978)
40. M. Green, R. Godfrey, M. Willison, A. Blakers, in *Proceedings of the 14th IEEE Photovoltaic Specialists Conference*, San Diego (1980), p. 684
41. R. Godfrey, M. Green, Appl. Phys. Lett. **34**, 790 (1979)
42. R. Thomas, C. Norman, R. North, in *Conference Record of the 14th IEEE Photovoltaic Specialist Conference* (1980), p. 1350
43. R. Hezel, W. Hoffmann, K. Jaeger, in *Proceedings of the 10th European Photovoltaic Solar Energy Conference, Lisbon* (1991), p. 511
44. W. Hoffmann, Metall **44**(7), 658 (1990)
45. C. Peters, R. Meyer, R. Hezel, in *Proceedings of the European Photovoltaic Solar Energy Conference, Rome* (2002), p. 127

46. M. Alonso, R. Pottbrock, R. Voermans, J. Villard, B. Joshi, in *Proceedings of the 12th European Photovoltaic Solar Energy Conference, Amsterdam* (1994), p. 1163
47. W. Hoffmann, *The Economic Competitiveness of Renewable Energy* (Scrivener Publishing Wiley, 2014)
48. J. Schmidt, T. Lauinger, A. Aberle, R. Hezel, in *Proceedings of the 25th PVSC, Washington D.C.* (1996), p. 413
49. T. Lauinger, J. Schmidt, A. Aberle, R. Hezel, Appl. Phys. Lett. **68**, 1232 (1996)
50. D. Ruby, W. Williams, C. Fleddermann, in *Proceedings of the 1st World Conference on Photovoltaic Energy Conversion IEEE, New York* (1994), p. 1355
51. B. Lenkheit, T. Lauinger, A. Aberle, R. Hezel, in *Proceedings of the 2nd World Conference on Photovoltaic Energy Conversion* (1998), p. 1434
52. A. Metz, R. Hezel, in *Conference on Record of the 26th IEEE PVSC* (1997), p. 283
53. S. Dauwe, L. Mittelstädt, A. Metz, J. Schmidt, R. Hezel, in *Proceedings of the 3rd World Conference on Photovoltaic Energy Conversion*, Osaka (2003), p. 1395
54. K. Blumenstock, R. Hezel, in *Insulating Films on Semiconductors* ed. by J. Simone, J. Buxo. Elsevier Science Publications B.V. North Holland (1986)
55. R. Hezel, R. Auer, M. Rammensee, *Progress in Plasma processing of Materials* (1999), p. 891
56. A. Aberle, R. Hezel, Progr. Photov. Res. Appl. **5**(1), 29 (1997)
57. T. Lauinger, A. Aberle, R. Hezel, in *Proceedings of the 14th European Photovoltaic Solar Energy Conference, Barcelona* (1997), p. 853
58. A. Aberle, T. Lauinger, R. Hezel, in *Proceedings of the 14th European Photovoltaic Solar Energy Conference, Barcelona* (1997), p. 684
59. M. Rammensee, Ph.D. thesis, University of Erlangen (1995)
60. J. Moschner, A. Metz, R. Hezel, in *Proceedings of the 17th European Photovoltaic Solar Energy Conference, Munich* (2001), p. 1917
61. S. Roth, *Themen 2007: Jahrestagung des Forschungsverbunds Solarenergie in Kooperation mit dem Bundesverband Solarwirtschaft e. V. (BSE Solar), Hannover, Leibniz Univ*. (2007)
62. R. Hezel, Prog. Photovolt. Res. Appl. **11**, 549 (2003)
63. R. Hezel, in *High-Efficient Low Cost Photovoltaics*, vol. Springer Series in Optical Science (Springer, Berlin, 2009), p. 86
64. A. Cuevas, in *Proceedings of the 20th European Photovoltaic Solar Energy Conference, Barcelona* (2005), p. 801
65. K. Jaeger, R. Hezel, in *Proceedings of the 19th IEEE Photovoltaic Specialist Conference, New Orleans* (1987), p. 388
66. A. Hübner, A. Aberle, R. Hezel, Appl. Phys. Lett. **70**, 1008 (1997)
67. K. Jaeger, G. Bende, W. Hoffmann, R. Hezel, in *Conference Record 23th IEEE Photovoltaic Specialist Conference, Louisville* (1993), p. 1235
68. K. Jaeger-Hezel, W. Schmidt, W. Heit, K. Rasch, in *Proceedings of the 13th European Photovoltaic Solar Energy Conference, Nice* (1995), p. 1515
69. A. Hübner, A. Aberle, R. Hezel, in *Proceedings of the 14th European Photovoltaic Solar Energy Conference, Barcelona* (1997), p. 92
70. J. Müller, A. Merkle, R. Hezel, in *Proceedings of the 20th European Photovoltaic Solar Energy Conference, Barcelona* (2005), p. 1020
71. S. Dauwe, L. Mittelstädt, A. Metz, R. Hezel, Prog. Photov. Res. Appl. **10**, 271 (2002)
72. G. Agostinelli, P. Chonlet, H. Dekkers, E. Vermerien, G. Beancarne, in *Proceedings of the 4th World Conference on Photovoltaic Energy Conversion* (2006), p. 1004
73. K. Münzer et al., *Proceedings of the 26th European Photovoltaic Solar Energy Conference, Hamburg* (2011), p. 2292
74. J. Schmidt, F. Werner, B. Veith, D. Zielke, S. Steingrube, P. Altermatt, S. Gatz, T. Dullweber, R. Brendel, Energy Procedia **15**, 30 (2012)
75. J. Schmidt, A. Merkle, R. Bock, P. Altermatt, A. Cuevas, N. Harder, B. Hoex, R. Sanden, E. Kessels, R. Brendel, in *Proceedings of the 23rd European Photovoltaic Solar Energy Conference, Valencia* (2008), p. 974

76. R. Preu, S. Glunz, S. Schäfer, R. Lüdemann, W. Wettling, W. Pfleging, in *Proceedings of the 16th European Photovoltaic Solar Energy Conference, Glasgow* (2000), p. 1181
77. T. Lauermann, A. Zuschlag, S. Scholz, G. Hahn, B. Terheiden, in *Proceedings of the 26th European Photovoltaic Solar Energy Conference, Hamburg* (2011), p. 1137
78. J. Müller et al. (2011). *IEEE Trans. Electron Devices* **58**(10), 3239
79. T. Dullweber, C. Kranz, R. Peibst, U. Baumann, H. Hannebauer, A. Fülle et al., Prog. Photov. Res. Appl. **24**, 1487 (2016)
80. K. Krauß, F. Fertig, J. Greulich, S. Rein, R. Preu, Phys. Stst. Solidi. A **213**(1), 68 (2016)
81. H. Hannebauer, T. Dullweber, U. Baumann, T. Falcon, R. Brendel, Phys. Status Solidi RRL **8**, 675 (2014)
82. J. Schmidt, B. Veith, R. Brendel, Phys. Stat. Sol. **RRC**, 287 (2009)
83. D. Kray, M. Hermle, S. Glunz, Prog. Photov. Res. Appl. **16**, 1 (2008)
84. H. Sperlich, D. Decker, P. Saint-Cast, E. Erben, L. Peters, in *Proceedings of the 25th European Photovoltaic Solar Energy Conference, Valencia* (2010), p. 1352

Chapter 5
High-Efficiency Industrial PERC Solar Cells for Monofacial and Bifacial Applications

Thorsten Dullweber

Abstract The passivated emitter and rear cell (PERC) concept is currently rapidly being introduced into industrial mass production and is expected to be the new silicon wafer based solar cell technology standard in the photovoltaics industry. In 2018, PERC-type solar cells accounted for approximately 40% of the worldwide produced solar cells and their share is expected to rapidly increase up to 70% within the next few years. Compared to the previous industrial silicon solar cell technology which applied a full-area aluminum rear contact, PERC cells passivate the rear silicon wafer surface with a dielectric layer and only locally contact the silicon wafer with an aluminum metal contact, which reduces charge carrier recombination and hence increases the conversion efficiency. Present record conversion efficiencies up to 22.8% of industrial PERC cells hence exceed the efficiency of conventional Al-BSF silicon solar cells by more than $2\%_{abs}$. In addition, PERC solar cells can be made bifacial by substituting the full-area rear aluminum layer with an aluminum finger grid design. This so-called PERC+ solar cell design enables large volume industrial manufacturing of bifacial silicon solar cells which absorb stray light from the rear side and hence increase the energy yield by 5–25% depending on the detailed module installation conditions. This chapter describes the most important research results and technology developments of the past decades as well as the present status of industrial PERC and PERC+ solar cells.

The passivated emitter and rear cell (PERC) concept is currently rapidly being introduced into industrial mass production and is expected to be the new silicon wafer based solar cell technology standard in the photovoltaics industry. In 2018, PERC-type solar cells accounted for approximately 40% of the worldwide produced solar cells and their share is expected to rapidly increase up to 70% within the next few years. Compared to the previous industrial silicon solar cell technology which applied

This chapter contains text adapted from [1] and [2] with permission of The Institution of Engineering and Technology.

T. Dullweber (✉)
Institut für Solarenergieforschung Hameln, Am Ohrberg 1, 31860 Emmerthal, Germany
e-mail: dullweber@isfh.de

V. Petrova-Koch et al. (eds.), *High-Efficient Low-Cost Photovoltaics*,
Springer Series in Optical Sciences 140,
https://doi.org/10.1007/978-3-030-22864-4_5

a full-area aluminum rear contact, PERC cells passivate the rear silicon wafer surface with a dielectric layer and only locally contact the silicon wafer with an aluminum metal contact, which reduces charge carrier recombination and hence increases the conversion efficiency. Present record conversion efficiencies up to 22.8% of industrial PERC cells hence exceed the efficiency of conventional Al-BSF silicon solar cells by more than $2\%_{abs}$. In addition, PERC solar cells can be made bifacial by substituting the full-area rear aluminum layer with an aluminum finger grid design. This so-called PERC+ solar cell design enables large volume industrial manufacturing of bifacial silicon solar cells which absorb stray light from the rear side and hence increase the energy yield by 5–25% depending on the detailed module installation conditions. This chapter describes the most important research results and technology developments of the past decades as well as the present status of industrial PERC and PERC+ solar cells.

5.1 Introduction

When the diffusion length of the minority charge carriers exceeds the silicon wafer thickness, charge carrier recombination at the rear side of the silicon solar cells becomes important. During the past decades, around 90% of the solar cells worldwide have been manufactured applying silicon wafers and a screen-printed full-area aluminum (Al) layer which contacts the complete rear silicon wafer surface by forming an aluminum back surface field (Al-BSF). The carrier recombination at the full-area aluminum rear contact is only marginally suppressed by the local Al doping of the Al-BSF. Also, the full-area Al layer partly absorbs the infrared light which reduces the light absorption of the solar cell. Due to these two loss mechanisms, the conversion efficiency of industrial silicon solar cells with full-area Al-BSF is limited to around 20%. Already in 1989, Blakers et al. [3] in the research group of M. A. Green at the University of New South Wales (UNSW), Australia, introduced the "Passivated Emitter and Rear Cell" (PERC) which was designed to overcome the efficiency limitations of the Al-BSF solar cell by introducing a dielectric passivation of the silicon wafer rear side using only local metal contacts. The PERC solar cell in 1989 did not apply a production-feasible manufacturing process but instead mostly laboratory-type processes and wafer materials which increased the conversion efficiency to a world record value of 22.8% at that time. Very expensive 0.2 Ωcm p-type float-zone silicon wafers were used. The rear passivation consisted of a thermally grown silicon dioxide layer which was locally opened by photolithography and etching followed by evaporation of a full-area aluminum layer which resulted in point-shaped local aluminum rear contacts. The solar cell's front side was processed with several photolithography steps forming inverted pyramids, a selective phosphorus emitter and evaporated TiPdAg front contacts. The resulting 4 cm^2 laboratory-type PERC solar cell of 1989 is shown schematically in Fig. 5.1. In contrast to Al-BSF cells, the rear side of PERC cells is largely covered by SiO_2 thereby suppressing the recombination of minority charge carriers (electrons) at the metal rear contact. Majority charge car-

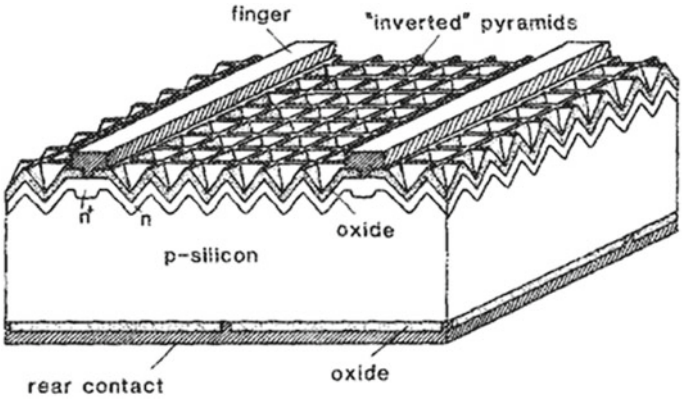

Fig. 5.1 Schematic drawing of the laboratory-type PERC solar cell published by Blakers et al. in 1989 [3] applying a thermal silicon dioxide rear passivation, rear-side point contacts patterned by photolithography, and a full-area evaporated aluminum rear metal layer. This figure is reproduced from [3] with the permission of AIP Publishing

riers (holes) are transported through the local Al contacts at the rear thereby ensuring the current flow through the PERC solar cell. Also, the SiO_2/Al layer stack at the PERC rear side serves as a very good optical mirror reflecting infrared light which has not yet been absorbed in the silicon wafer back into the solar cell instead of being absorbed in the Al layer. In the following years, the PERC concept was further developed into the passivated emitter and rear locally diffused (PERL) solar cell resulting in an efficiency of 25.0% by present standards [4] which remained the world record efficiency for silicon solar cells for almost two decades. The PERL cell applied a high local p+ doping below the Al rear contacts thereby reducing carrier recombination at the local rear contacts which increased the conversion efficiency.

The PERC and PERL solar cell designs of the UNSW provided the foundation and basic concept of today's industrial PERC solar cells. However, as outlined in the next sections, a broad variety of process and technology developments regarding surface passivation and metallization were required to develop an industrial PERC manufacturing process sequence applying novel low-cost and high-throughput processes with sufficient quality for high conversion efficiencies. Since a few years, the new production processes, in particular, for chemical rear surface polishing, aluminum oxide/silicon nitride rear surface passivation, laser contact opening, and aluminum screen printing are available with sufficient quality and throughput and now most solar cell companies are manufacturing PERC solar cells in mass production with a present market share of the PERC technology of 40% [5]. The International Technology Roadmap for Photovoltaics (ITRPV) predicts a further strong increase up to 70% of the market share of the PERC technology within the next years [6, 7] as shown in Fig. 5.2a. Several review papers and book chapters [1, 8–10] provide an overview of the research and development and the present status of the PERC solar

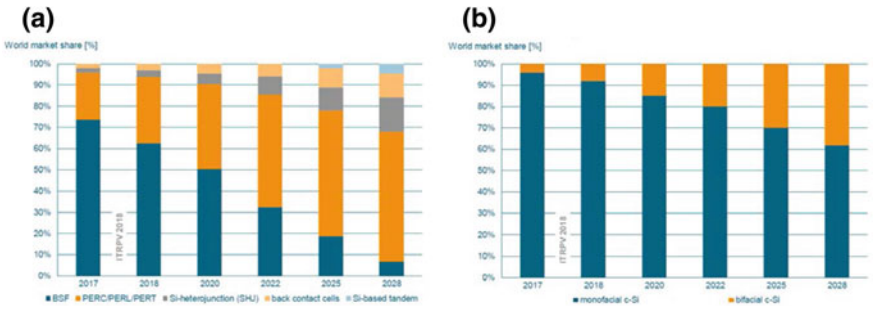

Fig. 5.2 **a** Forecasted market share of different solar cell technologies according to the International Technology Roadmap for Photovoltaics (ITRPV) as published in 2017 [6]. PERC cells are expected to gain approx. 60% market share within the next 10 years. **b** The ITRPV roadmap predicts a market share of bifacial silicon solar cells of 40% until 2028. The bifacial PERC+ cell concept (see Fig. 5.3c) combines both trends, PERC and bifacial, by changing the full-area aluminum rear layer of PERC to an aluminum finger grid layout. This figure is reproduced from [6] with the permission from VDMA

cell technology. The following sections will describe the development, status, and prospects of industrial PERC solar cells in detail.

Since a few years, bifacial solar cells and modules are gaining attention by the photovoltaics industry due to the increased energy yield by converting the solar irradiation to electricity not only with the solar cell's front side but by also utilizing diffuse light which illuminates the solar cell's rear side. As shown in Fig. 5.2b, the International Technology Roadmap for Photovoltaics (ITRPV) forecasts a steadily increasing market share of bifacial silicon solar cells of up to 40% till 2028. As will be described in this chapter, PERC+ solar cells enable a straightforward implementation of a bifacial solar cell concept into mass production. Hence, several companies are already producing bifacial PERC+ solar cells and modules. Review articles of the development and present status of PERC+ solar cells are published in [2, 11].

5.2 Industrial PERC Solar Cells

As described in Sect. 5.1, the first PERC solar cell fabricated at the UNSW in 1989 [3] applied mostly lab-type processes such as photolithography for structuring, thermal oxidation for masking and surface passivation as well as evaporation of metals for contact deposition. One important step toward an industrial PERC production sequence was introduced by the research institute IMEC, Belgium, in 2005 [12, 13] proposing a process combination of PECVD SiN_x as rear surface passivation, rear contact structuring by laser contact opening, and rear metallization via aluminum screen printing. However, also the PERC process sequence proposed by IMEC still applied several lab-type plasma processes, e.g., for texturing and rear emitter removal [12].

Today, a mainstream process flow for industrial production of PERC solar cells is applied by most of the PERC cell manufacturers as summarized in Table 5.1 and described in detail in [10]. First, the boron-doped multi- or monocrystalline silicon wafers with around 180 μm starting thickness and 156 × 156 mm^2 area are unisotropically etched in an acidic or alkaline chemical solution thereby forming pyramids on the wafer surface, a so-called texture, which reduce the reflection of light. Afterward, the phosphorus emitter is diffused applying phosphorus oxychloride ($POCl_3$) at temperatures around 850 °C in a quartz tube furnace. Since the texturing and $POCl_3$ diffusion process both, the front and the rear wafer surface, a wet chemical etching and polishing process removes the rear-side phosphorus doping and smoothens the rear pyramids [14, 15]. Afterward, the wafer surface is cleaned by alkaline and acidic chemical steps which also remove the remaining phosphorus silicate glass. Then, the wafer surfaces are coated by surface passivation layer stacks. The rear surface receives a layer stack consisting of 5–20 nm aluminum oxide (AlO_x) and 80–120 nm of silicon nitride (SiN_y) which are typically deposited by plasma-enhanced chemical vapor deposition (PECVD) [16, 17]. AlO_x has been shown to obtain very low surface recombination velocities of minority charge carriers on p-type wafer surfaces due to its built-in negative fixed charges [18, 19]. The SiN_y capping layer is required in order to protect the AlO_x layer against the following Al screen printing and firing processes, which otherwise would dissolve the AlO_x layer. The phosphorus-doped front surface is passivated by a SiN_y layer, which due to its built-in positive charges [20] is well suited to minimize carrier recombination of n-type wafer surfaces. The front SiN_y layer is typically around 80 nm thick which minimizes the reflection of

Table 5.1 Typical production process sequence of industrial PERC and PERC+ solar cells. Whereas the principal process flow of monofacial PERC and bifacial PERC+ solar cells is identical, the individual recipes vary between PERC and PERC+ in order to optimize the front-side efficiency for PERC and the bifaciality for PERC+

PERC recipes	PERC/ PERC+ process	PERC+ recipes
	Texturing	
	$POCl_3$ diffusion	
3–5 μm polishing removal	Rear chemical polishing	Reduced polishing removal
	PSG etch	
Thickness ca. 130 nm optimized for passivation and internal reflectance	AlO_x/SiN_y rear passivation	Thickness ca. 80 nm optimized for antireflection
	Front SiN_y	
Contact pattern optimized for front-side efficiency	Laser contact opening	Contact pattern optimized for bifaciality
	Ag rear screen printing	
Full-area print	Al rear screen printing	Fingerprint
	Ag front screen printing	
	Firing	Reduced set peak temperature

light from the front surface to below 3% in average over the whole visible wavelength range due to destructive interference. The rear metal contact pattern is defined by local laser ablation of the AlO_x/SiN_y stack, a process named laser contact opening (LCO) [21]. Typically, either line-shaped [22] or dashed-line-shaped [23] pattern is used in production. Then, the front and rear metal contacts are deposited by printing silver (Ag) or aluminum (Al) containing pastes through a mesh screen. The metal pastes consist of an Ag or Al powder with a particle size of a few micrometers (μm) and organic binders and solvents which define the viscosity and printability of the paste. The mesh screen consists of around 15 μm thin metal wires with around 300–400 wires per inch, which are coated by an organic emulsion. At areas where the Ag or Al paste should be printed on the wafer, the emulsion is removed from the mesh screen allowing the metal paste to penetrate through the screen. First, the rear Ag pads which are later required for module interconnection are screen-printed. Afterward, the Ag paste is dried at 200 °C thereby removing the solvent. The Al rear layer is screen-printed full area at the rear side and is dried. Then, the Ag front contact is screen-printed and dried. The typical Ag front contact layout consists of around 100 very thin Ag conductor lines (fingers) with a finger width around 40 μm, which are interconnected by four or five perpendicular Ag busbars which are required for module interconnection. After drying the Ag paste, the whole PERC process sequence is completed by a rapid thermal process called firing which heats the wafers for a few seconds up to around 800 °C. At this temperature regime, the glass frites of the Ag paste etch through the SiN_y front layer allowing the Ag to alloy with the phosphorus-doped silicon forming an electrical contact on the front side. At the same time, the Al paste on the rear-side alloys with the silicon wafer at areas where the rear passivation has been removed by LCO thereby forming an electrical contact at the rear side. The Al pastes contain a very small amount of glass frites and hence do not etch the rear passivation layer stack. The resulting industrial PERC solar cell is shown schematically in Fig. 5.3b.

The production process sequence described above applies to both monofacial PERC solar cells and bifacial PERC+ solar cells. However, as listed in Table 5.1, several process recipes are optimized differently for PERC versus PERC+ solar cells. Most importantly, the full-area Al layer print of PERC cells is changed to an Al finger grid print for PERC+ solar cells [24]. The LCO pattern for PERC is optimized for a high front-side efficiency by balancing wafer bulk spreading resistance losses versus recombination losses at the Al rear contacts. For PERC+, an additional optimization criterion is a high rear-side efficiency which favors larger LCO pitches and hence higher spacing of the Al fingers in order to minimize reflection losses of the PERC+ cell when illuminated from the rear side. For the same reason, PERC+ cells apply a thinner rear AlO_x/SiN_y stack around 80 nm [24] which is optimized for antireflection and the rear polishing removal maybe reduced in order to maintain part of the rear texture, both minimizing reflection losses. For PERC cells, the polishing process and rear passivation thickness are optimized for high front-side efficiencies which typically favors slightly higher polishing removals and thicker passivation layers to maximize the internal reflection at the rear. Finally, the set peak temperature of the firing process for PERC+ is typically around 20 °C lower as for PERC since the

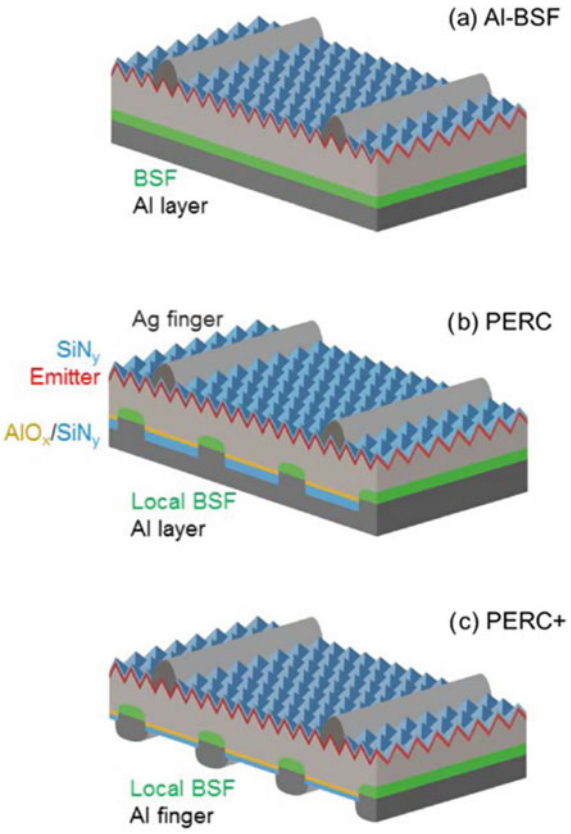

Fig. 5.3 Schematic drawings of **a** an industrial Al-BSF solar cell where the screen-printed Al layer alloys with the silicon wafer forming a full-area Al-doped back surface field (BSF or Al-BSF); **b** an industry-typical PERC solar cell with AlO_x/SiN_y rear passivation, local BSF formed by laser contact opening, and a full-area rear Al layer; **c** a bifacial PERC+ solar cell applying a screen-printed Al finger grid on top of the laser contact openings on the rear side thereby enabling light absorption from the front and rear sides

reduced amount of aluminum paste requires less external heating power to obtain the same physical wafer temperature. Figure 5.3c shows a schematic cross section of a PERC+ solar cell, which is described in detail in the next section.

For comparison, Fig. 5.3a shows a schematic drawing of a full-area Al-BSF solar cell, which has been dominating industrial production for many years as illustrated in Fig. 5.2a. The Al-BSF cell applies the same front side as an industrial PERC cell, whereas at the rear side the Al layer is printed directly to the silicon wafer surface without any dielectric rear surface passivation. Hence, the Al-BSF cell process sequence does not require AlO_x/SiN_y rear passivation deposition and no laser contact opening making it shorter and hence cheaper compared to the PERC process sequence in Table 5.1. Consequently, PERC cells need to demonstrate at least 1%

absolute higher energy conversion efficiencies compared to Al-BSF cells in order to enable lower photovoltaic electricity generation costs on module level (Euro per Watt peak; €/Wp) or electricity level (Euro per kilo Watt hour; €/kWh). Figure 5.4 shows a numerical simulation published in the year 2011 [25] applying the solar cell simulation software PC1D of the conversion efficiency versus the rear surface recombination velocity $S_{\text{eff,rear}}$ and the internal rear reflectance R_{rear}. The full-area Al-BSF forms a p/p+ doping gradient and hence a built-in electric field which limits $S_{\text{eff,rear}}$ to around 400 cm/s. The internal reflectance R_{rear} of the silicon/ aluminum interface is around 65%. As can be seen in Fig. 5.4, both parameters limited the conversion efficiency of Al-BSF cells to about 18.5%. Due to the dielectric rear passivation, PERC cells exhibit a much lower $S_{\text{eff,rear}}$ around 50 cm/s and a higher R_{rear} around 90% and hence demonstrated conversion efficiencies close to 20% already in the year 2011. The simulation in Fig. 5.4 assumed values for the Ag finger, emitter, and wafer properties which were typical in the PV industry in the year 2011. In the following years till today, the solar cell process technology has been constantly improved which increased the efficiencies of Al-BSF cells toward 20% and the efficiencies of PERC cells beyond 22% as shown in Fig. 5.5.

Due to continuous optimization of all process steps in Table 5.1 such as improved Ag pastes enabling narrower Ag fingers, selective emitters with advanced doping profiles, improved front and rear surface passivation layers, further developed Al pastes, LCO pattern, and busbar designs, the conversion efficiency of industrial PERC solar

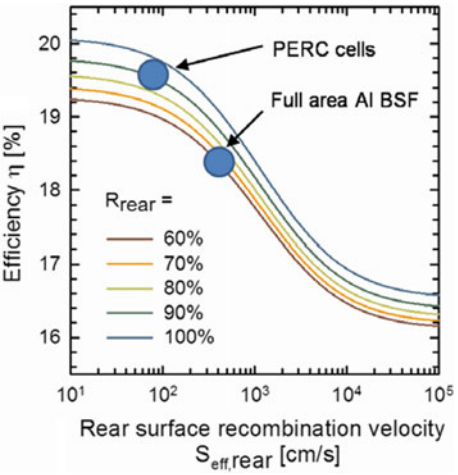

Fig. 5.4 PC1D simulation from the year 2011 [25] of the conversion efficiency in dependence of the rear surface recombination velocity $S_{\text{eff,rear}}$ for different internal rear reflectance values R_{rear}. The full-area Al-BSF with $S_{\text{eff,rear}}$ around 400 cm/s and R_{rear} around 65% limited the conversion efficiency of Al-BSF cells to about 18.5%. Due to the dielectric rear passivation, PERC cells exhibited a much lower $S_{\text{eff,rear}}$ around 50 cm/s and a higher R_{rear} around 90% and hence demonstrated conversion efficiencies close to 20%. In the following years, the efficiencies of Al-BSF improved toward 20% and of PERC cells beyond 22% as shown in Fig. 5.5

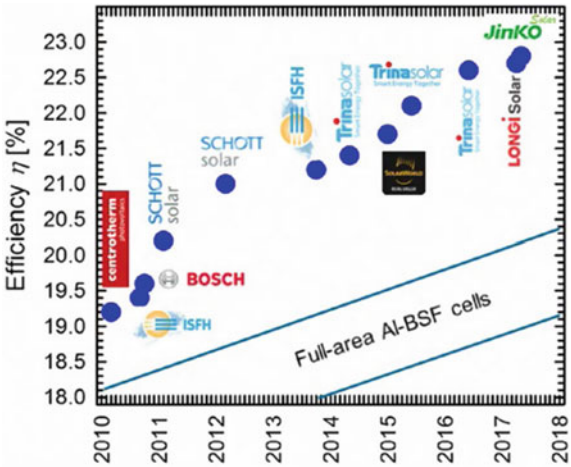

Fig. 5.5 Independently confirmed record conversion efficiencies of industrial-type PERC solar cells with screen-printed metal contacts using monocrystalline large-area p-type Cz silicon wafers. Typical efficiencies of full-area Al-BSF solar cells are indicated as well. Graph updated from [11]

cells has been constantly increased over the years. Figure 5.5 shows the evolution of record conversion efficiencies during the years 2010–2018 obtained with industrial PERC solar cells (large area >148 cm^2 p-type monocrystalline Czochralski-grown (Cz) silicon wafers, screen-printed metal front and rear contacts with conventional busbar layout) [22, 26–37]. Starting with an efficiency of 19.2% [26] reported by Centrotherm in 2010, the benchmark in 2012 has been 21.0% [28, 29] as demonstrated by Schott Solar. In 2014, the efficiency has been further increased to 21.2% by ISFH [30] and in July 2015 to 21.7% by SolarWorld [32]. Trina Solar was the first to surpass the 22% efficiency barrier by reporting a 22.1% efficient industrial PERC cell in December 2015 [33]. The present champion efficiencies of 22.7% and 22.8% have been obtained by LONGi Solar and JinkoSolar in October 2017, respectively [36, 37]. As can be derived from Fig. 5.5, the record efficiencies of industrial PERC cells increased by approximately $0.5\%_{abs.}$ per year as average value over the past 8 years. Simply extrapolating this trend predicts that in 2020 record PERC cell efficiencies will approach 24% applying industrially feasible production processes.

It took a lot of research and development effort to transfer the lab-type PERC concept of the UNSW into an industrially manufacturable PERC solar cell concept. A quite detailed summary of the historic development steps toward industrial PERC cells is given in [11]. Here, we just want to highlight the most important R&D achievements which enabled industrial PERC solar cells. As can be seen in Fig. 5.2a, for many years the so-called BSF or Al-BSF silicon solar cell was the dominant cell concept in industrial production. In order to upgrade a conventional industrial full-area Al-BSF production process into a PERC production process, mainly the rear passivation layer and the laser contact opening have to be introduced. Also, the phosphorus diffusion in the PERC process should only dope the wafer front surface and not the rear surface in order to avoid a floating rear junction or shunting of the electrodes. Hence, most of the R&D efforts for industrial PERC processes where directed toward low-cost and high-performance processes for the rear passivation

layer, for the rear contact structuring as well as for the wet chemical polishing process as outlined in the following paragraphs.

As described in the previous section, high-efficiency laboratory-type PERC solar cells often passivate the silicon wafer surfaces by means of silicon dioxide (SiO_2) grown at high temperatures ($\geq$800 °C) in a furnace [3]. However, this process is rather long and expensive and the SiO_2 passivation is dissolved by screen-printed Al pastes during firing. Hence, high-throughput low-cost surface passivation processes were required for industrial high-efficiency silicon solar cell manufacturing. Hezel and Jaeger [38] evaluated silicon nitride (SiN_x) grown by plasma-enhanced chemical vapor deposition (PECVD) at temperatures around 400 °C for surface passivation of silicon solar cells. PECVD obtains a high deposition rate resulting in short process times of just several seconds per wafer enabling high-throughput and low-production costs. Hence, PECVD SiN_x is already since many years applied as a front-side passivation layer of the phosphorus-doped emitter in industrial Al-BSF solar cells and seemed to be a promising candidate for the rear-side passivation of industrial PERC solar cells [12, 39, 40]. However, it was shown that on p-type rear silicon surfaces of PERC cells SiN_x passivation layers induce an inversion of the surface due to the positive fixed charges within the SiN_x layer leading to an enhanced carrier recombination which was identified and denoted as "parasitic shunting" by Dauwe et al. [20] in 2002. In contrast, aluminum oxide (AlO_x) was found to exhibit a high negative fixed charge density thereby being well suited to passivate p-type silicon surfaces [18, 19]. Hezel and Jaeger [38] reported already in 1989 that AlO_x passivates crystalline silicon surfaces quite well. Almost two decades later in 2006, Agostinelli et al. [41] and Hoex et al. [42] demonstrated excellent surface passivation properties of AlO_x single layers on p-type silicon wafers. The initial research applied lab-type low-throughput atomic layer deposition (ALD) of AlO_x layers [19, 43]. After demonstrating the high surface passivation quality, high-throughput deposition processes and tools have been developed such as PECVD [16, 17, 44–46] and spatial ALD [47, 48] which are capable of processing several thousand silicon wafers per hour and per production tool. For application of AlO_x as rear passivation in industrial PERC solar cells, the AlO_x layer has to be capped with a SiN_y layer in order to prevent the dissolution of the AlO_x layer by the Al paste during firing. Additionally, the SiN_y capping layer increases the internal optical reflectance which in turn leads to improved light trapping [49].

Regarding low-cost rear contact patterning instead of very expensive photolithography, in the year 2000 Preu et al. [21] demonstrated that laser ablation of the rear passivation layer is a promising industrial process to define the rear contact pattern as it removes the passivation layer with only minimal damage of the silicon crystal structure. Also, laser ablation allows to pattern the whole wafer rear side within just a few seconds enabling a throughput of several thousand wafers per production tool. The laser ablation approach was further developed by Agostinelli et al. [12, 13] in 2005 into the so-called "i-PERC" concept which proposed for the first time to combine laser ablation of the rear passivation layer with screen-printed Al layers, thereby forming local Al-BSF regions by alloying of the silicon and the aluminum through the laser contact openings (LCO) during the furnace firing step. This

approach resulted then in large-area i-PERC solar cells with efficiencies up to 17.2% [13] which outperformed the corresponding full-area Al-BSF cells by $0.7\%_{abs}$. Gatz et al. [22] were the first to apply line-shaped instead of point-shaped LCOs in combination with improved aluminum pastes which resulted in PERC cell conversion efficiencies of 19.4% in 2011. The company Sunrise proposed to combine the benefits of LCO lines for the Si–Al alloying process with the benefit of LCO points for minimizing the contact area fraction by applying for the first time dashed-line LCO contact geometry [23]. In parallel to the aforementioned LCO research activities, the composition of Al pastes has been further developed to improve Al–Si alloying and local Al-BSF formation resulting in better Al contact properties. In 2006, Meemongkolkiat et al. [50] demonstrated that a key requirement is to use a low content of glass frits in the Al paste in order to prevent etching of the rear passivation layer during furnace firing. Also, it was shown that the addition of certain materials to the Al paste resulted in a strongly increased Al-BSF depth [50]. However, at that time it was not disclosed neither what type of material was added to the Al paste nor what the physical mechanism was that enabled the deeper Al-BSF. In 2011, Rauer et al. [51] demonstrated that the addition of up to 24 wt% silicon to the Al paste increases the Si concentration in the Al–Si melt during furnace firing resulting in a thicker epitaxially regrown Al-BSF.

In order to obtain a single-sided phosphorus doping of the PERC cell front side, the company Centrotherm developed an industrial PERC process flow where the rear passivation layer (in this case a PECVD SiO_x/SiN_y stack) is deposited prior to the phosphorus diffusion thereby acting as a diffusion barrier and protecting thecells manufacturers rear side from being phosphorus doped [52]. This so-called "Centaurus process" was the first turnkey solution for industrial PERC production lines becoming available in 2011 [53]. A technological challenge of the Centaurus process is that the rear passivation layer has to maintain its passivation properties after being exposed to a high-temperature $POCl_3$ diffusion. Centrotherm achieved this by applying an optimized PECVD SiO_x/SiN_y passivation stack, whereas AlO_x/SiN_y stacks severely degrade during $POCl_3$ diffusion. A second approach to obtain a single-sided phosphorus doping relied on wet chemical etching of the rear wafer surface. Early work in 2009 on rear side etching [54, 55] applied the process sequence texturing - wet chemical polishing of the rear wafer surface—$POCl_3$ diffusion—wet chemical junction isolation. This process sequence allowed very long polishing of the rear surface resulting in smooth wafer rear surfaces without impacting the front-side phosphorus emitter by the reactive gas phase of the chemical polishing bath. However, it was shown by Kranz et al. [56] that, in particular, when applying an AlO_x/SiN_y passivation stack the rear surface roughness can be quite high without detrimental impact on the conversion efficiency. Accordingly, further work by RENA and ISFH in 2013 [14, 15] simplified the process sequence to texturing—$POCl_3$ diffusion—wet chemical rear polishing by developing a less reactive wet chemical polishing chemistry resulting in less emitter front etching and a higher rear surface roughness. Compared to the Centaurus process, one advantage of the polishing PERC process is that it is compatible with the favorable AlO_x/SiN_y rear passivation stack. This maybe

one reason why the polishing process sequence as shown in Table 5.1 became the most widely used process sequence for industrial PERC solar cell production.

5.3 Bifacial PERC+ Solar Cells

As described in the previous section and displayed in Fig. 5.6, industrial PERC cells apply p-type wafers and a full-area screen-printed aluminum (Al) rear layer which only locally contacts the silicon wafer at areas where the rear passivation has been removed by laser contact opening (LCO). The full-area aluminum layer prevents any transmission of diffuse sunlight from the rear side into the silicon wafer and hence any bifacial applications of these industrial PERC cells. On the other hand, bifacial solar cell concepts receive increasing interest for applications, e.g., in PV power plants where the produced electricity can be increased by up to 25% using bifacial instead of monofacial solar modules due to the absorption of diffuse light by the module's rear side [57, 58]. Accordingly, the photovoltaic technology roadmap

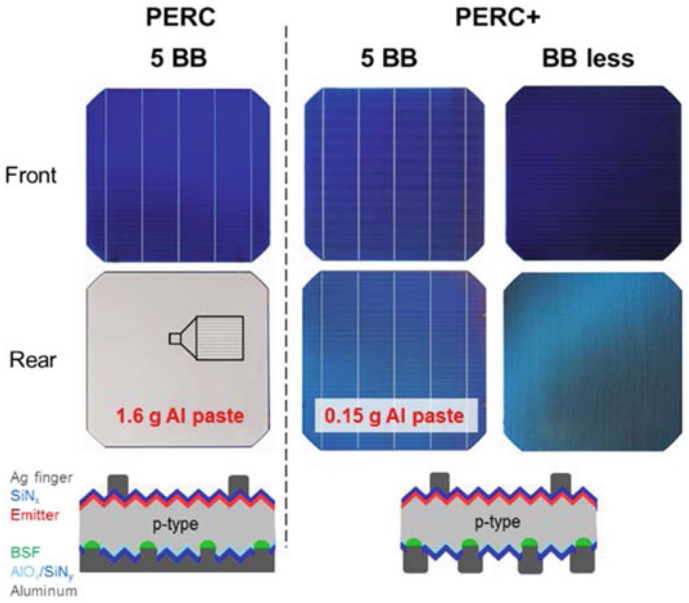

Fig. 5.6 Photographs of the front and rear sides as well as schematic cross-section drawings of industrial PERC and PERC+ solar cells. PERC+ cells enable bifacial applications and reduce the Al paste consumption while applying the same processing sequence in Table 5.1 as industrial PERC solar cells. Applying a busbar-less metal grid design ISFH demonstrated a PERC+ cell with 22.1% front-side efficiency. Figure reproduced from [11]. Copyright (2018) The Japan Society of Applied Physics

ITRPV predicts a market share of bifacial solar cells of 40% until 2028 as shown in Fig. 5.2b [8].

The concept of a bifacial solar cell absorbing sunlight from the front and rear sides has first been published in a patent by H. Mori in 1960 [59]. At that time, the idea was to use pn-junctions at the front and rear sides in order to improve the collection of photogenerated charge carriers at both wafer surfaces. Bifacial solar cells with industrially applicable manufacturing technologies have been developed from the year 2000 onward mostly by applying n-type wafers. The passivated emitter and rear totally diffused (PERT) solar cell concept has been adopted by ECN and Yingli to the bifacial PANDA solar cell [60, 61] and by ISC and Bosch to the BiSoN solar cell [62]. The so-called heterojunction solar cells which apply n-type wafers and doped amorphous Si surface passivation layers have been developed by Sanyo which now belongs to Panasonic as HIT solar cell [63] and by Meyer Burger and CSEM to a turnkey process solution [64]. A challenge of these n-type PERT and heterojunction cell concepts is that they typically apply screen-printed silver (Ag) finger grids on both wafer sides and hence consume a high amount of expensive Ag paste. Also, the n-PERT cells apply single-sided boron and phosphorus doping which requires additional or other process steps compared to p-type PERC cells. Industrial bifacial silicon solar cell concepts applying p-type wafers and a screen-printed Al rear finger grid have been investigated as well. In 2001, ISFH introduced a bifacial p-type solar cell where the rear Al grid fired through the SiN_x rear passivation layer without using any laser contact opening or rear-side boron doping [40]. ECN further developed this approach to the so-called p-PASHA cell concept [65]. However, the published efficiencies of these bifacial p-type solar cells with fired through Al fingers were just similar to full-area Al-BSF cells and significantly lower compared to typical industrial PERC cell efficiencies probably due to insufficient local Al-BSF formation.

ISFH and SolarWorld first published a bifacial PERC solar cell in 2015 by applying a screen-printed rear Al finger grid instead of the conventional full-area aluminum (Al) rear layer [24, 66], see Figs. 5.3c and 5.6. As shown in Table 5.1, the bifacial PERC cell used the same manufacturing sequence compared to monofacial PERC cells with only minimal recipe modifications for rear passivation, laser contact opening, and Al screen printing in order to produce bifacial PERC solar cells without investing into new or different production tools. Dullweber et al. named this novel cell concept PERC+ and demonstrated several advantages in the initial publications [24, 66]. The Al finger grid enabled bifacial applications of the PERC+ cells with rear-side efficiencies up to 16.7% while still obtaining very high front-side efficiencies above 21% comparable to monofacial PERC cells [66]. The corresponding bifaciality was up to 80.0%. Also, as outline in the next sections, PERC+ improves the Al-BSF contact properties, and when combined, e.g., with a white back sheet, obtains a higher rear-side reflectance [66]. Another advantage is that Al paste consumption of the PERC+ cells with Al finger grid is reduced up to 90% compared to PERC cells with full-area Al layer [24]. In 2015, two additional papers addressed the concept of bifacial PERC+ cells. Trina Solar developed glass/glass modules applying bifacial PERC+ solar cells with colored rear-side passivation designed for aesthetic optical appearance in building integrated photovoltaic applications [67]. These mod-

ules where, however, not designed and optimized for maximizing bifacial energy yield, e.g., in PV power plants. Krauß et al. performed numerical simulations of the potential front and rear conversion efficiencies of bifacial PERC+ cells and their corresponding bifacial gains [68].

Meanwhile, PERC+ solar cells have been introduced into mass production by many solar cells manufacturers. Table 5.2 summarizes published PERC+ conversion efficiencies when illuminated from the front or rear side. ISFH sets the benchmark in 2015 for high PERC+ front and rear-side efficiencies as outlined above. First published PERC+ conversion efficiencies of solar cell manufacturers were 20.3% [67] in 2015 and 20.7% [69] in 2016 which then continuously improved to 22.0% in 2017 as reported by LONGi Solar [70]. The highest PERC+ efficiency so far has been reported by ISFH by developing a busbar-less PERC+ solar cell [11] by screen printing only the Ag fingers on the front side without the Ag busbars as shown in Fig. 5.6, thereby reducing the shading losses of the Ag front grid. Industrially, this approach is attractive when combined with wire-based module interconnection technologies as will be described in a later paragraph. The busbar-less PERC+ cell exhibits an independently confirmed conversion efficiency of 22.1% [11] when illuminated from the front side, see the last line in Table 5.2. Due to the continuous efficiency improvements of industrial PERC solar cells as shown in Fig. 5.5, very likely even higher PERC+ front-side efficiencies will be obtained soon. At the same time, the conversion efficiency when illuminated from the rear side of PERC+ cells produced by cell manufacturers improved from 13.9% [69] in 2016 to 17.5% [70] in 2017 as shown in Table 5.2. For the 22.1% efficient PERC+ cell fabricated by ISFH in 2017 [11], the rear-side efficiency was not published as the rear Al finger grid has been optimized for monofacial applications and not for high bifaciality. Unfortunately, several leading solar cell manufacturers such as SolarWorld and Trina Solar which are producing

Table 5.2 Published efficiencies of industrial PERC+ solar cells when illuminated from the front or from the rear side. Several leading solar cell manufacturers such as SolarWorld and Trina Solar are producing bifacial PERC+ cells and modules (see Table 5.3) but did not publish any or recent PERC+ cell efficiencies

Year	Efficiency [%] front/rear	Organization	Source/comments
2015	21.5/16.7	ISFH	[66]; industrial process flow. No rear Ag pads
2015	20.3/n.p.	Trina Solar	[67]; optimized for optical appearance in BIPV
2016	20.7/13.9	Big Sun Energy Technology Inc	[69]
2017	21.5/16.1	JinkoSolar	[71]
2017	21.4/n.p.	Neo Solar Power	[72]
2017	22.0/17.5	LONGi Solar	[70]
2017	22.1[a]/n.p.	ISFH	[11] busbar-less Ag front grid

n.p.: not published; [a]independently confirmed

Table 5.3 Commercially available bifacial modules applying PERC+ solar cells. Maximum rating power stated for front-side illumination under standard test conditions (STC, AM1.5, 25 °C) and without rear-side illumination

Company/Product	Maximum rating power [Wp]	Comments	Source/year
SolarWorld/Bisun	290	5 BB, 60 cells	[73]/2017
Neo Solar Power/Glory Bifi	300	4 BB, 60 cells	[74]/2017
Trina Solar/DUOMAX	300	5 BB, 60 cells	[75]/2017
LONGi Solar/LR6-60PD	305	4 BB, 60 cells	[76]/2017
Jinko Solar/Swan bifacial 60H	330	5 BB, 60 cells	[77]/2019
Canadian Solar/Biku Module	315	5 BB, 60 cells	[78]/2019
LONGi Solar/Hi-MO4 bifacial	365	6 BB, 60 cells	[79]/2019

bifacial PERC+ cells and modules (see Table 5.3) did not publish any or no recent PERC+ cell efficiencies and hence do not appear at all or only with initial results in Table 5.2.

One key issue with the development of bifacial PERC+ cells is the very high specific resistivity of 20 μΩcm [25] of screen-printed Al fingers which is approximately six times higher compared to screen-printed Ag fingers. This is probably the main reason why most alternative industrial bifacial solar cell concepts focus on Ag finger grids on both wafer sides as outlined at the beginning of this section. Hence, in case of PERC+, the rear Al finger grid has to be designed in a way to minimize series resistance losses caused by the Al finger lines. Dullweber et al. calculated the series resistance contribution $R_{s,L}$ of the Al finger grid [11] in dependence of the number of busbars/wires and the Al finger width applying the equation

$$R_{s,L} = \frac{2}{3}\rho_f \frac{l_f}{A_f} \cdot A_{uc} \tag{5.1}$$

with the specific resistivity ρ_f of the Al paste, the finger length l_f, and the finger cross-section area A_f. The area of the unit cell of the Al finger grid layout (half finger pitch times half busbar distance) is described by the parameter A_{uc}. The calculated series resistance contribution $R_{s,L}$ of the Al finger grid is shown in Fig. 5.7 [11]. In order not to significantly reduce the front-side efficiency when changing from PERC to PERC+, as a rule of thumb $R_{s,L}$ should remain below 0.05 Ωcm^2. As this is not possible with a three-busbar configuration due to the high Al finger length l_f in between the busbars, the five-busbar design can be considered as an enabling technology of bifacial PERC+ cells when applying wide Al fingers around 150 μm. When moving to narrow Al fingers below 100 μm width, multi-wire module interconnection technologies with, e.g., 10 or 20 wires per PERC+ cell drastically minimize resistive losses of the Al fingers below 0.02 Ωcm^2.

The fine-line-print capability of Al finger pastes strongly improved over the past few years when Al paste vendors started to develop PERC+ specific Al pastes which

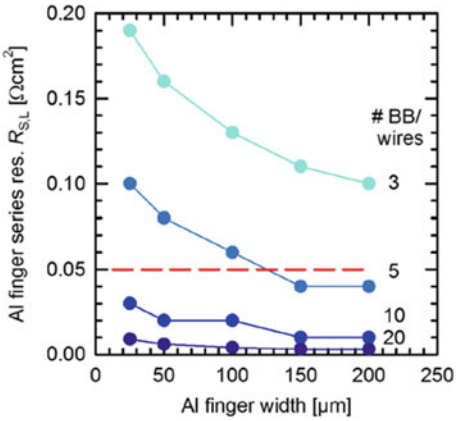

Fig. 5.7 Calculated series resistance contribution $R_{s,L}$ of the Al finger grid in dependence of the number of busbars/wires and the Al finger width. In order not to reduce the front-side efficiency when changing from PERC to PERC+, the series resistance increase caused by the Al finger grid should remain below 0.05 Ωcm^2. As this is not possible with a three-busbar configuration due to the high Al finger length, the five-busbar design can be considered as an enabler of bifacial PERC+ cells. When moving to very narrow Al fingers below 100 µm width, multi-wire technologies with, e.g., 10 or 20 wires help to minimize resistive losses of the Al fingers. Figure reproduced from [2, 11] with permission. Copyright (2018) The Japan Society of Applied Physics

reduce the spreading behavior of Al pastes during screen printing. Figure 5.8 shows the measured Al finger widths in dependence of the screen opening widths obtained with different Al pastes [12]. Whereas conventional PERC Al pastes designed for full-area Al screen print show an extreme spreading behavior resulting in wide Al fingers, and the novel PERC+ Al pastes enable 50–100 µm narrow Al fingers when applying 50–75 µm screen openings as shown in Fig. 5.8. The latest Al finger pastes with 50 µm Al finger width approach the fine-line printing capability of actual Ag finger pastes with printed Ag finger widths of only 35 µm as sketched in Fig. 5.8. When printing very narrow Al fingers, it becomes challenging to precisely align the Al fingerprint on top of the laser contact openings (LCO). In case of extreme misalignment when the Al finger does not overlap the LCO area, the open and laser-damaged silicon surface of the LCO area leads to very high surface recombination of minority charge carriers [11]. Accordingly, the alignment tolerance between Al fingerprint and LCO of approximately ±30 µm depending on the detailed Al finger and LCO geometries needs to be fulfilled for high PERC+ conversion efficiencies. This requires high precision laser processes and Al screens as well as camera-based alignment schemes between LCO and Al screen print.

First commercial bifacial PERC+ glass/glass modules have been introduced by SolarWorld at the Intersolar 2015 [80] followed by Neo Solar Power, Trina Solar, and LONGi Solar in 2017 [74–76]. Meanwhile, almost all major solar cell manufacturer offer commercial bifacial glass/glass modules applying PERC+ solar cells as summarized in Table 5.3. The interconnection of PERC+ cells to strings is accomplished

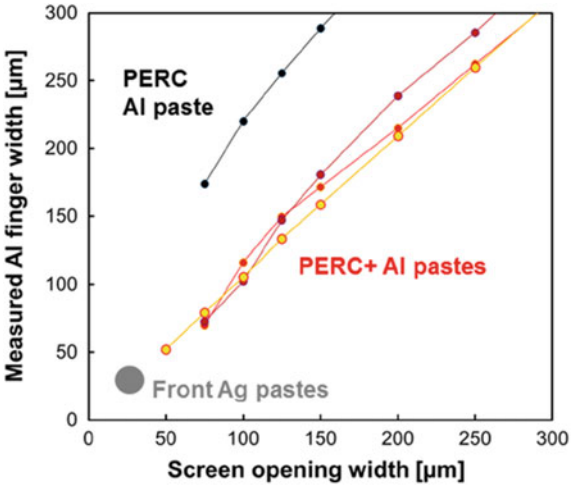

Fig. 5.8 Measured aluminum finger widths in dependence of the screen opening widths. Whereas conventional Al pastes designed for full-area print of PERC solar cells exhibit an extreme spreading, recently developed Al pastes for PERC+ fingerprints enable Al finger widths close to 50 µm. In comparison, Ag pastes obtain final finger widths around 35 µm with screen opening widths of 25–30 µm. Graph updated from [11]

using conventional tabbing–stringing technology where the Cu ribbons are soldered to the Ag front busbars and to Ag pads on the PERC+ rear side. All manufacturers apply four or five busbar designs in order to minimize Al finger resistance losses as shown in Fig. 5.7 and Table 5.3. Since the first publication by Hannebauer et al. in 2014 of a PERC cell applying a five-busbar design [30], the PV industry has migrated from three busbars to four or five busbars which is beneficial to the industrial adoption of PERC+ cells. As shown in Table 5.3, the commercially available maximum rating powers range between 315 and 365 W_p with 60 PERC+ cells per module [77–79]. The rating power is stated for front-side illumination only. When applying additional rear-side illumination, the output power increases accordingly. For example, with 10% additional rear-side illumination, the output power will increase by approx. 8% approaching 400 W_p total output power. The resistive losses caused by PERC+ rear Al fingers can be further reduced by moving from four or five busbar designs to PERC+ solar cells without any busbars. In this case, the module interconnection is accomplished by, e.g., 10 or 20 wires which reduce the Al finger lengths to a few millimeters, and hence drastically minimizing its grid line resistance as shown in Fig. 5.7. The reduced grid line resistance allows a further reduction of the Al finger width to well below 100 µm which minimizes shadowing losses of the Al finger grid and increases rear efficiency and bifaciality. In 2017, ISFH has developed a wire-interconnected PERC+ prototype module [81] where 18 wires are soldered directly to the Ag front and Al rear fingers applying the smart wire connection technology (SWCT) of Meyer Burger [82] without using Ag busbars or Ag pads. The PERC+

SWCT module exhibits an independently confirmed front-side efficiency of 19.8%, a rear-side module efficiency of 16.4%, and a bifaciality of 83% [81].

When applying bifacial PERC+ modules to outdoor field installations, in particular, the albedo of the ground and the mounting height of the module are important parameters to maximize the additional diffuse illumination of the module's rear side and hence the additional energy yield of bifacial PERC+ modules compared to monofacial PERC modules. Numerical simulations predict that the energy yield of PERC+ modules can increase up to 25% when mounted 0.5 m above ground with an albedo of 80% [24]. SolarWorld took the effort to measure the energy yield of Bisun modules in two different small-scale outdoor test installations. A 3.2 kWp installation on top of a flat roof with a high albedo of 74% due to white ballast stones demonstrated an increased energy yield of 13% compared to a monofacial PERC reference module which compared well to the calculated energy yield of 13.3% [83]. When mounted to a two-axis tracker system, the Bisun modules obtained 10% additional energy yield compared to monofacial PERC modules mounted on a two-axis tracker where the sandy ground had an albedo of 30% [83]. Trina Solar measured the energy yield of bifacial DUMAX modules either with a fixed mounted installation or mounted on a one-axis tracker and compared the results to a fixed mounted monofacial PERC module [84]. The fixed mounted bifacial modules demonstrated a 10% increased energy yield and the bifacial DUOMAX modules mounted on a one-axis tracker demonstrated a 24% increased energy yield compared to the fixed mounted monofacial modules [84], both on sandy ground. Hence, the combination of bifacial PERC+ modules with one-axis trackers is a very promising option to strongly increase the energy yield of photovoltaic power plants. Meanwhile, several large scale PV power plants with electricity generation capacity up to 224 MWp applying bifacial PERC+ solar cells are under construction [85–88]. Latest solar bids for new PV power plants approach an electricity price of $0.02/kWh where the combination of bifacial PERC+ cells with one-axis-trackers strongly contributes to reducing the PV electricity price [89] (Fig. 5.9). Accordingly, a recent market research study predicts that bifacial

Fig. 5.9 Photograph of a large scale 20 MWp PV power plant installed by LONGi in Golmud, China, applying bifacial PERC+ solar cells in combination with one-axis trackers thereby maximizing the energy yield from the modules front and rear side [91]

PERC+ module production capacity will strongly increase to 17% of the global solar module production capacity in 2021 [90].

5.4 AlO_x/SiN_y Rear Passivation and Local Al Rear Contacts

In order to obtain high conversion efficiencies with PERC and PERC+ solar cells, as shown in Fig. 5.4, the effective minority charge carrier recombination velocity $S_{\text{eff,rear}}$ at the rear side has to be as low as possible. $S_{\text{eff,rear}}$ can be calculated from the surface recombination velocities S_{pass} in the AlO_x/SiN_y passivated area and in the Al contacted area S_{cont} according to an analytical model proposed by Fischer [92] for contact patterns where the Al contact spacing is large compared to the wafer thickness:

$$S_{\text{eff,rear}} = \left(\frac{R_s - \rho W}{\rho D} + \frac{1}{f S_{\text{cont}}} \right)^{-1} + \frac{S_{\text{pass}}}{1 - f} \tag{5.2}$$

The parameters in (2) are the wafer bulk spreading resistance contribution R_S and the diffusion coefficient of the minority charge carriers $D = 26.9$ cm^2/s. The silicon wafer related parameters are the specific resistivity which is typically between 1 and 2 Ωcm for PERC cells and the wafer thickness W around 180 µm. The area fraction f of the Al rear contacts is typically between 1 and 5%. In order to obtain high conversion efficiencies by a low $S_{\text{eff,rear}}$, a low surface recombination velocity S_{pass} in the AlO_x/SiN_y passivated area of below 10 cm/s is required as well as a low surface recombination velocity S_{cont} below 500 cm/s at the local Al rear contacts. Applying these parameter settings to (2) results in $S_{\text{eff,rear}} < 50$ cm/s which is a typical value for high-efficiency PERC solar cells. An easy to use and hence practical approximation of (2) calculates the saturation current density of the whole rear-side $J_{0,\text{rear}}$ based on the saturation current densities of the rear passivation $J_{0,\text{pass}}$ and the local Al contacts $J_{0,\text{cont}}$ applying the equation $J_{0,\text{rear}} = (1 - f) \times J_{0,\text{pass}} + f \times J_{0,\text{cont}}$. Both equations favor small contact area fractions f which can be obtained either by reducing the laser contact opening line widths or dot diameter or by increasing the spacing of the laser contact openings. However, both approaches have their limitations. When reducing the laser contact opening line width or dot diameter too much, the Al–Si alloying is affected resulting in narrower Al-BSF depths and increased contact recombination as will be described in the following paragraphs. When increasing the spacing of the laser contact openings, the bulk spreading resistance increases since the majority charge carrier has to travel a longer distance to reach the rear contacts. Hence, optimizing the rear contact geometry of industrial PERC and PERC+ solar cells is a complex task since many parameters have to be considered. In any case, reducing the specific surface recombination velocities S_{pass} and

S_{cont} of PERC solar cells was and still is an important task for further improvements as outlined in the following paragraphs.

Aluminum oxide (AlO_x) was first published by Hezel and Jaeger [38] in 1989 to passivate crystalline silicon wafer surfaces with measured surface recombination velocities around 100 cm/s. However, it took until 2006 when Agostinelli et al. [41] and Hoex et al. [42] demonstrated excellent surface recombination velocities below 15 cm/s by applying atomic layer deposited (ALD) AlO_x layers on p-type silicon wafer surfaces. Meanwhile, many publications have reported excellent surface passivation properties of AlO_x layers [19, 43, 92–96] by applying many different deposition processes such as atomic layer deposition (ALD) [19, 43], plasma-enhanced chemical vapor deposition (PECVD) [16, 17], inductively coupled plasma (ICP) deposition [44, 45], atmospheric pressure chemical vapor deposition (APCVD) [38, 97], or reactive sputtering [94]. AlO_x is ideally suited to the rear passivation of p-type PERC solar cells, as the parasitic shunting observed with SiN_x layers is completely absent—thanks to the fixed *negative* charges [18, 19]. Figure 5.10 displays the surface recombination velocity S of AlO_x layers deposited by ALD and ICP versus an external charge Q_c applied to the AlO_x layers by corona discharge [45]. Without external charges, both layers obtain S values below 10 cm/s. At a positive corona charge around 4×10^{12} cm^{-2}, the internal negative charge is compensated resulting in highest S values of around 200 cm/s. Hence, this measurement nicely demonstrates the importance of the negative charges of AlO_x layers which repel minority charge carriers (electrons in case of PERC cells) from the rear side thereby minimizing carrier recombination. Industrial-type PERC solar cells use screen printing

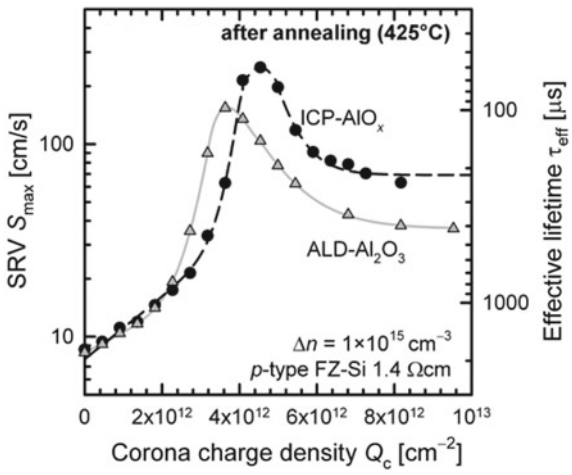

Fig. 5.10 Surface recombination velocity S of AlO_x layers deposited by ALD and ICP versus an external charge Q_c applied by corona discharge. Without external charges, both AlO_x layers obtain excellent S values below 10 cm/s. At a positive external corona charge around 4×10^{12} cm^{-2}, the internal negative charge is compensated resulting in highest S values of around 200 cm/s. Figure taken from [45]

of metal pastes and firing in a belt-line furnace at high temperatures (750–850 °C) for contact formation, which makes an excellent thermal stability of the surface passivation indispensable. As demonstrated by Schmidt et al., thin AlO_x layers tend to degrade during firing; however, a hydrogen-containing SiN_y capping layer deposited by PECVD improves the firing stability considerably [95]. The SiN_y capping layer also serves as a protection layer since the AlO_x is not stable against the aluminum paste during firing. The annealing step which is required for an excellent passivation quality of the AlO_x layer can be integrated into the SiN_y deposition by heating the wafers in the PECVD chamber before depositing the SiN_y [17, 45, 98]. Meanwhile, AlO_x/SiN_x stacks deposited by PECVD are the preferred choice as rear passivation of industrial PERC solar cells in mass production [6].

In addition to the AlO_x/SiN_x rear passivation, the local aluminum (Al) rear contacts strongly influence the current voltage parameters of industrial PERC solar cells. As can be seen in (5.2), the surface recombination velocity S_{cont} of charge carriers at the local Al contacts has to be small. The carrier recombination at the Al contact can be reduced by the local aluminum p+ doping called the aluminum back surface field (Al-BSF) surrounding the contact. The Al-BSF forms a p/p+ doping gradient and hence a built-in electric field which repels the electrons from the Al contact, whereas the hole transport is not blocked by the Al-BSF. Hence, understanding the Al–Si alloying process and Al-BSF growth during furnace firing is the key in order to optimize the electrical Al contact properties. When the wafer temperature during furnace firing exceeds 660 °C, the aluminum melts and according to the Al–Si phase diagram [99], silicon from the wafer dissolves in the aluminum paste at areas where the rear passivation has been removed by LCO. If the firing temperature and time are sufficiently high, the silicon concentration in the aluminum melt exceeds the eutectic concentration of 12.6 wt% of silicon in aluminum [99]. During cooldown of the firing process, excess silicon in the Al paste beyond the eutectic concentration epitaxially recrystallizes at the silicon wafer surface thereby incorporating aluminum up to its solid solubility limit which is in the range of 5×10^{18}cm^3. Aluminum acts as p-type dopant in the silicon crystal lattice thereby forming the local Al-BSF. The specific challenges of optimizing local Al–Si contacts of PERC solar cells as well as screen printing Al fingers in PERC+ cells are outlined in the following sections.

Whereas the lab-type PERC cell of Blakers et al. [3] applied point-shaped local rear contacts in combination with evaporated Al, in 2011 it was shown by Lauermann et al. [100] that point contacts in industrial-type PERC cells processed with local removal of the passivation layer, Al screen printing and firing cause severe void formation similar to Fig. 5.11a resulting in a scattering of the Al-BSF depth from 0 to 6 μm. In contrast, according to [100], line-shaped local rear contacts decrease the amount of voids and increase the Al-BSF depth to 4–7 μm thereby reducing contact recombination and increasing PERC conversion efficiencies. Further investigations applying carrier lifetime measurements demonstrated that compared with point contacts line contacts achieve a lower surface recombination velocity down to 800 cm/s [101]. Gatz et al. [102] revealed that the Al-BSF depth increases with increasing LCO line width thereby reducing the contact recombination velocity down to 300 cm/s. The application of an LCO line width of 80 μm, full-area Al screen printing and

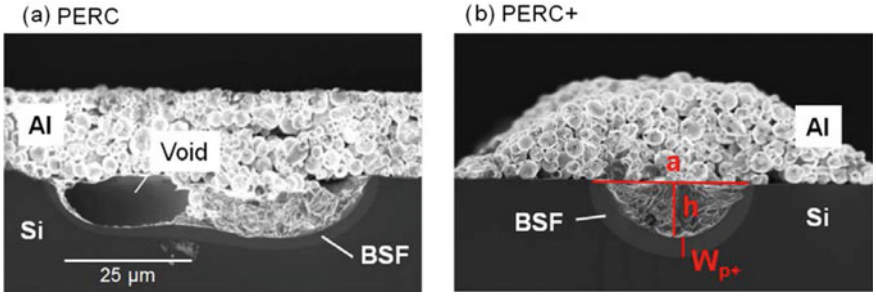

Fig. 5.11 Typical scanning electron microscope (SEM) images of locally alloyed aluminum contacts of **a** PERC and **b** PERC+ solar cells. Whereas the local Al contacts of PERC cells often show voids and a thin back surface field (BSF), PERC+ cells exhibit filled contacts and a deep BSF. Al contact geometries used for physical models in Fig. 5.12 are shown in image **b** such as the Al contact width a, the contact height h, and the Al-BSF depth W_{p+}. Figure (**a**) is reproduced from [2] with permission

firing to industrial-type PERC solar cells resulted in a record efficiency of 19.4% in 2011 [22]. In the same year, Urrejola et al. [103] systematically investigated the diffusion of silicon from the wafer through local line-shaped contact openings into the aluminum paste during furnace firing. One main result was that the maximum spread of silicon in the aluminum paste ranges between 300 and 1000 µm depending on the peak firing temperature and on the opening width. Hence, the silicon diffusion and following Al–Si alloy formation extend several hundred µm beyond the local rear contact edges into the aluminum paste. Taking this finding into account, in 2012, Müller et al. [104] proposed an analytical model which calculates the Al-BSF thickness in dependence of the contact geometry and several other process parameters. The model assumes a box-shaped silicon distribution in the aluminum paste with eutectic concentration after firing. The width of the box is used as a fit parameter to adjust the model to experimental Al-BSF values. The assumption of a box profile rather than the more realistic Gaussian silicon concentration profile greatly simplifies the model since no differential equations for the silicon diffusion have to be solved. The model further assumes that the excess silicon in the aluminum paste above the eutectic concentration recrystallizes as Al-BSF during cooldown of the firing step. The model reproduces the experimental finding that a certain minimum line width or a minimum point diameter is required to obtain several µm deep Al-BSFs as needed for low contact recombination and high-efficiency PERC cells. According to the model, the physical reason is that in case of thin lines or small points the large silicon spread beyond the LCO edges in the aluminum paste significantly reduces the silicon concentration in the aluminum paste and hence the amount of silicon which is available for the Al-BSF formation. In the extreme situation of very small LCO contacts, the silicon concentration in the aluminum paste is reduced below the eutectic concentration and hence no silicon is available for the Al-BSF growth. The model also describes accurately that line-shaped LCO contacts limit the Si diffusion to one direction, and hence obtain a high Si concentration and deeper Al-BSF

compared to point-shaped contacts, where the Si diffuses in all directions from the LCO into the Al layer. In addition to optimizing the LCO geometry another approach to deeper Al-BSF is to modify the composition of the Al paste, e.g., by adding Si powder in order to increase the Si concentration available for Al-BSF regrowth. In 2006, Meemongkolkiat et al. [50] showed that the addition of certain materials to the Al paste resulted in a strongly increased Al-BSF depth, however, without disclosing what type of materials was added to the Al paste. In 2011, Rauer et al. [51] demonstrated that the addition of up to 24 wt% silicon to the Al paste increased the Si concentration in the Al–Si melt during furnace firing resulting in a thicker epitaxially regrown Al-BSF.

All investigations of the Al-BSF formation as described above favor either wide line-shaped rear contacts or point-shaped rear contacts with very large diameter in order to fabricate a deep Al-BSF and hence to reduce the surface recombination velocity at the Al rear contacts. Nevertheless, for optimum PERC conversion efficiencies, the contacted area fraction should be small in order to keep the absolute contact recombination small as shown in (5.2). Also, the wafer bulk spreading resistance increases with wider contact spacing, hence limiting the efficiency. These considerations favor rear contact geometries which achieve a sufficiently deep Al-BSF with as small as possible contact area. An interesting approach to achieve this was introduced in 2013 by the company Sunrise [23]. They proposed a dashed-line rear contact geometry which potentially achieves a deep Al-BSF due to the line-shaped LCO contacts and simultaneously a small metalized area fraction in combination with low bulk resistance contribution due to the arrangement of the dashed lines similar to point-shaped contact patterns [23]. Another reason why industrial PERC cells favor as small as possible LCO contact areas is to limit the LCO process time to a few seconds per wafer enabling throughputs of several thousand wafers per hour per LCO production tool. This is the main reason why a typical industrial LCO line width today is in the range of 20–40 μm [105]. Thanks to huge progress in optimizing PERC-specific Al pastes as discussed above, today several μm deep Al-BSFs can be obtained with industrially feasible 30 μm narrow LCO openings.

In case of PERC+ solar cells, the Al finger width confines the diffusion of silicon in the Al paste thereby potentially increasing the Si concentration resulting in deeper Al-BSFs compared to full-area Al layer in PERC cells [24]. Figure 5.11 shows typical SEM images of local Al contacts of PERC and PERC+ solar cells. Whereas the local Al contacts of PERC cells often show voids and a thin BSF, PERC+ cells exhibit filled contacts and a deep BSF [24, 106]. Figure 5.12a shows measured Al-BSF depths demonstrating that PERC+ cells obtain up to 8 μm deep Al-BSFs compared to PERC with up to 6 μm. The black line represents a fit applying the model of Mueller [104] to the PERC data. The red line shows a fit to the PERC+ data using an extended model that takes the limited Al volume of the Al fingers into account [106]. According to the model, the limited Al volume of the Al fingers leads to a higher silicon concentration in the screen-printed aluminum during furnace firing causing thicker Al-BSFs during the epitaxial regrowth in the cooldown phase [106]. This effect becomes more pronounced for narrow Al contact widths around 50 μm which are industrially preferred in order to increase the throughput of the LCO tool.

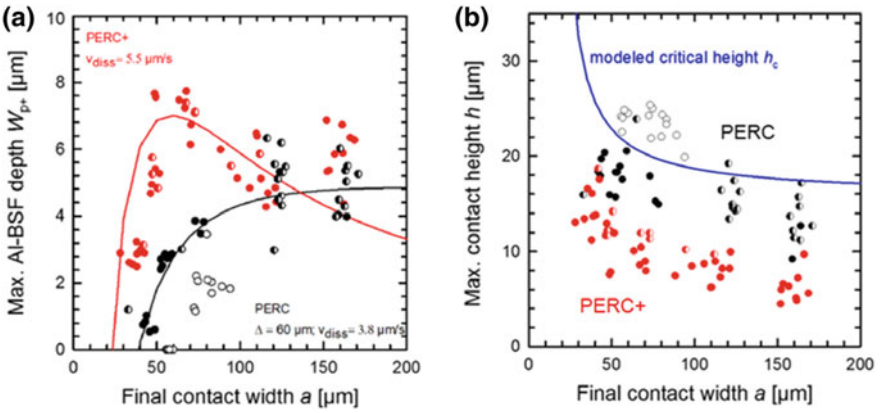

Fig. 5.12 **a** Maximum Al-BSF depth of PERC (black) and PERC+ (red) solar cells in dependence of the Al contact width a. PERC+ cells obtain a deeper Al-BSF compared to PERC since the Al fingers confine the Si diffusion during firing according to experimental data (dots) and analytical models (lines). **b** Voided Al contacts symbolized by open circles are often found for large contact heights were the Al alloys deeply into the silicon wafer. This finding is explained by modeling the surface energies of the Si wafer, the Al particles, and the liquid Al–Si melt. The Al contact parameters W_{p+}, h, and a are defined in Fig. 5.11b. Both graphs are reproduced from [107] with permission

Figure 5.12a, b uses different symbol styles where filled circles indicate a filled local Al contact, e.g., similar to Fig. 5.11b, half-filled circles a partially voided Al contact similar to Fig. 5.11a and open circles a fully voided Al contact where the void extends across the whole contact width a. According to Fig. 5.12b, voids, in particular, occur for Al contacts with large contact height h where the Al–Si eutectic extends more than 20 µm deep into the Si wafer [107]. This finding is explained by an analytical model proposed by Kranz et al. that calculates the surface energies of the liquid Al–Si melt, the Si wafer surface, and the screen-printed Al particle surface [107]. According to this model, voids form for large contact heights since then a sufficient amount of Al–Si melt is available in order to wet the large surface area of the Al particles rather than the small Si wafer surface area thereby minimizing the total surface energy of the Al–Si system. The PERC+ Al fingers reduce the Al contact height by about 7 µm which is the reason why PERC+ cells do not exhibit voids in contrast to PERC cells [107]. The increased Al-BSF thickness and the reduced amount of voids of PERC+ cells compared to conventional PERC cells result up to 3 mV higher open-circuit voltages V_{oc} due to reduced rear contact recombination [24].

References

1. T. Dullweber, J. Schmidt, Surface passivation of industrial PERC solar cells, in *Surface Passivation of Crystalline Silicon Solar Cells*, ed. by J. John (The Institution of Engineering and Technology, 2018, in press)
2. T. Dullweber, p-PERC+ solar cells, in *Bifacial Photovoltaics: Technology, Applications and Economics*, ed. by R. Kopecek, J. Libal (The Institution of Engineering and Technology, 2018), pp. 46–54
3. A.W. Blakers, A. Wang, A.M. Milne, J. Zhao, M.A. Green, 22.8% efficient solar cell. Appl. Phys. Lett. **55**, 1363–1365 (1989)
4. J. Zhao, A. Wang, M.A. Green, F. Ferrazza, Novel 19.8% efficient "honeycomb" textured multicrystalline and 24.4% monocrystalline silicon solar cells. Appl. Phys. Letters **73**, 1991–1993 (1998)
5. IHS Markit - PV Module Supply Chain Tracker 2018
6. International Technology Roadmap for Photovoltaic (ITRPV.net), 2017 Results, March 2018, http://www.itrpv.net/Reports/Downloads/
7. International Technology Roadmap for Photovoltaic (ITRPV.net), 2018 Results, March 2019, http://www.itrpv.net/Reports/Downloads/
8. A. Metz, D. Adler, S. Bagus, H. Blanke, M. Bothar, E. Brouwer, S. Dauwe, K. Dressler, R. Droessler, T. Droste, M. Fiedler, Y. Gassenbauer, T. Grahl, N. Hermert, W. Kuzminski, A. Lachowicz, T. Lauinger, N. Lenck, M. Manole, M. Martini, R. Messmer, C. Meyer, J. Moschner, K. Ramspeck, P. Roth, R. Schönfelder, B. Schum, J. Sticksel, K. Vaas, M. Volk, K. Wangemann, Industrial high performance crystalline silicon solar cells and modules based on rear surface passivation technology. Sol. Energy Mat. Sol. Cells **120**, 417–425 (2014)
9. M.A. Green, The Passivated Emitter and Rear Cell (PERC): From conception to mass production. Solar Energy Mat. Solar Cells **143**, 190–197 (2015)
10. T. Dullweber, J. Schmidt, Industrial silicon solar cells applying the Passivated Emitter and Rear Cell (PERC) concept—a review. IEEE J. Photovolt. **6**, 1366–1381 (2016)
11. T. Dullweber, H. Schulte-Huxel, S. Blankemeyer, H. Hannebauer, S. Schimanke, U. Baumann, R. Witteck, R. Peibst, M. Köntges, R. Brendel, Y. Yao, Present status and future perspectives of bifacial PERC+ solar cells and modules. *Jpn. J. Appl. Phys.* **57**, 08RA01 (2018)
12. G. Agostinelli, P. Choulat, H.F.W. Dekkers, S. de Wolf, G. Beaucarne, Screen printed large area crystalline silicon solar cells on thin substrates, in *Proceedings of the 20th European Photovoltaic Solar Energy Conference*, Barcelona, Spain, 2005, pp. 647–650
13. G. Agostinelli, J. Szlufcick, P. Choulat, G. Beaucarne, Local contact structures for industrial PERC-type solar cells, in *Proceedings of the 20th European Photovoltaic Solar Energy Conference*, Barcelona, Spain, 2005, pp. 942–945
14. C. Kranz, S. Wyczanowski, U. Baumann, K. Weise, C. Klein, F. Delahaye, T. Dullweber, R. Brendel, Wet chemical polishing for industrial type PERC solar cells. Energy Procedia **38**, 243–249 (2013)
15. D. Pysch, C. Schmitt, B. Latzel, J. Horzel, R. Sastrawan, O. Voigt, B.-U. Sander, S. Patzig-Klein, A. Pediaditakis, S. Queißer, A. Heeren, H. Nussbaumer, H. Kühnlein, X. Mao, X. Qu, S. Yang, I. Melnyk, X. Gay, F. Souren, R. Görtzen, H. Heezen, Implementation of an ALD-Al2O3 PERC-Technology into a multi- and monocrystalline industrial pilot production, in *Proceedings of the 29th European Photovoltaic Solar Energy Conference*, Amsterdam, Netherlands, 2014, pp. 612–616
16. P. Saint-Cast, D. Kania, M. Hofmann, J. Benick, J. Rentsch, R. Preu, Very low surface recombination velocity on p-type c-Si by high-rate plasma-deposited aluminum oxide, *Appl. Phys. Lett.* **95**, 151502-1–151502-3 (2009)
17. H.-P. Sperlich, D. Decker, P. Saint-Cast, E. Erben, L. Peters, High productive solar cell passivation on Roth & Rau MAiAs MW-PECVD inline machine—a comparison of Al_2O_3, SiO_2 and SiN_x–H process conditions and performance, in *Proceedings of the 25th European Photovoltaic Solar Energy Conference*, Valencia, Spain, 2010, pp. 1352–1357

18. G. Agostinelli, A. Delabie, P. Vitanov, Z. Alexieva, H.F.W. Dekkers, S. De Wolf, G. Beaucarne, Very low surface recombination velocities on p-type silicon wafers passivated with a dielectric with fixed negative charge. Sol. En. Mat. Sol. Cells **90**, 3438–3443 (2006)
19. B. Hoex, J. Schmidt, P. Pohl, M.C.M. van de Sanden, W.M.M. Kessels, Silicon surface passivation by atomic-layer-deposited Al2O3. *J. Appl. Phys.* **104**, 044903/1–12 (2008)
20. S. Dauwe, L. Mittelstädt, A. Metz, R. Hezel, Experimental evidence of parasitic shunting in silicon nitride rear surface passivated solar cells. Prog. Photovolt. Res. Appl. **10**, 271–278 (2002)
21. R. Preu, S.W. Glunz, S. Schäfer, R. Lüdemann, W. Wettling, W. Pfleging, Laser ablation—a new low-cost approach for passivated rear contact formation in crystalline silicon solar cell technology, in *Proceedings 16th European Photovoltaic Solar Energy Conference*, Glasgow, United Kingdom, 2000, pp. 1181–1184
22. S. Gatz, H. Hannebauer, R. Hesse, F. Werner, A. Schmidt, T. Dullweber, J. Schmidt, K. Bothe, R. Brendel, 19.4%-efficient large-area fully screen-printed silicon solar cells. Phys. Stat. Sol. RRL **5**, 147–149 (2011)
23. B. Tjahjono, M.J. Yang, V. Wu, J. Ting, J. Shen, O. Tan, T. Sziptalak, B. Liu, H.-P. Sperlich, T. Hengst, B. Beilby, K.-C. Hsu, Optimizing CELCO technology in one year of mass production, in *Proceedings of the 28th European Photovoltaic Solar Energy Conference*, Paris, France, 2013, pp. 775–779
24. T. Dullweber, C. Kranz, R. Peibst, U. Baumann, H. Hannebauer, A. Fülle, S. Steckemetz, T. Weber, M. Kutzer, M. Müller, G. Fischer, P. Palinginis, D.H. Neuhaus, PERC+: industrial PERC solar cells with rear Al grid enabling bifaciality and reduced Al paste consumption. Prog. Photovolt: Res. Appl. **24**, 1487–1498 (2016)
25. T. Dullweber, S. Gatz, T. Falcon, H. Hannebauer, High efficiency rear-passivated screen-printed silicon solar cells. *Photovolt. Int.* **13** (2011)
26. K.A. Münzer, J. Schöne, A. Teppe, R.E. Schlosser, M. Hein, D. Hammer, S. Hüls, M. Hanke, S. Keller, P. Fath, Advanced rear side technology for industrial high efficiency solar cells, in *Proceedings of the 25th European Photovoltaic Solar Energy Conference*, Valencia, Spain, 2010, pp. 2314–2318
27. T. Boscke, R. Hellriegel, T. Wutherich, L. Bornschein, A. Helbig, R. Carl, M. Dupke, D. Stichtenoth, T. Aichele, R. Jesswein, T. Roth, C. Schollhorn, T. Geppert, A. Grohe, J. Lossen, H. Krokoszinski, Fully screen-printed PERC cells with laser-fired contacts—an industrial cell concept with 19.5% efficiency, in *Proceedings of the 37th IEEE Photovoltaic Specialists Conference*, Seattle, USA, 2011, pp. 3663–3666
28. Schott Solar AG, press release August 24th 2011, http://www.presseportal.de/pm/23114/2101260
29. A. Lachowicz, K. Ramspeck, P. Roth, M. Manole, H. Blanke, W. Hefner, E. Brouwer, B. Schum, A. Metz, Nox-free solution for emitter etch-back, in *Proceedings of the 27th European Photovoltaic Solar Energy Conference*, Frankfurt, Germany, 2012, pp. 1846–1850
30. H. Hannebauer, T. Dullweber, U. Baumann, T. Falcon, R. Brendel, 21.2%-efficient fineline-printed PERC solar cell with 5 busbar front grid. Phys. Status Solidi RRL **8**, 675–679 (2014)
31. Trina Solar, press release, November 17th 2014, http://www.prnewswire.com/news-releases/trina-solar-announces-new-efficiency-records-for-silicon-solar-cells-282907361.html
32. SolarWorld AG, press release July 17th 2015, http://www.solarworld.de/en/group/investor-relations/news-announcements/corporate-news/single-ansicht/article/solarworld-ag-sets-new-world-record-for-solar-cell-efficiency/
33. Trina Solar, press release, December 16th 2015, http://www.prnewswire.com/news-releases/trina-solar-announces-new-efficiency-record-of-2213-for-mono-crystalline-silicon-solar-cell-300193727.html
34. Trina Solar, press release, December 19th 2016, http://www.prnewswire.com/news-releases/trina-solar-announces-new-efficiency-record-of-2261-for-mono-crystalline-silicon-perc-cell-300380906.html
35. W.W. Deng, F.Y. Ye, R. Liu, Y. Li, H. Chen, Z. Xiong, Y. Yang, Y. Chen, Y. Wang, P.P. Altermatt, Z. Feng, P.J. Verlinden, *44th IEEE Photovoltaic Specialists Conference*, 2017, in press

36. LONGi Solar, press release, October 23rd 2017, https://www.pv-tech.org/news/longi-solar-plans-22-record-perc-cell-in-production-at-end-of-2017
37. JinkoSolar, press release, October 25th 2017, https://www.pv-tech.org/news/jinkosolar-pushes-p-type-monocrystalline-perc-solar-cell-to-new-efficiency
38. R. Hezel, K. Jaeger, Low-temperature surface passivation of silicon for solar cells. J. Electrochem. Soc. **136**, 518–523 (1989)
39. A. Hübner, A.G. Aberle, R. Hezel, Novel cost-effective bifacial silicon solar cells with 19.4% front and 18.1% rear efficiency. Appl. Phys. Lett. **70**, 1008–1010 (1997)
40. S. Steckemetz, A. Metz, R. Hezel, Thin Cz-silicon solar cells with rear silicon nitride passivation and screen printed contacts, in *Proceedings of the 17th European Photovoltaic Solar Energy Conference*, Munich, Germany, 2001, pp. 1902–1905
41. G. Agostinelli, A. Delabie, P. Vitanov, Z. Alexieva, H.F.W. Dekkers, S. De Wolf, G. Beaucarne, Very low surface recombination velocities on p-type silicon wafers passivated with a dielectric with fixed negative charge. Sol. Energy Mat. Sol. Cells **90**, 3438–3443 (2006)
42. B. Hoex, S.B.S. Heil, E. Langereis, M.C.M. van de Sanden, W.M.M. Kessels, Ultralow surface recombination of c-Si substrates passivated by plasma-assisted atomic layer deposited Al2O3. Appl. Phys. Letters **89**, 042112 (2006)
43. J. Schmidt, A. Merkle, R. Brendel, M.C.M. van de Sanden, W.M.M. Kessels, Surface passivation of high-efficiency silicon solar cells by atomic-layer-deposited Al2O3. Prog. Photovolt. Res. Appl. **16**, 461–466 (2008)
44. B. Veith, T. Dullweber, M. Siebert, C. Kranz, F. Werner, N.-P. Harder, J. Schmidt, B.F.P. Roos, T. Dippell, R. Brendel, comparison of ICP-AlOx and ALD-Al2O3 layers for the rear surface passivation of c-Si solar cells. Energy Procedia **27**, 379–384 (2012)
45. T. Dullweber, C. Kranz, B. Beier, B. Veith, J. Schmidt, B.F.P. Roos, O. Hohn, T. Dippell, R. Brendel, Inductively coupled plasma chemical vapour deposited AlO_x/SiN_y layer stacks for applications in high-efficiency industrial-type silicon solar cells. Sol. Energy Mat. Sol. Cells **112**, 196–201 (2013)
46. F. Schwarz, R. Beckmann, N. Kohn, S. Nölker, S. Kastl, M. Hofmann, R. Ferré, T. Pernau, H. Wanka, J. Rentsch, Advanced anti-reflection and passivation layer systems produced by high-power plasma in the new Manz PECVD system, in *Proceedings of the 27th European Photovoltaic Solar Energy Conference*, Frankfurt, Germany, 2012, pp. 1938–1941
47. F. Werner, W. Stals, R. Goertzen, B. Veith, R. Brendel, J. Schmidt, High-rate atomic layer deposition of Al2O3 for the surface passivation of Si solar cells. Energy Procedia **8**, 301–306 (2011)
48. P.G. Vermont, V. Kuznetsov, E.H.A. Granneman, High-throughput solar cell passivation on in-line Levitrack ALD Al2O3 system—demonstration of process performance, in *Proceedings of the 26th European Photovoltaic Solar Energy Conference*, Hamburg, Germany, 2011, pp. 1644—1647
49. D. Kray, M. Hermle, S.W. Glunz, Theory and experiments on the back side reflectance of silicon wafer solar cells. Prog. Photovolt: Res. Appl. **16**, 1–15 (2008)
50. V. Meemongkolkiat, K. Nakayashiki, D.S. Kim, S. Kim, A. Shaikh, A. Kuebelbeck, W. Stockum, A. Rohatgi, Investigation of modified screen-printing Al pastes for local back surface field formation, in *Proceedings of the 4th World Conference Photovoltaic Energy Conversion*, Hawaii, USA, 2006, pp. 1338–1341
51. M. Rauer, R. Woehl, K. Rühle, C. Schmiga, M. Hermle, M. Hörteis, D. Brio, Aluminum alloying in local contact areas on dielectrically passivated rear surfaces of silicon solar cells. IEEE Electron Device Lett. **32**, 916–918 (2011)
52. K.A. Münzer, M. Hein, J. Schöne, M. Hanke, A. Teppe, R.E. Schlosser, J. Maier, A. Yodyunyong, S. Krümberg, S. Keller, P. Fath, Technical performance and industrial implementation in favour of centaurus technology. Energy Procedia **27**, 631–637 (2012)
53. K.A. Münzer, J. Schöne, M. Hein, A. Teppe, R.E. Schlosser, M. Hanke, J. Maier, K. Varner, S. Keller, and P. Fath, Development and implementation of 19% rear passivation and local contact centaurus technology, in *Proceedings of the 26th European Photovoltaic Solar Energy Conferene*, Hamburg, Germany, 2011, pp. 2292–2297

54. S. Queisser, K. De Keersmaecker, T. Borgers, E. Wefringhaus, D. Nagel, B.-U. Sander, M. Loehmann, M. Weber, F. Delahaye, Inline single side polishing and junction isolation for rear side passivated solar cells, in *Proceedings of the 24th European Photovoltaic Solar Energy Conference*, Hamburg, Germany, 2009, pp. 1792–1794
55. E. Cornagliotti, M. Ngamo, L. Tous, R. Russell, J. Horzel, D. Hendrickx, B. Douhard, V. Prajapati, T. Janssens, J. Poortmans, Integration of inline single-side wet emitter etch in PERC cell manufacturing. Energy Procedia **27**, 624–630 (2012)
56. C. Kranz, S. Wyczanowski, S. Dorn, K. Weise, C. Klein, K. Bothe, T. Dullweber, R. Brendel, Impact of the rear surface roughness on industrial-type PERC solar cells, in *Proceedings of the 27th European Photovoltaic Solar Energy Conference*, Frankfurt, Germany, 2012, pp. 557–560
57. C. Comparotto, M. Noebels, L. Popescu, A. Edler, J. Ranzmeyer, T. Klaus, V.D. Mihailetchi, R. Harney, J. Lossen, T.S. Böscke, D. Schär, H. Nussbaumer, T. Baumann, F.P. Baumgartner, Bifacial n-type solar modules: indoor and outdoor evaluation, in *Proceedings of the 29th European Photovoltaic Solar Energy Conference*, Amsterdam, The Netherlands, 2014, pp. 3248–3250
58. G.J.M. Janssen, B.B. Van Aken, A.J. Carr, A.A. Mewe, Outdoor performance of bifacial modules by measurements and modelling. Energy Procedia **77**, 364–373 (2015)
59. H. Mori, Radiation energy transducing device, U.S. Patent 3.278.811, October 1966 (priority October 1960)
60. I.G. Romijn, B.B. Van Aken, J. Anker, P. Barton, A. Gutjahr, Y. Komatsu, M. Koppes, E.J. Kossen, M.W.P.E. Lamers, D.S. Saynova, K.C.J.J. Tool, Y. Zhang-Steenwinkel, P.R. Venema, A.H.G. Vlooswijk, C. Schmitt, H. Kühnlein, N. Bay, M. König, A. Stassen, Industrial cost effective n-PASHA solar cells with >20% cell efficiency, in *Proceedings of the 28th European Photovoltaic Solar Energy Conference*, Paris, France, 2013, pp. 736–740
61. D. Song, J. Xiong, Z. Hu, G. Li, H. Wang, H. An, B. Yu, B. Grenko, K. Borden, K. Sauer, T. Roessler, J. Cui, H. Wang, J. Bultman, A.H.G. Vlooswijk, P.R. Venema, Progress in n-type Si solar cell and module technology for high efficiency and low cost, in *Proceedings of the 38th IEEE Photovoltaic Specialists Conference,* Austin, USA, 2012, pp. 3004–3008
62. V.D. Mihailetchi, J. Jourdan, A. Edler, R. Kopecek, R. Harney, D. Stichtenoth, J. Lossen, T. Boescke, H.J. Krokoszinski, Screen printed n-type silicon solar cells for industrial application, in *Proceedings of the 26th European Photovoltaic Solar Energy Conference*, Hamburg, Germany, 2010, pp. 1446–1448
63. M. Taguchi, A. Yano, S. Tohoda, K. Matsuyama, Y. Nakamura, T. Nishiwaki, K. Fujita, E. Maruyama, 24.7% record efficiency HIT solar cell on thin silicon wafer. IEEE J. Photovolt. **4**, 96–99 (2014)
64. B. Strahm, D. Lachenal, D. Bätzner, W. Frammelsberger, B. Legradic, J. Meixenberger, P. Papet, G. Wahli, E. Vetter, M. Despeisse, A. Faes, A. Lachowicz, C. Allebé, P.J. Alet, M. Bonnet-Eymard, C. Ballif, Y. Yao, C. Rychen, T. Söderström, J. Heiber, G. Schiltges, S. Leu, J. Hiller, V. Fakhfouri, The Swiss Inno-HJT project: fully integrated R&D to boost Si-HJT module performance, in *Proceedings of the 29th European Photovoltaic Solar Energy Conference*, Amsterdam, The Netherlands, 2014, pp. 467–471
65. I. Cesar, I.G. Romijn, D.M. Borsa, G. Galbiati, N.J. C.M. van der Borg, E.E. Bende, A.W. Weeber, Benchmark of open rear side solar cell with improved Al-BSF process at ECN, in *Proceedings 23rd European Photovoltaic Solar Energy Conference*, Valencia, Spain, 2008, pp. 1770–1775
66. T. Dullweber, C. Kranz, R. Peibst, U. Baumann, H. Hannebauer, A. Fülle, S. Steckemetz, T. Weber, M. Kutzer, M. Müller, G. Fischer, P. Palinginis, D.H. Neuhaus, The PERC+ cell: a 21%-efficient industrial bifacial PERC solar cell, in *Proceedings of the 31st European Photovoltaic Solar Energy Conference*, 2015, pp. 341–350
67. B. Liu, Y. Chen, Y. Yang, J. Dong, H. Shen, Z. Feng, P.J. Verlinden, Rear-colored double glass module fabricated with rear-colored bifacial p-type PERC cells, in *Proceedings of the 31st European Photovoltaic Solar Energy Conference*, 2015, pp. 659–661

68. K. Krauß, F. Fertig, J. Greulich, S. Rein, R. Preu, biPERC silicon solar cells enabling bifacial applications for industrial solar cells with passivated rear sides. Phys. Status Solidi A **213**, 68–71 (2016)
69. S.-Y. Chen, H.-C. Liu, H.-Y. Chang, Y.-Y. Chiu, Y.-H. Wang, Y.-H. Lin, S.-H. Yu, W.-J. Lih, C.-H. Du, Bifacial solar cells fabricated by PERC process for mass production, in *Proceedings of the 32nd European Photovoltaic Solar Energy Conference*, 2016, pp. 772–774
70. M. Xiajie, Y. Bin, C. Yongmei, X. Xinxing, F. Jianbin, T. Hongbo, L. Hua, in *Proceedings of the 27th International Photovoltaic Science and Engineering Conference*, Otsu, Japan, 2017, p. 138
71. Communication with JinkoSolar
72. Neo Solar Power data sheet, 2017, https://www.nsp.com/nspsolarcells?lang=en
73. SolarWorld data sheet of Bisun module, 2017, https://www.solarworld.de/en/products/sunmodule-bisun-protect/
74. Neo Solar Power data sheet of Glory Bifi module, 2017, https://www.nsp.com/nspsolarmodules?lang=en
75. Trina Solar data sheet of DUOMAX module, 2017, http://www.trinasolar.com/de/product/duomax4060/duomax-twin-deg5c07ii
76. LONGi Solar data sheet of LR6-60PD module, 2017, http://en.longi-solar.com/Home/Products/module/id/12_.html
77. https://www.jinkosolar.com/product_detail_311.html?lan=en
78. https://www.canadiansolar.com/upload/c3ee005ae8689897/8c800b00f763e4e9.pdf
79. https://en.longi-solar.com/home/products/Hi_MO4.html
80. SolarWorld press release, 2015, http://www.pv-tech.org/news/intersolar_europe_solarworld_to_launch_glass_glass_bifacial_modules
81. T. Dullweber, H. Schulte-Huxel, C. Kranz, S. Blankemeyer, U. Baumann, R. Witteck, M. Köntges, R. Brendel, Bifacial PERC+ solar cells and modules: an overview, in *Proceedings of the 33rd European Photovoltaic Solar Energy Conference*, 2017, pp. 649–656
82. A. Faes, M. Despeisse, J. Levrat, J. Champliaud, N. Badel, M. Kiaee, T. Söderström, Y. Yao, R. Grischke, M. Gragert, J. Ufheil, P. Papet, B. Strahm, B. Cattaneo, J. Cattin, Y. Baumgartner, A. Hessler-Wyser, C. Ballif, SmartWire solar cell interconnection technology, in *Proceedings of the 29th European Photovoltaic Solar Energy Conference*, 2014, pp. 2555–2561
83. H. Neuhaus (SolarWorld), Progress & perspectives in high-volume PERC manufacturing, in *Presented at the PV CellTech Conference*, Penang, Malaysia, 2017
84. L.C. Boon (Trina Solar), Bifacial and halfcut technology, in *Presented at the PV ModuleTech Conference*, Penang, Malaysia, 2017
85. https://www.power-technology.com/news/longi-bifacial-perc-modules/
86. https://www.pv-tech.org/news/ja-solars-bifacial-perc-modules-used-in-two-pv-projects-in-south-korea
87. https://www.pv-tech.org/news/trina-solar-supplying-edf-renewables-with-bifacial-modules-for-french-low-c
88. https://www.pv-tech.org/news/neo-solar-powers-mono-perc-bifacial-modules-selected-for-100mw-pv-plant-in
89. https://www.pv-tech.org/guest-blog/ultra-low-solar-bid-of-0.01997-kwh-in-the-us-not-quite-so-sunny
90. http://taiyangnews.info/business/5-42-gw-bifacial-solar-module-capacity-by-2019/
91. https://en.longi-solar.com/Home/Events/press_detail/id/36_World_s_largest_Bifacial_Solar_Power_Project_Installed_in_China_s_Qinghai_Province.html
92. B. Fischer, Loss analysis of crystalline silicon solar cells using photoconductance and quantum efficiency measurements. Ph.D. thesis, University of Konstanz, Germany, 2003
93. S. Miyajima, J. Irikawa, A. Yamada, M. Konagai, Hydrogenated aluminum oxide films deposited by plasma enhanced chemical vapor deposition for passivation of p-type crystalline silicon, in *Proceedings of the 23rd European Photovoltaic Solar Energy Conference*, Valencia, Spain, 2008, pp. 1029–1032

94. T.T. Li, A. Cuevas, Effective surface passivation of crystalline silicon by rf sputtered aluminum oxide. Phys. Status Solidi RRL **3**, 160–162 (2009)
95. J. Schmidt, B. Veith, R. Brendel, Effective surface passivation of crystalline silicon using ultrathin Al_2O_3 films and Al_2O_3/SiN_x stacks. Phys. Status Solidi RRL **3**, 287–289 (2009)
96. G. Dingemans, R. Seguin, P. Engelhart, M.C.M. van de Sanden, W.M.M. Kessels, Silicon surface passivation by ultrathin Al2O3 films synthesized by thermal and plasma atomic layer deposition. Phys. Status Solidi RRL **4**, 10–12 (2010)
97. L.E. Black, T. Allen, A. Cuevas, K.R. McIntosh, B. Veith, J. Schmidt, Thermal stability of surface passivation by APCVD Al_2O_3. Sol. En. Mat. Sol. Cells **120**, 339–345 (2014)
98. X. Gay, F. Souren, B. Dielissen, M. Bijker, R. Gortzen, D. Pysch, K. Weise, B. Sander, R. Sastrawan, Post-deposition thermal treatment of ultrafast spatial ALD Al2O3 for the rear side passivation of p-type PERC solar cells, in *Proceedings of the 28th European Photovoltaic Solar Energy Conference*, Paris, France, 2013, pp. 1220–1224
99. J.L. Murray, A.J. McAlister, The Al-Si (aluminum-silicon) system. Bull. Alloy. Phase Diagr. **5**, 74–84 (1984)
100. T. Lauermann, A. Zuschlag, S. Scholz, G. Hahn, B. Terheiden, The influence of contact geometry and sub-contact passivation on the performance of screen-printed Al2O3-passivated solar cells, in *Proceedings of the 26th European Photovoltaic Solar Energy Conference*, Hamburg, Germany, 2011, pp. 1137–1143
101. J. Müller, K. Bothe, S. Gatz, H. Plagwitz, G. Schubert, R. Brendel, Contact formation and recombination at screen-printed local aluminum-alloyed silicon solar cell base contacts. IEEE Trans. Electron Devices **58**, 3239–3245 (2011)
102. S. Gatz, J. Müller, T. Dullweber, R. Brendel, Analysis and optimization of the bulk and rear recombination of screen-printed PERC solar cells. Energy Procedia **27**, 95–102 (2012)
103. E. Urrejola, K. Peter, H. Plagwitz, G. Schubert, Silicon diffusion in aluminum for rear passivated solar cells. Appl. Phys. Lett. **98**, 153508 (2011)
104. J. Müller, K. Bothe, S. Gatz, R. Brendel, Modeling the formation of local highly aluminum-doped silicon regions by rapid thermal annealing of screen-printed aluminum. Phys. Status Solidi RRL **6**, 111–113 (2012)
105. Y. Gassenbauer, K. Ramspeck, B. Bethmann, K. Dressler, J.D. Moschner, M. Fiedler, E. Brouwer, R. Drössler, N. Lenck, F. Heyer, M. Feldhaus, A. Seidl, M. Müller, A. Metz, Rear-surface passivation technology for crystalline silicon solar cells: a versatile process for mass production. *IEEE J. Photovolt.* **3**, 125–130 (2012)
106. C. Kranz, B. Wolpensinger, R. Brendel, T. Dullweber, Analysis of local aluminum rear contacts of bifacial PERC+ solar cells. IEEE J. Photovolt. **6**(4), 830–836 (2016)
107. C. Kranz, U. Baumann, B. Wolpensinger, F. Lottspeich, M. Müller, P. Palinginis, R. Brendel, T. Dullweber, Void formation in screen-printed local aluminum contacts modeled by surface energy minimization. Sol. Energy Mat. Sol. Cells **158**, 11–18 (2016)

Chapter 6
High Efficient, Cost-Effective, and Reliable Silicon Solar Cells and Modules in Mass Production

J. W. Müller

Abstract Over the last decade, significant improvements in cost reduction as well as in conversion efficiency increase were achieved in large-scale industrial production, making PV cost competitive with other means of electricity generation. In many regions worldwide, PV achieves the lowest levelized cost of electricity. Several different factors made this tremendous achievement possible-namely economy of scale, a lean and efficient production process, and high conversion efficiencies. In this work, some of the key concepts and methods are described based on Hanwha Q CELLS' experience. The methods and approaches for the fast transfer of cell technologies from laboratory to production and for accelerated progress in cell efficiency, quality, and reliability of the cell and module product are described. Over the last decade, the cell conversion efficiency increased by 0.5%abs per year. Currently, average cell conversion efficiencies exceeding 20% using boron-doped *p*-type multicrystalline (mc-Si) and 22%, using Czochralski-grown silicon (Cz-Si) substrates, are achieved on a multi-GW scale. Currently (as of Jan 2018) produced Q.ANTUM solar modules from these cells exhibit output powers of 325 Wp based on 120 half Cz cells and of 350 Wp based on 72 full multicrystalline cells. Besides just the performance, it is critical to investigate the reliability of solar modules based on *p*-type solar cells with dielectrically passivated rear. In terms of reliability, light-induced degradation (LID) is examined in detail, with conditions relevant for the activation of both the boron–oxygen (BO) defect, and "Light and Elevated Temperature Induced Degradation" (LeTID). While the formation of the BO defect has been considered the most prominent LID mechanism in boron-doped *p*-type Cz-Si, recently it was shown that LeTID is another important issue for passivated emitter and rear cells (PERC) on both mc-Si and Cz substrates. When not adequately suppressed, LeTID can occur on *p*-type PERC with degradation in output power of >6%; critically, it cannot be suppressed in a straightforward manner by conventional processing steps used to permanently deactivate the BO defect. In contrast to conventional PERC, Hanwha Q

J. W. Müller (✉)
Hanwha Q CELLS GmbH, Sonnenallee 17 – 21, 06766 Bitterfeld-Wolfen OT Thalheim, Germany
e-mail: j.mueller@q-cells.com
URL: https://www.q-cells.com

V. Petrova-Koch et al. (eds.), *High-Efficient Low-Cost Photovoltaics*,
Springer Series in Optical Sciences 140,
https://doi.org/10.1007/978-3-030-22864-4_6

CELLS' Q.ANTUM technology is shown to reliably suppress both LID due to BO defect formation and LeTID, for both *p*-type mc-Si and Cz-Si substrates.

6.1 Introduction

Hanwha Q CELLS was one of the first companies to start the production of Si PERC-like cells in 2012. From the first internal PERC cell samples in mid-2009 to the transfer of the Q.ANTUM [1] process sequence to our production facility in end 2010 and finally to 24/7 cell and module production mode in 2012 took more than 2 years. Reflecting on this and other developments, the timeline and efforts to make laboratory developments feasible in mass production should not be underestimated. In the last decade, Hanwha Q CELLS developed concepts for an efficient transfer of new cell processes from the laboratory to mass production and fast development of high-quality cell and module products [2]. In this work, these methods are described and cover the technological progress at Hanwha Q CELLS over the last 10 years of R&D concerning cell efficiencies, module power, and reliability.

Within the last 4 years, the market share of solar cells with dielectrically passivated rear side has increased from less than 5% in 2013 [3] to about 15% in 2016 [4] and is expected to further increase in the upcoming years [4]. The majority of these cells is represented by the passivated emitter and rear cell (PERC [5]) structure and is processed on boron-doped *p*-type silicon substrates. Besides challenges in process technology, stability issues due to light-induced degradation (LID) have been a key challenge for high efficiency *p*-type Cz-Si solar cells. In particular, two LID mechanisms have hindered a wider adoption of the industrial manufacturing of PERC-like solar cells on boron-doped *p*-type silicon substrates: LID due to boron–oxygen (BO) defect formation [6–8] and "Light and elevated Temperature Induced Degradation" (LeTID) [9–13]. LID and LeTID are most pronounced for PERC on Cz- and mc-Si substrates, respectively.

This work reports on the results of mass production of Hanwha Q CELLS' cell technology on boron-doped *p*-type mc-Si and Cz-Si substrates. Over the last decade, an annual average cell conversion efficiency increase of 0.5%abs. was achieved by optimizing every process parameter and by the switch from the aluminum back-surface field (Al-BSF) technology to the Q.ANTUM technology. This efficiency increase was achieved while keeping a lean process sequence and significantly lowering costs, e.g., by reducing the silver paste consumption. Besides device performance upon fabrication, LID of Q.ANTUM and PERC is investigated in detail. It is shown that when not adequately suppressed, LeTID can occur not only in *p*-type mc-Si PERC but also in *p*-type Cz-Si PERC. The suppression of both the BO defect and LeTID is of utmost importance for both mc-Si and Cz-Si substrates. In contrast to conventional PERC, Hanwha Q CELLS' Q.ANTUM technology is shown to reliably suppress both LID due to BO defect formation and LeTID in modules manufactured from both *p*-type mc-Si and Cz-Si substrates [9–13].

6.2 Approaches for Efficient Cell Development and Production

Table 6.1 shows an overview of the essential steps for a successful technology transfer to mass production. HANWHA Q CELLS developed and optimized these approaches during the last years of cell and module development and transfer activities. According to our findings, most of the work in the development of a new cell technology suitable for mass production takes place on production equipment. The proof of concept of a new process or process sequence is typically done in the setting of research institutes. Subsequently, the replacement of standard processes by production processes, and the stepwise introduction of new processes into the routine of stable and well monitored 24/7 manufacturing conditions should be targeted. In this way, it is also ensured that processes to be introduced are evaluated and optimized directly in the context of a production process chain. Herewith the advantage of evolutionary cell development becomes visible. Replacing only one new laboratory process at a time by a production process enables a systematic benchmarking of both processes and the investigation of both expected and unexpected interdependencies on cell and module level. According to our experience, it is thereby essential that research laboratory and production line facilities are closely connected to each other. Running experiments on mass production tools furthermore reduce the run-time, thus increases the experimental rate and offers the possibility to improve the statistical relevance by flexibly increasing the amount of cells. The above-described process, accompanied by the development of suitable sampling analysis on cell and module level, enables fast and precise detection of potential targets for optimization. When all new processes are fully integrated into mass production with a positive business case and the electrical safety and reliability of the modules are certified for the process sequence, the first generation of a new cell concept can be produced. It is therefore essential to define suitable upper and lower process parameter limits (specifications) for each process as well as action instructions in case of limit violations. This comes along with the effort to install suitable parameter measurement tools and recipes. Any change in processes beyond these specifications should be critically examined concerning product and cost-relevant impacts on cell parameters as well as on production yield, breakage, throughput, optical criteria, solderability of cells, and module reliability. The high number of product and cost-relevant criteria in cell and module development leads to development efforts that can be easily underestimated. The existence of a single wafer tracking system in combination with a manufacturing execution system (MES) is another key enabler for fast and efficient development and tight process control.

Table 6.1 Chronological roadmap of approaches for fast production cell and module development. Table taken from [2]

Approach	Enabled actions and benefits
First sampling in laboratories	– First cell technology evaluation and experience – Determination of physical parameters → simulations
R&D pilot production/regular experiment runs in research environment (proof of concept)	– Improved level of process stability – Detection of N_{cell} improvement potentials >0.15%$_{abs}$ (single exp. mc-Si) – Evaluation of new processing tools – Start of module reliability investigations – Development of process monitoring and analysis test structures
Stepwise replacing of laboratory processes by production processes	– Benchmarking all processes between R&D and production tool
Full process sequence in production line (experiment level)	– Production relevant throughput and handling – Enlarged number of cells per time → extended module tests possible – Start calibration of inline measurement recipes and equipment – Resolution of N_{cell} improvement potentials >0.1%$_{abs}$ (process stability)
Application of tracking systems for evaluation of the joined data on wafer level	– Detection of process interdependencies and deviation root causes
Defining process parameter specifications (design freeze)	– Definition of standard operation procedures to stay within process specifications (in-spec condition)
Cell and module test productions with standard cell process	– Evaluation of tool uptimes, throughput, and yield in production – Determination of optical sorting criteria – More detailed production cost calculation possible
Module certification (EC/VDE)	– External and independent confirmation of electrical safety and reliability of modules
Start pilot cell and module production (handover to production)	– Find process instabilities and tool uptimes for 24/7 production conditions
In-spec parameter variations (ISV) in raining production or test production	– Efficiency improvement for this and next product generation – N_{cell} improvement resolution <0.03%$_{abs}$ due to large statistics

6.2.1 Improved Statistical Resolution of Experiments via Tra.Q

With our unique Tra.Q [14] wafer tracking system, each wafer gets an individual dot matrix code on the front surface of the wafer at the very beginning of the process sequence. Using this hard mark, we can accurately track process control data for each wafer throughout the entire manufacturing sequence from incoming inspection to final quality inspection at the end of the module line. By combining specific process data with the corresponding cell tester data via the identification number of each wafer, we are able to improve the statistical resolution of single experiments from >0.1%abs (100 cell batch experiment) to <0.03%abs [2]. This can be achieved by either (1) iteratively switching during the running production between two (or more) parameter settings of one process tool or (2) loading two parallel running process tools (with nominally the same or differing parameter settings) thus splitting the incoming material. To analyze the cell results by the corresponding parameter setting on cell level, we use Tra.Q data. No additional cell handling is required and all cells remain in the production chain. These two features enable the use of large numbers of cells for parameter variations. In order to secure the quality of the cells, the parameter variation needs to be kept within the process specification, leading to the term "in-spec variation" (ISV) for this approach. Figure 6.1 illustrates the results of a 100 cell batch experiment versus an 8000 cell ISV comparing two rear SiNx deposition recipes (other processes identical). As a measure of statistical significance of the results for both approaches, the mean of the 95% median confidence interval (CI) of both recipes is given in the graph. The results state that in the case of the ISV approach, the statistical resolution for all cell parameters is increased by one order of magnitude compared to the experiment mode. The improved resolution permits a very precise optimization of production processes. In our experience, a major part of continuous cell efficiency improvement is based on such measures of fine-tuning optimization. Further benefits of the ISV approach are clearly reduced experimental efforts, costs, and experiment run-times.

6.2.2 Root Cause Finding via Tra.Q

Combining Tra.Q process data together or with cell tester data on the wafer level furthermore enables the finding of process interactions and hidden root causes for process deviations or interdependencies. An example of a hidden root cause found by this approach is the analysis shown in Fig. 6.2 for a fill factor deviation [2]. The contour plot shows the (interpolated) relative fill factor (FF) distribution of 18,000 Q.ANTUM cells from mass production over the tray position of the AlOx/SiNx rear passivation deposition tool. By tracking the exact tray position of each cell via the Tra.Q system, up to 1%rel decreased, FF become visible for three specific tray positions on the mid-track (blue FF range in plot). Based on this characteristic plot, the

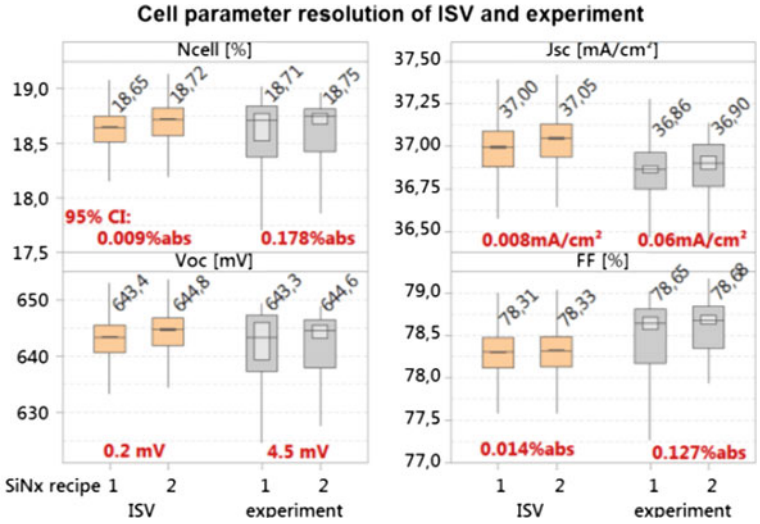

Fig. 6.1 Box and whisker plot of mc-Si cell results of a rear SiNx recipe comparison via an ISV (>8000 cells per recipe) contrasted with a corresponding batch experiment (100 cells per recipe). The 95% confidence interval (CI) for the median of cell parameters is given in the graph. The red text contains the mean CI value of recipe 1 and 2. Graph taken from [2]

origin of the FF decrease was found in a temporary imprecision in wafer positioning by one of the two loading stations serving the deposition tool. The positioning was subsequently corrected and additionally, a tighter control procedure for positioning was established. This issue would not be easily detectable in cell production lines without a wafer tracking system. Via Tra.Q, we know the identification number of each cell affected by such process deviations and if necessary are able to sort them out before module manufacturing. Thus, our cell and module production stands out for having the highest quality standards. The benefit of such a single wafer tracking system becomes more important with the size of a production site. In a 2 GW production line with several hundreds of individual processing tools and more than a million cells per day, it is almost impossible to ensure tight process control and efficient failure analysis without such a tracking system. A tracking system also paves the way for "Industry4.0" and opens the possibility for future self-learning fabs.

6.3 Cell Efficiency Development of Q.ANTUM Solar Cells on *p*-type Silicon Substrates

Figure 6.3 shows sketches of a standard Al-BSF and the Q.ANTUM solar cell structure. The Q.ANTUM solar cell resembles a PERC-like structure, i.e., it features a dielectrically passivated rear side with local contacts, front-side junction formation by phosphorus diffusion and screen-printed metallization.

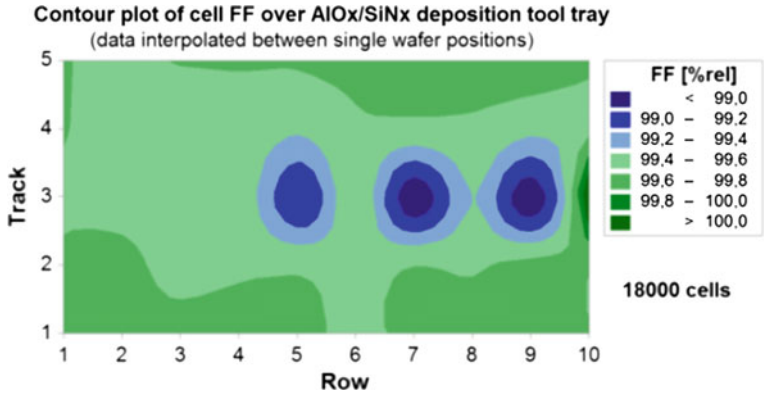

Fig. 6.2 Contour plot of the interpolated relative fill factor distribution of 18,000 Q.ANTUM cells from mass production over the tray position of the rear passivation deposition tool with imprecise tray loading. Graph taken from [2]

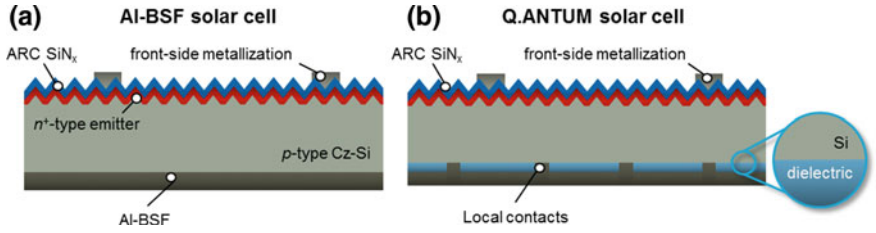

Fig. 6.3 Sketches of **a** aluminum back-surface field and **b** Q.ANTUM solar cell structures

Figure 6.4 shows the average cell conversion efficiency as a function of production date at Hanwha Q CELLS of *p*-type mc- and Cz-Si Al-BSF and Q.ANTUM solar cells, respectively. An increase in average efficiency of +0.5%abs/year is observed over the last decade. This constant average annual learning rate of 0.5%abs is achieved both on mc- and Cz-Si substrate. In the case of Cz substrates, the learning curve for Al-BSF cells is disrupted in the beginning of 2013 leading to a significantly flatter increase compared with the Q.ANTUM solar cell [15, 16]. By switching to the Q.ANTUM solar cell structure, the increase in conversion efficiency of + 0.5%abs/year could be maintained, and therefore the efficiency curves of both structures are decoupled with an increasing gap between Q.ANTUM and Al-BSF cells. A similar but less pronounced effect is shown in case of mc-Si substrates. Within the next 2 to 3 years, we do not expect a significant slowdown in the yearly efficiency increase of Q.ANTUM solar cells, leading to average cell conversion efficiencies exceeding 23% and 21% for Cz-Si and mc-Si, respectively. This steady increase in cell efficiency is achieved while maintaining a lean manufacturing process and significantly reducing the manufacturing costs per Wp, e.g., by lowering the silver paste consumption.

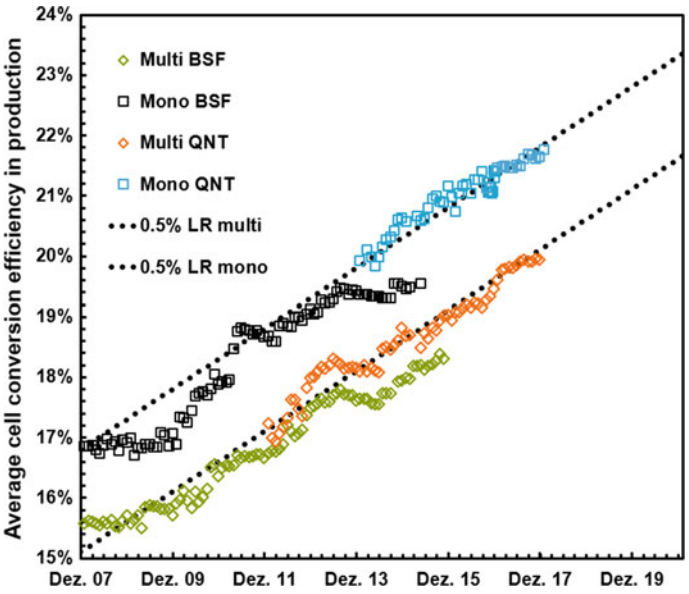

Fig. 6.4 Average solar cell conversion efficiency of mass production as a function of time at Hanwha Q CELLS. Over the last decade, an average annual learning rate of 0.5%abs. is reached both on mc-Si and Cz-Si substrates

Figure 6.5b shows a typical distribution of cell conversion efficiency of more than 3 million Q.ANTUM solar cells on *p*-type Cz-Si substrates in mass production in January 2018. A tight distribution with maximum frequencies between 21.9 and 22.1% can be seen, resulting in an average efficiency of 22.0%. Figure 6.5a shows a similar distribution of cell conversion efficiency of Q.ANTUM solar cells on cost-effective *p*-type mc-Si substrates. The distribution is slightly broader than in case of Cz-Si with maximum frequencies between 19.8% and 20.2% resulting in an average efficiency of 20.0%. These cell efficiencies lead to manufactured Q.ANTUM solar modules based on mc-Si substrates exhibiting power classes of 350 Wp, utilizing 72 6 inch full-square 4-busbar solar cells and standard module interconnection technology. In other words, no power-enhancing measures such as the use of half-cells, multi-wire approaches (e.g., soldering of multiple wires [17, 18] or connection of embedded wires during lamination [19, 20]), or light-capturing ribbons have been applied for the modules with mc-Si. For Cz-Si substrates, a more advanced module technology based on half-cells and six wire interconnection is applied. The half-cell technology halves the electrical current in the copper interconnects, thus the power loss due to series resistance in the interconnects is reduced by a factor of four, leading to a relative increase in module power by 3%rel. Moreover, using round wires instead of rectangular ribbons reduces the effective shaded area by roughly 60% of the wire diameter due to total internal refection at the glass–air interface of the module. This leads to an additional relative module power increase of 2%rel. Using cells with six busbars instead of four busbars reduces the power loss due to shorter finger lengths

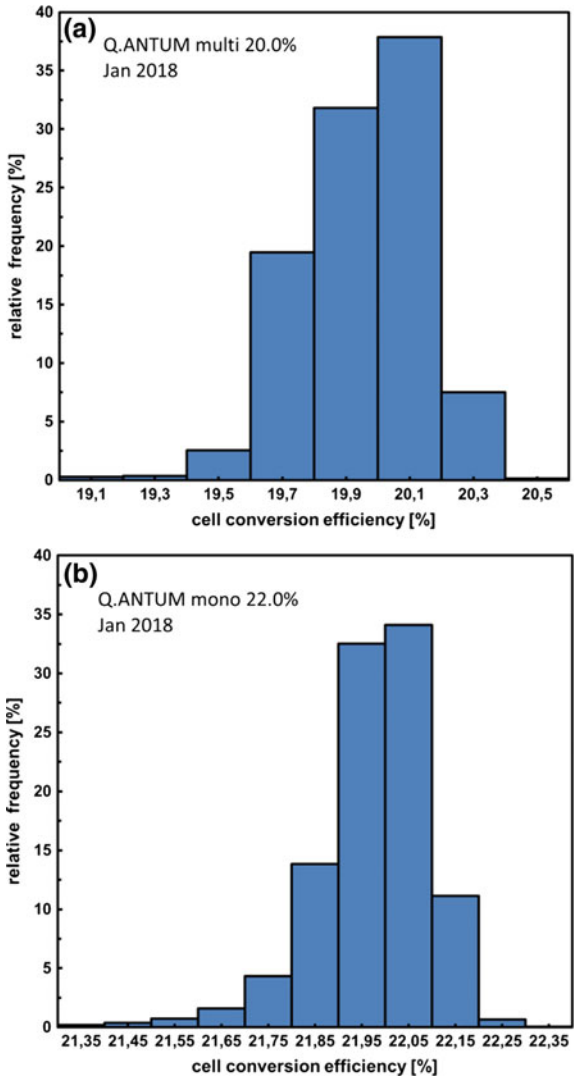

Fig. 6.5 Cell conversion efficiency distribution of several million Q.ANTUM solar cells on *p*-type silicon substrates in mass production in January 2018. **a** Q.ANTUM cells on mc-Si with average efficiency of 20.0%, **b** Q.ANTUM cells on Cz-Si with average efficiency of 22.0%

contributing an additional 0.5%rel module power increase. All three measures sum up to a gain of 5.5%rel compared to a module technology based on full-cells and four rectangular ribbon interconnection. Module powers of 320 Wp and 325 Wp are reached based on 120 half-cut *p*-type 6 inch pseudo squared Cz-Si substrates and six wire interconnection. These output powers are at the same level or even higher than those for modules with industrial PERT-like (passivated emitter, rear totally diffused [21]) solar cells on *n*-type silicon substrates. Furthermore, the gap to the power classes of modules with the highest efficiency *n*-type Cz-Si solar cell structures such as heterojunction [22–25] and rear-contact solar cells [26–29] is

rapidly narrowing. Importantly, compared to the comparably complex and thus higher cost manufacturing process of those *n*-type cells, the Q.ANTUM technology has an extremely competitive manufacturing cost.

6.4 Light-Induced Degradation of PERC

Besides maximizing conversion efficiency and output power, the long-term stability of solar cells and modules is of crucial importance. Two key mechanisms that are potential hazards for the reliability of solar cells and modules based on boron-doped *p*-type PERC-like technology are the boron–oxygen (BO) defect and "Light and elevated Temperature Induced Degradation" (LeTID). The impact of these mechanisms on PERC cell and module performance is discussed in this section and it is shown that Q.ANTUM technology suppresses both LID and LeTID in mc- and Cz-Si.

To separate BO defect formation and the formation of LeTID, different temperatures, excess charge carrier densities, and treatment times are applied. The applied nomenclature is as follows: CID describes current-induced degradation, which means that the same excess charge carrier densities are established by current injection in the dark as with LID. Two levels of excess charge carrier density are considered: OC and MPP mode, which correspond to the excess charge carrier concentrations at open-circuit and at maximum power point at an illumination intensity of $E_{ill} = 1\ kWm^{-2}$.

6.4.1 Boron–Oxygen Defect

To investigate the impact of BO defect formation on device performance, Q.ANTUM solar cells and PERC without treatment to permanently deactivate the BO defect have been processed on boron-doped *p*-type Cz-Si substrates from different industrial suppliers. These samples are then subjected to light soaking with an illumination intensity of ~1 sun-equivalent for 24 h at a temperature of 25 °C. For typical boron and oxygen concentrations, the formation of the BO defect has been shown to be almost independent of illumination intensity in the range of $0.01\ kWm^{-2} < E_{ill} < 1\ kWm^{-2}$ [6] and to typically be close to saturation after 24 h of light soaking at 25 °C [26, 27]. Figure 6.6 shows values of relative degradation in maximum output power upon light soaking. While a significant degradation of 4 to 5%rel is observed for PERC without BO defect stabilization, LID can be suppressed to less than 0.5%rel by applying Q.ANTUM technology [12].

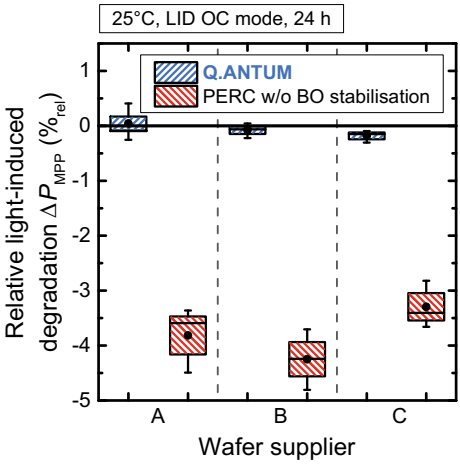

Fig. 6.6 Light-induced degradation of maximum output power of Q.ANTUM solar cells and PERC without BO stabilization on Cz-Si substrates from different suppliers (~1 sun-equivalent/25 °C/24 h). Graph taken from [12]

6.4.2 Light and Elevated Temperature Induced Degradation (LeTID)

In contrast to BO defect formation, LeTID has so far mainly been associated with a potential issue for mc-Si PERC [9–11]. In previous studies by Hanwha Q CELLS [11, 12], solar modules have been fabricated from mc- and Cz-Si PERC with intentionally manipulated LeTID sensitivity ("high LeTID"/"medium LeTID") along with LeTID-suppressing mc- and Cz-Si Q.ANTUM modules, and these have been subjected to different treatments. Figure 6.7 (right) shows the results for mc-Si: relative module power degradation as a function of treatment time. Severe degradation of more than 10% is observed for "high LeTID" PERC modules. While the "medium LeTID" treatment reduces degradation to about 4%, Q.ANTUM technology is shown to thoroughly suppress LeTID. Note: the applied test conditions are CID in MPP mode at elevated temperature. Compared with OC mode, the lower excess charge carrier densities in MPP mode lead to slower formation of LeTID but to a higher extent since regeneration sets in at a later point of time [11]. Hence, to test worst-case conditions at a reasonable speed, Hanwha Q CELLS suggests the testing conditions of CID in MPP mode at 75 °C to evaluate the long-term stability of silicon solar modules in terms of LeTID susceptibility.

As recently published by Hanwha Q CELLS [12], LeTID also occurs in Cz-Si cells. Three sorts of solar modules have been manufactured: (i) PERC modules without permanent deactivation of the BO defect, (ii) PERC modules with a commercially available processing step to permanently deactivate the BO defect, and (iii) LID- and LeTID-suppressing Q.ANTUM modules. To separate the formation of the BO defect and LeTID, two different CID treatments have been applied: (i) OC mode at $T_{LID} = 25$ °C, which corresponds to the conditions applied in Sect. 6.4.1 to test for BO defect formation and (ii) MPP mode at $T_{LID} = 75$ °C, which corresponds to the conditions suggested by Hanwha Q CELLS to test LeTID.

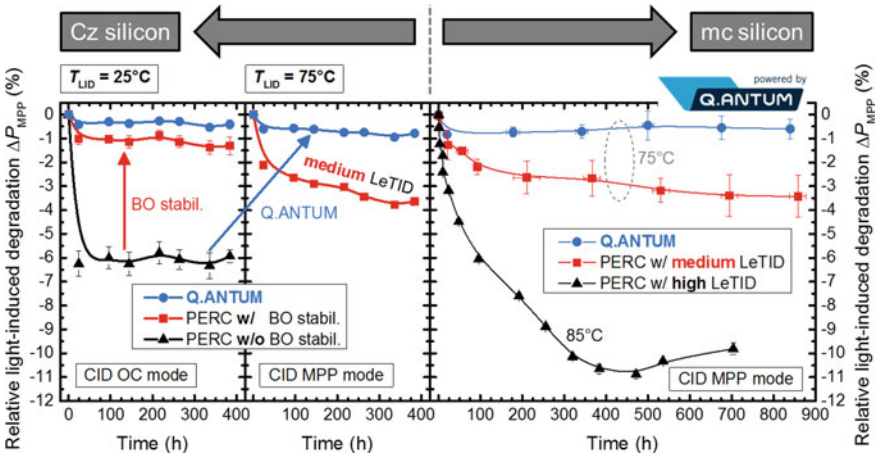

Fig. 6.7 (left) Relative degradation in maximum output power of modules with Cz-Si solar cells as a function of treatment time at temperatures of 25 and 75 °C in OC and MPP mode, respectively. Resulting degradation values for PERC modules with and without BO stabilization are displayed, along with LID- and LeTID-suppressing Q.ANTUM modules. (right) Relative power degradation of modules with mc-Si solar cells as a function of treatment time at temperatures of 75 and 85 °C in MPP mode. Resulting degradation values for PERC modules with maximum and medium LeTID sensitivity are displayed, along with LeTID-suppressing Q.ANTUM modules. It can be seen that Hanwha Q CELLS Q.ANTUM technology suppresses LID and LeTID for both mc- and Cz-Si. Graph taken from [12]

Figure 6.7 (left) shows values of relative module power degradation as a function of treatment time. In OC mode at $T_{LID} = 25$ °C, the Cz-Si PERC modules without BO stabilization show a degradation of around 6%, which is in the same order as for the PERC discussed in Sect. 6.4.1. By applying a commercially available processing step to permanently deactivate the BO defect (PERC w/BO stabilization), this degradation can be reduced to about 1%. However, when subjecting the PERC modules w/BO stabilization to CID in MPP mode at $T_{LID} = 75$ °C, a severe degradation of about 4% is observed. As expected from the discussion in Sect. 6.4.1, LID due to BO defect formation is close to saturation after 24 h of light soaking at 25 °C while degradation due to LeTID at 75 °C progresses in the considered time scale. When comparing Fig. 6.8 (left) and (right), it can be seen that the extent of LeTID of the Cz-Si PERC modules w/BO stabilization and its formation rate approximately correspond to the mc-Si PERC modules w/medium LeTID [12]. In conclusion, a strong LeTID signal is observed also on *p*-type Cz-Si PERC modules, despite the suppression of excessive LID due to BO defect formation by commercially available BO stabilization processing. As illustrated in Fig. 6.7, Hanwha Q CELLS' Q.ANTUM technology not only suppresses LID and LeTID on mc-Si but also on Cz-Si substrates [12].

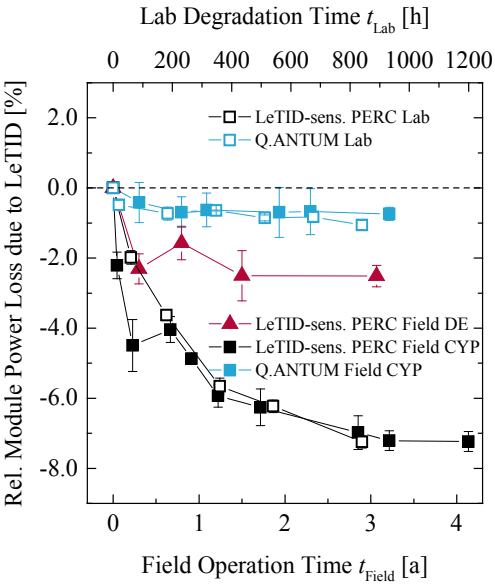

Fig. 6.8 Relative module power loss over time due to LeTID in the laboratory (upper x-axis) and from field operation in Thalheim (DE) and Nicosia (CYP) (lower x-axis). Graph taken from [13]

6.4.3 LeTID Under Real Field Condition

The impact of LeTID was investigated not only in the laboratory but also under real outdoor field conditions [13]. Standard industrial mc-Si substrates were neighbor sorted into two batches, for a direct comparison of PERC vs. Q.ANTUM technology that excludes material variability. LeTID-sensitive PERC modules were manufactured with one of the batches and Q.ANTUM modules with the other. The module degradation experiments in the laboratory were performed at a temperature of 75 °C in a climate chamber with CID (MPP) and 1 sun illumination.

LeTID-sensitive PERC and LeTID-suppressing Q.ANTUM modules were installed on outdoor test fields in Thalheim, Germany (DE) and Nicosia, Cyprus (CYP). The test fields represent temperate and Mediterranean climates, respectively. The irradiance (E_{mod}) in the module plane and module temperature (T_{mod}) as well as the energy yield of each system was logged regularly. Once every 3 months, the modules installed in Germany and Cyprus were removed from the system racks and tested by means of current–voltage measurements under standard test conditions (STC) in the laboratory. After each testing cycle, the modules were reinstalled outdoors.

For Thalheim, both the temperature and irradiances are significantly lower than in Nicosia. While in Thalheim, the modules operate for ~30% of all operation time in comparably lowlight conditions with Emod < 400 W/m^2, in Nicosia, the highest irradiance was measured to be in the range of 900–1000 W/m^2. These relatively high irradiances around 1000 W/m^2 in Cyprus resulted in comparably high module temperatures. The weighted average T_{mod} of 35–40 °C in Nicosia is significantly higher compared to Thalheim with 5–10 °C. In Nicosia, elevated temperatures with

$T_{mod} > 50$ °C occurred for ~25% of annual field operation time. Hence, these climatic conditions in Cyprus are well-suited for the characterization of LeTID in comparison to the temperate climate in Germany with ~70% of annual field operation time having $T_{mod} < 25$ °C [13].

The irradiance in the module plane and the module temperatures at two different test fields in Cyprus and Germany were measured. Together with a model for the irradiance- and temperature-dependence of LeTID kinetics, a site-specific time constant corresponding to the proposed accelerated laboratory test performed at 75 °C is deduced; e.g., 290 h laboratory test time corresponds to 1 year of field installation time in Cyprus. Figure 6.8 shows as filled symbols the relative module power loss due to LeTID for LeTID-sensitive PERC and LeTID-suppressing Q.ANTUM modules vs. field operation time (lower x-axis) in Cyprus and Germany. Furthermore, the corresponding values for degradation tests in the laboratory are shown as open squares. The time-dependent relative module power loss under laboratory testing at 75 °C with CID in MPP mode corresponds to the upper x-axis (lab degradation time t_{Lab}). The field performance can be modeled well by laboratory tests, see Fig. 6.10. LeTID-sensitive PERC modules showed a significant loss in module power of more than 7% due to LeTID, both in the field and under accelerated aging in the laboratory. Equivalent modules in Germany showed a degradation of ~2.5% for the same time period. Due to lower irradiance values and module temperature in Germany, the LeTID rate is less pronounced than in Cyprus. Figure 6.9 shows the relative loss of specific yield on the left and LCOE on the right y-axis compared with a reference system during 3 years of field installation in Cyprus. The loss in system output power due to LeTID is shown in Fig. 6.8 affects one-to-one the energy yield and the LCOE. It can be seen that the LeTID-suppressing Q.ANTUM modules show a higher

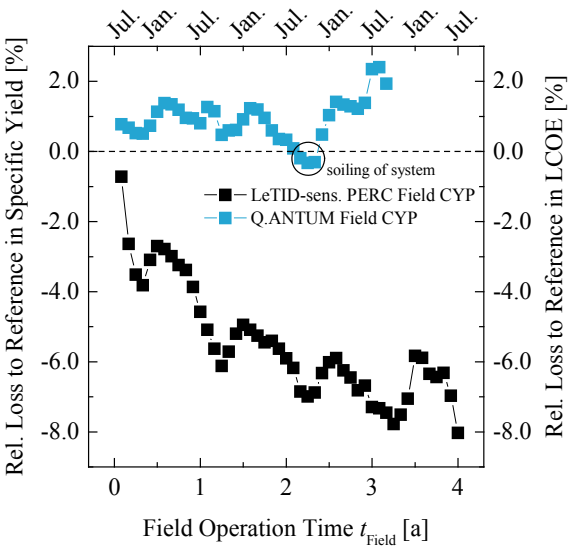

Fig. 6.9 Loss in specific yield and LCOE relative to reference due to LeTID during field operation in Nicosia (CYP). Graph taken from [13]

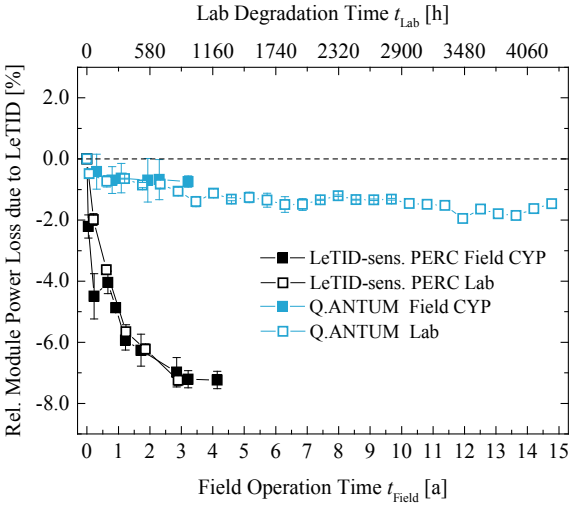

Fig. 6.10 Relative module power degradation over time due to LeTID. The lower x-axis corresponds to field operation time in Nicosia (CYP) and the upper x-axis to CID laboratory time in MPP mode at 75 °C in a climate chamber. Graph taken from [13]

specific yield and thus higher revenue than the reference system. The lower specific yield after approximately 2 years field installation time was due to soiling of the Q.ANTUM system in Cyprus from nearby construction, which was removed at the end of October. As shown in Figs. 6.8, 6.7, 6.8, and 6.9, by applying the optimized defect engineering of the Q.ANTUM process, LeTID could be fully suppressed in the field [13]. Figure 6.10 shows that Q.ANTUM modules do not degrade appreciably even after extended laboratory testing of several thousand hours. With the model that was developed and the site-specific time constant, the laboratory degradation time of 4300 h is predicted to correspond to 15 years of field installation in a Mediterranean climate [13].

6.5 Summary and Conclusion

This work addresses three crucial points for cost-effective PV cell and module production: first, lean and efficient production and development methods; second, high module power based on high efficiency cell and module technology; third, high reliability and energy yield by effective suppression of any light-induced degradation (LID).

A single wafer tracking system in combination with a manufacturing execution system was proven to be a powerful tool to detect process deviation and find their root causes. By using in-spec variation in combination with large amount of cells, statistically significant differences in conversion efficiency of less than 0.03%abs. are resolvable. This allows a very efficient fine-tuning of the whole process sequence and thus improves the average conversion efficiency of a production line. Using a systematic development process to mature and upscale lab results was found to speed

up implementation of innovations in a production environment. Thus, over the last decade, the average cell conversion efficiency of industrial solar cells fabricated on boron-doped *p*-type Czochralski-grown silicon (Cz-Si) and multicrystalline silicon (mc-Si) substrates increased by 0.5%abs. per year. Apart from process optimizations, one major technology platform change was implemented—going from the Al-BSF technology to Hanwha Q CELLS' Q.ANTUM technology, a PERC-based technology. Currently (Jan 2018), average solar cell conversion efficiencies of 22% and 20% are achieved in mass production on *p*-type Cz- and mc-Si substrates, respectively. We still see significant efficiency headroom for the Q.ANTUM technology and expect to approach 24% and 22% average conversion efficiency within the next years while maintaining a lean and cost-effective manufacturing process.

In combination with advanced interconnection and module technology, namely half-cell and six wire technology, Q.ANTUM module output powers of >325 Wp are achieved using 120 Cz-Si half-cells. The reliability of the wire connection technology is now well-established, with a soldering technique proven by yearlong studies. Q.ANTUM technology on cost-effective mc-Si substrates leads to solar modules exhibiting output powers of >350 Wp with 72 full 4-busbar cells and standard module technology.

One key concern for the long-term stability of Cz-Si and PERC cells in the field has been LID due to boron–oxygen (BO) defect formation and "Light and elevated Temperature Induced Degradation" (LeTID). By applying a commercially available processing step for the permanent deactivation of the BO defect, LID due to BO defect formation can be reduced from up to 6% to around 1% in conventional Cz-PERC. However, despite this BO defect stabilization, LeTID can be a severe issue for the long-term stability of PERC if not adequately suppressed, especially on mc-Si but also on Cz-Si substrates. The extent of LeTID in mc-Si and Cz-Si PERC can be manipulated, showing power degradation values of up to 11% on top of LID for different scenarios, despite "standard" permanent BO defect deactivation. Hence, the suppression of the BO defect is not sufficient, but instead, additional measures are necessary to detect and suppress LeTID to ensure long-term stability in the field.

The results presented show performance loss measurements due to LeTID not only in the lab but also in real field system installations. The observed degradation behavior in the field can be adequately predicted by using a site-specific time constant, which is easily adaptable to any climate zone.

In contrast to conventional PERC, Hanwha Q CELLS' Q.ANTUM technology is shown to reliably suppress both LID due to BO defect formation and LeTID in modules manufactured from both p-type mc-Si and Cz-Si substrates. Outdoor field operation data and long-term laboratory testing in climate chambers, corresponding to a field installation time of 15 years in a Mediterranean climate, validated the effective LeTID suppression of Q.ANTUM. This enables the superior long-term stability and field performance of Q.ANTUM compared with conventional PERC modules.

Acknowledgements The author acknowledges the staff of the R&D department and production at Hanwha Q CELLS for their contribution to this work.

References

1. P. Engelhart et al., Q.ANTUM—Q-Cells Next Generation High-Power Silicon Cell & Module Concept, in *Proceedings of the 26th European Photovoltaic Solar Energy Conference and Exhibition*, Hamburg, Germany (2011), pp. 821–826
2. S. Engelhart et al., 3 years of high quality mc-Si Q-ANTUM production experience—approaches for efficient cell and module development, in *Proceedings of the 31st European Photovoltaic Solar Energy Conference and Exhibition*, Hamburg, Germany (2015), pp. 273–278
3. International Technology Roadmap for Photovoltaic (ITRPV): 2013 Results, Fifth Edition, Revision 1, March 2014. http://www.itrpv.net/
4. International Technology Roadmap for Photovoltaic (ITRPV): 2016 Results, Eighth Edition, March 2017. http://www.itrpv.net/
5. A.W. Blakers, A. Wang, A.M. Milne, J. Zhao, M.A. Green, 22.8% efficient silicon solar cell. Appl. Phys. Lett. **55**(13), 1363 (1989)
6. S. Rein, T. Rehrl, W. Warta, S.W. Glunz, G. Willeke, Electrical and thermal properties of the metastable defect in boron-doped Czochralski silicon (Cz-Si), in *Proceedings of the 17th European Photovoltaic Solar Energy Conference*, Munich, Germany (2001), pp. 1555–1560
7. J. Schmidt, K. Bothe, Structure and transformation of the metastable boron- and oxygen-related defect center in crystalline silicon. Phys. Rev. B **69**(2), 24107 (2004)
8. V.V. Voronkov, R. Falster, Latent complexes of interstitial boron and oxygen dimers as a reason for degradation of silicon-based solar cells. J. Appl. Phys. **107**(5), 53509 (2010)
9. K. Ramspeck et al., Light induced degradation of rear passivated mc-Si solar cells, in *Proceedings of the 27th European Photovoltaic Solar Conference and Exhibition*, Frankfurt, Germany (2012), pp. 861–865
10. F. Fertig, K. Krauß, S. Rein, Light-induced degradation of PECVD aluminium oxide passivated silicon solar cells. Phys. Stat. Sol. (RRL) **9**(1), 41–46 (2015)
11. F. Kersten et al., Degradation of multicrystalline silicon solar cells and modules after illumination at elevated temperature. Sol. Energy Mater. Sol. Cells **142**, 83–86 (2015)
12. Fertig et al., Mass production of *p*-type Cz silicon solar cells approaching average stable conversion efficiencies of 22%. Energy Procedia **124**, 338–345 (2017)
13. F. Kersten et al., System performance loss due to LeTID. Energy Procedia **124**, 540–546 (2017)
14. S. Wanka et al., Tra.Q—laser marking for single wafer identification—production experience from 100 million wafers, in *Proceedings of the 26th European Photovoltaic Solar Energy Conference and Exhibition*, Hamburg, Germany (2011), pp. 1104–1107
15. A. Mohr et al., 20%-efficient rear side passivated solar cells in pilot series designed for conventional module assembly, in *Proceedings of the 26th European Photovoltaic Solar Energy Conference and Exhibition*, Hamburg, Germany (2011), pp. 2150–2153
16. M. Schaper et al., The Q.ANTUM technology platform applied to *p*-Cz to maintain constant efficiency increase per year, in *Proceedings of the 32nd European Photovoltaic Solar Energy Conference and Exhibition*, Munich, Germany (2016)
17. J. Walter, M. Tranitz, M. Volk, C. Ebert, U. Eitner, Multi-wire interconnection of busbar-free solar cells. Energy Procedia **55**, 380–388 (2014)
18. S. Braun, G. Hahn, R. Nissler, C. Pönisch, D. Habermann, Multi-busbar solar cells and modules: high efficiencies and low silver consumption. Energy Procedia **38**, 334–339 (2013)
19. T. Söderström, P. Paper, J. Ufheil, Smart wire connection technology, in *Proceedings of the 28th European Photovoltaics Solar Energy Conference and Exhibition*, Paris, France (2013), pp. 495–499
20. A. Schneider, L. Rubin, G. Rubin, Solar cell efficiency improvement by new metallization techniques—the Day4 electrode concept, in *Proceedings of the 4th World Conference on Photovoltaic Energy Conversion*, Waikoloa, HI, USA (2006), pp. 1095–1098
21. J. Zhao et al., High efficiency PERT cells on n-type silicon substrates, in *Conference Record of the 29th IEEE Photovoltaic Specialists Conference*, New Orleans, LA, USA (2002), pp. 218–221

22. K. Yoshikawa et al., Silicon heterojunction solar cell with interdigitated back contacts for a photoconversion efficiency over 26%. Nat. Energy **2**, 17032 (2017)
23. K. Masuko et al., Achievement of more than 25% conversion efficiency with crystalline silicon heterojunction solar cell. IEEE J. Photov. **4**(6), 1433–1435 (2014)
24. M. Tanaka et al., Development of new a-Si/c-Si heterojunction solar cells: ACJ-HIT (Artificially Constructed Junction-Heterojunction with Intrinsic Thin-Layer). Jpn. J. Appl. Phys. **31**, Part 1, No. 11, 3518–3522 (1992)
25. S. de Wolf, A. Descoeudres, Z.C. Holman, C. Ballif, High-efficiency silicon heterojunction solar cells: a review. Green **2**(1), 7–24 (2012)
26. E. van Kerschaver, G. Beaucarne, Back-contact solar cells: a review. Prog. Photovolt Res. Appl. **14**(2), 107–123 (2006)
27. D.D. Smith, Silicon solar cells with total area efficiency over 25%, in *Proceedings of the 42nd IEEE Photovoltaics Specialists Conference*, Portland, Oregon, USA, 2016
28. M.D. Lammert, R.J. Schwartz, The interdigitated back contact solar cell: a silicon solar cell for use in concentrated sunlight. IEEE Trans. Electron Devices **24**(4), 337–342 (1977)
29. R.M. Swanson et al., Point-contact silicon solar cells. IEEE Trans. Electron Devices **31**(5), 661–664 (1984)

Chapter 7
Silicon Heterojunction Technology: A Key to High Efficiency Solar Cells at Low Cost

A. S. Abramov, D. A. Andronikov, S. N. Abolmasov and E. I. Terukov

Abstract Solar cells made of silicon wafers have dominated the terrestrial photovoltaic (PV) market since the beginning of industrial commercialization of PV.

7.1 High-Efficiency Silicon PV Technologies Overview

Solar cells made of silicon wafers have dominated the terrestrial photovoltaic (PV) market since the beginning of industrial commercialization of PV. Today, about 90% of solar modules are made of silicon solar cells. There are two main reasons for this. First, silicon is one of the most common elements on the Earth, which is abundant and eco-friendly. Second, silicon is the main semiconductor material in the microelectronic industry. The presence of a vast market of the equipment for microelectronics, the high level of development of individual technological steps and the possibility of their transfer greatly facilitated and speeded up the growth of silicon PV. Since the very beginning, Si solar cells have demonstrated high conversion efficiencies among other technologies used in mass production of solar modules for

Dedicated to the 100 Anniversary of Ioffe Institute.

A. S. Abramov (✉) · D. A. Andronikov · E. I. Terukov
Ioffe Institute, 26 Polytechnicheskaya Str., St. Petersburg 194021, Russia
e-mail: a.abramov@hevelsolar.com

D. A. Andronikov
e-mail: d.andronikov@hevelsolar.com

E. I. Terukov
e-mail: e.terukov@hevelsolar.com

A. S. Abramov · D. A. Andronikov · S. N. Abolmasov · E. I. Terukov
R&D Center of Thin Film Technologies in Energetics, 28 Polytechnicheskaya Str., St. Petersburg 194064, Russia
e-mail: s.abolmasov@hevelsolar.com

V. Petrova-Koch et al. (eds.), *High-Efficient Low-Cost Photovoltaics*,
Springer Series in Optical Sciences 140,
https://doi.org/10.1007/978-3-030-22864-4_7

terrestrial PV market [1]. Multijunction solar cells fabricated from III to V semiconductor compounds have demonstrated significantly higher efficiencies (~38% for an InGaP/GaAs/InGaAs cell at one sun [2]) and are currently the mainstream product for spacecraft solar panels; however, these are still on their way to full-scale terrestrial applications due to elevated production costs.

High efficiency silicon-based PV technologies require advanced approaches in the solar cell design to address such issues as effective light absorption and collection of photo-generated carriers, suppression of carrier recombination losses, reduction of shadow losses caused by front electrodes and cell assembly in the module. The specific feature of high efficiency silicon solar cells is the implementation of surface passivation layers that allow decreasing significantly recombination losses of photo-generated carriers at the interfaces. Effective surface passivation is usually achieved by using dielectric layers such as silicon nitride (SiN_x), silicon oxide (SiO_2), aluminum oxide (Al_2O_3) (see Chap. 4 of this book for more details) or intrinsic hydrogenated amorphous silicon or their combinations, depending on the type of technology used for manufacturing of high efficiency silicon solar cells.

Among commercially available silicon solar cells, there are three main types of cells (see Fig. 7.1), which currently have conversion efficiency of above 22%. They include: (1) interdigitated back contact (IBC) cells, (2) passivated emitter and rear contact cells (PERC) and (3) silicon heterojunction (SHJ) cells. Up to now, the IBC cells, introduced into terrestrial PV market by SunPower Corporation around 2004 [3], have demonstrated the highest cell (>24%) and module (>22%) efficiency in

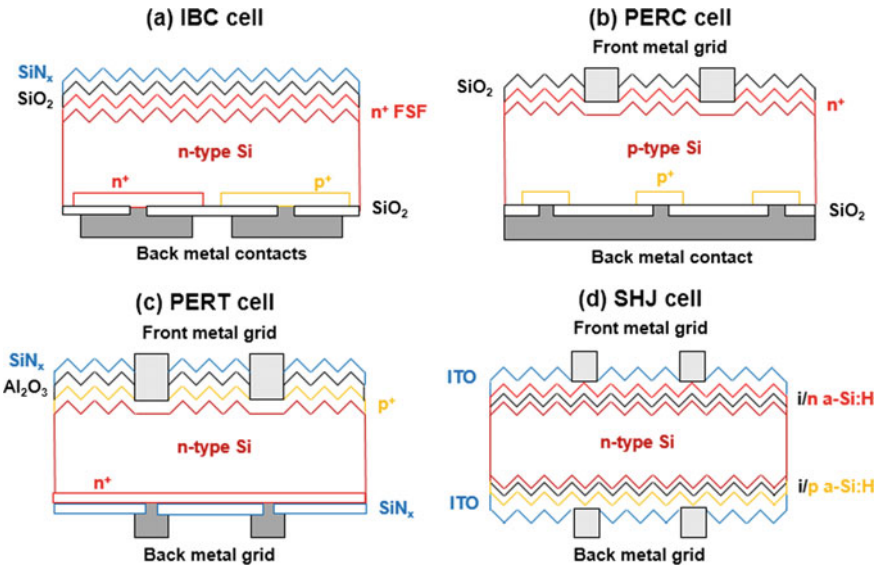

Fig. 7.1 Schematic cross-sectional view of high efficiency c-Si solar cells: **a** IBC cell (FSF—front surface field), **b** PERC cell, **c** PERT cell and **d** SHJ cell (ITO—indium tin oxide, i-a-Si:H—intrinsic hydrogenated amorphous silicon) ; bifacial, rear emitter design is shown

mass production [4] among these three designs. The record efficiency of SunPower R&D IBC cells is 25.2% [4]. The key design features that contribute to very high efficiency are: (1) a gridless front surface, which permits to avoid shadow losses and optimize front surface passivation, (2) localized back contacts with reduced contact recombination losses due to SiO_2 passivation, and (3) backside metallization that provides internal rear surface reflection and very low series resistance. An additional benefit of IBC cell design is that the cell interconnection is made at one (rear) side allowing to reduce the distance between cells and hence to increase the module efficiency. High efficiency and aesthetic appearance of IBC modules make them very attractive for mobile PV systems that can be used as an energy source in cars, trucks, planes, boats and so on [5]. However, their large-scale application (e.g., in centralized power stations or as a part of building integrated PV) is limited by comparatively complex manufacturing process resulting in high production costs.

On the other hand, the PERC cell has an advantage of being more compatible with existing production lines used for the standard technology—aluminum back surface field (Al-BSF) on p-type silicon, which represents a very large proportion (>90%) of world PV market. For this reason, many cell producers consider the PERC concept as a natural development of standard technology. The PERC cell concept was proposed by researchers from University of New South Wales (UNSW) in the late 1980s [6]. In this device, the back surface of the cell is oxidized and then p^+ regions are formed in localized areas of the device by opening windows in the oxide layers and then diffusing dopant impurities into these regions, as schematically shown in Fig. 7.1b. The silicon dioxide passivates the back surface of the cell and is much more effective at reflecting light back into the cell than the Al-BSF contact and p^+ regions alone. Such cells made of boron-doped, p-type c-Si are already in production on a large scale in Asia, with an efficiency of about 22% [7], not taking into account light-induced degradation (LID) effect due to boron–oxygen complex formation [8]. To avoid the LID effect, there have been suggestions that the industry needs to move as a whole to phosphorus-doped, n-type c-Si wafers, which is also a feasible substrate for high-performance PERC cells. Since phosphorus does not form such detrimental defects with oxygen, this allows higher lifetimes in standard Czochralski (CZ) grown ingots. For this reason, the passivated emitter rear totally diffuse (PERT) cell—a close cousin of PERC cell—has attracted much attention recently [9, 10]. This technology, however, requires additional steps to execute it (e.g., to grow SiN_x and Al_2O_3 layers, as can be seen in Fig. 7.1c), which increase the production costs compared to the PERC technology. A specific feature of PERT cell is its high (>90%) bifaciality. This means that such cells assembled in a module can benefit from an albedo of surrounding area and the gain in the energy yield can be rather impressive. Although the procedure for measuring the gain of bifacial modules having transparent protective cover at the rear side is not certified yet, recent studies have demonstrated that the gain could be in the range from 10 to 20%, depending on the albedo and design of solar station. For example, as shown in [11], an 18.5% cell mounted over a surface with intermediate albedo can yield a bifacial gain of 20%, corresponding to an equivalent cell efficiency of 22%. Hence, it is reasonable

to assume that 21–22% bifacial PERT cells could behave in outdoor conditions like 24–25% IBC cells, which have rather moderate bifaciality.

Another solar cell concept with inherent bifaciality is heterojunction with intrinsic thin layer (HIT) cell invented by Sanyo in the early 1990s [12]. In this device (as well as in other SHJ cells), excellent surface passivation is achieved by deposition of very thin intrinsic hydrogenated amorphous silicon (a-Si:H) layers on both sides of n-type wafer, as schematically shown in Fig. 7.1d. The a-Si:H passivation layers grown at low temperature allow to reach much higher open-circuit voltages (up to 750 mV [13]) and smaller temperature coefficients (below—0.3%/°C [14, 15]) in SHJ cells in comparison to high temperature (thermal diffusion) approaches employed in IBC, PERC or PERT cells. The simple structure of SHJ cells makes them also suitable for the IBC cell design. As recently demonstrated by Kaneka, 6″ SHJ cells having the IBC design can even outperform the standard IBC cells and reach an efficiency of 26.3% [16]. All these benefits make SHJ solar cells very attractive for the PV industry. Today many cell producers already use SHJ technology for large-scale manufacturing of solar cells with an efficiency of 22–23%.

In this chapter, the main features of SHJ technology are considered. As IBC-SHJ technology is still a subject of R&D and not industrialized yet, we focus on two-side contacted bifacial technology, depicted in Fig. 7.1d, which is the mainstream in the mass production of SHJ solar cells.

7.2 Key Features of SHJ Solar Cell Technology

7.2.1 SHJ Cell Technology at a Glance

The concept of a diode using a heterojunction formed on the contact between doped amorphous silicon layers and c-Si wafer was initially proposed in 1974 [16]. However, the concept was commercialized only in 1990s with implementation of very thin intrinsic a-Si:H layers between doped layers and c-Si wafer [12], as mentioned above. This ultra-thin a-Si:H layers with typical thickness of few nanometers have crucial effect on the performance of SHJ cells. Their aim is to suppress surface recombination by chemical passivation of dangling bonds on c-Si wafer surface with forming of Si–Si and Si–H bonds and to prevent defect generation by dopant atoms during deposition of doped layers [17].

A cross-sectional view of the conventional SHJ solar cell and main steps of its manufacturing process sequence are given in Fig. 7.2. Typically, the SHJ cell is composed of n-type c-Si wafer coated on both sides with thin intrinsic and doped a-Si:H layers. These layers then fully covered with indium tin oxide (ITO) films followed by screen-printing of contact metal grids for current collection using of low-temperature Ag conductive paste.

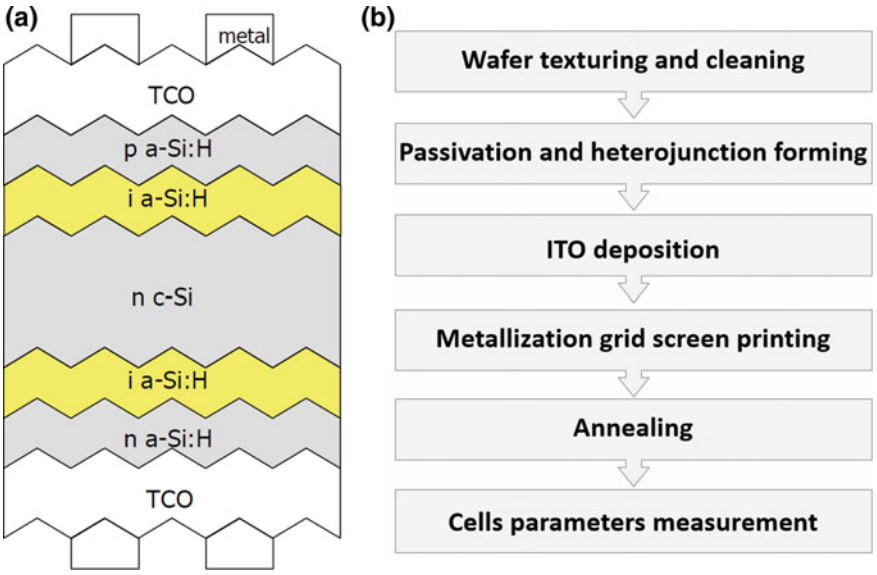

Fig. 7.2 **a** Schematic cross-sectional view of conventional SHJ solar cell and **b** main steps of its fabrication process sequence

7.2.2 Wafers for SHJ Cells

Like for all high performance c-Si solar cells, wafer quality is a key to high efficiency SHJ cells. Although record efficiency values reported in the literature have been obtained using high-purity float zone (FZ) c-Si wafers, the development of Czochralski process and continuous improvement of polysilicon quality allowed to reduce impurity concentrations in CZ wafers with reasonable production costs. As a result, the open-circuit voltage (V_{oc}) of SHJ cells has recently reached values as high as 750 mV [13].

Up to now, only monocrystalline CZ wafers are used for large-scale manufacturing of SHJ solar cells. Despite promising results have been reported by several research groups for SHJ cells made of epitaxial Si wafers or so-called "monolike wafers" [18], produced by advanced directional solidification process [19], the use of these potentially low-cost wafers in mass production requires further developments.

Both n- and p-doped c-Si wafers have been used for manufacturing SHJ solar cells, however, the highest efficiency was obtained for n-doped wafers [20]. The asymmetry between conduction and valence band offsets is generally assumed as a reason of worse performance of p-type SHJ solar cells [21]. It has also been speculated that in the case of n-type Si strong bending of conductive band at p/n junction prevents back diffusion of electrons and, therefore reduces their surface recombination, while hole transport through narrow "spike" barrier is facilitated by comparatively high density of localized states in the valence band tail of a-Si:H (see Fig. 7.3). Thus, for

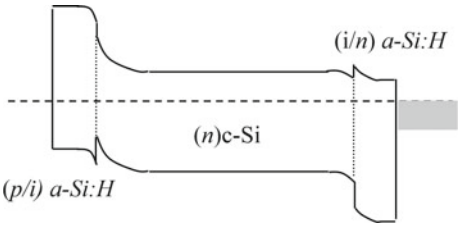

Fig. 7.3 Schematic of band diagram of a bifacial SHJ solar cell based on n-type silicon wafer

n-type wafers, intrinsic a-Si:H passivation layer along with field effect passivation, resulted from the large valence band offset, decreases recombination rate at the p/n interface, which almost approaches the intrinsic recombination limit of the high-quality c-Si [22]. Additional benefits of n-type c-Si are the absence of LID, associated with boron–oxygen complexes in p-type material, as explained above, and lower sensitivity of n-type silicon to metal impurities [23], which are usually present in the silicon feedstock, therefore less effort has to be made to obtain n-type silicon wafers with high electronic quality.

The electronic properties of monocrystalline silicon wafers for high efficiency solar cells are determined by impurities and dopant concentrations. Since measurements of these parameters require special techniques that can hardly be used in mass production process, the minority carrier lifetime and wafer resistance are usually measured in practice as the main parameters to trace the quality of wafers or ingots. These parameters usually vary along and across ingots and their profiles depend on the details of ingot growth process and post treatment. Therefore, it has been proposed to use the measured lifetime/resistance ratio as a cumulative measure of wafer and heterojunction qualities [24]. Recent studies have also shown that for SHJ cells with $V_{oc} > 750$ mV one has to use passivated wafers with a lifetime-to-resistance ratio above 4 ms/Ohm [25].

The most significant advantage of SHJ technology in terms of cost reduction is that all process steps are performed at low temperatures (<250 °C) favoring the use of thin wafers for SHJ solar cell production. Recent progress in wafer slicing technology due to implementation of diamond wire technology has resulted in mass production of low-cost wafers with thickness less than 160 μm. Wafers with as cut thickness of 150 μm have recently been successfully implemented in the SHJ production process without losses in the power of modules [26]. Although further reduction of SHJ cell thickness is also possible without significant losses in the efficiency [27], currently implementation of thinner wafers in mass production is limited by handling issues resulting in excess wafer brakeage rates.

7.2.3 Wafer Texturing and Cleaning

Similar to other c-Si PV technologies, wet chemical treatment is the first step in production sequence of SHJ cells. It usually includes the following steps:

– etching of highly defective surface part of wafer (surface damage etch—SDE);
– forming of special surface morphology (texture) reducing light reflection from wafer surface (TEX);
– cleaning of wafer surface from organic and metal impurities.

If first two steps based on isotropic (SDE) and anisotropic (TEX) alkali etching are similar to those used in other silicon PV technologies, the last step significantly differs. To obtain high-quality surface passivation the wafer surface should be extra clean. Therefore, enhanced cleaning procedure is necessary for production of high-efficiency SHJ cells, and includes removal of residual organic, ionic and metallic contamination (coming from wet etching/texturing solutions) from c-Si wafer surface. In addition, heavy deionized (DI) water rinse steps are used between each chemical treatment. The wet chemical treatment ends up with a short HF dip, which removes native oxide and passivates c-Si surface with hydrogen atoms prior to a-Si:H PECVD processes.

At the beginning of SHJ technology development, the RCA cleaning process, which is common in microelectronics [28], was adapted for wafer cleaning [29]. The RCA process, however, includes hydrogen peroxide, which has high decomposition rate at process temperatures above 65 °C that are required to reach reasonable throughput during mass production of SHJ solar cells. On the other hand, a substitution of H_2O_2 with ozone (O_3) as an oxidizing agent has also been used in microelectronics for a long time [30]. The O_3-based cleaning process allows reducing chemical consumption and waste generation, and facilitates the process control. It has been shown that O_3-based process is effective not only for cleaning of organic residuals but also in removing metallic contamination [31, 32]. Consequently, an industrial cleaning procedure usually includes three steps—cleaning from organics in DI water/O_3 mixture (DIO), cleaning from metallic contamination in HCl/HF solution either with or without O_3 and final oxidation in HCl/O_3 solution. A recent study [33] has shown that this process sequence can be reduced down to two process steps or even to a single cleaning step by fine tuning of concentration of chemicals.

7.2.3.1 Surface Passivation and Junction Formation

High-quality surface passivation is a key to achieve high values of V_{oc} in high-efficiency silicon-based solar cells. An insertion of thin (<10 nm) hydrogenated amorphous silicon (a-Si:H) layers between c-Si wafer and doped a-Si:H layers lead to higher V_{oc} values in comparison to those registered in case when intrinsic a-Si:H layers are absent [34]. In the last two decades the surface passivation of SHJ cells has been essentially improved, resulting in V_{oc} values close to 750 mV [13], which approach the theoretical limit (~760 mV) and underline the particular appeal of this technology. From a microscopic point of view, surface passivation of c-Si by a-Si:H is most likely closely linked to hydrogenation of surface states [35], where the hydrogen is supplied from the passivating film during its growth and post-annealing process. Generally, low temperature annealing of a-Si:H films in ambient air (which in some

extend mimics curing process of low temperature silver paste during manufacturing of SHJ solar cells) improves the passivation properties. As a rule, a necessary condition for good surface passivation is that the a-Si:H/c-Si interface should be atomically sharp, meaning that silicon epitaxial growth is avoided, that is, no crystalline material is deposited [36]. This can be achieved by a proper tuning of a-Si:H film properties during deposition process.

In practice, a-Si:H layers are commonly grown by plasma-enhanced chemical vapor deposition (PECVD) method using parallel-plate capacitively coupled plasma (CCP) discharge in pure silane or in silane-hydrogen mixtures at temperatures close to 200 °C. It appears that the most critical process parameters for surface passivation are the hydrogen-to-silane gas flow ratio and power density, whereas the gas pressure may affect the film thickness uniformity. It has been reported that plasma regimes close to the amorphous-to-microcrystalline transition are well suited for deposition of device-grade passivating a-Si:H layers [37]. These regimes can be produced either in silane plasmas highly diluted with hydrogen or in highly depleted pure silane plasmas [38]. The use of hydrogen plasma treatments during the a-Si:H deposition might also be beneficial [39]. Note that today most industrial CCP reactors employ RF (13.56 MHz) power for plasma generation. This is mainly due to the fact that the low excitation frequency allows better control of a-Si:H film thickness over large areas (>1 m^2). Nevertheless, the main drawbacks of standard RF PECVD reactors are: 1) low a-Si:H deposition and etching (during in situ plasma cleaning) rates due to low plasma density limiting the PECVD system throughput and 2) high-energy ion bombardment of the a-Si/c-Si interface due to high sheath voltages resulting in higher defect densities in passivating a-Si:H layers. Owing to these reasons, alternative deposition techniques such as very high frequency (VHF) PECVD [35, 39], hot wire (or catalytic) CVD [40, 41], expanding thermal plasmas [42], and so on [43, 44] have also been investigated in the recent years for c-Si surface passivation both in academia and industry. Currently, Hevel is the only company, which employs VHF (40.68 MHz) PECVD reactors for mass production of high efficiency HJT solar cells. It has been shown [45] that Gen5 KAI PECVD reactors, originally designed by the former Oerlikon Solar for mass production of micromorph modules, can provide an excellent uniformity (<5%) of optical and electrical properties of a-Si:H layers across entire surface of a 110 × 130 cm^2 wafer carrier. Since spring of 2017 [46], Gen5 KAI PECVD reactors have successfully been used for mass production of high-efficiency SHJ solar cells at the Hevel production facility, as described in Sect. 7.3.

To fabricate SHJ solar cells, the passivating intrinsic a-Si:H layers should be coated with p- and n-doped a-Si:H layers for the front emitter and back surface field formation, respectively. However, as shown in [47], their electronic passivation properties are often found to be inferior in comparison to those of their intrinsic counterparts despite the fact that they may yield a field effect at the a-Si:H/c-Si interface. Deterioration of surface passivation is more pronounced for p-doped layers rather than for n-doped layers. On the other hand, n-doped a-Si:H layers can have electric conductivity one or two orders in magnitude higher compared to p-doped a-Si:H layers [48]. Besides, n-doped layers can easily be made nano- or microcrystalline, which makes them even more conductive and transparent. As a result,

the rear emitter (RE) design in which the emitter is located at the rear surface of c-Si wafer is more suitable for manufacturing of high-efficiency SHJ solar cells. For RE configuration the front lateral current collection is facilitated by the Si wafer itself, as electrons abundant in the n+ region near the cells front surface have a very high diffusion length. Since the electron transport is supported by the wafer, some limitations are lifted for the front TCO layer as well as the current collection grid allowing making them more transparent and less dense, respectively. In other words, this leads to cell with higher fill-factor at higher short-circuit current compared to the FE (front emitter) counterpart. It should also be mentioned that in recent years there has been growing interest in developing of amorphous and nano-crystalline silicon oxide layers [49, 50] acting as passivation and window layers for high-efficiency SHJ solar cells due to their higher optical band-gap energy, resulting in less parasitic absorption.

As mentioned above, the c-Si wafer surface should be clean and nonoxidized in order to obtain good solar cell performance in terms of surface passivation. In this matter ex situ photoluminescence (PL) imaging is a useful technique for process optimization, in particular during mass production process in industry. This is because PL measurements are nondestructive, environment-insensitive and contactless, and hence can practically be applied at any process step. Although several mechanisms affect the PL response, it is generally found that intense PL signals correlate with good interface properties. A strong PL response is widely regarded as an indicator of a high-quality surface passivation. *In situ* PL measurements can also be used for more precise control of a-Si:H passivation properties [51, 52].

7.2.4 Transparent Conductive Oxides

Since thin-doped a-Si:H layers have high resistance, they are commonly coated with transparent conductive oxides (TCO) layers to collect the photo-generated current. The total current produced by 6″ in size SHJ solar cells usually exceeds 9 A, therefore additional metallic electrodes are required for efficient current collection, which are the subject of next section. The sheet resistance of TCO layers must be sufficiently low (typically below 100 Ω/sq.) to avoid deteriorating of the fill factor. Direct current (DC) sputtering is commonly used in industry for double-side deposition of TCO layers simplifying the manufacturing process of bifacial HJT solar cells. In this case, the wafer carrier acts as the edge shadowing mask at the rear surface resulting in edge insolation between front and rear ITO layers. The size of edge insolation should be minimal to obtain maximum short-circuit current. The use of cylindrical rotary targets allows increasing TCO target utilization factor (up to 80%) and, in turn, to extend their exchange period, minimizing the production costs [53]. On the contrary, planar TCO targets that are widely used in R&D studies have a target utilization factor of only 30%. Ceramic indium tin oxide (ITO) targets of various composition (In_2O_3:SnO_2 = 90:10, 95:5, 97:3, etc.) are often the TCO material of choice in SHJ cells, in particular for the front TCO layer, which also acts as an antireflection

coating (ARC). The refractive index of most TCO layers is close to 2 at a wavelength of 600 nm, therefore the thickness of the front ITO layer must be fixed at about 75 nm to minimize reflection losses.

Carrier mobility of ITO $\mu = 20–40$ cm^2/Vs are typical for DC sputtered ITO layers, and carrier density can be tuned from 10^{19} to 10^{21} cm^{-3} by adjusting the flow of oxygen in argon atmosphere during sputtering, giving front ITO layers with sheet resistances below 100 Ω/sq. and optical transmittance above 90% for 80–100 nm thick layers [54, 55]. Among typical ITO target compositions 97:3 ITO targets yield thin films with high mobility and optical transparency, making them suitable for the front TCO. Nevertheless, alternative TCO materials with even higher motilities and therefore lower absorption for the same sheet resistance have also been extensively investigated in recent years. These include hydrogen (IO:H) and tungsten (IWO) doped indium oxide [56, 57] or their combination (IWOH) [58], however, to obtain such high mobility layers on large scale is challenging. It should also be emphasized that the high UV content of magnetron sputtering discharges in combination with high energy neutrals can lead to damage of underlying a-Si:H layers [59]. Therefore, there has also been interest in the development of "soft" deposition techniques for TCO layers such as low pressure chemical vapor deposition (LPCVD) (mainly used for aluminum-doped zinc oxide (AZO) [60]), remote plasma deposition (RPD) [58] and most recently atomic layer deposition (ALD) [61]. Nevertheless, inline magnetron sputtering is still the workhorse of the PV industry for depositing of various TCO layers.

7.2.5 Metallization

The process requirements for manufacturing SHJ solar cells have several advantages in comparison to those of conventional homojunction c-Si solar cells. First of the advantages is low thermal budget during the heterojunction formation. The deposition temperature of a-Si:H and ITO layers is usually less than 250 °C. Second, the time required to form the a-Si:H/c-Si junctions and contact layers is also shorter for SHJ cells than for conventional c-Si solar cells based on thermal diffusion processes. Third, wafer bowing is suppressed due to the low process temperature and symmetric structure of SHJ solar cells. However, the main disadvantage of using low temperature processes is that standard firing-through metallization techniques (with firing temperatures in the range of 800–900 °C) cannot be implemented in SHJ cells. This is because the a-Si/c-Si heterojunction does not withstand process temperatures above 200–250 °C, at which hydrogen effusion from internal surfaces of the heterojunction leads to detrimental effects on the cell performance. Due to this reason, the so-called low curing temperature (LCT) silver paste is commonly used for metallization of SHJ cells via screen-printing, which is currently the state-of-the-art technology for the metal grid deposition. The LCT Ag paste, however, has a typical bulk resistivity in the range of 5–6 μΩ*cm [62], that is, 2–3 times higher than the bulk resistivity of conventional firing pastes. Unlike firing-through paste printed fingers, which after

firing step became dense and highly conductive (their conductivity is almost equal to bulk Ag), fingers made of LCT Ag paste represent a polymeric matrix containing Ag particles even after curing. Hence, the contact resistance of the particles limits the conductivity of fingers made of LCT Ag paste. On the other hand, the LCT paste is in direct contact with thin TCO layer rather than with Si surface, therefore the contact resistance between ITO and LCT Ag paste is another important parameter directly affecting the SHJ solar cell performance. Consequently, it is obvious that five busbar (5BB) or multiwire concepts are favorable for interconnection of SHJ cells with LCT Ag paste contact grids in order to minimize the current collection ohmic losses and to increase the cell efficiency. In addition, the resistivity of LCT Ag paste can be controlled by changing the form and size of Ag particles, ranging from microscopic flakes to spherical nanoparticles. Several ideas have also been proposed for decreasing the Ag content of LCT paste to minimize its cost such as replacing the Ag particles by silver-coated copper or graphite; however, to the best of our knowledge, none of these alternatives has been implemented in mass production yet.

To obtain the best cell performance, fine-tuning of the LCT Ag paste properties (such as viscosity, polymeric and silver content) should be performed as well as a trade-off between its printability, adhesion, aspect ratio and bulk conductivity should be found. For the state-of-the-art products a finger width of as low as 30–40 μm and an aspect ratio of 1:3—1:2 can be achieved in combination with busbarless design, resulting in SHJ cell efficiencies above 23% [63, 64].

It should be mentioned that the cell interconnection is one of the factors that have an impact on the total cost of SHJ solar modules. Since conventional soldering is, as a rule, not compatible with LCT Ag paste [65], alternative approaches like SWCT [66] or ECA [67] ribbon gluing have been implemented. Both technologies have proven their reliability; however both have higher cost compared to conventional soldering due to incorporation of expensive materials (such as Ag or In) in the interconnection elements.

As of today, the only alternative to LCT Ag paste for SHJ cell metallization is Cu electroplating [68]. This process can boast very small finger line width down to 20–25 μm, very high bulk conductivity of the fingers (bulk resistivity <2 μΩ*cm), allows for acceptable peel-force after soldering, good module reliability, lower production costs, however suffers from significant cost of the manufacturing equipment. Nevertheless, future scenarios predict significant decrease of the overall equipment and production costs placing Cu electroplating as a serious competitor to standard Ag paste screen-printing for HJT solar cell metallization [69].

7.3 Conversion of "Micromorph" to SHJ Technology

Recently, record SHJ solar cell efficiencies have attracted attention of companies manufacturing equipment for mass production of c-Si solar cells. In recent years, not only production tools designed for different process steps of SHJ technology but also turnkey production lines have appeared on the PV market [70]. Despite these lines

allowed production of high-efficiency SHJ cells, there was a question behind—can PV production tools originally designed for silicon thin film PV be reused in production lines for SHJ cells? Indeed, in the late 2000s, many production lines designed for single or double-junction amorphous silicon PV have been installed worldwide and became noncompetitive in next few years with drastic drop in polysilicon price. The core equipment of these lines—PECVD reactors—are similar to those required for producing of SHJ solar cells. Reuse of these complex and expensive systems can yield significant cost savings to the companies deciding to enter SHJ solar cell market and give them a chance for return of initial investments made in Si thin film PV. Moreover, such approach can enhance positive ecological effect of PV by suppression of CO_2 emission required for production of new PV mass production tools and for recycling old ones.

The answer to the abovementioned question was found at the Ioffe Institute. This leading Russian research center in semiconductor physics and PV technology, which celebrates its 100th anniversary in 2018, is alma mater of three Nobel Prize winners. It is remarkable that the last of them, Professor Alferov, got his Noble price for works on heterojunctions. Despite the main focus of the Ioffe Institute was on heterojunctions made of III–V semiconductor compounds for CPV and space applications, there were also significant activities on amorphous silicon technology since 1980s [71]. Research activity on silicon thin film PV at the Ioffe Institute has particularly been intensified in 2010 with start of Hevel PV project, launched by Renova group of companies and Rusnano. In frame of the project, Thin Film Technology in Energetics (TFTE) R&D Center was established at the Ioffe Institute as a research unit focused on technological support of Hevel's production line. For that purpose, the R&D center was equipped with a pilot line having process tools similar to those used in micromorph production lines, but with lower production capacity, and a set of laboratory tools needed for solar cell characterization and material studies. Consequently, Hevel project was initially aimed for mass production of micromorph PV modules. Nevertheless, the sharp drop in polysilicon price and continuous progress in the development of conventional c-Si PV made micromorph modules noncompetitive soon after the beginning of Hevel project. Therefore, a demand for significant improvements of the micromorph production line has been addressed to the Ioffe Institute. The proposed solution was to convert Hevel's production line into SHJ solar cell line. This proposal was supported by demonstration that KAI PECVD reactors, originally designed by Oerlikon Solar for micromorph technology, can be effectively used in SHJ cell production process [45]. Soon after the so-called HJT (heterojunction technology) project has been started, the most challenging part of the project was to adapt PECVD reactors, designed for micromorph module production, to the requirements of SHJ technology. Besides, all process steps described in Sect. 7.2 were developed and optimized at TFTE R&D center. As a result, the efficiency of laboratory cells above 22% has been achieved within 3 years from the start of the project, as demonstrated in Fig. 7.4. The implementation of this technology into the mass production allowed to double Hevel's production capacity and resulted in an average cell efficiency of 21.5% at the beginning of mass production in April, 2017 [46]. In the next one and half years, the average SHJ cell efficiency was enhanced up to 22.8% by continuous technology improvement.

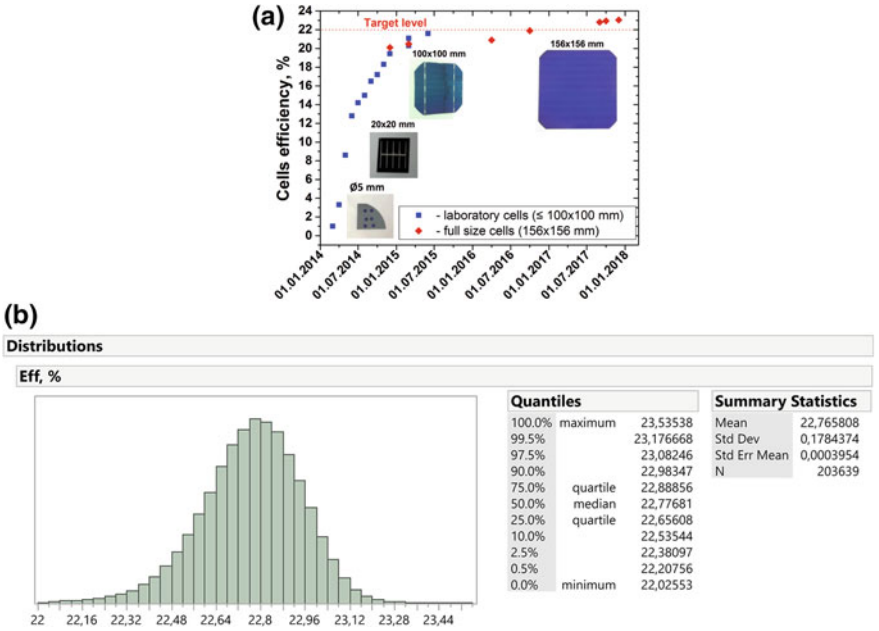

Fig. 7.4 **a** Progress in R&D SHJ solar cell efficiency achieved at TFTE R&D Center in collaboration with the Ioffe Institute and **b** an example of SHJ cell efficiency distribution for a weekly mass production at the Hevel production facility

7.4 SHJ Module Technology and Reliability Issues

7.4.1 Cell Requirements

One of the main challenges in assembling of c-Si solar cell module is to minimize the so-called cell to module losses (CTM) that have both optical and electrical origins. To tackle the optical losses the front glass with antireflective coating (ARC) is generally used today for field PV applications. On the other hand, applications such as building integrated photovoltaics (BIPV) and automotive integrated photovoltaics (AIPV) tend to avoid ARC due to visual appearance issues, which allows for up to 3% relative power gain compared to standard solar glass. To minimize electrical losses, current collecting and interconnecting ribbons with higher cross-section are being used. In this respect, one should admit an inherent advantage of SHJ cells compared to traditional Al:BSF or even PERC cells, since the same power can be achieved by SHJ cells at lower operating current due to significantly higher operating voltage values, caused by excellent passivation properties of a-Si:H layers introduced at the cell

surface [20]. Lower cell operating current leads to lower requirements to electrical resistance of interconnection elements, hence lowering resistive CTM losses.

Furthermore, to avoid unnecessary CTM losses related to the cell current mismatch in a module, it is very beneficial to perform sorting by maximum power point current additionally to the standard efficiency bin cell sorting. At Hevel production facility, this has proved to result in a power gain of up to 2 W on a 60-cell module compared to standard efficiency bin sorting strategy and at the same time minimizing the risk of appearance of hot cells due to the current mismatch.

Typical electroluminescence (EL) images of SHJ modules with current matched (a) and current mismatched (b) cells are presented in Fig. 7.5. The advantage of current match sorting is clearly seen by homogeneous EL light intensity distribution for the current matched case.

7.4.2 Cells Interconnection

Interconnection of SHJ cells is a stumbling stone for the whole process chain [72], as soldering which is used for interconnection of conventional c-Si cells is not compatible with LTC Ag paste, which has to be applied instead of the standard firing through silver paste due to temperature restrictions for the a-Si/c-Si heterojunction. This type of pastes has higher bulk resistivity (2–3 times that of the high temperature pastes) and low adhesion after soldering. Usually, Ag busbars are easily peeling off the ITO surface with force well below 1 N/mm [73].

To overcome this limitation, new cell interconnection technologies have been proposed, for example, gluing of ribbon using electrical conductive adhesive (ECA) [67, 74] or multiwire interconnection using low-temperature attachment of a foil with embedded InSn coated wires called SmartWire Connection Technology (SWCT®) [66, 75]. InSn alloy with a low melting temperature of around 120 °C has a good adhesion, both to Ag paste and ITO-layer itself; hence a metallurgic contact between the wire and the cell surface is established after temperature treatment. SWCT technology does not require very precise positioning of the ribbons relative to the metallization grid, which is one of the major challenges for multiwire technology. The initial attachment of the cells to the wires in SWCT does not require precise soldering of the wires to the solder pads and is commonly done by an adhesive layer-containing foil, which allows using a large number (up to 24) of relatively thin wires of 200–250 μm in diameter.

Optimizing the SWCT module assembly bill of materials (BOM)—by tuning the optical properties of the lamination foils and electrical properties of the wires—we have achieved at Hevel a gain of 9 W on a 60-cell module compared to standard BOM without increasing the material costs and changing the cell manufacturing process and efficiency (see Table 7.1).

Table 7.1 Best production values for module IV-characteristics with standard and optimized BOM

	Standard BOM	Optimized BOM
P_{max} (W)	310	326
V_{pmax} (V)	35.5	36.67
I_{pmax} (A)	8.75	8.89
I_{sc} (A)	9.37	9.33
V_{oc} (V)	43.34	44.15
FF (%)	76.33	79.14

7.4.3 Module Types

SHJ solar cells possess an inherent property of having bifacial light sensitivity. Unlike competitors, SHJ cells do not require any special process steps to become bifacial—only an additional screen printing step for the back cell side. At the same time, producing bifacial SHJ cells allows to avoid full metallization of the backside, simplifying significantly the PVD equipment that is no more required to deposit metallic

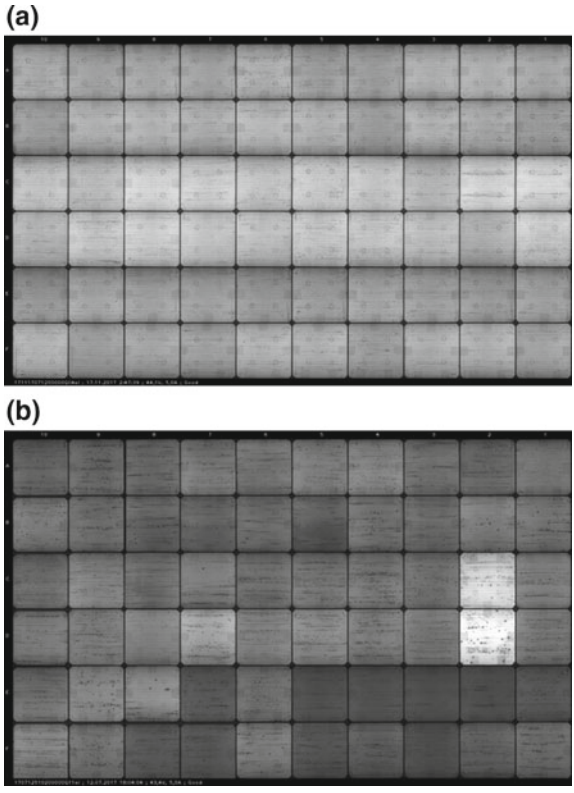

Fig. 7.5 EL images of SHJ modules composed of current matched sorted cells (**a**) and cells without current sorting

layers and thus allowing significant CAPEX savings [55]. The bifaciality factor measured for SHJ bifacial solar cells is as high as 95% [76], which is significantly higher than that of the PERC cells—80% [77]. In combination with white backsheet when assembled into the module, bifacial cells yield the same power as monofacial cells of the same quality, since lack of Ag back side reflector is compensated by light reflection from the white backsheet. At the same time, full benefit of cell bifaciality can be fulfilled when they are assembled with transparent backsheet or back glass. In this case, taking into account the albedo of the module surroundings and the amount of scattered light, the yield of bifacial SHJ modules can surpass that of any monofacial module—even the most efficient IBC cell-based products. The yield of bifacial modules can exceed the yield of monofacial ones of the same class by 13% even for moderate albedo (green grass in summer and snow coverage in winter), according to measurements conducted at Hevel [78].

In this respect, two types of modules are being produced at Hevel's production facility:

– Monofacial glass/backsheet modules with bifacial SHJ solar cells that allow reaching maximum module power at STC IV-curve measurements. These modules are the best option for application in environment where the bifacial effect cannot be utilized (rooftop applications, BIPV, locations with low albedo levels).
– Bifacial glass/glass modules with bifacial SHJ solar cells (at the moment at development stage at Hevel) allow obtaining maximum yield in environment with high backside reflection. Best applications for them are large area solar farms in snowy regions or in regions with a large number of overcast days when scattered light plays a significant role.

A typical daily statistic of the module power distribution (glass/white backsheet, 60 cell modules) at Hevel's production line is presented in Fig. 7.6.

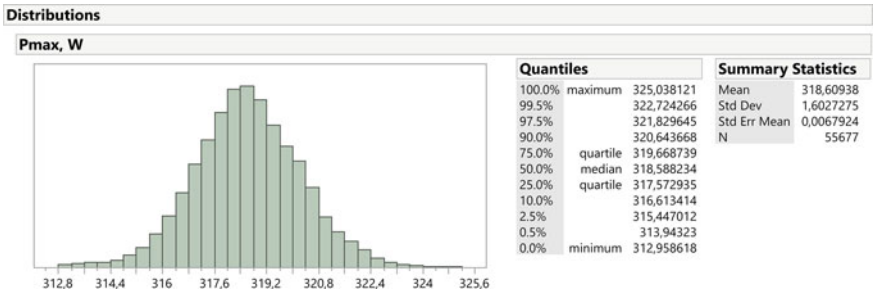

Fig. 7.6 Typical daily glass/white backsheet 60 cell module production statistics at Hevel

Table 7.2 The measured cell efficiency values of Hevel SHJ cells before and after laser cutting

	Isc	Voc	FF	Eff	Rs	Rsh
As produced	9.230	0.728	79.43	21.83	0.0052	8795.0
After cut	9.219	0.723	78.92	21.54	0.0050	4803.3

7.4.4 Perspective Products

One of the perspective products emerging at global market is a half-cut cell module. Designed to incorporate two half-cut cell modules connected in parallel to each other on one glass (alternative configurations also apply) it allows to keep the output IV-characteristics the same as for standard full-cell modules, while significantly reducing resistive losses due to two times lower current generated by the half-cells.

A critical process in producing half-cells is laser cutting of the cell. To avoid unnecessary modifications to cell production equipment and handling tools, it is preferable to make the laser cut as the last process step on a finished cell. This brings certain complications, as very special care has to be taken not to shunt the cell by melting the ITO layers together on the cell sides in the cut area. The cut region also suffers from lack of surface passivation, as the border area loses passivation after the cut. Taking into account these facts, it is natural to expect a certain decrease of the cell efficiency for half-cut cells. The results of cell efficiency measurement of Hevel SHJ cells before and after the cut are presented in Table 7.2. Note that the cells have not been specially selected by efficiency values.

The drop in efficiency comprises from a slight decrease of V_{oc} (5 mV) and FF (0.51%). The difference in I_{sc} is caused by deletion of cell material during the cutting process. The total efficiency loss is below 0.3% abs, which is quite acceptable and is the state-of-the-art for existing laser cutting technology. It should also be noted that the laser cut does not influence significantly the cell shunt resistance; hence the reverse current value remains in the acceptable range for the modules to pass reliability testing.

The observed cell efficiency drop is fully compensated on a module level by the decrease of CTM due to lower overall cell current. At Hevel, we have achieved a 4–5 W relative increase of module power at STC when comparing 144 half-cell and 72 full-cell modules assembled from the same power class cells. For our 144 half-cell glass/glass module prototype, we have achieved the power figures shown in Table 7.3. The module is characterized by a high fill-factor value that evidences decreased ohmic losses due to lower current generated by each half-cell. The values for 10 and 20% albedo clearly indicate that bifacial modules when used in the right environment can ensure unsurpassed energy yield by far exceeding that of the monofacial modules.

Table 7.3 Parameters of bifacial 144 half-cell glass/glass module prototype

Measurement conditions	STC	BiFi + 10%[a]	BiFi + 20%[a]
P_{max} (W)	389	425	460
I_{mpp} (A)	8.78	9.55	10.31
V_{mpp} (V)	44.30	44.47	44.67
I_{sc} (A)	9.33	10.21	11.09
V_{oc} (V)	53.06	54.15	54.81
FF (%)	78.53	76.87	75.68

[a]Calculated values based on 10 and 20% backside illumination and module power bifaciality factor of 93%

7.5 Summary

Nowadays, SHJ technology yields the highest conversion efficiencies at R&D level for both double- and one-side contacted silicon solar cells due to excellent surface passivation properties of a-Si:H layers. Low temperature processes used for manufacturing of SHJ solar cells can result in potential cost savings when wafer thickness is reduced below 150 μm, which is currently limited by higher breakage rates caused by the use of standard automation equipment in mass production. In addition, SHJ technology can be implemented in a-Si thin-film production lines in a cost-effective way, as has been demonstrated by Hevel company under the leadership of the Ioffe Institute. Despite great challenges in interconnecting of HJT solar cells, reliable solutions exist, which enable assembling HJT solar modules with ultra-high output power. One of the main advantages of HJT technology is an inherent bifaciality of the cells that allows obtaining record energy yields for solar modules with backside sensitivity in outdoor environments where reflected or scattered light can be utilized. In combination with half-cell approach benefiting from lower ohmic losses due to decreased cell current passing through the conductive elements of the module, an output power as high as 460 W at STC+20% bifacial gain could be obtained for glass/glass 72 cell modules at Hevel.

References

1. M.A. Green et al., Prog. Photovolt. **26**, 427 (2018)
2. K. Sasaki, et al., in *Proceeding of the 9th International Conference on Concentrating Photovoltaics Systems,* Miyazaki, 2013
3. K.R. McIntosh, et al., in *Proceeding of the 3rd World Conference on Photovoltaic Energy Conversion,* Osaka, 2003, p. 971
4. D.D. Smith, et al., in *Proceeding of the 43rd IEEE Photovoltaic Specialists Conference,* Portland, 2016, p. 3351
5. P. Verlinden, Interdigitated back contact solar cells, in *Photovoltaic Solar Energy: From Fundamentals to Applications*, 1st edn., Wiley & Sons, 2017, pp. 92–102

6. M.A. Green, Sol. Energy Mater. Sol. Cells **143**, 190 (2015)
7. Y. Feng et.al., in *IEEE 43rd Photovoltaic Specialists Conference (PVSC)*, Portland, 3360 (2016)
8. S. Wilking, C. Beck, S. Ebert, A. Herguth, G. Hahn, Sol. Energy Mater. Sol. Cells **131**, 2 (2014)
9. T. Blevin et al., Sol. Energy Mater. Sol. Cells **131**, 24 (2014)
10. W. Cai et al., Energy Proc. **92**, 399 (2016)
11. L. Kreinin, N. Bordin, N. Eisenberg, *1st BifiPV Workshop*, Konstanz, 2012
12. M. Taguchi, et al., in *Proceeding of the 5th International Photovoltaic Science and Engineering Conference*, Kyoto, 1990, p. 689
13. M. Taguchi et al., IEEE J. Photovoltaics **4**, 96 (2014)
14. A.V. Sachenko et al., J. Appl. Phys. **119**, 225702 (2016)
15. K. Yoshikawa et al., Nature Energy **2**, 17032 (2017)
16. W. Fuhs, K. Niemann, J. Sruke, Bull. Am. Phys. Soc. **19**, 394 (1974)
17. M. Schaper, J. Schmidt, H. Plagwitz, R. Brendel, Prog. Photovolt., Res. Appl. **13**, 381 (2005)
18. E. Kobayashi, Y. Watabe, R. Hao, T.S. Ravi, Prog. Photovolt: Res. Appl. **24**, 1295 (2016)
19. F. Jay, D. Muñoz, T. Desrues, E. Pihan, V. Amaralde-Oliveira, N. Enjalbert, A. Jouini, Sol. Energy Mater. Sol. Cells **130**, 690 (2014)
20. S. De Wolf, A. Descoeudres, Z.C. Holman, C. Ballif, Green **2**, 7 (2012)
21. W. Fuhs, L. Korte, M. Schmidt, J. Optoelectron. Adv. M. **8**, 1989 (2006)
22. J. Melskens, B.W.H. van de Loo, B. Macco, L.E. Black, S. Smit, W.M.M. Kessels, IEEE J. Photovolt. **8**, 373 (2018)
23. D. MacDonald, L.J. Geerligs, Appl. Phys. Lett. **85**, 4061 (2004)
24. D. L. Bätzner, et al., in *Proceeding of the 31st European Photovoltaic Solar Energy Conference*, Hamburg, 2015, p. 1042
25. A. Danel, S. Harrison, F. Gérenton, R. Varache, J. Veirman, in *Proceeding of the 35th European Photovoltaic Solar Energy Conference*, Brussels, 2018, 2DO.1.2
26. D. Andronikov, et al., in *Proceeding of the 35th European Photovoltaic Solar Energy Conference*, Brussels, 2018
27. A. Abramov, et al., in *Proceeding of the 35th European Photovoltaic Solar Energy Conference*, Brussels, 2018
28. W. Kern, J. Electrochem. Soc. **137**, 1887 (1990)
29. Q.Wang, et al., in *Proceeding of the 33rd IEEE Photovoltaic Specialist Conference*, San Diego, 2008
30. G.Chen, in *Proc. Int. Conf. Wafer Rinsing,* 1999
31. T.Bearda et al., Solid State Phenom. **187**, 341 (2012)
32. F.Sevenig et al., Energy Proc. **8**, 288 (2011)
33. V. Breus et al., in *Proceedings of the 35th European Photovoltaic Solar Energy Conference*, Brussels, 2018
34. M. Tanaka et al., Jpn. J. Appl. Phys. **31**, 3518 (1992)
35. S. De Wolf, S. Olibert, C. Ballif, Appl. Phys. Lett. **93**, 032101 (2008)
36. H. Fujiwara, M. Kondo, Appl. Phys. Lett. **90**, 013503 (2007)
37. A. Descoeudres, L. Barraud, R. Bartlone, G. Choong, S. De Wolf, F. Zicarelli, C. Ballif, Appl. Phys. Lett. **97**, 183505 (2010)
38. B. Strahm, A.A. Howling, L. Sansonnens, Ch. Hollenstein, Plasma Sourc. Sci. Technol. **16**, 80 (2007)
39. A. Descoeudres et al., Appl. Phys. Lett. **99**, 123506 (2011)
40. J.J.H. Gielis et al., Phys. Rev. B **77**, 205329 (2008)
41. J.W. Schuttauf et al., Appl. Phys. Lett. **98**, 153514 (2011)
42. A. Illiberi, K. Sharma, M. Creatore, M.C.M. van de Sanden, Phys. Stat. Sol. RRL **4**, 172 (2010)
43. K. Maydell, E. Conrad, M. Schmidt, Prog. Photovolt. **14**, 289 (2006)
44. U.K. Das, M.Z. Burrows, M. Lu, S. Bowden, R.W. Birkmire, Appl. Phys. Lett. **92**, 063504 (2008)
45. S. Abolmasov, et al., in *Proceedings of the 31th European Photovoltaic Solar Energy Conference*, Hamburg, 2015, p. 1046

46. D. Andronikov, et al., in *Proceedings of the 33rd European Photovoltaic Solar Energy Conference*, Amsterdam, 2017, p. 732
47. S. De Wolf, M. Kondo, J. Appl. Phys. **105**, 103707 (2009)
48. A. Shah, *Thin-film silicon solar cells*, 1st edn. (EPFL Press, Lausanne, 2010)
49. T. Mueller, J. Wong, A.G. Aberle, Energy Proc. **15**, 97 (2012)
50. K. Ding, U. Aeberhard, F. Finger, U. Rau, J. Appl. Phys. **113**, 134501 (2013)
51. S.N. Abolmasov, P. Roca i Cabarrocas, J. Vac. Sci. Technol. A **33**, 021201 (2015)
52. F. Lebreton, S.N. Abolmasov, F. Silva, P. Roca I Cabarrocas, Appl. Phys. Lett. **108**, 051603 (2016)
53. P. Lippens, M/ Büchel, D. Chiu, C. Szepesi, Thin Solid Films **532**, 94 (2013)
54. C. Frei, D. Chiu, P. Lippens, in *Proceedings of the 28th European Photovoltaic Solar Energy Conference*, Paris, 2012, p. 2029
55. S. Abolmasov, et al., in *Proceedings of the 33rd European Photovoltaic Solar Energy Conference*, Amsterdam, 2017, p. 787
56. L. Barraud et al., Sol. Energy Mater. Sol. Cells **115**, 151 (2013)
57. Z. Lu, F. Meng, Y. Cui, J. Shi, Z. Feng, Z. Liu, J. Phys. D Appl. Phys. **46**, 075103 (2013)
58. E. Kobayashi, N. Nakamura, Y. Watabe, in *Proceedings of the 27th European Photovoltaic Solar Energy Conference*, Frankfurt, 2012, p. 1619
59. B.M. Meiners, S. Holinski, P. Schäfer, S. Hohage, D. Borchert, in *Proceedings of the 31st European Photovoltaic Solar Energy Conference*, Hamburg, 2015
60. G. Choong, P. Bole, L. Barraud, F. Zicarelli, A. Descoeudres, S. De Wolf, C. Ballif, in *Proceedings of the 25th European Photovoltaic Solar Energy Conference*, Valencia, 2010, p. 2505
61. Y. Kuang et al., Sol. Energy Mater. Sol. Cells **163**, 43 (2017)
62. A. Bettinelli, et al., in *Proceedings of the Metallization and Interconnection Workshop*, 2017
63. A. Descoeudres et al., Solar Energy, in Press (2018)
64. D. Andronikov et al., in *Proceedings of the 35th European Photovoltaic Solar Energy Conference*, Brussels, 2018
65. S. Hoffmann, in *Proceedings of the 33rd European Photovoltaic Solar Energy Conference*, Amsterdam, 2017
66. T. Söderström et al., in *Proceedings of the 42nd IEEE PVSC,* New Orleans, 2015
67. T. Geipel, Z. Huq, U. Eitner, Energy Proc. **55**, 336 (2014)
68. A. Lachowicz et al., in *Proceedings of the 33rd European Photovoltaic Solar Energy Conference*, Amsterdam, 2017
69. A. Faes et al., Photovolt. Int. **41** (2018)
70. T. Soderstrom et al., in *IEEE Proceedings of the of 42nd Photovoltaic Specialists Conference (PVSC)*, 3703, 2015
71. A. Kosarev et al., Sov. Tech. Phys. Lett. **11**, 28 (1985)
72. A. De Rose et al., Photovolt. Int., **40**, 2018
73. S. Hoffmann et al., in *Proceedings of the 33rd European Photovoltaic Solar Energy Conference*, Amsterdam, 2017
74. A. Schneider et al., Energy Proc. **38**, 387 (2013)
75. A. Schneider, L. Rubin, G. Rubin, in *Proceedings of the 4th WCPEC*, Waikoloa, 1095 (2006)
76. B. Strahm et al., in *Proceedings of the of 7th International Conference on Crystalline Silicon PV*, Freiburg, 2017
77. T. Dullweber et al., in *Proceedings of the of 31st European Photovoltaic Solar Energy Conference*, Hamburg, 2015
78. K. Emtsev et al, in *Proceedings of the 33rd European Photovoltaic Solar Energy Conference*, Amsterdam, 2017

Chapter 8
III–V Solar Cells and Concentrator Arrays

Zh. I. Alferov, V. M. Andreev and M. Z. Shvarts

Abstract Semiconductor heterostructures allow solving the problems of controlling the fundamental parameters of semiconductor devices owing to the possibility of change in the electronic band structure, bandgaps and refractive indices of a material itself during epitaxial growth, as well as effective masses and mobilities of charge carriers in it.

8.1 Introduction—From Primary Heterostructures to III–V Solar Cells

Semiconductor heterostructures allow solving the problems of controlling the fundamental parameters of semiconductor devices owing to the possibility of change in the electronic band structure, bandgaps and refractive indices of a material itself during epitaxial growth, as well as effective masses and mobilities of charge carriers in it. The development of the physics and technology of semiconductor heterostructures has resulted in remarkable changes in our everyday life. Heterostructure electronics is widely used in many areas of our civilization. It is hardly possible to imagine our life without dual heterostructure (HS) laser-based telecommunication systems, heterostructure solar cells (SCs), light-emitting diodes (LEDs), heterostructure bipolar transistors (HEMTs), and low-noise high electron mobility transistors for high-frequency applications including, for example, satellite television. Now dual HS

This chapter is dedicated to the memory of Valery Rumyantsev (Ioffe Institute).

Zh. I. Alferov (✉)
St Petersburg Academic University, 8/3 Khlopina Str, 194021 St.-Petersburg, Russia
e-mail: zhores_alferov@spbau.ru

V. M. Andreev · M. Z. Shvarts
Ioffe Institute, 26 Polytechnicheskaya str, 194021 St.-Petersburg, Russia
e-mail: Vmandreev@mail.ioffe.ru

M. Z. Shvarts
e-mail: Shvarts@scell.ioffe.ru

V. Petrova-Koch et al. (eds.), *High-Efficient Low-Cost Photovoltaics*,
Springer Series in Optical Sciences 140,
https://doi.org/10.1007/978-3-030-22864-4_8

laser has entered practically every house as CD players. Heterostructure solar cells are widely used in space and terrestrial applications.

The idea of using heterojunctions in semiconductor electronics had already been put forward at the beginning of the electronics era. Already in his first patent concerned with p-n junction transistors, W. Shockley proposed a wide-gap emitter to obtain unidirectional injection of charge carriers [1]. A. Gubanov was the first to analyze theoretically current–voltage characteristics of isotype and anisotype heterojunctions [2]. However, the most important theoretical investigations at this early stage of heterostructure research were done by H. Kroemer, who introduced the concept of quasi-electric and quasi-magnetic fields in a graded-band heterojunction and made an assumption that heterojunctions might exhibit extremely high injection efficiencies in comparison to homojunctions [3]. During the same period, various concepts were developed regarding application of heterostructures in semiconductor SCs. The next important step was done several years later when a concept of double-heterostructure lasers had been formulated independently by Alferov [4] and Kroemer [5]. In 1966, it was predicted that the density of injected charge carriers could be by several orders of magnitude higher than the carrier density in the wide-gap emitter ("superinjection" effect) [6]. In the same year, in the paper [7] the main advantages of the dual HS concept were summarized for the use in various devices, especially lasers and high-power rectifiers.

At that time, general skepticism existed with respect to the possibility of creating an "ideal" heterojunction with a defect-free interface, where theoretically predicted excellent injection properties would be realized. In fact, the pioneering study of the first lattice-matched epitaxial single-crystal Ge–GaAs heterojunctions by Anderson [8] gave no proof of non-equilibrium charge carrier injection in heterostructures. Mostly owing to this general skepticism, only few groups had been trying to find an "ideal couple", which seemed to be a quite difficult problem. Many conditions of compatibility between thermal, electrical and chemical properties, as well as the crystalline and band structures of the contacting materials are to be met.

A lucky combination of certain properties of gallium arsenide, that is, small charge carrier effective mass, wide energy gap, effective radiation recombination, sharp optical absorption edge due to the "direct" band structure, high electron mobility at the absolute minimum of the conduction band and its strong reduction at the nearest minimum at the (100) point ensured for this material a place of "active region" in different electronic devices, even at that initial stage of research. Since the maximum effect would be achieved by using it in the heterostructures with wide-bandgap materials, the most promising systems considered at that time were GaP-GaAs and AlAs-GaAs. To be "compatible", materials of the "couple" must have, as the first and the most important condition, close lattice constants; therefore, heterojunctions in the AlAs-GaAs system were preferable. However, before starting the work on preparation and study of these heterojunctions, one had to overcome a certain psychological barrier. By that time, AlAs had long been synthesized, but many properties of this compound remained poorly studied, since AlAs was known to be chemically unstable and it decomposes in moist air. The possibility of preparing stable and applicable heterojunctions in this system seemed to be not promising.

Initially, attempts to create double heterostructures were related to a lattice-mismatched GaAsP system. Zh. Alferov et al. succeeded in fabricating first dual HS lasers in this system by vapor phase epitaxy. However, due to lattice mismatch, the lasing occurred only at liquid nitrogen temperature, similar to the behavior of the homojunction lasers. At the same time, it was alighted that small crystals of AlGaAs solid alloys of different compositions, which had been prepared by growing from a melt, were stable at least for 2 years. It immediately became clear that AlGaAs is suitable for preparing durable heterostructures and devices. Studies of the phase diagrams and growth kinetics in this system and the development of a version of the liquid phase epitaxial growth method resulted soon in the fabrication of the first lattice-matched AlGaAs heterostructures [9, 10].

Then the progress in the semiconductor heterostructure field was very rapid. The following properties and effects had been experimentally proved: unique injection properties of a wide-gap emitter and effect of superinjection [11]; stimulated emission at recombination [12]; the band diagram of the AlGaAs–GaAs heterojunction and carefully studied luminescence properties [13]; effect of carrier diffusion in a graded-band heterostructure. At the same time, majority of the most important devices with realization of the main advantages of the heterostructure concept have been created: low threshold room temperature lasers [14–17]; high-efficient LEDs [10, 18]; SCs [19]; bipolar transistors [20]; and p-n–p-n switching devices [21].

At that early stage of the heterostructure physics and technology, it became clear that new lattice-matched structures are needed in order to cover a wider range of wavelength spectrum. The first important step was done in the works [22, 23], in which various lattice-matched heterojunctions based on quaternary III–V solid solutions were proposed for independent variation of the lattice constant and the bandgap. Soon, InGaAsP compositions were recognized among the most important ones for many different practical applications: InGaAsP/InP for lasers in the infra-red intervals suitable for fiber optics communications [24], and InGaAsP/GaAs lasers in the visible region [25]. In the early 1970s, ideal lattice-matched heterostructures were limited by the mentioned materials only. Later this “world map” of the III–V heterostructures was drastically expanded.

Since the first solar-powered satellites Vanguard-1 and Sputnik-3 were launched in 1958, SCs based on Si had become the main sources of electricity on the spacecrafts. The first space arrays were based on single crystal silicon SCs characterized by efficiency of about 10%. During the 1960s and 1970s, considerable improvements in the Si cell design and technology were introduced that allowed increase in the efficiency of up to 18%. This was achieved owing to fabrication of “violet” cells with increased short-wavelength photosensitivity, formation of so-called back surface field, application of photolithography to ensure optimal front grid pattern; reduction of optical losses by front surface texturing and improved antireflection coating deposition. These advanced Si cells are used till now for such space missions that do not strictly require III–V SCs with their higher efficiency and better radiation stability [26, 27].

At the beginning of 1960s, it was found that GaAs-based SCs with the Zn-diffused p-n junction ensured better temperature stability and higher radiation resistance. One

of the first scaled applications of the temperature-stable GaAs SCs took place on the Russian spacecrafts Venera-2 and Venera-3 launched in November 1965 to the "hot" planet Venus. The area of each GaAs solar array fabricated by the Russian Enterprise KVANT for these spacecrafts was 2 m^2. Then the Russian moon-cars were launched in 1970 (Lunokhod-1) and in 1972 (Lunokhod-2) with GaAs 4 m^2 solar arrays in each. The operating temperature of these arrays on the illuminated surface of the moon was about 130 °C. Therefore, silicon-based SCs could not operate effectively in these conditions. GaAs solar arrays have shown efficiency of 11% and have provided the energy supply during the life-time of these moon-cars.

The first AlGaAs/GaAs SCs with passivating wide-bandgap window were created in 1970 [19]. In the following decades, by means of the liquid-phase epitaxy (LPE) of AlGaAs/GaAs heterostructures [19–36], their AM0 efficiency was increased up to 18–19% [34–38] owing to the intensive investigations in the fields of physics and technology of space SCs [39–42]. These investigations were stimulated and supported by ambitious space programs in the former USSR [33] and in the USA [26, 27].

High efficiency and improved radiation hardness of the AlGaAs/GaAs SCs stimulated for the high-scale production of AlGaAs/GaAs space arrays for the spacecrafts launched in 1970–1980s. For example, an AlGaAs/GaAs solar array with a total area of 70 m^2 was installed in the Russian space station MIR launched in 1986 (Fig. 8.1). During 15 years on the orbit, the array degradation appeared to be lower than 30% under trying conditions of its operation, of appreciable shadowing, effects of numerous docking and ambient environment of the station. At that time, it was the most scaliest demonstration of the advantages of AlGaAs/GaAs SC in space applications.

Fig. 8.1 Command module of "MIR" space station was launched into orbit on March 13, 1986 with PV array based on AlGaAs/GaAs SCs developed at Ioffe Institute and fabricated in NPO "Kvant". The array has been operating during the 15-year space station span-time

Further improvement of the LPE technology allowed obtaining [43, 44] the efficiencies of 24.6% (AM0, 100 suns) on the base of the heterostructures with an ultra-thin window AlGaAs layer and a back surface field layer.

Since the late 1970s, AlGaAs/GaAs heterostructures were produced also by the metal organic chemical vapor deposition (MOCVD) technique (later known as MOVPE—metal-organic vapor phase epitaxy) [45, 46]. The advantage of MOVPE is a possibility to fabricate multi-layer structures in high-yield reactors with layers of a specified composition, and its precise thickness varied from 1 to 10 nm to several microns. AlGaAs/GaAs heterostructures with an ultra-thin (~0.03 μm) top window layer and with a back surface wide-bandgap barrier were fabricated by MOVPE for space cells. AlGaAs/GaAs 4 cm^2 space SCs with efficiencies of 21 [47] and 21.7% [48] were fabricated on the base of these structures.

Enhanced light absorption was provided in the cells with an internal Bragg reflector [49–51]. This dielectric mirror increases the effective absorption length of sunlight within the long-wavelength part of the photoresponse spectrum and allows making the base layer thinner. In this case, the cell efficiency is more tolerant to reduction of the carrier diffusion length; as a result, these cells are more radiation-resistant [51].

Owing to the fact that MOVPE is capable of producing single crystal layers on silicon and germanium substrates, it has a potential for fabrication of low-cost, high-efficiency III–V SCs on these substrates. The lattice mismatch of 4% between Si and GaAs does not allow growing GaAs on Si with a sufficient quality. However, there is a progress in improving the GaAs/Si structure quality by using special structures and growth techniques: strained superlattice, thermo cyclic growth and cyclic structure annealing.

Ge is a quite good lattice matched to GaAs material. Therefore epitaxial growth of GaAs with high quality was realized by MOVPE, which is now the basic technique for the growth of multi-layer AlGaAs/GaAs/Ge single-junction and GaInP/GaAs/Ge multi-junction (MJ) SCs. This method provides a good crystal quality of epitaxial structures on Ge substrates, high productivity and reproducibility.

Among other single-junction SCs, the InP-based cells are rather promising for the space application owing to the fact that InP has a higher radiation resistance [27, 41, 52] than GaAs. However, there are some obstacles in the scale application of InP-based cells in space arrays. First, there is no lattice-matched wide-bandgap window for InP to make stable passivation of the front surface. Second, it is difficult to grow this material with high quality on the Ge and Si substrates due to lattice mismatches as high as 8% between InP and Si and 4% between InP and Ge.

Multi-junction (tandem) SCs ensured further increase of III–V SC efficiencies. Despite a large number of theoretical studies of tandem SCs [53–56], their efficiencies remained low for a long time, since the ohmic and optical losses in available designs were unacceptably large. Monolithic and mechanically stacked tandem cells with increased efficiencies were developed in the beginning of 1990s. In mechanically stacked tandems with GaAs-GaSb, GaInP/GaAs-GaSb and similar configurations, including spectrum splitting concept [57–62], the efficiencies exceeding 30% were achieved under the concentrated sunlight. Monolithic tandem SCs have

been developed and fabricated by MOVPE on the structures of GaInP/GaAs [63–65], GaInP/GaInAs [66], GaInP/Ga(In)As/Ge [67–70], GaInP/GaAs/GaInNAsSb [71] and other heterostructures [70, 72–74]. The latest highly efficient results were demonstrated on multi-junction SCs fabricated with inverted metamorphic and wafer-bonded technologies and with the use of modern III–V/Si and III–V/SiGeSn structures [75–83].

8.1.1 Single-Junction AlGaAs/GaAs Concentrator Solar Cells

The creation of AlGaAs/GaAs heterostructure SCs opened up the new possibilities of increasing the efficiency of solar energy conversion. The idea of wide-bandgap window was realized for SCs, which allowed protecting the photoactive region of the cells against the influence of surface electronic states. Defect-free heterojunctions between AlGaAs (wide-gap window) and p-n GaAs (photoactive region) were successfully formed, which provided ideal conditions for the photogeneration of electron–hole pairs and their collection at the p-n junction. Since SCs with a GaAs photoactive region turned out to be even more radiation-resistant, they quickly found an application in space solar arrays, despite their significantly higher cost compared to silicon cells.

First, the development of AlGaAs/GaAs SCs was based on relatively simple structures and technologies. The relatively simple LPE technique was applied. Only one wide-gap p-AlGaAs layer had to be grown, whereas the p-n junction was formed by the diffusion of a p-type impurity from the melt into the base material of n-GaAs (Fig. 8.2a, c). From the middle of the 1980s, high-tech methods began to penetrate the sphere of semiconductor solar photovoltaics. The progress in the field of GaAs-based SCs was stimulated by the application of new epitaxial techniques for heterostructure growth. The main achievement here was metal-organic chemical vapor deposition.

New technologies allowed for improving the SC structure parameters. First, the wide-gap AlGaAs window was optimized, and its thickness became comparable with that of the nanosized active regions in heterolasers. The AlGaAs layer also served as the third component in the triple-layered interference antireflection coating (ARC) of a cell. Prismatic cover was applied to reduce the shadowing losses on the top grid finger contacts in concentrator SCs (Fig. 8.3a). A heavily doped GaAs contact layer was grown on the top of the wide-gap AlGaAs window, and it was removed during the post-growth treatment in the areas between the contact stripes (Fig. 8.3b). Second, a back (behind the p-n junction) wide-gap layer was introduced, which ensured, along with the front wide-gap layer, a double-sided confinement of photogenerated carriers within the region of light absorption (Figs. 8.2b and 8.3). The recombination losses of carriers before their collection at the p-n junction were reduced. At this stage of the optimization of single-junction AlGaAs/GaAs photocell heterostructures, the modified low-temperature LPE technique was still competing with the newly developed MOVPE technique.

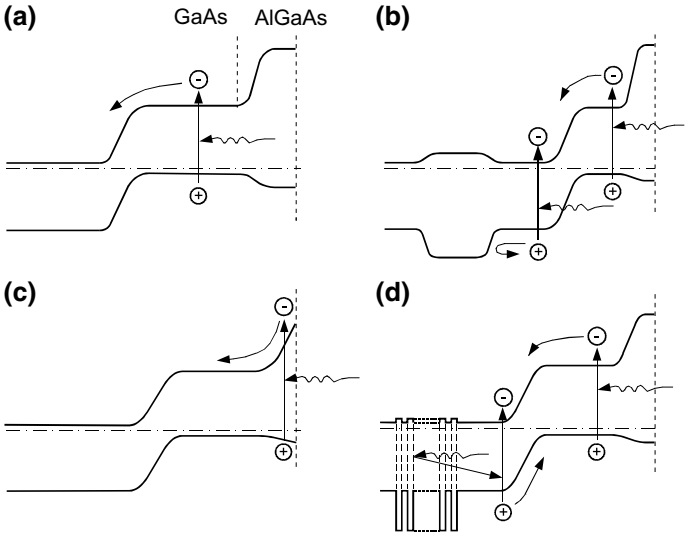

Fig. 8.2 Energy band diagrams of SCs based on AlGaAs/GaAs heterostructures: **a** structure with a p-n-junction in GaAs and with a frontal wide-gap "window" of p-AlGaAs; **b** structure with a back potential barrier in the n-region; **c** structure with a frontal p-AlGaAs layer of variable composition; **d** structure with a Bragg mirror

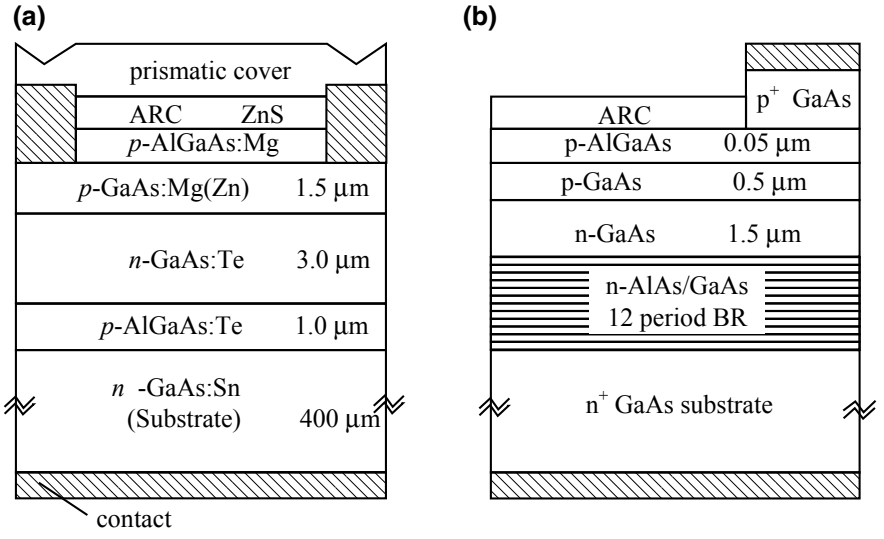

Fig. 8.3 Heterostructure of the AlGaAs/GaAs-based SCs: **a** prepared by LPE with thick (3 μm) base n-GaAs layer, **b** prepared by MOVPE with internal Bragg reflector and thin (1.5 μm) base n-GaAs layer

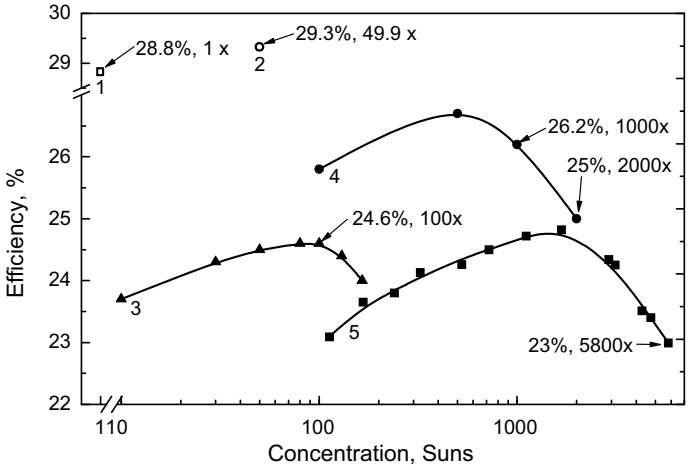

Fig. 8.4 Highest efficiencies in the AlGaAs/GaAs single-junction SCs under AM0 (curve 3), AM1.5 g (dot 1) and AM1.5d (data 2, 4, 5) spectrum irradiation [27, 43, 70, 84, 85]

For these structures the record efficiency of 29.3% for illumination with the concentrated (49.9 suns, AM1.5d) sunlight was measured in MOVPE-grown SCs [70]. At the same time, the record efficiency of 24.6% for single-junction cells at illumination with 100 × concentration of AM0 sunlight (Fig. 8.4) still belongs to LPE-grown SCs [27, 43]. Also, the highest efficiencies for high concentration ratios in the range of 1000–2000 suns (AM1.5d) were measured in the LPE-grown AlGaAs/GaAs single-junction SCs (Fig. 8.4): 26.2% (1000×) and 25.0% (2000×) [84]. These cells can operate under ultra-high sunlight concentration with efficiency as high as 23% at 5800 suns (AM1.5d) [85].

In MOVPE-grown AlGaAs/GaAs SC structures, a single wide-bandgap AlGaAs layer, which forms the back potential barrier, can be replaced by a system with pairs of AlAs/GaAs layers making a Bragg mirror (Figs. 8.3b and 8.5) [51]. The wavelength of the reflection peak for such a mirror is chosen in the vicinity of the absorption edge of the photoactive spectrum region, so that the long-wavelength light that was not absorbed in this region can be absorbed during the second passage after reflection from the mirror (Fig. 8.2d). At the same time, the wide-gap mirror layers continue to serve as the back potential barrier for photogenerated carriers. In these conditions, the thickness of the photoactive region can be reduced by half without loss of current as compared to the thickness of structures without a mirror (Fig. 8.3b). This factor led to a significant increase in the radiation resistance of such type of photocells, because the number of lattice defects generated under irradiation by high-energy particles decreases proportionally to the thickness of the photoactive region.

More complicated structures with several Bragg reflectors [86] tuned for several IR bands of solar radiation allow increasing the reflection of the sub-bandgap IR radiation to reduce SC operation temperature and, as a result, to increase the cell efficiency.

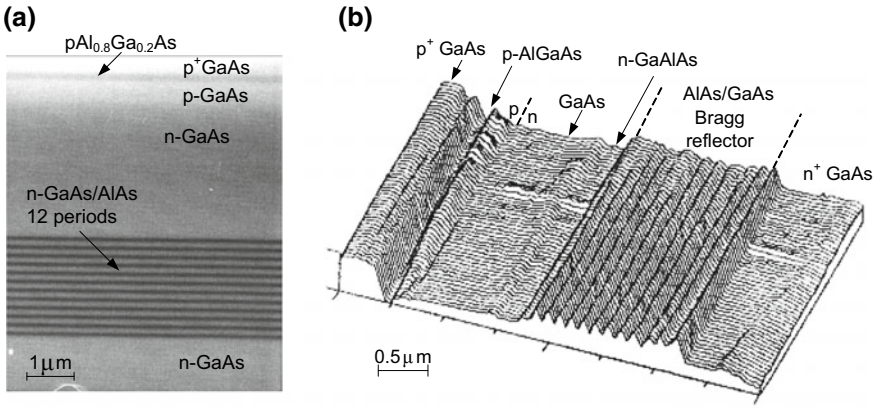

Fig. 8.5 SEM (**a**) and STM (**b**) images of the SC heterostructure with internal Bragg reflector

The effect of the start-up processes on re-reflection and recycling of radiation can be enforced essentially using thin-film GaAs-based SCs. Application of the new epitaxial lift-off (ELO) process for fabricating thin-film single-junction GaAs SCs without light concentration has allowed raising the efficiency of up to 28.8% and simultaneously registering extremely high open-circuit voltage of 1.122 V [70]. This voltage value is an indicator of the efficiency of the photon recycling process, at which photons absorbed in the GaAs photoactive layers can be radiatively re-emitted, and then again re-absorbed in the same GaAs device. Efficient photon recycling ensures higher carrier density generated by a SC, because, in the ideal case, photons that are absorbed in the semiconductor either create an electron–hole pairs that are given an impact into current of the device, or are radiatively re-emitted in order to be re-absorbed with new electron–hole pairs generation. Photon recycling therefore results from the combination of minimizing the loss of photons to processes other than carrier generation, as well as minimizing the non-radiative recombination of carriers. This leads to increased carrier density within the device, which in turns leads to increasing the *Voc* of the device owing to greater quasi-Fermi-level splitting.

The processes of photon recycling can be started-up also in using the above-mentioned Bragg reflectors, which opens the possibility of thickening photoactive layers in MJ SC subcells, thus being a contributory factor in raising their efficiency and radiation tolerance [51, 87, 88].

8.2 Multi-junction Solar Cells

The idea of tandem solar cells began to be discussed in the early 1960s and was considered to be promising. However, increasing the efficiency seemed a long way away. The situation started to be changed in the late 1980s, when many research

groups concentrated their efforts on developing different types of multi-junction SCs. The optimal bandgaps for dual and triple-junction SCs are shown in Fig. 8.6.

At the first stage, the best results on efficiency were obtained in mechanically stacked MJ SC concept started in 1989 by Fraas and Avery with the demonstration of a 32.6% (AM1.5d, 100×) efficient concentrator GaAs/GaSb mechanically stacked dual-junction cell [89]. However, everyone understood that the real promising cells would be those with a monolithic structure.

The first high-efficiency monolithic tandem SCs were fabricated by MOVPE on GaInAs/InP [90], GaAs/AlGaAs [91]. To prepare GaInAs/InP tandem cells [90], GaInAs n- and p-layers are grown on an InP substrate to form the bottom subcell. InP n- and p-layers were grown on the top of this structure to form the top subcell. The contacts were made according to a three-terminal scheme: one back contact covering the entire surface and two ridge-like contacts to the illuminated surface. One of them served to connect the top of the bottom cell and the back of the top cell. The cell efficiencies were 8.9% for the bottom GaInAs cell and 22.9% for the top InP cell, the total efficiency being as high as 31.8% AM 1.5 at concentration ratio of 50×.

High-efficiency AlGaAs/GaAs monolithic tandem cells have been made with bottom GaAs and top $Al_{0.37}Ga_{0.63}As$ subcells [91]. An efficiency of 27.6% measured under AM1.5g spectrum irradiation was achieved in this tandem (top cell: Eg = 1.93 eV). The component cells were electrically connected by a metallic contact fabricated during the post-growth processing.

Two-terminal monolithic tandem SCs based on AlGaAs/GaAs heterostructures were fabricated by low-temperature LPE [92]. The top and bottom cells were connected by a tunnel junction formed in GaAs. The heterostructure was grown by a two-stage LPE procedure. The bottom GaAs-based cell structure was grown at the

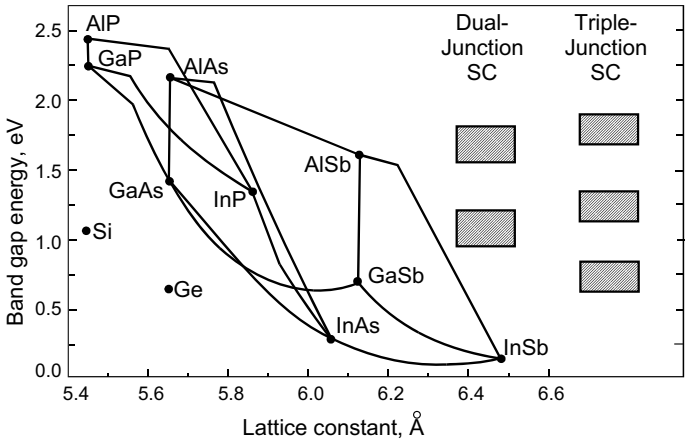

Fig. 8.6 Band gaps of III–V compounds and their solid solutions versus the lattice constants of these materials. The optimum E_g is shown for the dual- and triple-junction SCs

first stage. Heavily doped p^+-GaAs and n^+-GaAs layers were grown on this structure to prepare a tunnel junction. Their thickness was chosen as thin as possible (8–10 nm) to minimize the sunlight absorption losses within a GaAs-based subcell. The doping levels were as high as 10^{20} cm^{-3} when Ge or Te is added to the melt. This is quite sufficient to form a tunnel junction. The top AlGaAs layer was grown to protect tunnel diode during the second LPE growth. Reference samples of such GaAs subcells (without p^+ and n^+ layers and with thin $pAl_{0.9}Ga_{0.1}As$ window layer) have demonstrated outdoor efficiency exceeding 27% (AM1.5, 100–300 suns). At the second stage, the top AlGaAs subcell was grown with the photoactive region made of $Al_xGa_{1-x}As$ ($x > 0.3$). These cells demonstrated rather high external quantum yield of 80–90% in the spectral range of 650–450 nm. An open-circuit voltage of 2.53 eV and fill factor of 0.8 at 50 suns were obtained using these tandem cells. Further developments of monolithic tandem SCs by LPE had not been continued because the reproducibility of two-stage LPE progress was not ensured.

Researchers from the NREL (National Renewable Energy Laboratory, USA) were the first to obtain the sufficient efficiency increase in the monolithic dual-junction SCs [93]. Using the MOVPE technique, they grew GaInP/GaAs structures matched by their lattice constants, in which the top photocell had a p-n junction in $In_{0.5}Ga_{0.5}P$ and the bottom one was in GaAs. The cells were electrically connected in series by means of a tunnel p-n junction specially formed between the cascades. Efficiency of 30.2% (AM1.5d, 180×) was obtained in these dual-junction SCs.

At the same time, the interest on triple-junction cells was growing. As a consequence of well-directed efforts, efficiency as high as 35–42% has been demonstrated in monolithic GaInP/Ga(In)As/Ge SCs [69, 94–97].

8.3 Lattice-Matched GaInP/Ga(In)As/Ge Triple-Junction Solar Cells

The vast structures for modern high-efficient MJ SCs are fabricated by the metal-organic vapor phase epitaxy (MOVPE technique) on highly productive commercial reactors. Ge of p-type is used as an active substrate, on which a lattice-matched (LM) triple-junction (3J) heterostructure—$Ga_{0.50}In_{0.50}P/Ga_{0.99}In_{0.01}As/Ge$ (widely used abbreviation is GaInP/GaAs/Ge)—of high crystalline perfectness is formed. Emitters of n-type Ge are obtained with the help of diffusion processes. Series connections of junctions are provided by means of low-resistance and optically transparent tunnel diodes. Each layer in the 3J GaInP/GaAs/Ge LM heterostructure brought to perfection (see Fig. 8.7) is optimized by composition, doping level and thickness [98].

Top and middle subcells include the following layers: back-surface field (BSF) layer, base, spacer, emitter and window. The Ge subcell consists of a base (substrate), a diffused emitter and a window. Subcells are connected in series by tunnel diodes, which in turn include highly doped thin (10–20 nm) layers.

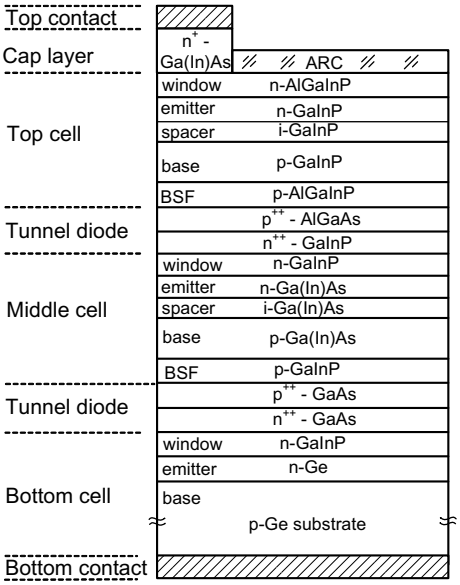

Fig. 8.7 Typical GaInP/Ga(In)As/Ge structure of a monolithic triple-junction SC on p-Ge substrate

However, the combination of forbidden gaps for subcells in the GaInP/GaInAs/Ge LM heterostructure is not the optimal one: the bottom narrowband Ge p-n junction generates substantially greater current than GaInP and GaAs subcells. A part of sunlight energy corresponding to the "excess" photons absorbed in Ge is lost without the use, thus limiting the MJ SC efficiency. For this reason, a substantial increase of the 3J SC with a Ge substrate should not be expected. The investigations being carried out on raising the MJ SC efficiency are associated with the increase in the number of p-n junctions based on materials with optimum combinations of Eg values.

Estimations show that the 3J SC efficiency can be raised substantially by replacing the narrowband Ge subcell with wider band one based on the GaInAs solid solution isolattice to GaAs with Eg in the range of 0.7–0.5 eV with a prospect to approach to Eg ~1 eV [71]. Further increase in the SC efficiency is ensured by introducing additional narrowband junctions isolattice to GaAs with Eg in the range of 0.7–0.5 eV to the structure.

Since the technology of the wideband tandem GaInP/GaInAs (1.86/1.41 eV) is well developed, it is, as a rule, the basis for designing 3–4J SCs. Efforts are mainly directed to develop narrowband subcells, that is, to search for materials with the forbidden gap smaller than that of GaAs (Eg = 1.41 eV).

For this reason, researchers try to replace active Ge (at a p-n junction) with more effective, strong and light Si [99–101]. However, owing to great difference between lattice constants and between coefficients of thermal expansion (CTE), it was not possible up to now to obtain good quality GaAs/Si layers by direct epitaxial growth [101]. Good results have been demonstrated for the technology of direct bonding of III–V heterostructures with Si plates [100–103]. Impressive achievements have been

obtained by inverted growth of a monolithic 4J architecture with two metamorphic layers of GaInAs with Eg equal to 1 and 0.7 eV [104]. Break-through results on obtaining device quality of a new class of GaInAsNSb were obtained by the MBE technique [71, 105]. In these compounds, the forbidden gap width varied depending on the N portion from 1.3 to 0.7 eV at complete matching with the GaAs or Ge lattice. This opens up for the possibilities of fabricating 4, 5 and even 6J SCs with a record efficiency. Besides, at present, for narrowband subcells, 3J Si-Ge-Sn solid solutions of the IV group are developed. Combination of these three elements allows obtaining compounds lattice matched with GaAs and Ge with a forbidden gap from 0.5 to 1.2 eV [82].

8.4 Lattice-Mismatched (Metamorphic) Heterostructures for Multi-junction Solar Cells

In developing modern high-effective MJ SCs, the following main methods and technologies are applied:

Upright metamorphic growth (UMM). It is monolithic growth of several crystals with different lattices, as a rule, in the direction from narrowband subcells to wideband ones. For acceptable crystallographic quality of photoactive layers, intermediate compensating (buffer) layers with gradually varying lattice constant are usually applied [67, 68].

Inverted metamorphic growth (IMM). At IMM, the MJ SC structure is formed starting from the wideband, isolattice subcell to the substrate of a MJ SC with following going to the layers of narrowband metamorphic materials [80, 104, 106–108]. Advantage of the mentioned approach compared to the "direct" structure is the transfer of the growth of metamorphic (not lattice matched) layers to later stages of epitaxial process, what allows creating perfect wideband subcells. One can select an optimal forbidden gap for narrowband subcells, since they are not associated with grown substrate. Then the structure is separated from the substrate (technology ELO—epitaxial lift-off) and transferred to a new carrier.

Separation of MJ SC thin layers from a massive isolattice substrate is performed by selective etching in hydrofluoric acid along the "sacrificial" layer (usually the AlGaAs layer) specially formed during structure growth. Selectivity of etching by "sacrificial" layer with respect to the adjacent GaAs layers reaches 10^6. After separation, the epitaxial film is transferred to a new supporting substrate, which can be thin, flexible, superlight and with better heat conduction than the growth one [109]. The initial substrates are re-usable, which reduces the structure cost substantially. Owing to super-small structure thickness, the ratio of power/mass of standard and flexible solar arrays has improved significantly.

Wafer bonding technology for MJ SCs is connection of heterostructures grown separately on different substrates. This opens up the wide possibilities in choosing

the substrates for growing and avoids the use of metamorphic buffer layers that compensate variation in the lattice constant along the direction of growth of buffer layers. Usually one of the structures is obtained by the IMM growth. Then the plates are pressed followed by removal of one of the substrates by the ELO technique. The given process of creating MJ SCs is rather complicated and requires high technological culture [102, 103, 110–113]. The highest efficiencies for MJ SCs fabricated by the combined technology "IMM-bolding" are: 46.1% for 4J GaInP/GaAs//GaInAsP/GaInAs SC (C = 312, AM1.5d) [76]; 30.2% for 3J GaInP/AlGaAs//Si SC (C = 1, AM1.5g) [78]; 35.8% (C = 1, AM0) and 38.8% (C = 1, AM1.5d) for 5J SC [75].

The problem in the crystal quality arises during the development of growth procedure for such metamorphic SCs. It should be noted that GaInAs with near to ideal bandgap of 1.1 eV has the lattice mismatch of 1.6% with the Ge substrate. In spite of the higher theoretical efficiency of such metamorphic cells, the achieved cell efficiencies are approximately equal to those for lattice-matched cells. Nevertheless, the highest efficiency (>40%) has been reached by Spectrolab, Inc. in the metamorphic $Ga_{0.44}In_{0.56}P/Ga_{0.92}In_{0.08}As$/Ge 3-junction concentrator SCs [69].

The following statement may be formulated on the basis of the presented data: heterostructures of high-efficiency multi-junction SCs are the most complicated structures among all semiconductor devices. The confirmation of this declaration is as follows:

- Full range of the III–V materials in view of the binaries and solid alloys is involved in the formation of the MJ SC structure (including nitrides for advanced cells). A very wide range of the layer bandgaps covering photon spectrum from UV to IR should be ensured. All the layers are lattice matched, or moderately metamorphic.
- Triple-junction SC consists of about 20 layers and the quantity of layers will be higher or more than in the advanced 4÷6-junction cells, or in the cells with Bragg reflectors, as well as in the cells incorporating superlattices and quantum dots. Layer thickness varied in a very wide range from 10 nm in the tunnel diodes up to a few micrometers in the photoactive regions.
- Doping level varied from 10^{15} to 10^{16} cm^{-3} in the spacer layers up to 10^{19}–10^{20} cm^{-3} in commutating tunnel diodes. A drastic change in the doping level should be ensured in the tunnel diodes and this sharpness should be conserved in the structure during further crystallization at enough high growth temperatures. Also, the operating capacity of the tunnel junctions should be ensured during all the life-time of outdoor SC operation at various temperatures and high photocurrent densities.
- III–V SC structures are grown on Ge substrate, being the foreign material in relation to the cell one. A number of additional technological problems are expected, if Ge substrate is substituted to Si one, which is more promising from economical point of view.
- Individual cell dimensions varied from 1 mm^2 in the terrestrial concentrator modules with mini-lenses up to about 30 cm^2 in arrays without concentration for space application. It means that extremely high quality of growth and post-growth technologies must be ensured.

– SCs are among such semiconductor devices that operate under inclement climatic conditions. A thin glass sheet or dielectric layer is the only barrier between environment and the cell structure.
– In concentrator SCs, optically transparent protectors and front layers are subjected to action in a highly intensive light (up to 1000 suns and higher in the center of the focal spot), so that a radiation resistance of corresponding materials should be ensured.
– Conflicting demands to the cell structure are accompanied by a requirement to provide the lowest cell cost as an essential issue in the balance-of-system cost of solar electricity.

8.5 Multi-junction Solar Cells: Current Status of High-Efficiency Data

In spite of the complexity of MJ SC structures and technology, a number of institutes and companies are continuing their MJ cells development for PV applications, including concentrator approach, because it opens the perspectives for significant increase in efficiency and reduction in the solar electricity cost.

It is clear that SCs are the key elements in the concentrator PV installations. Table 8.1 summarizes the efficiencies of terrestrial single- and multi-junction (from 2 to 4 junctions) III–V concentrator SCs demonstrated in this century (after the year 2000). Cell producers, sunlight concentration ratios (suns), conditions at measurements (air mass) and the cell structure (type of SCs) are shown in the table. The cells in the upper part of the table are characterized by a rather high efficiency. Involving the high-power companies (Spectrolab, AZUR Space, EMCORE Photovoltaics, Sharp, SolAero Technologies Corp., etc.) into "terrestrial" concentrator activity allowed organizing a high-scale production of MJ concentrator SCs for concentrator modules [114–116].

MJ SCs are characterized by a complicated structure. In a triple-junction SC, three photoactive *p*-*n* junctions are connected in series by two intermediate *n*+ -*p*+ tunnel junctions, biased by voltage in the forward direction. Very high doping concentrations of the tunnel junction regions require small thicknesses of the corresponding layers in the structure to reduce the non-photoactive light absorption. In addition, two enclosing barrier layers with the purpose to minimize dopant diffusion from the *n*+ and *p*+ layers in both tunnel junctions should be introduced in a multi-junction SC structure. Often, technological difficulties associated with the formation of tunnel junctions are the reason for lower conversion efficiency of a cell. This is especially true in the case of cells intended for operation under high sun concentration conditions.

If the generated photocurrent density in a SC exceeds the density of the peak tunnel current (J_p) of one or both tunnel junctions, in this case there exists a part of the *I*–*V* curve near the open circuit voltage point, where a trace from the action of

Table 8.1 Selected efficiencies of the concentrator solar cells based on III–V compounds

Year	Producer (test lab)	Eff (%)	Suns	Air mass	Type of solar cell	Ref.
2001	FhG-ISE	30.2	300	AM1.5d	GaInP/GaInAs 2J monolithic	[117]
2001	IOFFE/IES-UPM	26.2	1000	AM1.5d	AlGaAs/GaAs single-junction	[84]
		25	2000			
2001	JX Crystals	34	15	AM0	GaInP/GaAs-GaSb 3J hybrid circuit	[118]
2005	Fraunhofer ISE RWE-SSP	35.2	600	AM1.5d	GaInP/GaInAs/Ge, monolithic	[119]
2006	IOFFE	35	50	AM1.5 low-AOD	GaInP/GaAs/GaSb 3J hybrid monolithic/mech.stacked	[59]
2006	Toyota TI Sharp Corp.	38.9	489	AM1.5g	GaInP/GaInAs/Ge, 3J monolithic	[97]
2006	Spectrolab	39.3	179	AM1.5 low-AOD	GaInP/GaInAs/Ge, 3J monolithic	[117]
2006	Spectrolab	40.7	240	AM1.5 low-AOD	GaInP/GaInAs/Ge, 3J monolithic	[69]
2009	Spectrolab (NREL)	41.6	364	AM1.5d	GaInP-Ga(In)As-Ge 3J, lattice matched, commercially available	[69]
2009	FhG-ISE (FhG-ISE)	41.1	454	AM1.5d	GaInP-GaInAs-Ge 3J, upright metamorphic; commercially available from AZUR SPACE, Spectrolab	[68]
2011	Spire (NREL)	42.3	406	AM1.5d	GaInP-GaAs-wafer-GaInAs 3J, epi growth lattice matched on front and inverted metamorphic on back of GaAs wafer	[72]
2012	Alta Devices (NREL)	28.8	1	AM1.5 g	GaAs single-junction	[120]
2012	Solar Junction (NREL)	43.5	925	AM1.5d	GaInP/GaAs/GaInNAs 3J, MBE, lattice matched, dilute nitrides, grown on GaAs	[71]

(continued)

Table 8.1 (continued)

Year	Producer (test lab)	Eff (%)	Suns	Air mass	Type of solar cell	Ref.
2013	Sharp (FhG-ISE)	43.5	306	AM1.5d	GaInP/GaAs/GaInAs 3 J, inverted metamorphic	[121]
2013	NREL (NREL)	42.6	327	AM1.5d	GaInP/Ga(In)As/GaInAs 3 J, inverted metamorphic	[122]
	Emcore (NREL)	42.4	325			[80]
2014	Fraunhofer ISE/Soitec/CEA (AIST)	46	508	AM1.5d	GaInP/GaAs//GaInAsP/GaInAs 4 J, wafer bonding, lattice matched grown on GaAs and InP	[123]
2014	NREL (NREL)	45.7	234	AM1.5d	GaInP/GaAs/GaInAs/GaInAs 4J, inverted metamorphic	[124]
2017	NREL (NREL)	35.9	1	AM1.5 g	GaInP/GaAs//Si mechanically stacked	[125]

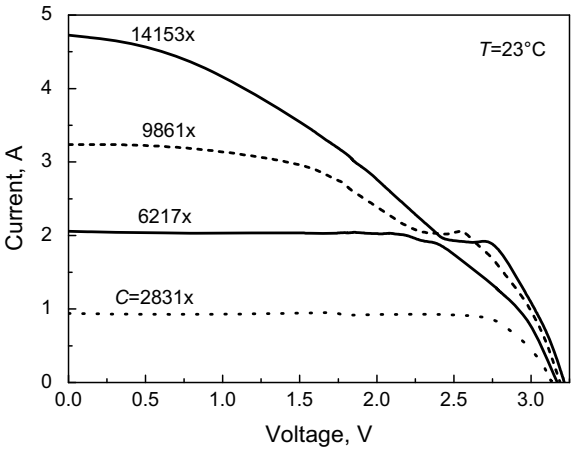

Fig. 8.8 A family of the illuminated *I–V* curves at different light intensities from the high power flash solar simulator for 3J SC (designated illumination area is 2 mm in diameter)

the internal tunnel diode(s) can be revealed. The J_p value is an important parameter of a SC, establishing the limit in the photocurrent density for efficient operation. In Fig. 8.8, a family of the illuminated *I–V* curves for a 3J SC is shown. It was measured at different light intensities from a high power flash solar simulator [126].

A tunnel peak is revealed at sun concentration beginning from ~9800×. Resolution of the tunnel peaks is difficult, when *I–V* curves are strongly deformed due to obvious action of the cell internal resistance. The value of J_p as high as 65 A·cm^{-2} has been calculated from *I–V* curve for $C = 9861\times$, when considering only the designated illumination area.

The main result of Fig. 8.8 is that 3J SCs can operate at illumination intensities as high as several thousand suns. Tunnel peaks have a tendency to move toward the open-circuit voltage point, when illumination increases. At the same time, peak current decreases. Probably, it is caused by overlapping of the tunnel curves with a part of the curve related to the photoactive junctions being more vertical near the open-circuit point at higher photocurrents. Other reasons may be regarded as well. Among them is a parasitic photoactivity of the tunnel junctions, where the generated photocurrent reduces peak current. Another reason can be associated with the carrier transport through the cell structure, where the thickness of all the layers is smaller than the diffusion length of the photogenerated carriers. Further investigations could make clear this phenomenon.

Ohmic losses reduction obtained by lowering both series and sheet resistances ensures a high fill factor value exceeding 0.87 at concentration ratios up to 1000 suns and FF = 0.8 at 4000 suns (Fig. 8.9). Efficiencies of about 37% at 1000×, 36% at 2500 × and 34.5% at 4000 × have been measured in one of the Spectrolab's cells available in the market.

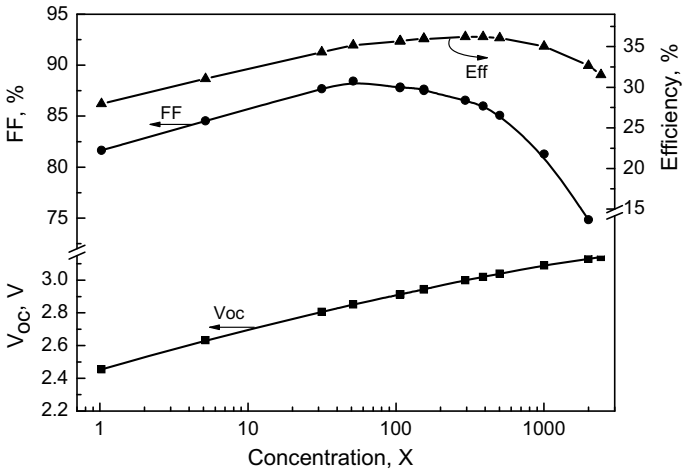

Fig. 8.9 Efficiency (Eff), fill factor (FF) and open-circuit voltage (V_{oc}) versus sunlight concentration ratio (AM1.5d low AOD) for a GaInP/GaInAs/Ge triple-junction SC developed in IOFFE Institute (total area is 4 mm^2 and designated illumination area is 1.7 mm in diameter)

8.6 Concentrator PV Modules and Installations with III–V Solar Cells

The concentrator approach is the only way for the large-scale use of high-efficiency III–V SCs for terrestrial applications. Indeed, optical elements made of relatively cheap materials can focus the sunlight on small-in-area cells, which allows reducing drastically the consumption of semiconductor materials in production of solar arrays. The costs for optical elements and mechanical sun tracking systems are covered at the expense of larger amount of "solar" electricity produced in higher-in-efficiency cells and owing to normal positioning of the PV modules with respect to sunrays during the daytime. For more than 30 years, many research groups were engaged in the development of concentrator PV systems. Under the development were the SC structure and fabrication technology, effective concentrator optical systems, module design and sun trackers [28, 40, 127, 128]. Interest in concentrator PV systems grew substantially after promoting in practice the higher-in-efficiency MJ SCs which proved promising in achieving photovoltaic conversion efficiencies of nearly 35–40% at high-level sunlight concentration.

In the first concentrator modules and installations, large-area mirrors (0.5–1 m in diameter) focused the sunlight on cells of several square centimeters in area. Cooling by water or by means of thermal pipes was necessary [127–130] (Fig. 8.10a). Appearance of the technology accessible for Fresnel lens (FL) fabrication determined the revision of the photovoltaic module design. SCs could be placed behind the concentrators in this case. The module housing could serve as a protector from the environment (Fig. 8.10b). Since the FLs had smaller dimensions (25 × 25 cm^2), the

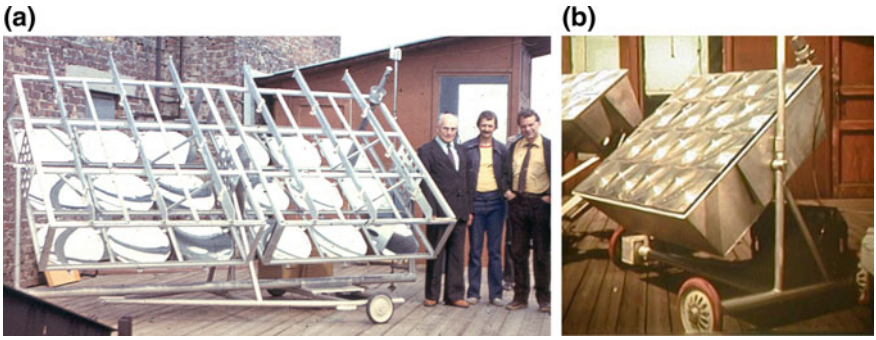

Fig. 8.10 Solar PV installations with AlGaAs/GaAs SCs and with: **a** parabolic mirrors, 1981 [130]. In photo: Zh. Alferov (on the right), V. Rumyantsev (in the center) and V.Tuchkevich (on the right); **b** Fresnel lenses (25 × 25 cm^2 each) 1986 [131]

photocell dimensions were also decreased down to less than 1 cm^2. Characteristics of such photocells were improved owing to lower internal ohmic losses and simplified assembly. For cooling the cells, it was suffice to use heat conductivity of the module metallic housing with walls of reasonable thickness [131].

In the late 1980s, the concept of radical decrease in the concentrator dimensions on retention of a high sunlight concentration ratio has been proposed [132, 133]. The first experimental modules of such type consisted of a panel of lenses, each of 10 × 10 or 25 × 25 mm^2, focusing radiation on the AlGaAs/GaAs cells of 1–3 mm in size (see Fig. 8.11). At that time, the main advantages of a module with small-aperture area concentrators were formulated: the requirements are essentially relieved imposed on the capability of heat sinking material to conduct heat, on its thermal expansion coefficient and on its thickness. The focal distance of such lenses appears to be comparable with the structural thickness of the conventional modules without concentrators.

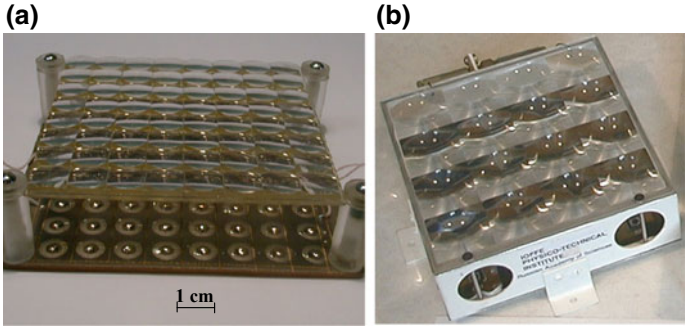

Fig. 8.11 PV modules employing small-size aperture concentrators and AlGaAs/GaAs cells [132, 133]: **a** glass smooth-surface lenses; **b** plastic Fresnel lenses (Flight experiment on communication satellite Molniya-3K in 2001)

The advantages of small-size concentrator cells are the following: low ohmic losses at collection of low current in the conditions of non-uniform light intensity distribution at high local photocurrent density; high cell chip throughput from a wafer; possibility to apply the high-productive mounting methods. Somewhat later, this approach resulted in creation of the "all-glass" photovoltaic modules with III–V cells and panels of small-aperture area FLs (each lens is 4×4 cm^2). The lens panels had a "glass-silicone" composite structure. This work was carried out owing to close cooperation between the research teams at the Ioffe Institute (St. Petersburg, Russia) and Fraunhofer Institute for Solar Energy Systems (Freiburg, Germany) [134–137].

In recent years, the team of the Ioffe Institute has developed the concentrator modules in which FLs are arranged on a common superstrate with a panel of 12 $\times$ 12 lenses. The cells as small as 2×2 mm^2 with designated area of 1.7 mm in diameter operating at mean concentration ratio of 500–700 $\times$ are used (see Fig. 8.12) [138–147].

In the case of the use of the monolithic MJ cells, the following fundamental advantage should be noted. They operate at lower photocurrent, so that ohmic losses, say, in a 5-junction cell, would be a factor of 5 low of the losses in a one-junction cell operating within the same spectral range. Non-uniformity in the illumination distribution along the cell surface is a negative feature of concentration. For MJ cells, an important factor is chromatic aberrations in concentrators of the refractive type. Negative influence of this type of non-uniformity in the illumination cannot be compensated by the use of a more dense contact grid, because lateral currents arise between subcells inside the cell structure. Small-size cells have certain advantages

Fig. 8.12 PV tracker equipped with Fresnel lens concentrator modules

in this respect. On the other hand, parameters of a concentrator as an element of a PV system should be optimized in the required way.

8.6.1 Design of Fresnel Lens Sunlight Concentrators

Different lens as sunlight concentrators finds its expanding application in photovoltaic installations. The main disadvantage of lenses as concentrators is conditioned with the chromatic aberrations (CA), which, at the wide range of the sunlight spectrum and finite angular dimension of the sun, leads to "blurring" of the concentrated radiation in the plane of the photoreceiver location and to the considerable decrease in the average level of the irradiance due to the spatial and spectral energy redistribution.

This negative effect can be essentially diminished by a correct choice of the optimum combination of the lens dimension, its focal distance and optical parameters determining the refracting surface profile. The optimization criterion is the maximum of the average sunlight concentration corresponding to the focal spot minimum size. The optical parameter controlling the profile of the lens at its pre-assigned dimensions and focal distance is the refractive index, the values of which are taken from its precisely determined dependence on wavelength for a chosen lens material. Any optimization procedure may be used for solving the problem.

Such is suggested general approach for designing lens concentrators, which will be illustrated by an example of choosing design parameters of flat-plane FLs, being among the most promising ones for solar photovoltaic installations [148–152]. All calculations could be performed using two concentration process models based on the geometrical optics and photometry (power optics) concepts [153, 154].

To account for the physical essence of the proposed approach, it is appropriate to consider the problem in the geometrical optics approximation. It is known [155] that, when there is no CA, the concentration ratio of an ideal lens $C_g^{\max}$ is determined by its opening angle (or by the ratio of the diameter $2r_l$ to the focal distance f) and by the angular diameter of the sun $2\varphi_s = 32'$. At the optimum ratio $r_l/f = 1$, the $C_g^{\max}$ value is 11,500 and the focal spot radius is approximately 107 times smaller than the lens radius. The presence of CA, which stems from the dependence of the refractive index of the lens material on the radiation wavelength, $n = n(\lambda)$, leads to a significant increase in the focal spot radius r_s and, as a result, to the considerable decrease of the geometrical concentration $C_g = (r_l/r_s)^2$.

Figure 8.13 shows schematically how a sunlight beam passing through the terminal tooth of a lens decomposes due to light dispersion into several monochromatic beams (each with its own wavelength) with an angular divergence of $2\varphi_s$. The central ray of a beam with the wavelength corresponding to the refractive index n_{calc} chosen for calculations of the FL profile strikes the center F_0 of the focal spot. Beams with wavelengths other than that corresponding to n_{calc} will cross the optical axis above (UV radiation) or below (IR radiation) the focal plane, thus forming additional foci (F_{UV} and F_{IR}, respectively) on the optical axis. In this case, the spot radius in the focal plane will be determined by its intersection with the extreme ray of the beam

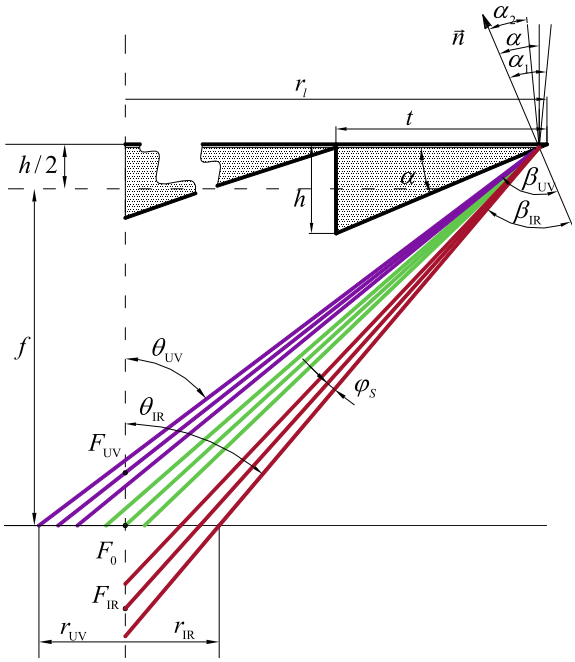

Fig. 8.13 Schematic diagram of sunlight beam dispersion on the terminal tooth of a FL

with the wavelength at the corresponding end of the radiation spectrum in the UV or IR region.

Following the geometrical concept presented in [156], the dependences of maximal values of geometrical concentration ratio and minimal focal spot radii on n_{calc} could be found. It can be seen (Fig. 8.14) to what extent the maximum concentration is sensitive to the accuracy of n_{calc} selection. Thus, the influence of CA can essentially be lowered down by choosing the correct combination of $n_{\text{calc}}^{\text{opt}}$ and f^{opt} and the lens profile corresponding to these parameters and hence the geometrical concentration can be increased by 1.5–2 times.

The main lens characteristic is the distribution of the concentrated radiation density in the focal plane. This so-called optical-power characteristic (OPC) allows estimating comprehensively the lens quality—its concentrating capability and optical efficiency. From the calculation results or OPC measurements, one can determine the average radiation concentration in a spot of any diameter (i.e., for a SC of any size) and the corresponding optical efficiency of the concentrator–receiver system. Besides, the OPC gives a possibility to estimate the character of the irradiance distribution in the focal spot and its effect on the SC I–V curve.

In the photovoltaic model of the concentration process developed by us before [154, 156], the parameter controlling profile of the lens at its pre-assigned dimensions and focal distance is the refraction index, values of which are taken from its precisely determined dependence on the wavelength for a chosen lens material, and

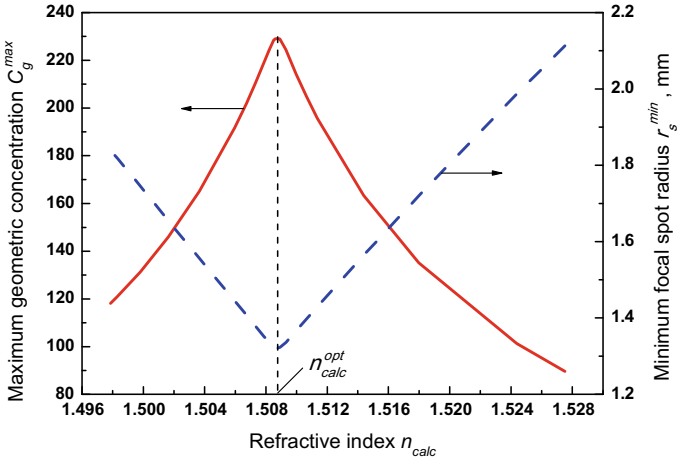

Fig. 8.14 Maximum geometrical concentration $C_g^{\max}$ and minimum focal spot radius $r_s^{\min}$ versus refractive index n_{calc}

the optimization parameter is the maximum of the average sunlight concentration corresponding to the focal spot minimum size. The basis for calculation is the OPC of a lens, which characterize the concentrated radiation density distribution in its focal plane. In determining the average values of the concentration ratio and optical efficiency, not the entire focal spot area is considered, but the circle area, in which 95–98% of the concentrated radiation power is collected. This allows obtaining a higher average concentration on a receiver without essential losses of the power of the radiation passed through a lens.

A preliminary analysis of different type of optical materials for manufacturing FLs has shown that an increase in the refraction index affects positively the lens concentrating capability. For the 40 × 40 mm^2 lenses, selection of the optimum profile parameters for the terrestrial solar spectrum in the range of 320–920 nm was done. FL profile designing was carried out for two practically available materials: silicon compound (Wacker 604) and urethane polymer (Fig. 8.15). It has been found that by choosing the material with greater refraction index, the average radiation concentration in the spot increased by 1.5 times, and, in the ideal case, reaches 780× (Fig. 8.16). In this case, 95% of the power is concentrated within the spot of 1.5 mm in diameter, whereas for a FL of silicon compound the spot diameter was approximately 1.9 mm.

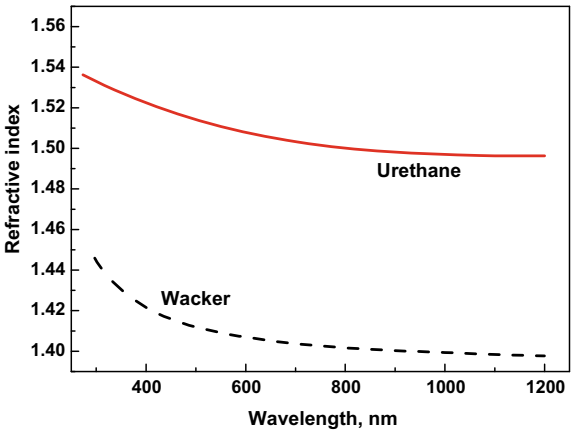

Fig. 8.15 Optical materials refraction index curves

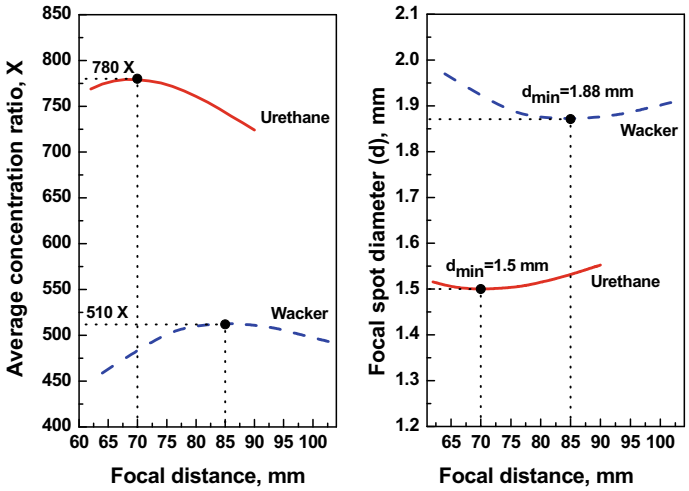

Fig. 8.16 Maximum average concentration ratio (left plot) and minimum focal spot diameter (right plot) versus focal distance for 40 mm × 40 mm Fresnel lenses made of Wacker 604 and urethane

8.7 Module Efficiency Improvement

8.7.1 Compensation of Chromatic Aberration Negative Effect

As discussed earlier, the main disadvantage of FL as a concentrator is conditioned by the chromatic aberration. It is obvious that the actual problem is of lowering the negative effect of the CA on the power efficiency of the system "FL-SC" [157–160].

This problem can be solved, both by a purposeful change of the concentrated light characteristics by means of varying the FL profile [153, 154, 156] and matching these

characteristics with those of a SC [160, 161] and by correct choice of the mutual location of a FL and a SC [151, 162, 163].

In previous section, a procedure for diminishing the negative effect of the CA by optimizing the FL profile has been proposed with the aim of achieving the maximum level of average sunlight concentration on a SC at a sufficiently high value of the "FL-SC" system optical efficiency [162]. However, it was obvious that the proposed procedure is best suited for the systems based on non-selective photoreceivers, which are insensitive to spectrum content variations on their photosensitive surface. In the case of systems based on MJ SCs, an additional study is required to analyze the feasibility of the procedure application, since the effect of CA leads to differences in spatial and spectral irradiance distributions on the separate p-n junctions of a MJ SC, and if the lens is preliminary assigned or designed by allowing for the requirements pointed out above, it is not clear at what distance between FL and SC the maximum power efficiency can be achieved.

In [151, 162, 163] on investigating the behavior of the 3J SC current–voltage characteristic parameters, it was experimentally shown that there exists for a SC such a position on the FL optical axis at which the "FL-SC" pair maximum efficiency can be achieved.

However, in some practical cases the optimum position of a SC with respect to a lens could be found on the basis of preliminary investigations of lens optical-power characteristics and their analysis accounted for the 3J SC spectral response. Herein, the optimal position of the SC with respect to the lens has been found by direct laboratory experiment, leaving open the question of the correspondence of the detected lens-to-cell distance to the designed focal one. The theoretical study results have been verified experimentally under natural sun [164].

Consider, as an example, a silicone-on-glass lens (Wacker 604) of size 40 mm × 40 mm. The refractive profile parameters have been chosen for the terrestrial solar spectrum of 320–920 nm, which corresponds to the spectral response range for the top and middle junctions of the GaInP/GaAs/Ge 3J SC, since just these junctions are mainly contributing to the photocurrent of a SC and determine its efficiency. The FL focal distance, at which the minimum focal size and the maximum average concentration were ensured, was of 85 mm (see Fig. 8.16). Values of the tilt angles and tooth highs of the designed optimal profile were used in the manufacture of negatively profiled mold by means of the diamond cutting.

For designed lens an optical-power characteristic (OPC) has been rated within the three wavelength ranges: 340–680 nm (blue light), 600–920 nm (red light) and 880–1840 nm (infrared light) corresponding to the spectral responses of separate junctions of the 3J SC at different distances from the lens (Fig. 8.17a).

However, on the basis of these characteristics, it is impossible to estimate the efficiency of converting the radiation concentrated by a lens into the photocurrent by the separate junctions and to determine the cell optimal position on the lens optical axis. To do this, it is necessary to normalize OPC with consideration for the spectral response of individual subcells of 3J SC. Figure 8.17b presents distributions of densities of photocurrents generated by p-n junctions at different distances of a SC from a lens.

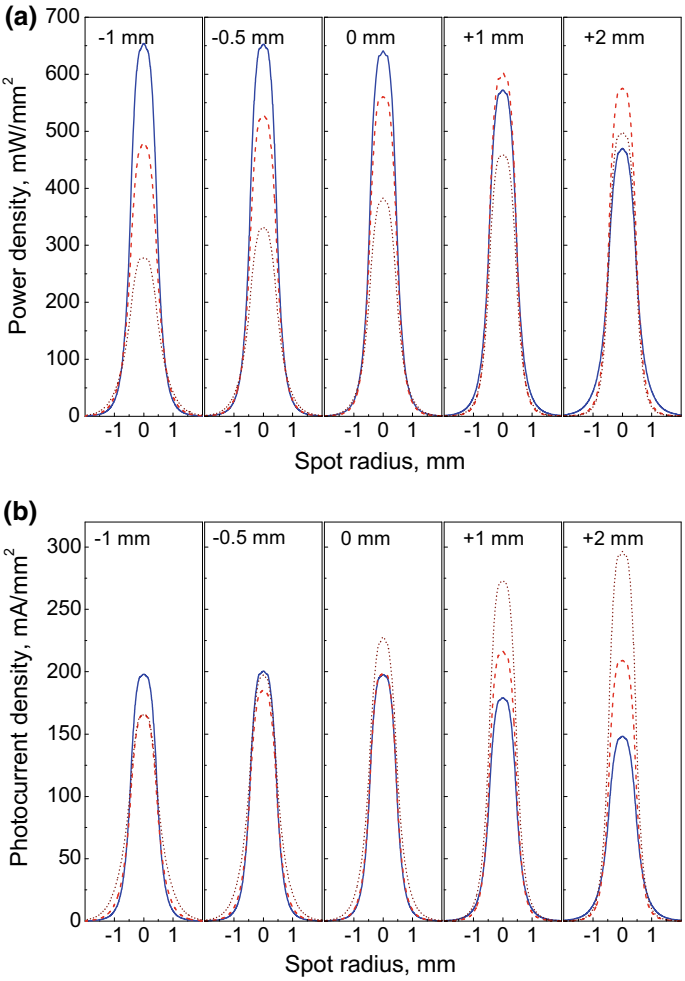

Fig. 8.17 Rated optical-power characteristics **a** for three wavelength ranges (340–680 nm—blue solid lines, 600–920 nm—red dash lines and 880–1840 nm—wine short dash lines) at different distances from a lens (designing focal distance is 85 mm, defocusing is equal to 0) and corresponding distributions of photocurrent densities generated by p-n junctions of 3J SC (**b**) (GaInP—blue solid lines, GaAs—red dash lines, Ge—wine short dash lines)

Recalculation of the power distributions into the "current" ones using data on the cell spectral response shows that, going from the top p-n junction to the bottom one, the areas under the photocurrent density distribution curves and also the values of the maximum density of the photocurrent generated in the SC center rise due to differences in the spectral responses and, hence, in the efficiencies of converting solar radiation into current.

Since, in converting the concentrated radiation, an essential part of power losses in a 3J SC is conditioned by the non-uniform distribution of the photocurrent density along photoactive layers of separate junctions and by the difference in the values of the photocurrent generated by the junctions (the latter is due to smearing out the light spots caused by the CA), in determining the 3J SC optimum position on the lens optical axis, the distribution of the generated photocurrent density in mA/mm^2 should be considered instead of the distribution of the radiation flux density in mW/mm^2.

Analysis of the obtained dependences from the point of view of their effect on the "FL-SC" system power characteristics indicates the following. A drastic luminance differential from the periphery to the center of the focal spot leads to a high local density of the photocurrent generated by a p-n junctions in the cell center, which, depending on the position of the receiver with respect to the lens, results in rising power losses on the internal resistance of the top junction, when "blue" light is strongly focused; the same for the middle junction and "red" light and the bottom junction and "infrared" light.

Figure 8.18 presents the dependencies of densities of the local photocurrents generated in the cell centers on the cell–lens distance. The dependencies show that the strongest negative effect on the SC fill factor is from the GaInP cell side, when the 3J SC is closer to the lens by 0.5 mm than the rated focal distance (85 mm), but from the GaAs and Ge cells, when the SCs are farther by 1.1 mm and 1.5 mm, respectively, since the local photocurrent generation in the center of each cell at these 3J SC positions appears to be maximum.

However, for the 3J SC, not only the high level of the locally generated photocurrent can have a negative effect on the FF. Integrating the dependencies presented in Fig. 8.17b allows obtaining values of the photocurrents generated by the junctions at different distances of a SC from a FL, which are shown in Fig. 8.19 for a SC with the photosensitive area of 2.3 mm in diameter. Practically for the whole range of the defocusing (from −1 to +2 mm), the "FL-SC" system will operate in the mode of current limiting by the top GaInP junction. Only in the case of very strong shift of

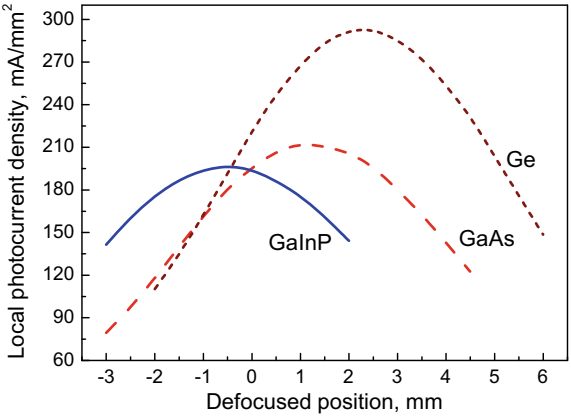

Fig. 8.18 Densities of local photocurrents generated in the center of subcells as a function of the distance between 3J cell and FL

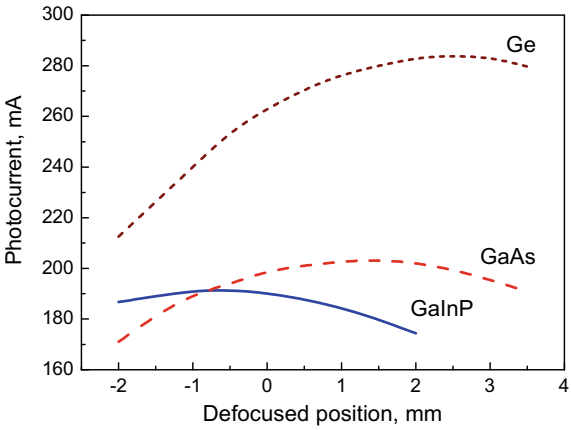

Fig. 8.19 Photocurrents of subcells versus cell–lens distance

a SC toward a lens (defocusing is – 2 mm), which, apparently, is not optimal one from the point of view of red and infrared light focusing, the current limitation by the middle GaAs junction arises. In the –0.8 mm position, the currents of the GaInP and GaAs junctions coincide, and, hence, the SC FF should be minimal at this position. Besides, the Ge junction current is also very close to the GaInP and GaAs cells' currents, which will also increase the FF drop in the defocusing range from –1.5 to –0.5 mm.

But, as shown earlier (see Fig. 8.18), when the 3J SC is by 0.5 mm closer to the lens, the negative effect on the SC I–V characteristic will take place in the GaInP cell side due to the local generation photocurrent density being maximum. Therefore, when 3J SC is located at a distance of 84–85.5 mm from the lens, one could expect a maximum drop in the FF resulting in the considered "FL-SC" system efficiency reduction.

The second minimum of the FF should be expected, when a SC is placed within the defocusing range from +1.1 mm to +1.4 mm, due to the maximum of local density of the photocurrent generated by GaAs junction (see Fig. 8.18) and the absolute maximum of its integrated current (see Fig. 8.19).

The following minimum of FF may be caused by the Ge junction in the defocusing range from +1.5 mm to +2.5 mm (see Figs. 8.18 and 8.19). However, since at the +2.5 mm defocusing the top junction current becomes too small, only the +1.5 mm position is worthy of consideration. Power losses on the internal resistance of the Ge junction will lead to broadening of the second FF minimum due to the high local photocurrent density in the cell center.

Between two minima of the I–V characteristic fill factor, when a SC is placed from a lens at distances of 84–84.5 and 86.1–86.5 mm, respectively, there must be a FF maximum, which resulted from decrease in the load on the top GaInP cell from generation of the local photocurrent and its integral value and from the limitation of the current from the top junction side at simultaneous increase in the difference

between the photocurrents of all three cells. This maximum should be expected in the defocusing range close to +0.5 mm.

Thus, the results of the analysis presented have allowed one to determine preliminarily the optimum distance between a SC and a lens, at which there must be a maximum of the "FL-SC" system efficiency.

The verification of theoretical analysis data and the study of the effect of 3J SC position on the "FL-SC" system efficiency were carried out outdoors at natural sunlight. Controlled positioning of the 3J SC on the lens optical axis and variation in the distance between the lens and the cell was performed by means of X-Y-Z translation stage. The lens position required with respect to the cell location plane was ensured by a rotation stage for varying its fixing angle. A 3J SC with a designated illumination area of 2.3 mm in diameter was mounted on a heat-sink base with a vacuum chuck and connected electrically with the I–V tracer.

The whole system, the picture of which is presented in Fig. 8.20, was established on the sun two-axis tracker at the Ioffe Institute and adjusted normally to the incident sunlight by an optical sighting device. The I–V curves outdoor measurements for "FL-SC" pair were made on midday of 22 June in Saint-Petersburg. The direct sunlight irradiation was checked concurrently using pyrheliometer CH 1 mounted on the tracker. The average value of irradiation during the tests was 750 ± 10 W/m^2. Dependencies of the I–V characteristic parameters (I_{SC}, V_{OC}, FF) and efficiency of the cell-to-lens distance are presented in Fig. 8.21.

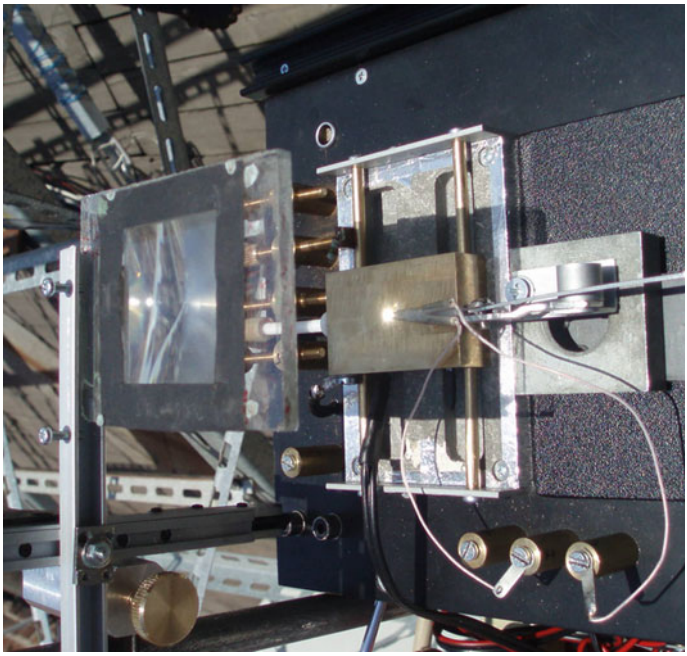

Fig. 8.20 An experimental "FL-SC" pair at outdoor testing

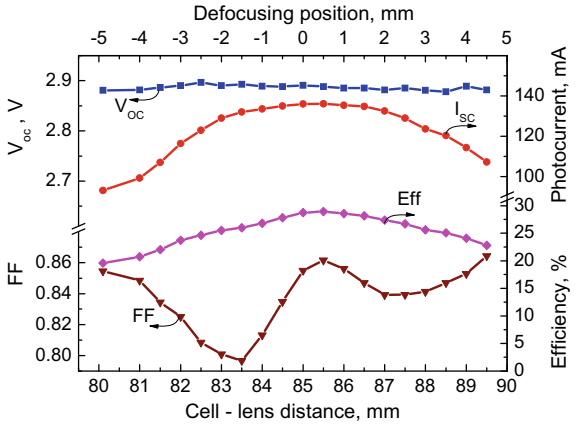

Fig. 8.21 Dependencies of the I_{SC}, V_{OC}, FF and efficiency of the cell–lens distance

The shape of the dependence of the FF on the "cell–lens" distance containing two minima and one maximum confirms completely the theoretical estimations made before. Actually, in the defocusing range of interest, at which the level of the photocurrent generated by a cell changes a little (i.e. the whole light, practically, is focused on the SC photosensitive area), there is an absolute maximum of the FF equal to 86% and a corresponding maximum efficiency to it. These maxima are achieved at a distance of the SC from the lens equal to 85.5 mm (defocusing is +0.5 mm), which corresponds exactly to the value obtained from the preliminary theoretical analysis.

The first FF minimum position (FF = 80%) is found at the SC location of 83.5 mm from the lens, which is by 0.5 mm closer to the lens, than shown by theoretical analysis. The second broad minimum is achieved at the SC location of 87–88 mm from the lens, which is almost by 1 mm farther. Such a shift in the minima positions may be explained by imperfection of the lens refracting surfaces, both at the step of fabricating the negative mold and also in forming the Fresnel profile on glass by the direct copying technique.

By and large, it can be concluded that the data obtained at the experimental investigation step on the SC position with respect to the lens coincide quite precisely with the theoretical analysis results concerning primarily the determination of the real SC position, at which the "FL-SC" system maximum efficiency is achieved. It has been shown that, for the "FL-SC" pair considered, the optimum distance, at which a SC should be placed with respect to a lens, is +0.5 mm to the designing focal distance.

Allowing for the gently sloping efficiency curve in the maximum region, one may conclude that a weakened effect of the CA on the "FL-SC" system characteristics can be achieved in using the proposed procedure for designing lenses. In this case, a SC can be placed in the focal plane of such a lens or somewhat farther (+0.5 mm) from the designing distance. It might be well pointed out that, in the real system, the efficiency

maximum is achieved at the FF maximum, which allows using the dependence of the latter on the "FL-SC" distance as a probe for funding the optimum SC location.

8.8 Conclusion

At present, III–V heterostructure solar cells are widely used for space applications. Progress in terrestrial applications of III–V solar cells is associated with the development of cells with efficiencies exceeding 45% at the concentrated sunlight. These devices can form a technical basis for large-scale solar power engineering in the future. In this case, considerable amount of electrical energy supply to our homes will be generated by heterostructure solar cells illuminated by the sun through the concentrators.

With the development of solar power engineering and the increase in capacity of solar PV installations, it becomes increasingly necessary to satisfy two conflicting requirements—increase of the installation efficiency and reduction of the generated electricity cost. To raise the efficiency, it is necessary to use expensive III–V semiconductor materials, such as GaAs, and complex multilayer semiconductor structures including those for SCs with several p-n junctions. However, the high cost of the materials and technologies for fabricating MJ SCs does not allow achieving a low cost of installations with plane cells of such type, which makes their wide application difficult. The problem can be solved by successively creating and applying SPVIs with sunlight concentrators. In this case, the size of a SC, which is located in the concentrator focus, is decreased proportionally to the radiation concentration ratio—in tens and hundreds of times. Hence, consumption of expensive semiconductor materials and structures and their contribution into the cost of the generated power unity are reduced radically. Moreover, due to the SC efficiency rise, the installation area required for obtaining the electric power unity lowers. This gives an additional economy of means expended for designing, construction and mounting works in creating terrestrial solar PV installations, or for launching space solar arrays, for maintaining parameters of a spacecraft orbit and so on. As a result, the cost of the unit electric power of installations with radiation concentrators will be substantially lower than that in the case of conventional plane space arrays. Thus, it is obvious that SPVIs with radiation concentrators have wide prospects to be applied in developing solar power engineering.

The main functional element of PV installations with radiation concentrators is a PV module, which is a set of definite amount of structurally integrated "concentrator-SC" systems, each of which contains one initial concentrator (e.g., Fresnel lens) and a SC on a heat sink in its focus. In a number of cases, a secondary concentrating element is installed above the SC.

Combination of optically effective concentrators with modern heterostructure SCs ensures the maximum efficiency of sunlight conversion by PV modules and is superior to all other types of radiation power converters. By 2020, the photovoltaic community predicts overcoming 50% of MJ SC efficiencies (AM1.5d, concentrated

radiation). To achieve these indices, at present, transfer from a standard three-junction SC to more efficient four-, five- and six-junction SCs architectures is observed; new materials with optimal forbidden gaps are being improved and created; combined technologies are being developed with the aim to use lattice-mismatched semiconductor materials.

Practice in developing the sunlight PV conversion technique shows that high values of SC and PV system efficiencies demonstrated in indoor conditions, as a rule, appear on the large-scale market of PV production in 2–3 years, promoting humanity to an energetically secure "green" future.

References

1. W. Shockley, Circuit Element Utilizing Semiconductor Material. U.S. Patent 2269347, September 25, 1951
2. A.I. Gubanov, Theory of the contact between two semiconductors with different types of conduction. Zh. Tekh. Fiz. **20**, 1287 (1950)
3. H. Kroemer, Theory of a wide-gap emitter for transistors. Proc. IRE **45**(11), 1535–1537 (1957)
4. Zh.I. Alferov, *The double heterostructure: concept and its applications in physics, electronics and technology* (Norstedts Tryckeri, Stockholm, Les prix Nobel, 2001), pp. 65–93
5. H. Kroemer, A proposed class of heterojunction injection lasers. Proc. IEEE **51**(12), 1782–1783 (1963)
6. Zh. I. Alferov, V.B. Khalfin, R.F. Kazarinov, A characteristic feature of injection into heterojunctions. Fiz. Tverd. Tela **8**, 3102–3105 (1966) [Sov. Phys. Solid State **8**, 2480 (1967)]
7. Z.I. Alferov, Possible development of a rectifier for very high current densities on the bases of a p-i-n (p-n-n, n-p-p) structure with heterojunctions. Fiz. Tekh. Poluprovodn. **1**, 436–438 (1966) [Sov. Phys. Semicond. **1**, 358–361 (1967)]
8. R.L. Anderson, Germanium-gallium arsenide heterojunctions. IBM J. Res. Dev. **4**(3), 283–287 (1960)
9. Z.I. Alferov, V.M. Andreev, V.I. Korol'kov, D.N. Tret'yakov, V.M. Tuchkevich, High-voltage p-n junctions in Ga_xAl_{1-x} crystals. Fiz. Tekh. Poluprovodn. **1**, 1579–1581(1967) [Sov. Phys. Semicond. **1**, 1313–1314 (1968)]
10. H.S. Rupprecht, J.M. Woodall, G.D. Pettit, Efficient visible electroluminescence at 300 K from $Ga_{1-x}Al_xAs$ p-n junctions grown by liquid-phase epitaxy. Appl. Phys. Lett. **11**(3), 81–83 (1967)
11. Z.I. Alferov, V.M. Andreev, V.I. Korol'kov, E.L. Portnoi, D.N. Tret'yakov, Injection properties of n–$Al_xGa_{1-x}As$-p-GaAs heterojunctions. Fiz. Tekh. Poluprovodn. **2**, 1016–1017 (1968) [Sov. Phys. Semicond. **2**, 843–844 (1969)]
12. Z.I. Alferov, V.M. Andreev, V.I. Korol'kov, E.L. Portnoy, D.N. Tret'yakov, Coherent radiation of epitaxial heterojunction structures in the AlAs–GaAs system. Fiz. Tekh. Poluprovodn. **2**, 1545–1547 (1968) [Sov. Phys. Semicond. **2**, 1289–1291 (1969)]
13. Z.I. Alferov, V.M. Andreev, V.I. Korol'kov, E.L. Portnoi, D.N. Tret'yakov, Recombination radiation in epitaxial structures in the AlAs–GaAs system, in *Proceedings of IX International Conference on the Physics of Semiconductors*, Moscow, vol. 1 (Nauka, Leningrad, 1968), pp. 504–510
14. Z.I. Alferov, V.M. Andreev, E.L. Portnoy, M.K. Trukan, AlAs–GaAs heterojunctions injection lasers with a low room-temperature threshold. Fiz. Tekh. Poluprovodn. **3**, 1328–1332 (1969) [Sov. Phys. Semicond. **3**, 1107–1110 (1970)]
15. I. Hayashi, Heterostructure lasers. IEEE Trans. Electr. Devices **31**(11), 1630–1642 (1984)

16. Z.I. Alferov, V.M. Andreev, D.Z. Garbuzov, Y.V. Zhilyaev, E.P. Morozov, E.L. Portnoi, V.G. Trofim, Investigation of the influence of the AlAs–GaAs heterostructure parameters on the laser threshold current and the realization of continuous emission at the room temperature. Fiz. Tekh. Poluprovodn. **4**, 1826–1829 (1970) [Sov. Phys. Semicond. **4**, 1573–1575 (1971)]
17. I. Hayashi, M.B. Panish, P.W. Foy, S. Sumski, Junction lasers which operate continuously at room temperature. Appl. Phys. Lett. **17**, 109–111 (1970)
18. Z.I. Alferov, V.M. Andreev, V.I. Korol'kov, E.L. Portnoi, A.A. Yakovenko, Spontaneous radiation sources based on structures with AlAs–GaAs heterojunctions. Fiz. Tekh. Poluprovodn. **3**, 930–933 (1969) [Sov. Phys. Semicond. **3**, 785–787 (1970)]
19. Z.I. Alferov, V.M. Andreev, M.B. Kagan, I.I. Protasov, V.G. Trofim, Solar-energy converters based on p-n $Al_xGa_{1-x}As$-GaAs heterojunctions. Fiz. Tekh. Poluprovodn. **4**, 2378–2379 (1970) [Sov. Phys. Semicond. **4**, 2047–2048 (1971)]
20. Z.I. Alferov, F.A. Ahmedov, V.I. Korol'kov, V.G. Nikitin, Phototransistor utilizing a GaAs–AlAs heterojunction. Fiz. Tekn. Poluprovodn. **7**, 1159–1163 (1973) [Sov. Phys. Semicond. **7**, 780–782 (1973)]
21. Z.I. Alferov, V.M. Andreev, V.I. Korol'kov, V.G. Nikitin, A.A. Yakovenko, p-n-p-n structures based on GaAs and on $Al_xGa_{1-x}As$ solid solutions. Fiz. Tekn. Poluprovodn. **4**, 578–581 (1970) [Sov. Phys. Semicond. **4**, 481–483 (1971)]
22. Z.I. Alferov, V.M. Andreev, S.G. Konnikov, V.G. Nikitin, D.N. Tret'yakov, Heterojunctions on the base of III–V semiconducting and of their solid solutions, in *Proceedings of International Conference Physical Chemical Semiconductors Heterojunctions and Layer Structures*, Budapest, 1970, vol. 1, ed. by G. Szigeti (Academiai Kiado, Budapest, 1971), pp. 93–106
23. G.A. Antipas, R.L. Moon, L.W. James, J. Edgecumbe, R.L. Bell, in *Gallium Arsenide and Related Compounds*, vol. 17. 1972 Conference Series IOP, London: Institute of Physics, 1973, p. 48
24. A.P. Bogatov, L.M. Dolginov, L.V. Druzhinina, P.G. Eliseev, L.N. Sverdlova, E.G. Shevchenko, Heterolasers on the base of solid solutions $Ga_xIn_{1-x}As_yP_{1-y}$ and $Al_xGa_{1-x}Sb_yAs_{1-y}$. Kvantovaya Electron. **1**, 2294 (1974) [Sov. J. Quant. Electr. **1**, 1281, 1974]
25. Zh. I. Alferov, I.N. Arsent'ev, D.Z. Garbuzov, S.G. Konnikov, V.D. Rumyantsev. Generation of coherent radiation in $nGa_{0.5}In_{0.5}P$-$pGa_{x\sim0.55}In_{1-x}As_{y\sim0.10}P_{1-y}$—$nGa_{0.5}In_{0.5}P$. Pisma Zh. Tech. Fiz. **1**, 305–310, 1975 [Sov. Phys.-Tech. Phys. Lett. **1**, 147–148, 1975]
26. D. Flood, H. Brandhorst, Space solar cells, in *Current Topics in Photovoltaics,* vol. 2, ed. by T.J. Coutts, J.D. Meakin (Academic Press, New York, 1987, London), pp. 143–202
27. S.G. Bailey, D.J. Flood, Space photovoltaics. Prog. Photovolt. Res. Appl. **6**(1), 1–14 (1998)
28. V.M. Andreev, V.A. Grilikhes, V.D. Rumyantsev, *Photovoltaic conversion of concentrated sunlight* (Wiley & Sons Ltd., New York, 1997)
29. H.J. Hovel, J.M. Woodall, High-efficiency AlGaAs-GaAs solar cells. Appl. Phys. Lett. **21**, 379–381 (1972)
30. V.M. Andreev, T.M. Golovner, M.B. Kagan, N.S. Koroleva, T.A. Lubochevskaya, T.A. Nuller, D.N. Tret'yakov, Investigation of high efficiency AlGaAs-GaAs solar cells. Sov. Phys. Semicond. **7**(12) (1973)
31. Zh.I. Alferov, V.M. Andreev, G.S. Daletskii, M.B. Kagan, N.S. Lidorenko, V.M. Tuchkevich. Investigation of high efficiency AlAs-GaAs heteroconverters, in *Proceedings of World Electrotechnology, Congress*, Moscow, 1977, Section 5A, report 04
32. H.J. Hovel, Solar cells, in *Semiconductors and Semimetals*, ed. by R.K. Willardson, A.C. Beer, vol. 11 (New York, London: Acad. Press, 1975)
33. V.M. Andreev, III–V heterostructure photovoltaics in Russia, in *Proceedings of the 17th European Photovoltaic Solar Energy Conference*, Munich, 2001, pp. xxxi–xxxii (2001)
34. J.M. Woodall, H.J. Hovel, An isothermal etchback-regrowth method for high efficiency $Ga_{1-x}Al_xAs$-GaAs solar cells. Appl. Phys. Lett. **30**, 492–493 (1977)
35. V.M. Andreev, V.R. Larionov, V.D. Rumyantsev, O.M. Fedorova, Sh.Sh. Shamukhamedov, P AlGaAs-pGaAs-nGaAs solar cells with efficiencies of 19% at AM0 and 24% at AM1.5. Sov. Tech. Phys. Lett. **9**(10), 537–538 (1983)

36. H.J. Hovel, Novel materials and devices for sunlight concentrating systems. IBM J. Res. Develop. **22**, 112–121 (1978)
37. E. Fanetti, C. Flores, G. Guarini, F. Paletta, D. Passoni, High efficiency 1.43 and 1.69 eV band gap Ga_{1-X} Al_xAs-GaAs solar cells for multicolor applications. Solar cells **3**, 187–194 (1981)
38. R.C. Knechtly, R.Y. Loo, G.S. Kamath, High-efficiency GaAs solar cells. IEEE Trans. Electron Devices **31**(5), 577–588 (1984)
39. H.S. Rauschenbach, *Solar cell array design handbook* (Litton Educational Publishing Inc, The principles and technology of photovoltaic energy conversion. New York, 1980)
40. A. Luque, G. LAraujo. *Solar cells and optics for photovoltaic concentration*. Bristol-Philadelphia: Adam Hilger, 1989, 531 p
41. L.D. Partain (ed.), *Solar Cells and Their Application* (New York: Wiley, 1995)
42. P.A. Iles, Future of Photovoltaic for Space Applications. Prog. Photovoltaics Res. Appl. **8**, 39–51 (2000)
43. V.M. Andreev, A.B. Kazantsev, V.P. Khvostikov, E.V. Paleeva, V.D. Rumyantsev, M.Z. Shvarts. High-efficiency (24.6%, AM0) LPE Grown AlGaAs/GaAs concentrator solar cells and modules. In *Conference Record of the First World Conference on Photovoltaic Energy Conversion (WCPEC)* (Waikoloa, Hawaii, 1994), pp. 2096–2099
44. V.M. Andreev, V.D. Rumyantsev, A^3B^5 based solar cells and concentrating optical elements for space PV modules. Sol. Energy Mater. Sol. Cells **44**, 319–332 (1996)
45. R.D. Dupuis, P.D. Dapkus, R.D. Vingling, L.A. Moundy, High-efficiency GaAlAs/GaAs heterostructure solar cells grown by metalorganic chemical vapor deposition. Appl. Phys. Lett. **31**, 201–203 (1977)
46. N.J. Nelson, K.K. Jonson, R.L. Moon, H.A. Vander Plas, L.W. James, Organometallic-sourced VPE AlGaAs/GaAs concentrator solar cells having conversion efficiencies of 19%. Appl. Phys. Lett. **33**. 26–27 (1978)
47. J.G. Werthen, G.F. Virshup, C.W. Ford, C.R. Lewis, H.C. Hamaker, 21% (one sun, air mass zero) 4 cm^2 GaAs space solar cells. Appl. Phys. Lett. **48**, 74–75 (1986)
48. S.P. Tobin, S.M. Vernon, S.J. Woitczuk, C. Baigar, M.M. Sanfacon, T.M. Dixon. Advanced in high-efficiency GaAs solar cells, in *Conference Record of the 21st IEEE Photovoltaic Specialists Conference (PVSC)*, Kissimimee, pp. 158–162 (1990)
49. S.P. Tobin, S.M. Vernon, M.M. Sanfacon, A. Mastrovito, Enhanced light absorption in GaAs solar cells with internal Bragg reflector, in *Conference Record of the 22nd IEEE Photovoltaic Specialists Conference*, pp. 147–152 (1991)
50. V.M. Andreev, V.V. Komin, I.V. Kochnev, V.M. Lantratov, M.Z. Shvarts, High-efficiency AlGaAs-GaAs solar cells with internal Bragg reflector, in *Conference Record of the First World Conference on Photovoltaic Energy Conversion (WCPEC)* (Waikoloa, Hawaii, 1994), pp. 1894–1897
51. M.Z. Shvarts, O.I. Chosta, I.V. Kochnev, V.M. Lantratov, V.M. Andreev, Radiation resistant AlGaAs/GaAs concentrator solar cells with internal Bragg reflector. Sol. Energy Mater. Sol. Cells **68**, 105–122 (2001)
52. M. Yamaguchi, Space solar cell R&D activities in Japan, in *Proceedings of the 15th Space Photovoltaic Research and Technology Conference*, pp. 1–10 (1997)
53. C.C. Fan, B.-Y. Tsaur, B.J. Palm, Optimal design of high-efficiency tandem cells, in *Conference Record of the 16th IEEE Photovoltaic Specialists Conf. (PVSC)*, pp. 692–698 (1982)
54. M.A. Green, *Solar Cells* (Prentice-Hall Inc., New Jersey, 1982)
55. M.F. Lamorte, D.H. Abbott, Computer modeling of a two-junction, monolithic cascade solar cell. IEEE Trans. Electron Devices **27**, 231–249 (1980)
56. M.B. Spitzer, C.C. Fan, Multijunction cells for space applications. Solar Cells **29**, 183–203 (1990)
57. L. Fraas, B. Daniels, Han-Xiang Huang, J. Avery, C. Chu, P. Iles, M. Piszczor, Over 30% efficient InGaP/GaAs/GaSb cell-interconnected-circuits for line-focus concentrator arrays, in *Proceedings of the 28th IEEE Photovoltaic Specialists Conference (PVSC)* (Anhorage, Alaska, 2000), pp. 1150–1153

58. L. Fraas, J. Avery, D. Scheiman, AM0 calibration of 34% efficient mechanically stacked GaInP/GaAsGaSb circuits, in *Proceedings of the 29th IEEE Photovoltaic Specialists Conference (PVSC)* (New Orleans, 2002), pp. 912–915
59. M.Z. Shvarts, P.Y. Gazaryan, V.P. Khvostikov, V.M. Lantratov, N.K. Timoshina, InGaP/GaAs-GaSb and InGaP/GaAs/Ge-InGaAsSb hybrid monolithic/stacked tandem concentrator solar cells, in *Proceedings of the 21st European Photovoltaic Solar Energy Conference* (Dresden, 2006), pp. 133–136
60. I. Mathews, D. O'Mahony, K. Thomas, B. Corbett, A.P. Morrison, Adhesive bonding for mechanically stacked solar cells. Prog. Photovolt. Res. Appl. **23**(9), 1080–1090 (2015)
61. J.D. McCambridge, M.A. Steiner, B.A. Unger, K.A. Emery, E.L. Christensen, M.W. Wanlass, A.L. Gray, L. Takacs, R. Buelow, T.A. McCollum, J.W. Ashmead, G.R. Schmidt, A.W. Haas, J.R. Wilcox, J.V. Meter, J.L. Gray, D.T. Moore, A.M. Barnett, R.J. Schwartz, Compact spectrum splitting photovoltaic module with high efficiency. Prog. Photovoltaics Res. Appl. **19**, 352–360 (2011)
62. M.A. Green, M.J. Keevers, I. Thomas, J.B. Lasich, K. Emery, R.R. King, 40% efficient sunlight to electricity conversion. Prog. Photovoltaics Res. Appl. **23**(6), 685–691 (2015)
63. M.A. Green, K. Emery, D.L. King, Y. Nishikawa, W. Warta, E.D. Dunlop, D.H. Levi, A.W.Y. Ho-Baillie, Solar cell efficiency tables (version 49). Prog. Photovoltaics Res. Appl. **25**, 3–13 (2017)
64. B.M. Kayes, L. Zhang, R. Twist, I.K. Ding, G.S. Higashi, Flexible thin-film tandem solar cells with >30% efficiency. IEEE Journal of Photovoltaics **4**, 729–733 (2014)
65. I. Garcia, I. Rey-Stolle, B. Gallana, C. Algora, A 32.6% efficient lattice-matched dual-junction solar cell working at 1000 suns. Appl. Phys. Lett. **94**(5), 053509 (2009)
66. J. Ohlmann, D. Lackner, J.F. Sanchez, M. Zedda, A. Wekkeli, M. Steiner, A. Fallisch, F. Dimroth, 35.1% efficient dual-junction solar cells optimized for direct hydrogen generation, in *Proceedings of the 44th IEEE Photovoltaic Specialists Conference (PVSC)*, Washington (2017)
67. R.R. King, D.C. Law, K.M. Edmondson, C.M. Fetzer, G.S. Kinsey, H. Yoon, R.A. Sherif, N.H. Karam, 40% efficient metamorphic GaInP/GaInAs/Ge multijunction solar cells. Appl. Phys. Lett. **90**, 183516 (2007)
68. W. Guter, J. Schöne, S. P. Philipps, M. Steiner, G. Siefer, A. Wekkeli, E. Welser, E. Oliva, A.W. Bett, F. Dimroth, Current-matched triple-junction solar cell reaching 41.1% conversion efficiency under concentrated sunlight. Appl. Phys. Lett. **94**(22), 223504–223506 (2009)
69. R.R. King, A. Boca, W. Hong, X.-Q. Liu, D. Bhusari, D. Larrabee, K.M. Edmondson, D.C. Law, C.M. Fetzer, S. Mesropian, N.H. Karam, Band-Gap engineered architectures for high-efficiency multijunction concentrator solar cells, in *Proceedings of the 24th European Photovoltaic Solar Energy Conference*, Hamburg (2009), pp 55–61
70. M.A. Green, Y. Hishikawa, E.D. Dunlop, D.H. Levi, J. Hohl-Ebinger, Anita W.Y. Ho-Baillie, Solar cell efficiency tables (version 51). Prog. Photovoltaics Res. Appl. **26**, 3–12 (2018)
71. V. Sabnis, H. Yuen, M. Wiemer, High-efficiency multijunction solar cells employing dilute nitrides. AIP Conf. Proc. **1477**, 14–19 (2012)
72. P. Chiu, S. Wojtczuk, X. Zhang, C. Harris, D. Pulver, M. Timmons, 42.3% efficient InGaP/GaAs/InGaAs concentrators using bifacial epigrowth, in *Proceedings of the 37th IEEE Photovoltaic Specialists Conference (PVSC)*, Seattle (2011), pp. 771–774
73. Press release, Sharp Corporation, 31 May 2012. Accessed at http://www.sharp-world.com/corporate/news/120531.html
74. A. Yoshida, T. Agui, N. Katsuya, K. Murasawa, H. Juso, K. Sasaki, T. Takamoto, Development of InGaP/GaAs/InGaAs inverted triple junction solar cells for concentrator application, in *Proceedings of the 21st International Photovoltaic Science and Engineering Conference* (PVSEC-21), Fukuoka (2011)
75. P.T. Chiu, D.L. Law, R.L. Woo, S. Singer, D. Bhusari, W.D. Hong, A. Zakaria, J.C. Boisvert, S. Mesropian, R.R. King, N.H. Karam, 35.8% space and 38.8% terrestrial 5J direct bonded cells, in *Proceedings of the 40th IEEE Photovoltaic Specialists Conference (PVSC)*, Denver, Colorado, pp. 11–13

76. F. Dimroth, T.N.D. Tibbits, M. Niemeyer et al., Four-junction wafer-bonded concentrator solar cells. IEEE Journal of Photovoltaics **6**, 343–349 (2016)
77. https://www.ise.fraunhofer.de/en/press-media/news/2017/31–3-percent-efficiency-for-silicon-based-multi-junction-solar-cell.html
78. R. Cariou, J. Benick, P. Beutel et al., Monolithic two-terminal III–V//Si triple-junction solar cells with 30.2% efficiency under 1-Sun AM1.5g. IEEE J. Photovoltaics **7**(1), 367–373 (2017)
79. A.P. Kirk, High efficacy thinned four-junction solar cell. Semicond. Sci. Technol. **26**(12), 125013 (2011)
80. D. Aiken, E. Dons, S.-S. Je, N. Miller, F. Newman, P. Patel, J. Spann, Lattice matched solar cells with 40% average efficiency in pilot production and a roadmap to 50%. IEEE J. Photovoltaics **3**(1), 542–547 (2013)
81. M. Ochoa, I. García, I. Lombardero et al., Advances towards 4J lattice-matched including dilute nitride subcell for terrestrial and space applications, in *Proceedings of the IEEE 43rd Photovoltaic Specialists Conference (PVSC)*, Portland, 2016, pp. 0052–0057
82. R. Roucka, A. Clark, B. Landini, Si-Ge-Sn Alloys with 1.0 eV Gap for CPV Multijunction Solar Cells. AIP Conf. Proc. **1679**, 040008–040008 (2015)
83. T. Wilson, T. Thomas, M. Führer, N.J. Ekins-Daukes, R. Roucka, A. Clark, A. Johnson, R. Hoffman, D. Begarney, Single and multi-junction solar cells utilizing a 1.0 eV SiGeSn junction, in *AIP Conference Proceedings,* vol. 1766 (2016), pp. 060006
84. C. Algora, E. Ortiz, I. Rey-Stolle, V. Diaz, P. Pena, V.M. Andreev, V.P. Khvostikov, V.D. Rumyantsev, A GaAs solar cell with efficiency of 26.2% at 1000 suns and 25.0% at 2000 suns. IEEE Trans. Electron Devices **48**(5), 840–844 (2001)
85. V.M. Andreev, V.P. Khvostikov, V.R. Larionov, V.D. Rumyantsev, E.V. Paleeva, M.Z. Shvarts, C. Algora, 5800 Suns AlGaAs/GaAs concentrator solar cells, in *Proceedings of Technical Digest of the International Photovoltaic Science and Engineering Conference*, Sapporo (1999), pp. 147–148
86. V.M. Andreev, I.V. Kochnev, V.M. Lantratov, S.A. Mintairov, V.D. Rumyantsev, M.Z. Shvarts, Ultra-violet sensitive infra-red reflective AlGaAs/GaAs solar cells with two Bragg reflectors, in *Proceedings of the 16th European Photovoltaic Solar Energy Conference*, Glasgow (2000), pp. 1019–1021
87. I. García, J. Geisz, M. Steiner, J. Olson, D. Friedman, S. Kurtz, Design of semiconductor-based back reflectors for high voc monolithic multijunction solar cells, in *Preprint Presented at the IEEE Photovoltaic Specialists Conference,* Austin, 2012
88. R. Campesato, G. Gori, M. Casale, G. Gabetta, G. Muthusamy, Sankaran, P. Suresh, E.R. Uma, Radiation effects on advanced multi junction solar cells for space missions, in *Proceedings of the 32nd European Photovoltaic Solar Energy Conference and Exhibition*, Munich (2016), pp. 1411–1414
89. L.M. Fraas, J.E. Avery, J. Martin, V.S. Sundaram, G. Giard, V.T. Dinh, T.M. Davenport, J.W. Yerkes, M.J. O'Neil, Over 35-percent efficient GaAs/GaSb tandem solar cells. IEEE Trans. Electron Devices **37**(2), 443–449 (1990)
90. M.W. Wanlass, J.S. Ward, K.A. Emery, T.A. Gessert, C.R. Osterwald, T.J. Coutts, High performance concentrator tandem solar cells based on IR-sensitive bottom cells. Solar cells **30**(1–4), 363–371 (1991)
91. B.-C. Chung, G.F. Virshup, S. Hikido, N.R. Kaminar, 27.6% efficiency (1 sun, air mass 1.5) monolithic $Al_{0.37}Ga_{0.63}As$/GaAs two junction cascade solar cell with prismatic cover glass. Appl. Phys. Lett. **55**, 1741–1743 (1989)
92. V.M. Andreev, V.P. Khvostikov, E.V. Paleeva, V.D. Rumyantsev, S.V. Sorokina, M.Z. Shvarts, V.I. Vasilev, Tandem solar cells based on AlGaAs/GaAs and GaSb structures, in *Proceedings of the 23rd International Symposium on Compound Semiconductors* (St. Petersburg, Russia, 1996), pp. 425–428
93. D.J. Friedman, S.R. Kurtz, K.A. Bertness, A.E. Kibbler, C. Kramer, J.M. Olson, D.L. King, B.R. Hansen, J.K. Snyder, GaInP/GaAs monolithic tandem concentrator cells, in *Proceedings of the 1st World Conference on Photovoltaic Energy Conversion (WCPEC)* (Waikoloa, Hawaii, 1994), pp. 1829–1832

94. R.R. King, D.C. Law, C.M. Fetzer, R.A. Sherif, K.M. Edmondson, S. Kurtz, G.S. Kinsey, H.L. Cotal, D.D. Krut, J.H. Ermer, N.H. Karam, Pathways to 40%-efficient concentration photovoltaics, in *Proceedings of the 20th European International Photovoltaic Science and Engineering Conference (PVSEC-20)*, Barcelona (2005), pp. 6–10
95. F. Dimroth, R. Beckert, M. Meusel, U. Schubert, A.W. Bett, Metamorphic $Ga_yIn_{1-y}P/Ga_{1-x}In_xAs$ tandem solar cells for space and for terrestrial concentrator applications at C > 1000 suns. Prog. Photovoltaics Res. Appl. **9**(3), 165–178 (2001)
96. D.J. Aiken, M.A. Stan, S.P. Endicter, G. Girard, P.R. Sharps, A loss analysis for a 28% efficient 520× concentrator module, in *Proceedings of the IEEE 4th World Conference on Photovoltaic Energy Conversion(WCPEC)*, Hawaii (2006), pp. 686–689
97. M. Yamaguchi, Y. Okada, A. Yamamoto, T. Takamoto, K. Araki, Y. Ohshita, Novel materials and structures for high efficiency multi-junction solar cells, in *Proceedings of the 21st European Photovoltaic Solar Energy Conference*, Dresden (2006), pp. 53–56
98. A.W. Bett, S.P. Philipps, S. Essig, S. Heckelmann, R. Kellenbenz, V. Klinger, M. Niemeyer, D. Lackner, F. Dimroth, Overview about technology perspectives for high efficiency solar cells for space and terrestrial applications, in *Proceedings of the 28th European International Photovoltaic Science and Engineering Conference* (PVSEC-28) (2013), pp. 1–6
99. S.A. Ringel, J. Carlin, C. Andre, M. Hudait, M. Gonzalez, D. Wilt, E.B. Clark, P. Jenkins, D. Scheiman, A. Allerman, E.A. Fitzgerald, C.W. Leitz, Single-junction InGaP/GaAs solar cells grown on Si substrates with SiGe buffer layers. Prog. Photovoltaics Res. Appl. **10**(6), 417–426 (2002)
100. K. Derendorf, S. Essig, E. Oliva, V. Klinger, T. Roesener, S.P. Philipps, J. Benick, M. Hermle, M. Schachtner, G. Siefer, W. Jäger, F. Dimroth, Fabrication of GaInP/GaAs//Si solar cells by surface activated direct wafer bonding. IEEE J. Photovoltaics **3**(4), 1423–1428 (2013)
101. F. Dimroth, T. Roesener, S. Essig, C. Weuffen, A. Wekkeli, E. Oliva, G. Siefer, K. Volz, T. Hannappel, D. Häussler, W. Jäger, A.W. Bett, Comparison of direct growth and wafer bonding for the fabrication of beam GaInP/GaAs dual-junction solar cells on silicon. IEEE J. Photovoltaics **4**(2), 620–625 (2014)
102. J.M. Zahler, K. Tanabe, C. Ladous, T. Pinnington, F.D. Newman, H. Atwater, High efficiency InGaAs solar cells on Si by InP layer transfer. Appl. Phys. Lett. **91**(1), 012108 (2007)
103. M.J. Archer, D.C. Law, S. Mesropian, M. Haddad, C.M. Fetzer, A.C. Ackerman, C. Ladous, R.R. King, H.A. Atwater, GaInP/GaAs dual junction solar cells on Ge/Si epitaxial templates. Appl. Phys. Lett. **92**, 103503–103503 (2008)
104. P. Patel, D. Aiken, A. Boca, B. Cho, D. Chumney, M.B. Clevenger, A. Cornfeld, N. Fatemi, Y. Lin, J. McCarty, F. Newman, P. Sharps, J. Spann, M. Stan, J. Steinfeldt, C. Strautin, T. Varghese, Experimental results from performance improvement and radiation hardening of inverted metamorphic multijunction solar cells. IEEE J. Photovoltaics **2**, 377–381 (2012)
105. D. Jackrel, S. Bank, H. Yuen, M. Wistey, J. Harris, A. Ptak, S. Johnston, D. Friedman, S. Kurtz, Dilute nitride GaInNAs and GaInNAsSb solar cells by molecular beam epitaxy. J. Appl. Phys. **101**, 114916 (2007)
106. A.B. Cornfeld, M. Stan, T. Varghese et al. Development of a large area inverted metamorphic multi-junction (IMM) highly efficient AM0 solar cell, in *Proceedings of the 33rd IEEE Photovoltaic Specialists Conference (PVSC)*, San Diego, CA (2008), pp 88–92
107. J.F. Geisz, D.J. Friedman, J.S. Ward et al., 40.8% efficient inverted triple-junction solar cell with two independently metamorphic junctions. Appl. Phys. Lett. **93**, 123505 (2008)
108. R.M. France, J.F. Geisz, M.A. Steiner, D.J. Friedman, J.S. Ward, J.M. Olson, W. Olavarria, M. Young, A. Duda, Pushing inverted metamorphic multijunction solar cells toward higher efficiency at realistic operating conditions. IEEE J. Photovoltaics **3**, 893–898 (2013)
109. C. Youtsey, J. Adams, R. Chan, V. Elarde, G. Hillier, M. Osowski, D. McCallum, H. Miyamoto, N. Pan, C. Stender, R. Tatavarti, F. Tuminello, A. Wibowo, Epitaxial lift-off of large-area GaAs thin-film multi-junction solar cells, in *Proceedings of the CS MANTECH Conference*, Boston, Massachusetts (2012), on CD
110. H. Moriceau, F. Rieutord, F. Fournel, Y. Le Tice, L. Di Cioccio, C. Morales, A.M. Charvet, C. Deguet, Overview of recent direct wafer bonding advances and applications, in *Advances in Natural Sciences: Nanoscience and Nanotechnology*, vol. 1 (2010), p. 043004

111. Q.-Y. Tong, U. Gosele, *Semiconductor Wafer Bonding: Science and Technology* (Electrochemical Society, N.Y., 1999)
112. D.C. Law, D.M. Bhusari, S. Mesropian, J.C. Boisvert, W.D. Hong, A. Boca, D.C. Larrabee, C.M. Fetzer, R. R. King, N.H. Karam, Semiconductor-bonded III–V multijunction space solar cells, in *Proceedings of the 34th IEEE Photovoltaic Specialists Conference (PVSC)*, Philadelphia, PA (2009), pp 2237–2239
113. J. Boisvert, D. Law, R. King, D. Bhusari, X. Liu, A. Zakaria, W. Hong, S. Mesropian, D. Larrabee, R. Woo, A. Boca, K. Edmondson, D. Krut, D. Peterson, K. Rouhani, B. Benedikt, N. H. Karam, Development of advanced space solar cells at Spectrolab, in *Proceedings of the 35th IEEE Photovoltaic Specialists Conference (PVSC)*, Honolulu, HI (2010), pp 123–127
114. *Handbook of Photovoltaic Science and Engineering*. 2nd edn. A. Luque, S. Hegedus ed. by John Wiley & Sons, Ltd. (2011)
115. Terrestrial concentrator solar cell systems, in *Solar Cells and Their Applications*, 2nd edn., Part III, ed. by L.M. Fraas, L.D. Partain (Hoboken, New Jersey: John Wiley & Sons, Inc., 2010)
116. *Handbook on Concentrator Photovoltaic Technology*, ed. by A. Carlos, Rey-Stolle Ignacio. (John Wiley & Sons, Ltd. 2016)
117. M.A. Green, K. Emery, D. L. King, Y. Nishikawa, W. Warta, Solar cell efficiency tables (version 29), in *Progress in Photovoltaics*: *Research and Applications,* vol. 15, pp. 35–40 (2007)
118. L.W. Fraas, W.E. Daniels, H.X. Huang, L.E. Minkin, J.E. Avery, M.J. O'Neill, A.J. McDanal, M.F. Piszczor, 34% efficient InGaP/GaAs/GaSb cell-interconnected-circuits for line-focus concentrator arrays, in *Proceedings of the 17th European Photovoltaic Solar Energy Conference*, Munich (2001), pp. 2300–2303
119. Zh.I. Alferov, V.M. Andreev, V.D. Rumyantsev, III–V heterostructures in photovoltaics, in *Concentrator Photovoltaics*, vol. 130, ed. by A. Luque, V. Andreev (New York: Springer Series in Optical Sciences, 2007), pp. 25–50
120. B.M. Kayes, H. Nie, R. Twist, S.G. Spruytte, F. Reinhardt, I.C. Kizilyalli, S. Gregg, Higashi, 27.6% conversion efficiency, a new record for single-junction solar cells under 1 sun illumination, in *Proceedings of the* 37th *IEEE Photovoltaic Specialists Conference* (PVSC), Seattle (2011), pp. 4–8
121. K. Sasaki, T. Agui, K. Nakaido, N. Takahashi, R. Onitsuka, T. Takamoto, "Development of InGaP/GaAs/InGaAs inverted triple junction concentrator solar cells». AIP Conf. Proc. **1556**, 22–25 (2013)
122. J.F. Geisz, A. Duda, R.M. France, D.J. Friedman, I. Garcia, W. Olavarria, J.M. Olson, M.A. Steiner, J.S. Ward, M. Young, Optimization of 3-junction inverted metamorphic solar cells for high-temperature and high-concentration operation, in *9th International Conference on Concentrator Photovoltaic Systems*, ed. by J. Mendiguren Olaeta, B. Rolfe, E. Atzema, D. Hanselman, L. Galdos Errasti, P. Hodgson, M. Weiss, *AIP Conference Proceedings*, vol. 1477 (2013), pp. 44–48
123. F. Dimroth, M. Grave, P. Beutel, U. Fiedeler, C. Karcher, T.N.D. Tibbits, E. Oliva, G. Siefer, M. Schachtner, A. Wekkeli, A.W. Bett, R. Krause, M. Piccin, N. Blanc, C. Drazek, E. Guiot, B. Ghyselen, T. Salvetat, A. Tauzin, T. Signamarcheix, A. Dobrich, T. Hannappel, K. Schwarzburg, Wafer bonded four-junction GaInP/GaAs//GaInAsP/GaInAs concentrator solar cells with 44.7% efficiency. Prog. Photovoltaics Res. Appl. **22**(3), 277–282 (2014)
124. R.M. France, J.F. Geisz, I. Garcia, M.A. Steiner, W.E. McMahon, D.J. Friedman, T.E. Moriarty, C. Osterwald, J. Scott Ward, A. Duda, M. Young, W.J. Olavarria, Quadruple-junction inverted metamorphic concentrator devices. IEEE J. Photovoltaics **5**(1), 432–437 (2015)
125. Essig, S. et al., Raising the one-sun conversion efficiency of III–V/Si solar cells to 32.8% for two junctions and 35.9% for three junctions. Nat. Energy, 2, article number 17144 (2017)
126. V.M. Andreev, E.A. Ionova, V.R. Larionov, V.D. Rumyantsev, M.Z. Shvarts, G. Glenn, Tunnel diode revealing peculiarities at I–V measurements in multijunction III–V solar cells, in *Proceedings of the IEEE 4th World Conference on Photovoltaic Energy Conversion (WCPEC)*, Hawaii (2006), pp. 799–802

127. G. Sala, A. Luque, Past experiences and new challenges of PV concentrators, in *Concentrator Photovoltaics*, vol. 130, ed. by A. Luque, V. Andreev. New York: Springer Series in Optical Sciences (2007), pp. 1–24
128. V.D. Rumyantsev, Terrestrial concentrator PV systems in *Concentrator Photovoltaics*, vol. 130, ed. by A. Luque and V. Andreev. New York: Springer Series in Optical Sciences (2007), pp. 151–174
129. Zh.I. Alferov, V.M. Andreev, Kh.K. Aripov, V.R. Larionov, V.D. Rumyantsev, Pattern of autonomal solar installation with heterostructure solar cells and concentrators. Geliotechnica, **2**, 3–6 (1981) [Appl. Solar Energy **2**, 1981]
130. Zh.I. Alferov, V.M. Andreev, Kh.K. Aripov, V.R. Larionov, V.D. Rumyantsev, Solar photovoltaic installation with 200 Watt output based on AlGaAs-heterophotocells and reflective concentrators, Geliotechnika, **6**, 3–6 (1981) [Appl. Solar Energy **6**, 1981]
131. A.A. Vodnev, A.V. Maslov, V.D. Rumyantsev, Sh.Sh. Shamukhamedov, Experience on creation of the solar installations based on AlGaAs/GaAs-photocells with concentrators, in *Sunlight Concentrators for Photovoltaic Power Installations*, ed. by V.A. Grilikhes, Leningrad: Energoatomizdat (1986), pp. 25–29 (in Russian)
132. V.M. Andreev, A.A. Alaev, A,B. Guchmazov, V.S. Kalinovsky, V.R. Larionov, K.Ya. Rasulov, V. D. Rumyantsev, High-efficiency AlGaAs-heterophotocells operating with lens panels as the solar energy concentrators, in *Proceedings of the all-Union Conference "Photovoltaic phenomena in semiconductors"*, Tashkent, 1989, pp. 305–306 (in Russian)
133. M.Z. Shvarts, V.D. Rumyantsev, V.A. Grilikhes, A.A. Soluyanov, Investigation of a Fresnel lens concentrator photovoltaic module. Appl. Solar Energy **36**(4), 19–28 (2000)
134. Project: INTAS96–1887, 1997-2000 years, "Photovoltaic installation with sunlight concentrators", Final Report (2000)
135. V.D. Rumyantsev, M. Hein, V.M. Andreev, A.W. Bett, F. Dimroth, G. Lange, G. Letay, M.Z. Shvarts, O.V. Sulima, Concentrator array based on GaAs cells and Fresnel lens concentrators, in *Proceedings of the 16th European Photovoltaic Solar Energy Conference and Exhibition*, Glasgow (2000), pp. 2312–2315
136. V.D. Rumyantsev, V.M. Andreev, A.W. Bett, F. Dimroth, M. Hein, G. Lange, M.Z. Shvarts, O.V. Sulima, Progress in development of all-glass terrestrial concentrator modules based on composite Fresnel lenses and III–V solar cells, in *Proceedings of the 28th IEEE Photovoltaic Specialists Conference (PVSC)*, Anhorage, Alaska (2000), pp. 1169–1172
137. A.W. Bett, C. Baur, F. Dimroth, G. Lange, M. Meusel, S. van Riesen, G. Siefer, V.M. Andreev, V.D. Rumyantsev, N.A. Sadchikov, FLATCON^{TM}–modules: technology and characterization, in *Proceedings of the 3rd World Conference on Photovoltaic Energy Conversion (WCPEC)*, Osaka (2003), pp. 634–637
138. V.D. Rumyantsev, Solar concentrator modules with silicone-on-glass Fresnel lens panels and multijunction cells. Optics Express **18**(S1), 17–A24 (2010)
139. V.M. Andreev, N.Y. Davidyuk, E.A. Ionova, P.V. Pokrovskii, V.D. Rumyantsev, N.A. Sadchikov, Parameter optimization of solar modules based on lens concentrators of radiation and cascade photovoltaic converters. Tech. Phys. **55**(2), 277–284 (2010)
140. NYu. Davidyuk, E.A. Ionova, D.A. Malevskii, V.D. Rumyantsev, N.A. Sadchikov, Effect of secondary lens concentrators on the output parameters of solar modules with cascade photovoltaic converters. Tech. Phys. **55**(7), 1003–1008 (2010)
141. V.D. Rumyantsev, Yu.V. Ashcheulov, N.Yu. Davidyuk, E.A. Ionova, P.V. Pokrovskiy, N.A. Sadchikov, V.M. Andreev, CPV modules based on lens panels, in *Proceedings of the 5th Forum on New Materials, CIMTEC 2010–12 International Ceramics Congress and 5th Forum on New Materials*, Montecatini Terme, Italy. *Advances Science Technology*, vol. 74 (2010), pp. 211–218
142. V.D. Rumyantsev, N.Yu. Davidyuk, E.A. Ionova, D.A. Malevskiy, P.V. Pokrovskiy, N.A. Sadchikov, M. Sturm, HCPV modules with primary and secondary minilens panels, in *Proceedings of the 6th International Conference on Concentrating Photovoltaic Systems*, Freiburg, 2010, *AIP Conference Proceedings*, vol. 1277 (2010), pp. 97–100

143. V.M. Andreev, V.D. Rumyantsev, N.Yu. Davidyuk, E.A. Ionova, V.R. Larionov, D.A. Malevskiy, A.O. Monastyrenko, P.V. Pokrovsky, N.A. Sadchikov, Concentrator PV installations based on modules with Fresnel minilens parquets, in *Proceedings of the 25th European Photovoltaic Solar Energy Conference and Exhibition/5th World Conference on Photovoltaic Energy Conversion(WCPEC)*, Valencia (2010), pp. 102–107
144. V.D. Rumyantsev, V.M. Andreev, A.V. Chekalin, NYu. Davidyuk, O.A. Im, E.V. Khazova, N.A. Sadchikov, Progress in developing HCPV modules of SMALFOC-design. AIP Conf. Proc. **1556**, 185–188 (2013)
145. V.M. Andreev, N.Y. Davidyuk, E.A. Ionova, V.D. Rumyantsev, Photovoltaic modules with cylindrical waveguides in a system for the secondary concentration of solar radiation. Tech. Phys. **58**(9), 1323–1328 (2013)
146. V.M. Andreev, N.Yu. Davidyuk, D.A. Malevski, A.N. Pan'chak, V.D. Rumyantsev, N.A. Sadchikov, A.V. Chekalin, A. Luque, New-generation concentrator modules based on cascade solar cells: design and optical and thermal properties. Tech. Phys. **59**(11), 1650–1657 (2014)
147. V.D. Rumyantsev, V.M. Andreev, A.V. Chekalin, N.Yu. Davidyuk, N.A. Sadchikov, HCPV modules of SMALFOC Design in Versions for PV and PV/T Operation, in *Proceedings of the 40th IEEE Photovoltaic Specialists Conference (PVSC)*, Denver, Colorado (2014), pp. 2720–2723
148. V. Grilikhes, V. Rumyantsev, M. Shvarts, Indoor and outdoor testing of space concentrator AlGaAs/GaAs photovoltaic modules with Fresnel lenses, in *Proceedings of the 25th IEEE Photovoltaic Specialists Conference (PVSC),* Washington (1996), pp 345–348
149. R. Leutz, A. Suzuki, A. Akisawa, T. Kashiwagi, Developments and designs of solar engineering Fresnel lenses, in *Proceedings of Symposium on Energy Engineering in the 21st Century (SEE2000)*, vol.2, *2000*, pp. 759–765
150. V.D.Rumyantsev, O.I.Chosta, V.A.Grilikhes, N.A.Sadchikov, A.A.Soluyanov, M.Z.Shvarts, V.M.Andreev. "Terrestrial and space concentrator PV modules with composite (glass-silicone) Fresnel lenses" in *Proc. of the 29th IEEE Photovoltaic Specialists Conference (PVSC)*, New Orleans, 2002, pp. 1596–1599
151. H. Cotal, R. Sherif, The effects of chromatic aberration on the performance of GaInP/GaAs/Ge concentrator solar cells from fresnel optics, in *Proceedings of the 31 st IEEE PV Specialists Conference(PVSC)*, Lake Buena Vista, USA (2005), pp. 747–750
152. V.D. Rumyantsev, N.A. Sadchikov, A.E. Chalov, E.A. Ionova, D.J. Friedman, G. Glenn, Terrestrial concentrator PV modules based on GaInP/GaAs/Ge TJ cells and minilens panels, in *Proceedings of the 4th World Conference on Photovoltaic Energy Conversion (WCPEC)*, Hawaii (2006), pp. 632–635
153. E.V. Bobkova, V.A. Grilikhes, A.A. Soluyanov, M.Z. Shvarts, Effect of chromatic aberration on the concentration of solar radiation by fresnel lenses. Tech. Phys. Lett. **32**(12), 1039–1042 (2006)
154. E. Bobkova, V. Grilikhes, A. Soluyanov, M. Shvarts, The method for choosing the optimal parameters of flat-plane Fresnel lenses, intended for sunlight concentration. *Geliotekhnica,* vol. 3, pp. 50–57 (2006) [Translated into English in Applied Solar Energy]
155. V. Weinberg, *Optical in the solar power plants* (Oborongiz, Leningrad, 1959), p. 256
156. V.A. Grilikhes, M.Z. Shvarts, A.A. Soluyanov, E.V. Vlasova, V.M. Andreev, The new approach to design of Fresnel lens sunlight concentrator, in *Proceedings of the Forth International Conference on Solar Concentrators for the Generation of Electricity or Hydrogen*, El Escorial, Spain (2007), pp. 49–52
157. L. James, Effects of concentrator chromatic aberrations on multi-junction cells, in *Conference Record of the First World Conference on Photovoltaic Energy Conversion (WCPEC)*, Waikoloa, Hawaii (1994), pp. 1799–1802
158. S. Kurtz, D. Friedman, J. Olson. The effect of chromatic aberrations on two-junction, two-terminal devices in a concentrator system, in *Conference Record of the First World Conference on Photovoltaic Energy Conversion (WCPEC)*, Waikoloa, Hawaii (1994), pp. 1791–1794
159. S. Kurtz, M. O'Neill, Estimating and controlling chromatic aberration losses for two-junction, two-terminal devices in refractive concentration systems, in *Proceedings of the 25th IEEE PV Specialists Conference(PVSC), Washingon, DC* (1996), pp. 361–364

160. K. Araki, M. Yamaguchi, Improvement of mismatching in concentrator modules using III–V cells, in *Proceedings of the 17th European Photovoltaic Solar Energy Conference*, Munich, 2001, pp. 2187–2190
161. M.J. O'Neill, Color-mixing lens for solar concentrator system and methods of manufacture and opreation thereof, U.S. Patent 6031179 (2000)
162. K. Nishioka, T. Takamoto, W. Nakajima, T. Agui, M. Kaneiwa, Y. Uraoka, T. Fuyuki, Analysis of triple-junction solar cell under concentration by spice, in *Proceedings of the 3rd World Conference on Photovoltaic Energy Conversion(WCPEC),* Osaka (2003), pp. 869–872
163. A. Yoshida, H. Juso, T. Agui, K. Nakamura, K. Sasaki, T. Takamoto, M. Tanaka, M. Kaneiwa, K. Okamoto, Characteristics of concentrator triple junction cell optimized for current matching, in *Proceedings of the 4th World Conference on Photovoltaic Energy Conversion (WCPEC), Hawaii* (2006), pp. 757–759
164. M.Z. Shvarts, V.A. Grilikhes, N.H. Timoshina, A.A. Soluyanov, E.V. Vlasova, Weakening of the chromatic aberration negative effect on the performance of concentrator multi-junction solar cells, in *Proceedings of the 22nd European Photovoltaic Solar Energy Conference*, Milan (2007), pp. 126–131

Chapter 9
CIGS Thin Film Photovoltaic—Approaches and Challenges

F. Kessler, D. Hariskos, S. Spiering, E. Lotter, H. P. Huber and R. Wuerz

Abstract After a short overview of the historical development of the Cu(In, Ga)Se_2 (CIGS) thin film solar cell and its special features, we give an overview of the deposition and optimization of the p-type CIGS absorber as well as the subsequent n-type buffer layer and the molybdenum back contact. Developments to increase efficiency by optimizing the implemented bandgap grading via the local gallium content as well as the specific doping of the CIGS absorber by means of various alkali elements deepen the understanding. Finally, modern approaches to monolithic cell interconnection are discussed, e.g. via the use of modern ultra-short pulse lasers. Numerous literature references enable the reader to gain an even deeper insight if required.

F. Kessler (✉) · D. Hariskos · S. Spiering · E. Lotter · R. Wuerz
ZSW – Zentrum für Sonnenenergie- und Wasserstoff-Forschung Baden-Württemberg, Meitnerstr. 1, 70563 Stuttgart, Germany
e-mail: friedrich.kessler@zsw-bw.de

D. Hariskos
e-mail: dimitrios.hariskos@zsw-bw.de

S. Spiering
e-mail: stefanie.spiering@zsw-bw.de

E. Lotter
e-mail: erwin.lotter@zsw-bw.de

R. Wuerz
e-mail: roland.wuerz@zsw-bw.de

H. P. Huber
Laserzentrum Hochschule München, Fakultät für angewandte Wissenschaften und Mechatronik, Hochschule für angewandte Wissenschaften München, Lothstr. 34, 80335 Munich, Germany
e-mail: heinz.huber@hm.edu

V. Petrova-Koch et al. (eds.), *High-Efficient Low-Cost Photovoltaics*,
Springer Series in Optical Sciences 140,
https://doi.org/10.1007/978-3-030-22864-4_9

9.1 Introduction

9.1.1 Brief History

Harry Hahn et al. were the first to synthesize the ternary chalcopyrite $CuInSe_2$ (CIS) and some others in the laboratory [1]. This first CIS ($CuInSe_2$) material was grown by mixing two binary and stoichiometric educts at a temperature of 900 °C for 12 h. They determined the lattice constants by the Debye-Scherrer method and focused on structural analysis of the new material. It took about 20 years (1974) for a team from Bell Laboratories Holmdel to investigate the electronic and optical properties in more detail. The Wagner, Shay, Migliorato and Kasper group produced the first heterostructures consisting of a p-type $CuInSe_2$ absorber and an n-type CdS layer [2]. They were looking for a broad-band detector in the visible and NIR as an alternative to Si or CdS/Cu_2S junctions. The $CuInSe_2$ single crystals were produced by melt growth from stoichiometric mixtures, which were subsequently annealed under Se atmosphere at 600 °C for 24 h to achieve p-type conductivity. The n-type CdS layer was evaporated to a thickness of 5–10 μm. Indium on CdS and gold on $CuInSe_2$ were used as ohmic contacts. After all the processes, the solar cell efficiency was around 5%.

Just one year later, the Wagner et al. group stated that they had achieved a PV conversion efficiency of 12% with the same heterostructure [3]. An important leap forward has been taken by leaving the approach of manufacturing PV devices from thick and single-crystalline $CuInSe_2$ absorbers. Instead, some scientists discovered the real potential of this direct bandgap CIS absorber which should require only a few micrometers to absorb the entire solar spectrum above its bandgap of $E_g = 1.01–1.04$ eV. Kazmerski et al. [4] were the first to fabricate thin film CIS/CdS devices. The CdS layer ($d = 6$ μm) and the CIS absorber (5–6 μm) were still quite thick and reached a conversion efficiency of 4–5%. But Mickelsen and Chen [5] (Boeing Aerospace, 1981) achieved a breakthrough. They attained a CIS/CdS efficiency of 9.4% by using thin film vacuum deposition processes for all functional layers and a total stack thickness of only 5 μm.

Many other scientific discoveries such as the introduction of Ga to increase the bandgap from about 1 eV toward the optimum value of 1.3–1.5 eV (depending on the sun spectrum), the installation of a bandgap grading and the defined admixture of alkali elements (“dopants”) could boost the cell efficiency of $Cu(In,Ga)Se_2$ (CIGS)-based solar cells up to values around 23%. The CIGS-based solar cells have not only survived the ups and downs of PV from 2000 to 2012, that is, the unrealistic expectation of market growth, but also established competition in Si technology and other thin film PV technologies such as CdTe and a-Si:H-based approaches. Nevertheless, the production volume of CIGS modules is still around 2%, whereas Si dominates the scenario with a share of >90%. The optimistic assumptions of Chopra et al. [6] and Mitchell et al. [7], according to which the manufacturing costs of thin film devices from 2004 would be lower than those of Si thick film technology, could not be verified at least until 2004.

Advantageous features of CIGS

There are numerous reasons explaining why CIGS is currently one of the most promising PV technologies:

- CI(G)S is a semiconductor with direct bandgap and high optical absorption coefficient in the range of 10^5 cm^{-1}, allowing a low absorber thickness of 2–3 μm or even less if multi-reflection technologies are applied.
- Adjustable graded bandgap between 1.04 and 1.14 eV without degradation of optoelectronic properties.
- Dopability via alkali metals, especially Na and K.
- Short energy payback time of about 1 year.
- Microcrystalline absorbers with saturated defects and electrical properties that can be even better than a single crystal.
- Large variety of deposition methods, both in vacuum and vacuum-free.
- The typical substrate structure allows for the free choice of substrates from glass (typically float glass) to polymer or metal foils. Cost-effective coating approaches such as roll-to-roll in vacuum or vacuum-free can be used; energy savings can be done through low heat capacities of the thin functional layers and/or the use of thin substrates.
- The manufacture of highly flexible, lightweight and material-saving devices enables optimum integration into facades (BIPV), the automotive sector, aerospace applications and leisure applications.
- The possibility to fabricate heterojunction structures and tandems, to modify device properties by interface modifications and intermediate thin functional layers.
- Cell connections via monolithic connections enable the production of customized modules with minimal effort (only possible on insulating substrates/foils); however, if cell sorting is desired, other techniques can also be used; for example, shingling of cells (metallic substrates), wiring and screening technology.
- Very high stability in space against high-energy electrons, making CIGS generators a suitable candidate for special space missions in highly radiant regions [8, 9] (e.g. the Van Allen belt).

9.1.2 Structure of a CIGS Solar Cell

CI(G)S crystallizes in a tetragonal chalcopyrite lattice (Fig. 9.1). The ratio of the lattice constants c/a is close to 2. The unit cell can be deduced from the face-centered cubic lattice of ZnSe (II–VI group), where Zn is substituted by Cu (group I) and In (resp. Ga) (group III) ordered according to the Grimm-Sommerfeld rule. In this way, the CIS or CIGS unit cell can be constructed by two sphalerite unit cells. Each Se atom is surrounded by four metal atoms (Cu, In/Ga), which form a tetrahedron [10].

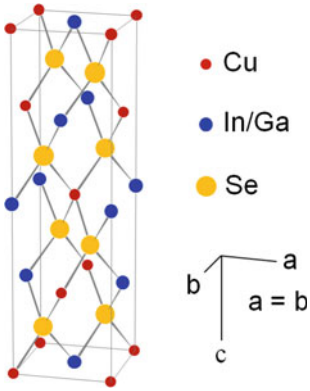

Fig. 9.1 Tetragonal chalcopyrite unit cell of CI(G)S

CI(G)S thin films with a thickness of typically 1–3 μm are multicrystalline and range from very small crystallites ≪1 μm to crystallites of a few micrometers diameter. Attempts and expectations to improve the quality of optoelectronic materials by using single crystals failed and no longer make sense, as the grain boundaries can be passivated very successfully. It is even not straightforward to give substantial evidence that absorbers with smaller grain size must result in devices with worse optoelectronic properties, at least if the grains are not too small and the passivation of grain boundary states (e.g. by alkali doping) was successful. Multicrystalline CIGS thin film absorbers are inherently p-type which is mainly caused by Cu vacancies. However, early investigations on CIS report the existence of both n- and p-type single crystals, depending on growth conditions [11].

The structure of a typical CIGS-based solar cell is shown in Fig. 9.2. Owing to the relatively low total thickness of the active layers of approx. 4 μm, the solar cell or module requires a suitable carrier substrate that meets all technical and economic

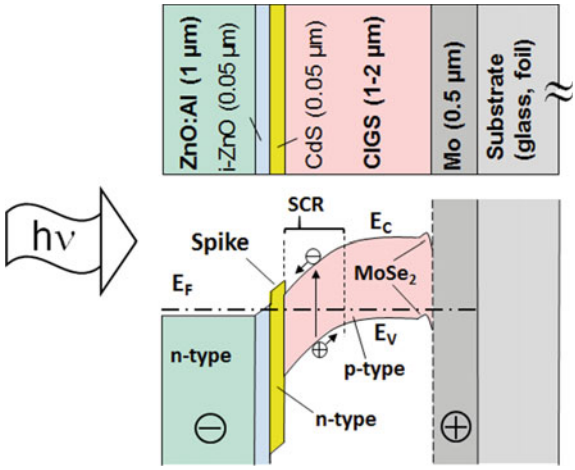

Fig. 9.2 Sketch of the cell structure (upper picture) and corresponding band diagram of a "standard" CIGS type PV device (lower picture)

requirements such as high temperature stability of 400–700 °C without degassing or decomposition, low roughness with regard to the layer thicknesses and commercial availability at reasonable costs. Standard float glass, a mass product widely used in the window industry, is a pretty good compromise, especially when it is not about high weight and brittleness. In addition, float glass or soda-lime glass has a reproducible and extremely low average roughness (R_a) of a few nanometers. In combination with its relatively hard surface and high optical transparency, glass is also an ideal material for monolithic cell connection by laser and mechanical scribing.

According to Fig. 9.2, the active stack deposition normally starts with the molybdenum (Mo) back contact, followed by a p-type absorber layer (CIGS) , an n-type buffer layer (e.g. CdS, Zn(O,S), In_2S_3 or others), a thin high-resistance undoped zinc oxide layer (i-ZnO) and a highly n-type Al-doped ZnO (ZnO:Al or AZO) layer as transparent conductive oxide (TCO) front contact. The high AZO thickness of up to 1 μm in Fig. 9.2 is used to achieve a sufficient lateral conductivity for the fabrication of monolithically integrated modules (normally) without a metal grid on top. However, to verify the highest efficiency at small cell level, the ZnO:Al thickness is reduced to approx. 200 nm and a fine Ni–Al–Ni grid is applied for the transport of the charge carriers. An anti-reflective layer of MgF_2 with a typical thickness of 105 nm reduces the reflection losses.

CIGS-based thin film devices are preferably manufactured in "substrate configuration" (see Fig. 9.2) to protect the buffer and window layers from damage from the CIGS process temperature (400–700 °C). In substrate structures, light enters through the finally deposited layer (here: ZnO:Al), in contrast to superstrate configurations such as CdTe-based devices, in which the photons first penetrate into the PV device via the transparent substrate. The advantage of the superstrate approach is that opaque films/carriers can also be used as carrier material. The beneficial consequences are manifold and concern both the fabrication procedure (e.g. roll-to-roll manufacturing on stainless steel foil or polyimide) and the end product (weight, brittleness, flexibility). A substrate configuration also offers a wide range of possibilities when looking at hetero tandem structures with (e.g.) CIGS as back cell and perovskite as front cell.

The lower picture of Fig. 9.2 indicates the direction of the electron minority carriers in the conduction band and the hole majority carriers in the valence band, as well as the space charge region (SCR). The little spike in the conduction band is a result of the CdS buffer layer. However, the potential electron-blocking behavior is only observed at low temperatures. Igalson et al. [12] showed by admittance spectroscopy, dark and light I–V–T analysis and C–V profiling that the electron barrier at the front is significantly more pronounced for CdS buffers compared to In_2S_3 buffered samples.

For instance, the I–V curves at 120 K showed a pronounced kink in the first quadrant (roll-over effect), which was not observed with In_2S_3 buffers. The small hump near the Mo back contact is due to the formation of a thin $MoSe_2$ layer [13, 14] which is responsible for the back-surface field formed for the electrons and holes. A further discussion can be found in Sect. 9.2.2.1.

9.2 Device Fabrication

Some advantageous features of CIGS-based PV modules are:

- The possibility to grow the absorber by a comparably large number of thin film deposition methods, including both non-vacuum and vacuum approaches.
- The possibility of choosing very different carrier materials and thus being able to supply PV generators for almost all conceivable areas of application such as conventional applications (on-roof and free-field), well-coordinated building integration (BIPV), automotive applications (cars, truck tarpaulins), leisure activities, aviation and space applications.
- Material and energy savings in production by reducing the absorber thickness and optimizing multiple reflection effects.
- The continuing increase in generator efficiencies.
- The potential to fabricate tandem devices, for example, in a perovskite/CIGS structure with CI(G)S as the bottom cell; even CIGS/CI(G)S tandem structures may be a future option consisting of a high and low bandgap CIGS device. However, some obstacles still need to be overcome for both approaches.

The multitude of implementation options and diversification, on the other hand, carries the risk that optimization processes for a certain product would take considerably longer than with a PV concept with only one meaningful manufacturing process, which is developed and applied in parallel by all users.

The core process bearing the most profound know-how within a CIGS-based PV device is the deposition of the p-type CIGS absorber. To produce a highly efficient solar cell, however, a deep understanding of all other layers is also necessary, especially the adjacent layers such as buffer and back contact. In addition to the bulk-correlated layer properties, particular attention must be paid to the CIGS interfaces, which can significantly hamper the carrier transport, for example, by implementing increased recombination states in the gap or the formation of barriers in the conduction or valence band, which impede the transport of charge carriers (see also Fig. 9.2). Especially the optimization of the pn-junction, that is the p-CIGS/n-buffer interface, is complex, especially if a Cd-free alternative buffer has to be applied due to environmental reasons. The following discussions are only intended to show how small changes can have a big impact.

9.2.1 CIGS Layer

9.2.1.1 Phase Diagram, Copper and Gallium Content

Figure 9.3 shows the phase diagram along the pseudobinary Cu/In/Se system Cu_2Se–In_2Se. A detailed discussion of the ternary Cu/In/Se phase diagram including the history on the way to calculation and verification of this system was provided by

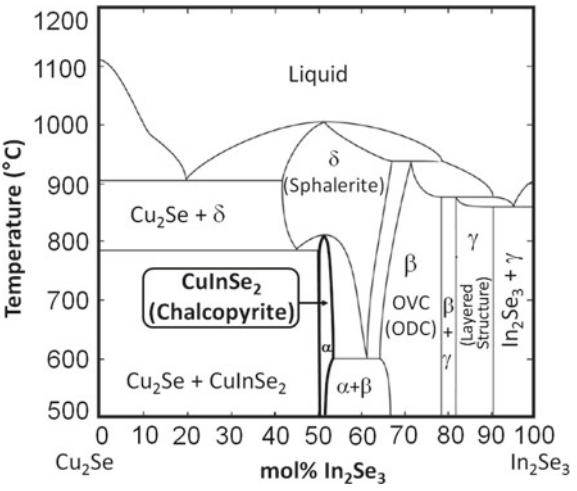

Fig. 9.3 Pseudobinary phase diagram of the ternary Cu/In/Se system along the Cu_2Se and In_2Se_3 axis (original graphic by Chang et al. [20], later revised by Stanbury et al. [15] and in this publication)

Stanbery [15]. The Cu/In/Ga/Se diagram is even more complicated and less understandable, but usually the ternary Cu/In/Se system is also useful to explain the quaternary system. The desired crystalline chalcopyrite region suitable for the production of efficient thin film solar cells is the p-type phase ($CuInSe_2$). The phase is stable from room temperature to approx. 810 °C and is only present at a substoichiometric Cu content of 24–24.5% [16]. The copper deficient n-type β-phase $CuIn_3Se_5$ should be avoided or reduced to a minimum in the bulk, in order to achieve a homogeneous and strongly p-type semiconductor. At the interface to the n-type buffer/TCO interface, however, the n-type and β-phase $CuIn_3Se_5$ (resp. $Cu(In,Ga)_3Se_5$) or the so-called ordered vacancy compound (OVC or ordered defect compound, ODC) is intended and very helpful to provide a proper hetero interface. The OVC layer is automatically formed at high temperatures in the direction of the interface to the n-type CdS buffer. This buried pn junction in the absorber reduces recombination at the heterogeneous CI(G)S/CdS interface [17, 18]. Another beneficial effect of Cu poor grown absorbers as postulated by Schock, Rau and Turcu [14, 19] is the Fermi level pinning close to the conduction band and the bandgap widening at the absorber surface. In summary, as a consequence of type conversion, bandgap widening and Fermi level pinning at the interface, the heterojunction losses of Cu-poor CIGS absorbers are low and the recombination essentially takes place in the space charge region (SCR).

The parameter range for the fabrication of an efficient chalcopyrite absorber is rather limited, as demonstrated in Figs. 9.3 and 9.4 [21] by the PV-active α-phase.

For the fabrication of suitable PV absorbers the $Cu(In,Ga)Se_2$ layers should be slightly Cu deficient as the Cu vacancies contribute to the p-type conductivity. Devices with the potential of high efficiencies should have a Cu content in the range of $0.88 < Cu/(In + Ga) < 0.95$ [23]. However, if all Cu vacancies corresponded to a doping state, the defect or dopant concentration would be $>10^{20}/cm^3$ and thus more than three orders of magnitude higher than any reasonable doping level. Additionally, only a part of the excess vacancy states can be compensated by the higher

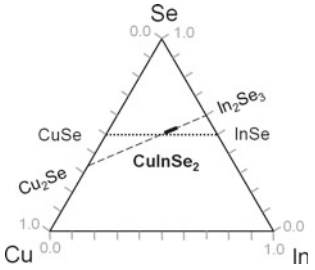

Fig. 9.4 Simplified ternary Cu/In/Se phase diagram indicating the α-phase region for the fabrication of PV-relevant CIS-material by a solid bold line (original diagram by Gödecke et al. [22], redrawn in this publication). The dashed axis corresponds to the phase diagram of Fig. 9.3

Cu deficiency of the $Cu(In,Ga)_3Se_5$ OVC layer. Its thickness increases with the Cu deficiency of the bulk material and varies between 5 and 60 nm [24]. The main reason, however, describing the electronically extremely tolerant behavior of CIGS is not the OVC layer, but the formation of inactive and neutral defect complexes. Defect complexes consisting of two Cu vacancies (2 V_{Cu}) and an In-Cu anti-site (In_{Cu}) are particularly suitable candidates that allow a Cu deficiency as low as 22%, as it results from measurements [14] and calculations [25]. The defect chemistry of CIGS and its derivatives is complex. However, understanding the interactions between charged and neutral defects under illumination and temperature activation is necessary to describe all experimentally observed effects and to further improve efficiency and reduce metastability. A detailed description of the defect models can be found elsewhere [26–30].

According to the early detailed balance calculations of Shockley and Queisser [31] (Shockley-Queisser limit) the ideal bandgap of a single-junction cell should be in the range of 1.3 eV. Later, their estimates of black-body solar radiation with a surface temperature of 6000 °C and the assumption of pure radiation recombination were refined by the introduction of the AM1.5g spectrum, which better describes the solar spectrum on Earth, corresponding to a lower integrated light intensity/m^2 by slightly more than a factor of 1.5 [32]. If small fluctuations of the maximum efficiency are neglected by different input parameters (e.g. assumed spectrum), it is obvious that the $CuInSe_2$ band spacing should be increased from 1.04 eV to slightly above $E_g = 1.3$ eV. Hanna et al. [33] investigated the bandgap E_g as a function of the Ga content $x = GGI = Ga/(Ga + In)$ from $x = 0$ ($CuInSe_2$)) to $x = 1$ ($CuGaSe_2$). Up to a Ga content of $x = 0.3$, the bandgap was not only increased to E_g 1.2 eV, but the bulk defect concentration was also reduced to a minimum. The number of defect states depends on the CIGS deposition method but their minimum is always at $x \approx 0.3$. The evaluation of the losses of the open-circuit voltage V_{oc} relative to E_g by applying the difference $E_g - qV_{oc}$ versus E_g could show an analog minimum of $E_g - qV_{oc}$ at $E_g \approx 1.2$ eV [33]. Up to a Ga concentration Ga/(Ga + In) of $x < 0.3$, the open-circuit voltage V_{oc} increases superlinear but sublinear with $x > 0.3$. With $x > 0.3$ [34] the defect concentration in the bulk rises. Thus, the admixture

of Ga is limited. Nevertheless, Jackson et al. [35] showed that high IV conversion efficiencies of $\eta \geq 19\%$ can be achieved with $Cu(In_{(1-x)},Ga_x)Se_2$ based devices up to a Ga content of $0.21 \leq Ga/(Ga + In) \leq 0.38$ corresponding to a bandgap of 1.11–1.23 eV, which demonstrates that the materials tolerance is higher than expected due to the defect concentrations [33]. Other authors [36] could even slightly expand the useful bandgap region up to 1.35 eV.

$Cu(In,Ga)Se_2$ based thin film solar cells have already achieved efficiencies close to 23% with the two main and currently most industry-relevant deposition methods, such as co-evaporation [37] and sequential sputtering plus annealing [38]. The multicrystalline CIGS semiconductor shows a rather good-natured behavior and high-efficiency cells >20% can be achieved not only by large grains over the whole absorber thickness but also by a structure with many small grains. Fortunately, the grain boundaries can be easily neutralized and passivated (e.g. by alkali supply) and do not hamper the device. Some mechanisms and details on how to optimize the CIGS absorber by treatments with alkali metals are described in Sect. 9.2.1.5.

Many attempts have been made to increase the bandgap toward 1.4 eV and above in order to improve the efficiency or to develop a wide-bandgap material to be applied as front cell of a tandem device. Experiments are still ongoing and physically challenging. After all, a sulfur-based $Cu(In,Ga)S_2$ solar cell with a relatively high V_{oc} of 920 meV has achieved a maximum efficiency of 15.5% [39]. Best efficiencies with absorbers of $CuInS_2$ ($E_g = 1.53$ eV) reached an efficiency of 11.4% [40]; with $CuGaSe_2$ ($E_g = 1.68$ eV) the record efficiency is 11.9% [41]. Goto et al. [42] reported on the improvement of a $CuInS_2$ absorber by adding a $CuGaS_2$ seed layer prior to the $CuInS_2$. With the absorber formed after some sulfurization and KCN etching steps, a cell efficiency of 13.0% could be demonstrated ($V_{oc} = 690$ meV).

9.2.1.2 CIGS Co-evaporation

The CIGS co-evaporation of the pure elements copper, indium, gallium and selenium at an elevated substrate temperature of 400–700 °C is one of the first and still most successful deposition methods. The layer composition can be adjusted relatively precisely by the quantity and time of the evaporated elements Cu, In, Ga and Se. The contamination of the absorber depends essentially on the purity of the evaporated elements. Excess selenium is provided over the entire coating time. The so-called three-stage process introduced by Contreras et al. (NREL) [43] at laboratory level gained great importance in the CIGS community, as reproducible results with high efficiency could be achieved using this formulation. The basic idea was to grow the absorber via a Cu-rich phase and to finish the film with a Cu poor phase, so that the final absorber is slightly Cu-deficient. The original flux and temperature profile of the metals over time is shown in Fig. 9.5. The evaporation begins with a Cu-free first deposition phase at a moderate temperature of 300–350 °C. During the second phase the temperature increased to 500–560 °C, while the metal flux is dominated by Cu. After the Cu-rich second phase the deposition is terminated by In and Ga evaporation

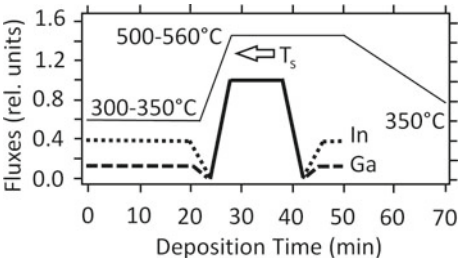

Fig. 9.5 Flux profiles of a three-stage CIGS process versus deposition time (original diagram by Contreras et al., redrawn in this publication [43])

converting the absorber back to a Cu-poor total composition. Se is present in excess in all phases, including the cooling phase.

Another finding of NREL in connection with the three-stage CIGS processing was the discovery of the beneficial effect of a double profiling structure of the absorber composition, that is, variation of the bandgap (via the Ga content) over the thickness. A simplified and schematic notch structure is shown in Fig. 9.6. The band is bent essentially within the conduction band (CB) and corresponds to a bandgap minimum in the bulk toward the front interface. The highest bandgap is implemented at the back contact and a slightly enhanced E_g at the front interface in order to reduce interface recombination of minority carriers. The minimum bandgap at the notch (E_{gn}) is necessary to absorb low energy photons and corresponds with the photogeneration gap and thus the short circuit current density (J_{sc}) [44]. It is advantageous that the enlarged gap in the space charge region (E_{gSCR}) toward the front side is correlated with the open-circuit voltage (V_{oc}). The difference between the photogeneration distance and the electrical distance ($E_{gSCR} - E_{gn} \cong 100$ meV) is therefore the performance gain resulting from the double grading.

Based on the double grading and in conjunction with the three-stage processing, many institutes [45–48] were able to produce CIGS solar cells with high efficiency. By varying and fine-tuning the bandgap profile (or Ga/(Ga + In)) highest efficiencies >20% could be demonstrated [49, 50], especially at low (<500 °C) temperature on polyimide substrates [51].

The bandgap formation (resp. Ga/(Ga + In)) and thus the multistage deposition formulations with Cu-rich phase were modified in various ways, for example, by introducing a double-notch [48], widening of the notch width, or shifting the notch forward or backward and so on. Tests with differently shaped Ga double profiles show that different shapes can be selected to achieve high efficiencies ≥20.0% (Fig. 9.7). Moreover, the achieved efficiency is not only dependent on the Ga gradient. For example, the right alkali elements must be added to the absorber in the right quantity

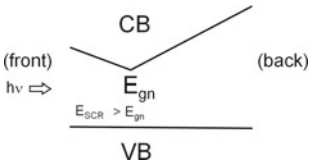

Fig. 9.6 Simplified band diagram with notch profile as introduced by NREL first (adopted from Contreras et al. [43], redrawn in this publication)

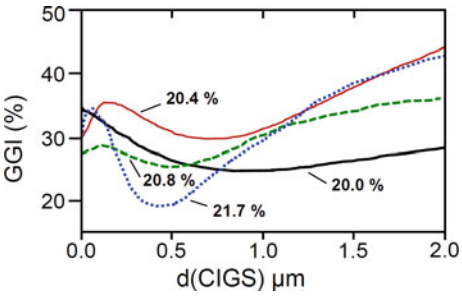

Fig. 9.7 CIGS solar cells with different double-graded Ga/(Ga + In) profiles and efficiencies ≥20% [50, 52]. A deeper notch, which is shifted further forward, seems to be advantageous (dotted curve)

and at the right time (see Sect. 9.2.1.5). Further points to consider are: the interfaces, especially the band alignment to the buffer layer, spikes or cliffs in the CB or defect states impeding the carrier transport.

Owing to the complexity of the three-stage process with regard to production, alternative multistage or single-stage evaporation processes, which are more compatible with inline processing, were pushed forward. Salomé et al. [53] compared single-stage and three-stage CIGS depositions with the same total Ga content and confirmed the typical expectations: The three-stage sample consisted of larger grains, had a 28 meV higher V_{oc}, a 0.1 mA/cm^2 higher J_{sc} and an efficiency of 17.0%. The efficient three-stage sample was 0.7% higher than that of the single-stage sample. As a result, however, the differences were surprisingly low. In addition, the notch of the three-stage sample was quite deep (too deep) in the absorber so that its full benefit could not be unfold. The single-stage device showed a quasi-linear increase in Ga content from front to back and crossed the Ga/(Ga + In) curve at a depth of 0.7 µm.

The co-evaporation process offers the possibility of a precise determination of the absorber composition and the local Ga content already during the film growth. Doping elements can also be added during the desired growth phase. Another important parameter is the temperature profile of the substrate which controls the interdiffusion of the elements. The main challenges in production are process control, acceleration of deposition rates, large-area efficiencies and process yield to reduce costs. In most cases, therefore, no real three-stage process is preferred for production, but rather various modifications from single-stage inline to multistage processes of all kinds. Development is not yet complete.

In an early development stage, the focus was not only on controlling material flows and film growth, but also on the commercial availability of suitable evaporation sources for large-area inline deposition. In the meantime, the deposition width is no longer limited by the sources, and various tools such as in situ microbalances and AAS measurements have proven themselves for flow control [54]. In continuous inline production, XRF can be used indirectly to control film composition through a loop-back mechanism in conjunction with the evaporation sources. Other advanced process control tools such as laser light scattering (LLS), Raman or time-resolved photoluminescence are discussed by Scheer et al. [55] and can also be used for all CIGS coating processes.

9.2.1.3 CIGS by Sequential Deposition and Subsequent Annealing

The sequential precursor separation and the subsequent selenization and annealing is the second main approach for the separation of CIGS absorbers on an industrial level. The driving force behind these developments was the search for a large area, compatible CIGS coating method that enables the reproducible and easily controllable growth of homogeneous layers. The sequential approach can be traced back to the early 1980s and is based on the developments of ARCO Solar, Inc. (ASI) [56], where the metallic precursors (Cu,In) have been deposited by electrodeposition. After the evaporation of selenium, the stack was annealed. Further development steps were the introduction of gallium, the conversion from galvanic deposition to sputtered precursors and the improvement of selenization through the use of gaseous H_2Se as a Se source. In the early 1990s, Siemens Central R&D group (next owner and successor of ASI) developed a rapid thermal processing (RTP) with a vaporized Se precursor and finally Siemens Solar Industries introduced an additional "sulfurization after selenization" process (SAS) [57].

This SAS processing by H_2Se and H_2S annealing of a sputtered Cu–In–Ga precursor is currently one of the most advanced deposition methods which has been continuously and very successfully optimized within the last few years by Solar Frontier K.K. (established 2006). In 2017 Solar Frontier K.K. had reached a production capacity of >1 GW on glass substrates.

Physically and with a view on process control, the selenization and sulfurization via H_2Se and H_2S is sufficient and works well [58]. The record efficiency of 22.9% [38] (cell area: 1 cm^2) achieved in 2017 by Solar Frontier is based on this technology. However, since H_2Se is highly toxic (much more than H_2S) and highly flammable, other supply methods such as Se vapor or the deposition of a Se layer on the top side have been extensively tested [59–63]. Avancis, another CIGS manufacturer on glass, starts the absorber deposition with a low temperature DC magnetron sputtered Cu–In–Ga stack with an evaporated Se layer on the top [57, 63]. The second step is a high temperature RTP treatment ($\leq$550 °C) in sulfur-containing gas, which forms the $Cu(In,Ga)(S,Se)_2$ absorber, which is very similar to the Solar Frontier process but less dangerous due to the Se supply by elemental selenium. The disadvantage of using elemental Se vapor is that Ga accumulates at the back contact and thus forms a Ga-free low bandgap absorber at the front after the RTP process. A method for overcoming this challenge was described by Schmidt et al. [64].

Both the admixture of gallium and sulfur to the $CuInSe_2$ matrix increases the bandgap. In the gaseous sulfur treatment by the RTP process, the S atoms are replaced [65] by the Se atoms near the front surface and form a kind of double or multi-stage bandgap over the absorber thickness, similar to the double sorting described above for the highly efficient co-evaporated CIGS. While the substitution of In by Ga essentially affects the conduction band (CB), the addition of sulfur mainly influences the valence band (VB) [65]. Owing to the S-conditioned widening of the bandgap to the front, the VB is pulled downwards, whereby the photogenerated holes are rejected from the front interface and thus a carrier recombination at the interface is prevented. Another beneficial effect is the increased V_{oc} compared to samples without sulfurization.

9.2.1.4 Alternatives

CIGS absorbers were produced not only by co-evaporation of the elements, but also by evaporation from binary, ternary or quaternary sources. Flash evaporation and pulsed laser deposition were investigated with the aim of improving deposition control. Some other alternative methods have also been investigated and are described in the overview of Kemell et al. [24] but will not be described here. Perhaps the third most important deposition method is the galvanic deposition of the elements or binary compounds, followed by a selenization and annealing step [66] (two-stage process). Although the single-step deposition of $CuInSe_2$ has been investigated over a long period of time [67–69], two-stage processing has finally proven superior by better control of composition and performance [70, 71]. Before the closure of NEXCIS (France) in 2015 the company had achieved an efficiency of 14.00% on 60 cm × 120 cm [70] and 17.3% [70] on small area cell level with a two-stage process. The US company Solopower [71] is able to fabricate flexible electrodeposited CIGS modules at a length of 1.5 m on metal foil with efficiencies >13%.

Other non-vacuum and solution [72] or nanoparticle-based deposition processes [73] may also have reasonable efficiencies, but the process control and absorber composition is still less mature to compete with electrodeposition, sequential sputtering and co-evaporation. Compared to vacuum-based processes, however, the material utilization in solution or galvanic processes is significantly higher. In addition, the non-vacuum investments for production are significantly lower. Since module efficiency has a direct and linear effect on production costs, its effect is often much more serious than reducing the material costs of a single layer by a few percent, as it accounts for only a part of the total module costs. The share of each layer in the total costs depends on the applied CIGS approach, the country of production, abundance of materials and many other things. For instance, according to the estimations of ISET [74] for its ink approach, the expenses for the glass substrate plus cover glass amounts to 32% of the total materials costs. A discussion of manufacturing costs of glass–glass CIGS devices is given (e.g.) by Horowitz et al. [75].

9.2.1.5 Alkali Doping

In contrast to silicon-based solar cells, alkali metals show a positive impact on the performance of CIGS solar cells. The positive effect of sodium (Na) on cell efficiency was first demonstrated in 1993 when CIGS solar cells were deposited on sodium oxide containing glass substrates [76]. The main effect of Na is a strong increase in the open-circuit voltage V_{oc} and the fill factor FF [77, 78] caused by an increase in the net acceptor concentration [79]. For flexible or Na-free substrates, an external supply of Na is necessary for high cell efficiencies. Here Na can be supplied before CIGS growth by a Na-doped Mo layer [80], by a NaF precursor layer [77], during the CIGS growth by NaF co-evaporation [81] or after the CIGS growth by NaF post-deposition treatment (PDT) [78]. The time at which Na is applied has a strong impact on the growth of the CIGS layer: Since Na hinders the interdiffusion of Ga and In, steeper

Ga gradients and smaller grains are obtained if Na is present during growth [81]. In addition, Na impedes the annihilation of stacking faults [82] so that in case of temperature-sensitive substrates such as polyimide, where the CIGS layer must be grown at low temperature, the CIGS should be first grown alkali-free and then Na should be added by a NaF-PDT process [78]. It is not yet clear whether the positive effect of Na is a grain boundary-related [83, 84] or a bulk-related [85, 86] effect. Atom probe tomography measurements (APT) revealed a strong segregation of Na at grain boundaries up to a concentration of 1.7 at.% [87]. On the other hand, Na was also found in the bulk of grains up to a concentration of 60 ppm or 2.6×10^{18} cm^{-3} by APT [87] which is much higher than the typical doping concentration of $1 \times 10^{15} - 1 \times 10^{16}$ cm^{-3} in Na-doped CIGS layers. Na was thus able to passivate the grain boundaries and dope the bulk of CIGS layers. The influence of the heavier alkali elements potassium (K) and cesium (Cs) on the cell performance was investigated as early as 1997, but was small compared to Na [88] and not the subject of research. In 2012, potassium was re-discovered as an efficiency booster.

Within the framework of an EU project (hipoCIGS), R. Wuerz (ZSW) observed that CIGS solar cells deposited on enamelled steel showed higher efficiencies than on soda-lime glass (SLG), whereas SLG was previously considered the substrate with the highest efficiency potential. Potassium was found as the reason for the efficiency increase, as the enamel layer provided much more potassium than the SLG substrate, while the supply of Na was comparable for both substrates. A detailed analysis of the subsequent incorporation of potassium via a KF-PDT treatment was first performed by Chirilă et al. (EMPA) [51] in 2013. At the same time and independently, the influence of KF-PDT on the absorber properties was investigated at ZSW [89].

KF-PDT increased cell efficiency in a similar way to NaF-PDT [89]. The application of KF-PDT on a Na-doped layer resulted in a record efficiency of 20.4% on flexible polyimide film [51], which is still (2018) the highest efficiency for a thin film solar cell on a flexible substrate. When applying the KF-PDT on Na-doped CIGS layers on SLG, the cell efficiency was further ramped up to 20.8% [90], 21.0% [91] and 22.3% [92]. The KF-PDT is also effective for sulfur-containing absorbers based on Cu(In,Ga)(S,Se)$_2$ [92]. It has further improved the efficiency of the modules in a full-scale industrial production process [93]. The main effect of the KF-PDT is an increase in the open-circuit voltage V_{oc} and fill factor. This effect can be explained by various experimental findings.

The potassium treatment:

(1) leads to a strong depletion of copper (Cu) at the surface of the CIGS layer [51] and to the formation of K–In–Se surface species [94].
(2) leads to a widening of the surface bandgap of the CIGS layer to 2.52 eV [95], which corresponds well to the bandgap of $KInSe_2$ with $E_g = 2.68$ eV [96]. Hence, formation of $KInSe_2$ at the surface of the CIGS layer due to the KF-PDT seems to be likely.
(3) reduces surface recombination [97, 98], due to the changed surface composition
(4) allows a reduction of the CdS layer thickness without loss at fill factor [51] and thus increases quantum efficiency in the UV range

(5) enhances the charge carrier density of the CIGS layer [99]
(6) increases carrier lifetime [99, 100]
(7) increases the photoluminescence intensity [99], indicating reduced non-radiative recombination
(8) reduces band fluctuations [100].

A combined NaF- and KF-PDT proved to be more effective in increasing cell efficiency than a single NaF or KF-PDT [97].

In the meantime, PDT has also been successfully extended to the heavier alkali elements Rb and Cs. Efficiency was even increased to 22.6% [37] and 22.9% [38], respectively, through RbF and CsF PDT. APT measurements showed that Rb strongly segregates at grain boundaries (GB) and that Rb pushes Na and K out of GBs [101]. Further, nanoXRF (X-ray fluorescence) measurements combined with electron back scatter diffraction (EBSD) have demonstrated, that Rb only segregates at random GBs, but not at Σ3 GBs [102]. Time-resolved photoluminescence measurements revealed a strong increase of carrier lifetime due to the RbF PDT [103]. Furthermore, the formation of an $RbInSe_2$ interfacial layer at the CdS/CIGS interface was supposed to be the reason for a strong increase in V_{oc} by the RbF-PDT [104]. A combination of light (Na) and heavy (Rb, Cs) alkali metals is therefore necessary to achieve maximum cell efficiencies.

9.2.2 Back and Front Contact

9.2.2.1 Mo Back Contact

Molybdenum has been identified as one of the most suitable back contact materials since the beginning of the development of CI(G)S solar cells. It meets all the required specifications—such as sufficient stability in selenium and sulfur atmosphere, relatively stable and inert at high temperatures, formation of a low-resistance contact to the absorber [105], virtually no reactions with Cu, In, Ga at CIGS growth conditions and no diffusion of Mo into the absorber. Furthermore, the high material hardness enables mechanical scribing (second and third scribe) on glass substrates for monolithic interconnection without impairing the glass matrix. On the other hand, the Mo layer is permeable for diffusion of sodium from the soda-lime glass (SLG) into the growing CI(G)S. Thus, Na doping of the absorber can be controlled at least partially by the substrate temperature and the Mo properties.

Molybdenum has a relatively low coefficient of linear thermal expansion (CTE_{Mo}: 4.8–5.9 × 10^{-6} K^{-1}) compared to the soda-lime glass substrate (CTE_{SLG}: ≈9 × 10^{-6} K^{-1}) or the absorber. The experimentally determined linear CTE of $CuInSe_2$ [106] at $T = 300$ K according to the work of Paszkowicz et al. is $CTE_L = 8.62 \times 10^{-6}\ K^{-1}$. Along the a-axis of the chalcopyrite crystal the thermal expansion coefficient is 9.15 × 10^{-6} K^{-1}, and along the c-axis it is 7.61 × 10^{-6} K^{-1}. The strong difference in CTE can lead to adhesion problems during the high-temperature deposition process of the

CIGS layer or bending of the glass substrate due to stresses. The Mo back contact is normally deposited by e-gun evaporation or sputtering. Especially the DC magnetron sputtering from planar or rotatable targets is the method of choice today due to its excellent suitability for homogeneous industrial large-area deposition. The intrinsic properties of the Mo layer can be modified via the sputtering parameters, especially the gas pressure [107]. Low-pressure sputtering leads to denser material with high conductivity and compressive stress, while comparatively high-pressure sputtering leads to tensile stress, lower density and low conductivity. These properties can be used to adapt the Mo layer to the respective substrate, for example, to ensure sufficient film adhesion without cracks or delamination or to ensure the correct amount of Na diffusion through back contact, that is, to adjust the barrier properties. Often a Mo bilayer is deposited, starting with a more flexible and less dense layer to compensate for CTE mismatch between the substrate and the back contact, improving adhesion to the substrate, followed by a denser, that is at lower pressure deposited layer of high conductivity. In principle, the back contact can be adapted to all common substrates such as soda-lime glass, stainless steel and polyimide. If required, an additional thin adhesive layer can be sputtered under the molybdenum.

Another important property of molybdenum is the formation of a thin (a few nanometers up to some tens of nanometers) $MoSe_2$ layer depending on the selenium exposure time and the substrate temperature [108, 109]. The $MoSe_2$ layer is responsible for the formation of an ohmic or quasi-ohmic back contact [110]. Without $MoSe_2$ layer a Schottky contact with a barrier height of about 0.87 eV [111] is created which impedes the CIGS/Mo hole flux [112]. It has a direct bandgap of 1.35–1.55 eV [110, 113] and an indirect bandgap of 1.06–1.19 eV [114–116]. The details of the CIGS/$MoSe_2$/Mo band alignment are still the subject of discussions. We assume that the CIGS/$MoSe_2$ contact is an ohmic and the $MoSe_2$/Mo transition is a Schottky contact to holes. Since the $MoSe_2$ layer thickness is very thin, however, tunneling of holes is possible and the measured current–voltage behavior is ohmic [112, 117] (see also Fig. 9.2). Therefore, a thin $MoSe_2$ layer is very important to achieve highly efficient CIGS devices that have been proven not only for co-evaporated absorbers but also for the industrialized sequential sputtering plus selenization process (SAS) [117]. Even with conductive alternative ZnO-based back contacts, a thin $MoSe_2$ layer improves device performance and forms a quasi-ohmic contact [118].

A molybdenum back contact works at both low and high CIGS deposition temperatures (400 °C < T < 750 °C).

Orgassa et al. [119] investigated a variety of electron beam evaporated alternative back contact metals such as tungsten (W), molybdenum (Mo), chromium (Cr), tantalum (Ta), niobium (Nb), vanadium (V), titanium (Ti) and manganese (Mn) for CIGS solar cells on soda-lime glass. Best cell efficiencies obtained with evaporated single-stage CIGS and substrate temperature of 550 °C were 14.2% on W, 13.8% on Mo, 13.3% on Ta, 10% on Nb, 5.9% on Cr and 3.4% on V. While almost no Se reactions were observed for W, Mo, Ta and Nb, titanium and manganese layers were completely consumed by chemical reactions. The authors also had in mind to find a back contact of higher reflectivity than Mo, which is one of the main drawbacks of a Mo back contact layer. A highly reflective back contact would allow the absorber

thickness to be reduced to 0.5–1 μm by multiple reflections. From that perspective Ta and Nb were superior to Mo or W, at least at wavelengths $\lambda > 700$ nm. The search for suitable highly reflective back contacts is still ongoing and various approaches have been described in the literature based on the sputtering of a thin ZrN [120, 121] or an Al/InZnO (IZO) layer onto a standard Mo contact. Bissig et al. [122] achieved with such a Mo(500 nm)/Al(100 nm)/InZnO(260 nm)/Mo(2.6 nm) back contact with improved reflectivity and high-quality three-stage CIGS an improvement in efficiency from 19.5% (ref.) to 19.9%.

9.2.2.2 Transparent Front Contact

The transparent, highly conductive front contact is probably the least CIGS-specific layer. Therefore, this topic is only briefly addressed and the reader is referred to the extensive literature.

Usually aluminum-doped ZnO [50, 51, 63] (ZnO:Al or AZO) is deposited by dc magnetron sputtering as a wide bandgap window layer (undoped ZnO: $E_g = 3.3$ eV [123], E_g increases with doping), after a highly resistive undoped ZnO (i-ZnO) layer, which is deposited by rf sputtering. We prefer here to discuss the thin (approximately 50 nm) i-ZnO layer in conjunction with the buffer (see Sect. 9.2.3.2).

Owing to its low carrier mobility of $\leq 30\ cm^2/(Vs)$ AZO has to be heavily doped so that the Fermi level is raised up to or above the conduction band edge to achieve sufficiently high conductivity. However, due to optical losses with increased wavelength in the NIR/IR region resulting from undesired free carrier absorption, a compromise between conductivity and transparency is sought for monolithically connected modules. The thickness to be selected depends on the width of the cell stripes (a few mm) and is about 300–1000 nm for modules without an additional metal grid. The use of boron-doped ZnO (ZnO:B or BZO), which is characterized by better optoelectronic properties with a lower degree of doping, has also proven to be an industrial alternative. This transparent conductive oxide is widely used by [58] Solar Frontier applying the soft MOCVD method for deposition.

In the search for more transparent, conductive and, in terms of degradation by moisture, more stable n-conducting window layers, numerous other potentially suitable TCOs were investigated, such as ITO [124] (In_2O_3:Sn), IOH [125] (In_2O_3:H), Al-doped ZMO [126] ($Zn_{1-x}Mg_xO$:Al, $x \leq 0.1$), FTO (F-doped SnO_2 [127]) or a-IZO [128] (amorphous InZnO) . For example, ITO or IZO have proven to be much more stable than ZnO in the damp-heat test (1000 h at 85 °C and 85% rel. hum.) [127, 128]. The significantly higher costs can be partially compensated by the higher conductivity and thus lower layer thickness. Another promising TCO is IOH which is characterized by high electron mobility and—like ITO and IZO—can be produced with an amorphous structure [125].

Especially with regard to further efficiency increases, the full theoretical potential of the TCO must be exploited as well. Interesting additional options result, for example, from the combination of monolithic cell connection and the use of a metal grid

[93]. For instance, the TCO thickness can be reduced while simultaneously increasing transmittance and lateral conductivity. With the help of simulations, the optimum compromise between dead surface, light incidence and electrical conductivity can be determined and thus the module efficiency is optimized [93].

9.2.3 Buffer

9.2.3.1 Main Buffer Approaches

Based on the research in CdS solar cells in the 1960s [129], this n-type material was already well known and a potential and within a short time successfully working counterpart for the chalcopyrite absorber to build the p-n junction [3]. In the course of prospecting new ways of efficiency improvement and for environmental aspects, alternative buffer materials gained more interest toward turn of the century. CIGS solar modules with buffer layers based on zinc or indium chalcogenides entered the industrial production in recent years.

The electronic properties of the heterojunction are essential for the device performance. The exact role of the buffer layer has been studied for decades but not yet fully understood. However, thanks to the intensive investigations on various buffer materials, the progress in understanding the mechanisms at the heterojunction took many steps forward.

(i) **CdS buffer**

At the initial stage of development of $CuInSe_2$ solar cells, evaporated CdS, doped with indium (CdS:In), with a thickness of 1–6 μm was used as a negatively conducting front electrode first on $CuInSe_2$ single crystals [2] and later on $CuInSe_2$ thin films [4]. Optionally, ZnS was admixed forming CdZnS to increase the bandgap of the front electrode [130].

This first device structure was successively modified by replacing the thick CdS front contact with a significantly more transparent window layer consisting of a thin CdS buffer and a zinc oxide double layer structure, which in turn consists of a thin undoped high-resistance layer and a thicker doped conductive layer [131, 132]. Optionally, CdZnS was applied instead of the pure CdS buffer [131]. The choice of doping element for ZnO was influenced to some extent on the deposition method, that is, B doping for chemical vapor deposition (CVD) and Al doping for magnetron sputtering.

A solution growth process, known as chemical bath deposition (CBD), was established for the deposition of the CdS buffer layer [133, 134]. The major advantage of the CBD process is the possibility to grow very thin and dense layers with excellent step coverage even on very rough CIGS surfaces (Fig. 9.8).

Furthermore, the interaction of the solution chemistry with the CIGS surface in the initial stage of CdS growth also leads to cleaning and mixing effects on the CIGS

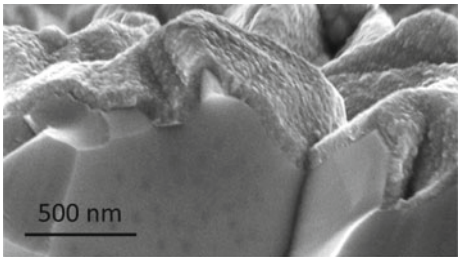

Fig. 9.8 SEM image of a CdS(top layer)/CIGS(bottom layer) cross-section demonstrating the excellent covering capability of CBD CdS

surface, which are assumed to have a positive effect on the p/n junction formation [135, 136].

Over the last three decades, CdS/i-ZnO/ZnO:Al has been one of the most prominent window layer structures in CIGS solar cells and continues to dominate parts of the CIGS technology enabling the highest conversion efficiencies compared to other alternative structures. Important milestones in the development of the CIGS technology such as the incorporation of Ga in $CuInSe_2$, process development (three-stage co-evaporation, sequential processing), and doping with alkali metals were accompanied with CBD CdS as buffer material [137, 138].

New trends in the CIGS technology, which are mainly influenced by the alkali post-deposition treatment (PDT), are a further reduction of CBD CdS thickness [51] and the replacement of the i-ZnO layer by other more transparent materials such as i-ZnMgO [139] or TiO_2 [140]. However, a reduction of the CdS thickness well below 10 nm can be accompanied by incomplete coverage of the rough CIGS surface. Sparse CdS growth on the CIGS surface at the very first stage of the CBD process is influenced by the different CIGS grain orientation [141]. An improvement of the initial CdS growth could be demonstrated after modification of the CIGS surface composition with alkali metals [142] or after oxide formation by annealing the CIGS in air [143]. All these developments are aimed at reducing parasitic absorption in the blue wavelength region without any V_{OC} loss and thus increasing the power conversion efficiency.

A schematic representation of the device structure evolution correlated with the quantum efficiency improvement is shown in Figs. 9.9 and 9.10.

(ii) **Alternative buffer layers**

The motivation to replace CdS with other materials was driven by two aspects:

(a) The potential for increasing the short current density by avoiding parasitic absorption in the blue wavelength range between 300 and 550 nm.
(b) Compliance with the RoHS[1] directives for the reduction of Cd in electronic devices.

[1]RoHS: Acronym for **R**estriction **o**n the use of certain **H**azardous **S**ubstances.

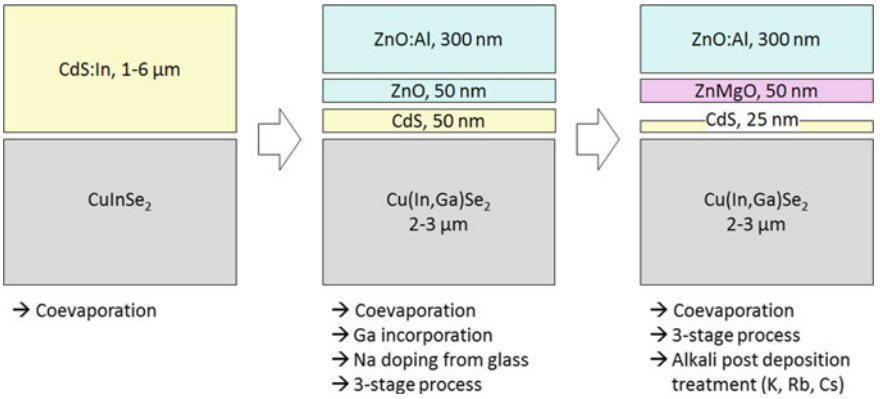

Fig. 9.9 Optimization steps of the interface of CIGS-based solar cells including a CdS buffer

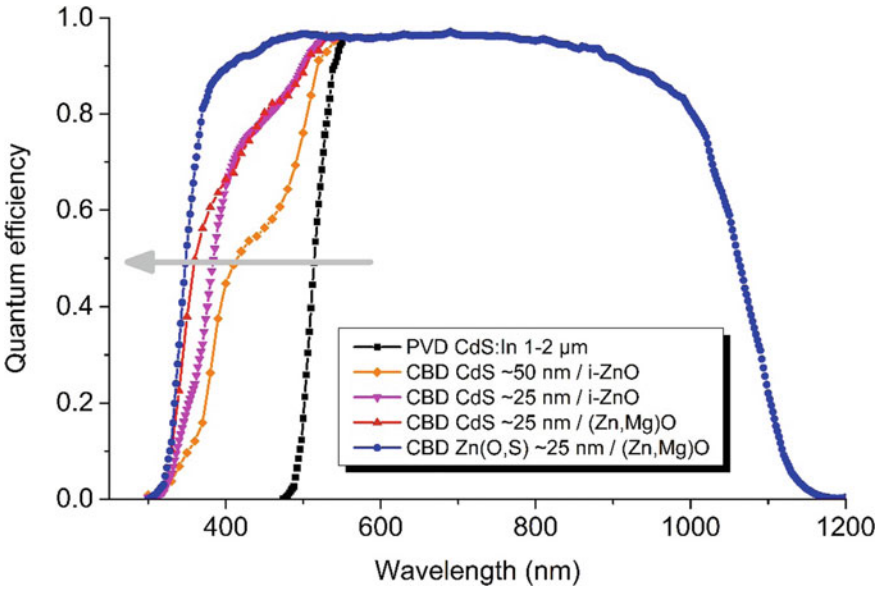

Fig. 9.10 The effect of reduction of parasitic light absorption in the blue wavelength region by reducing the CdS thickness as demonstrated by external quantum efficiencies in the wavelength region between 300 and 550 nm of different CIGS-based cells [131, 144, 145] according to the structures in Fig. 9.9. The potential for maximum gain in spectral response is demonstrated with an internal quantum efficiency of a CdS-free cell with Zn(O,S)/(Zn,Mg)O buffer

Over the last two decades, various more transparent and environmentally friendly materials have been tested than CdS. Most of the works dealt with chalcogenides based on indium or zinc, such as Zn(S,O), ZnSe, $ZnInSe_x$, (Zn,Mg)O, In_2S_3 and In_2Se_3. An elaborate review of the buffer layer development is provided by Naghavi et al. [146].

In addition to the CBD process used for CdS, a large number of other deposition methods for the various Cd-free buffer materials, such as atomic layer deposition (ALD), metal organic vapor deposition (MOCVD), sputtering, ion layer gas reaction (ILGAR), thermal evaporation, electrodeposition (ED), and so on, were investigated. From an industrial perspective, gas phase processes attract more attention because they offer the advantage of improved process integrity in the almost vacuum-dominated CIGS module production lines [147]. However, the characteristics of a material deposited by different methods can have a wide variety [148] and must be carefully adapted to the specific absorber material applied. Pre- or post-deposition treatments such as annealing or light-soaking may be necessary [149, 150]. Mughal et al. [151] show an overview about champion cell efficiencies for different materials and deposition methods.

As shown in Fig. 9.10 using a CIGS cell with CBD-Zn(S,O) buffer as an example, a lower parasitic absorption in the blue wavelength range can also offer a gain in quantum efficiency even in comparison with improved devices with a thinner CdS buffer layer. Nevertheless, it can be observed that a gain in short-circuit current is often accompanied by losses in the open-circuit voltage [152].

The performance of Cd-free cells is significantly influenced by the absorber material used and matters related thereto such as band-alignment, surface composition and interface chemistry. As described in Sects. 9.2.1.2 and 9.2.1.3 co-evaporated absorbers have a similar bandgap grading compared to sequentially prepared absorbers by selenization/sulfurization of metallic stacks but they are realized by different composition gradients resulting in different chemical surface compositions. The surface bandgap of co-evaporated CIGS depends on the Ga concentration while the surface bandgap of sequentially prepared absorbers depend on the sulfur concentration. Thus, the band alignment between absorber and buffer is affected in different ways. An increased Ga surface concentration results in an increased conduction band-offset (CBO) but an increased S surface concentration results in an increased valence band-offset (VBO) [150].

So far, Cd-free buffers have not been industrially established in co-evaporated CIGS-based modules. Realized cell peak efficiencies are comparable, but statistically below those of the reference devices with CdS. The reason for this is losses in the open-circuit voltage, which reverse short-circuit current gains, combined with a reduced reproducibility of the device properties. Progress in reducing or compensating V_{oc} loss for cells with Zn(O,S) buffer has been demonstrated by CIGS post-deposition treatment with heavier alkali metals. A certified small-area cell efficiency of 21% could be realized [153].

For sequentially processed sulfur-containing $CuIn_{1-x}Ga_xSe_{2-y}S_y$ (CIGSS) modules, Cd-free materials such as CBD-Zn(S,O) and thermally evaporated In_2S_3 are already well-established in industrial production. The company Solar Frontier

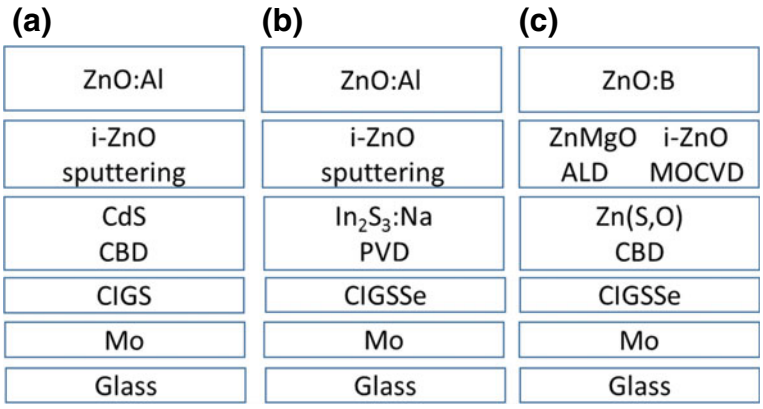

Fig. 9.11 Scheme of CIGS cell stacks on glass/Mo substrates established in the industry with CdS/i-ZnO buffer system and alternative buffer layers: **a** co-evaporation—Solibro GmbH [158], **b** sequential—Avancis GmbH [147], **c** sequential—Solar Frontier [58]

demonstrated a 19.2% efficient 30 × 30 cm^2 record mini-module and a small-area cell efficiency of 22.0% with CBD-Zn(S,O) buffer layer [58, 154]. Using In_xS_y as buffer the company AVANCIS GmbH realized a 17.9% 30 × 30 cm^2 module [155].

For the In_2S_3 buffer aspects such as the elementary interdiffusion between absorber and buffer layer during buffer deposition or in the following process steps significantly influence the chemical and electrical properties of the interface, instancing copper and sodium diffusion. Barreau [156] gives an overview of earlier investigations on the indium sulfide buffer layer and the influence of the incorporation of a third atom on its behavior on co-evaporated CIGS devices. Avancis GmbH controls the sodium content and the resulting electronic properties of their sequentially processed solar modules by direct deposition of a PVD-In_2S_3:Na buffer layer [157].

Well-established device structures for the production of commercial CIGS modules are shown in Fig. 9.11.

9.2.3.2 The i-ZnO Layer

Historically, the undoped ZnO layer is correlated with the window layer, especially since both layers, i-ZnO and ZnO:Al, are usually deposited by sputtering processes. The thin i-ZnO layer has no direct influence on the electrical performance of solar cells, but has a positive effect on module stability and shunt reduction [159].

Within the framework of buffer development, the n-junction of the buffer system became interesting and important again, so that both layers can also be considered as a double buffer layer. Alternative materials such as ZnMgO were explored [160]. For Zn(S,O) buffer layers the replacement of i-ZnO by ZnMgO shows a much more favorable electronic structure [161].

9.2.4 Substrate-Related Issues

CIGS thin film solar cells are only a few micrometer thick, and deposited as standard to several millimeter thick float glass substrates. Since float glass is produced in large quantities for the window industry, it can be produced very cost-effectively. A theoretically possible thin, light and flexible PV generator is thus transformed into a relatively heavy and fragile module, especially as the front encapsulation usually also consists of a glass plate. Hence, to exploit the full potential of CIGS technology, roll-to-roll production (R2R) of light and flexible devices should be aimed for. Numerous metallic and non-metallic foils have been successfully tested [162], but the variety of possible carrier foils is rather limited with regard to an industrial application in which economic aspects play an important role.

The most important requirements for a flexible substrate are:

- High temperature resistance in vacuum and selenium atmosphere: wider range of deposition parameters
- no outgassing at high temperatures in vacuum and no water absorption: no contamination of the absorber
- suitable coefficient of thermal expansion CTE in comparison to CIGS: higher film adhesion
- smooth, hard and reproducible surface: simplified scribing via laser or mechanical tool, less shunts, higher yield
- electrically insulating (advantageous): monolithic interconnection possible
- lightweight, flexible and low cost foils available: improved competitiveness.

Since none of the commercially available films meet all criteria, compromises still have to be made, depending on the application. Owing to the low thickness of the active layers and the large surface-to-volume ratio, surface roughness and diffusion processes play a large and often essential role. For example, a change of carrier material can require a considerable re-optimization of the individual PV layers. Especially important is the back contact, which often has to be readapted in order to ensure good layer adhesion without cracking.

The thermal conductivity and heat capacity of the film also influences layer growth and layer quality, not only of the absorber.

The optimal parameters for CIGS deposition and the type of doping depend strongly on the substrate temperature applied, so that an absorber optimized at high substrate temperatures cannot be deposited with the same parameters at low temperatures. High CIGS substrate temperatures ($T \geq 600$ °C) have the advantage that the desired CIGS crystallites are formed faster, which has an effect on maximum web speed and thus on production costs. Lower substrate temperatures ($T \leq 450$ °C), on the other hand, have the advantage that undesired diffusion processes are less pronounced and the CIGS composition can be better controlled.

Other aspects that are strongly substrate-correlated are the alkali doping of the CIGS absorber and the monolithic or non-monolithic series connection of cells. If the end product is to be flexible or lightweight, glass encapsulation must be dispensed

with, which is less a technical than a cost issue, especially as both the Mo back contact and the ZnO front contact are very sensitive to moisture and must be well protected.

Metal foils

Metal foils are ideal for R2R coating in vacuum. They do not deform or tear even under relatively high tensile stress and temperatures. Due to the production-related rolling process, they are relatively rough compared to glass or polyimide. The different roughness of each individual batch, which depends on the rollers used, can pose a certain challenge. An even greater challenge is the cost-effective electrical insulation of the metal foil. Technically, however, this is now possible and a cost-effective solution can be expected in the future. The most important metal substrate is currently ferritic stainless steel foil. Normally, this must be provided with a diffusion barrier [163–165] against iron to prevent contamination of the absorber. Within the framework of technical progress, the use of low-cost structural steel would also be conceivable in the foreseeable future.

All commercial CIGS companies that work with metal foils currently use non-insulated stainless steel foils such as Miasolé (CIGS sputtering and selenization), Global Solar Energy (CIGS co-evaporation) or Solopower (electrodeposition).

Electrically insulating films

Thin glass is currently no alternative due to its high costs/m^2, although it is available in a thickness <50 μm. There is not much choice of polymers either: The only material currently on the market that can withstand temperatures up to 450 °C is polyimide. Polyimide is available from a thickness of 7.5 μm. The reasons for choosing polyimide film for R2R production are that PI is electrically insulating and lightweight and has a well reproducible and relatively smooth surface. At high temperatures, polyimide films do not melt but begin to decompose, making them increasingly brittle. The films can be heated up to 600 °C for a short time without tearing. Depending on the manufacturer and storage prior to coating, polyimide films can absorb a few percent water, which can then degas during the CIGS process at 400–450 °C and affect the growing CIGS layer. To prevent this, the film is usually degassed and pretreated prior to the coating process.

The two companies Ascent Solar and Flisom deposit CIGS on polyimide film by low temperature co-evaporation using the R2R process.

A detailed discussion of substrate-related issues and the fabrication of flexible CIGS devices can be found elsewhere [166–168].

9.2.5 Series Interconnection of Cells

9.2.5.1 Monolithic Interconnection

The monolithic interconnection of solar cells, that is the series interconnection of PV cells via at least three pattering steps between the deposition of functional layers, is a special unique feature of thin film solar cells [169]. As a minimum requirement, the

substrate has to be electrically insulating, such as glass, polyimide or insulated metal foil. Monolithic interconnection means that on a single sheet of substrate several solar cells are serially connected by reasonable overlapping of parts of the front and back contact of neighbored cells. The classic and simplest way to do this is via three patterning steps (P1, P2 and P3) performed after the back contact, semiconductors and conductive window deposition.

The sequential deposition of the individual layers of thin film solar cells allows dividing the module area into individual cells and monolithically interconnect these cells in series without any additional interconnection elements like wires, metal grids or ribbons, for instance. Thus, the high current density parallel to the surface, which results from the large area of the thin film modules can be significantly reduced by a factor which correlates directly with the number of subcells. Thus, the application of a metallic grid, which collects the current on, for example, silicon wafer cells, is dispensable. In parallel, the voltage of a given PV active area can be increased from typically less than one volt (one cell) to some tens or even 100 V depending on the number of solar cells [170].

The basic sequence of the patterning steps for the interconnection outlined in Fig. 9.12 is initiated with the separation of the back contact layer into galvanic isolated stripes a few mm wide, typically around 5 mm, which define the individual cells and the width that the cell current must bridge (P1). After deposition of the absorber and possibly further layers such as the CdS buffer and the i-ZnO, a second scribe (P2) next to the P1 groove removes all layers except the back contact and thus creates contact opening for the subsequent conductive connection between the back contact and the AZO front contact of adjacent solar cells.

Finally, a third line (P3) is necessary to galvanically separate the cell stripes which have been short-circuited so far by the AZO layer (Fig. 9.12).

The scribing processes P1 and P3 have to be optimized for maximum isolation resistance. The required values for P1 and P3 are a minimum of about 0.1 MΩ cm. The P2 scribe must be optimized for minimum contact resistance. Here in literature, specific interconnect resistances in the range of 0.3–0.8 Ω cm for mechanically scribed contacts and 0.1–0.2 Ω cm for laser structured contacts have been reported [171].

The distance from P1 to P3 in lateral direction forms a photovoltaic inactive zone and has to be minimized to minimize aperture losses [172]. Mechanical scribing leads to an about 300 μm wide dead area. The first reported all-laser structuring

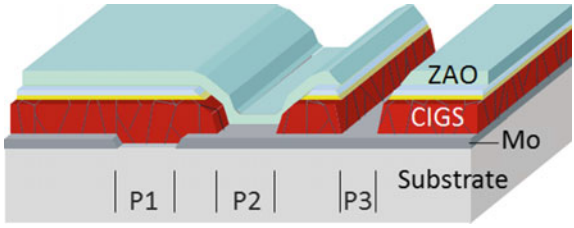

Fig. 9.12 Schematic drawing illustrating the monolithic series interconnection

could reduce the dead area to 190 μm, which seems to be a good value for a reliable process in production. The reported minimum value lies at 70 μm, which is difficult to maintain in production [173].

Completely different methods can be used to implement the individual patterning steps. Some possible techniques for performing P1–P3 are:

- chemical etching by means of lithographic masks
- shingling: cutting of CIGS material on flexible substrates and connecting back and front contact with a metal tape [174, 175]
- mechanical scribing with needles
- selective structuring or lift-off by localized energy input, in particular pulsed laser radiation, but also more exotic other means such as electron beams.

There are also other methods such as the local application of an anti-sticking layer below a functional layer, which supports the detachment or even totally prevents the layer deposition on this area.

Chemical etching is suitable for all three structuring steps of CIGS modules. However, the need to apply and remove masks for photolithography increases the number of process steps and thus the effort and costs, as does the alternative use of printing technology.

Nowadays, industry standard is using selective picosecond laser structuring for P1 and P2, and mechanical [176] or laser scribing for P3 [177, 178].

Laser scribing

P1: Laser ablation is the preferred method for the patterning of the back contact (P1). In CIGS modules this layer usually is molybdenum with a thickness of 200–1000 nm. Since Mo is normally deposited on a glass substrate which has a much lower melting point, the laser power has to be applied via short or ultrashort pulses in the nanosecond or picosecond range in order to evaporate the highly absorbing metal layer before too much heat has flowed into the substrate [179] (Fig. 9.13).

The absorption length of Mo at commercial available laser green (523 nm) and infrared (1064 nm) lies in a range of 10–20 nm [180]. Heat diffusion lengths for pulse durations of 10 ps and 10 ns lie at about 50 nm and 1.5 μm, respectively [181], leading to a heat-affected zone in the same range. Selective laser structuring can be performed from the film side and the substrate side in a single pulse process [182].

Owing to the long heat diffusion length, short pulses in the nanosecond range heat the Mo film homogenously, remove the film mainly in the liquid phase and support the removal process through the formation of thermomechanical forces that lift off the layer from the substrate. The removal fluence threshold lies at about 1–2 J/cm^2 for about 500 nm thick Mo films [181, 183]. The nanosecond process always leads to unwanted cracks and burr in the film and substrate or barrier layer (e.g. SiNx) melting or damage (see Fig. 9.13, left side).

Ultrashort pulses in the picosecond or femtosecond range lead to a confined energy situation, where a strong pressure wave is generated in the laser-irradiated interface [184]. The laser pulse is heating a relatively thin contact layer on a thick, stiff substrate (e.g. 3 mm thick glass). If the laser is irradiated from the film side, the ablation threshold is at about 1.7 J/cm^2, the fluence needed for a removal of the complete film

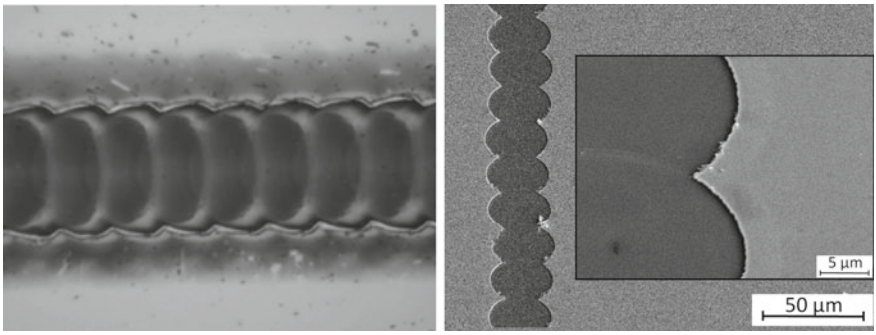

Fig. 9.13 P1 groove performed by use of a nanosecond laser (left) and a picosecond laser with 10.2 ps pulse duration from the substrate side (right). The nanosecond laser leads to rims at the edge of the ablated Mo-film, which are comparable to the thickness of the Mo layer of about 500 nm. Additionally, microcracks and partial material lift-offs are produced in a range of 5 µm to the sides of the groove. The substrate glass shows faint melting zones in the pulse overlapping areas. The edges of the scribe have a molten appearance and are paralleled by darker zones which are covered by condensed glass vapor. The picosecond laser process is free from thermal damages

lies between 5 and 10 J/cm^2 [170, 182]. The film removal is accomplished by direct laser ablation, evaporation of a surface layer, thermal expansion and pressure wave assisted, photo-mechanical ablation of the Mo film. In this way melting and damage of the film and substrate can be almost completely avoided [185].

The confined energy situation can be further assisted by passing the laser beam through the glass substrate onto the backside of the Mo layer and thus directly heating the interface. In a so-called direct-induced ablation, the Mo film is lifted-off by an ultrafast melting of an about 50 nm thick interface layer, heat expansion and subsequent pressure wave generation, which causes the layer to be directed away from the substrate after about 100 ps. The conservation of this momentum pulls on the layer with a force which can become high enough to overcome the adhesion and the layer is tearing off after about 10 ns. The film removal is performed by punching out intact film disks leaving behind very well-defined circular edges without thermal damage, melting and debris [182, 185, 186] (see Fig. 9.13, right side).

For these reasons, the application of picosecond laser pulses via the glass side (i.e. the back side) is considered to be the preferred P1 method with the best results. Additionally, according to Heise et al., the threshold fluence of the laser is 0.1 J/cm^2, which is more than one order of magnitude smaller compared to P1 laser patterning from the front side [178]. The process window lies between about 0.5 and 1 J/cm^2.

Nevertheless, in case of opaque substrates, P1 patterning from the back is no option. P1 laser scribing has been carried out with nanosecond (ns) and picosecond (ps) lasers of green (532 nm) or infrared (1064 nm) wavelength and a pulse overlap of $\geq$30%. Thus, ultrashort pulse lasers (femtosecond or picosecond range) are very advantageous, but not mandatory. The wavelength plays only a minor role [187]. In order to minimize damage to the substrate and to obtain the smoothest possible, the pulse duration should lie in the ultrafast domain and the energy should be kept as low

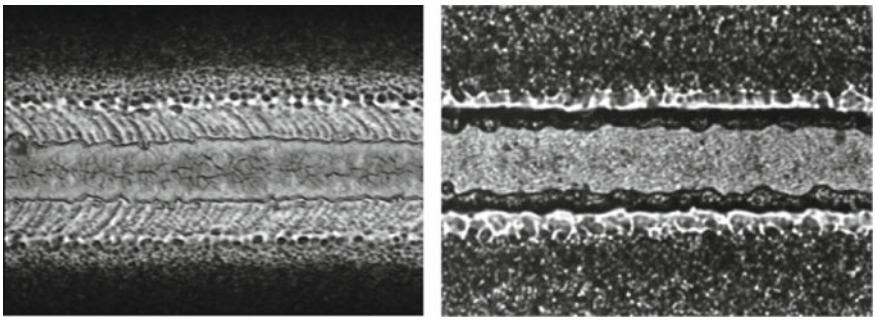

Fig. 9.14 Left: Removal of CIGS by a pulsed nanosecond laser (P2). Owing to excess energy in the centre of the trace, the Mo back contact shows cracks. Right: The picosecond laser process avoids microcracks in the Mo and leads to a lower contact resistance

as possible. With average powers of 5–10 W line scribing speeds of 10 m/s and more can be realized from the substrate side, while powers of 50–100 W are necessary to reach the same scribing speeds from the film side.

P2: The removal of the absorber layer for the contact opening step P2 can be done with multiple highly overlapping pulses with direct laser ablation (Fig. 9.14). As with P1, thin parts of the absorber material can be vaporized with short and ultrashort pulses [170]. However, the energy input has to be carefully controlled. If the absorber is incompletely removed, an increased contact resistance results. On the contrary, if the fluence is too high, the back contact will be damaged. Since the back contact is usually significantly thinner than the absorber, fluctuations in the absorber thickness can quickly lead to excess energy being capable of melting or cracking the back contact (Fig. 9.14, left).

The ablation threshold of a single 10 ps laser pulse for the absorber lies at fluence of 0.1–0.2 J/cm^2. Only a few 10 nm thick part of the absorber is removed at the threshold. For a reliable structuring process of 2–3 μm thick absorber, the fluence and the average number of pulses per position are increased to 1–2 J/cm^2 and about 10–30 pulses per position (Fig. 9.14, right). The short thermal diffusion length of the picosecond pulse limits the thermal damage and avoids microcracks. In addition, the precise depth control of the picosecond laser process enables a removal of a weakly conducting MoSe or MoS layer (remaining from the absorber formation) without damaging the Mo film, thus the contact resistance of the later deposited ZnO film can be reduced to about 50% compared to mechanical scribing [170]. A formation of ripples, so-called laser-induced periodic surface structures (LIPSS [188]) at the Mo surface is observed and might have also a positive impact on lowering the contact resistance.

Another variation of the P2 laser processing is the CIGS decomposition due to selective evaporation of the selenium. The metallized absorber does not need to be completely removed due to its increased conductivity compared to the original composition. However, a noticeable additional contact resistance remains [171, 189].

P2 can even be performed after deposition of the AZO layer by de-selenization of the CIGS absorber with a so-called P2 microwelding; however, it is challenging to achieve a sufficiently low contact resistance [190]. The potential advantage of this method is that P2 and P3 can be done simultaneously, for example, by two different lasers or P2 by laser and P3 mechanically. Hence, one alignment and process interruption step could be avoided in production [191].

To remove CIGS by lift-off instead of CIGS direct ablation by heating and evaporation, Moser et al. [192] and Burn et al. [187] suggested using a long wavelength laser of 1550 nm that is not absorbed by the absorber but by the underlying Mo.

P2 can be performed by a wide range of methods and lasers, such as continuous wave, pulsed, nanosecond, picosecond, long and short wavelengths. Nevertheless, the most reliable and CIGS process-tolerant laser parameters that can be used in production seems to be the multipulse direct ablation with picosecond lasers due to avoiding of unwanted microcracks and superior contact properties [176–178].

P3: To achieve a solar cell separation, the transparent conductive front contact has to be galvanically separated with a P3 scribe by either removing just the ZnO layer on top of the CIS or both, ZnO and CIS on top or the Mo back electrode. Both processes can be performed with picosecond lasers [170, 177, 178].

However, the direct approach to couple the laser energy into the contact layer material by interband absorption, which corresponds to UV radiation, requires a high fluence input when using nanosecond pulses. As a consequence, the edge zones of the P3 groove are thermally damaged. An improvement for the selective structuring of transparent thin films is to apply UV picosecond pulses with reduced absorption length and thermal diffusion length [193].

Indirect ablation with picosecond lasers has proven to be much more effective [194]. For this, a wavelength is needed for which the window layer is transparent and which is absorbed at the interface in the first layers of the absorber. Additionally, the pulse duration has to be short enough to create a confined energy situation [184]. Indirect ablation is not yet fully understood, but the mechanism should be similar to the pressure wave, that is, mainly photomechanical lift-off as described for the Mo film removal (P1) over the substrate side. The heat expansion of a few 10 nm thin absorber material interface, combined with melting and eventually evaporating, is creating a pressure wave, which lifts-off the front contact mainly photo-mechanically. The amount of energy required for this is very small and typically in the range of only one-tenth of the energy required to evaporate the window layer [170]. But the CIGS surface has undergone substantial heating and results in some thermal damage, leading to shunts at the P3 edge, which can be detected in thermography. In summary, the picosecond laser P3 achieves the efficiency of the mechanical P3, but does not improve it. However, the advantages of the P3 laser scribing are the reduction of the dead zone and a non-contact, wear-free process (Fig. 9.15).

P3 laser scribing is also possible by removing the entire layer stack down to the back contact [170, 187]. However, this is not only unnecessary but even unfavorable [195] as the increased energy input (fluence) required to remove the CIGS also increases the thermal damage of the P3 edges.

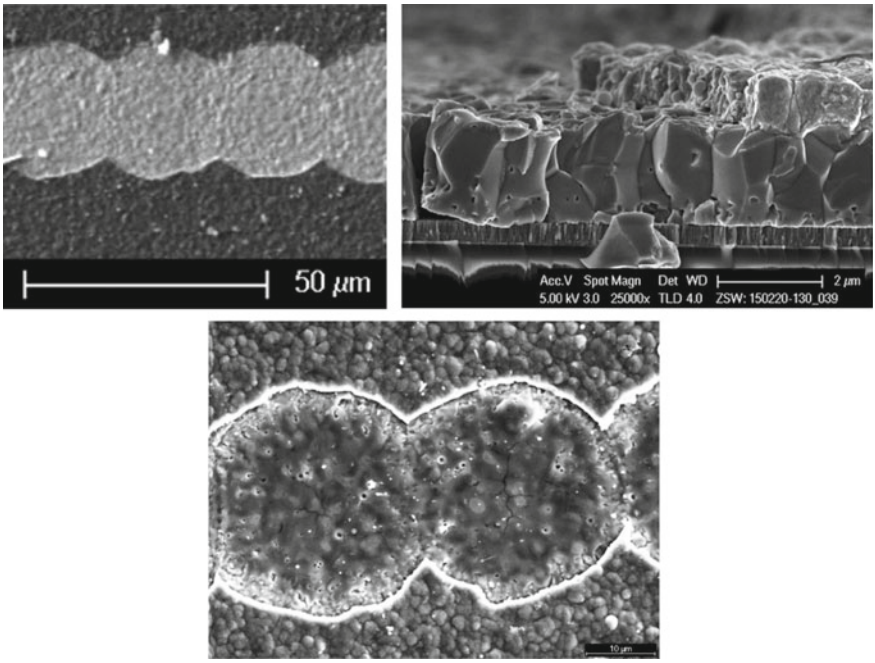

Fig. 9.15 SEM images of a P3 scribe performed with a 10 picosecond laser at 532 nm (top row) and 1064 nm (bottom). The AZO and the buffer layers are removed from the CIGS. The CIGS surface has been thermally damaged within the scribe and shows some microcracks in the REM image (bottom)

In literature all fiber laser scribing [196] of CIGS modules has been investigated and discussed, as well as the possibility of high-speed scribing [172, 187]. Owing to the progress in laser technology, development in the direction of robust, powerful and industrial ultrashort-pulse lasers introduces a 10–15% solar efficiency increase by reducing the dead area and lowering the contact resistance of front and back contact [172, 177, 195].

Monolithic solar cell connection on sensitive flexible substrates

All laser scribing is mandatory if the monolithic cell interconnection has to be performed on thin (25–50 µm) temperature-sensitive polyimide substrates or rough or soft substrates (in comparison to glass). Polyimide (PI) films, for instance, absorb water, start to decompose at rather low temperatures ($T > 450$ °C), are highly flexible and normally have a linear coefficient of thermal expansion (CTE) which is clearly higher than soda lime glass or molybdenum.

P1: To prevent thermally induced irreversible dilatation of the plastic film at the P1 grooves and to avoid thermal damage of the substrate by the laser, the energy input via the laser should be as low as possible. Thus, picosecond or even femtosecond short pulse visible (532 nm) or near IR lasers (1064 nm) combined with the lowest possible fluence should be preferred. Stress-related Mo detachment is preferred to

thermally induced removal and should dominate the P1 process. Although the process can be carried out in such a way that the plastic substrate remains almost undamaged, some excess energy is advantageous in order to overcome the inhomogeneities and height fluctuations that could otherwise locally lead to residual material bridges in the scribe [197]. The Mo-on-PI adhesion is generally worse than the Mo-on-glass adhesion, which would support P1 laser scribing. However, in view of the entire solar cell and the other patterning steps, Mo adhesion should be as good as possible. Depending on the back-contact properties, the thickness of the polymer film and the applied wavelength, P1 can also be performed with nanosecond lasers and even from the rear.

P2: P2 performed on polyimide substrates seems to be the most challenging scribe especially with view on high-speed laser patterning. Moderate Mo adhesion on polyimide is advantageous for P1, but for P2 the adhesion on the substrate should be as high as possible in order not to remove the Mo layer. The P2 laser processing on polyimide (PI) is much more delicate compared to soda-lime glass substrates as the layer stack can absorb much less energy without harming the PI film. Thus, short pulse lasers with low pulse energy and high overlap would be a good choice to remove the absorber step by step without damaging the layers underneath [172, 197]. In this process, the CIGS layer is gradually evaporated pulse by pulse. High repetition rates of up to 1 MHz are therefore the means of choice for implementing the high-speed patterning required for successful industrialization.

P3: The P3 scribe is independent of the substrate type, at least if only the TCO window is removed as recommended also on glass (see previous chapter).

There is currently no uniform or universally valid concept for laser patterning on polymer film. However, the method of choice should be flexible and not depend on the individual layer properties such as adhesion or layer thickness.

Mechanical scribing

Owing to the relatively low adhesion of CIGS on the molybdenum back contact and the much higher hardness of Mo, the absorber can be brushed off the back contact with mechanical scribing tools such as needles. Even brushes may be used if larger areas need to be decoated. A common tool used for P2 and P3 is a cone-shaped pen with a flat tip. The tip diameter determines the minimum groove width. It is typically in the range of a few tens of microns.

Owing to the stiffness of the TCO layer, the P3 groove is considerably more chipped than P2 (Fig. 9.16). In order to achieve a long service life, a very hard material such as carbide is preferred. But even though there is only very little abrasion with such hardened tools, they need to be replaced quite frequently, because they break from time to time due to accidental bumps on the substrate surface. Another problem that may arise from this mechanical scribing technique is related to the aggregation of rubbed layer material under the tip of the tool. In case of P3 this is a mixture of CIGS and ZnO particles, which are hard enough to scratch the underlying molybdenum layer. Such scratches can substantially increase the contact resistance between the cells, especially if corrosion due to humidity additionally attacks this contact (Fig. 9.17).

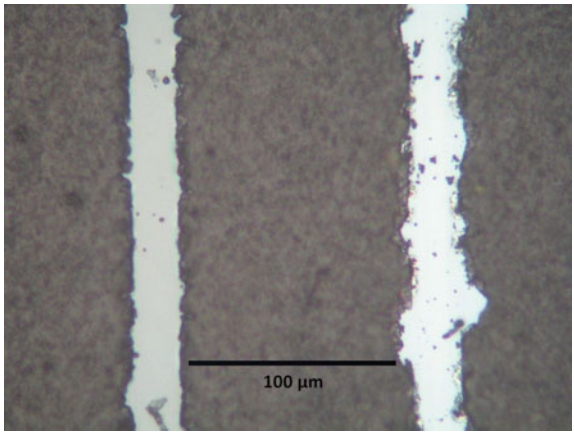

Fig. 9.16 P2 (left) and P3 (right) by mechanical scribing

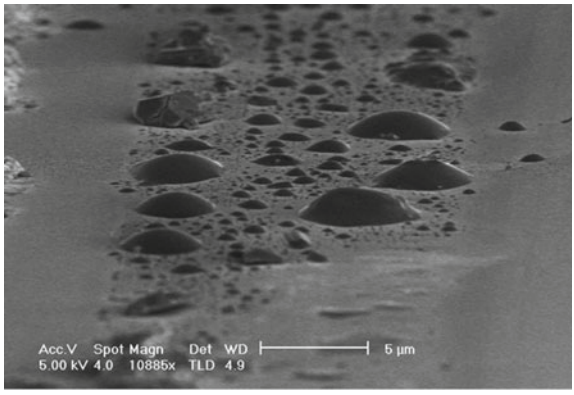

Fig. 9.17 SEM image of P3 scribe after storage in humid air for some days. Moisture penetrated the Mo layer through barely visible cracks and led to chemical reactions between glass, Mo und H_2O. The deposits on the surface consist of carbonates and other compounds of sodium and molybdenum

9.2.5.2 Alternative Concepts

Alternative concepts for the integrated serial interconnection shift one or more patterning steps toward the end of the process chain [190, 198–200]. This is particularly important if several processes have to be carried out without interruption of vacuum processing, such as in the roll-to-roll coating. In this quasi-monolithic or post-deposition approach P1, P2 and P3 are performed simultaneously after all active layers have been deposited. This, however, eliminates the functional contribution of the stacked layers to the serial interconnection making two additional work steps necessary: The connection of neighbored cells across P1 is no longer achieved "automatically" by the deposition of the AZO layer, but has to be provided by an additionally applied contact material such as a conductive Ag paste. As the P1 grooves are no more filled by isolating CIGS material, the uncovered P1 groove now has to be filled with an additional insulator (paste, ink) to prevent short circuits [169, 198, 200] (Fig. 9.18).

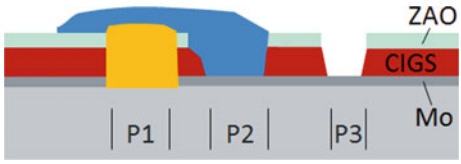

Fig. 9.18 Modified interconnection scheme: P1 and P2 are performed after all layers have been deposited. As a consequence, P1 must be filled with an insulator (drawn in orange) and an additional contact material is required to connect adjacent cells by bridging P1 and connecting the TCO of the left cell with the Mo back contact of the right cell via P2 (drawn in blue)

A compromise between the initial three-step and the five-step approach is the four-step method [200] in which P1 is postponed only and applied together with P2 before the TCO top contact layer deposition. This method only requires the additional printing of an isolation line while the AZO layer continues to establish the cell connection.

The discussion of a non-monolithic connection, for example, of large solar cells on metal substrates separated from each other, is to be dispensed with here. In principle, however, individual cells can be connected in series via contact strips and grids such as Si wafers [201].

9.3 Future Prospects

Although CIGS technology has long since matured, new findings have enabled a continuous and gradual increase in efficiency, as has been demonstrated in recent years, for example, by the introduction of a defined gallium gradient and precisely performed alkali doping. It can be assumed that further insights to increase the quantum yield and reduce the radiation-free recombination will bring the efficiencies closer to the theoretical limit. Another possibility to increase the efficiency already with the existing CIGS quality is the possibility to integrate CIGS as a back cell into a tandem structure with perovskite as front solar cell. The efficiency of a perovskite CIGS tandem structure is currently 23.9% [202], achieved by a four-terminal configuration.

With the help of CIGS thin film solar cell technology, the most efficient flexible solar generators currently available can be produced. The most commonly used substrate films are made of stainless steel or polyimide. Advances in materials science, for example in the deposition of efficient and cost-effective functional layers for substrate isolation, substrate modification or as a diffusion barrier, can further reduce the influence of the substrate on the properties of the solar cell.

By producing cost-effective, lightweight, flexible and efficient PV modules on mild steel, for example in mobile systems or as a roll-out for shading elements, CIGS technology can reach people at all levels of everyday life and thus contribute to reducing CO_2 emission and achieving climate protection targets.

References

1. H. Hahn, G. Frank, W. Klingler, A.-D. Meyer, G. Störger, Untersuchungen über ternäre Chalkogenide. Über einige ternäre Chalkogenide mit Chalkopyritstruktur. Zeitschrift für anorganische und allgemeine Chemie, Band **271**, 153–170 (1953)
2. S. Wagner, J.L. Shay, P. Migliorato, CulnSe2/CdS heterojunction photovoltaic detectors. Appl. Phys. Lett. **25**, 434 (1974). https://doi.org/10.1063/1.1655537
3. S. Wagner, J. Shay, H. Kasper, The p-CuInSe2/n-CdS Heterodiode: photovoltaic detector, solar cell and light emitting diode. J. Phys. Colloq. **36**(C3), C3-101–C3-104 (1975). https://doi.org/10.1051/jphyscol:1975319. jpa-00216289
4. L.L. Kazmerski, F.R. White, G.K. Morgan, Thin-film CuInSe2/CdS heterojunction solar cells. Appl. Phys. Lett. **29**, 268 (1976). https://doi.org/10.1063/1.89041
5. R.A. Mickelsen, W.S. Chen, Development of a 9.4% efficient thin-film CuInSe2/CdS solar cell, in *Conference Record of the IEEE Photovoltaic Specialists Conference, Proceedings of the Fifteenth IEEE Photovoltaic Specialists Conference* (Kissimmee, FL, 1981), pp. 800–804
6. K.L. Chopra, P.D. Paulson, V. Dutta, Thin-film solar cells: an overview. Prog. Photovolt. Res. Appl. **12**, 69–92 (2004). https://doi.org/10.1002/pip.541
7. R.L. Mitchell, C.E. Witt, R. King, D. Ruby, PVMaT advances in the photovoltaic industry and the focus of future PV manufacturing R&D. in *Conference Record of the 29th IEEE Photovoltaic Specialists Conference* (IEEE, New Orleans, Louisiana, 2002), pp. 1444–1447
8. A. Jasenek, U. Rau, T. Hahn, G. Hanna, M. Schmidt, M. Hartmann, H.W. Schock, J.H. Werner, B. Schattat, S. Kraft, K.-H. Schmid, W. Bolse, Defect generation in polycrystalline Cu(In,Ga)Se2 by high-energy electron irradiation. Appl. Phys. A **70**, 677–680 (2000). https://doi.org/10.1007/s003390000512
9. S. Dabbabi, T.B. Nasr, N.T. Kamoun, CIGS solar cells for space applications: numerical simulation of the effect of traps created by high-energy electron and proton irradiation on the performance of solar cells. JOM, Miner. Metals Mater. Soc. (2018). https://doi.org/10.1007/s11837-018-2748-9
10. J. Ramanujam, U.P. Singh, Copper indium gallium selenide based solar cells—a review. Energy Environ. Sci. **10**, 1306–1319 (2017). https://doi.org/10.1039/c7ee00826k
11. H. Neumann, N. Van Nam, H.-J. Hobler, G. Kuhn, Electrical properties of n-TYPE CuInSe2 single crystals. Solid State Commun. **25**, pp. 899–902 (1978)
12. M. Igalson, A. Urbaniak, K. Macielak, M. Tomassini, N. Barreau, S. Spiering, Barriers for current transport in CIGS structures, in *Conference Record of the IEEE Photovoltaic Specialists Conference* (2011). https://doi.org/10.1109/pvsc.2011.6186511
13. T. Wada, N. Kohara, T. Negami, M. Nishitani, Chemical and structural characterization Cu(In,Ga)Se2/Mo in Cu(In,Ga)Se2 solar cells. Jpn. J. Appl. Phys. **35**, 1253 (1996)
14. H.-W. Schock, U. Rau, The role of structural properties and defects for the performance of Cu-chalcopyrite-based thin-film solar cells. Phys. B **308–310**, 1081–1085 (2001)
15. B.J. Stanbery, Copper indium selenides and related materials for photovoltaic devices. Crit. Rev. Solid State Mater. Sci. **27**(2), 73–117 (2002). https://doi.org/10.1080/20014091104215
16. N.G. Dhere, Present status and future prospects of CIGSS thin film solar cells. Sol. Energy Mater. Sol. Cells **90**, 2181–2190 (2006)
17. H.-W. Schock, R. Noufi, Prog. Photovolt.: Res. Appl. **8**, 151 (2000)
18. R. Klenk, Thin Solid Films **387**, 135–140 (2001)
19. M. Turcu, U. Rau, Fermi level pinning at CdS/Cu(In, Ga)(Se, S)2 interfaces: effect of chalcopyrite alloy composition. J. Phys. Chem. Solids **64**, 1591–1595 (2003)
20. C.H. Chang, A. Davydov, B.J. Stanbery, T.J. Anderson, Thermodynamic assessment of the Cu-In-Se system and application to thin film photovoltaics, in *The Conference Record of the 25th IEEE Photovoltaic Specialists Conference* (IEEE, Piscataway, 1996), p. 849
21. H.-W. Schock, Properties of chalcopyrite-based materials thin-film solar cells, in *Thin-Film Solar Cells, Next Generation Photovoltaics and Its Applications*, ed. by Y. Hamakawa (Springer, Berlin, Heidelberg, New York, 2004)

22. T. Gödecke, T. Haalboom, F. Ernst, Phase Equilibria of Cu-In-Se. Z. Metallkd. **91**, 622–662 (2000)
23. M.A. Contreras, K. Ramanathan, J. AbuShama, F. Hasoon, D.L. Young, B. Egaas, R. Noufi, Diode characteristics in state-of-the-art ZnO/CdS/Cu(In_{1-x}Gax)Se2 solar cells. Prog. Photovolt: Res. Appl. **13**, 209–216 (2005). https://doi.org/10.1002/pip.626
24. M. Kemell, M. Ritala, M. Leslkelä, Thin film deposition methods for CuInSe2 solar cells. Crit. Rev. Solid State Mater. Sci. **30**(1), 1–31 (2005). https://doi.org/10.1080/10408430590918341
25. S.B. Zhang, S.H. Wei, A. Zunger, H. Katayama-Yoshida, Defect physics of the CuInSe2 chalcopyrite semiconductor. Phys. Rev. B **57**, 9642 (1998)
26. M. Malitckaya, H.-P. Komsa, V. Havu, M.J. Puska, First-principles modeling of point defects and complexes in thin-film solar-cell absorber CuInSe2. Adv. Electron. Mater. **3**, 1600353 (2017)
27. J. Pohl, K. Albe, Intrinsic point defects in CuInSe2 and CuGaSe2 as seen via screened-exchange hybrid density functional theory. Phys. Rev. B **87**, 245203 (2013)
28. C. Persson, Y.-J. Zhao, S. Lany, A. Zunger, n-type doping of CuInSe2 and CuGaSe2. Phys. Rev. B **72**, 035211 (2005)
29. S. Siebentritt, M. Igalson, C. Persson, S. Lany, The electronic structure of chalcopyrites—bands, point defects and grain boundaries. Prog. Photovolt: Res. Appl. **18**, 390–410 (2010). https://doi.org/10.1002/pip.936
30. S. Siebentritt, Chalcopyrite compound semiconductors for thin film solar cells. Curr. Opin. Green Sustain. Chem. **4**, 1–7 (2017). https://doi.org/10.1016/j.cogsc.2017.02.001
31. W. Shockley, H.J. Queisser, Detailed balance limit of efficiency of *p-n* junction solar cells. J. Appl. Phys. **32**(3), 510–519 (1961). https://doi.org/10.1063/1.1736034
32. S. Rühle, Sol. Energy **130**, 139–147 (2016). https://doi.org/10.1016/j.solener.2016.02.015
33. G. Hanna, A. Jasenek, U. Rau, H.W. Schock, Influence of Ga-content on the bulk defect densities of Cu(In, Ga)Se2. Thin Solid Films **387**, 71–73 (2001)
34. U. Rau, M. Schmidt, A. Jasenek, G. Hanna, H.W. Schock, Electrical characterization of Cu(In, Ga)Se2 thin-film solar cells and the role of defects for the device performance. Sol. Energy Mater. Sol. Cells **67**, 137–143 (2001)
35. P. Jackson, R. Würz, U. Rau, J. Mattheis, M. Kurth, T. Schlötzer, G. Bilger, J.H. Werner, High quality baseline for high efficiency, Cu(In1-x, Gax)Se2 solar cells. Prog. Photovolt. Res. Appl. **15**, 507–519 (2007). https://doi.org/10.1002/pip.757
36. M.A. Contreras, L.M. Mansfield, B. Egaas, J. Li, M. Romero, R. Noufi, E. Rudiger-Voigt, W. Mannstadt, Wide bandgap Cu(In, Ga)Se2 solar cells with improved energy conversion efficiency. Prog. Photovolt: Res. Appl. **20**, 843–850 (2012). https://doi.org/10.1002/pip.2244
37. P. Jackson, R. Wuerz, D. Hariskos, E. Lotter, W. Witte, M. Powalla, Effects of heavy alkali elements in Cu(In,Ga)Se2 solar cells with efficiencies up to 22.6%. Phys. Status Solidi RRL **10**(8), 583–586 (2016). https://doi.org/10.1002/pssr.201600199
38. V. Bermudez, A. Perez-Rodriguez, Understanding the cell-to-module efficiency gap in Cu(In, Ga)(S, Se)2 photovoltaics scale-up. Nat. Energy **3**, 466–475 (2018)
39. H. Hiroi, Y. Iwata, S. Adachi, H. Sugimoto, A. Yamada, New world-record efficiency for pure-sulfide Cu(In, Ga)S2 thin-film solar cell with Cd-free buffer layer via KCN-free process. IEEE J. Photovolt. **6**(3), 760–763 (2016)
40. K. Siemer, J. Klaer, I. Luck, J. Bruns, R. Klenk, D. Bräunig, Efficient CuInS2 solar cells from a rapid thermal process (RTP). Sol. Energy Mater. Sol. Cells **67**, 159–166 (2001)
41. F. Larsson, N.S. Nilsson, J. Keller, C. Frisk, V. Kosyak, M. Edoff, T. Törndahl, Record 1.0 V open-circuit voltage in wide band gap chalcopyrite solar cells. Prog. Photovolt. Res. Appl. **25**, 755–763 (2017). https://doi.org/10.1002/pip.2914
42. H. Goto, Y. Hashimoto, K. Ito, Efficient thin film solar cell consisting of TCO/CdS/CuInS2/CuGaS2 structure. Thin Solid Films **451–452**, 552–555 (2004). https://doi.org/10.1016/j.tsf.2003.11.045
43. M.A. Contreras, J. Tuttle, A. Gabor, A. Tennant, K. Ramanathan, S. Asher, A. Franz, J. Keane, L. Wang, J. Scofield, R. Noufi, High efficiency Cu(ln,Ga)Se2-based solar cells: processing of novel absorber structures, in *Proceedings 1st World Conference on Photovoltaic Energy Conversion* (IEEE, Piscataway, NJ, 1994), p. 68

44. T. Dullweber, G. Hanna, U. Rau, H.W. Schock, A new approach to high-efficiency solar cells by band gap grading in Cu(In, Ga)Se2 chalcopyrite semiconductors. Sol. Energy Mater. Sol. Cells **67**, 145–150 (2001)
45. Y. Hahsimoto, N. Kohara, T. Negami, M. Nishitani, T. Wada, Surface characterization of chemically treated Cu(In, Ga)Se2 thin films. Jpn. J. Appl. Phys. **35**, 4760–4764 (1996)
46. K. Ramanathan, M.A. Contreras, C.L. Perkins, S. Asher, F.S. Hasoon, J. Keane, D. Young, M. Romero, W. Metzger, R. Noufi, J. Ward, A. Duda, Properties of 19.2% efficiency ZnO/CdS/CuInGaSe2 thin-film solar cells. Prog. Photovolt: Res. Appl. **11**, 225–230 (2003). https://doi.org/10.1002/pip.494
47. E. Avancini, R. Carron, B. Bissig, P. Reinhard, R. Menozzi, G. Sozzi, S. Di Napoli, T. Feurer, S. Nishiwaki, S. Buecheler, A.N. Tiwari, Impact of compositional grading and overall Cu deficiency on the near-infrared response in Cu(In, Ga)Se2 solar cells. Prog. Photovolt: Res. Appl. (2016). https://doi.org/10.1002/pip.2850
48. A. Chirilă, S. Buecheler, F. Pianezzi, P. Bloesch, C. Gretener, A.R. Uhl, C. Fella, L. Kranz, J. Perrenoud, S. Seyrling, R. Verma, S. Nishiwaki, Y.E. Romanyuk, G. Bilger, A.N. Tiwari, Highly efficient Cu(In, Ga)Se2 solar cells grown on flexible polymer films. Nat. Mater. **10**, 857–861 (2011)
49. S. Niki, M. Contreras, I. Repins, M. Powalla, K. Kushiya, S. Ishizuka, K. Matsubara, CIGS absorbers and processes. Prog. Photovolt: Res. Appl. **18**, 453–466 (2010). https://doi.org/10.1002/pip.969
50. P. Jackson, D. Hariskos, R. Wuerz, O. Kiowski, A. Bauer, T.M. Friedlmeier, M. Powalla, Properties of Cu(In,Ga)Se2 solar cells with new record efficiencies up to 21.7%. Phys. Status Solidi RRL **9**(1), 28–31 (2015). https://doi.org/10.1002/pssr.201409520
51. A. Chirilă, P. Reinhard, F. Pianezzi, P. Bloesch, A.R. Uhl, C. Fella, L. Kranz, D. Keller, C. Gretener, H. Hagendorfer, D. Jaeger, R. Erni, S. Nishiwaki, S. Buecheler, A.N. Tiwari, Potassium-induced surface modification of Cu(In, Ga)Se2 thin films for high-efficiency solar cells. Nat. Mater. **12**, 1107–1111 (2013). https://doi.org/10.1038/NMAT3789
52. M. Powalla, P. Jackson, W. Witte, D. Hariskos, S. Paetel, C. Tschamber, W. Wischmann, High-efficiency Cu(In, Ga)Se2 cells and modules. Sol. Energy Mater. Sol. Cells **119**, 51–58 (2013)
53. P.M.P. Salomé, V. Fjällström, P. Szaniawski, J.P. Leitão, A. Hultqvist, P.A. Fernandes, J.P. Teixeira, B.P. Falcão, U. Zimmermann, A.F. da Cunha, M. Edoff, A comparison between thin film solar cells made from co-evaporated $CuIn_{1-x}Ga_xSe2$ using a one-stage process versus a three-stage process. Prog. Photovolt: Res. Appl. **23**, 470–478 (2015). https://doi.org/10.1002/pip.2453
54. M. Powalla, B. Dimmler, Scaling up issues of CIGS solar cells. Thin Solid Films **361–362**, 540–546 (2000)
55. R. Scheer, A. Pérez-Rodríguez, W.K. Metzger, Advanced diagnostic and control methods of processes and layers in CIGS solar cells and modules. Prog. Photovolt: Res. Appl. **18**, 467–480 (2010)
56. V.K. Kapur, U.V. Choudary, A.K. P. Chu, US patent no. 4,581,108 (1986)
57. V. Probst, W. Stetter, W. Riedl, H. Vogt, M. Wendl, H. Calwer, S. Zweigart, K.-D. Ufert, B. Freienstein, H. Cerva, F.H. Karg, Rapid CIS-process for high efficiency PV-modules: development towards large area processing. Thin Solid Films **387**, 262–267 (2001)
58. T. Kato, Cu(In,Ga)(Se,S)2 solar cell research in solar Frontier: progress and current status. Jpn. J. Appl. Phys. **56**, 04CA02 (2017). https://doi.org/10.7567/jjap.56.04ca02
59. G.D. Mooney, A.M. Hermann, J.R. Tuttle, D.S. Albin, R. Noufi, Formation of CuInSe2 thin films by rapid thermal recrystallization. Appl. Phys. Lett. **58**, 2678 (1991). https://doi.org/10.1063/1.104805
60. J.A. Frantz, J.D. Myers, R.Y. Bekele, V.Q. Nguyen, B.M. Sadowski, S.I. Maximenko, R.J. Walters, J.S. Sanghera, Recent progress in sputtered Cu(In,Ga)Se2 absorbers for photovoltaics. https://www.researchgate.net/publication/282960353, https://doi.org/10.1364/noma.2015.ns3b.2

61. C.-H. Chen, W.-C. Shih, C.-Y. Chien, C.-H. Hsu, Y.-H. Wua, C.-H. Lai, A promising sputtering route for one-step fabrication of chalcopyrite phase Cu(In, Ga)Se2 absorbers without extra Se supply. Sol. Energy Mater. Sol. Cells **103**, 25–29 (2012)
62. Y.-C. Wang, H.-P.D. Shieh, Double-graded bandgap in Cu(In, Ga)Se2 thin film solar cells by low toxicity selenization process. Appl. Phys. Lett. **105**, 073901 (2014). https://doi.org/10.1063/1.4893713
63. F. Karg, High efficiency CIGS solar modules. Energy Procedia **15**, 275–282 (2012)
64. S.S. Schmidt, C. Wolf, H. Rodriguez-Alvarez, J.-P. Bäcker, C.A. Kaufmann, S. Merdes, F. Ziem, M. Hartig, S. Cinque, I. Dorbandt, C. Köble, D. Abou-Ras, R. Mainz, R. Schlatmann, Adjusting the Ga grading during fast atmospheric processing of Cu(In, Ga)Se2 solar cell absorber layers using elemental selenium vapor. Prog. Photovolt: Res. Appl. **25**, 341–357 (2017). https://doi.org/10.1002/pip.2865
65. T. Kobayashi, H. Yamaguchi, Z.J.L. Kao, H. Sugimoto, T. Kato, H. Hakuma, T. Nakada, Impacts of surface sulfurization on Cu(In1_x, Gax)Se2 thin-film solar cells. Prog. Photovolt: Res. Appl. **23**, 1367–1374 (2015). https://doi.org/10.1002/pip.2554
66. N.B. Chaure, Electrodeposited $CuIn_{1-x}Ga_xSe2$ thin films from non-aqueous medium for solar cell Applications. J. Renew. Sustain. Energy **5**, 031604 (2013). https://doi.org/10.1063/1.4808023
67. R.N. Bhattocharya, Solution growth and electrodeposited CulnSe2 thin films. J. Electrochem. Soc. **130**(10), 2040 (1983)
68. A. Kampmann, V. Sittinger, J. Rechid, R. Reineke-Koch, Large area electrodeposition of Cu(In, Ga)Se2. Thin Solid Films **361–362**, 309–313 (2000)
69. S.N. Qiu, L. Li, C.X. Qiu, I. Shih, C.H. Champness, Study of CulnSe2 thin films prepared by electrodeposition. Sol. Energy Mater. Sol. Cells **37**, 389–393 (1995)
70. C. Broussillou, C. Viscogliosi, A. Rogee, S. Angle, P.P. Grand, S. Bodnar, C. Debauche, J.L. Allary, B. Bertrand, C. Guillou, L. Parissi, S. Coletti, Statistical process control for Cu(In,Ga)(S,Se)2 electrodeposition-based manufacturing process of 60 × 120 cm^2 modules up to 14,0% efficiency, in *Conference Record of the 42nd IEEE Photovoltaic Specialist Conference* (2015). https://doi.org/10.1109/pvsc.2015.7356224
71. S. Aksu, S. Pethe, A. Kleiman-Shwarsctein, S. Kundu, M. Pinarbasi, Recent advances in electroplating based CIGS solar cell fabrication, in *Conference Record of the 38th IEEE Photovoltaic Specialist Conference* (2012). https://doi.org/10.1109/pvsc.2012.6318235
72. A.R. Uhl, C. Fella, A. Chirilă, M.R. Kaelin, L. Karvonen, A. Weidenkaff, C.N. Borca, D. Grolimund, Y.E. Romanyuk, A.N. Tiwari, Non-vacuum deposition of Cu(In, Ga)Se2 absorber layers from binder free, alcohol solutions. Prog. Photovolt: Res. Appl. **20**, 526–533 (2012). https://doi.org/10.1002/pip.1246
73. V. Kapur, R. Kemmerle, A. Bansal, J. Haber, J. Schmitzberger, P. Le, D. Guevarra, V. Kapur, T. Stempien, Manufacturing of "ink based" CIGS SOLAR cells/modules, in *Conference Record of the 33rd IEEE Photovoltaic Specialist Conference* (2008), pp. 1–5. https://doi.org/10.1109/pvsc.2008.4922496
74. V.K. Kapur, A. Bansal, S. Roth, Roadmap for manufacturing cost competitive CIGS modules, in *Conference Record of the 38th IEEE Photovoltaic Specialist Conference* (2012), pp. 3343–3348. https://doi.org/10.1109/pvsc.2012.6318289
75. K.A.W. Horowitz, R. Fu, M. Woodhouse, An analysis of glass-glass CIGS manufacturing costs. Sol. Energy Mater. Sol. Cells **154**, 1–10 (2016)
76. J. Hedström, H. Ohlsén, M. Bodegård, A. Kylner, L. Stolt, D. Hariskos, M. Ruckh, H. W. Schock, ZnO/CdS/Cu(In,Ga)Se2 thin film solar cells with improved performance, in *Conference Record of the 23rd IEEE Photovoltaic Specialists Conference* (IEEE, Piscataway, NJ, 1993), pp. 364–371
77. K. Granath, M. Bodegård, L. Stolt, The effect of NaF on Cu(In, Ga)Se2 thin film solar cells. Sol. Energy Mater. Sol. Cells **60**, 279–293 (2000)
78. D. Rudmann, D. Brémaud, H. Zogg, A.N. Tiwari, Na incorporation into Cu(In, Ga)Se2 for high-efficiency flexible solar cells on polymer foils. J. Appl. Phys. **97**, 084903 (2005)

79. M. Ruckh, D. Schmid, M. Kaiser, R. Schäffler, T. Walter, H.W. Schock, *Conference Record of the 24th IEEE Photovoltaic Specialists Conference* (Waikoloa, Hawaii, 1994), pp. 156–159
80. R. Wuerz, A. Eicke, F. Kessler, P. Rogin, O. Yazdani-Assl, Alternative sodium sources for Cu(In, Ga)Se2 thin-film solar cells on flexible substrates. Thin Solid Films **519**, 7268–7271 (2011)
81. W. Thongkham, A. Pankiew, K. Yoodee, S. Chatraphorn, Enhancing efficiency of Cu(In, Ga)Se2 solar cells on flexible stainless steel foils using NaF co-evaporation. Sol. Energy **92**, 189–195 (2013)
82. H. Stange, S. Brunken, H. Hempel, H. Rodriguez-Alvarez, N. Schäfer, D. Greiner, A. Scheu, J. Lauche, C.A. Kaufmann, T. Unold, D. Abou-Ras, R. Mainz, Effect of Na presence during $CuInSe_2$ growth on stacking fault annihilation and electronic properties. Appl. Phys. Lett. **107**, 152103 (2015)
83. A. Urbaniak, M. Igalson, F. Pianezzi, S. Buecheler, A. Chirilă, P. Reinhard, A.N. Tiwari, Effects of Na incorporation on electrical properties of Cu(In, Ga)Se2-based photovoltaic devices on polyimide substrates Sol. Energy Mater. Sol. Cells **128**, 52–55 (2014)
84. C. Persson, A. Zunger, Anomalous grain boundary physics in polycrystalline CuInSe2: the existence of a hole barrier. Phys. Rev. Lett. **91**, 266401 (2003)
85. S.H. Wei, S.B. Zhang, A. Zunger, Effects of Na on the electrical and structural properties of $CuInSe_2$. J. Appl. Phys. **85**, 7214–7218 (1999)
86. Z.K. Yuan, S. Chen, Y. Xie, J.S. Park, H. Xiang, X.G. Gong, S.H. Wei, Na-diffusion enhanced p-type conductivity in Cu(In, Ga)Se2: a new mechanism for efficient doping in semiconductors. Adv. Energy Mat. **6**, 1601191 (2016)
87. O. Cojocaru-Mirédin, T. Schwarz, P.P. Choi, M. Herbig, R. Wuerz, D. Raabe, Atom probe tomography studies on the $Cu(In,Ga)Se_2$ grain boundaries. J. Vis. Exp. (74), e50376. https://doi.org/10.3791/50376 (2013)
88. M.A. Contreras, B. Egaas, P. Dippo, J. Webb, J. Granata, K. Ramanathan, S. Asher, A. Swartzlander, R. Noufi, On the role of Na and modifications to Cu(In,Ga)Se2 absorber materials using thin MF (M = Na, K, Cs) precursor layers, in *Conference Record of the 26th IEEE Photovoltaic Specialists Conference* (Anaheim, California, 30 September–3 October 1997), pp. 359–362
89. A. Laemmle, R. Wuerz, M. Powalla, Efficiency enhancement of Cu(In, Ga)Se2 thin-film solar cells by a post-deposition treatment with potassium fluoride. Phys. Status Solidi RRL **7**, 631–634 (2013). https://doi.org/10.1002/pssr.201307238
90. P. Jackson, D. Hariskos, R. Wuerz, W. Wischmann, M. Powalla, Compositional investigation of potassium doped Cu(In,Ga)Se2 solar cells with efficiencies up to 20.8%. Phys. Status Solidi RRL **8**, 219–222 (2014)
91. D. Herrmann, P. Kratzert, S. Weeke, M. Zimmer, J. Djordjevic-Reiss, R. Hunger, P. Lindberg, E. Wallin, O. Lundberg, L. Stolt, CIGS module manufacturing with high deposition rates and efficiencies, presented at the *IEEE 40th Photovoltaic Specification Conference* (Denver, CO, USA, 8–13 June 2014)
92. K.F. Tai, R. Kamada, T. Yagioka, T. Kato, H. Sugimoto, From 20.9 to 22.3% Cu(In,Ga)(S,Se)2 solar cell: reduced recombination rate at the heterojunction and the depletion region due to K-treatment. Jpn. J. Appl. Phys. **56**, 08MC03 (2017)
93. O. Lundberg, E. Wallin, V. Gusak, S. Södergren, S. Chen, S. Lotfi, F. Chalvet, U. Malm, N. Kaihovirta, P. Mende, G. Jaschke, P. Kratzert, J. Joel, M. Skupinski, P. Lindberg, T. Jarmar, J. Lundberg, J. Mathiasson, L. Stolt, Improved CIGS modules by KF post deposition treatment and reduced cell-to-module losses, in *43rd Photovoltaic Specialist Conference* (Denver, 2016), pp. 1293–1296
94. E. Handick, P. Reinhard, R.G. Wilks, F. Pianezzi, T. Kunze, D. Kreikemeyer-Lorenzo, L. Weinhardt, M. Blum, W. Yang, M. Gorgoi, E. Ikenaga, D. Gerlach, S. Ueda, Y. Yamashita, T. Chikyow, C. Heske, S. Buecheler, A.N. Tiwari, M. Bär, Formation of a K-In-Se surface species by NaF/KF postdeposition treatment of Cu(In, Ga)Se2 thin-film solar cell absorbers. ACS Appl. Mater. Interfaces. **9**, 3581–3589 (2017)

95. E. Handick, P. Reinhard, J.-H. Alsmeier, L. Köhler, F. Pianezzi, S. Krause, M. Gorgoi, E. Ikenaga, N. Koch, R.G. Wilks, S. Buecheler, A.N. Tiwari, M. Bär, Potassium postdeposition treatment-induced band gap widening at Cu(In, Ga)Se2 surfaces—reason for performance leap? ACS Appl. Mater. Interfaces. **7**, 27414–27420 (2015)
96. Z.Z. Kish, V.B. Lazarev, E.Y. Peresh, E.E. Semrad, Compounds in In_2Se_3-K_2Se. Neorg. Mater. **24**, 1602–1605 (1988)
97. F. Pianezzi, P. Reinhard, A. Chirilă, B. Bissig, S. Nishiwaki, S. Buecheler, A.N. Tiwari, Unveiling the effects of post-deposition treatment with different alkaline elements on the electronic properties of CIGS thin film solar cells. Phys. Chem. Chem. Phys. **16**, 8843–8851 (2014)
98. H. Elanzeery, F. Babbe, M. Melchiorre, E. Robert, A. Zelenina, S. Siebentritt, Potassium fluoride ex-situ treatment on both Curich and Cu-poor $CuInSe_2$ thin film solar cells. IEEE J. Photovolt. **7**, 684–689 (2017)
99. I. Khatri, H. Fukai, H. Yamaguchi, M. Sugiyama, T. Nakada, Effect of potassium fluoride post-deposition treatment on Cu(In, Ga)Se2 thin films and solar cells fabricated onto sodalime glass substrates. Sol. Energy Mater. Sol. Cells **155**, 280–287 (2016)
100. S.A. Jensen, S. Glynn, A. Kanevce, P. Dippo, J.V. Li, D.H. Levi, D. Kuciauskas, Beneficial effect of post-deposition treatment in high-efficiency Cu(In, Ga)Se2 solar cells through reduced potential fluctuations. J. Appl. Phys. **120**, 063106 (2016)
101. A. Vilalta-Clemente, M. Raghuwanshi, S. Duguay, C. Castro, E. Cadel, P. Pareige, P. Jackson, R. Wuerz, D. Hariskos, W. Witte, Rubidium distribution at atomic scale in high efficient Cu(In, Ga)Se2 thin-film solar cells. Appl. Phys. Lett. **12**, 103105 (2018)
102. P. Schöppe, S. Schönherr, R. Wuerz, W. Wisniewski, G. Martínez-Criado, M. Ritzer, K. Ritter, C. Ronning, C.S. Schnohr, Rubidium segregation at random grain boundaries in Cu(In, Ga)Se2 absorbers. Nano Energy **42**, 307–313 (2017)
103. T. Unold, Talk at EMRS (2018)
104. S. Ishizuka, N. Taguchi, J. Nishinaga, Y. Kamikawa, S. Tanaka, H. Shibata, Group III elemental composition dependence of RbF post deposition treatment effects on Cu(In, Ga)Se2 thin films and solar cells. J. Phys. Chem. C **122**, 3809–3817 (2018)
105. W.N. Shafarman, J.E. Phillips, Direct current-voltage measurements of the Mo/CuInSe2 contact on operating solar cells, in *Conference Record of the 25th IEEE Photovoltaic Specialist Conference* 1996 (Washington DC, USA, 1996), pp. 917–919
106. W. Paszkowicz, R. Minikayev, P. Piszora, D. Trots, M. Knapp, T. Wojciechowski, R. Bacewicz, Thermal expansion of CuInSe2 in the 11–1,073 K range: an X-ray diffraction study. Appl. Phys. A **116**, 767–780 (2014). https://doi.org/10.1007/s00339-013-8146-9
107. G. Gordillo, F. Mesa, C. Calderon, Electrical and morphological properties of low resistivity Mo thin films prepared by magnetron sputtering. Braz. J. Phys. **36**(3B), 982–985 (2006)
108. D. Abou-Ras, G. Kostorz, D. Bremaud, M. Kälin, F.V. Kurdesau, A.N. Tiwari, M. Döbeli, Formation and characterisation of MoSe2 for Cu(In, Ga)Se2 based solar cells. Thin Solid Films **480–481**, 433–438 (2005). https://doi.org/10.1016/j.tsf.2004.11.098
109. T. Klinkert, B. Theys, G. Patriarche, M. Jubault, F. Donsanti, J.-F. Guillemoles, D. Lincot, New insights into the Mo/Cu(In, Ga)Se2 interface in thin film solar cells: Formation and properties of the MoSe2 interfacial layer. J. Chem. Phys. **145**, 154702 (2016). https://doi.org/10.1063/1.4964677
110. T. Wada, N. Kohara, S. Nishiwaki, T. Negami, Characterization of the Cu(In, Ga)Se2/Mo interface in CIGS solar cells. Thin Solid Films **387**, 118–122 (2001)
111. J.A. Spies, R. Schafer, J.F. Wager, P. Hersh, H.A.S. Platt, D.A. Keszler, G. Schneider, R. Kykyneshi, J. Tate, X. Liu, A.D. Compaan, W.N. Shafarman, p in double-heterojunction thin-film solar cell p-layer assessment. Sol. Energy Mater. Sol. Cells **93**, 1296–1308 (2009)
112. X. Zhang, M. Kobayashi, A. Yamada, Comparison of Ag(In, Ga)Se2/Mo and Cu(In, Ga)Se2/Mo interfaces in solar cells. ACS Appl. Mater. Interfaces. **9**(19), 16215–16220 (2017). https://doi.org/10.1021/acsami.7b02548
113. B.K. Choi, M. Kim, K.-H. Jung, J. Kim, K.-S. Yu, Y.J. Chang, Temperature dependence of band gap in MoSe2 grown by molecular beam epitaxy. Nanoscale Res. Lett. **12**, 492 (2017). https://doi.org/10.1186/s11671-017-2266-7

114. W. Kautek, H. Gerischer, H. Tributsch, The role of carrier diffusion and indirect optical transitions in the photoelectrochemical behavior of layer type d-band semiconductors. J. Electrochem. Soc. **127**, 2471–2478 (1980)
115. S.M. Delphinec, M. Jayachandranb, C. Sanjeeviraja, Pulsed electrodeposition and characterization of molybdenum diselenide thin film. Mater. Res. Bull. **40**, 135–147 (2005). https://doi.org/10.1016/j.materresbull.2004.09.008
116. A.M. Vora, Effect of indium intercalation on various properties of MoSe2 single crystals. Cryst. Res. Technol. **42**(3), 286–289 (2007). https://doi.org/10.1002/crat.200610814
117. K.-J. Hsiao, J.-D. Liu, H.-H. Hsieh, T.-S. Jiang, Electrical impact of MoSe2 on CIGS thin-film solar cells. Phys. Chem. Chem. Phys. **15**, 18174 (2013)
118. J.B. Pang, Y.A. Cai, Q. He, H. Wang, W.L. Jiang, J.J. He, T. Yu, W. Liu, Y. Zhang, Y. Sun, Preparation and characteristics of MoSe2 interlayer in bifacial Cu(In, Ga)Se2 solar cells. Phys. Procedia **32**, 372–378 (2012)
119. K. Orgassa, H.W. Schock, J.H. Werner, Alternative back contact materials for thin film Cu(In, Ga)Se2 solar cells. Thin Solid Films **431–432**, 387–391 (2003)
120. J. Malmström, S. Schleussner, L. Stolt, Enhanced back reflectance and quantum efficiency in thin film solar cells with a ZrN back reflector. Appl. Phys. Lett. **85**, 2634 (2004). https://doi.org/10.1063/1.1794860
121. S. Schleussner, T. Kubart, T. Törndahl, M. Edoff, Reactively sputtered ZrN for application as reflecting back contact in Cu(In, Ga)Se2 solar cells. Thin Solid Films **517**, 5548–5552 (2009)
122. B. Bissig, R. Carron, L. Greuter, S. Nishiwaki, E. Avancini, C. Andres, T. Feurer, S. Buecheler, A.N. Tiwari, Novel back contact reflector for high efficiency and double-graded Cu(In,Ga)Se2 thin-film solar cells. Prog. Photovolt. Res. Appl. 1–7 (2018). https://doi.org/10.1002/pip.3029
123. V. Srikant, D.R. Clarke, On the optical band gap of zinc oxide. J. Appl. Phys. **83**(10), 5447–5451 (1998)
124. C.P. Thompson, S. Hegedus, P. Carcia, R.S. McLean, The effects of device geometry and TCO/Buffer layers on damp heat accelerated lifetime testing of Cu(In, Ga)Se2 solar cells. IEEE J. Photovolt. **3**, 494 (2013)
125. T. Jäger, Y.E. Romanyuk, S. Nishiwaki, B. Bissig, F. Pianezzi, P. Fuchs, C. Gretener, M. Döbeli, A.N. Tiwari, Hydrogenated indium oxide window layers for high-efficiency Cu(In, Ga)Se2 solar cells. J. Appl. Phys. **117**, 205301 (2015)
126. Y. Kuwahata, T. Minemoto, Impact of Zn1-xMgxO: Al transparent electrode for buffer-less Cu(In, Ga)Se2 solar cells. Renew. Energy **65**, 113–116 (2014)
127. F.J. Pern, R. Noufi, X. Li, C. DeHart, B. To, Damp-heat induced degradation of transparent conducting oxides for thin-film solar cells, in *Conference Record of the IEEE PVSC* (2008), pp. 43–48
128. R. Menner, S. Paetel, W. Wischmann, M. Powalla, Indium zinc oxide window layer for high-efficiency Cu(In, Ga)Se2 solar cells. Thin Solid Films **634**, 160–164 (2017)
129. T. Shitaya, H. Sato, Single crystal CdS solar cells. J. Appl. Phys. **7**, 1348–1353 (1968)
130. R.A. Mickelsen, W. Chen, Polycrystalline thin-film $CuInSe_2$ solar cells, in *Records of IEEE PVSC* (1982), pp. 781–785
131. R.R. Potter, C. Eberspacber, L.B. Fabick, Device analysis of CuInSe2/CdZnS/ZnO Solar cells, in *Records of IEEE PVSC* (1985), pp. 1659–1664
132. K. Mitchell, C. Eberspacher, J. Ermer, D. Pier, Single and tandem junction CuInSe2 cell and module technology, in *Records IEEE PVSC* (1988), pp. 1384–1389
133. J. Kessler, K.O. Velthaus, M. Ruckh, R. Laichinger, H.-W.. Schock, D. Lincot, R. Ortega, J. Vedel, Chemical bath deposition of CdS on CuInSe2, etching effects and growth kinetics, in *6th International Photovoltaic Science and Engineering Conference (PVSEC-6)* (1992), pp. 1005–1010
134. M.A. Contreras, M.J. Romer, B. To, F. Hasoon, R. Noufi, S. Ward, K. Ramanathan, Optimization of CBD CdS process in high-efficiency Cu(In, Ga)Se2-based solar cells. Thin Solid Films **403–404**, 204–211 (2002)
135. A. Kylner, The chemical bath deposited CdS/Cu(In, Ga)Se2 interface as revealed by X-ray photoelectron spectroscopy. J. Electrochem. Soc. **146**(5), 1816–1823 (1999)

136. C. Heske, D. Eich, R. Fink, E. Umbach, T. van Buuren, C. Bostedt, L.J. Terminello, S. Kakar, M.M. Grush, T.A. Callcott, F.J. Himpsel, D.L. Ederer, R.C.C. Perera, W. Riedl, F. Karg, Observation of intermixing at the buried CdS/Cu(In, Ga)Se2 thin film solar cell heterojunction. Appl. Phys. Lett. **74**, 1451–1453 (1999)
137. D. Abou-Ras, S. Wagner, B.J. Stanbery, H.-W. Schock, R. Scheer, L. Stolt, S. Siebentritt, D. Lincot, C. Eberspacher, K. Kushiya, A.N. Tiwari, Innovation highway: breakthrough milestones and key developments in chalcopyrite photovoltaics from a retrospective viewpoint. Thin Solid Films **633**, 2–12 (2017)
138. S. Kurtz, I. Repins, W.K. Metzger, P.J. Verlinden, S. Huang, S. Bowden, I. Tappan, K. Emery, L.L. Kazmerski, D. Levi, Historical analysis of champion photovoltaic module efficiencies. IEEE J. Photovolt. **8**, 363 (2018)
139. P. Jackson, R. Wuerz, D. Hariskos, E. Lotter, W. Witte, M. Powalla, Effects of heavy alkali elements in Cu(In,Ga)Se2 solar cells with efficiencies up to 22.6%. Phys. Status Solidi RRL **10**, 583–586 (2016)
140. J. Löckinger, S. Nishiwaki, T.P. Weiss, B. Bissig, Y.E. Romanyuk, S. Buecheler, A.N. Tiwari, TiO_2 as intermediate buffer layer in Cu(In, Ga)Se2 solar cells. Sol. Energy Mater. Sol. Cells **174**, 397–404 (2018)
141. W. Witte, D. Abou-Ras, D. Hariskos, Chemical bath deposition of Zn(O, S) and CdS buffers: influence of Cu(In, Ga)Se2 grain orientation. Appl. Phys. Lett. **102**, 051607 (2013)
142. T.M. Friedlmeier, P. Jackson, D. Kreikemeyer-Lorenzo, D. Hauschild, O. Kiowski, D. Hariskos, L. Weinhardt, C. Heske, M. Powalla, A closer look at Initial CdS growth on high-efficiency Cu(In,Ga)Se_2 absorbers using surface-sensitive methods, in *Proceedings IEEE PVSC* (2016), pp. 457–461
143. W. Witte, D. Abou-Ras, D. Hariskos, Improved growth of solution-deposited thin films on polycrystalline Cu(In, Ga)Se2. Phys. Status Solidi RRL **10**, 300–304 (2016)
144. D. Hariskos, R. Menner, P. Jackson, S. Paetel, W. Witte, W. Wischmann, M. Powalla, L. Bürkert, T. Kolb, M. Oertel, B. Dimmler, B. Fuchs, New reaction kinetics for a high-rate chemical bath deposition of the Zn(S, O) buffer layer for Cu(In, Ga)Se2-based solar cells. Prog. Photovolt: Res. Appl. **20**, 534–542 (2012)
145. T.M. Friedlmeier, P. Jackson, A. Bauer, D. Hariskos, O. Kiowski, R. Wuerz, M. Powalla, Improved photocurrent in Cu(In,Ga)Se2 solar cells: from 20.8% to 21.7% efficiency with CdS buffer, and 21.0% Cd-free. IEEE J. Photovolt. **5**, 1487–1491 (2015)
146. N. Naghavi, D. Abou-Ras, N. Allsop, N. Barreau, S. Bücheler, A. Ennaoui, C.-H. Fischer, C. Guillen, D. Hariskos, J. Herrero, R. Klenk, K. Kushiya, D. Lincot, R. Menner, T. Nakada, C. Platzer-Björkman, S. Spiering, A.N. Tiwari, T. Törndahl, Buffer layers and transparent conducting oxides for chalcopyrite Cu(In, Ga)(S, Se)2 based thin film photovoltaics: present status and current developments. Prog. Photovoltaics Res. Appl. **18**, 411–433 (2010)
147. J. Palm, T. Dalibor, R. Lechner, S. Pohlner, R. Verma, R. Dietmüller, A. Heiß, H. Vogt, F. Karg, Cd-free CIS thin film solar modules at 17% efficiency, in *Proceedings of the 29th European Photovoltaic Solar Energy Conference* (2014), pp. 1433–1438
148. K. Ramanathan, J. Mann, S. Glynn, S. Christensen, J. Pankow, J. Li, J. Scharf, L. Mansfield, M. Contreras, R. Noufi, A comparative study of Zn(O,S) buffer layers and CIGS solar cells fabricated by CBD, ALD, and sputtering, in *Proceedings 38th IEEE Photovoltaic Specialists Conference* (2012), pp. 1677–1680
149. W. Witte, D. Hariskos, A. Eicke, R. Menner, O. Kiowski, M. Powalla, Impact of annealing on Cu(In, Ga)Se2 solar cells with Zn(O, S)/(Zn, Mg)O buffers. Thin Solid Films **535**, 180–183 (2013)
150. A. Wachau, J. Schulte, P. Agoston, F. Hübler, A. Steigert, R. Klenk, F. Hergert, H. Eschrich, V. Probst, Sputtered Zn(O, S) buffer layers for CIGS solar modules—from lab to pilot production. Prog. Photovoltaics Res. Appl. **25**, 696–705 (2017)
151. M.A. Mughal, R. Engelken, R. Sharma, Progress in indium (III) sulfide (In_2S_3) buffer layer deposition techniques for CIS, CIGS, and CdTe-based thin film solar cells. Solar Energy **120**, 131–146 (2015)

152. W. Witte, D. Hariskos, M. Powalla, Comparison of charge distributions in CIGS thin-film solar cells with ZnS/(Zn, Mg)O and CdS/i-ZnO buffers. Thin Solid Films **519**, 7549–7552 (2011)
153. D. Hariskos, P. Jackson, W. Hempel, S. Paetel, S. Spiering, R. Menner, W. Wischmann, M. Powalla, Method for a high-rate solution deposition of Zn(O, S) buffer layer for high-efficiency Cu(In, Ga)Se2-based solar cells. IEEE J. Photovolt. **6**, 1321–1326 (2016)
154. T. Kato, A. Handa, T. Yagioka, T. Matsuura, K. Yamamoto, S. Higashi, J.-L. Wu, K.F. Tai, H. Hiroi, T. Yoshiyama, T. Sakai, H. Sugimoto, Enhanced efficiency of Cd-Free Cu(In, Ga)(Se, S)2 minimodule via (Zn, Mg)O second buffer layer and alkali metal post-treatment. IEEE J. Photovolt. **7**, 1773–1780 (2017)
155. Module with record efficiency from AVANCIS: Fraunhofer ISE certifies CIGS solar module with an efficiency of 17.9% (2016). http://www.avancis.de/en/press/news/article/avancis-erzielt-erneuten-wirkungsgradrekord-fraunhofer-ise-zertifiziert-cigs-solarmodul-mit-wirkung/
156. N. Barreau, Indium sulfide and relatives in the world of photovoltaics. Sol. Energy **83**, 363–371 (2009)
157. D. Hauschild, F. Meyer, A. Benkert, D. Kreikemeyer-Lorenzo, T. Dalibor, J. Palm, M. Blum, W. Yang, R.G. Wilks, M. Bär, F. Reinert, C. Heske, L. Weinhardt, Improving performance by Na doping of a buffer layer—chemical and electronic structure of the InxSy:Na/CuIn(S, Se)2 thin-film solar cell interface. Prog. Photovolt. Res. Appl. **26**, 359–366 (2018)
158. E. Wallin, U. Malm, T. Jamar, O. Lundberg, M. Edoff, L. Stolt, World-record Cu(In,Ga)Se2-based thin-film sub-module with 17.4.% efficiency. Prog. Photovolt. **20**, 851–854 (2012)
159. K. Ellmer, A. Klein, B. Rech (eds.), *Transparent Conductive Zinc Oxide: Basics and Applications in Thin Film Solar Cells*, Chapter 9 (Springer, Berlin/Heidelberg, 2008), pp. 418–419
160. J.V. Li, X. Li, Y. Yan, C.-S. Jiang, W.K. Metzger, I.L. Repins, M.A. Contreras, D.H. Levi, Influence of sputtering a ZnMgO window layer on the interface and bulk properties of Cu(In, Ga)Se2 solar cells. J. Vac. Sci. Technol. **27**, 2384–2389 (2009)
161. D. Hariskos, B. Fuchs, R. Menner, N. Naghavi, C. Hubert, D. Lincot, M. Powalla, The Zn(S, O, OH)/ZnMgO buffer in thin-film Cu(In, Ga)(Se, S)2-based solar cells part II: magnetron sputtering of the ZnMgO buffer layer for in-line co-evaporated Cu(In, Ga)Se2 solar cells. Prog. Photovolt. Res. Appl. **17**, 479–488 (2009)
162. F. Kessler, D. Rudmann, Technological aspects of flexible CIGS solar cells and modules. Sol. Energy **77**, 685–695 (2004). https://doi.org/10.1016/j.solener.2004.04.010
163. K. Herz, A. Eicke, F. Kessler, R. Wächter, M. Powalla, Diffusion barriers for CIGS solar cells on metallic substrates. Thin Solid Films **43–432**, 392–397 (2003)
164. R. Wuerz, A. Eicke, M. Frankenfeld, F. Kessler, M. Powalla, P. Rogin, O. Yazdani-Assl, CIGS thin-film solar cells on steel substrates. Thin Solid Films **517**, 2415–2418 (2009)
165. K.-B. Kim, Effect of metal barrier layer for flexible solar cell devices on stainless steel substrates. Appl. Sci. Converg. Technol. **26**(1), 16–19 (2016). https://doi.org/10.5757/ASCT.2017.26.1.16
166. P. Reinhard, A. Chirilă, P. Blasch, F. Pianezzi, S. Nishiwaki, S. Buecheler, A.N. Tiwari, Review of progress toward 20% efficiency flexible CIGS solar cells and manufacturing issues of solar modules. IEEE J. Photovolt. **3**(1), 572–580 (2013). https://doi.org/10.1109/JPHOTOV.2012.2226869
167. R. Zhang, D.R. Hollars, J. Kanicki, High efficiency Cu(In, Ga)Se2 flexible solar cells fabricated by roll-to-roll metallic precursor co-sputtering method. Jpn. J. Appl. Phys. **52**, 092302 (2013). https://doi.org/10.7567/JJAP.52.092302
168. R. Birkmire, E. Eser, S. Fields, W. Shafarman, Cu(InGa)Se2 solar cells on a flexible polymer web. Prog. Photovolt: Res. Appl. **13**, 141–148 (2005). https://doi.org/10.1002/pip.605
169. S. Nakano, T. Matsuoka, S. Kiyama, H. Kawata, N. Nakamura, Y. Nakashima, S. Tsuda, H. Nishiwaki, M. Ohnishi, I. Nagaoka, Y. Kuwano, Laser patterning method for integrated type a-Si solar cell submodules. Jpn. J. Appl. Phys. **25**, 1936 (1986)
170. G. Heise, A. Börner, M. Dickmann, M. Englmaier, A. Heiss, M. Kemnitzer, J. Konrad, R. Moser, J. Palm, H. Vogt, H.P. Huber, Demonstration of the monolithic interconnection on CIS

solar cells by picosecond laser structuring on 30 by 30 cm^2 modules. Prog. Photovolt: Res. Appl. (2014). https://doi.org/10.1002/pip.2552
171. P.-O. Westin, U. Zimmermann, M. Edoff, Laser patterning of P2 interconnect via in thin-film CIGS PV modules. Sol. Energy Mater. Sol. Cells **09**, 1230 (2008). https://doi.org/10.1016/j.solmat.2008.04.015
172. G. Heise, A. Heiss, H. Vogt, H.P. Huber, Ultrafast lasers improve the efficiency of CIS thin film solar cells. Phys. Procedia **39**, 702–708 (2012)
173. S. Nishiwaki, A. Burn, S. Buecheler, M. Muralt, S. Pilz, V. Romano, R. Witte, L. Krainer, G.J. Spühler, A.N. Tiwari, A monolithically integrated high-efficiency Cu(In, Ga)Se2 mini-module structured solely by laser. Prog. Photovolt Res. Appl. **23**, 1908–1915 (2015). https://doi.org/10.1002/pip.2583
174. O. Tober, J. Wienke, M. Winkler, J. Penndorf, J. Griesche, Mater. Res. Soc. Symp. Proc. **763**, 371 (2003)
175. F. Kessler, D. Hermann, M. Powalla, Approaches to flexible CIGS thin-film solar cells. Thin Solid Films **480–481**, 491 (2005)
176. H. Vogt, A. Heiss, J. Palm, F. Karg, H. P. Huber, G. Heise, All laser patterning serial interconnection for highly efficient CIGSSe modules, in *Proceedings of 26th EUPVSEC* (Hamburg, 3DV.2.9, 2011)
177. G. Heise, M. Domke, J. Konrad, F. Pavic, M. Schmidt, H. Vogt, A. Heiss, J. Palm, H.P. Huber, Monolithical serial interconnects of large CIS solar cells with picosecond laser pulses. Phys. Procedia **12**, 149–155 (2011)
178. G. Heise, A. Heiss, C. Hellwig, T. Kuznicki, H. Vogt, J. Palm, H.P. Huber, Optimization of picosecond laser structuring for the monolithic serial interconnection of CIS solar cells. Prog. Photovolt: Res. Appl. **21**, 681–692 (2013). https://doi.org/10.1002/pip.1261
179. S. Zoppel, H. Huber, G.A. Reider, Selective ablation of thin Mo and TCO films with femtosecond laser pulses for structuring thin film solar cells. Appl. Phys. A **89**, 161–163 (2007)
180. M.M. Kirillova, L.V. Nomerovannaya, M.M. Noskov, Optical properties of molybdenum single crystals. Sov. Phys. JETP **33**, 1210–1214 (1971)
181. M. Domke, L. Nobile, S. Rapp, S. Eiselen, J. Sotrop, H.P. Huber, M. Schmidt, Understanding thin film laser ablation: the role of the effective penetration depth and the film thickness. Phys. Proc. **56**, 1007–1014 (2014)
182. G. Heise, M. Englmaier, C. Hellwig, T. Kuznicki, S. Sarrach, H. Huber, Laser ablation of thin molybdenum films on transparent substrates at low fluencies. Appl. Phys. A **102**, 173–178 (2011)
183. J. Bovatsek, A. Tamhankar, R.S. Patel, N.M. Bulgakova, J. Bonse, Thin film removal mechanisms in ns-laser processing of photovoltaic materials. Thin Solid Films **518**, 2897 (2010)
184. L. Zhigilei, Z. Lin, D. Ivanov, Atomistic modeling of short pulse laser ablation of metals: connections between melting, spallation, and phase explosion. J. Phys. Chem. C **113**, 11892 (2009)
185. M. Domke, S. Rapp, M. Schmidt, H. Huber, Ultrafast movies of thin film laser ablation. Appl. Phys. A **109**, 409–420 (2012)
186. J. Sotrop, A. Kersch, M. Domke, G. Heise, H.P. Huber, Numerical simulation of ultrafast expansion as the driving mechanism for confined laser ablation with ultra-short laser pulses. Appl. Phys. A **113**, 397 (2013)
187. A. Burn, V. Romano, M. Muralt, R. Witte, B. Frei, S. Buecheler, S. Nishiwaki, Selective ablation of thin films in latest generation CIGS solar cells with picosecond pulses, in *Proceedings of SPIE 8243, Laser Applications in Microelectronic and Optoelectronic Manufacturing (LAMOM) XVII* (2012), p. 824318. https://doi.org/10.1117/12.906919
188. J. Bonse, S. Hoehm, S. Kirner, A. Rosenfeld, J. Krueger, Laser-induced periodic surface structures a scientific evergreen. IEEE J. Sel. Top. Quant. Electron. **23**(3) (2017)
189. E. Lotter, B. Freilinger, R. Wächter, M. Powalla, Laser patterning of the semiconductor layer of CIGS modules under industrial conditions, in *Proceedings of the 16th* European Photovoltaic *Solar Energy* Conference (Glasgow, UK, 1–5 May 2000), pp. 779–782

190. P.-O. Westin, U. Zimmermann, M. Ruth, M. Edoff, Next generation interconnective laser patterning of CIGS thin film modules. Sol. Energy Mater. Sol. Cells **95**, 1062–1068 (2011)
191. P. Gecys, E. Markauskas, A. Zemaitis, G. Raciukaitis, Variation of P2 series interconnects electrical conductivity in the CIGS solar cells by picosecond laser-induced modification. Sol. Energy **132**, 493–502 (2016)
192. R. Moser, M. Domke, G. Heise, G. Marowsky, H.P. Huber, Nanosecond laser lift-off of a copper-Indium-diselenide thin film at a wavelength of 1342 nm. Phys. Procedia **41**, 739–744 (2013)
193. S. Rapp, M. Schmidt, H.P. Huber, Selective femtosecond laser structuring of dielectric thin films with different band gaps: a time-resolved study of ablation mechanisms. Appl. Phys. A **122** (2016)
194. G. Heise, M. Dickmann, M. Domke, A. Heiss, T. Kuznicki, J. Palm, I. Richter, H. Vogt, H. Huber, Investigation of the ablation of zinc oxide thin films on copper–indium-selenide layers by ps laser pulses. Appl. Phys. A **104**, 387–393 (2011)
195. P. Gečys, E. Markauskas, S. Nishiwaki, S. Buecheler, R. De Loor, A. Burn, V. Romano, G. Račiukaitis, CIGS thin-film solar module processing: case of high-speed laser scribing. Sci. Rep. **7**, 40502 (2017). https://doi.org/10.1038/srep40502
196. A. Burn, M. Muralt, S. Pilz, V. Romano, R. Witte, B. Frei, S. Buecheler, S. Nishiwaki, L. Krainer, All fiber laser scribing of Cu(In, Ga)Se2 thin-film solar modules. Phys. Procedia **41**, 713–722 (2013)
197. D.J. Hwang, S. Kuk, Z. Wang, S. Fu, T. Zhang, G. Kim, W.M. Kim, J. Jeong, Laser scribing of CIGS thin-film solar cell on flexible substrate. Appl. Phys. A **123**, 55 (2017)
198. V. Probst, A. Jasenek, C. Sandfort, A. Letsch, I. Koetschau, T. Hahn, J. Feichtinger, H. Eschrich, Innovative front end processing for next generation CIS module production. Jpn. J. Appl. Phys. **54**, 08KC12 (2015). http://dx.doi.org/10.7567/JJAP.54.08KC12
199. M.L. Crozier, A. Brunton, S.J. Henley, J.D. Shephard, A. Abbas, J.W. Bowers, P.M. Kaminski, J.M. Walls, Inkjet and laser hybrid processing for series interconnection of thin film photovoltaics. Mater. Res. Innovations **18**(7), 509–514 (2014). https://doi.org/10.1179/1433075X14Y.0000000260
200. J. Britt, S. Wiedeman, S. Albright, Process development for CIGS-based thin-film photovoltaic modules. Phase II technical report. NREL/SR-520–29227 (2000)
201. E. Niemi, J. Sterner, P. Carlsson, J. Oliv, E. Jaremalm, S. Lindström, All-sputtered flexible CIGS cells at high speed, in *Proceedings of 31st EU PVSEC* 2015 (Hamburg, 2015), pp. 1010–1013
202. H. Shen, T. Duong, J. Peng, D. Jacobs, N. Wu, J. Gong, Y. Wu, S.K. Karuturi, X. Fu, K. Weber, X. Xiao, T.P. White, K. Catchpole, Energy Environ. Sci. **11**, 394 (2018). https://doi.org/10.1039/c7ee02627g

Chapter 10
Perovskite Photovoltaics: From Laboratory to Industry

D. Forgacs, K. Wojciechowski and O. Malinkiewicz

Abstract The following pages of this book will discuss the current state-of-the-art of 'perovskite' photovoltaic technology, that has been awe-inspiring in the last decade. Since the first edition of HELC-PV, perovskite solar cells appeared and have been the dominating research topic in photovoltaics, attracting tremendous scientific and public interest. The technology advanced rapidly, and now in 2018, there are already several companies existing with the aim of bringing this technology to the market. As such, it has been a pleasure and an honour for Saule Technologies to be approached by the editors to review the advancement of this swiftly developing field. While the fabrication of devices with record high efficiencies has been achieved already, there are still open questions regarding fundamental physical and chemical processes taking place in such a device. There are a vast number of publications available that scrutinize the accumulated knowledge and observations regarding this unique class of materials. As such, it is a challenging—yet rewarding task to write a chapter that gives an objective perspective on the topic. Our aim was to create something that provides the readers with a valuable overview that will stay relevant even when the current state-of-the art will be outdated. We intended to describe the basic principles that guide the characteristics of perovskites, and then connect them with their function in solar cells and the related scientific discoveries. We hope that

The original version of this chapter was revised: Typos correction has been updated. The correction to this chapter is available at https://doi.org/10.1007/978-3-030-22864-4_13

D. Forgacs (✉)
Director of Knowledge Management, Saule Technologies,
Dunska 11. (WPT, Sigma building 1st floor), 54-427 Wroclaw, Poland
e-mail: david.forgacs@sauletech.com

K. Wojciechowski
Scientific Director, Saule Technologies,
Dunska 11. (WPT, Sigma building 1st floor), 54-427 Wroclaw, Poland
e-mail: konrad.wojciechowski@sauletech.com

O. Malinkiewicz
Chief Technology Officer, Saule Technologies,
Dunska 11. (WPT, Sigma building 1st floor), 54-427 Wroclaw, Poland
e-mail: olga@sauletech.com

V. Petrova-Koch et al. (eds.), *High-Efficient Low-Cost Photovoltaics*,
Springer Series in Optical Sciences 140,
https://doi.org/10.1007/978-3-030-22864-4_10

this chapter will provide the reader with a basic framework of knowledge that can be referred to when reading future works dealing with perovskites. We hope that you will find this work helpful, and in case you do so—please do not hesitate to recommend it to your colleagues, friends and acquaintances.

10.1 Introduction

Dear reader,

The following pages of this book will discuss the current state-of-the-art of 'perovskite' photovoltaic technology, that has been awe-inspiring in the last decade. Since the first edition of HELC-PV, perovskite solar cells appeared and have been the dominating research topic in photovoltaics, attracting tremendous scientific and public interest. The technology advanced rapidly, and now in 2018, there are already several companies existing with the aim of bringing this technology to the market. As such, it has been a pleasure and an honour for Saule Technologies to be approached by the editors to review the advancement of this swiftly developing field. While the fabrication of devices with record high efficiencies has been achieved already, there are still open questions regarding fundamental physical and chemical processes taking place in such a device. There are a vast number of publications available that scrutinize the accumulated knowledge and observations regarding this unique class of materials. As such, it is a challenging—yet rewarding task to write a chapter that gives an objective perspective on the topic. Our aim was to create something that provides the readers with a valuable overview that will stay relevant even when the current state-of-the art will be outdated. We intended to describe the basic principles that guide the characteristics of perovskites, and then connect them with their function in solar cells and the related scientific discoveries. We hope that this chapter will provide the reader with a basic framework of knowledge that can be referred to when reading future works dealing with perovskites. We hope that you will find this work helpful, and in case you do so—please do not hesitate to recommend it to your colleagues, friends and acquaintances.

Solar cells based on halide perovskites have been a scientific sensation for the last 5 years preceding the writing of this book. One reason why perovskite solar cells attracted tremendous interest is that these class of materials possess intrinsically beneficial qualities, as well as offer the possibility to engineer their properties to match the requirements and mitigate the effect of their less desirable traits. This peculiar quality stems from perovskites' unique characteristics among semiconductors. While in the case of solar cell technologies that utilize inorganic semiconductors as light harvesting materials, such as silicon (Si), cadmium-telluride (CdTe), copper-indium-gallium-diselenide (CIGS), gallium-arsenide (GaAs) and copper-tin-zinc-selenide (CZTSe), there are covalent bonds between the atoms in the crystal lattice, the case of perovskite solar cells is different. The perovskite lattice is comprised of ions and held together by ionic interactions—although it has been suggested that there is some

covalent character present as well, due to the low electronegativity of heavier halides [1].

While halide perovskites are heavily investigated as solar cell materials only recently, this class of compounds is not new in the field of optoelectronics. Their history started back in the early nineties, when they were extensively studied by David Mitzi in the laboratories of IBM [2–4]. He used perovskites as an active material for diodes and transistors. However, his concerns regarding their sensitivity to moisture delayed the pursuit of perovskites as viable photovoltaic (PV) materials. The change came in 2009, when a Japanese research group introduced a perovskite layer into a liquid dye-sensitized solar cell (DSSC) architecture for the first time [5]. The team led by prof. Miyasaka used methylammonium lead iodide ($CH_3NH_3PbI_3$) perovskite as a sensitizer on mesostructured titanium dioxide (TiO_2) achieving a power conversion efficiency (PCE) of 3.8%. In 2011, a 6.5% efficient device was reported from the research group of Nam-Gyu Park [6]. Unfortunately, the traditional iodide/iodine liquid electrolyte used in these architectures was dissolving the photoactive material, leading to the rapid degradation of fabricated solar cells. Three years later, the group of prof. Kanatzidis announced a dramatic improvement of the efficiency of DSSCs by replacing the liquid electrolyte with a tin-based ($CsSnI_3$) perovskite as a hole transporting material (HTM). In doing so, they have created the first perovskite-containing solid-state DSSC [7]. Power conversion efficiency exceeding 10% was achieved, significantly overpassing state-of-the-art ss-DSSC values. Another breakthrough came soon after, when 2 research groups reported similar results in a very close succession. Henry Snaith from the University of Oxford, and Nam-Gyu Park together with the team of École polytechnique fédérale de Lausanne (EPFL) have replaced the liquid electrolyte with the solid state spiro-OMeTAD to be used as the HTM, eliminating the cause of perovskite's fast degradation observed in Miyasaka's cells [8, 9]. Furthermore, the Oxford group reported an additional ground-breaking discovery. By replacing the mesoporous TiO_2 film with an insulating Al_2O_3 scaffold, their devices reached even higher performances than the reference ones. This highlighted that perovskites are capable of ambipolar charge transport over large distances (exceeding the material's absorption lengths), and there is no explicit need for a mesoporous electron accepting material to be present for efficient charge collection [10]. Consequently, this paved the way for the realization of perovskite-based traditional thin-film architectures. These seminal works attracted the attention of many scientists working on DSSCs and organic photovoltaics (OPVs). Due to architectural similarities, years of OPV and DSSC research expertise turned out to be very relevant for the emerging perovskite PV technology. The joint effort and the accumulated knowledge facilitated a rapid development, and in a few years' time many breakthrough achievements have been reached. The following sections will attempt to give a straightforward explanation on why these group of materials have been so successful, as well as review the challenges associated with their industrialization.

10.2 Perovskite Properties

Since the first observation of the photoelectric effect by Becquerel in 1839, scientists around the globe were seeking for the perfect material that could be used to produce power from the most ubiquitous power source in our vicinity—the Sun [11]. The ultimate goal is to make a great solar cell—efficient, cheap, long lasting, and environmentally friendly. To reach this goal, a special photoactive material has to be developed that fulfils several unique requirements. The most important features are excellent absorption and transport properties, combined with an easy and low-cost fabrication. While different semiconducting materials offer some of these features, the peculiarity of halide perovskites is that they fulfil most of the above mentioned requirements. This originates from their special crystal structure which will be discussed first, examining how the components contribute to the properties of the material.

Methylammonium lead iodide ($MAPbI_3$) is up to date the most heavily researched, archetypical halide perovskite material, and can therefore be seen as a standard perovskite and a model compound [12, 13]. Like most of the perovskites used in photovoltaics it consists of three main components: a monovalent cation (MA^+), a divalent metallic cation (Pb^{2+}), and halogenic anions (I^-). Before we dive into the physics that govern the exact role of each of these components, it is worth to take a closer look at the whole picture. Organic-inorganic metal halides are actually only a small part of a much bigger perovskite family, that adopt similar crystal structures. Figure 10.1. represents the crystal structure of perovskites, and highlights the different types of materials in this family.

10.2.1 General Structure

The ionic structure can be described by the general formula ABX_3 with a specific spatial distribution of the components. Here, A is a mono/divalent cation, B is a di/tetravalent cation, and X is a mono/divalent anion. The first classification of such a crystal lattice arrangement was made by Gustav Rose, who had found $CaTiO_3$ in the Ural mountains in 1839, and it has been named after the Russian mineralogist and nobleman, Lev Perovski. Over time, it has been discovered that there are hundreds of compositions that adopt a perovskite structure. It was first described by Victor Goldschmidt [14]. Initially discovered materials were minerals of natural origin, however a scientific interest stimulated appearance of synthetic perovskites as well. Researchers demonstrated piezoelectric and ferroelectric properties, and even high temperature superconductivity in perovskite material, all due to their structure.

In order to form a perovskite crystal, the constituting ions must fulfil requirements regarding their size and charge. These parameters can be described by the tolerance factor, which was studied in different works addressing both oxide and halide perovskites [15].

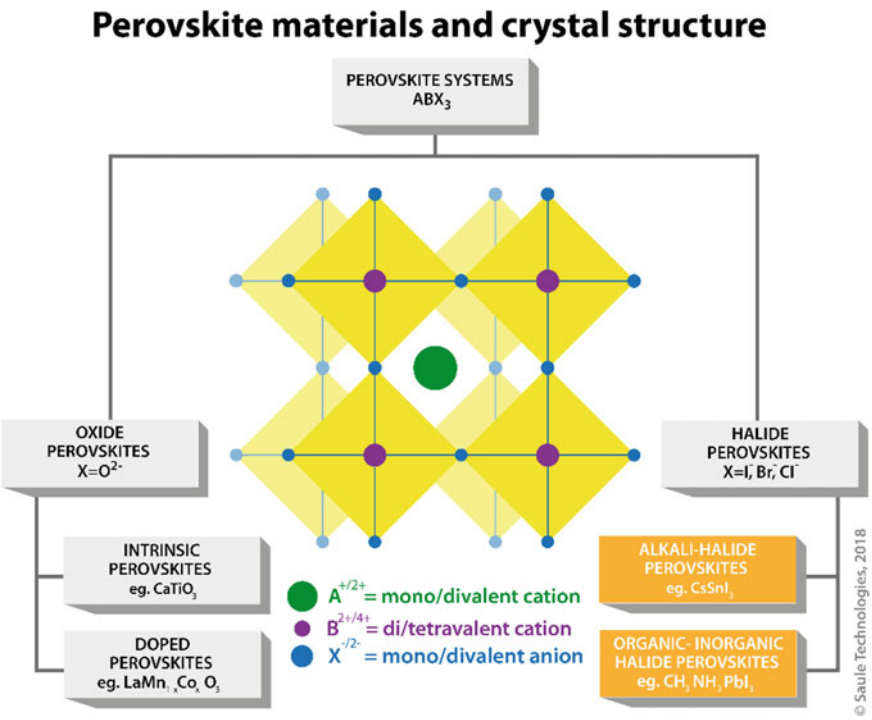

Fig. 10.1 The crystal structure of perovskites, and the different types of materials in this family. A is a mono/divalent cation, B is a di/tetravalent cation, and X is a mono/divalent anion. Courtesy of saule technologies. https://onlinelibrary.wiley.com/doi/abs/10.1002/solr.201900144 [144]

In an ideal case, this structure has a cubic symmetry, corresponding to the tolerance factor values that are close to 1. To fulfil this, the A-site ion must be much larger than the B-site one. Orthorhombic, rhombohedral or tetragonal structures can also form, based on the size of the constituting ions. Importantly, the type of crystalline phase affects the photovoltaic performance. As the structure is dependent on the temperature as well, the same material can exist in different symmetries based on thermal conditions [16]. As such, the phase transition points have to be taken into account when designing a solar cell that has to withstand thermal cycling.

Now, having an insight into the general structure of perovskites, we can take a closer look at how its individual components contribute to their properties.

10.2.2 The Role of the Metallic Cation

First of all, in order to harvest energy from the light that reaches the surface of a solar cell, the photoactive material has to be a semiconductor with desirable absorption

properties. In an ideal case, it has a direct band gap that allows the harvesting of most of the incident photons with the least possible losses. The state-of-the-art high efficiency semiconductor for photovoltaics is GaAs [17]. Can perovskites compete with them? To answer this question, let's take a look at the electronic structure of these materials.

Each semiconductor material can be classified as having either an indirect or a direct band gap, and it has a strong implication on how the lattice can interact with photons [18]. In the case of indirect band gap materials, the electromagnetic radiation has to interact with phonons—the vibrational motion of the atoms in the condensed matter—in order to be absorbed. Due to this requirement of the change in crystal momentum, the chance that a photon can be harvested in a solar cell that is based on an indirect band gap material are orders of magnitude less than in the case of a direct one. Consequently, the thickness of the active layer in such a solar cell has to be orders of magnitude larger, to have a comparable light harvesting capability. Indirect bandgap semiconductors, like silicon, need to be much thicker in order to efficiently harvest all the usable energy of sunlight. This was partially overcome by structuring their surfaces to increase the optical path length, nevertheless their optimal thickness remains in the range of around 100 μm [19, 20]. This value is more than 2 orders of magnitude larger than the ones reported for optimized perovskite photovoltaics, ranging from 300 to 1000 nm.

DFT calculations have shown that in the case of $MAPbI_3$ the $[PbI_6]^{4-}$ octahedra framework is dominating the energetic levels near the band edge [21]. There are controversies remaining about the electronic contribution of the A-site MA^+ cations. Some studies claim them to be electronically inactive, only influencing the tolerance factor and the structural stability of the material [22]. However, a recent work has demonstrated an experimental evidence that the nitrogen atom in the MA^+ cation actually has an effect on the electronic structure of $MAPbI_3$ [23]. Nevertheless, the valence band maximum (VBM) has strong Pb s and I p antibonding character, whereas the conduction band minimum (CBM) is mostly contributed from the Pb p state [24]. In the case of GaAs, the VBM has a p character, and the CBM has an s one [21]. The main difference comes from the states near the conduction band minimum, with the s-type displaying more dispersity and p-type ones being more dense. Simply put, the presence of the p-character in the CBM of perovskites leads to a very high density of states near the band edge, leading to substantial absorption characteristics that outclass Si and even GaAs especially in the visible part of the spectrum (Fig. 10.2).

With the advancement of the perovskite field, an interest arose in developing perovskites with altered B-site cations. One reason behind this intention is to replace the most commonly used lead in halide perovskite absorbers, which is frequently considered as a limitation in their large-scale application.

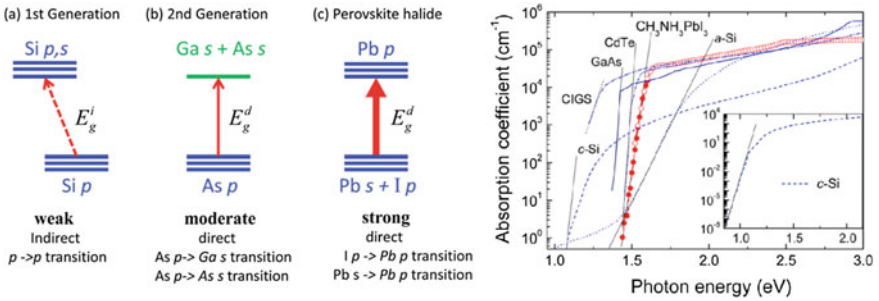

Fig. 10.2 (left) The comparison of transitions in **a** Silicon, **b** GaAs and **c** Halide perovskites, and (right) the absorption coefficient of the most common semiconductor materials for solar cell applications as the function of photon energy. Reprinted from [21, 140]. Copyright 2015 Royal Society of Chemistry and 2014 American Chemical Society

10.2.3 The Role of the Halide Anion

As mentioned earlier, having a direct band gap has beneficial effects in itself for the application of the material in photovoltaics. However, due to the unique ionic nature of perovskite materials, they offer an additional advantage that the bandgap can be engineered over the whole visible spectrum, extending into the ultraviolet and near infrared as well [25]. This is again due to the $[PbX_6]^{4-}$ octahedra, and its strong impact on the electronic characteristics. An exchange of a halide ion X alters the size of the unit cell, resulting in a change of the band gap. It was observed that if phase stability requirements are met, the absorption onset can be shifted easily [26, 27].

This feature motivated researchers to investigate alternative perovskite compositions displaying different band gap levels than the archetypical $MAPbI_3$ to fit to the requirements of the particular applications. The initial investigation of this topic was carried out by Noh et al. [28]. With a simple solution mixing approach, the successful alloying of $MAPbI_3$ and $MAPbBr_3$ was achieved. In this work, it was highlighted that increased bromide inclusion leads to a larger extent of unit cell contraction, which in turn leads to an increase in the material's band gap, which is in line with Vegard's law [29]. Figure 10.3 represents the change in absorption coefficient in $MAPb(I_xBr_{1-x})_3$ systems as a function of composition.

With the decreasing size of the halides, the band gap increases. In the case of $MAPbX_3$ the values shift from 1.55 eV for X = I to 2.3 eV and 3.4 eV for X = Br and X = Cl, respectively, making this class of materials interesting for both single- and multi-junction photovoltaics, as well as light emitting applications. Besides the versatility in applications, this also enables the design of solar cells with different colours. Mixed halide compositions however exhibit a photo-instability, leading to phase segregation under illumination [30]. When aiming to tune the band gap in the range that is interesting for tandem applications, researchers have encountered that solar cells exhibit a subpar V_{oc} with respect to their band gap energy. Photoluminescence measurements have indicated that this originates from the formation

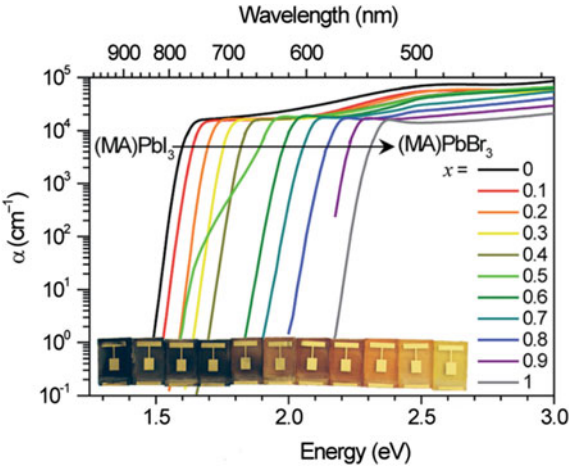

Fig. 10.3 The change in absorption coefficient in $MAPb(I_xBr_{1-x})_3$ systems as a function of composition. Reprinted from [102]

of iodine-rich phases with below band gap energy, acting as recombination centres [30].

10.2.4 The Role of Monovalent Cations

As mentioned before, the role of cations in the electronic structure of perovskites is still under debate. They however contribute significantly to the solution processability of these semiconductors. The small monovalent cations are easily solubilized by strong polar solvents, while the halide counterions in their salts help in the complexation of plumbate ions [31]. Besides, they have a strong implication on the geometry of the lattice, which enables the rational design and engineering of the perovskite material, giving rise to special features when done properly. Let's take a look at them.

The exchange of A-site cations was first explored when researchers have reported perovskite solar cells that incorporated formamidinium (FA) A-site cations instead of the traditional MA ones [32]. The slightly larger size of the FA cation changes the lattice constant, resulting in a redshift of the absorption onset. $FAPbI_3$ exhibits a band gap of 1.48 eV, leading to an increment of the maximum achievable short-circuit current. The tunability of the material was also demonstrated, with a transition between a tetragonal and cubic phase [27].

Inspired by the tunability of the band gap and the improved thermal stability of perovskites with cations other than MA, the rational engineering of perovskite alloys emerged as a robust approach to fabricate materials with desired qualities. The first work was carried out by Jeon et al. [33]. In this work, $MAPbBr_3$ was utilized to stabilize the perovskite phase of $FAPbI_3$, enabling the thermal treatment to be lowered to 100 °C, and leading to highly efficient solar cells, setting the record performance at the time with 17.9%.

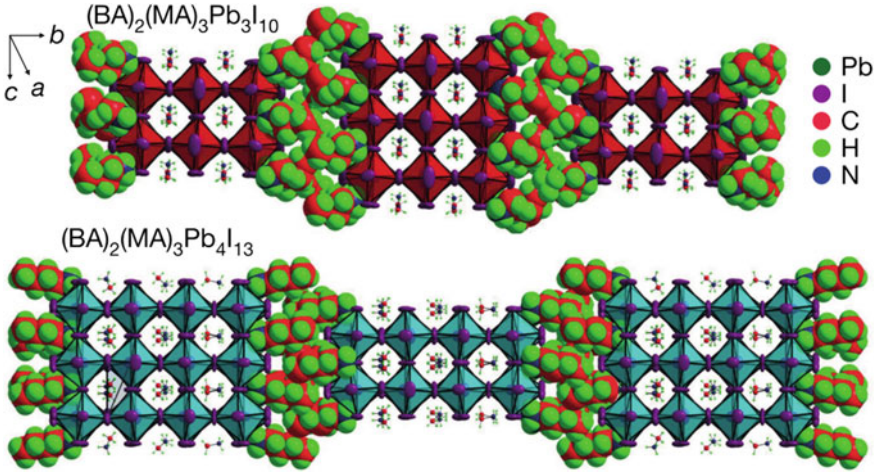

Fig. 10.4 The structure of 2D/3D perovskites with two different stoichiometries, as simulated by Tsai et al. [44]. Reprinted from [44]

This initiated an important research direction, and various compositions were then explored with the aim of improving the performance of the materials. It was found that besides the organic MA^+ and FA^+ cations, inorganic cations, such as Cs^+, Rb^+ or K^+ can be successfully mixed into a composition of halide perovskites [34–38]. Besides the mixed compositions, solar cells based on fully inorganic perovskites have also been demonstrared [39, 40]. One of the advantages of these compounds is high thermal stability, which is in contrast with $MAPbI_3$ that has been shown to degrade even when kept at moderate temperatures of around 60 °C for a prolonged time [41, 42] (Fig. 10.4).

Besides the combination of inorganic cations, alternative organic cations have also been investigated, with longer chain amines being one of specific interest. Their larger size results in the formation of a 2D, Ruddlesden-Popper layered perovskite structure [43]. By tuning the stoichiometry of the material, hybrid 2D/3D compositions can be achieved, enabling the tuning of perovskite properties, such as the band gap, conductivity, and stability [44, 45]. When an appropriate composition is chosen, this provides an interesting avenue to reach higher stability without compromising charge transport. In 2017, Grancini et al. have demonstrated a 2D/3D perovskite solar cell with a stability over 10000 h under constant illumination [46].

10.3 Processing Methods

So now we understand the factors that contribute to the attractiveness of perovskite absorbers. Let's take a look at the possibilities of creating the photoactive layer in this PV technology.

Perovskites are unique in this aspect as well. In their case, the deposition is followed by a crystallization step, which will have a great impact on the resulting performance of the solar cell. This is a facile process, as it can happen spontaneously in the presence of the required precursors [47]. Achieving a material with the desired properties however, requires the complex understanding of the system and the multitude of contributing factors guiding its evolution [38].

Polycrystalline perovskite thin films can be processed from solution, by evaporation, or by hybrid/alternative methods that combine these approaches [48]. Processing methods can be further categorized based on the number of deposition steps used to form perovskite layers, and in most cases films are formed in a one-step or a two-step method. The processing conditions are closely related to the material's composition that is aimed to be formed, but in this chapter we will discuss these two factors separately, in an attempt to give a more structured overview (Fig. 10.5).

We will start with the discussion on a solution-based processing, as it has been by far the most common way of producing perovskite films. Also, it holds the highest prospect of delivering ultimately low manufacturing costs [49].

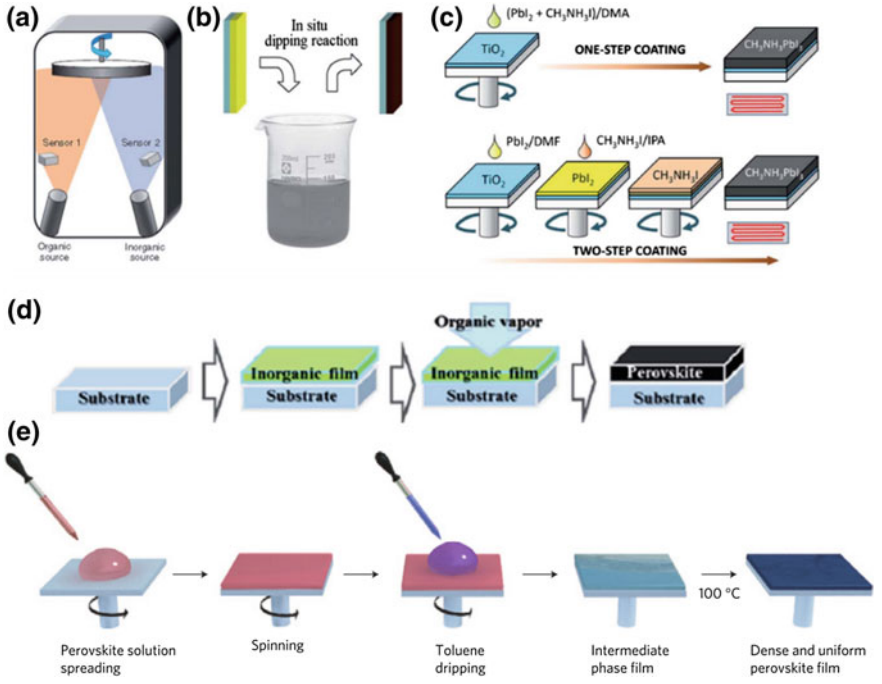

Fig. 10.5 Processing methods of perovskite thin films. **a** co-evaporation [76], **b** 2-step solution processing via in situ dipping [141], **c** one- and two-step solution processing via sequential coating [142], **d** vapor assisted solution processing [79], **e** antisolvent method [66]. Reprinted from ref [66, 76, 79, 141, 142]. Copyright 2013–2014 Nature publishing, 2014 American Chemical Society, 2014 AIP publishing

10.3.1 Solution Processing

The chemical quality, the age, the concentration and the stoichiometry of the precursors, the coordinating strength and boiling point of the solvents, the atmospheric composition of the processing environment, the type and duration of post treatments as well as the surface onto which perovskite is grown—everything will have an effect on the thin-film morphology and the optoelectronic properties [50, 51]. This will in turn define its crystallographic properties and greatly affect the device performance. Separating these parameters is a difficult task, and even though several research works have addressed these topics, drawing definitive conclusions from the results requires a careful approach.

The most straightforward approach is the one-step solution processing. In this case, the precursors (halide salts of the metal B and of the cation A) are dissolved in a polar aprotic solvent and deposited onto a substrate, using a spin-coating method for instance. Subsequently, the samples are annealed, leaving a thin film of perovskite on the substrate (Fig. 10.6c). Dimethylformamide (DMF) or dimethyl sulfoxide (DMSO) are the most widely used solvents, however alternatives such as γ-butyrolactone (GBL), N-methyl-2-pyrrolidone (NMP), 2-methoxyethanol and various solvent mixtures have also been investigated [52, 53]. While the implementation of this approach is easy, gaining control over the morphology of the resulting film requires profound understanding of the complex processes involved in the perovskite formation.

In the previous sections, it has been described that the A-site cations affect the geometry of the perovskite structure. It also has to be noted that their contribution to processability is of significant importance. It was observed that perovskite precursor formulations do not contain only solvated ions, but also various colloidal networks, comprising metal-halide based coordination complexes [31]. It was also

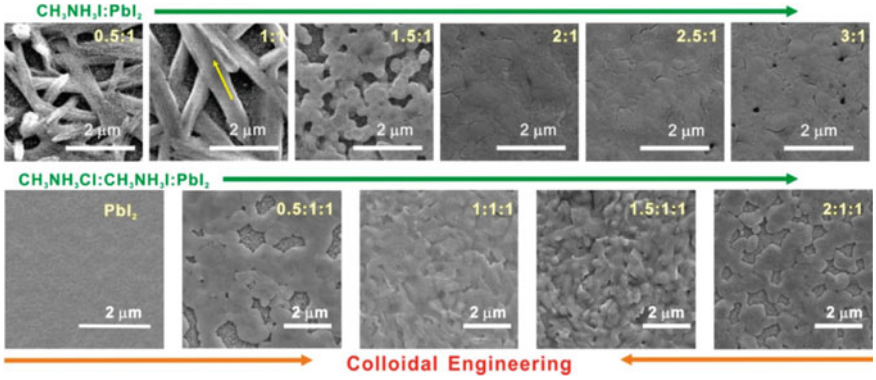

Fig. 10.6 SEM images of perovskite layers deposited from precursor solutions with different stoichiometries. The ratio of the components is represented in the top-right corner of the images. Reprinted from [31]

shown that the size and density of these colloids can have a defining effect on the nucleation and growth pathways of perovskite crystals, and as such, gaining control over these processes is of high importance. The colloidal framework is associated with lead polyhalides, which is accompanied by coordinating solvent molecules, forming Lewis acid-base adducts [13, 52]. It was shown that by engineering the strength of the bonds between the solvent molecules and the lead halide species the morphology of the perovskite films can be improved [54].

Initial works that utilized stoichiometric PbI_2: MAI precursor ratios have reported poor substrate coverage, with needle-like morphologies of the perovskite [55, 56]. This was attributed to the existence of lead-polyhalide complexes with a preferred rapid axial growth orientation. It led to poor device performance with a high variation depending on the measurement area. For high efficiency and reproducible solar cells, uniform, pinhole-free perovskite layers are needed with large grain sizes. As such, various approaches and materials have been investigated to provide a greater extent of control on perovskite formation by enlarging the time window available for processing [57, 58]. It was proposed that highly coordinative species form slow down the nucleation and crystallization of perovskites [59]. Additives (e.g.: DMSO, 1,8-diiodooctane (DIO)) aiming to reach this goal have been utilized with a success to various extents [56, 60, 61].

It was observed that the presence of Cl^- ions can also be beneficial for the morphology of the perovskite layer [62]. Thin films prepared from a mixture of $PbCl_2$ and MAI were initially considered as a 'mixed halide' perovskite, with chloride ions partially replacing iodide in a material's composition [9]. Later reports, and more in-depth analyses have shown that chloride ions are present in the film in very little amounts (less than 3–4%), and due to their size being too small to fit in, they are unlikely to be incorporated into the crystal lattice [63]. The improved performance is more likely a combination of improved growth with electronic effects that arise from the presence of chloride ions.

The observation that the stoichiometry of the perovskite thin film can be very different from the precursor composition opened up new avenues for processing these layers. It was found that there are various ionic species that can be considered as 'spectating', forming volatile compounds and leaving the system during the growth of the film [58, 62]. The examination of the processing window for different precursor materials and compositions was first carried out by Moore et al. [58]. Utilizing in situ wide angle X-ray scattering WAXS, they analysed the transformation kinetics of different lead salts to perovskite. They found especially attractive characteristics in the case of lead acetate.

The nucleation and the growth of perovskite polycrystalline films strongly depend on the interactions of a solvent with the precursors and the substrate. The solvent vapour's partial pressure determines the speed of liquid evaporation, which has an impact on formation kinetics. As the solvent evaporates, the concentration of the precursor is increasing, eventually reaching supersaturation [64]. This leads to nucleation, which can be either homogeneous or heterogeneous. The surface tension of the precursor dispersion and the surface energy and chemistry of the substrate will have a strong impact on the quality of the grown perovskite layer [65]. As such,

engineering these parameters became an important part of the solution-processed perovskite solar cell field.

A breakthrough came in 2014, when Jeon et al. and Xiao et al. reported a method in which they treated the sample with a non-polar solvent during spinning [66, 67]. Toluene and chlorobenzene were utilized for this purpose, as they are miscible with the commonly used GBL, DMF and DMSO, however they are poor solvents for the perovskite precursors. If the wet film is treated with the antisolvent in the proper time window, the residual solvents will be washed out immediately, and a uniform and smooth solid layer will be left on the substrate with high coverage. This approach gave researchers the possibility to lock-in and freeze a perovskite structure during its evolution, quenching its further progression. After optimizing the precursor composition and processing conditions—with special attention to the time window when the antisolvent is applied—this method can provide a reproducible approach for deposition of uniform layers that yield high performance devices [68]. As such, most efficient solar cells to date are fabricated with an anti-solvent strategy [34, 69, 70]. The main limitation of this approach is its scalability to industrial formats.

In a two-step processing, the lead compound is deposited first, and subsequently it is converted to perovskite by interdiffusion with the organic salt by a second coating step [71, 72]. The advantage of this method is that it is simpler to control the deposition of a single compound, and it allows the formation of homogeneous and continuous films. A crucial requirement of this approach is to enable the penetration of the organic cation deep into the inorganic layer, as its maximum depth will determine the obtainable perovskite thickness limiting the maximum achievable photocurrent and hence the maximum efficiency of the solar cell. This represented a challenge for initial experiments utilizing the 2-step approach. With the advancement of this technique, it was found that the infiltration of the cations can be facilitated by improving the deposition of the first inorganic layer [73]. The reported methods include varying the solvents used for deposition, utilizing complexing additives, and even structuring the metal halide [74]. Using these approaches, the best performing devices reached PCEs higher than 20% [75].

10.3.2 Evaporation

Evaporated perovskites can also be fabricated by one and two-step methods. The deposition is done by placing the precursors into separate crucibles in an enclosed chamber, and then heating them up to their sublimation temperature in high vacuum. The vapours of the materials condense and react on the substrates situated at a given distance from the sources, forming compact perovskite films at low temperature. One major advantage of this approach is its intrinsic additivity, as any combination of materials can be deposited in a stack, without the necessity of fulfilling solvent orthogonality requirement as it is in a solution-based process. Vacuum-grown perovskites reported in literature were shown to have highly smooth and uniform layers, providing a reliable processing approach [76]. On the other hand, being a vacuum

based process, it requires a sophisticated equipment and higher maintenance cost—which increases the cost of production.

The first vacuum deposited perovskite solar cells were reported in 2013 by Liu et al. [76]. This work highlighted the first perovskite solar cell in a planar n-i-p architecture, utilising TiO_2 and spiro-MeOTAD as electron and hole selective layers, respectively. The photoactive layer was based on co-deposited $PbCl_2$ and MAI. In order to form a stoichiometric composition, these layers had to be exposed to thermal annealing to remove the excess materials. A breakthrough in vacuum deposited perovskites was achieved by the group of Bolink only a few months later [77]. In that report, a co-evaporation process was carried out from stoichiometric MAI and PbI_2, and no further thermal treatment was needed to achieve a high quality perovskite layer, and in turn highly efficient solar cell performance. This in combination with utilizing organic interfacial layers resulted in a great reduction of processing temperatures, making it a versatile method compatible with flexible substrates.

The upcoming years of development in this processing method led to fully vacuum deposited perovskite solar cells, harnessing the full potential of this approach [78]. By finding organic interfacial layers with suitable energy levels and appropriate dopants, Momblona et al. have prepared highly efficient p-i-n and n-i-p perovskite solar cells by a sequential evaporation of the complete device architecture for the first time. A significant aspect of the above mentioned work is that it provides an approach towards perovskite/perovskite tandem solar cells.

10.3.3 Hybrid Processes

Vapor-Assisted Solution Processing (VASP) is a hybrid technique aimed to combine the high quality layers and control on growth provided by vapor methods, meanwhile maintaining the simplicity of solution processing [79]. First demonstrated by Chen et al. in 2013, this approach led to the highest performance in a planar architecture at the time. The method consists of depositing a metal-halide layer from solution, then exposing it to the vapours of the organic halide material. Several alternative hybrid techniques have been developed and reported since then, with various performances [80].

10.4 Device Architectures

In most perovskite solar cells, the photoactive layer is contacted with charge transport layers to selectively allow only one type of charge carrier to be extracted [81]. Doing so will have beneficial effect on the performance of a solar cell, as it will prevent the recombination of carriers in the electrode layer The transport material has to meet several requirements to fulfil this role.

Creating a contact with pertinent selectivity requires the energy levels of the valence and conduction band, the Fermi-level and the band gap of the transport layer to be of appropriate values [82]. This facilitates the extraction of one type of charge carrier, while blocking the other. Fulfilling these requirements will reduce fundamental electrical losses. A good selective layer will also have negligible optical losses, and as such it is important to minimize its absorption, as well as detrimental contributions from interference. An additional basic prerequisite is processability. In the case of solution processed perovskite solar cells, it means that the layer has to provide good wetting properties and withstand the aggressive polar solvents used for perovskite precursors, in case it is processed below the photoactive layer. Solvent orthogonality has to be met also when the selective layer is deposited on top of the perovskite. This limits the possible formulations to the ones based on non- and weak polar solvents, as polar solvents damage and dissolve halide perovskites.

Evolving from dye-sensitized solar cells (DSSCs), the first perovskite solar cells were fabricated using a mesoscopic TiO_2 film to harvest electrons from the photoactive material [5]. Its initial purpose was to provide an extraction interface in the bulk of the absorber to prevent losses from transport limitations. After discovering the excellent ambipolar transport properties of halide perovskites, this layout has developed over time to thinner layers, as the role of mesoscopic TiO_2 shifted towards facilitating crystallization [10]. However, it is still the most commonly used for perovskite cells, hence it is often referred to as the standard architecture. With the rapid development of perovskite devices, a wide range of selective charge transport layers and device architectures have been investigated [83].

A conventional method to categorize these solar cells is differentiating them based on the polarity of the front contact, the side on which light enters the device [84]. When the electron transport layer (ETL) is deposited on the front contact, the device has an n-i-p structure, whereas if the polarity is inverted (holes are extracted at the substrate side), the architecture is called p-i-n. Figure 10.7. represents the examples of common materials and architectures used for the fabrication of perovskite solar cells.

10.4.1 N-I-P

An archetypical n-i-p perovskite solar cell uses TiO_2 as the ETL, and spiro-OMeTAD as the hole transport layer (HTL) [8]. Notably, the highest reported power conversion efficiencies were achieved with devices in an n-i-p architecture [85]. Initially, a high temperature processing was required to achieve high quality TiO_2 layers, but with the advancements of the perovskite field several routes have been explored to overcome this limitation [86].

Alternative synthesis routes for metal oxides have been proposed, with one prominent method being atomic layer deposition (ALD) [87]. This allows the formation of compact and high quality thin films, providing additional barrier properties. It was used for depositing various materials, such as TiO_2, SnO_2, ZnO, NiO and Al_2O_3.

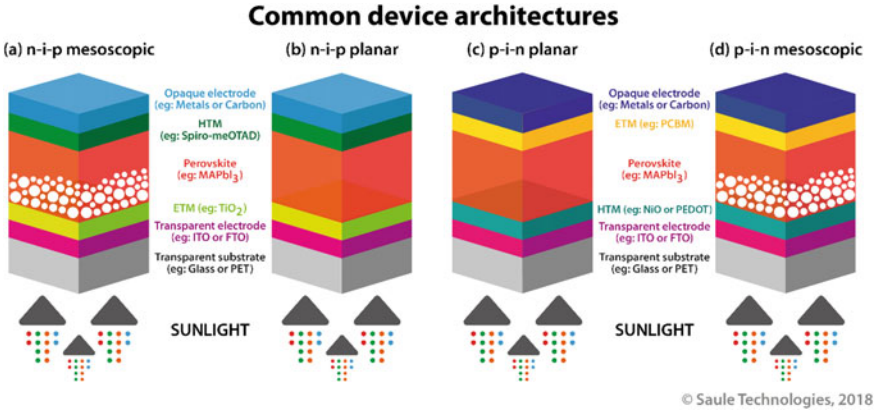

Fig. 10.7 Examples of common materials and architectures used for the fabrication of perovskite solar cells. Courtesy of Saule Technologies

Another approach is to use metal foils such as titanium as substrates, that enable higher temperature fabrication. In this case, finding a viable transparent top electrode is imperative [88]. Besides, module fabrication poses another challenge, as a solution has to be found to form the series connections without interrupting the conductive substrate. Different organic materials have been explored as well, both as stand-alone selective layers and in conjunction with metal oxides to improve their performance [83].

The most commonly used HTM in n-i-p perovskite solar cells is spiro-OMeTAD [89]. The deposition of this material has been very well optimized over the years to yield high efficiency devices, however there are a couple of shortcomings that has to be overcome. First of all, the fabrication of this material requires a complex synthesis, leading to a high price. Besides, there are concerns regarding the instability of solar cells based on spiro-OMeTAD induced by doping agents—a typical example being a highly hygroscopic Li-TSFI [90]. These additives are used to improve conductivity. Their detrimental effect point towards the necessity to develop novel hole transporters. This is an important research direction, and a plethora of novel materials have been proposed and reported already [89, 91, 92]. Many of them offer attractive properties with price, stability and efficiency outperforming the established spiro-OMeTAD.

10.4.2 P-I-N

The traditional p-i-n layout—also referred to as the inverted one—originates from OPV [93]. Utilization of organic semiconductors as transport layers provides the inherent advantage of low processing temperatures. Various PEDOT:PSS-type materials have been reported as viable HTMs, however usually a lower V_{oc} value is

observed in devices based on them [94]. This could be associated with interfacial defects leading to SRH recombination. One explanation is a reaction between the intrinsically p-doped PEDOT:PSS and the perovskite, that could reduce the work function of the transport layer. Alternative organic HTMs, as well as p-type metal oxides (such as NiO_x, Cu_2O, etc.) were utilized successfully to replace PEDOT, leading to improved performance and longevity [92].

The most commonly used ETL materials in a p-i-n architecture are fullerene derivatives, with PCBM being one prominent example [95]. To improve its performance, alternative functionalization methods have been reported, that enhance its solubility and/or promote a uniform arrangement on the surface of the active layer, leading to a more favourable morphology. Alternative organic materials and metal oxides have also been investigated [83].

As a general conclusion, metal oxides are an attractive group of materials as charge selective layers, due to their robustness and moisture barrier properties combined with a low cost. With appropriate interfacial engineering and processing, they are an interesting class of materials for transport layers in perovskite solar cells. Organic materials on the other hand offer tailoring of energy levels and simple low temperature processing routes.

10.4.3 Tandem Solar Cells

The band gap of $MAPbI_3$ is measured to be around 1.55 eV in a thin film, which is close to 1.34 eV—a value yielding the theoretical maximum efficiency (33.7%) for a single junction solar cell, as derived by Shockley and Queisser (SQ) [96]. This limitation can be overcome by the construction of tandem architectures, where several absorbers are connected electrically, reducing spectral losses from carrier thermalization. In this case, the performance will be dependent on the band gap energy of the complementary absorbers [97].

The preparation of a double junction solar cell incorporating commercially available mature technologies, such as crystalline silicon (c-Si) or CIGS solar cells (with band gaps between 1.1–1.3 eV), requires a complementary absorber with a band gap between 1.7–1.9 eV [98]. While this approach can improve device efficiency, it also makes the fabrication more complex, which is a crucial subject to consider in the perspective of a viable commercialization (Fig. 10.8).

Due to the above mentioned reasons, halide perovskite solar cells are particularly interesting for tandem applications, as their band gap can be engineered by an appropriate choice of the compound stoichiometry, and they also offer low cost fabrication methods combined with high performance. Their exceptional tunability makes them promising candidates to couple with c-Si or CIGS solar cells, and the realization of an efficient perovskite/perovskite tandem holds an attractive commercial potential [99–101].

Several works reported solar cells utilizing perovskite absorbers with an optimized band-gap for tandem applications [101]. A commonly observed challenge of

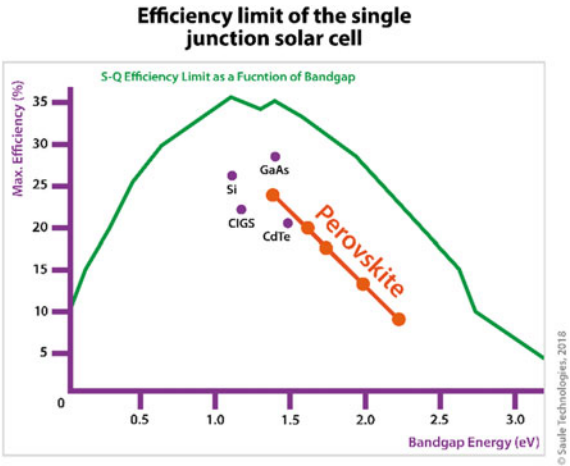

Fig. 10.8 The Shockley-Queisser efficiency limit as the function of the band gap. The current efficiency records of different technologies are highlighted. Courtesy of Saule Technologies

such systems is the segregation of halide species under illumination, forming recombination centres that limit performance [102]. This effect is especially pronounced in mixed I^-/Br^- compositions that exhibit a band gap in the above mentioned optimal range.

It was reported, that when alloying lead and tin based perovskites, the band gap changes in an anomalous way, reaching lower levels than either of the pure materials [103]. This change is accompanied with an improved material stability, making these compositions interesting for single junction and perovskite/perovskite tandem applications.

Tandem architectures can be categorized based on the arrangement between the sub-cells [104]. Two-terminal monolithic (2T), and four-terminal (4T) devices have been the most extensively investigated in case of perovskites. 4T tandem solar cells have so far yielded higher performances, however it requires 2 complete devices with front and back electrodes to be prepared. The monolithic connection is the most challenging and rewarding layout, as it enables a simple series electronic connection, and requires only 2 electrode layers. There are however several challenges that have to be met in order to fabricate highly efficient 2T solar cells. These include processability, current matching between the sub-cells, an efficient charge recombination layer between the sub-cells, and optical management.

The combination of these demands have so far limited the performance of perovskite-based monolithic tandem cells to be below that of the single junction record of the respective sub-cells [104]. Nevertheless, there is a rapid development, and it is expected that perovskite tandems will soon outperform their single junction counterparts (Fig. 10.9).

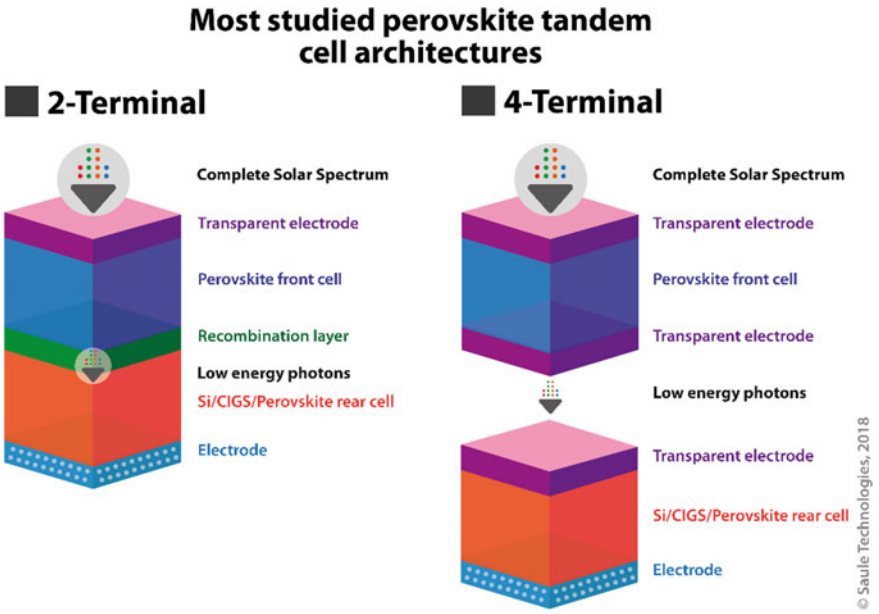

Fig. 10.9 The most studied perovskite tandem cell architectures (left) 2-terminal (right) 4-terminal. Courtesy of Saule Technologies

10.5 Device Operation

10.5.1 Charge Generation and Transport

Once an incoming photon interacts with an electron near the VBM, charge carriers are generated [105]. An electron will be excited to a higher energy state, leaving behind a hole with a positive charge. As these are carriers with an opposite charge, an electrostatic Coulomb interaction will bind them together, creating a quasiparticle called an exciton [106]. In order to generate electricity, these charge carriers have to be separated and transported to their respective electrodes. Let's take a look, how perovskites perform at these tasks!

Materials with a high dielectric constant (like Si or GaAs) allow the formation of Wannier-Mott excitons. These excitons have binding energies on the order of 10 meV [107]. It is comparable with the thermal energy at room temperature, which amounts to 25.7 meV. Consequently, the generation of free charge carriers is facilitated as excitons easily dissociate, which is beneficial for high performance solar cells. There are several reports examining the dielectric constant and the exciton binding energies of halide perovskites, in particular $MAPbI_3$ [108]. The findings are that perovskites exhibit a high dielectric constant, which is increased further by orders of magnitude upon illumination. The origin of this behaviour is under scrutiny, with one possible explanation it being correlated with mobile ions in the lattice. Nevertheless, as the

high dielectric constant implies, the exciton binding energy in this material is low. Values between 2 and 55 meV have been reported using different approaches, with a direct measurement method that showed it to amount to 16 meV [107, 109]. The preferred generation of free charge carriers is supported by the lack of excitonic peaks in the absorption spectrum of $MAPbI_3$ at room temperatures. Temperature-dependent PL measurements have highlighted that the excitonic peak is present in $MAPbI_3$ at low temperatures, below 100 K [16]. As the temperature increases, the excitonic peak diminishes and completely disappears at 160 K. At the same time, a new, higher energy peak appears, indicating the radiative band-to-band recombination of free charge carriers (Fig. 10.10).

Once the charge carriers are generated, they have to be transported through the photoactive material, to reach their respective electrodes [84]. This happens via the combination of two effects: drift—driven by an electric field, and diffusion—driven by a gradient in concentration. A good contact will extract charges at a rate that is higher than the rate of diffusion in the bulk of the absorber, and thus a concentration gradient will be created. However, when the extraction is slow, charge will build up at the vicinity of the interface retarding the extraction of carriers even further.

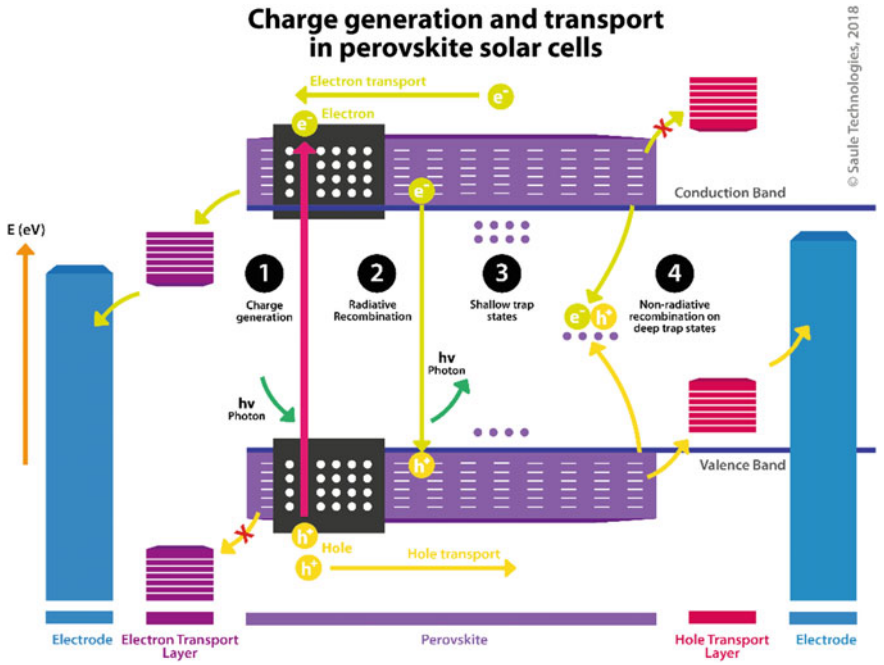

Fig. 10.10 Charge generation, transport, and recombination in perovskite solar cells. (1) A photon is absorbed, electron-hole pairs are generated. (2) Radiative recombination – photons are emitted. (3) Shallow trap states. (4) Deep trap states leading to non-radiative recombination. Courtesy of Saule Technologies

If the carriers recombine before being extracted, the energy of the absorbed photon will be lost, leading to a decreased power output [24]. Hence, it is important to understand what the diffusion length of the charge carriers is in a given material, as it will determine the maximal layer thickness that can be used for efficient transport properties. The examination of these characteristics were first carried out in 2013 [10]. Using transient absorption and time-resolved photoluminescence decay measurements, Stranks et al. found diffusion lengths that can exceed one micron in a perovskite film. These high values were surprising, but it corroborated well with the good performance of solar cells without a mesoporous TiO_2 which was previously thought to be necessary for efficient charge extraction. The observation of long PL-lifetimes, diffusion lengths and ambipolar transport led to the realization that there is no explicit need for this and perovskite solar cells can be efficient in a conventional planar thin-film structure [110]. This is in contrast with organic photovoltaics, where a bulk heterojunction is needed to provide a quick charge separation to prevent recombination. These findings provided a major breakthrough in understanding the basic principles of photophysical processes occurring in such systems.

10.5.2 Loss Mechanisms

Charge carriers that are not extracted will recombine. It is an inevitable process, and it is desirable for all the recombination to be of radiative type, like it would take place in an ideal solar cell material [111]. This way, under 1-sun illumination, it can enable a build-up of high internal photon densities resulting in higher operating voltages. Non-radiative recombination present in the material will act as a loss mechanism, restraining the maximum efficiency to lower values than that of the SQ limit. At the SQ limit, the external quantum efficiency (EQE) of the electroluminescence (EL) is 1, which means that there are no non-radiative losses. The EL can be recorded by operating the solar cell as an LED, applying forward bias that exceeds the V_{oc} value. It is an interesting tool for getting information on non-radiative losses, and optimizing record-breaking cells.

Non-radiative recombination typically originates from the presence of trap states [112]. A charge carrier can fall into this state, and subsequently recombine with a carrier of opposing charge. These trap states are formed due to defects in the crystalline material, and they can be categorized based on their depth. Deeper are more detrimental, providing an easier path for recombination. As such, it is crucial to analyse the defects in absorber materials, and their contribution to the loss mechanisms.

Crystallographic defects natively present in semiconductors are the product of the crystal growth, and their appearance cannot be completely avoided. The defect density is given as their number per cubic centimetre of the material. Semiconductor materials utilized for solar cell applications exhibit low to moderate densities, with values reported being sc-Si: 10^8 cm^{-3}, poly-Si: 10^{13}–10^{14} cm^{-3}, CIGS: 10^{13} cm^{-3}, CdTe: 10^{13}–10^{15} cm^{-3} [113]. $MAPbI_3$ single crystals have also been examined, and low values of around $10^{11}cm^{-3}$ have been found. Surface and interfacial defects are

considered to be the source of most non-radiative recombination present in perovskite solar cells.

In a polycrystalline film, the homogeneity of the semiconductor is interrupted at the grain boundary, and these areas are naturally prone to be more defective [114]. As such, the role of grain boundaries in perovskite films had been under intense investigation. The reported defect densities for polycrystalline $MAPbI_3$ films are several orders of magnitude larger than that of single crystals, with relatively high values of 10^{15}–10^{16} cm^{-3} [113]. While various works correlated the grain boundaries with the high density of defects and the primary source of non-radiative losses, other findings demonstrated them with a benign nature. It is generally accepted that they serve as a platform where moisture-induced degradation can initiate, and that larger grain sizes are generally beneficial for device performance and stability.

Despite the relatively high level of defect density present, solar cells based on perovskite thin films show excellent efficiencies with V_{oc} values that are quite high compared to their band gap energy, and deliver long carrier diffusion lengths [115]. These seemingly contradictory findings point towards an unusual defect tolerance. Various studies examined the origin of this phenomenon. [23, 24, 116] The findings indicate that the most likely defects with low formation energies result in shallow traps that are less detrimental to device performance. This behaviour can be explained by the characteristics of the valence band constituted by antibonding orbitals, which probably leads to states in the band and not the band gap in the presence of a broken bond [24]. Besides, dangling bonds typically present in covalent semiconductors will not be formed in a strongly ionic lattice, as the additional charge will be screened due to the high dielectric constant of the perovskite lattice, leading to shallow traps. It was also found that the less abundant iodine interstitials actually lead to deep level electron and hole traps in $MAPbI_3$ [117]. Nonetheless, due to the distinctive amphoteric nature of iodine, the electron traps are kinetically deactivated. This leaves only hole traps as harmful defects, and they can be passivated via a redox transformation. Interstitial iodine was also shown to have the lowest migration activation energy of all ionic species present in a perovskite material [118]. As such, it is an important research direction to find a robust strategy for the passivation of defects [115]. Various materials and post treatment methods were explored to achieve this, with promising improvements on the V_{oc} and stability of the solar cells [35, 119].

10.5.3 Device Measurement and Hysteresis

Solar cells are evaluated and characterized with a current-voltage measurement. This is a standardized method, that consists of illuminating a solar cell with the AM 1.5G spectrum with an intensity of 1000 W/m^2, and recording current values as a function of applied voltage. Three parameters are extracted from the measurement: the short-circuit current (J_{sc}), the open-circuit voltage (V_{oc}) and the fill factor (FF). These together are used to determine the solar to power conversion efficiency of a device. A voltage sweep is applied in two directions; forward and reverse direction. This method

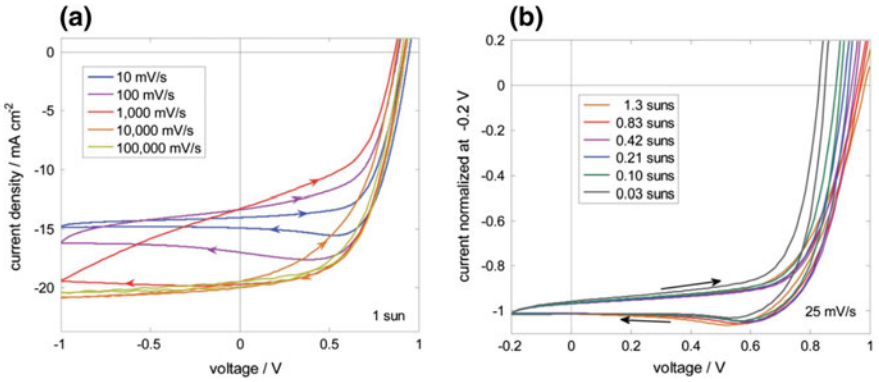

Fig. 10.11 Current-voltage characteristics of the same perovskite solar cell recorded under. **a** Various scanning speeds and **b** illumination intensities. Reprinted from [143]

is supposed to represent the steady state power output of a solar cell in operation under the given bias. The shape of the recorded curve and the corresponding figures of merit should be independent of the sweep direction, speed or biasing history—excluding minor deviations. It is however not the case when measuring perovskite solar cells.

Since the early days of perovskite solar cell research, the I-V characterization of the devices carried ambiguity. It has been observed that the current-voltage curves of perovskite solar cells display a loop, and this phenomenon is referred to as hysteresis [120] (Fig. 10.11).

The presence of this characteristic has been reported in many works, and while its extent have been different, it is pertained regardless of the deposition method of the perovskite as well as the interfacial layers utilized. It has been also noted, that these effects change based on the biasing history of the solar cell, as well as the speed at which the current-voltage sweep has been carried out [121]. This effect will create uncertainty in the evaluation of the photovoltaic characteristics of devices and the comparison of the performance of different processes and materials utilized for the fabrication of the solar cells.

Subsequently, many works addressed this phenomenon, reaching for different explanations, such as ferroelectricity, charge carrier trapping, or interfacial effects [122]. There is a rate-independent, slow response, and a rate-dependent, fast response. Currently there is a fairly broad consensus on the origin of hysteretic effects as majority of research findings suggest that migration of ionic species present in the perovskite material play a primary role [118]. In the presence of an electric field, mobile ions accumulate in the vicinity of the electrodes. This will build up a space charge adjacent to the collection layers, which in turn will have an effect on charge transport, extraction and recombination. It results in an enhancement or inhibition of carrier collection based on the pre-biasing history, and consequently, a hysteretic current-voltage response (Fig. 10.12).

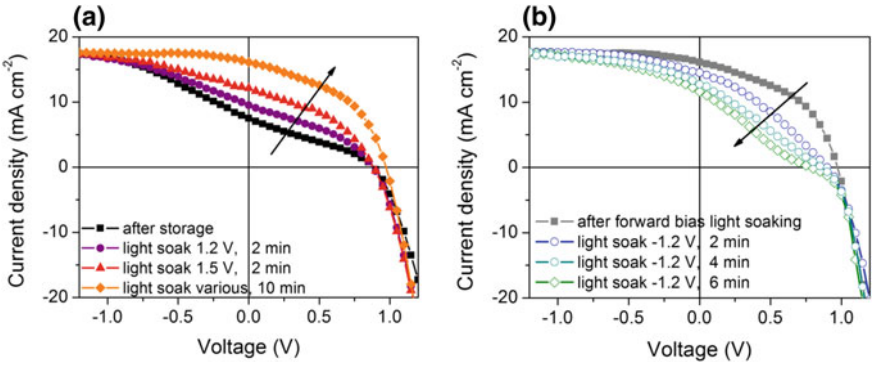

Fig. 10.12 The effect of light soaking on the I-V characteristics of perovskite solar cells. Reprinted from ref [121]

Besides the interaction with the electric field, mobile ionic species in perovskites were shown to interact with electromagnetic radiation and heat as well [123]. Light-soaking changes the photovoltage of solar cells, and corresponding PL-measurements have highlighted an increased lifetime and intensity under illumination.

The problems that the presence of mobile ions generate regarding the estimation of the actual performance of the solar cell can be overcome by slow I-V sweeps and maximum power point (MPP) tracking, which are now recommended by the perovskite community as measurement standards. However, there are concerns that it raises regarding the internal stability of perovskites, which are one of the major topics that are under scrutiny today [124].

10.6 Scale up

10.6.1 Commercialization Bottlenecks

Initially thought of as a sensitizer in DSSCs, perovskites were soon recognized as new thin-film absorbers [83]. The pioneering works initiated an extensive research on hybrid halide perovskites as a stand-alone PV technology. In the following years, various methods were explored to deposit high quality perovskite materials [66, 73, 76, 81]. The focus was to understand how the chemistry of diverse precursors is affected by a multitude of processing techniques and conditions, and how it influences the optoelectronic properties of the deposited perovskite thin film.

After several years of development, perovskite PV technology has grown into a viable solution with tangible prospects in the near future [125]. The next step is to develop appropriate production methodologies, and scrutinize the two major challenges regarding the material: its stability, and its environmental impact.

The origin of instability in perovskites can be categorized as either external or internal, based on the source that introduces it.

The intrinsic instability is related to the low heat of formation of perovskite from its precursors, PbI_2 and MAI in the case of $MAPbI_3$ [41]. It results in weak thermodynamic stabilization, and the material can easily decompose to its constituents at elevated temperatures. Overcoming these limitations can be achieved by the usage of alternative, thermodynamically more stable perovskite materials. The inclusion of FA and Cs ions were shown to improve the thermal stability, as well as an alloying with lower dimensionality perovskites [37].

The sensitivity towards environmental agents refers to decomposition that is induced by moisture, oxygen and UV-light [52]. The most straightforward way to overcome this issue is impervious encapsulation of solar cells, to prevent them from being exposed to harmful effects. Existing methods for alternative thin-film photovoltaic technologies as well as OLEDs might be utilized as a guidance here [126]. Besides, engineering the perovskite material to be intrinsically more endurant towards these effects will also be beneficial.

The degradation of interfaces arises from photoelectrochemical interactions between the perovskite and the transport materials and electrodes [127]. There is a well-known concern regarding the archetypical spiro-OMeTAD. Besides its high price, this material was shown to deteriorate quickly, especially in the presence of its common dopants that are used to oxidize spiro-OMeTAD and in turn increase its conductivity. It was also observed that metal ions from the electrode, and iodide ions from perovskite can migrate through organic transport layers severely affecting device performance. The usage of metal oxides and carbon-based electrodes were shown to reduce these effects [128]. The development of new, robust interfacial layers will also contribute to overcome this issue.

The migration of ionic species under illumination or via an electric field was shown to alter the output power of the solar cell [112]. These changes have shown to be reversible after a few cycles, however, concerns are present whether this has long-term implications, and intrinsic limitations on the lifetime of perovskite solar cells.

Besides the stability of the material, researchers are generally concerned about the lead content of the most efficient perovskite absorbers [129]. Being a heavy metal, there are obvious questions that arise regarding the environmental and health-related impacts of a large-scale production that involves lead. As such, it will be necessary to carry out thorough examinations of these topics, to understand and minimize the risks associated with them. One solution is to increase device stability and combine it with proper, fail-proof encapsulation. From a legislative point of view, there might be also a few limitations to overcome in order to enter the market, as there are precise indicatives on what levels of heavy metal contents are allowed in a commercial product.

An alternative approach is the development of lead-free perovskites [130]. However, due to the previously described electronic structure of these materials, the p-p transition in lead halide perovskites plays a crucial role in the excellent absorbing

properties of the material. As such, it is challenging to find an alternative formulation that allows the formation of a perovskite material with the same excellent properties.

Typically considered alternatives are tin-based perovskites [131]. $MASnI_3$ was shown to have a narrower band gap than $MAPbI_3$, which is closer to the optimum for single junction solar cells. However, due to the amphoteric nature of tin, there are difficulties that arise regarding the processing and the stability of these absorbers, as Sn^{2+} can easily oxidize to Sn^{4+} which does not form a perovskite structure [132]. The amphoteric nature of tin also contributes to the toxicological effect of perovskites based on it, as reported by Babaygit et al. [129]. When exposed to water, tin drastically lowers its pH value, and eventually it leads to the demise of living organisms at lower concentrations than lead. Nevertheless, perovskite solar cells based on tin are investigated, but their efficiencies are much below the state-of-the art devices based on lead.

Alternative materials, such as germanium- bismuth- or titanium-based perovskites have also been investigated, however solar cells based on them have so far always displayed a poor performance [130, 133, 134]. As perovskites cover a huge amount of formulations, computational methods might provide a viable, quick and efficient way to discover new photoactive materials. This has been demonstrated by Zhao et al., who identified 64 possible new formulations of double perovskites [135]. In these compositions, a mono- and a trivalent metal cation replaces two divalent ones. Due to the large number of possible compositions, the development of double perovskite materials might be a successful way to create efficient and lead-free perovskite solar cells [130, 134, 136].

10.6.2 Target Markets

A successful market entrance of perovskite solar cells will largely depend on how all the performance parameters will be related to their price. A commonly used figure of merit for energy generating assets is the levelized cost of electricity (LCOE) [137]. This provides an assessment of the minimal cost at which the energy has to be sold to reach break-even over the entire lifetime of the generating asset. It is calculated by dividing the total average cost of operating electricity source by the total generated energy. Cai et al. have performed the first detailed LCOE analysis on perovskite solar cells, taking realistic scenarios into account [138] (Fig. 10.13).

This work pointed out, that the LCOE values that perovskite solar cells can reach are much below all other currently available energy sources, provided that an efficiency of 12% can be reached with a lifetime of at least 15 years. These values were estimated for glass-sealed n-i-p modules deposited on a glass/FTO substrate. Several important conclusions were drawn from the performed analysis. First, the cost of the photoactive and transport layers, and the solvents used to deposit them contribute only a small amount to the final cost. More than half of the total module costs are constituted by the transparent conductive oxide. According to their calculations, the

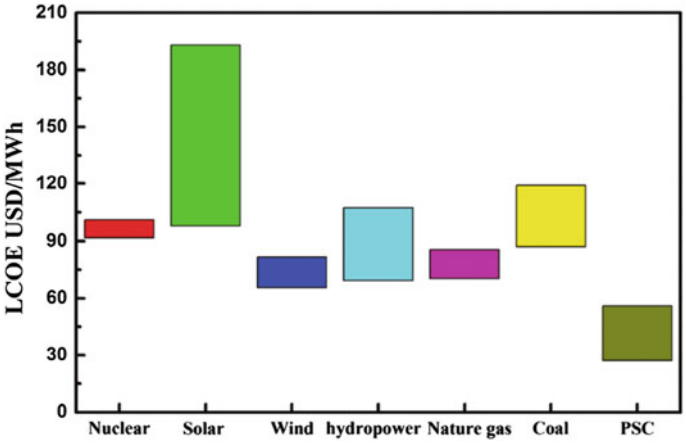

Fig. 10.13 Representation of an LCOE analysis of different energy. Sources [138]. Reprinted with permission from ref [135]

module efficiency plays one of the most important role in determination of the final price.

While these calculations are pointing towards the great potential that lies in the commercial entry of perovskites, there are few trends that should be taken into account. The price of silicon solar cells have been falling rapidly in the last decade, and continues to do so [139]. There is a learning curve which correlates the increased amount of cumulative production with the price of the product. However, since 2011 the costs fall under the value predicted by this curve. It has already led to the bankruptcy of many solar manufacturing companies, and it does not create a favourable landscape for a new technology to enter the market. As such, it is imperative for entrepreneurs that are planning to bring a new technology into the market to realize the implications of the above. As a first principle, targeting applications where crystalline silicon is not viable will be probably the easiest direction for stand-alone perovskite solar cells.

Considering the above mentioned limiting factors and the advantageous properties of perovskites, there are several target markets that could be accessed by such solar cells [137]. Building integrated photovoltaics is one segment, where perovskites are forecast to “shine”. This is mainly due to their high efficiency and excellent absorption properties, which enables them to generate power efficiently, even from indirect or scattered light. As such, perovskite solar modules could be implemented onto facades, enlarging the area available for photovoltaic energy generation and contributing to the development of zero-energy buildings. The favourable low-light performance also enables indoor applications, such as the powering smart home systems or various low-power electronics. There could be alternative applications, for instance charging portable electronic devices and electric vehicles.

An alternative approach is to create tandem structures, and doing so on silicon that already dominates the market seems to be an attractive option [99]. Capitalising

on the existing large-scale value chain of the dominant PV technology, this approach could enable a rapid development. While this can improve the performance of silicon solar cells, and potentially further reduce the cost of electricity, it also sets high requirements for perovskites. For this to be viable, the development of a high performance, wide bandgap perovskite is needed, that allows current matching of the sub-cells [104]. The material should also exhibit a stability comparable with silicon solar cells, and reaching this point might substantially postpone the realization of a viable product.

Due to their high efficiency and defect tolerance, perovskites are also promising candidates for space applications [138]. For the greatest impact, this requires the development of a light-weight substrate and encapsulation, that will maximize their power-to-weight ratio. It was shown already that perovskites can outperform the state of the art GaAs in this figure of merit as well [139].

The ultimate goal is to live on a planet fuelled by clean, safe and reliable energy. This should be the clear guidance to all organizations that work on perovskites, providing the paradigm for interinstitutional collaborations, and the design and development of future products. It is our responsibility to carefully evaluate all the risks associated with perovskites, and to find the way to eliminate any potentially harmful aspects. Maximal effort should be made with the aim of collaborating in the development of a technology that is beneficial for all humankind.

10.7 Advancements by Saule Technologies

Saule Technologies was established in 2014, shortly after the first breakthrough findings about perovskites were published. The sole purpose of the company is the commercialization of photovoltaic cells based on this new technology. Saule has pioneered the application of ink-jet printing for the fabrication of flexible, lightweight, and efficient perovskite solar modules.

As spin-coating—the most commonly used deposition method is not suitable for industrial size scaling, an alternative approach has to be utilized. Ink-jet printing has been chosen as a production method of perovskite solar cells, as it offers several favourable properties. In this approach, the ink-jet printer nozzle is applying the ink exactly at a pre-defined location with high resolution. Using this technique enables the creation of custom patterns, as the shapes and areas covered by each layer can be all tailored according to the requirements. This feature will allow architects to utilize BIPV with a great degree of design freedom.

The processing is carried out in ambient conditions with a negligible waste of materials. This is facilitated by the drop on demand approach, which is accomplished by driving the nozzles with a piezoelectric material. When the ink-jet head reaches the targeted location, a voltage signal is used to alter the shape of the transducer, forcing the drops out of the nozzles. Figure 10.14 (left) represents the operation of a nozzle. An industrial-scale ink-jet head has several hundreds of them, enabling a rapid and high-resolution printing at a low cost.

Utilizing ink-jet printing for large scale production requires a number of parameters to be engineered. For example, the ink used for printing has to fulfil viscosity and surface tension requirements set by the printhead, to enable a stable jetting. Besides, the solvent system has to provide the necessary solubility for the component to be deposited, as well as solvent orthogonality with the underlying layer. A common strategy to overcome these issues is to utilize solvent mixtures and additives to meet prerequisites for printability. The wetting properties of the ink also have to be optimized. If it is "too good", the deposited droplets will spread rapidly, and it will prevent a high resolution printing. Poor wetting on the other hand will lead to non-uniform coverage. Various surface treatment methods can be utilized to optimize the interaction between the ink and the surface onto which it is deposited.

Saule Technologies was the first company to present a working demonstrator in 2016. The device was a module that contained 24 solar cells with an active area of 1 cm^2, capable of charging a phone under intense illumination. During 2017, Saule has increased the scale of this technology from 1 cm^2 size solar cells deposited on a laboratory scale into an automated method that covers the size of an A4 paper (210 × 297 mm). In the same year, the company has also developed a robust encapsulation method compatible with perovskite solar cells, which prevents moisture and oxygen from penetrating into the solar cell. This technique has been shown to enable the undisturbed underwater operation of such modules, highlighting the viability of the approach.

The developments described above highlight that by 2019–10 years after their first demonstration—perovskite solar cells have matured to a technology that is close to its market entrance. It is the fastest developing field of photovoltaics to date, and while there are still some open questions about the peculiarities of the photoactive material, we at Saule are sure about its eventual success. We are striving to utilize the potential of this technology to its utmost extent, with the aim of contributing to

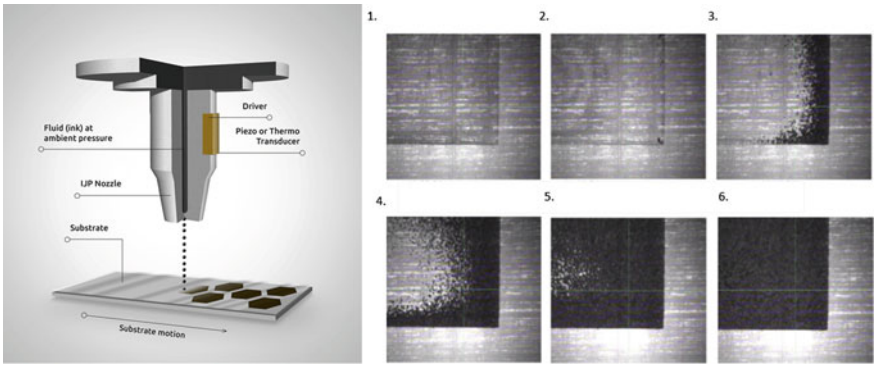

Fig. 10.14 (left) The schematic of an ink-jet printing nozzle, depositing materials on a substrate. (right) The crystallization of perovskite as seen by the fiducial camera. Courtesy of Saule Technologies

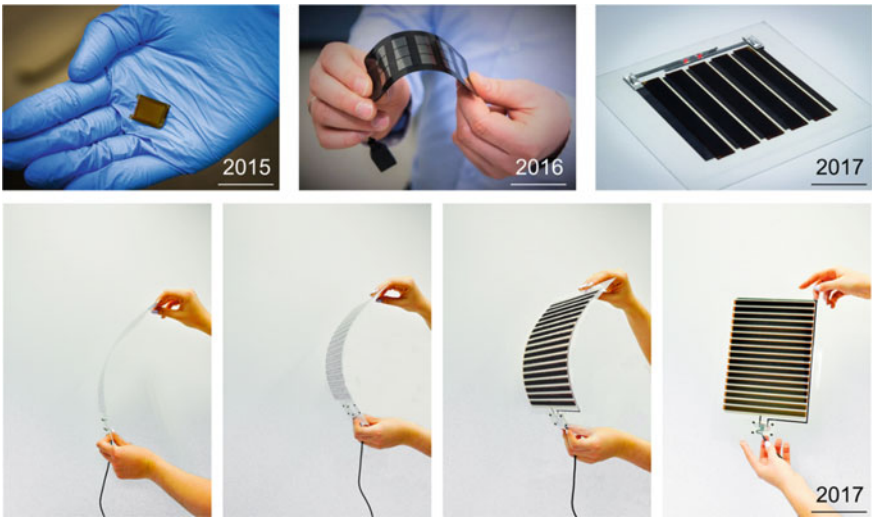

Fig. 10.15 The evolution of demonstrators by Saule technologies: (2015) An ink-jet printed perovskite solar cell. (2016) A perovskite solar module made of single cells externally connected in series. (2017, top) Ink-jet printed flexible perovskite solar module (2017, bottom) An A4 paper-sized, ink-jet printed perovskite solar module, capable of charging portable electronic devices. Courtesy of Saule Technologies

a global change leading to clean, safe, sustainable and low-cost energy production (Fig. 10.15).

Currently, Saule is collaborating with Skanska to develop offices with a BIPV solution, where semi-transparent and opaque perovskite solar modules will be utilized on the windows and facades of office buildings respectively. The possibilities in using perovskites for space applications are also being explored in collaboration with JAXA, the Japanese space agency. The high specific power of light-weight perovskite modules provides the technology with great potential, and the initial tests regarding their tolerance to radiation present in such conditions supports this research direction (Fig. 10.16).

By the end of 2018, the technology development has enabled Saule to create two major demonstrators, initiating the real-life test of printed perovskite photovoltaics. Skanska has installed a façade element into their Spark office situated in Warsaw, Poland consisting of 54 ink-jet printed perovskite solar modules. Henn-na Hotel in Nagasaki, Japan has erected a curved glass structure containing 72 perovskite modules. These modules are used to power the illumination of the logos of the respective companies, and the performance of the solar cells are monitored. The greatest importance of these demonstrators is to highlight that the technology has matured to the point that enables ambient processing of hundreds of functional perovskite modules in a semi-automated manner, and prospects good views towards the upcoming commercial entrance of such devices (Fig. 10.17).

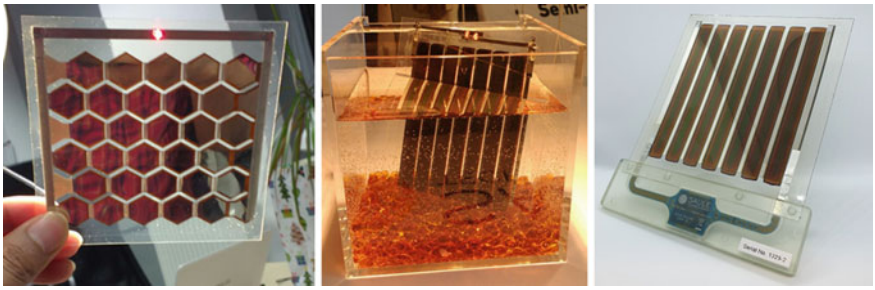

Fig. 10.16 (left) Perovskite solar module with a hexagonal pattern (middle) A perovskite solar module operating underwater (right) An autonomous, battery-free Bluetooth beacon operating in indoor lighting conditions. Courtesy of Saule Technologies

Fig. 10.17 (left) Curved glass façade element in Nagasaki, Japan with 72 printed perovskite modules (right) Visualization of a BIPV application: perovskite modules integrated into windows of a skyscraper. Courtesy of Saule Technologies

References

1. Q. Chen et al., Under the spotlight: The organic–inorganic hybrid halide perovskite for optoelectronic applications. Nano Today **10**, 355–396 (2015)
2. D.B. Mitzi, C.A. Feild, Z. Schlesinger, R.B. Laibowitz, Transport, optical, and magnetic properties of the conducting halide perovskite CH3NH3SnI3. J. Solid State Chem. **114**, 159–163 (1995)
3. S. Wang, D.B. Mitzi, C.A. Feild, A. Guloys, Synthesis and characterization of [NH2C(I) = NH2]3MI5 (M = Sn, Pb): stereochemical activity in divalent tin and lead halides containing single (110) perovskite sheets. J. Am. Chem. Soc. **117**, 5297–5302 (1995)
4. D.B. Mitzi, Solution-processed inorganic semiconductors. J. Mater. Chem. **14**, 2355 (2004)
5. A. Kojima, K. Teshima, Y. Shirai, T. Miyasaka, Organometal halide perovskites as visible-light sensitizers for photovoltaic cells. J. Am. Chem. Soc. **131**, 6050–6051 (2009)
6. J.-H. Im, C.-R. Lee, J.-W. Lee, S.-W. Park, N.-G. Park, 6.5% Efficient perovskite quantum-dot-sensitized solar cell. *Nanoscale* **3,** 4088 (2011)
7. I. Chung, B. Lee, J. He, R.P.H. Chang, M.G. Kanatzidis, All-solid-state dye-sensitized solar cells with high efficiency. Nature **485**, 486–489 (2012)
8. H.-S. Kim et al., Lead iodide perovskite sensitized all-solid-state submicron thin film mesoscopic solar cell with efficiency exceeding 9%. Sci. Rep. **2**, 591 (2012)
9. M.M. Lee, J. Teuscher, T. Miyasaka, T.N. Murakami, H.J. Snaith, Efficient hybrid solar cells based on meso-superstructured organometal halide perovskites. Science (80-.). **338**, 643–647 (2012)
10. S.D. Stranks, et al., Electron-hole diffusion lengths exceeding 1 micrometer in an organometal trihalide perovskite absorber. Science (80-.). **342**, 341–344 (2013)
11. L.M. Fraas, *Low-Cost Solar Electric Power*. *Low-Cost Solar Electric Power* **9783319075**, (Springer International Publishing, 2014)
12. S.D. Stranks, H.J. Snaith, Metal-halide perovskites for photovoltaic and light-emitting devices. Nat. Nanotechnol. **10**, 391–402 (2015)
13. N.-G. Park, M. Grätzel, T. Miyasaka, K. Zhu, K. Emery, Towards stable and commercially available perovskite solar cells. Nat. Energy **1**, 16152 (2016)
14. V.M. Goldschmidt, Die Gesetze der Krystallochemie. Naturwissenschaften **14**, 477–485 (1926)
15. W. Travis, E.N.K. Glover, H. Bronstein, D.O. Scanlon, R.G. Palgrave, On the application of the tolerance factor to inorganic and hybrid halide perovskites: a revised system. Chem. Sci. **7**, 4548–4556 (2016)
16. K. Wu et al., Temperature-dependent excitonic photoluminescence of hybrid organometal halide perovskite films. Phys. Chem. Chem. Phys. **16**, 22476–22481 (2014)
17. M.A. Green et al., Solar cell efficiency tables (version 51). Prog. Photovolt. Res. Appl. **26**, 3–12 (2018)
18. U.K. Mishra, J. Singh, *Semiconductor Device Physics and Design* 28–91 (Springer Netherlands, 2008). https://doi.org/10.1007/978-1-4020-6481-4_2
19. A.S. Lin, et al., High mechanical strength thin HIT solar cells with graphene back contact. IEEE Photonics J. **9**, (2017)
20. K. Yoshikawa, et al., Silicon heterojunction solar cell with interdigitated back contacts for a photoconversion efficiency over 26%. Nat. Energy **2**, (2017)
21. W.-J. Yin, J.-H. Yang, J. Kang, Y. Yan, S.-H. Wei, Halide perovskite materials for solar cells: a theoretical review. J. Mater. Chem. A **00**, 1–17 (2015)
22. P. Umari, E. Mosconi, F. De Angelis, Relativistic GW calculations on CH3NH3PbI3 and CH3NH3SnI3 perovskites for solar cell applications. Sci. Rep. **4**, 4467 (2015)
23. M. Kot, K. Wojciechowski, H. Snaith, D. Schmeißer, Evidence of nitrogen contribution to the electronic structure of the CH3NH3PbI3 perovskite. Chem. A Eur. J. **24**, 3539–3544 (2018)
24. W. Tress, Perovskite solar cells on the way to their radiative efficiency limit—insights into a success story of high open-circuit voltage and low recombination. Adv. Energy Mater. **7**, 1602358 (2017)

25. P. Gao, M. Grätzel, M.K. Nazeeruddin, Organohalide lead perovskites for photovoltaic applications. Energy Environ. Sci. **7**, 2448–2463 (2014)
26. S. A. Kulkarni, et al., Band-gap tuning of lead halide perovskites using a sequential deposition process. J. Mater. Chem. A **2**, 9221 (2014)
27. G.E. Eperon et al., Formamidinium lead trihalide: a broadly tunable perovskite for efficient planar heterojunction solar cells. Energy Environ. Sci. **7**, 982 (2014)
28. J.H. Noh, S.H. Im, J.H. Heo, T.N. Mandal, S.I Seok, Chemical management for colorful, efficient, and stable inorganic-organic hybrid nanostructured solar cells. Nano Lett. **13,** 1764–1769 (2013)
29. A.R. Denton, N.W. Ashcroft, Vegard's law. Phys. Rev. A **43**, 3161–3164 (1991)
30. D.J. Slotcavage, H.I. Karunadasa, M.D. McGehee, Light-induced phase segregation in halide-perovskite absorbers. ACS Energy Lett. **1**, 1199–1205 (2016)
31. K. Yan et al., Hybrid halide perovskite solar cell precursors: colloidal chemistry and coordination engineering behind device processing for high efficiency. J. Am. Chem. Soc. **137**, 4460–4468 (2015)
32. T.M. Koh et al., Formamidinium-containing metal-halide: an alternative material for near-IR absorption perovskite solar cells. J. Phys. Chem. C **118**, 16458–16462 (2014)
33. N.J. Jeon et al., Compositional engineering of perovskite materials for high-performance solar cells. Nature **517**, 476–480 (2015)
34. M. Saliba, et al., Incorporation of rubidium cations into perovskite solar cells improves photovoltaic performance. Science (80-.) **354**, 206–209 (2016)
35. M. Abdi-Jalebi et al., Maximizing and stabilizing luminescence from halide perovskites with potassium passivation. Nature **555**, 497–501 (2018)
36. G.E. Eperon et al., Inorganic caesium lead iodide perovskite solar cells. J. Mater. Chem. A **3**, 19688–19695 (2015)
37. M. Saliba et al., Cesium-containing triple cation perovskite solar cells: improved stability, reproducibility and high efficiency. Energy Environ. Sci. **9**, 1989–1997 (2016)
38. P. Gratia et al., The many faces of mixed ion perovskites: unraveling and understanding the crystallization process. ACS Energy Lett. **2**, 2686–2693 (2017)
39. J. Liang, et al., CsPb0. 9Sn0. 1IBr2 based all-inorganic perovskite solar cells with exceptional efficiency and stability. J. Am. Chem. Soc. **139**, 14009–14012 (2017)
40. H. Chen et al., Inorganic perovskite solar cells: a rapidly growing field. Sol. RRL **2**, 1700188 (2018)
41. B. Brunetti, C. Cavallo, A. Ciccioli, G. Gigli, A. Latini, on the thermal and thermodynamic (in) stability of methylammonium lead halide perovskites. Sci. Rep. **6**, (2016)
42. B. Conings, Intrinsic thermal instability of methylammonium lead trihalide perovskite. Adv. Energy Mater. (2015)
43. C.C. Stoumpos et al., Ruddlesden-popper hybrid lead iodide perovskite 2D homologous semiconductors. Chem. Mater. **28**, 2852–2867 (2016)
44. H. Tsai et al., High-efficiency two-dimensional ruddlesden-popper perovskite solar cells. Nature **536**, 312–316 (2016)
45. I.C. Smith, E.T. Hoke, D. Solis-Ibarra, M.D. McGehee, H.I. Karunadasa, A layered hybrid perovskite solar-cell absorber with enhanced moisture stability. Angew. Chem. Int. Ed. **53**, 11232–11235 (2014)
46. G. Grancini et al., One-year stable perovskite solar cells by 2D/3D interface engineering. Nat. Commun. **8**, 15684 (2017)
47. P.K. Nayak et al., Mechanism for rapid growth of organic–inorganic halide perovskite crystals. Nat. Commun. **7**, 13303 (2016)
48. A. Dubey et al., Strategic review on processing routes towards highly efficient perovskite solar cells. J. Mater. Chem. A (2018). https://doi.org/10.1039/C7TA08277K
49. Z. Song et al., A technoeconomic analysis of perovskite solar module manufacturing with low-cost materials and techniques. Energy Environ. Sci. **10**, 1297–1305 (2017)
50. D.P. McMeekin, et al., Crystallization kinetics and morphology control of formamidinium–cesium mixed-cation lead mixed-halide perovskite via tunability of the colloidal precursor solution. Adv. Mater. **29**, (2017)

51. S.I. Seok, M. Grätzel, N.-G. Park, Methodologies toward highly efficient perovskite solar cells. Small 1704177 (2018)
52. J.S. Manser, M.I. Saidaminov, J.A. Christians, O.M. Bakr, P.V. Kamat, Making and breaking of lead halide perovskites. Acc. Chem. Res. **49**, 330–338 (2016)
53. J.C. Hamill, J. Schwartz, Y.-L. Loo, Influence of solvent coordination on hybrid organic-inorganic perovskite formation. ACS Energy Lett. **3**, 92–97 (2018)
54. X. Cao et al., Elucidating the key role of a lewis base solvent in the formation of perovskite films fabricated from the lewis adduct approach. ACS Appl. Mater. Interfaces. **9**, 32868–32875 (2017)
55. L. Etgar et al., Mesoscopic $CH_3NH_3PbI_3/TiO_2$ Heterojunction Solar Cells. J. Am. Chem. Soc. **134**, 17396–17399 (2012)
56. Y.-J. Jeon et al., Planar heterojunction perovskite solar cells with superior reproducibility. Sci. Rep. **4**, 6953 (2014)
57. M. Yang et al., Perovskite ink with wide processing window for scalable high-efficiency solar cells. Nat. Energy **2**, 17038 (2017)
58. D.T. Moore, et al., Crystallization kinetics of organic–inorganic trihalide perovskites and the role of the lead anion in crystal growth. J. Am. Chem. Soc. 150209140709004 (2015). https://doi.org/10.1021/ja512117e
59. Y. Wu et al., Retarding the crystallization of PbI 2 for highly reproducible planar-structured perovskite solar cells via sequential deposition. Energy Environ. Sci. **7**, 2934–2938 (2014)
60. C.-C. Chueh et al., The roles of alkyl halide additives in enhancing perovskite solar cell performance. J. Mater. Chem. A **3**, 9058–9062 (2015)
61. P.-W. Liang et al., Additive enhanced crystallization of solution-processed perovskite for highly efficient planar-heterojunction solar cells. Adv. Mater. **26**, 3748–3754 (2014)
62. S.D. Stranks, P.K. Nayak, W. Zhang, T. Stergiopoulos, H.J. Snaith, Formation of thin films of organic-inorganic perovskites for high-efficiency solar cells. Angew. Chem. Int. Ed. **54**, 3240–3248 (2015)
63. S. Colella et al., MAPbI3-xClx mixed halide perovskite for hybrid solar cells: the role of chloride as dopant on the transport and structural properties. Chem. Mater. **25**, 4613 (2013)
64. A.R. Pascoe et al., Directing nucleation and growth kinetics in solution-processed hybrid perovskite thin-films. Sci. China Mater. **60**, 617–628 (2017)
65. C. Bi et al., Non-wetting surface-driven high-aspect-ratio crystalline grain growth for efficient hybrid perovskite solar cells. Nat. Commun. **6**, 1–7 (2015)
66. N.J. Jeon et al., Solvent engineering for high-performance inorganic-organic hybrid perovskite solar cells. Nat. Mater. **13**, 1–7 (2014)
67. M. Xiao et al., A fast deposition-crystallization procedure for highly efficient lead iodide perovskite thin-film solar cells. Angew. Chem. Int. Ed. **53**, 9898–9903 (2014)
68. H. Zhang et al., Understanding the effect of delay time of solvent washing on the performances of perovskite solar cells. ACS Omega **2**, 7666–7671 (2017)
69. T. Jesper Jacobsson, et al., Exploration of the compositional space for mixed lead halogen perovskites for high efficiency solar cells. Energy Environ. Sci. **9**, 1706–1724 (2016)
70. J.P. Correa-Baena, et al., Unbroken perovskite: interplay of morphology, electro-optical properties, and ionic movement. Adv. Mater. 5031–5037 (2016). https://doi.org/10.1002/adma.201600624
71. K. Liang, D.B. Mitzi, M.T. Prikas, Synthesis and characterization of organic − inorganic perovskite thin films prepared using a versatile two-step dipping technique. Chem. Mater. **10**, 403–411 (1998)
72. J. Burschka et al., Sequential deposition as a route to high-performance perovskite-sensitized solar cells. Nature **499**, 316–319 (2013)
73. H. Chen, Two-step sequential deposition of organometal halide perovskite for photovoltaic application. Adv. Funct. Mater. **27**, 1605654 (2017)
74. X. Cao et al., Control of the morphology of PbI 2 films for efficient perovskite solar cells by strong Lewis base additives. J. Mater. Chem. C **5**, 7458–7464 (2017)

75. W.S. Yang, et al., High-performance photovoltaic perovskite layers fabricated through intramolecular exchange. Science (80-.) **348**, 1234–1237 (2015)
76. M. Liu, M.B. Johnston, H.J. Snaith, Efficient planar heterojunction perovskite solar cells by vapour deposition. Nature **501**, 395–398 (2013)
77. O. Malinkiewicz et al., Perovskite solar cells employing organic charge-transport layers. Nat. Photonics **8**, 128–132 (2014)
78. C. Momblona et al., Efficient vacuum deposited p-i-n and n-i-p perovskite solar cells employing doped charge transport layers. Energy Environ. Sci. **9**, 3456–3463 (2016)
79. Q. Chen et al., Planar heterojunction perovskite solar cells via vapor-assisted solution process. J. Am. Chem. Soc. **136**, 622–625 (2014)
80. Y.H. Chiang, H.M. Cheng, M.H. Li, T.F. Guo, P. Chen, Low-pressure vapor-assisted solution process for thiocyanate-based pseudohalide perovskite solar cells. Chemsuschem **9**, 2620–2627 (2016)
81. H. Snaith, Perovskites: the emergence of a new era for low-cost, high-efficiency solar cells. J. Phys. Chem. Lett. **4**, 3623–3630 (2013)
82. U. Wurfel, A. Cuevas, P. Wurfel, Charge carrier separation in solar cells. IEEE J. Photovolt. **5**, 461–469 (2015)
83. Z. Guo, L. Gao, C. Zhang, Z. Xu, T. Ma, Low-temperature processed non-TiO 2 electron selective layers for perovskite solar cells. J. Mater. Chem. A **6**, 4572–4589 (2018)
84. Z. Song, S.C. Watthage, A.B. Phillips, M.J. Heben, Pathways toward high-performance perovskite solar cells: review of recent advances in organo-metal halide perovskites for photovoltaic applications. J. Photonics Energy **6**, 22001 (2016)
85. W.S. Yang, et al., Iodide management in formamidinium-lead-halide–based perovskite layers for efficient solar cells. Science (80-.) **356**, (2017)
86. J.M. Ball, M.M. Lee, A. Hey, H.J. Snaith, Low-temperature processed meso-superstructured to thin-film perovskite solar cells. Energy Environ. Sci. **6**, 1739 (2013)
87. R.W. Johnson, A. Hultqvist, S.F. Bent, A brief review of atomic layer deposition: from fundamentals to applications. Mater. Today **17**, 236–246 (2014)
88. Y. Xiao, G. Han, H. Zhou, J. Wu, An efficient titanium foil based perovskite solar cell: using a titanium dioxide nanowire array anode and transparent poly(3,4-ethylenedioxythiophene) electrode. RSC Adv. **6**, 2778–2784 (2016)
89. L. Calió, S. Kazim, M. Grätzel, S. Ahmad, Hole-transport materials for perovskite solar cells. Angew. Chem. Int. Ed. **55**, 14522–14545 (2016)
90. I. Lee, J.H. Yun, H.J. Son, T.S. Kim, Accelerated degradation due to weakened adhesion from Li-TFSI additives in perovskite solar cells. ACS Appl. Mater. Interfaces. **9**, 7029–7035 (2017)
91. M. Saliba et al., A molecularly engineered hole-transporting material for efficient perovskite solar cells. Nat. Energy **1**, 15017 (2016)
92. Chen, J. & Park, N.-G. Inorganic Hole Transporting Materials for Stable and High Efficiency Perovskite Solar Cells. *J. Phys. Chem. C* acs.jpcc.8b01177 (2018). https://doi.org/10.1021/acs.jpcc.8b01177
93. J.-Y. Jeng et al., $CH_3NH_3PbI_3$ perovskite/fullerene planar-heterojunction hybrid solar cells. Adv. Mater. **25**, 3727–3732 (2013)
94. J.C. Yu et al., Highly efficient and stable inverted perovskite solar cell employing PEDOT:GO composite layer as a hole transport layer. Sci. Rep. **8**, 1070 (2018)
95. Y. Fang, C. Bi, D. Wang, J. Huang, The functions of fullerenes in hybrid perovskite solar cells. ACS Energy Lett. **2**, 782–794 (2017)
96. K.A. Bush, et al., 23.6%-efficient monolithic perovskite/silicon tandem solar cells with improved stability. Nat. Energy **2**, 17009 (2017)
97. A. Guchhait, et al., Over 20% efficient CIGS–perovskite tandem solar cells. ACS Energy Lett. 807–812 (2017). https://doi.org/10.1021/acsenergylett.7b00187
98. De A. Vos, Detailed balance limit of the efficiency of tandem solar cells. J. Phys. D. Appl. Phys. **13**, 839–846 (1980)
99. G.E. Eperon, et al. Perovskite-perovskite tandem photovoltaics with optimized band gaps. Science (80-.). **354**, 861–865 (2016)

100. F. Hao, C.C. Stoumpos, R.P.H. Chang, M.G. Kanatzidis, Anomalous band gap behavior in mixed Sn and Pb perovskites enables broadening of absorption spectrum in solar cells. J. Am. Chem. Soc. **136**, 8094–8099 (2014)
101. G.E. Eperon, M.T. Hörantner, H.J. Snaith, Metal halide perovskite tandem and multiple-junction photovoltaics. Nat. Rev. Chem. **1**, 0095 (2017)
102. E.T. Hoke et al., Reversible photo-induced trap formation in mixed-halide hybrid perovskites for photovoltaics. Chem. Sci. **6**, 613–617 (2015)
103. C.S. Ponseca et al., Organometal halide perovskite solar cell materials rationalized: ultrafast charge generation, high and microsecond-long balanced mobilities, and slow recombination. J. Am. Chem. Soc. **136**, 5189–5192 (2014)
104. G.D. Scholes, G. Rumbles, Excitons in nanoscale systems. Nat. Mater. **5**, 683–696 (2006)
105. V. D'Innocenzo et al., Excitons versus free charges in organo-lead tri-halide perovskites. Nat. Commun. **5**, 3586 (2014)
106. E.J. Juarez-Perez et al., Photoinduced giant dielectric constant in lead halide perovskite solar cells. J. Phys. Chem. Lett. **5**, 2390–2394 (2014)
107. Q. Lin, A. Armin, R.C.R. Nagiri, P.L. Burn, P. Meredith, Electro-optics of perovskite solar cells. Nat. Photonics **9**, 106–112 (2015)
108. G. Xing, et al., Long-range balanced electron-and hole-transport lengths in organic-inorganic CH3NH3PbI3. Science (80-.). **342**, 344–347 (2013)
109. O.D. Miller, E. Yablonovitch, S.R. Kurtz, Intense internal and external fluorescence as solar cell approach the SQ efficiency limit. Photovolt. IEEE J. **2**, 1–27 (2012)
110. T.S. Sherkar et al., Recombination in perovskite solar cells: significance of grain boundaries, interface traps, and defect ions. ACS Energy Lett. **2**, 1214–1222 (2017)
111. D. Meggiolaro et al., Iodine chemistry determines the defect tolerance of lead-halide perovskites. Energy Environ. Sci. **11**, 702–713 (2018)
112. J.S. Yun et al., Critical role of grain boundaries for ion migration in formamidinium and methylammonium lead halide perovskite solar cells. Adv. Energy Mater. **6**, 1–8 (2016)
113. R. Brenes et al., Metal halide perovskite polycrystalline films exhibiting properties of single crystals. Joule **1**, 155–167 (2017)
114. W.J. Yin, T. Shi, Y. Yan, Unusual defect physics in CH3NH3PbI3perovskite solar cell absorber. Appl. Phys. Lett. **104**, (2014)
115. D. Meggiolaro, et al., Iodine chemistry determines the defect tolerance of lead-halide perovskites. Energy Environ. Sci. 0–30 (2018). https://doi.org/10.1039/c8ee00124c
116. C. Li et al., Iodine migration and its effect on hysteresis in perovskite solar cells. Adv. Mater. **28**, 2446–2454 (2016)
117. T. Niu et al., Stable high-performance perovskite solar cells via grain boundary passivation. Adv. Mater. **30**, 1706576 (2018)
118. H.J. Snaith et al., Anomalous hysteresis in perovskite solar cells. J. Phys. Chem. Lett. **5**, 1511–1515 (2014)
119. W. Tress, et al., Understanding the rate-dependent J–V hysteresis, slow time component, and aging in $CH_3NH_3PbI_3$ perovskite solar cells: the role of a compensated electric field. Energy Environ. Sci. 995–1004 (2015). https://doi.org/10.1039/c4ee03664f
120. W. Tress, Metal halide perovskites as mixed electronic-ionic conductors: challenges and opportunities—from hysteresis to memristivity. J. Phys. Chem. Lett. **8**, 3106–3114 (2017)
121. E.L. Unger et al., Hysteresis and transient behavior in current–voltage measurements of hybrid-perovskite absorber solar cells. Energy Environ. Sci. **7**, 3690–3698 (2014)
122. K. Domanski, E.A. Alharbi, A. Hagfeldt, M. Grätzel, W. Tress, Systematic investigation of the impact of operation conditions on the degradation behaviour of perovskite solar cells. Nat. Energy **3**, 61–67 (2018)
123. J.-P. Correa-Baena et al., The rapid evolution of highly efficient perovskite solar cells. Energy Environ. Sci. **10**, 710–727 (2017)
124. J.-S. Park, H. Chae, H.K. Chung, S.I. Lee, Thin film encapsulation for flexible AM-OLED: a review. Semicond. Sci. Technol. **26**, 034001 (2011)

125. A. Guerrero et al., Interfacial degradation of planar lead halide perovskite solar cells. ACS Nano **10**, 218–224 (2016)
126. E. Bi et al., Diffusion engineering of ions and charge carriers for stable efficient perovskite solar cells. Nat. Commun. **8**, 15330 (2017)
127. A. Babayigit et al., Assessing the toxicity of Pb-and Sn-based perovskite solar cells in model organism Danio rerio. Sci. Rep. **6**, 1–11 (2016)
128. A. Abate, Perovskite solar cells go lead free. Joule **1**, 659–664 (2017)
129. M. Konstantakou, T. Stergiopoulos, A critical review on tin halide perovskite solar cells. J. Mater. Chem. A **5**, 11518–11549 (2017)
130. S.J. Lee et al., Fabrication of efficient formamidinium tin iodide perovskite solar cells through SnF_2-pyrazine complex. J. Am. Chem. Soc. **138**, 3974–3977 (2016)
131. S. Nagane et al., Lead-free perovskite semiconductors based on germanium-tin solid solutions: structural and optoelectronic properties. J. Phys. Chem. C **122**, 5940–5947 (2018)
132. C. Wu et al., The dawn of lead-free perovskite solar cell: highly stable double perovskite $Cs_2AgBiBr_6$ film. Adv. Sci. **5**, 1700759 (2018)
133. X. Zhao et al., Design of lead-free inorganic halide perovskites for solar cells via cation-transmutation. J. Am. Chem. Soc. **139**, 2630–2638 (2017)
134. G. Volonakis et al., $Cs_2InAgCl_6$: a new lead-free halide double perovskite with direct band gap. J. Phys. Chem. Lett. **8**, 772–778 (2017)
135. M. Cai, et al., Cost-performance analysis of perovskite solar modules. Adv. Sci. **4**, (2017)
136. F. Taghizadeh-Hesary, N. Yoshino, Y. Inagaki, Empirical analysis of factors influencing price of solar modules (2018)
137. He, X. *Perovskite Photovoltaics 2018–2028*. (2018)
138. I. Cardinaletti et al., Organic and perovskite solar cells for space applications. Sol. Energy Mater. Sol. Cells **182**, 121–127 (2018)
139. M. Kaltenbrunner et al., Flexible high power-per-weight perovskite solar cells with chromium oxide-metal contacts for improved stability in air. Nat. Mater. **14**, 1032–1039 (2015)
140. S. De Wolf et al., Organometallic halide perovskites: sharp optical absorption edge and its relation to photovoltaic performance. J. Phys. Chem. Lett. **5**, 1035–1039 (2014)
141. S. Pang et al., $NH_2CH{=}NH_2PbI_3$: an alternative organolead iodide perovskite sensitizer for mesoscopic solar cells. Chem. Mater. **26**, 1485–1491 (2014)
142. J.-H. Im, H.-S. Kim, N.-G. Park, Morphology-photovoltaic property correlation in perovskite solar cells: one-step versus two-step deposition of CH_3 NH_3 PbI_3. APL Mater. **2**, 081510 (2014)
143. B. Chen, M. Yang, S. Priya, K. Zhu, Origin of J-V hysteresis in perovskite solar cells. J. Phys. Chem. Lett. 905–917 (2016)
144. K. Wojciechowski, D. Forgács, T. Rivera, Industrial opportunities and challenges for perovskite photovoltaic technology. Sol. RRL **3**, 1900144 (2019). https://doi.org/10.1002/solr.201900144

Chapter 11
Augsburger Tubular Photovoltaic (ATPV)

V. Petrova-Koch and J. Mayer

Abstract Nowadays, available PV modules are flat. The PV presented in this chapter is a glass tube with a flexible PV cell inside. The tubular diversification of the PV was initially inspired by the start-up company Solyndra in Silicon Valley CA, which manufactured CIGS cell directly on the surface of an inner glass tube. Unfortunately, Solyndra went bankrupt due to high manufacturing costs. In 2011, a leaner tubular PV was invented at Gate-East in Garching, which enabled substantial simplification compared to the Solyndra's ideas and design. It was named Augsburger Tubular Photovoltaics (ATPV) and patented with Osram, later Ledvance. It has numerous advantages as follows: the cell manufacturing is roll-to-roll technology, the absorption films can be thinner at the same efficiency, because the tubular shape extends the light path, compared to flat cells and modules. Simplified installation and operation: low weight; semitransparent for rain, wind, and snow; better cooling compared to a flat panel; leaner and cost-effective substructure. Agricultural application: protection against hail but permeability for sun and rain—homogenous plant growth as general: reduced evaporation, short-period shade and therefore, uniform growing; good protection at high temperatures and from destructive hail—dual as well as multiple use is possible. The concept of ATPV was successfully proven, and a small-scale manufacturing was built at the Osram, later Ledvance site in Augsburg.

Dedicated to Prof. Fred Koch (TU Munich).

V. Petrova-Koch (✉)
Gate-East, Schleissheimer Str. 17, Garching 85748, Germany
e-mail: vpkoch@yahoo.de

J. Mayer
Ledvance GmbH, Equipment Engineering, Berliner Allee 65, Augsburg 86153, Germany
e-mail: j.mayer@ledvance.com

V. Petrova-Koch et al. (eds.), *High-Efficient Low-Cost Photovoltaics*,
Springer Series in Optical Sciences 140,
https://doi.org/10.1007/978-3-030-22864-4_11

11.1 Introduction

The sun is the strongest energy source known to the humankind on one side, the growing population uses more and more electricity on the other. The PV, if affordable, is capable to supply with solar electricity to everybody on the planet, clean and environmentally friendly.

The PV has the potential to become one of the biggest industries of the twenty-first century. It is already bigger than the microelectronics, or the lighting industry. The recent PV reached in a relatively short time, the remarkable cumulative volume of 300 GW in 2017/1/). However this is only the beginning. The PV market share is expected to grow to approximately 400 GW in 2020 and to approximately 700 GW in 2030/2/.

Cost reduction is one of the main goals of the recent PV industry. There are two major ways to achieve lower cost: (i) via economy of scale in Gigawatt-sized fabs; or (ii) via next generation lean manufacturing at a smaller scale. Vertical integration along the value chain could further reduce the costs.

Many of the known big PV companies are upscaling the volume of their already established PV manufacturing to Giga-scale at the moment, in order to further lower the costs. Increasing the efficiency of the cells and of the modules at the same time, approaching the theoretical limits, became a must in the last years. Almost all single-junction PV cells manufactured on a big scale reached values around 20%.

Newcomers and game changer are focused on next generation PV, and on innovative and lean manufacturing/14–17/. New PV concepts promise to diversify the recent PV market. There is enough room for it. Affordable, competitive, and innovative PV modules, produced in substantially smaller fabs, are on the way to establish their market position and shares.

The **Augsburger Tubular Photovoltaic (ATPV)**, which we are presenting in this chapter, belongs to the second category. The ATPV targets a lean PV manufacturing and is a shaped PV.

Today, 99% of the PV modules are flat, no matter if they are c-Si wafer- or thin-film based. In both cases, they resemble big-size roof tiles and wall panels.

More than a decade ago, there was a start-up company Solyndra/3/in Silicon Valley CA, which put a lot of effort to shape TF PV and to bring to the market its patented tubular PV cells and modules/4/. Solyndra was founded in 2005, unveiled its greenfield manufacturing side in Silicon Valley Ca in 2008, and reached in a relatively short time, a manufacturing volume higher than 100 MWp/year. Unfortunately, it went bankrupt in 2011, together with many other PV start-up companies. Obviously, the cost of the tubular cells and modules were too high.

In 2011, a leaner tubular PV was invented by V. Petrova-Koch at Gate-East in Garching, which enabled substantial simplification compared to the Solyndra's ideas and design. It was named **Augsburger Tubular Photovoltaics (ATPV)**. A patent was applied together with Osram in 2014/5/. The new concept of this PV was successfully proven, and a small-scale manufacturing was built and explored more recently for ATPV module-production at small-scale at the Ledvance site in Augsburg.

Fig. 11.1 The Osram manufacturing site in Augsburg, known since 1961 for high scale manufacturing of world-class fluorescent tubes. Since 2016, it belongs to Ledvance

Osram was known since 1961 for its top-quality fluorescing **tube manufacturing** on big scale. This site in Augsburg, owned since 2016 by Ledvance (Fig. 11.1) was founded more than 100 years ago. The classical lighting business lost drastically its market shares worldwide in the last years. Alternative ideas, technologies, and solutions are welcome to prolong the life of excellent manufacturing sites like the one in Augsburg.

The ATPV concept, the cells, the modules, and several innovative installations and applications will be presented in this chapter. We compare the ATPV with the Solyndra's product at one side, and with the standard flat TF PV- and c-Si PV modules on the other.

11.2 Shaped PV Versus Flat PV

11.2.1 Advantages of the Cylindrical Tubular PV Design

Putting PV cells inside a cylindrical glass tube is not popular. Almost all Thin-Film PV (TFPV) developers and manufacturers are also focused on cells that lay flat on a panel. The TFPV modules have similar appearance and design as the crystalline silicon solar panels, commonly seen today.

The cylindrical shape has numerous advantages:

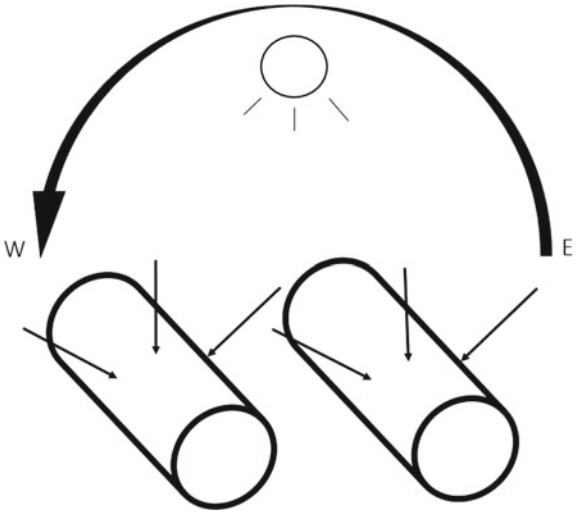

Fig. 11.2 Self-tracking the sun with cylindrically shaped horizontally installed PV power tubes

- It allows the PV cells to face the sun for longer periods of time in a day than a flat solar cell (Fig. 11.2). Hence, cylindrical power tubes can produce more electricity over the day. No trackers are needed. The self-tracking saves costs.
- The PV tubes can be installed horizontally, they don't need any inclination. This brings additional simplifications on system level, provides new appearance of the PV installations, and enables new applications.
- The absorbing films can be thinner when cylindrically shaped than the absorbing film used to manufacture flat PV cells with the same efficiency because the light path gets prolonged when the cells are curved. This means that there is a reduction of the material consumption, and also of the cell deposition and processing time, which at the end results in cost reduction.
- The cylindrical shape provides a certain concentration of solar radiation on the way to the cell surface (Fig. 11.3). The degree of concentration depends on the distance between the outer glass tube surface and the absorption layer top surface.
- The PV power tubes cool better than a flat power module, because of the discretization of the absorber area. Also, the air moves more efficiently around the power tubes and cools them more efficiently than a PV flat module.
- The wind, rain, and snow clean the tubes better than the flat glass panels.

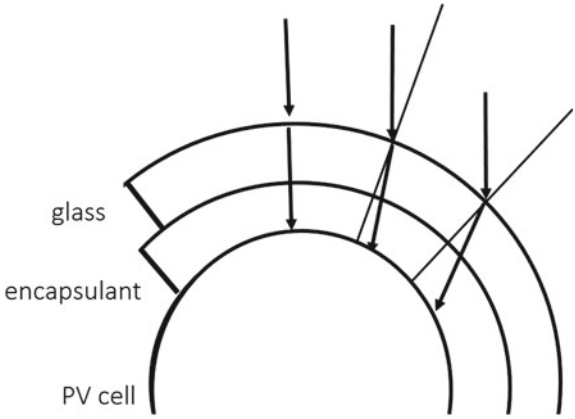

Fig. 11.3 Concentration (small degree) of the solar radiation on the way to the surface of a cylindrically shaped solar cell

11.2.2 Comparison Between an Array Cylindrical Glass Tubes and a Pair of Flat Glass Plates (Without PV Cells)

The top of almost all PV modules today is a soda-lime glass plate, solar grade. Plastic is used to wrap only flexible and very light PV modules, which make use of roll-to-roll TFPV cells.

Our cylindrically shaped tubular PV is making use of soda-lime glass, which is cost-effective. It is hard to imagine that plastic tubes could compete with soda-lime glass tubes, and be the choice to manufacture cylindrically shaped PV. Soda-lime glass tubes are an ultimate choice for outdoor applications if the preferred shape of the PV is tubular.

The glass tubing industry is very advanced, and it is cost-competitive to the flat glass manufacturing industry.

The diameters of the available cylindrical soda-lime glass tubes spread in a very broad range (from few mm in diameter to several hundreds of mm). Their wall thickness can be varied between several hundred μm and several mm.

The diameter the tubes we chose for ATPV, and also the diameter of the Solyndra's tubes is approximately one inch, (25 mm). These tubes are known from the classical lighting industry as T8 glass tubes and are very popular. This diameter is considerably smaller than the diameter of the tubes usually used to manufacture evacuated solar thermal tubular collectors, which is typically approximately 2 inch/6/.

The wall thickness of the Solyndra's T8 tubes was ca. 1.8 mm. In our case, it is around 1–1.2 mm.

The length of the tubes we and Solyndra chose is approximately one meter. We prefer this length because the width of the standard flat c-Si PV modules is also approximately one meter.

The weight of the ATPV tubes is about 200 grams/tube, versus ca. 300 g/tube in the case of Solyndra.

While Solyndra was buying tubes from companies specialized on glass tubbing, our strategy is to manufacture the glass tubes, the power tubes, and the ATPV modules vertically integrated at the manufacturing side of Ledvance in Augsburg.

The ATPV glass tubes need a hardening of 90–120 N/m^2. They have to satisfy also the required hail test for outdoor applications. We managed to toughen the tubes thermally, and **in-line**. This reduces the cost as compared to the thermal toughening of glass plates, which has to be performed after cutting the flat glass and c-shaping the glass edges. The edge processing and external thermal toughening elevate the cost by at least 30%/6.7/.

An array of thermally toughened glass tubes is cost-competitive to a sandwich of two flat glass plates with the same area, and in many cases, even less expensive. The comparison here concerns the glass only, without the PV cells.

The flat PV modules are usually covered on the top side with solar glass (typically with a thickness of 2, 3.2, or 4 mm). Their backside is glass for the case of all TFPV. Glass/glass modules also became popular for the c-Si modules more recently/8/. The thickness of the top and the bottom glass is usually the same. The weight of one square meter of flat glass sandwich varies in the range 10–20 kg/m^2. 2 mm glass could be toughened ESG recently/8/, and used more widely for manufacturing glass/glass PV modules..

One square meter area can be completely covered by 40 T8 tightly ordered T8 glass tubes (25 mm in diameter). Their weight is around 8 kg in our case, which is substantially lower than the weight per m^2 of the flat glass sandwich. This means a significant process energy and material savings, cost reduction, and more efficient transportation of the ATPV modules.

Many PV manufacturers believe nowadays, that using flat soda-lime glass plates is less expensive than to wrap PV cells in soda-lime glass tubes. It could be proven that tubular design is competitive and can even have lower costs.

The tubular lighting industry has more than half a century of successful history. A typical glass furnace enables today the manufacturing of about 1000 km glass tubes per day (with a diameter of approx. 1 inch). The highly automated lines used to assemble fluorescing tubes reach values up to 7000 tubes/h!

The high degree of automation and the in-line toughening of the glass tubes allows manufacturing a square meter of T8 tubes cost-competitive than a sandwich of two thermally toughened soda-lime glass plates of the same area. The main advantages of the tubes are they don't have edges, don´t need cutting, and because of it, they could be toughened thermally in-line! Tubes with walls as thin as 1 mm enable toughening comparable to one of flat solar glass plates with of a 2 mm thickness or more.

A cylindrical glass body could be vacuum sealed (Fig. 11.4). Its inside stays free of humidity this way for a very long time (for many decades). The sealing is of higher quality if we use the tubes fresh and don't wash them. Two glass plates in contrast can't be vacuum sealed so far. Numerous attempts have failed.

A vertically integrated highly automated production of Augsburger Tubular PV (ATPV) on the side of the glass tubbing fab is our target, where we start with sand and glass tube and end with cost-competitive ATPV Modules. High-efficient TFPV cells

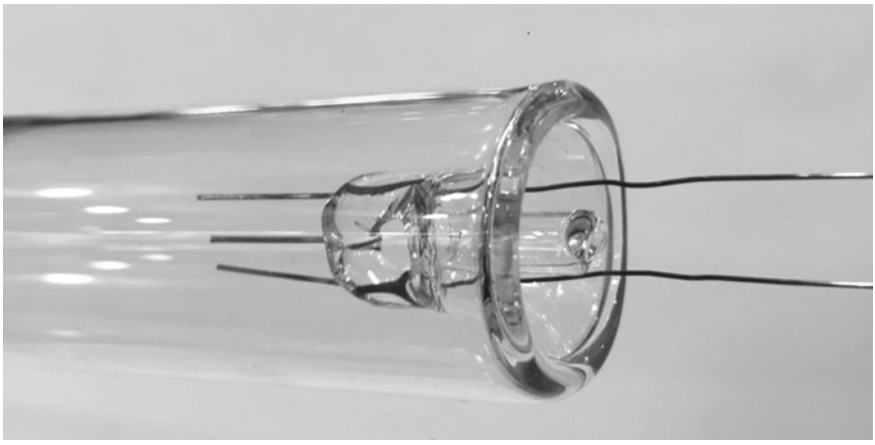

Fig. 11.4 Vacuum-sealed cylindrical glass tube

and stripes needed for the ATPV will face less degradation if the cell and module manufacturing is not separated at two sides.

The advantages of a vertical integrated tubular device manufacturing have been proven over decades by the fluorescing tube industry.

The thin-film PV manufacturing today is also vertically integrated into the 99% of all known fabs.

Our goal is to inherit the existing glass tubing experience and enable a second life of the glass fab and glass sealing production lines. This way, we will be able to reduce the cost.

11.2.3 Cell Designs and Semiconductor Materials, Suitable to Serve Tubular PV

The wafer-based c-Si PV cells are cost-effective and widely used today, but because of their rigidity, they can't serve a tubular PV in a simple manner.

The tubular PV is restricted to thin-film PV cells, which can be shaped much easier. A transparent counter electrode deposited on the top side of the absorbing layer (Fig. 11.5) is the preferred design for the cylindrically shaped cell.

The semiconductor CdTe, which is known for its low -ost TFPV manufacturing, is not in our focus. The widely spread architecture of the CdTe PV cells is inverted, their top electrode is not transparent; Also the issues around manufacturing and using PV cells containing Cd and their environmentally friendly recycling are open.

Several other semiconductor materials enable shaped architecture and would allow manufacturing of high-efficient shapeable cells and PV power tubes. The most mature and efficient is CIGS/9–12/, followed by perovskite TFPV/13–15/. Perovskite PV

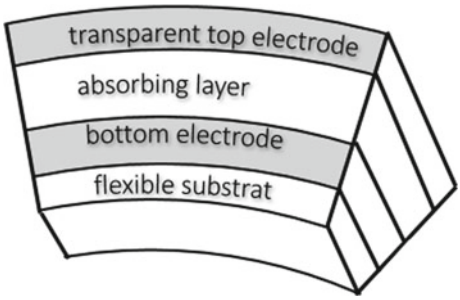

Fig. 11.5 Preferred cell design to serve a cylindrically shaped PV

became a hype in the last several years because of its rapidly improving efficiency at very low cost of manufacturing at the same time. Unfortunately, the perovskites with the highest efficiency obtained so far contain lead (Pb).

Numerous companies are manufacturing CIGS TFPV on a large scale//nowadays. Solar Frontier produces in Japan more than 1 GW/y flat CIGS PV Modules; Avancis and CNBM manufactures in China ca. 300 MW/y this year and plan on upscaling to more than one GW/y in the next 2 years; Manz, Shanghai Electric Group, and Shenhua Group in China will produce 250 MW this year, Hanergy, which owns Solibro's production side in Germany for rigid CIGS on glass, MiaSole's in CA, and Global Solar's in AZ, for flexible CIGS PV on stainless steel, manufactures a volume of more than 250 MW/y total; Solo Power in Oregon reached 250 MW/y for flexible CIGS PV on stainless steel, SIVA Power in CA ramping up a unique 200 MW CIGS novel highly productive CIGS manufacturing on glass, Ascent Solar in CO, US, manufactures flexible CIGS Modules on Steel at low manufacturing volume; Flisom in CH manufacturing 15 MW/y Flexible monolithically integrated CIGS PV on Polyimid foils and is going to build a much bigger plant in a very near future. All these companies are aiming to prove that CIGS TFPV is a mature PV technology, which is competitive to c-Si PV. There is a belief even that CIGS is "the next Big thing in PVs" because this TFPV reached efficiency in the lab higher than 20%, low manufacturing cost, and better environmental food print compared to the c-Si PV. The c-Si wafer-based PV still dominates more than 80% of the PV market at the moment. A serious competition race is taking place in the last years, and TFPV is gaining more and more shares.

A remarkable recent achievement in the field of TFPV and particularly for the CIGS TFPV is the laser processing and monomythical interconnection of the cells, including the flexible once/10/. Laser Processing improves the reproducibility, and the productivity of PV manufacturing, which saves costs. Stringing, and wiring, which is unavoidable in the case of c-Si wafer PV technology is not needed in the case of TFPV in general.

CIGS, which is a direct gap semiconductor, needs a thickness of 1.5–2 μm in order to totally absorb the solar radiation, which is roughly 100 times less than the thickness of a c-Si wafer-based Pv cell, which is in the range of 150–200 μm. c-Si

is a semiconductor with non-direct gap. Because of this, Si absorbs visible light one to two orders of magnitude that is less efficient, a thick absorber is needed.

A CIGS could either be deposited on curved surfaces (for example on so-called inner tubes, as Solyndra did) or via roll-to-roll on thin foils (our choice in the case of ATPV).

11.2.3.1 Solyndra'S CIGS PV Cells Deposition and Laser Processing on an Inner Glass Tube

Solyndra made use of CIGS deposition on permanently rotating soda-lime glass inner tubes (Fig. 11.6). The typical diameter of the inner tubes was 15–16 mm (T5 tubes). The company has developed a unique way to deposit and structure efficient Copper Indium Gallium Selenium (CIGS) cells on these tubes/10, 11/. The manufacturing equipment was specially designed and constructed for Solyndra. This probably was one of the serious obstacles to reduce cell manufacturing costs.

11.2.3.2 Roll-to-Roll Flexible CIGS Cells and Stripes for the ATPV

The Augsburger Tubular PV makes use of flexible CIGS PV cells (Fig. 11.7), manufactured by Roll-to-Roll (R2R) Technology.

The R2R CIGS technology has the following advantages:

1. The R2R deposition of semiconductor films is an established technology, which promises shortening of the deposition time and a substantial cost reduction. R2R is known from the textbooks as an example for lean and fast manufacturing.
2. High-efficient CIGS PV cells can be deposited on flexible foils. Several research labs like NRLEL in CO, US, ZSW in Stuttgart, and EMPA already demonstrated this. At ETH Zurich is holding the world record of 20.2% on Polyimid//.
3. A number PV start-up companies like MiaSole, Global Solar SoloPower, Ascent Solar in the US together with Hanergy Holding Group; Flisom in Switzerland, and Solar Frontier in Japan are manufacturing flexible CIGS PV cells and modules on industrial scale. All these companies except Flisom are depositing the cells on stainless steel foils. Monolithically interconnection of the cells is not

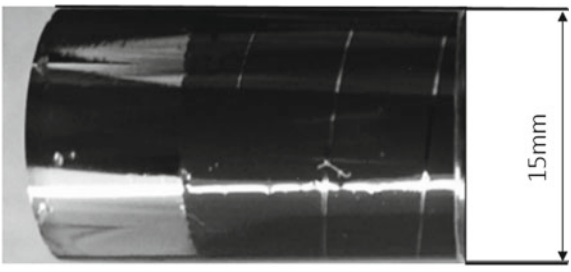

Fig. 11.6 Solyndra laser scribed monolithically interconnected CIGS cells, deposited on an inner glass tube

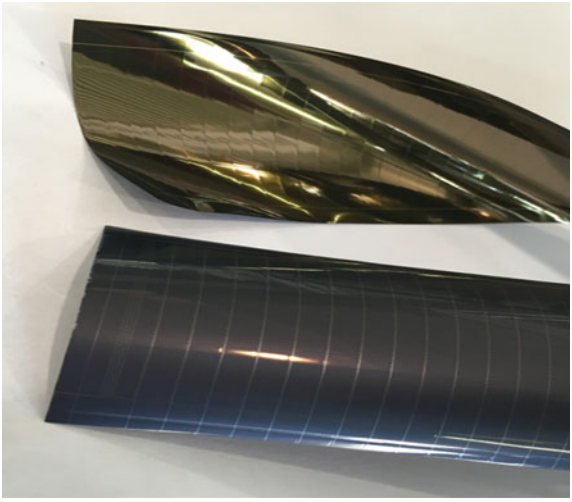

Fig. 11.7 CIGS R2R cells and stripes for ATPV on Polyimid or Steel foil

demonstrated so far on stainless steel foils. On Polyimid, Flisom has demonstrated recently good laser processing, and monolithically interconnection of the CIGS cells. For ATPV we focus at the moment mainly on CIGS cells, R2R deposited on Polyimid foils, because of the possibility to vertically interconnect the cells.

11.2.3.3 Other Cells Capable to Serve the ATPV

We expect that other cells will mature and serve the ATPV in the near future. These are

High-efficient CIGS cells on steel foils, monolithically interconnected. Such cells need a high-temperature insulating layer between the steel and the CIGS absorbing layer.

Flexible Perovskite PV Cells. Perovskite PV became a hype in the field of PV for two main reasons: the cells reached extraordinary high efficiency (around 20% in the last few years), while their manufacturing remains very easy and the costs are low as compared to the once of c-Si and CIGS PV cells. Recently, efficient flexible perovskite PV modules (ink-jet printed on PET) have been demonstrated (see Chap. 10 for more details).

There are two disadvantages of perovskite; they degrade easily when facing humidity and UV light, and the wanted high efficiency of about 20% is observed only with perovskite cells containing Pb.

If **the OPV** can reach **efficiencies higher than 12–13%** and the manufacturing technology remains low cost, then these cells will be a very promising candidate for ATPV too. At the moment, the cell efficiencies remain much lower than for example in the case of Perovskite cells. However, OPV has two major advantages: easy and

low-cost manufacturing is possible in the case of printed OPV, the composition of the OPV layers is not hazardous and poisoning; and the OPV is easy to recycle.

11.3 Power Tubes

11.3.1 Solyndra Power Tubes, the Forerunner of the Tubular PV

Solyndra caught a lot of attention in the solar world because it managed not only to deposit and process Copper Indium Gallium Selenium (CIGS) cells with an efficiency of about 13% on a glass tube but also to encase it in a second glass tube. Each Solyndra power tube is made up of two tubes. Silicone oil is added as an "optical coupling agent". The sunlight shines through the outer tube and concentrates on the way to the inner tube (Fig. 11.8a). After inserting the inner tube into the outer tube, each cylinder is hermetically sealed with glass and metal to keep out the moisture, which otherwise can seriously erode the CIGS' performance (Fig. 11.8b). Solyndra's power tubes need white back reflection foil to make use of the downside of the power tube (Fig. 11.8c).

With this technology, Solyndra reached efficiencies of the cells up to 12.5% in average, and 14% in the best case, enabling power tubes with a power of ca. 5 W each, which was used to assemble the 40 tube-modules, described later in this chapter.

11.3.2 Koch Power Tubes

A flexible CIGS stripe containing monolithically interconnected cells is placed and glued on the upper half of the Koch power tube, which is facing the sun (Fig. 11.9). If bifacial power tubes of this type are needed, they could be realized optionally. No white back refection foil is needed. The Koch Power Tube doesn't need an inner tube.

The silicon oil used as liquid optical coupling agent by "Solyndra" is replaced in the case of the Koch Power Tube with a solid encapsulation foil. It provides the needed optical matching of the cells to the glass tube, and also mechanical stability in the case that a power tube breaks. We cover the tube-inside completely with encapsulation foil and glue it, which helps to hold the glass shards in an emergency case (Fig. 11.10).

The Koch power tubes are vacuum sealed. We are making use of technology explored for a long time and proven by the lighting industry. The vacuum-sealed power tubes are filled at the end with a defined atmosphere (N2 or dry ear, slight overpressured), enabling a better cooling of the PV cells. The vacuum sealing of the glass body helps to protect the cells from humidity for decades. The long-lasting

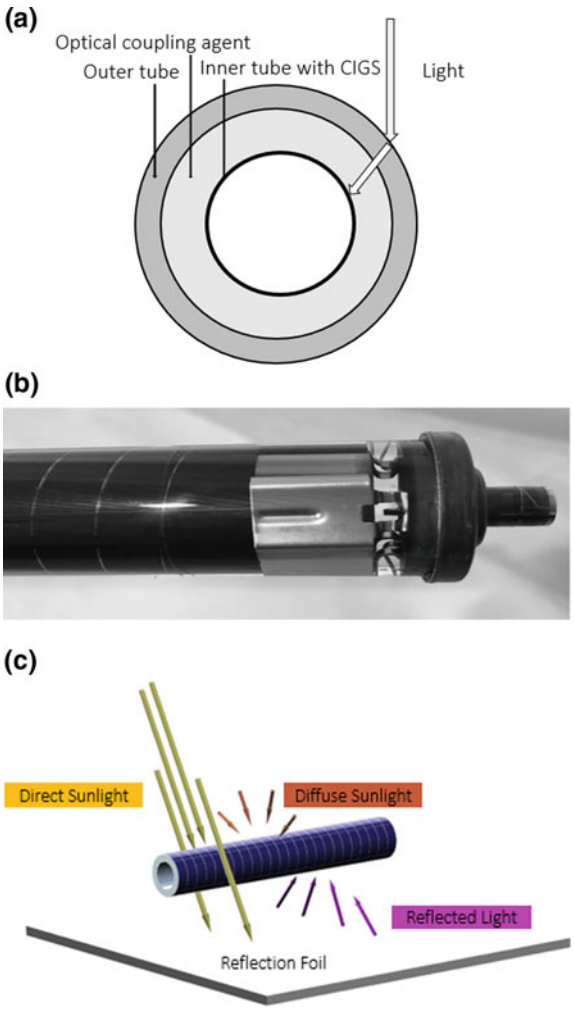

Fig. 11.8 **a** The way of light to the inner tube. **b** Solyndra power tube. **c** Solyndra power tube system

extremely dry conditions inside of the tubes are proven in the case incandescent lamps and in case of fluorescing lighting.

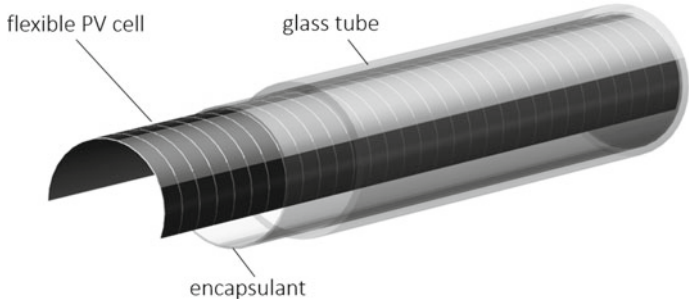

Fig. 11.9 General view of a typical Koch power tube

Fig. 11.10 The solid encapsulation helps to optically match the CIGS cells to the glass tubes, and also to hold the shards if some break

11.4 Tubular Modules

11.4.1 ATPV Versus Solyndra Modules

11.4.1.1 Similarities

The tubular power modules, no matter if Solyndra or ATPV, give a new meaning of rooftop and field PV installations and bring several unique characteristics:

– Each power cylinder is placed apart (at least one inch) and is connected at each end with wiring. The harnesses lie parallel to the cylinders. This design is intended to keep broken cylinders from affecting the performance of those that still work.
– Unlike many solar-power installations with flat PV modules, which have to be tilted to better capture sunlight, and tightly anchored, the tubular modules don't

need to be tilted and also don't need to be anchored on the roof with ballasts and adhesives.
- The cylindrical design and spacing between the power tubes make the tubular modules semitransparent: for light (Fig. 11.11a); for wind (Fig. 11.11b); for rain (Fig. 11.11c); and for snow (Fig. 11.11d).
  The major advantages for the solar conversion to electricity resulting from the semitransparency of the modules for solar radiation, wind, rain, and snow of the modules could be summarized as follows:
- The photons get scrambled and become better absorbed in thin films due to its oblique incidence.
- The wind comes through the modules and cools the tubes and the cells better than this in the case of the flat modules. The harnessing of the sun radiation improves. We measured a better cooling compared to the standard flat modules by 5 to 8 C. In addition to it, the CIGS TFPV has a substantially lower temperature coefficient of 0.3%/C, compared to the ca. 0.5%/C for the c-Si flat modules//, and generates more current than c-Si-based module at equal temperature.
- The rain washes the T8 tubes better, and the wind penetration helps too so that much better self-cleaning effects take place.
- The snow sticks much less to the tubes in winter. More electricity can be generated over the year by the tubular PV modules.

11.4.1.2 Major Advantages of ATPV Compared to Solyndra Modules

The major advantages of the ATPV compared to the Solyndra modules are the following:

- cell material saving: Only the tube side directed to the sun is covered with PV cells, which saves roughly 50% on cell material (Fig. 11.9).
- no back reflection foils needed: In contrast, Solyndra's bifacial power tubes, which are fit into aluminum-framed modules, have to be placed on a white mounting device a foot off the roof, and the clearing allows the CIGS tubes to capture sunlight reflected from the rooftop.
- the weight of the ATPV modules is roughly one-third of the weight of the Solyndra module because no inner tube and also no silicone oil optical agent is used, plus the outer tube is significantly thinner in the ATPV case.
- dual use of the encapsulation foil: The optical coupling agent used in the ATPV case is solid, enables but an optical coupling as valuable as the silicone oil in the case of Solyndra, plus it provides safety if a glass tube brakes. The shards are not spilled, they stick to the encapsulation foil.
- extremely dry conditions in the tubes were enabled, thanks to the vacuum sealing: The thin-film cells and their transparent conductive electrodes (usually made out of ZnO, which has low cost but is hygroscopic) remain protected against humidity during the entire life of the modules.

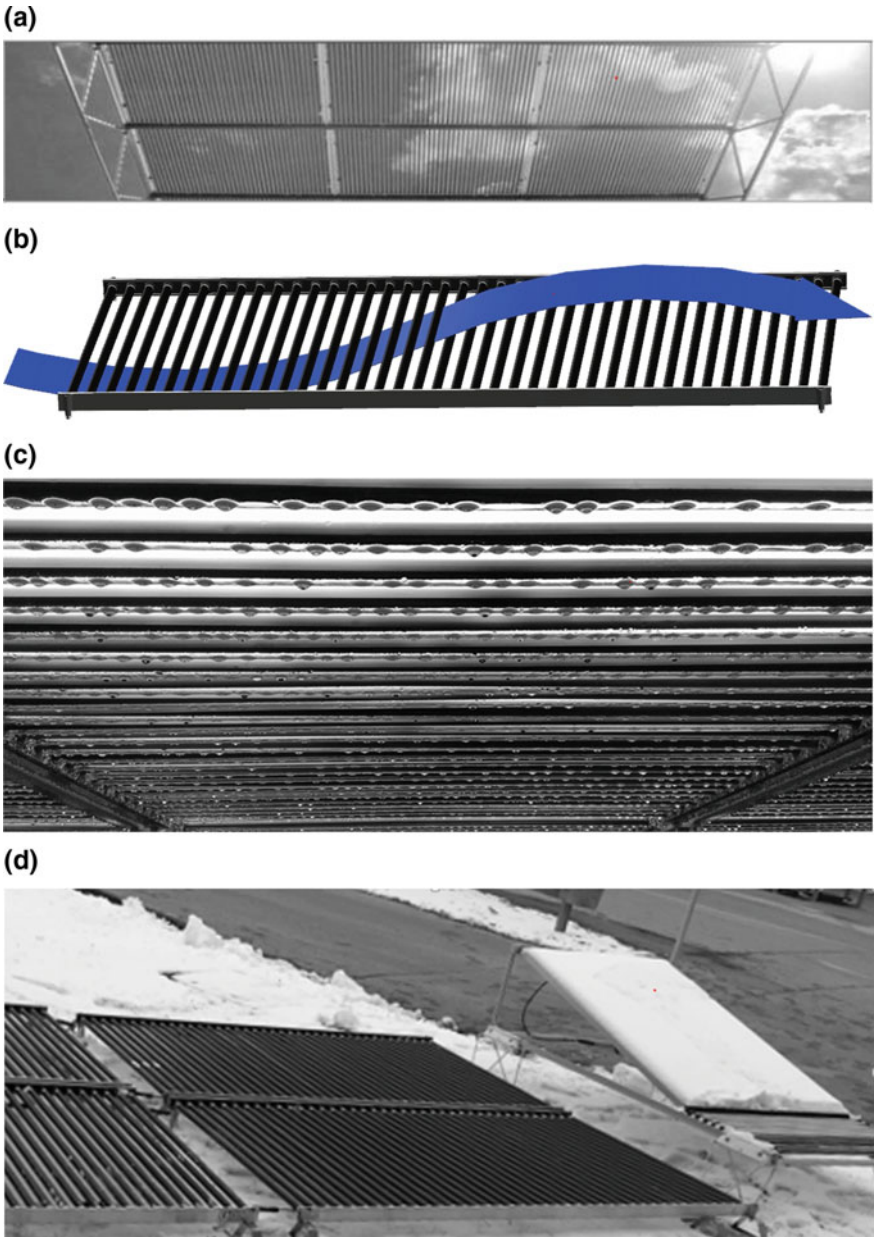

Fig. 11.11 **a**, **b**, **c**, **d** ATPV, semitransparent for solar radiation wind, rain, and snow

11.5 ATPV Rooftop Installation Versus Rooftop Installation with Flat PV Modules

Because of the spacing between the tubes, there is no lift when the wind blows through. "One can set the modules on the roof like a clothes horse". The mounting systems are very simple (Fig. 11.11) compared to the one used to install standard flat modules.

Because of the substantially lower wind resistance and the self-tracking effect, unlike many conventional solar-power installations, the tubular modules system doesn't need to be tilted and doesn't need to be anchored on the roof with ballasts and adhesives. The lightweight modules, particularly in the case of ATPV, are very suitable for flat roofs including light industrial and private house roofs.

Experienced system integrators say that tubular modules take one-third of the time to install.

Unlike many standard solar-power installations, which have to be tilted to better capture sunlight, the tubular system doesn't need to be anchored on the roof with ballasts and adhesives (Fig. 11.12).

The tubular modules perform optimally when mounted horizontally and packed closely together, covering significantly more of the typically available roof area and producing more electricity per rooftop on an annual basis than a conventional panel installation.

The transparency for wind is also a very big advantage, for example, when the tubular modules are used for rooftop-installations. PV Modules could be installed also on the rooftops of very tall buildings. In regions visited frequently by hurricanes, the wind semitransparency of the modules offers advantages too. The tubular modules can withstand winds up to 130 m/h, 200 km/h, on roofs and in solar farms as it was demonstrated first by Solyndra in Florida/US several years ago.

Green roofs could be combined with the ATPV. Particularly in big cities, where a lot more electricity and PV is needed, and the green area has to grow in order to clean the air, tubular modules can be combined with green roofing. A green roof combined with PV double-harvests the rain, for cleaning the tubular PV at one side,

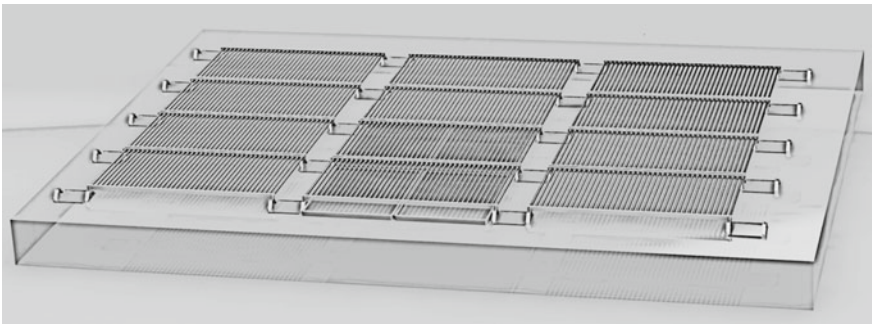

Fig. 11.12 Tubular modules as rooftop installation with service path; a combination with green roofing possible

and for irrigation of the plants on the other side. The plants need less water under the shadows of the tubular modules, and the modules will be better cooled, which is an obvious advantage and a win/win situation.

11.6 Agro-PV Under an ATPV Power Pergola

The semitransparency of the modules for light, wind, rain, and snow brings substantial advantages. A continuous power pergola (Fig. 11.13) can be with any size: small, medium, and big. The mounting systems could be much leaner than the one used today to build flat module free-field installations (Fig. 11.13).

The elevated ATPV modules allow plants, animals, and fish to grow, people to work, agro- machines having space to move. Agro-PV, sometimes also named in the literature as Sun-sharing, Double harvesting, etc. gets another appearance and meaning with tubular modules. The standard free-field PV installations need disruption in rows and strong anchoring of the module-blocks to withstand the wind. Normally, the blocks of flat modules are mounted very low above the ground, so that Agro-PV becomes impossible, their optical look is not very attractive and appealing, plus it does not allow simple maintenance of the solar farms The PV is frequently criticized in the last years for competing with the food chain, and in many countries, PV Farming gets banned because of it.

The ATPV power pergola enables more homogeneous growth of plants and harvest compared to an Agro-PV installation based on standard modules (Fig. 11.10) because the solar radiation gets scrambled by the glass tube surfaces before reaching the plants (only shadows with short periods interfere during a sunny day with the crop). Also, the rain can reach the plants under the pergola homogeneously, and the snow too.

An advantageous microclimate appears under the power pergola, which stimulates the growth of the protected crop. The shades reduce the need for irrigation, which is very attractive particularly for regions facing strong global climate change and desertification. In Bavaria, we observed that saving of water for irrigation was more than 20%. This issue is more attractive for regions with more sun like Germany, South Europe, CA, Africa, Middle East, etc. Compared with the systems build with standard flat modules, the advantages in the case of ATPV are obvious. ATPV modules could also be installed also in the standard way practiced at the moment. The pergola type of installation allows dual and even triple use of the land.

11.7 Other ATPV Applications

ATPV could improve the appearance of facades in combination with autonomous LED lighting.

ATPV could serve the street lighting sector.

Fig. 11.13 ATPV power Pergola build in 2014 in Weihenstephan, Freising

ATPV could power water desalination installations particularly on the sea coast, where the winds are strong.

Individual power tubes could serve many other niche-markets, which will not be discussed here.

11.8 Conclusions

The Augsburger Tubular PV(ATPV) presented here is a relatively photovoltaic technology. Its unique characteristics are as follows:

- the PV cells needed can be manufactured cost-effectively relying on R2R technology, laser processing, and monolithically interconnection of the thin-film cells. The efficiency of the flexible cells is competitive with the efficiency of many rigid cells and modules known from the flat PV business.
- Soda-lime glass tubes, known for their competitiveness from classical lighting industry, can find a new application and serve the PV industry on a large scale.
- the ATPV power tubes are very lean, lightweight, and easier to manufacture compared to the Solyndra power tubes, known already to the PV community.
- the tubular modules are lightweight and transparent for solar radiation, rain, wind, and snow. They allow to install easily in power pergola-manner for both: rooftops and Agro-PV free fields. The better combination of the tubular modules (power pergola) with plants, animals, fish, etc. is obvious, compared to installations based on flat PV modules.
- A lot more needs could be done for the manufacturing of high-efficient low-cost single and tandem flexible cells, needed for the manufacturing of Augsburger tubular PV modules.
- A lot more needs to be done to establish the ATPV and to contribute for market diversification. Innovative affordable applications in the field of PV are possible. We work to establish ATPV as a new product and as a part of this growing and booming PV market.

Acknowledgements We are thankful to all colleagues and partners supporting the ATPV efforts so far: Osram and more recently Ledvance in Augsburg, particularly the Equipment Engineering department and the GlassFab and also to our partners: Flisom in Switzerland; ZSW Stuttgart; the HM in Munich; and the HSWT in Weihenstephan/Freising, Germany.

Appendix

Worldwide, more than 16.330.000.000.000 kWh electricity is consumed by the seven billion inhabitants of our planet in 2016, with a rapidly increasing tendency for the feature.

The farming area around the world is estimated of the order.

To produce food, 4 060 000 km^2 of the US territory and 166500 km^2 of the German territory is used as farming land.

There are approximately 30 billion square feet (2.8 billion square meters) of flat roofs in the US., an area large enough to collect the sunlight needed to power 18 million American homes or replace 38 conventional coal-fired power plants.

The flat roofs in Germany have an area of one million square meters, this area is enough to supply electricity roughly to 5 Million German homes.

There is a hope that ATPV can be manufactured competitive and on the right scale in Bavaria in a very near future. There is no doubt that affordable PV will serve than at least a small share of this huge electricity and food demand on our planet.

References

1. E. Bellini, *PV-Magazine* (2017)
2. W. Hoffmann, *The Economic Competitiveness of Renewable Energy*, Scrivener Publishing, J. Wiley, New York (2014)
3. DOE invested 535 Million US-Dollar, Obama was proud oft the Solyndra unique PV. About $600 million in equity from investors since its inception in 2005 Investors: Virgin Green Fund, Madrone Capital Partners, RockPort Capital Partners, Argonaut Private Equity, Masdar, Redpoint Ventures, U.S. Venture Partners, Artis Capital Management and CMEA Ventures
4. Some Solyndra Patents 1. B Buller, ME Beck - US Patent 7235736, 2007 (Monolitical integration of cylindrical solar cells); 2. E. Milshtein, B. Buller - US Patent 7879685, 2011 (System and method for creating isolation between layers comprising solar cells); 3 B Buller, C Gronet, K Truman, T Brezoczky - US Patent 8,443,558, 2013 (Support system for solar energy generator panels)
5. Patent application US 7235736B1. Petrova-Koch, R. Mackh, J. Mayer (2014)
6. S. Arora, S. Chitkara, R. Udayakumar, M. Ali, J. Pet. Gas Eng. **2**(4), 74–82 (2011)
7. Lisec, Austria, Private Communications
8. Solar World-innovations, Private Communications
9. A. Tiwari et al., Review of progress toward 20% efficiency flexible CIGS Solar cells and manufacturing issues of solar modules, in *2012 IEEE 38th Photovoltaic Specialists Conference (PVSC)*, vol. 2 (2012)
10. F. Kessler, D. Hariskos, S. Spiering, E. Lotter, H.P. Huber, R. Wuerz, Chapter 9 of this in book
11. B. Buller, M. Back, Solyndra US Patent 7235736B1 (2007)
12. E. Milshtein, B. Buller, Solyndra US Patent 787968B2 (2011)
13. D. Forgacs, K. Wojciechowski, O.Malinkiewicz, Chapter 10 in this book
14. Tesla Solar Roof Tile Manufacturing: Business News (2018)
15. Hevel Solar: HJT c-Si bifacial cells and glass/glass Module manufacturing started in Russia (2017)
16. Longi c-Si PERC cells and halfcell module manufacturing started in 2017
17. Energetica in Austria announced Next Gn one Gigawatt Fab in Austria in August (2018)

Chapter 12
Fluorescent Solar Energy Concentrators: Principle and Present State of Development

Adolf Goetzberger

Abstract A review of the history and recent developments of fluorescent concentrators is given. The principle of this innovative device is based on light guiding in a transparent matrix doped with fluorescent centers, mainly organic dyes. The dyes strongly absorb a certain band of the solar spectrum and emit at a red-shifted frequency for which the concentrator is transparent. Since the light is emitted isotropically a large part is guided to the edges of the concentrator and arrives in concentrated form at the smaller side-edge. This concentrated light could be easily guided to an adapted solar cell. Work was done in the late seventies and early eighties, but then interest vanished because of several difficulties like unstable dyes and nonavailability of dyes in the infrared, which would be best adapted to silicon solar cells. Theoretically very high efficiencies can be reached if several plates with different colors are stacked and equipped with adapted solar cells. In recent years new interest has emerged in fluorescent concentrators. Two concepts are being most actively investigated now. The first is a band pass mirror on the front surface of the concentrator that reflects selectively the emitted light but transmits the light to be absorbed. In this manner also rays not within internal reflection are retained. It has been shown that only in this way the ultimate efficiency can be reached for a single plate concentrator. This efficiency is not much lower than for a directly illuminated ideal solar cell. A second new approach consists of replacing organic dyes with quantum dots. They offer the hope of greater stability, they can be tuned to different absorption wavelength by their size and by the spread of sizes their redshift can be tailored. A third approach is trying to put the dye centers in a surface coating, which opens the possibility to apply as a wafe guiding plates also more temperature resistive materials like glass.

A. Goetzberger (✉)
Fraunhofer Institute for Solar Energy Systems, Heidenhofstr. 2, 79110 Freiburg, Germany
e-mail: goetzberger@yahoo.de

V. Petrova-Koch et al. (eds.), *High-Efficient Low-Cost Photovoltaics*,
Springer Series in Optical Sciences 140,
https://doi.org/10.1007/978-3-030-22864-4_12

12.1 Principle

The use of transparent sheets doped with fluorescent dyes for the concentration of sunlight was suggested first in the 1970s [1, 2]. The principle itself is much older; it was first used in scintillation counters for atomic physics [3, 4]. Although significant advances were made in early work, after some years the further progress of work was limited by the materials available at that time—in particular the dyes—and interest was dormant for decades. Only recently new progress in materials, as well as theoretical advances, rekindled interest. In this article the historic work and the present state of the art will be reviewed.

Figure 12.1 shows the principle of the fluorescent concentrator, sometimes also called the luminescent collector: I represent an incident beam of light interacting with a dye molecule dissolved in a matrix of index of refraction n. The incident light will be absorbed and emitted at a different wavelength. (In the normal case of Stokes fluorescence the emitted wavelength will be shifted to a longer wavelength.) If the probability of emission is equal in all directions and part of the light will leave the transparent medium (F_1) while another part (F_2) will be reflected back because it intersects the surface at an angle leading to *total internal reflection*. It is important to note that this reflection is in principle *lossless.* Thus, the captured light is guided within the transparent sheet which will be also called the collector. Concentrated light can thus be obtained at the edge of the concentrator. The edges of the concentrator not contacted by solar cells have to be covered with mirrors. The fraction of light contained in the concentrator can be quite high. The fluorescent concentrator is the only concentrator known that can achieve high values of concentration without tracking. In contrast, concentrators based on geometric optics have to be tracked in order to achieve concentration of more than 2, and they can only use direct sunlight. This is a fundamental limitation following from nonimaging optics.

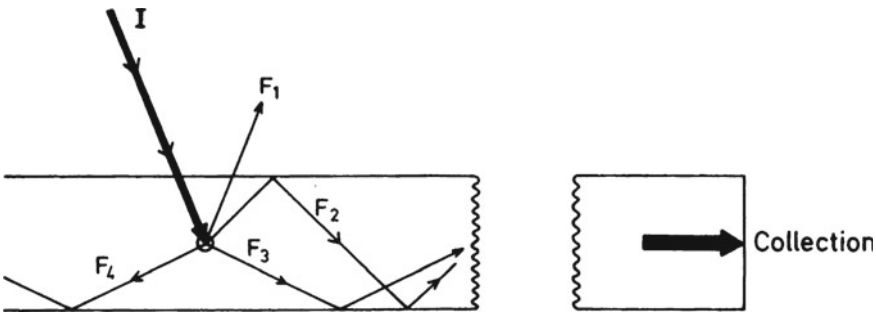

Fig. 12.1 Principle of fluorescent collection. Dye molecule D interacts with incoming light beam I. Secondary beams are partly lost (F_1) and partly guided in a transparent material (F_2–F_4)

In [5, 6] it has been shown that loss L due to light leaving the concentrator through the two boundary planes is given by:

$$L = 1 - (n^2 - 1)^{1/2}/n \tag{12.1}$$

where n is the index of refraction of the concentrator. For $n = 1.5$ for instance, $L = 0.2546$, for $n = 2$, L is 0.134 (it will be shown below that by the optimized design of concentrators these losses can be reduced significantly). The solid angle determined by the onset of total internal reflection is called the loss cone.

A basic requirement for efficient collection is that the incident wavelength has to have a short absorption length, the emitted wavelength a very long absorption length. This is accomplished by selecting a dye, whose absorption and emission wavelengths are well separated. Also, the fluorescence efficiency has to be high. The latter requirement is more easily met than the former. Quite a number of dyes are known to have a fluorescence efficiency of close to 100%. New dyes with better spectral properties and stability are being developed by the chemical industry. The emission and absorption characteristics are not only dependent on the nature of the molecule, but also on that of the solvent. The material of the collector has to be highly transparent and a good solvent for dyes. Plastics, glass, or organic solvents contained between plastic or glass sheets are possible candidates for this purpose. It is also possible to deposit the dye dissolved in a thin film on the surface of a completely transparent sheet.

Although prices for solar cells, including c-Si and other cells on wafers have come down considerably in recent years the cells are still the most expensive part of a flat plate solar generator. Conversion of concentrated solar light leads to a reduction of the cost of the PV systems if the concentrator applied has a significantly lower cost than the PV cells.

Fluorescent concentrators have the following advantages:

- Concentration of Sunlight without tracking
- Concentration of direct *and* diffuse light
- The concentrators are particularly well adapted to overcast conditions that occur frequently in temperate climates
- Possibility of spectrum splitting by use of several sheets doped with different dyes shown below

A single semiconductor can never convert sunlight with the highest possible efficiency because quanta with higher energy than the band gap lose their energy by thermalization and those with lower energy are not absorbed. Therefore, multijunction cells employing different semiconductors achieve the highest efficiency today. They consist of complex layers of III–V compounds but are very expensive and so they can only be used in concentrating systems.

12.2 Concentrator Stacks

Fluorescent concentrators offer the possibility to separate different portions of the solar spectrum just like multijunction cells and concentrate them at the same time [2]. Figure 12.2a shows a stack of three concentrators c_1–c_3 contacted by three different solar cells S_1–S_3. The ideal absorption and emission spectra of the fluorescent molecules in the collectors are sketched in Fig. 12.2b. Because every concentrator is fully transparent to the unabsorbed part of the spectrum a rather complete separation of the solar spectrum is possible in this manner. The solar cells S_1–S_3 have band gaps adjusted to the emission bands of the concentrators. A more detailed analysis carried out below demonstrates that the theoretical energy conversion efficiency is greater than 30% versus 24% for single-junction silicon cells (for AM 1.5).

For the calculation of quantum efficiency we put aside the energy loss due to Stokes shift and are only interested in quantum losses. It is assumed that the quantum efficiency of fluorescence is 100%. Reflection losses can be minimized with antireflection layers but even without antireflection coatings, the stack offers possibilities for minimizing reflection losses.

Much progress has occurred with antireflective coatings in the last 30 years. They have become more efficient and also more economical. Although such coatings have a lower index of refraction than the collector sheet they do not interfere with total internal reflection because only the difference between medium in which the light is emitted and air is of importance.

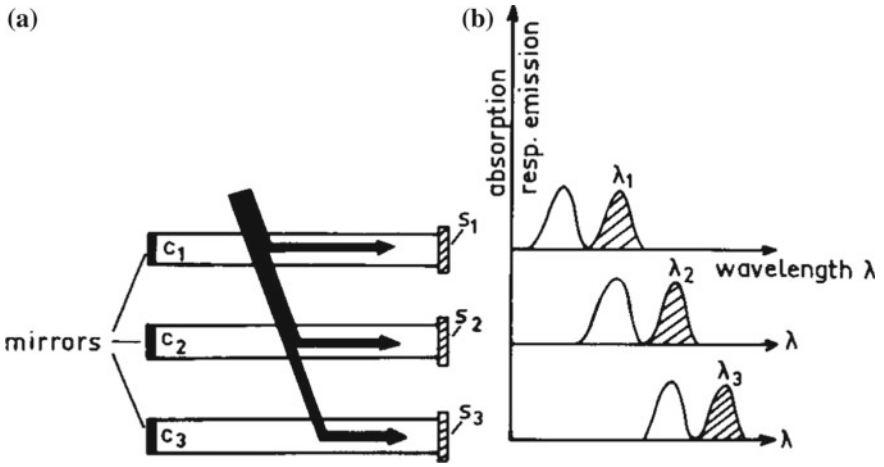

Fig. 12.2 **a** Fluorescent concentrator stack. Collectors c_1, c_2, c_3 are combined with solar cells S_1, S_2, S_3 of different bandgaps. **b** Absorption and emission (shaded) spectra of dyes in c_1–c_3, λ_1–λ_3 are peak emission wavelengths of c_1–c_3

For stacks, the following facts apply: The spectral range for these antireflective coatings becomes narrower and, therefore, easier to realize for the lower plates of the stack. It can be seen that c_1 has to be transparent for the entire solar spectrum, c_3 only has to operate in the long-wavelength range. An additional possibility is the use of photonic structures to decrease the loss cone angle as described below.

Now the quantum efficiency for a stack will is calculated. Again normal incidence is assumed. The procedure applied here is the following: The incident spectrum is divided into m parts such that each part contains an equal number of photons. This requirement is convenient for computation but not necessary for practical applications. An advantage of the stack is the fact that one-half of the escape cone losses of the preceding plate is recovered by the following one. This is seen from Fig. 12.2b. Collector c_1 emits at wavelength λ_1. If the absorption band of c_2 is arranged as shown in Fig. 12.2b, c_2 absorbs not only the solar radiation at the wavelength band λ_1 coming from above but also the radiation emitted by the dye in c_1 in the direction of c_2. The same is true for the lower parts of the stack. A recursion formula will now be derived for the quantum efficiency of a stack versus the number of collector plates in the stack. The symbols used in this calculation are given in Fig. 12.3.

The incident radiation S suffers reflection losses R at every interface traversed. Loss of fluorescent radiation not retained in the collectors is indicated by L. As was pointed out already, the loss cone losses directed towards c_2 are recoverable. A minor detail also indicated in Fig. 12.3 is the fact that reflection of this radiation in leaving c_1 does not have to be taken into account because exactly the same loss occurs at the top surface of the collector thus canceling the former loss (dashed lines in Fig. 12.3)

Let S_1 be the amount of radiation entering collector c_1 at the absorption band of this collector and C_1 be radiation collected there $S_2 \ldots S_m$ and $C_2 \ldots C_m$ are defined accordingly. Then $S_1(\lambda_1) = (1 - R)/m$

$$C_1 = S_1(1 - L)$$

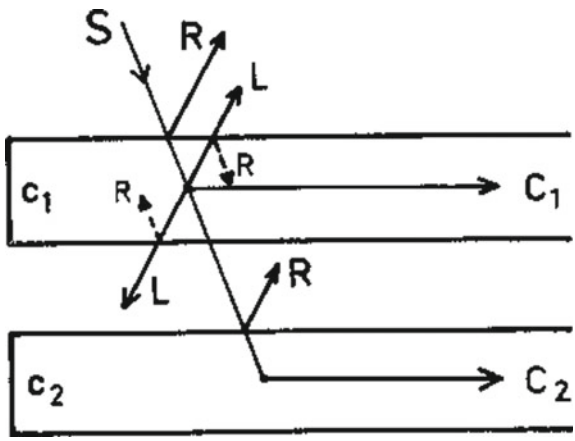

Fig. 12.3 Definition of quantities used in calculation of quantum efficiency. For details see text

Table 12.1 Quantum efficiency η_Q of collector stack

m	1	2	3	4
η_Q	0.7126	0.7299	0.7204	0.7030

The amount of radiation entering the second collector in the appropriate band is one mth of the incident spectrum attenuated by reflection (multiple reflections are neglected) and augmented by half of the loss from the preceding collector attenuated by reflection upon entering the second collector and so on:

$$\begin{aligned}
S_2(\lambda_2) &= (1-R)^3/m + (1-R)S_1L/2; \quad C_2 = S_2(1-L);\\
S_3(\lambda_3) &= (1-R)^5/m + (l-R)\,S_2L/2; \quad C_3 = S_3(1-L);\\
S_4(\lambda_4) &= (1-R)^7/m + (1-R)S_3L/2; \quad C_4 = S_4(1-L);\\
&\vdots\\
S_m(\lambda_m) &= (1-R)^{2m-1}/m + (l-R)S_{m-1}L/2; \quad C_m = S_m(1-L).
\end{aligned}$$

The quantum efficiency is the sum:

$$\eta_Q = \sum_{k=1}^{m} C_k \tag{12.2}$$

Equation (12.5) will now be evaluated for a realistic case: A common high transparency plastic-like Plexiglas with an index of refraction of 1.49 without antireflection coating and $L = 0.2587$ (Table 12.1).

Obviously, the stacking of collectors does not degrade quantum efficiency.

It should be pointed out that the order of dyes in the different sheets as shown in Fig. 12.2 can also be reversed—the longest wavelength on top and the highest at the bottom. This may be advantageous. In this case, a band pass mirror as described in the next section can be applied.

12.3 Light Guiding by Photonic Band Pass Mirrors

The loss of fluorescent light through the surfaces of the collector can be entirely avoided by covering the front surface with a wavelength selective mirror (hot mirror) [7, 8]. This mirror should have the following properties:

- A sharp cutoff edge at the onset wavelength of the dye's emission. All light below this wavelength should be transmitted, all above should be reflected.
- Near 100% reflection for light comes from all directions.

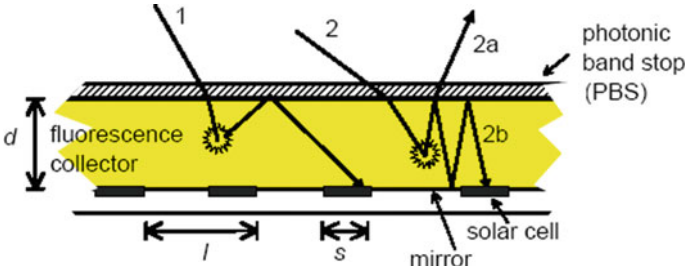

Fig. 12.4 Optimal design of fluorescent collector with band pass mirrors [9]. The coverage factor $f = s^2/l^2$

A band pass mirror with nonideal properties can be realized with commercial hot mirrors [8, 9]. Better results can be expected from photonic structures. First experiments with Rugate structures have shown promising results [10]. It features a continuously varying refractive index profile in contrast to the discrete structure of normal Bragg reflectors. This results in the suppression of side loops, which would cause unwanted reflection and loss of usable radiation. In [9, 11] it was shown that the ultimate efficiency limits of fluorescent concentrators can only be reached with selective mirrors. On the other hand, the light within the loss cone has a long path length before reaching the edges of the concentrator. In this case an arrangement as depicted in Fig. 12.4 is more advantageous.

12.4 Factors Determining Energy Efficiency of Fluorescent Concentrators

For the energy conversion efficiency, all energy losses in the collection process have to be taken into account. These are in detail:

- R: Surface reflection coefficient. This is either the Fresnel reflection coefficient or a lower value if an antireflection coating is applied
- η_{abs}: Absorption efficiency of the dye due to its absorption spectrum with respect to the solar spectrum
- η_{qua}: Quantum efficiency of dye
- η_{stok}: "Stokes efficiency"; $(1 - \eta_{\text{stok}})$ is the energy loss due to Stokes shift
- η_{trap}: Efficiency of light trapping by total internal reflection (Loss cone)
- η_{dye}: Efficiency of light conduction limited by self-absorption of dye
- η_{mat}: "Matrix efficiency"; $(1 - \eta_{\text{mat}})$ is the loss caused by light scattering or absorption in the matrix. η_{dye} and η_{mat} determine the mean free path of the emitted light in the collector
- η_{tref}: Efficiency of the light guiding by total internal reflection. This depends on the surface quality of the matrix

The overall optical efficiency can then be written as:

$$\eta_{\text{opt}} = (1 - R)\eta_{\text{abs}}\,\eta_{\text{qua}}\,\eta_{\text{stok}}\,\eta_{\text{trap}}\,\eta_{\text{dye}}\,\eta_{\text{mat}}\,\eta_{\text{tref}} \tag{12.3}$$

These loss factors will now be discussed.

The *surface reflection loss R* is usually the Fresnel reflection loss. It is given by $[(n-1)/(n+1)]^2$ where n is the refractive index. For most transparent materials it amounts to about 4% per surface. It can be minimized by employing an antireflection coating. If it has a smooth surface it will not interfere with total internal reflection.

The *absorption loss* η_{abs} is determined by the fraction of the solar spectrum absorbed by the dye. Practically all dyes absorb only part of the solar spectrum. It is possible to incorporate more than one dye into a collector, leading to a cascade of absorption and reemission. A disadvantage is that at every emission part of the radiation escapes through the loss cone. If the dyes are located very close to one another radiationless energy transfer can occur via the Förster mechanism. Therefore, doping of a thin surface region of the collector with a high concentration of dyes may have advantages.

The *quantum efficiencies* η_{qua} of the dyes can vary considerably. Only dyes with efficiency close to unity are usable. Fortunately, dyes with such efficiency and good stability are available but this refers only to the visible range.

The *stokes loss* η_{stok} is caused by the frequency shift between absorbed and emitted light. It is inherent in the fluorescence process. On one hand this shift should be small to minimize the energy loss, on the other it should be large enough to avoid overlap of absorption and emission loss (related to η_{dye}).

The light trapping efficiency η_{trap} is given by L (from (12.1)). It increases with an increasing refractive index of the collector material. In practice there are only little differences of available materials.

η_{dye} designates the efficiency limitation caused by *self absorption of the dye*. All known dyes have a certain overlap of absorption and emission spectrum as shown in Fig. 12.5. Also shown in this figure is how the spectrum is modified by multiple reabsorption and emission. The spectrum at the output is then redshifted. It has also been found that dyes cause a very small absorption within the emission region and beyond [12]. This absorption is difficult to determine but can have a great influence on the overall efficiency. A further effect causing unwanted absorption are photodegradation products caused by degradation of dyes [13]. These products can be annealed by heating in the dark.

η_{mat} is the *efficiency due to scattering or absorption in the matrix*. It depends strongly on the purity and preparation of the matrix.

Total internal reflection is theoretically lossless but in practice, it depends on the surface finish of the matrix. This loss η_{tref} can in principle be completely avoided by employing a reflecting band pass filter at the surface of the collector as pointed out above. Ideally this filter should also serve as an antireflection coating for the wavelength region absorbed by the dye to reduce R.

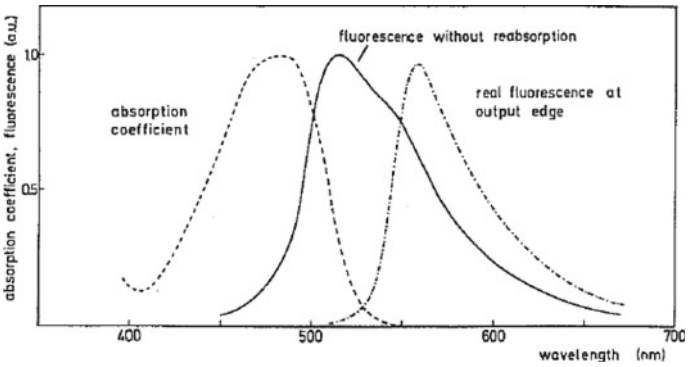

Fig. 12.5 Absorption and emission spectrum of typical dye. Output spectrum is modified by reabsorption

12.5 Theoretical Limits of Concentration and Efficiency

12.5.1 Limit of Concentration

Let us first consider a conventional concentrator based on geometric optics. In this case, the concentration is limited by the conservation of étendue or Liouville's theorem which relates the beam divergence at the input and output aperture. The most efficient concentrator is the CPC (Compound Parabolic Concentrator) that can approach the theoretical limits.

The concentration ratio C is given (for three dimensions) by:

$$C \leq \frac{n^2 \sin^2 \Theta_2}{\sin^2 \Theta_1} \tag{12.4}$$

where C is the concentration factor, $\theta_1 =$ input angle of light, $\theta_2 =$ output angle at receiver. If diffuse light is to be concentrated, $\theta_1 = 90°$ and, therefore, the maximum concentration is limited to n^2 which is about a factor of two for most available transparent materials.

On the other hand, geometrical concentration can be very effective at very small input angles. For solar radiation the limiting input angle is given by the viewing angle of the sun. Therefore, tracking concentrators for direct radiation permit very high concentration.

The maximum concentration of the fluorescent concentrator has been determined by Yablonovitch [14] and Smestad et al. [7]. They point out that because of the energy loss due to the Stokes effect the system operates as an optical heat pump. The radiance at a given energy is increased by changing some of the incoming energy to heat.

For fluorescent concentrators, the concentration factor is determined by:

$$C \leq \frac{(\nu_2)^2}{(\nu_1)^2} \exp\left(\frac{h(\nu_1 - \nu_2)}{KT}\right) \tag{12.5}$$

where ν_1, = frequency of absorbed light, ν_2 = frequency of emitted light. The concentration factor depends only on the magnitude of the Stokes shift. So concentration occurs at the sacrifice of energy efficiency.

12.5.2 Limit of Efficiency

The limits of efficiency were examined by Rau et al. [9], Glaeser and Rau [10], and Markvart et al. [15, 16]. They showed that the detailed balance principle introduced into solar cell physics by Shockley and Queisser [17] can also be used for the fluorescent concentrator solar cell system. They investigated a single-stage concentrator and found that very high efficiency is possible provided the concentrator surface is covered by a perfect band pass mirror. In [9, 10] Monte-Carlo simulations were employed to obtain relations between efficiency, band gap energy, and coverage fraction. In Fig. 12.6 the results of these calculations are presented.

The simulated efficiencies for a fluorescent concentrator ($f = 1$) *with PBS* (open squares) follow the radiative Shockley–Queisser efficiency limit η_{rad} (solid line) when calculated with reference to the photonic threshold energy E_{th}. The efficiencies *without PBS* (open circles) are at about $0.88 \times \eta_{\text{rad}}$ (dashed line) calculated with reference to the band gap energy $E_{\text{g}} = E_{\text{th}} - 0.2$ eV of the underlying solar cell. (b) Efficiencies for a band gap energy $E_{\text{g}} = 1.12$ eV and threshold energy $E_{\text{th}} =$

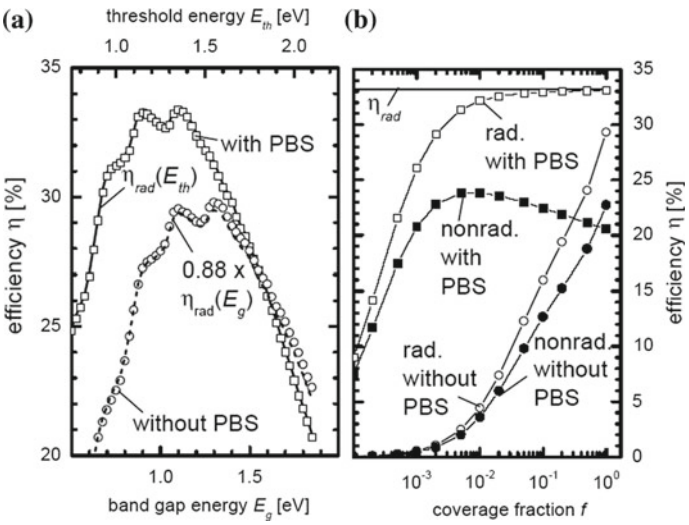

Fig. 12.6 **a** Monte-Carlo simulations [9, 10]. For explanations see text

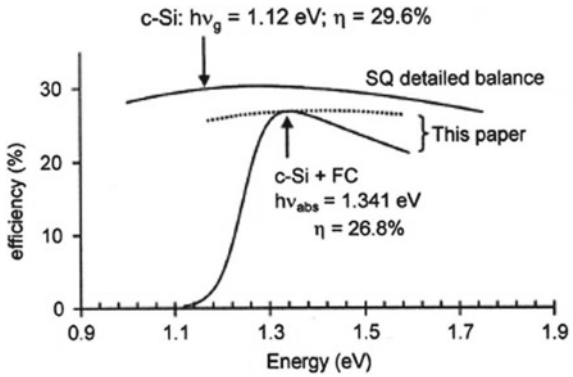

Fig. 12.7 Conversion efficiency of an ideal Si cell with and without a fluorescent concentrator

1.32 eV for ideal (rad.) and nonideal (nonrad.) solar cells. *Without* photonic band stop (PBS) the efficiencies degrade monotonically with decreasing coverage fraction f (full and open circles, for the radiative and the non-radiative case). *With* PBS the systems efficiency drops much slower for an ideal solar cell (open squares) and even achieves an optimum at $f \approx 10^{-2}$ in the non-radiative case (full squares). Comparable results were obtained by Markvart [15, 16] as shown in Fig. 12.7. It is seen that ideal efficiency is 26.8% versus 29.6% without concentrator.

12.6 Improvements in Basic Design

12.6.1 Optical Concentrators at the Collector Output

This is an old proposal [18]: At the edge of a collector plate a concentrating element (taper or more effective a CPC) is attached before the solar cell (Fig. 12.8). The additional concentration possible in this manner which is given by (12.4). Rests on two facts: The divergence angle of incoming rays is limited by the onset angle of total internal reflection and can then further be converted to 90°. The collector material

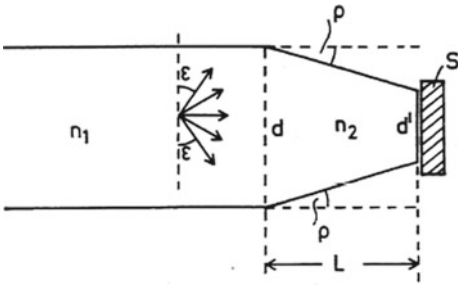

Fig. 12.8 Fluorescent collector with two stage concentration by attached taper with refractive index $n_2 > n_1$

can be made of a material of a higher index of refraction than the collector material. A concentration factor between 1.5 and 2 is thus possible.

12.6.2 *Combination of Fluorescent Collector with Large Area Si-Solar Cell*

Because at present no dyes emitting in the IR with acceptable properties are available a good compromise is the following concept [10] (Fig. 12.9).

A fluorescent concentrator doped with a dye emitting in the red or orange is equipped with a GaInP cell that has its maximum response in this range. The collector is transparent to all radiation not absorbed by the dye. The transmitted radiation is converted by a large area silicon cell at the bottom. Figure 12.10 shows the efficiencies of the silicon cell alone and the combined system. The silicon cell **without the**

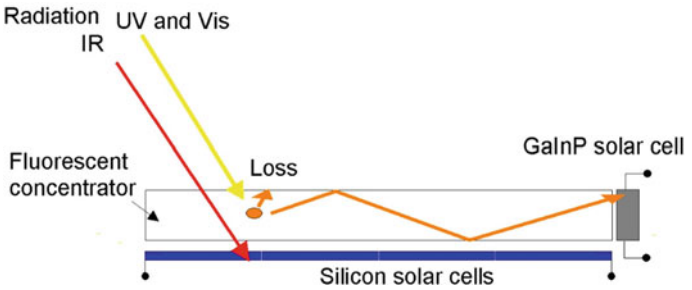

Fig. 12.9 Combination of a short wavelength fluorescent concentrator with attached GaInP cell and Si bottom cell

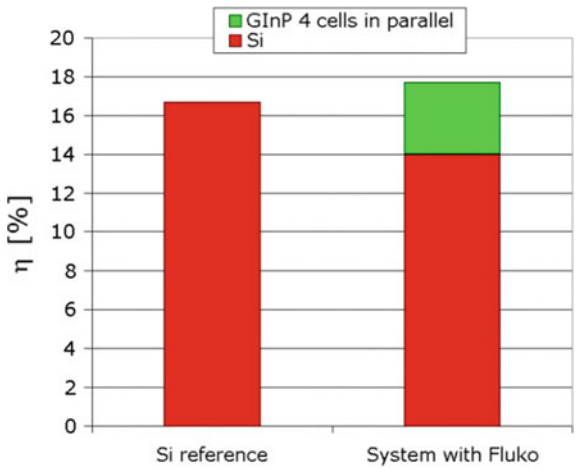

Fig. 12.10 Efficiency of silicon cell alone and of total system

concentrator had an efficiency of 16.7%. Under the fluorescent concentrator, the efficiency dropped to 14.0%. The total system efficiency was 17.7%, which is significantly higher than the silicon solar cell alone.

12.6.3 Combination of Fluorescent Concentrator with Up-conversion

Recently great progress has been achieved with up-converters—compounds that combine two or more quanta to a higher energy quantum [19].

This effect can also be useful for fluorescent concentrators as indicated in Fig. 12.11.

Below the fluorescent collector, an up-converter and a mirror is arranged. The spectral properties of the fluorescent collector and the up-converter are shown below. The dye in the collector shifts the absorbed wavelength range to longer wavelength above the band energy of the solar cell. The photons emitted downwards are converted by the up-converter to shorter wavelength to be reabsorbed by the collector. Furthermore, the collector is transparent to the solar spectrum within the emission range of the dye in the collector. These photons will also be converted to higher wavelengths.

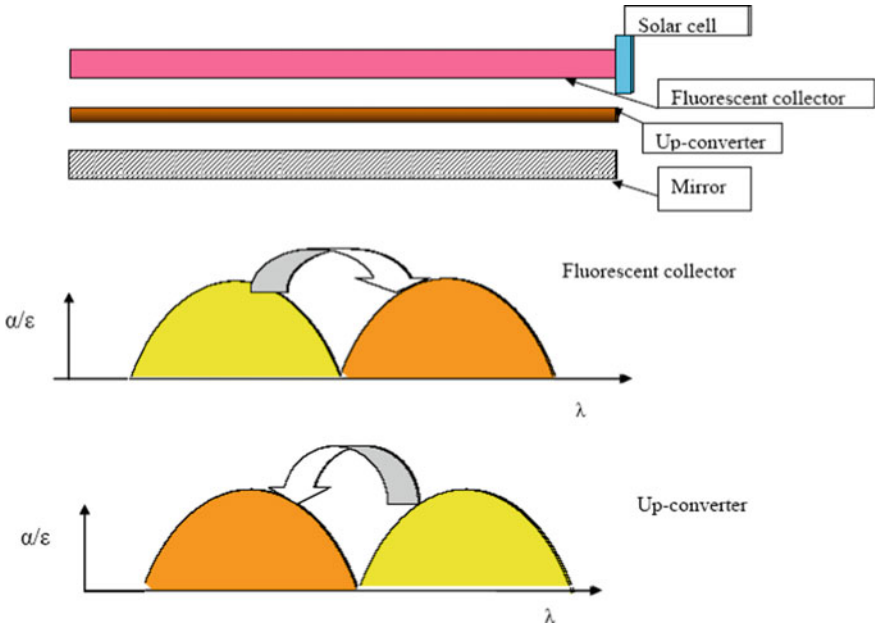

Fig. 12.11 Fluorescent collector combined with up-converter. For an explanation of function see text

12.6.4 Combination of Collector Stack with Band Pass Mirror

The collector stack can also be combined with a band pass mirror as described in Sect. 12.3. For this purpose the following conditions apply:

- Longest wavelength dye on top
- Solar cells placed below each other
- Transparent electrical connections

In Fig. 12.12a the stacking of the collectors is sketched, in Fig. 12.12b we see the wavelength diagram. Consider the top plate: The dye absorbs in the shorter wavelength and emits at longer once. The upper mirror reflects the emitted radiation but is transparent for all other wavelengths, downward emitted radiation is reflected by the lower mirror which extends into this wavelength region as indicated by the short arrows. The lower plates operate in the same manner.

The collector stack with band pass mirrors offers intriguing prospects: It is the only device that can concentrate diffuse radiation and could also approach highest conversion efficiency! While the original fluorescent concentrator shown in Fig. 12.2 has a theoretical efficiency of about 30%, the new design can go much higher. From Fig. 12.7 we derive that a one plate concentrator with a silicon cell has a theoretical efficiency of 90% of the thermodynamic efficiency. A collector stack is a spectrum splitting device and can now achieve an efficiency close to that of a multijunction cell. If we assume the theoretical efficiency to be 60%, the multi-stage fluorescent concentrator has a theoretical efficiency of 54%.

Obviously, many difficulties have to be overcome to reach this goal, such as: Near ideal band pass mirrors are needed, the dyes should have a well-defined absorption bands without absorption in the shorter wavelengths and appropriate wide gap solar cells have to be available. In addition the cost should be competitive.

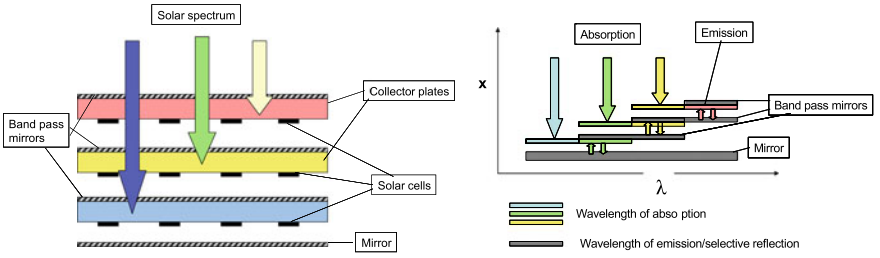

Fig. 12.12 Fluorescent collector stack with band pass reflectors. **a** The geometrical arrangement, **b** wavelength representation

12.7 Experimental Results

12.7.1 Results of the Initial Period

Experimental work can be divided into two periods: The initial period from 1977 to about 1985 and the more recent period which started about 2000. The older results are still meaningful because they represent benchmarks to be reached and exceeded in present work. The most interesting parameters are the overall electrical efficiency and the long term stability of the concentrators These are in turn influenced by the properties of matrix and dye. In comparing efficiencies the dimensions of the samples are very important. Results of the early period are summarized in review papers by Wittwer et al. [20] and Zastrow [21] (Table 12.2).

The efficiency of 4% is still the highest value that has been realized for such a large area. The second most important issue is the stability of the collector dye-system under illumination. It could be observed that by continued development the stability of the dyes improved during the course of the work. A representative measurement is shown in Fig. 12.13. The cumulative illumination corresponds to more than two years of outdoor exposure. Also clearly seen is the recovery of fluorescence during periods of darkness.

A problem that continues to limit efficiency is the lack of useful long-wavelength dyes. They still have low quantum efficiency and are not very stable. Figure 12.14

Table 12.2 Electrical efficiencies for 40 × 40 cm^2 collectors with Si and GaAs cells. The highest efficiency of 4.0% was obtained with a double stack and GaAs cells

Dimension (cm^3)	Absorption range (nm)	Efficiency (%)	
		Si	GaAs
40 × 40 × 0.3	360–550	2.1	2.5
40 × 40 × 0.3	490–610	1.4	2.5
Stack of both	360–610	3.0	4.0

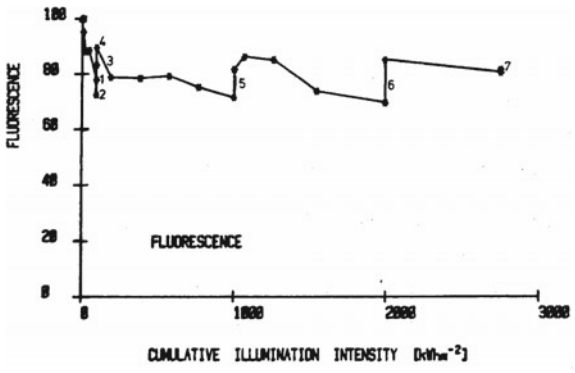

Fig. 12.13 Fluorescence during long term light exposure in kWh/m^2. Fluorescence is normalized to the maximum value

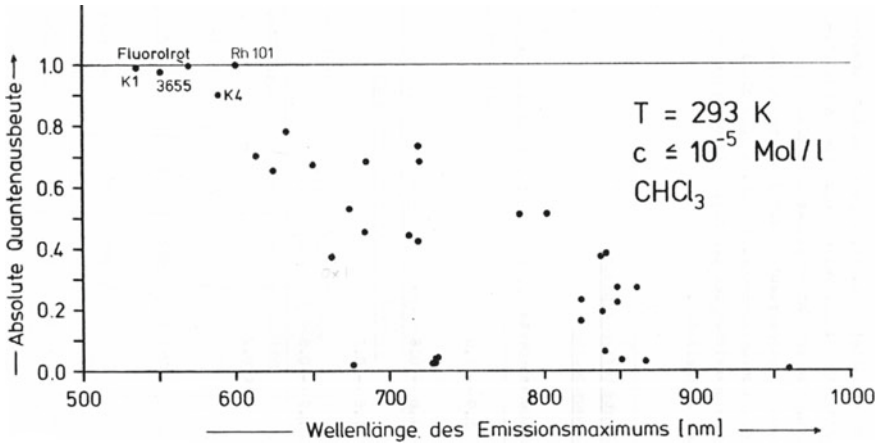

Fig. 12.14 Quantum efficiencies of different dyes versus peak emission wavelength

gives a compilation of quantum efficiencies found until 1984. It is evident that there is a general tendency is towards lower efficiency when emission wavelength increases.

12.7.2 Recent Experimental and Theoretical Work

Danos et al. [22] characterized fluorescent concentrators based on solid, liquid, and Langmuir Blodget films. Chatten et al. [23] have developed a self-consistent 3D thermodynamic model for planar concentrators, modules, and stacks. The results for test concentrators containing both quantum dots and organic dyes as the luminescent species show excellent agreement with experiment.

Organic dyes are still the best choice for fluorescent concentrators as shown in [24]. In this paper by Richards and McIntosh collectors doped with multiple dyes were investigated by ray tracing using experimental data from newly available dyes. In such a collector multiple are absorbed and reemitted by increasingly longer wavelength dyes. In this manner a large part of the solar spectrum is absorbed and emission occurs at a wavelength which is more suitable for silicon cells. They found that a mixture of five dyes including a near IR dye of 85% quantum efficiency gave the best result of 44% electrical efficiency. Only radiative transfer and high-efficiency solar cells were studied. They also state that all dyes show photostability under sunlight for at least 10 years. Lower stability was found by Reda with more conventional dyes [25].

A new possibility to obtain better performing luminescing centers consists of quantum dots as has been pointed out by Barnham et al. [26]. These are nanometer-sized semiconductor crystallites. Because they are inorganic there is a hope that they

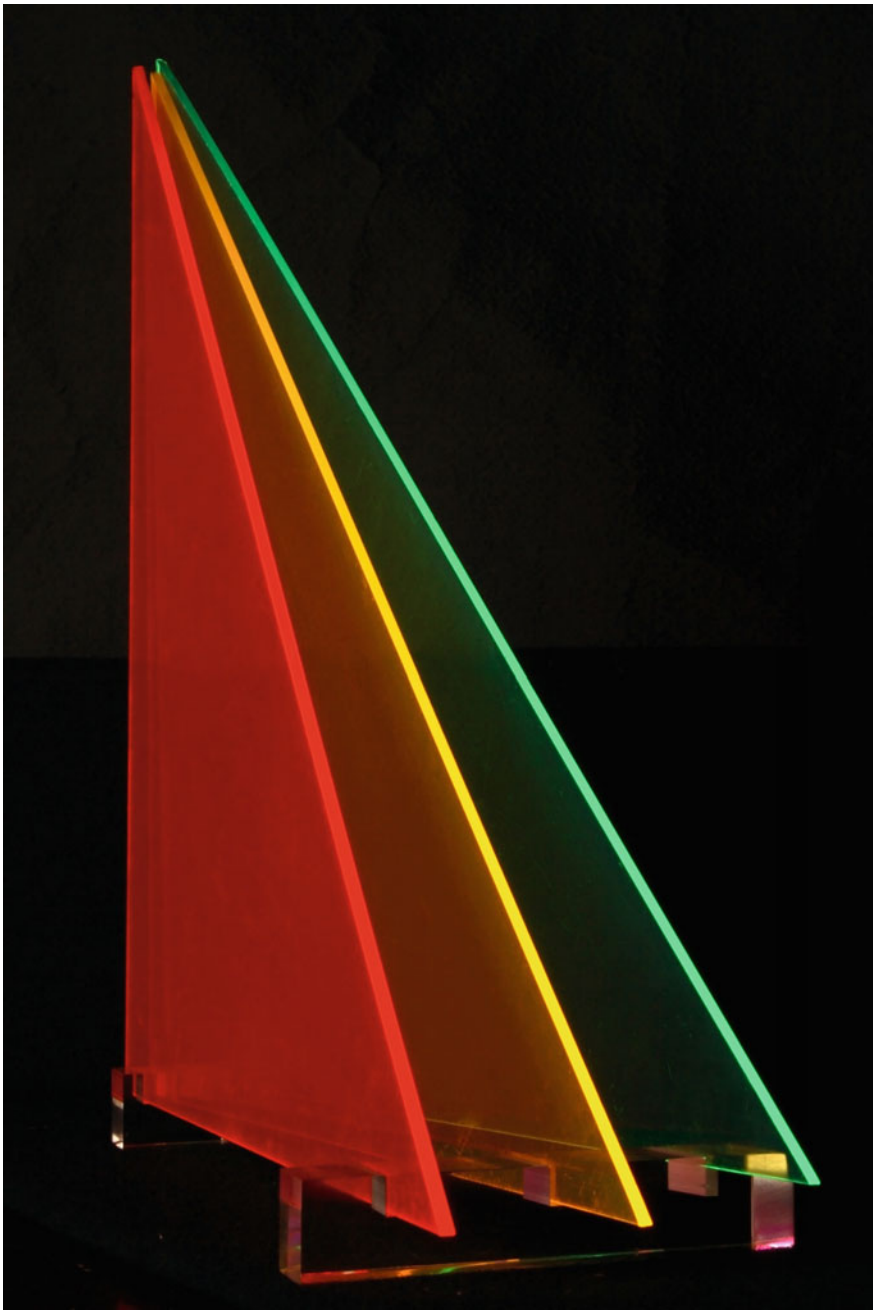

Fig. 12.15 Three PMMA plates doped with different color dyes. These plates are about 25 years old but not degraded, they were however mostly stored in the dark. Although the light output looks very spectacular only part of the light arriving at the edges is emitted because a big part is reflected back by total internal reflection

exhibit greater light stability than organic dyes. Another advantage is that the absorption threshold can be tuned by choice of the dot diameter. Furthermore, Williams et al. showed by a thermodynamic model that the red shift of emission is related to the spread of quantum dot sizes.

In view of these advantages, there is considerable interest in developing fluorescent concentrators doped with quantum dots. Numerous investigations were carried out in recent years. Mainly quantum dots based on CdS were used. Schüler [27] applied the dots by the solgel technique to glass surfaces but also core-shell quantum dots consisting of CdSe cores with CdS or ZnS shell were studied [28, 29]. So far the quantum dots show continued improvement but quantum efficiency is not yet as high as for the best organic dyes. Also some instability has been observed.

Further, it should be remarked that fluorescent concentrators have applications beyond photovoltaics. They have been in use for advertising for many years. They can also be used in green houses to convert the green light to red light which can be better absorbed by plants [20]. Application for daylighting has been studied in the early days [30] and recent work with newer dyes appears very promising [12].

Finally, I present a photograph of three collector plates as they appear in daylight (Fig. 12.15).

References

1. W.H. Weber, J. Lambe, Appl. Opt. **15**, 2299 (1976)
2. A. Goetzberger, W. Greubel, Solar energy conversion with fluorescent collectors. Appl. Phys. **12**, 123 (1977)
3. W.A. Shurcliff, R.C. Jones, J. Opt. Soc. Am. **39**, 912 (1949)
4. J.B. Birks, *The Theory and Practice of Scintillation Counting* (Pergarnon Press, London, 1964)
5. G. Keil, J. Appl. Phys. **40**, 3544 (1969)
6. G. Keil, Nucl. Instrum. Methods **87**, 111–123 (1970)
7. G. Smestad, H. Riess, R. Winston, E. Yablonovitch, Solar Energy Mater. **21**, 99 (1990)
8. B.S. Richards, A. Shilav, R. Corkish, in *19. EU PV Solar Energy Conference* (2004), p. 113
9. U. Rau, F. Einsele, G.C. Glaeser, Appl. Phys. Lett. **87**, 171101 (2005)
10. J.C. Goldschmidt, S.W. Glunz, A. Gombert, G. Willeke, in *21. EU PV Solar Energy Conference* (2006), p. 107
11. G.C. Glaeser, U. Rau, Proc. SPIE **6197**, 143 (2006)
12. A.A. Earp, G.B. Smith, P.D. Swift, J. Franklin, Sol. Energy **76**, 655 (2004)
13. A. Zastrow, H.R. Wilson, K. Heidler, V. Wittwer, A. Goetzberger, in *6th EU PV Conference* (1983), p. 202
14. E. Yablonovitch, J. Opt. Soc. Am. **70**, 1362 (1980)
15. T. Markvart, J. Appl. Phys. **99**, 026101 (2006)
16. T. Markvart, L. Danos, P. Kittidachachan, R. Greef, in *20. EU PV Solar Energy Conference* (2005), p. 171
17. W. Shockley, H.J. Queisser, J. Appl. Phys. **32**, 510 (1961)
18. A. Goetzberger, O. Schirmer, Appl. Phys. **19**, 53 (1979)
19. S. Balushev, T. Miteva, V. Yakutin, G. Nelles, A. Yasuda, G. Wegner, Appl. Phys. Lett. **14**, 143903 (2006)
20. V. Wittwer, W. Stahl, A. Goetzberger, Solar Energy Mater. **11**, 187 (1984)
21. A. Zastrow, SPIE **2255**, 534 (1993)

22. L. Danos, P. Kittidachachan, P.J.J. Meyer, R. Greef, T. Markvart, in *21. EU PV Solar Energy Conference* (2006), p. 443
23. A.J. Chatten, D.J. Farrell, B.F. Buxton, A. Büchtemann, K.W.J. Barnham, in *21. EU PV Solar Energy Conference* (2006), p. 315
24. B.S. Richards, K.R. McIntosh, in *21. EU PV Solar Energy Conference* (2006), p. 185
25. S.M. Reda, Sol. Energy **81**, 755 (2007)
26. K. Barnham, J.L. Marques, J. Hassard, P. O'Brien, Appl. Phys. Lett. **76**, 1197 (2000)
27. A. Schüler, Solar Energy (2007)
28. S.J. Gallagher, B. Norton, P.C. Eames, Sol. Energy **81**, 813 (2007)
29. S.J. Gallagher, B.C. Rowan, J. Doran, B. Norton, Sol. Energy **81**, 540 (2007)
30. A. Zastrow, V. Wittwer, Proc. SPIE **653**, 93 (1986)

Correction to: Perovskite Photovoltaics: From Laboratory to Industry

D. Forgacs, K. Wojciechowski and O. Malinkiewicz

Correction to:
Chapter 10 in: V. Petrova-Koch et al. (eds.), *High-Efficient Low-Cost Photovoltaics*, Springer Series in Optical Sciences 140, https://doi.org/10.1007/978-3-030-22864-4_10

The original version of the book was inadvertently published with typos in the abstract of Chapter 10, which have now been corrected. The book and chapter have been updated with the changes.

The updated version of this chapter can be found at
https://doi.org/10.1007/978-3-030-22864-4_10

V. Petrova-Koch et al. (eds.), *High-Efficient Low-Cost Photovoltaics*,
Springer Series in Optical Sciences 140,
https://doi.org/10.1007/978-3-030-22864-4_13

Index

V. Petrova-Koch et al. (eds.), *High-Efficient Low-Cost Photovoltaics*,
Springer Series in Optical Sciences 140,
https://doi.org/10.1007/978-3-030-22864-4